Advances in Electrochemical Science and Engineering

Volume 5

WILEY-VCH

Advances in Electrochemical Science and Engineering

Advisory Board

Prof. R. C. Alkire, University of Illinois, Urbana, Illinois, USA
Prof. E. J. Cairns, University of California, Berkeley, California, USA
Prof. M. Fleischmann, The University, Southampton, United Kingdom
Prof. M. Froment, Université Marie et Pierre Curie, Paris, France
Prof. K. Honda, Kyoto University, Kyoto, Japan
Prof. Yu. V. Pleskov, A. N. Frumkin Institute of Electrochemistry, Academy of Sciences, Moscow, Russia
Prof. S. Trasatti, Università di Milano, Milano, Italy
Prof. E. B. Yeager, Case Western Reserve University, Cleveland, Ohio, USA

Advances in Electrochemical Science and Engineering

Volume 5

Edited by Richard C. Alkire,
Heinz Gerischer,
Dieter M. Kolb
and Charles W. Tobias

Contributions from

A. Kapturkiewicz, Warsaw
O. A. Petrii, G. A. Tsirlina, Moscow
D. D. MacDonald, L. B. Kriksunov, University Park
S. Gottesfeld, Los Alamos
F. Beck, Duisburg

WILEY-VCH

Weinheim · New York · Chichester · Brisbane · Singapore · Toronto

Editors:
Prof. Richard C. Alkire
University of Illinois
Vice Chancellor for Research
601 East John Street
Champaign, IL 61820-5711
USA

Prof. Dieter M. Kolb
University of Ulm
Department of Electrochemistry
Albert-Einstein-Allee 11
D-89081 Ulm
Germany

This book was carefully produced. Nevertheless, authors, editors and publishers do not warrant the information contained therein to be free of errors. Readers are advised to keep in mind that statements, data illustrations, procedural details or other items may inadvertently be inaccurate.

© WILEY-VCH Verlag GmbH, D-69469 Weinheim (Germany), 1997

e-mail (for orders and customer service enquiries): sales-books@wiley-vch.de

Visit our Home Page on http://www.wiley-vch.de

All rights reserved. No part of this publication may be reproduced, stored in a retrieval system, or transmitted, in any form or by any means, electronic, mechanical, photocopying, recording, scanning or otherwise, except under the terms of the Copyright Designs and Patents Act 1988 or under the terms of a licence issued by the Copyright Licensing Agency, 90 Tottenham Court Road, London, UK W1P 9HE, without the permission in writing of the Publisher.

Other Editorial Offices

John Wiley & Sons, Inc., 605 Third Avenue,
New York, NY 10158-0012, USA

John Wiley & Sons Ltd
Baffins Lane, Chichester
West Sussex PO19 1UD, England

Jacaranda Wiley Ltd, 33 Park Road, Milton,
Queensland 4064, Australia

John Wiley & Sons (Asia) Pte Ltd, 2 Clementi Loop #02-01,
Jin Xing Distripark, Singapore 129809

John Wiley & Sons (Canada) Ltd, 22 Worcester Road,
Rexdale, Ontario M9W 1L1, Canada

A catalogue record for this book is available from the British Library

Deutsche Bibliothek Cataloguing-in-Publication Data
Advances in electrochemical science and engineering:
Weinheim; New York; Chichester; Brisbane; Singapore; Toronto : WILEY-VCH
ISSN 0938-5193
Erscheint unregelmässig. - Aufnahme nach Vol. 1 (1990)
Vol. 1. (1990) -
ISBN 3-527-29385-X

Typeset by Thomson Press (India) Ltd., New Delhi
Printed and bound in Great Britain by Bookcraft (Bath) Ltd
This book is printed on acid-free paper responsibly manufactured from sustainable forestation, for which at least two trees are planted for each one used for paper production.

Introduction

This publication represents the final volume in the editorial collaboration of Heinz Gerischer and Charles W. Tobias which began in 1976. Their efforts led in 1987 to the initiation of the present series entitled *Advances in Electrochemical Science and Engineering* with the publisher VCH Verlagsgesellschaft who committed to producing typeset volumes at regular intervals. The favorable reception of the first four volumes and an increased interest in electrochemical science and technology provide good reasons for the continuation of this series with the same high standards and purpose.

Richard C. Alkire
Heinz Gerischer
Dieter M. Kolb
Charles W. Tobias

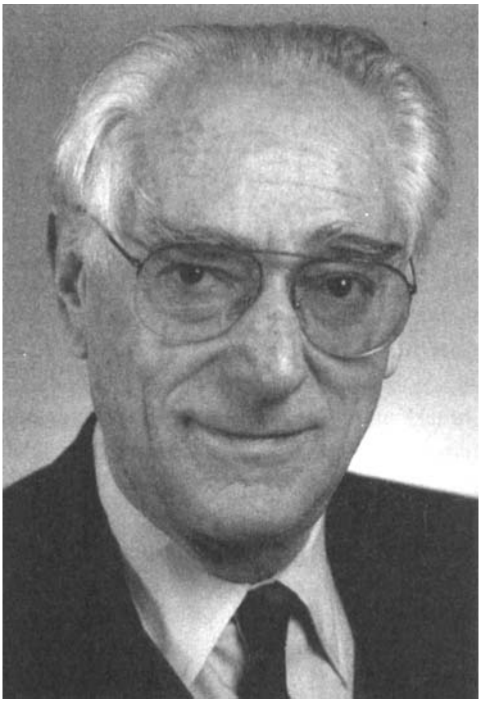

Photograph by Marianne Kischke, Fritz-Haber Institut der Max-Planck Gesellschaft

Heinz Gerischer

(1919–1994)

On September 14, 1994, Heinz Gerischer died of heart failure in Berlin. His name is intimately connected with the pioneering work in electrode kinetics, semiconductor- and photo-electrochemistry and electrochemical surface science. His scientific career started as a young assistant of K. F. Bonhoeffer in Berlin immediately after the war, and continued in Göttingen and Stuttgart. Then came Munich, where he accepted a professorship at the Technical University in 1962, and Berlin where in 1969 he became director of the Fritz-Haber-Institut der Max-Planck-Gesellschaft. He was a key person for the development of new methods in electrochemistry. Although a chemist by training, he recognized very early the important role of surface physics in gaining a fundamental understanding of electrode processes. Consequently, he was among the first to transform traditional electrochemistry into a branch of modern surface science. Heinz Gerischer was a man with a deep understanding of physical chemistry; his works have become landmarks for our future work.

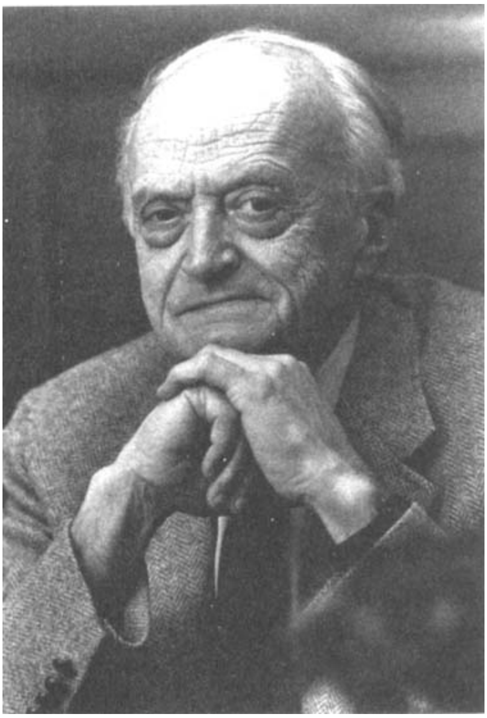

Charles Tobias

(1920–1996)

It is with deep sadness that we report the passing of Charles W. Tobias on March 6, 1996. Professor Tobias initiated the discipline of electrochemical engineering in the United States, and played a central role in its development for nearly fifty years. In so doing, he played a pivotal role in the development of one of the world's leading chemical engineering departments at the University of California at Berkeley. He founded the precursor to the present monograph series in 1961 with Paul Delahay, and in 1976 continued that co-editorship with Prof. Heinz Gerischer with whom he introduced in 1990 the present series, "*Advances in Electrochemical Science and Engineering*". Charles Tobias was a man of wisdom who had a profound influence on the lives of many individuals, and who contributed enormously to the advancement of electrochemical science and engineering.

Preface

During the recent past, electrochemical science and engineering has seen profound changes. The consequences of changing energy, feedstock, materials, and waste treatment demands have spurred the traditional electrolytic industries, and have sparked new inventions. These trends have been accompanied by a development in the understanding of the fundamental principles, as well as rapid advancement in many areas of electrochemical science and engineering. The chapters in the present volume treat topics of fundamental and applied interest associated with electrochemiluminescence phenomena, novel superconducting materials, the prevention of electrochemical corrosion through understanding of fundamentals of transport and reaction phenomena, the advancement of polymer fuel cell technology, and the development of metal-free batteries.

Andrzej Kapturkiewicz gives a thorough account on the theory of electron transfer reactions that lead to electrochemiluminescence (ECL). He discusses in detail the conditions under which the Marcus theory can give a more quantitative description of ECL processes.

Oleg Petrii and Galina Tsirlina describe a wide range of oxide high temperature superconductors, their electrochemical synthesis, their properties and degradation mechanisms, and analytical methods for the characterization of their surfaces and volumes. The recent advances in this field open new possibilities for elucidating the interface and charge-transfer at extremely low temperatures.

Digby Macdonald and Leo Kriksunov provide a broad perspective on the complex phenomena by which fluid flow influences the initiation and propagation of corrosion in pits and cracks. By focusing on the industrially important environment of high temperature aqueous systems, the authors provide an important link between theoretical understanding, well-designed experiments, and predictive capability.

Shimshon Gottesfeld provides a valuable perspective on the advancement of polymer electrolyte fuel cells in such key areas as lowering catalyst loading, decreasing susceptibility of anode catalyst to poisoning by the fuel, improving cathode performance, and achieving high proton conductivity. These activities cover a wide range of fundamental subjects in interfacial electrochemistry and material science, as well as chemical and electrochemical engineering.

Finally, Fritz Beck gives a comprehensive survey of materials that can be used as active electrodes in metal-free batteries. He discusses the advantages and disadvantages of various systems in terms of technical realization, electrochemical stability and power density, and mentions possible applications.

Contents

A. Kapturkiewicz
Marcus Theory in the Qualitative and Quantitative Description of Electrochemiluminescence Phenomena 1

O. A. Petrii and Galina A. Tsirlina
Electrochemistry of Oxide High-Temperature Superconductors 61

D. D. Macdonald and L. B. Kriksunov
Flow Rate Dependence of Localized Corrosion in Thermal Power Plant Materials 125

S. Gottesfeld
Polymer Electrolyte Fuel Cells 195

F. Beck
Graphite, Carbonaceous Materials and Organic Solids as Active Electrodes in Metal-Free Batteries 303

Index 413

List of Contributors

Fritz Beck
University of Duisburg
Fachgebiet Elektrochemie
D 47057 Duisburg
Germany

Shimshon Gottesfeld*
Materials Science and
Technology Division
Electronic and Electrochemical
Materials and Devices Group
Los Alamos National Laboratory
Los Alamos, NM 87545
USA

Andrzej Kapturkiewicz
Institute of Physical Chemistry of the
Polish Academy of Sciences
Kasprzaka 44/52
01-224 Warsaw
Poland

Leo B. Kriksunov
Center for Advanced Materials
The Pennsylvania State University
University Park, PA 16802
USA

Digby D. Macdonald
Center for Advanced Materials
The Pennsylvania State University
University Park, PA 16802
USA

Oleg A. Petrii
Department of Electrochemistry
Moscow State University
Vorob'evy Gory V-234
Moscow GSP-3
119889 Russia

Galina A. Tsirlina
Department of Electrochemistry
Moscow State University
Vorob'evy Gory V-234
Moscow GSP-3
119889 Russia

*With Tom A. Zawodzinski

Advances in Electrochemical Science and Engineering
Edited by Richard C. Alkire, Heinz Gerischer, Dieter M. Kolb and Charles W. Tobias
© WILEY-VCH Verlag GmbH, 1997

Marcus Theory in the Qualitative and Quantitative Description of Electrochemiluminescence Phenomena

Andrzej Kapturkiewicz

Institute of Physical Chemistry of the Polish Academy of Sciences,
Kasprzaka 44/52, 01-224 Warsaw, Poland

Contents

1 Introduction 3
2 Kinetics of Electron Transfer Reactions 5
  2.1 Main Concepts 5
  2.2 Normal and Inverted Marcus Region 7
  2.3 Radiative Electron Transfer in the Inverted Marcus Region 11
  2.4 Effects of Solvent Molecular Dynamics 14
  2.5 Unimolecular versus Bimolecular Electron Transfer Reaction 16
3 Formation of Excited States in Electron Transfer Reactions 18
  3.1 Routes of the Excited States Formation 18
  3.2 Energetics of Ions Annihilation 20
  3.3 Triple-Potential-Step Technique in Electrochemiluminescence 23
4 Efficiencies of the Excited States Formation 24
  4.1 Aromatic hydrocarbons 24
  4.2 Intramolecular Donor–Acceptor systems 33
  4.3 Ruthenium(II) Chelates 44
  4.4 Molybdenum(II) and Tungsten(II) Halide Cluster Ions 49
5 Conclusions 55
6 References 56

List of Symbols

c	velocity of light
C	molar concentration of solute
e_0	electron charge
E	energy/standard redox potential
f	force constant
F	Faraday constant
FC	Franck–Condon factor
G	Gibbs energy
h	Planck's constant
$\mathbf{H}$	energy operator
j	number of vibronically-excited sublevel

k	reaction rate
K_{act}	association constant for formation of precursor complex
L	optical path length
M	electronic transition moment
n	refractive index of medium
N_{A}	Avogadro constant
r	effective radius of redox center/reactants separation distance
R	gas constant
S	electron-vibration coupling constant/entropy
t	time
T	absolute temperature
V	electronic matrix element describing electronic coupling/potential energy
w	energy of precursor complex formation
$w(r_{12})$	energy functions for reactants 1 and 2 at distance r_{12}
x	reaction nuclear coordinate
β	parameter describing distance (exponential) decreasing of electronic coupling
δr	effective thickness of reaction layer
ε	static dielectric constant, dielectric permittivity
ε_0	dielectric permittivity of a vacuum
$\varepsilon(\tilde{\nu}_{\mathrm{a}})$	molar absorbance of charge-transfer absorption of a photon
η	viscosity
λ	inner/outer/reorganization energy and their 'force constants'
$\boldsymbol{\mu}$	dipole moment operator
ν	mean inner vibration frequency/mean outer rotation frequency
τ	relaxation time
ϕ	efficiency/fraction of electron transfer events
ϕ_{ecl}	electrochemiluminescence efficiency
ϕ_{o}	emission quantum yield
ε_{∞}	dielectric permittivity in near-infrared region
$\tilde{\nu}$	absorption/emission wave number
Ψ	electronic wavefunction
ω	angular frequency

Abbreviations

A	acceptor
ACN	acetonitrile
BA	bianthryl
biq	2,2′-biisoquiniline
BN	butyronitrile
bpy	2,2′-bipyridine
bpz	2,2′-bipyrazine
bqu	2,2′-biquinoline
cip	contact ion pair
D	donor
DA	10,10′-dimethoxybianthryl
DPA	9,10-diphenyl enthracene
dph	4,7-diphenyl-1,10-phenanthroline
ECL	electrochemiluminescence
HOMO	highest occupied atomic orbital
L	organic ligand
LUMO	lowest unoccupied atomic orbital
MO	molecular orbital
PF	pre-exponential factor

R	organic molecule
ssip	solvent-separated ion pair
TBAP	tetra-n-butylammonium perchlorate
TTA	triplet–triplet annihilation

1 Introduction

The understanding of the factors determining the rate of the electron transfer processes is important, because of the ubiquity and essential role of electron transfer in many physical, chemical, and biological processes. During the past three decades they have been the subject of extensive theoretical and experimental studies. Classical and quantum-mechanical treatments predict that the reaction rate will increase with increasingly negative Gibbs energy of the reaction, maximize for a moderately exergonic reaction (the normal Marcus region), and thereafter decrease as the Gibbs energy of the reaction becomes more negative (the inverted Marcus region) [1].

One of the most fascinating consequences of such behavior is the light emission during the reaction with very large exothermicity [2]. Chemiluminescence can be defined as the emission of light resulting from the generation of electronically excited states formed in a chemical reaction. Light emission arises at the expense of the energy released from an exothermic elementary step of a reaction. The understanding of the mechanism of chemiluminescence has advanced to the point that prediction of light emission during a chemical reaction is now possible (see, for example, [3–5]). However, much remains to be done in identifying the fundamental physical processes leading to electronic excitation. It is not possible to give a simple answer to the question "What are the factors controlling excited state formation?" Quantitative predictions are even more difficult, because of the large number of factors affecting the mechanism of a chemiluminescent reaction. The heart of the matter is the excitation step, which in most cases can be formulated as an inter- or intramolecular electron transfer. Kinetic considerations predict the occurrence of such electron transfer in a very short time scale (even shorter than the period of an intramolecular vibration) requiring rapid dissipation of a large amount of energy into the vibration modes of the molecular frames. This is very difficult for the reacting system, and only a limited fraction of the reacting species follows that pathway directly, leading to a direct formation of the stable ground-state products. The formation of the excited states is less exergonic and less thermodynamically favored. However, less energy needs to be vibrationally dissipated, and therefore the process may be kinetically preferred. Obviously, because the molecular energy levels are quantized, the reaction yielding the excitation must deliver, in one step, the appropriate amount of energy.

In the simplest case this may be realized in chemical reactions involving strong oxidants and reductants. Both methods for the preparation of the reactants, the common chemical (e.g., [6]), and electrochemical routes (reviewed in [7–13]), can be used, and the observations from these two methods can be nicely related. Employment of chemical oxidants and/or reductants seems to be more cumbersome, especially in quantitative work. The electrochemical route seems to be much more useful in cases of relatively unstable intermediates. Also it is advantageous because, when working at controlled potentials, very selective oxidation and reduction can be induced.

Electrochemiluminescence (or electrochemically generated chemiluminescence), ECL, can be defined as the generation of light-emitting species by means of homogeneous electron transfer between precursors in solution. Such precursors are obtained as a consequence of heterogeneous electron transfer (electrode) reactions, leading to the formation of very active oxidizing and reducing agents. To facilitate rapid encounters among themselves, precursors may be formed sequentially on one working electrode by application of the appropriate potential program (under diffusion-controlled electrolysis conditions using the triple potential-step technique [14]) or under steady-state convective electrolysis conditions (e.g., on the ring and on the disk of a rotating ring-disk electrode [15, 16] or at double-band microelectrodes [17]).

In some cases the excited states of molecules can also be achieved by means of heterogeneous electron transfer. Typically, electron transfer to or from an electrode results in formation of an excited state of the electrode [18–20]. However, the oxidized form of some luminescent species may be reduced by electrons transferred from the conduction band of an n-type semiconductor, showing evidence for the production of triplet states [21–23].

Electrochemical excitation, "photochemistry without light," exhibits many phenomena that are unique to ECL as compared to photochemistry. The efficient production of emission from excimers or exciplexes as compared to excited monomers, efficient generation of excited triplet states, and intense delayed fluorescence caused by triplet–triplet annihilation are the most typical examples. On the other hand, the method offers a chance to populate the excited states that are inaccessible by the processes following photoexcitation.

Three directions of the ECL investigations seem to be the most interesting: study of the mechanism of the phenomenon as such; use of electrical energy for obtaining excited molecules; and application of ECL for studying the kinetics and mechanism of electron transfer reactions. Up till now, eventual practical applications are less developed; ECL devices, such as displays and lasers [24–27], and the visualization of non-uniform current distribution on electrodes [28, 29] are the most interesting examples.

Quantitative study of ECL systems is a rather difficult task. The combined requirements of reductant and oxidant stability with high fluorescence efficiency of the parent molecule drastically limit the types of compounds suitable for use in the study of the ECL phenomenon. To these, we must add solubility and chemical stability in the presence of electrodes, electrolyte, and solvent. Photochemical stability is an additional requirement. Chemical complications following the initial electron transfer to and from the electrode are still a problem. The chemistry occurring in solution after electrolysis must therefore be examined carefully. Especially, the solvent-supporting electrolyte system should be chosen to prevent lack of reactivity with the electrogenerated species. All of the above complications may lead to misinterpretation of the essentially simple processes of electron transfer excitation. However, in some cases most of these interferences may be removed by appropriate experimental conditions and the ECL obtained data allow for quantitative discussion. An interpretation that is more general and more quantitative than hitherto is possible in view of new data presented in the literature.

2 Kinetics of Electron Transfer Reactions

2.1 Main Concepts

As mentioned above, the formation of excited states in chemical reactions may be understood in the context of an electron transfer model for chemiluminescence, first proposed by Marcus [2]. According to this model the formation of excited states is competitive with the formation of the ground state, even though the latter is strongly favored thermodynamically. Thus, understanding the factors that determine the electron transfer rate is of considerable importance. The theory of electron transfer reactions in solution has been summarized and reviewed in many reviews (e.g., [30–36]). Therefore, in this chapter the relevant ideas and equations are only briefly summarized, to serve as a basis for description of the ECL experiments.

Although a number of theories have been proposed, there is agreement that the crux of the electron transfer problem is the fact that the equilibrium nuclear configuration of a species (in the intramolecular bond, this includes lengths and angles as well as the vibrations and rotations of the surrounding solvent dipoles) changes when it gains or loses an electron. The equilibrium configurations of reduced and oxidized forms of a redox couple, like the ground and excited states of a molecule are generally different. As a consequence, the rates of thermally activated electron transfer reactions, radiative transitions and nonradiative deactivation processes can be discussed with common formalism in which the rate is a product of an electronic and a nuclear factor. The former is a function of the electronic interaction in the reacting system, whereas the latter depends on the nuclear configuration changes between the reactants and products. Of course the larger the electronic interaction, and the smaller the changes in nuclear configuration, the more rapid is the electron transfer process. The role of both factors in determining the rate of electron transfer can be described quantitatively. The formalism describing these processes provides a unified description of homogeneous (intra- and intermolecular) and heterogeneous electron transfer reactions, either radiative or radiationless in nature.

The theoretical description of the kinetics of electron transfer reactions starts from the pioneering work of Marcus [1]; in his work the convenient expression for the free energy of activation was defined. However, the pre-exponential factor in the expression for the reaction rate constant was left undetermined in the framework of that classical (activate-complex formalism) and macroscopic theory. The more sophisticated, semiclassical or quantum-mechanical, approaches [37–41] avoid this inadequacy. Typically, they are based on the Franck–Condon principle, i.e., assuming the separation of the electronic and nuclear motions. The Franck–Condon principle states that the interatomic distances and nuclear moment are identical in the final and initial states during the time of electron transfer. The transfer of an electron between two states is a relatively instantaneous event compared to the slower nuclear motions that must take place to accommodate the "new" electronic configuration. Nuclear changes must occur prior to electron transfer and they are possible due to collisions between reactants and surrounding solvent. Before the transfer of an electron, the nuclear geometry of the initial state, including the surrounding solvent molecules, must be converted into a high-energy, "nonequilibrium" or distorted configuration. The transition state consists of two high-energy species which posses the same nuclear conformation but different electronic configurations. Moreover, for simplicity, the inner-molecular motions (treated quantum-mechanically) are separated from the solvent motions (treated classically). Such an approach is justified at normal temperatures. Taking into account the assumptions presented above, the probability per unit time (first-order state constant k_{et}) that an initial state will pass to a final product may be given by the time-dependent perturbation theory as:

$$k_{et} = \frac{4\pi^2}{h} V_{12}^2(\mathrm{FC}) \tag{1}$$

where h is the Planck constant and V_{12} is the electronic matrix element describing the electronic coupling between the initial and final states, being defined as follows:

$$V_{12} = \langle \Psi_1 | \mathbf{H} | \Psi_2 \rangle \tag{2}$$

where Ψ_1 and Ψ_2 are the electronic wavefunctions of the reacting system in the initial and final states, respectively. $\mathbf{H} = (\mathbf{H}_1 + \mathbf{H}_2 + \mathbf{H}_{12})$ is the energy operator and contains $\mathbf{H}_{12}$, which, unlike $\mathbf{H}_1$ and $\mathbf{H}_2$, depends on the separation distance between two redox centers involved in the given electron transfer reaction. $\mathbf{H}_1$ and $\mathbf{H}_2$, however, depend on the reaction nuclear coordinate x. $\mathbf{H}_{12}$ corresponds to the interaction between of the initial and final state, but with the electron being required to remain localized on the substract or product. The potential energies of the system in its initial (V_1) and final (V_2) states are given by:

$$V_1 = \langle \Psi_1 | \mathbf{H} | \Psi_1 \rangle \quad \text{and} \quad V_2 = \langle \Psi_2 | \mathbf{H} | \Psi_2 \rangle \tag{3}$$

The quantity (FC) is the Franck–Condon factor: it is a sum of products of overlap integrals of the vibrational and solvation wavefunctions of the reactants with those of the products, suitably weighted by Boltzmann factors. The value of the Franck–Condon factor may be expressed analytically by considering the effective potential energy curves, of both the initial and the final states, as a function of their nuclear configurations. Relatively simple relationships can be derived if the appropriate curves are harmonic with identical force constants. Under these conditions:

$$V_1 = \lambda(x_1 - x)^2 \quad \text{and} \quad V_2 = \lambda(x_2 - x)^2 + \Delta G_{12} \tag{4}$$

where λ is the "force constant" (in units of energy) of the parabolas, x is the dimensionless nuclear (reaction) coordinate, ΔG_{12} is the Gibbs energy change between the initial and the final state, and x_1 and x_2 correspond to their thermodynamically equilibrated configurations.

The term λ is the sum of two contributions: an inner one (λ_i) required for the bond length and angle changes, and an outer one (λ_o) necessary for the reorganization of the solvent coordination shells. The energy λ_i can be estimated using a harmonic-oscillator approximation. The potential energy needed to change the inter-atomic distances from their equilibrium values in the initial state to those appropriate to the final state may be calculated, taking into account the force constants in the reactant and product ($f_{j,1}$ and $f_{j,2}$ respectively, where j = number of changing bond) and the change in equilibrium values of the given bond (Δq_{12}):

$$\lambda_i = \sum_j \frac{f_{j,1} f_{j,2}}{f_{j,1} + f_{j,2}} (\Delta q_{12})^2 \tag{5}$$

The quantities needed may be obtained from the IR-spectroscopic ($f_{j,1}$ and $f_{j,2}$) and crystallographic (Δq_{12}) data. Obviously Eq. (5) is valid only if no bonds are broken and new bonds are not formed in the given electron transfer reaction.

The energy required to reorganize the solvent, λ_o, is obtained by a different procedure. The medium outside the reactant (or reactants) is treated as a dielectric continuum with the polarization made up of two parts, a relatively rapid electronic polarization and a slower vibrational–orientational one. The latter has to adjust to a nonequilibrium value appropriate to the final state, contrary to the former. On the basis of the Born solvation theory λ_o (if one electron is transferred) is given by:

$$\lambda_o = \frac{N_A e_0^2}{4\pi\varepsilon_0} \left[\frac{1}{n^2} - \frac{1}{\varepsilon}\right] \left[\frac{1}{2r_1} + \frac{1}{2r_2} - \frac{1}{r_{12}}\right] \tag{6}$$

where ε and n are the static dielectric constant and the refractive index of the reaction medium; N_A, e_0 and ε_0 are the Avogadro constant, the electron charge and the permittivity of a vacuum, respectively; r_1 and r_2 are the effective radii of the redox centers involved in the electron transfer reaction, with the center-to-center separation distance r_{12}. Equation (6) is exactly valid only for spherical molecules, with a uniform charge distribution. In the cases in which the charge is nonuniformly redistributed and/or for nonspherical molecules, λ_o may be estimated on the basis of an appropriate, more sophisticated extension of the simple Born model (e.g., [42–44]).

2.2 Normal and Inverted Marcus Region

Using the formalism presented above, potential energy curves may be constructed in zero-order as well as in first-order approximations. Electron transfer can then be described in terms of crossing of the system from one potential energy curve to the other. In the zero-order approximation, the electron is required to remain localized to the individual system. No electron transfer is possible as long as this condition is imposed: electronic coupling of the reactants is necessary for the system to pass from the initial state to the final state. Electronic coupling removes the degeneracy at the intersection and leads to the formation of two new curves, the adiabatic states of the system. The adiabatic states are obtained by solving the secular equation:

$$\begin{vmatrix} V_1 - E & V_{12} \\ V_{12} & V_2 - E \end{vmatrix} = 0 \tag{7}$$

The roots of the equation are:

$$E_{\pm} = \frac{1}{2}(V_1 + V_2) \pm \frac{1}{2}\sqrt{(V_1 - V_2)^2 + 4(V_{12})^2} \tag{8}$$

where E_+ and E_- describe the lower and upper curve, respectively. The above considerations are valid if $V_{12} \ll V_1$, $V_{12} \ll V_2$ and $V_{12} < \lambda$. These requirements are fulfilled in most intermolecular (outer-sphere) reactions. The magnitude of the electronic interaction V_{12} between reactants is important. The approach presented above is generally true when the coupling of the initial and final states of the system is relatively weak. If the splitting at the intersection is very large, simple application of time-dependent perturbation theory is no longer possible, and a somewhat different approach must be used (e.g., [45]). Such systems, mostly intramolecular, are relatively rare.

For many reasons it is convenient to distinguish between two cases. The first is called the normal free-energy region (or the normal Marcus region) and is defined by $-\lambda < \Delta G_{12} < \lambda$ (Fig. 1) with the reaction rate expressed as follows:

$$k_{\mathrm{et}} = \frac{4\pi^2}{h} V_{12}^2 \sqrt{\frac{1}{4\pi\lambda_o RT}}\, \mathrm{e}^{-S} \exp\left[-\frac{(\lambda_o + \Delta G_{12})^2}{4\lambda_o RT}\right] \tag{9}$$

where R is the gas constant and T the absolute temperature. S is called the electron-vibration coupling constant and is equal to the inner reorganization energy λ_i, expressed in units of vibrational quanta $h\nu_i$:

$$S = \lambda_i / h\nu_i \tag{10}$$

where ν_i denotes mean vibration frequency of the reactant and product bonds. In this region the reaction rate will increase with increasing negative Gibbs energy ΔG_{12}. When $\Delta G_{12} = -\lambda$ the reaction rate is maximized and the process has no barrier.

If the given reaction is very exergonic, with $-\Delta G_{12} > \lambda$, the shapes of the potential energy curves are changed. Electron transfer involves a transition from one adiabatic curve to the other and therefore is inherently nonadiabatic (Fig. 2). The second region is called the abnormal or inverted free-energy region (also the inverted Marcus region) and is defined by $\Delta G_{12} < -\lambda$. In this region, the reaction rate usually decreases as the standard Gibbs energy becomes more negative.

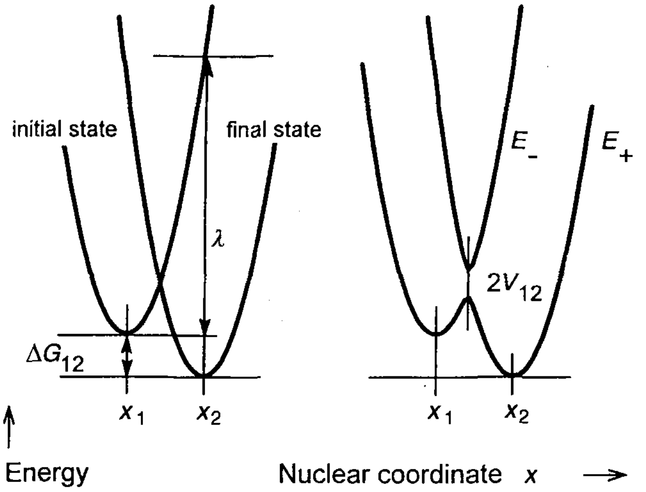
initial state
final state
λ
ΔG12
x1
x2
Energy
E-
E+
2V12
x1
x2
Nuclear coordinate x

Fig. 1. Electron transfer in the normal Marcus region. Potential energies of the reactant and product as a function of the nuclear (reaction) coordinate: the zero-order (left) and first-order (right) representations.

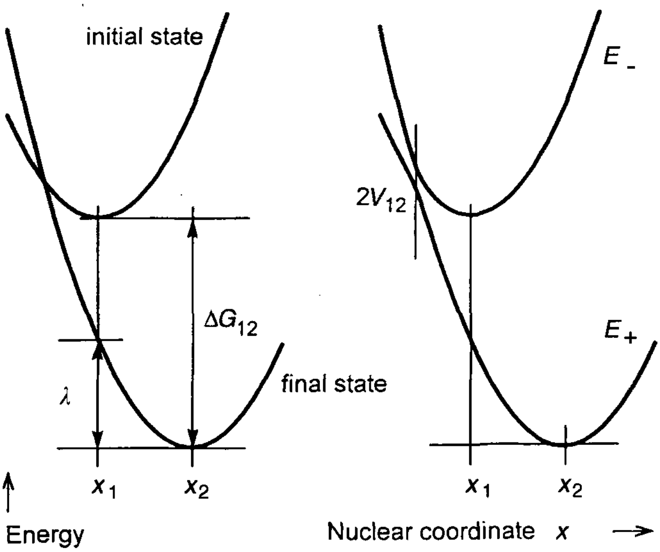
initial state
ΔG12
λ
final state
x1
x2
Energy
E-
2V12
E+
x1
x2
Nuclear coordinate x

Fig. 2. Electron transfer in the inverted Marcus region. Potential energies of the reactant and product as a function of the nuclear (reaction) coordinate: the zero-order (left) and first-order (right) representations.

In electron transfer reactions with relatively low exothermicity, $-\Delta G_{12} < \lambda$, the excess of the Gibbs energy leads only to vibrational and orientational excitation of the surrounding solvent shell. If the reaction is more exergonic, vibrational and/or electronic excitation of reaction products is generally possible. The overall reaction rate is then the superposition of many channels.

Electronic excitation is possible only for very exergonic electron transfer reactions with the energy excess larger than the energy for the given excited state, typically greater than 1.5 eV. Vibrational intramolecular excitation is, however, already possible for moderately exergonic processes (typically the energy of vibronic quanta is 0.1–0.3 eV). Consequently, the reaction rate in the inverted Marcus region (with $-\Delta G_{12} > \lambda$) may be faster than that expected from the simplified theory. Vibrational excitation of the high-frequency modes accompanying the electron transfer lowers the energy gap in the inverted Marcus region. This results in lowering of the effective activation energy and in enhancement of the reaction rate. Of course, the enhancement is even greater if additional channels (leading to electronically excited products) are also accessible. In the theoretical description of the resulting reaction rate the same main assumptions are applicable, but different Franck–Condon factors (FC) should be applied for all the accessible channels.

In the theoretical description of the overall reaction rate the modified Eq. (1) may be applied (with the assumption that the electronic coupling element does not depend on the quantum number, j, of the excited vibrational mode):

$$k_{\mathrm{et}} = \frac{4\pi^2}{h} V_{12}^2 \sum_j (\mathrm{FC}_j) \tag{11}$$

Each summand in Eq. (11) represents the rate for a single contribution to the total rate from a $0 \longrightarrow j$ nonradiative vibronic transition (Fig. 3). The Frack–Condon principle applies for each of the single contributions. Similarly, as in the single mode approximation, the corresponding Franck–Condon factors (FC_j) are a sum of product of overlap integrals of the vibrational wavefunction of the reactants with those of products, weighted by appropriate Boltzmann factors. It is assumed (for simplicity) that only one (averaged over all of the changing bonds and angles) high-frequency

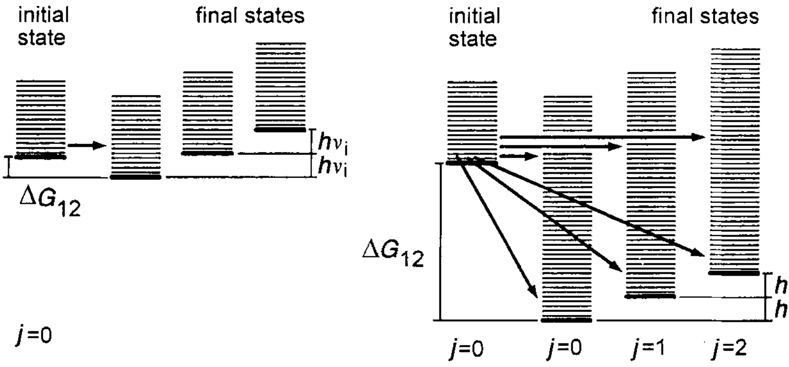

Fig. 3. Schematic illustration of non-radiative electron transfer (horizontal arrows) in the normal (left) and inverted (right) Marcus regions. Associated with each vibronic state is a stack of sublevels representing low-frequency (mainly) solvent modes. In the initial state only one vibrational mode, with $j = 0$, is mainly occupied, whereas in the final state various vibrational modes, with $j = 0, 1, 2...$, may be accessible. Diagonal arrows (in the inverted Marcus region) correspond to radiative electron transfer (charge-transfer fluorescence). Adapted from [55].

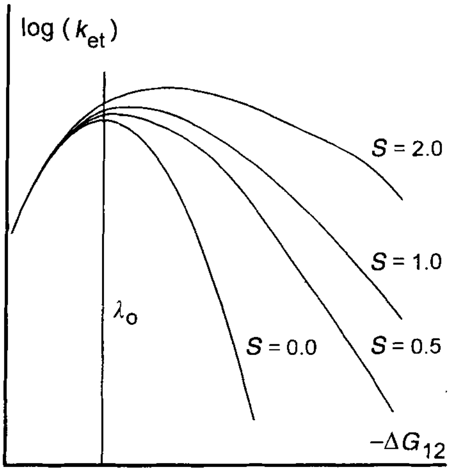

Fig. 4. Logarithm of the electron transfer rate as a function of reaction exothermicity. The case $S = 0$ corresponds to neglect of the vibrational excitation. If $S > 0$ the vibrational excitation is taken into account.

internal vibrational mode, of frequency ν_i, undergoes reorganization. (At normal temperatures $h\nu_i > RT$ and vibrational excitation of the reactants may be neglected.) Low-frequency modes, mainly associated with the solvent shell ($h\nu_s < RT$) are treated classically. Under the above assumptions the resulting expression for the total reaction rate is [46, 47]:

$$k_{et} = \frac{4\pi^2}{h} V_{12}^2 \sqrt{\frac{1}{4\pi\lambda_o RT}} \sum_{j=0} \frac{S^j e^{-S}}{j!} \exp\left[-\frac{(\lambda_o + \Delta G_{12} + jh\nu_i)^2}{4\lambda_o RT}\right] \tag{12}$$

In slightly exergonic electron transfer processes the reaction product is principally formed in the vibrational ground state ($j = 0$). However, when the process is more exergonic, vibrationally excited sublevels with $j < -(\Delta G_{12} + \lambda_o)/h\nu_i$ may be accessible (if $S > 0$). This results in the enhancement of the reaction rate (cf. Fig. 4). Sometimes the enhancement may be so large that the inverted Marcus region cannot be distinctly observed, especially for bimolecular reactions with additional diffusion limitations, e.g., [48, 49]. On the other hand, unequivocal evidence of the inverted Marcus region has recently been presented [50–58]. The quantum effects (in the inverted Marcus region) are expected not only to modify the free-energy relationship but also to affect the temperature dependence of the electron transfer rate [59], with the essential difference between systems with small and large λ_i values. In both cases the strong temperature dependence predicted by the classical Marcus model becomes considerably weaker.

2.3 Radiative Electron Transfer in the Inverted Marcus Region

Electronic coupling of the initial and final states of the system also allows radiative electron transfer between redox centers. Such a process, important in the case of

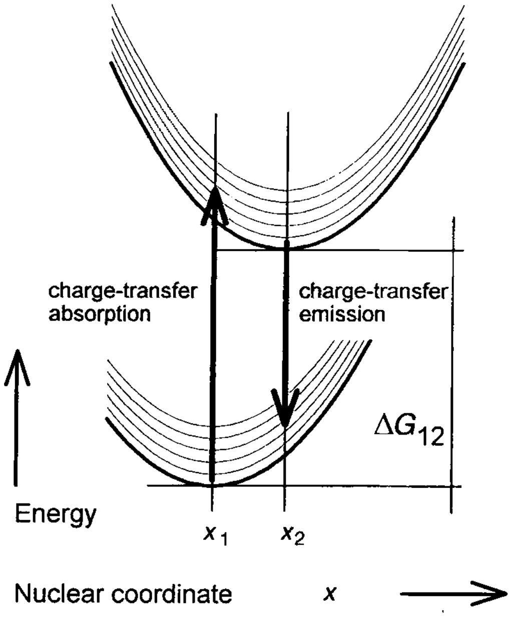

Fig. 5. Radiative transition in the inverted Marcus region: charge-transfer absorption (arrow up) and charge-transfer emission (arrow down).

excimer or exciplex ECL emission, may also be discussed in terms of the Marcus theory. There are two principal differences between themal (nonradiative) and optical (radiative) electron transfer processes. The first is the amount of energy dissipated. Both processes (radiative and nonradiative electron transfer) are spontaneous transitions in which the entire electronic energy is dissipated into intramolecular and solvent motions. The electronic energy dissipated in charge-transfer emission at a given photon with energy $hc\tilde{\nu}_f$ is $-\Delta G_{12} - hc\tilde{\nu}_f$, i.e., less than in the corresponding nonradiative electron transfer. In charge-transfer absorption however, the energy $hc\tilde{\nu}_a$ of an absorbed photon, is greater than ΔG_{12}, with the excess of the electronic energy equal to $hc\tilde{\nu}_a + \Delta G_{12}$, (Fig. 5). The second important difference is connected with the operator coupling initial and final states. In optical transitions the dipole moment operator $\boldsymbol{\mu}$, rather than the energy operator, is suitable:

$$M = \langle \Psi_1 | \boldsymbol{\mu} | \Psi_2 \rangle \tag{13}$$

where M is the electronic transition moment and $\boldsymbol{\mu}$ is the dipole moment operator. If the contribution of the excited states can be neglected, the quantity M is connected with the electronic matrix element V_{12} [60]:

$$M \approx (V_{12}/\Delta G_{12})\mu_{CT} \tag{14}$$

where μ_{CT} corresponds to the change of the dipole moment value between the initial and final state. This is usually not the case in excimer or exciplex emission, for which contribution of excited states must also be taken into account [61–64].

The rate $I(\tilde{\nu}_f)$ of emission of a given photon with energy $hc\tilde{\nu}_f$ (in photons per molecule per unit time per unit spectral energy) is given by Eq. (15) [65]. It is formally very similar to the expression for the nonradiative electron transfer rate (cf. Eq. (12)):

$$I(\tilde{\nu}_f) = \frac{64\pi^4}{3h}\frac{n^3\tilde{\nu}_f^3}{c^3}\frac{M^2}{4\pi\varepsilon_0}\sqrt{\frac{1}{4\pi\lambda_o RT}}\sum_{j=0}\frac{S^j e^{-S}}{j!}\exp\left[-\frac{(\lambda_o + \Delta G_{12} + jh\nu_i + hc\tilde{\nu}_f)^2}{4\lambda_o RT}\right] \tag{15}$$

where c is the velocity of light. Integration of Eq. (15) over whole range of $\tilde{\nu}_f$ leads to the familiar expression for the radiative rate constant k_f [66]:

$$k_f = \frac{64\pi^4 n^3 M^2}{12\pi\varepsilon_0 hc^3}(\tilde{\nu}_f^{\max})^3 \tag{16}$$

In a similar way, the molar absorbance $\varepsilon(\tilde{\nu}_a)$ of charge-transfer absorption of a given photon with the energy $hc\tilde{\nu}_a$ may be expressed thus:

$$\varepsilon(\tilde{\nu}_a) = \frac{8\pi^3 N_A}{3\ln(10)}\frac{n\tilde{\nu}_a}{c}\frac{M^2}{4\pi\varepsilon_0}\sqrt{\frac{1}{4\pi\lambda_o RT}}\sum_{j=0}\frac{S^j e^{-S}}{j!}\exp\left[-\frac{(\lambda_o - \Delta G_{12} + jh\nu_i - hc\tilde{\nu}_a)^2}{4\lambda_o RT}\right] \tag{17}$$

The quantity $\varepsilon(\tilde{\nu}_a)$ is defined by $\log(I/I_0) = -\varepsilon(\tilde{\nu}_a)CL$, where C is the molar concentration of the solute, I and I_0 are the transmitted and incident light intensity, and L is the optical path length.

From Eqs. (15) and (17) simple approximate expressions for the absorption $\tilde{\nu}_a^{\max}$ and emission $\tilde{\nu}_f^{\max}$ maxima may be obtained:

$$hc\tilde{\nu}_a^{\max} \approx -\Delta G_{12} + \lambda_o + \lambda_i \quad \text{and} \quad hc\nu_f^{\max} \approx -\Delta G_{12} - \lambda_o - \lambda_i \tag{18}$$

Both maxima are also simply connected with ΔG_{12}, allowing the independent determination of this quantity from the spectroscopic data:

$$\Delta G_{12} \approx -[hc\tilde{\nu}_a^{\max} + hc\tilde{\nu}_f^{\max}]/2 \tag{19}$$

Equations (15) and (17) also describe the shape of the emission and the absorption band, respectively. One can derive the expression for the full width at half-maximum, $\Delta\tilde{\nu}_{1/2}$:

$$[hc\Delta\tilde{\nu}_{1/2}]^2/8\ln(2) \approx \lambda_i h\nu_i + 2\lambda_o RT \tag{20}$$

Unlike the kinetic data for nonradiative electron transfer, analysis of the charge-transfer emission and/or absorption bands makes it possible to determine the quantities λ_o, λ_i, etc. It can be done by fitting the emission and/or absorption spectra using various parameters (e.g., [55, 67]). Combined analysis of the temperature and solvent effects on $\Delta\tilde{\nu}_{1/2}$ also seems to be a way of determining all of the parameters describing the given radiative process (e.g., [68]).

The formalism presented above makes possible the quantitative prediction of the rates of nonradiative electron transfer from the analysis of charge-transfer spectra, (e.g., [67]), and will probably be very useful in the quantitative interpretation of ECL processes following the E-route (Section 3.1). To our knowledge, however, such an approach to the description of electrochemiluminescence phenomena has not been applied until now.

2.4 Effects of Solvent Molecular Dynamics

The theoretical description of electron transfer reactions is limited by the frameworks of the perturbation theory of the interaction causing a transition. In this theory the dynamics of intramolecular as well as solvent motions have no influence on the rate constant of the reaction. The formation of some favorable geometry of reactant(s), which allows reaction, is fast compared to the intrinsic electron transfer step. In conjunction with this "frozen-reactant" approximation, the assumption is made that the orientation of the reactant(s) can be regarded as fixed. This is justified if the electron hopping frequency, expressed by the pre-exponential factors in Eqs. (9) and (12), is relatively small, and the intramolecular and solvent shell changes occur on a much faster time scale. In most cases this is fulfilled for the bond lengths and angles adjustment ($\nu_i \approx 10^{13}$–$10^{14}\,\mathrm{s}^{-1}$). The solvent motions, however, are much slower ($\nu_s \approx 10^{11}$–$10^{12}\,\mathrm{s}^{-1}$). Therefore, for relatively small values of the electronic coupling element $V_{12} \approx 0.01$–$0.02\,\mathrm{eV}$, the number of reacting subsystems (at the intersection point of the potential energy curves) is smaller than expected from the equipartition theorem, and the electron transfer reaction is slower than expected from Eqs. (9) and (12). According to a simplified interpretation, this corresponds to the lowering of the velocity with which the reacting system is moving on its potential energy curve.

It is generally recognized that the solvent affects the kinetics of such a reaction in two ways, namely through the magnitude of the Gibbs energy of activation and the pre-exponential factor. The role of the solvent in determining the activation barrier to electron transfer is already recognized on the basis the work of Marcus. For a quantitative description of the solvent effects on the pre-exponential factor it is necessary to go beyond the framework of perturbation theory. The stochastic approach to describing the effect of the solvent dynamics on the rate constant was developed in the early 1980s [69–73]. On the basis of this approach it was found that the rate of electron transfer is proportional to the frequency of longitudinal reorientational relaxation (expressed by the longitudinal relaxation time τ_L) of the solvent. At about the same time, the influence of the solvent dynamics was confirmed empirically [74–77]. Later the influence of the solvent dynamics was supported by other authors theoretically (e.g., [78–81]) as well as experimentally, (e.g., [82–85]).

The theory starts from description of the dielectric loss spectra, frequency-dependent permittivity of the solvent $\varepsilon(\omega)$, in the framework of the Debye model [86], in which the reorientation of the solvent dipoles gives the main contribution to the relaxation of solvent polarization:

$$\varepsilon(\omega) = \varepsilon_\infty + \frac{\varepsilon - \varepsilon_\infty}{1 + i\omega\tau_D} \quad \text{with} \quad i = \sqrt{-1} \tag{21}$$

where ω is the angular frequency. The longitudinal relaxation time $\tau_L = \tau_D\varepsilon_\infty/\varepsilon$ is related to the Debye relaxation time τ_D, and to the dielectric permittivity of the given solvent (in the near-infrared region, ε_∞; in the static electric field, ε).

It has been generally found that the possible influence of the solvent dynamics may be expressed by a modification of Eq. (9) (e.g., [81]):

$$k_{et} = \frac{4\pi^2}{h} V_{12}^2 \sqrt{\frac{1}{4\pi\lambda_o RT}} \frac{e^{-S}}{1 + 8\pi^2 V_{12}^2 e^{-s} \tau_L / \lambda_o h} \exp\left[-\frac{(\lambda_o + \Delta G_{12})^2}{4\lambda_o RT}\right] \tag{22}$$

Equation (21) exhibits the transition from the solvent-controlled limit (for sufficiently large values of V_{12}) when k_{et} is reciprocally proportional to τ_L:

$$k_{et} = \frac{1}{\tau_L} \sqrt{\frac{\lambda_o}{16\pi RT}} \exp\left[-\frac{(\lambda_o + \Delta G_{12})^2}{4\lambda_o RT}\right] \tag{23}$$

to the nonadiabatic limit (for small values of V_{12}) when k_{et} is essentially controlled by the frequency of electron hopping (cf. Eq. (9)). It should be noted that in the case of the electron transfer reactions controlled by the solvent molecular dynamics, the appropriate values of λ_i as well as V_{12} cannot be derived from the experimental rate constant; only the lower limit of V_{12} may be estimated. The possible eventual influence of the solvent molecular dynamics depends strongly on the value of V_{12}. Therefore, it should be more pronounced in the case of electrochemical, heterogeneous electron transfer reactions, compared with homogeneous ones (e.g., [87]). This results from the fact that, in electron transfer at an electrode, all the metal (electrode) states above (below) the Fermi level energy can receive (provide) electrons, not just one state as in the case of homogeneous electron transfer [88].

Equations (22) and (23), similarly to Eq. (9), are applicable to the electron transfer reactions in the normal Marcus region. In the inverted Marcus region, possible vibrational excitation of the reaction products should again be taken into account. Depending on the values of S and V_{12}, some of the accessible reaction channels may be affected by the solvent molecular dynamics. This problem has been discussed in [89], with the main conclusion that the overall reaction rate may be expressed as follows:

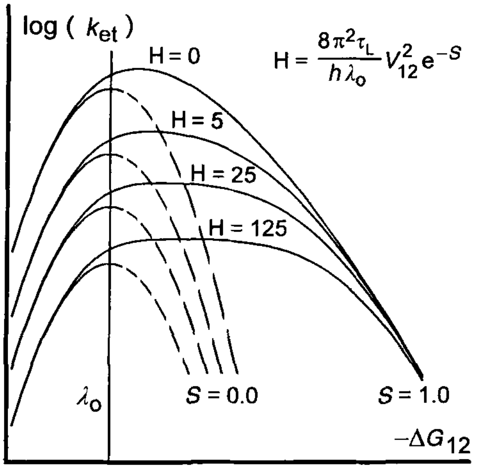

Fig. 6. Logarithm of the electron transfer rate as a function of the reaction exothermicity, without (H = 0) and with (H > 0) limitation caused by the solvent molecular dynamics. The case $S = 0$ corresponds to neglect of the vibrational excitation. If $S = 1$ the vibrational excitation is taken into account.

$$k_{et} = \frac{4\pi^2}{h} V_{12}^2 \sqrt{\frac{1}{4\pi\lambda_o RT}} \sum_{j=0} \frac{S^j e^{-S}/j!}{1 + \frac{8\pi^2\tau_L}{h\lambda_o} V_{12}^2 \frac{S^j e^{-S}}{j!}} \exp\left[-\frac{(\lambda_o + \Delta G_{12} + jh\nu_i)^2}{4\lambda_o RT}\right] \tag{24}$$

Vibrational excitation of the high-frequency intramolecular modes accompanying the electron transfer lowers the energy gaps in the inverted Marcus region. It results in the lowering of the effective activation energy and in the relative enhancement of the reaction rate. It may be concluded that the enhancement in the inverted Marcus region is more pronounced for reactions controlled by the solvent molecular dynamics. In the normal Marcus region, however, the influence of the solvent molecular dynamics leads to absolute reduction of the electron transfer rate (Fig. 6).

2.5 Unimolecular versus Bimolecular Electron Transfer Reactions

Electron transfer becomes more favorable with decreasing separation of the two reactants, because of the electronic interactions. These are the strongest when the two reactants are in contact. As a consequence, the first step in bimolecular electron transfer reactions is the formation of a precursor complex from the separated reactants. Therefore, in the case of the bimolecular reactions the association constant K_{act} for the formation of the precursor complex should be included in the expression for the observed overall reaction rate k_{obs}. Provided that the formation of the precursor complex is not rate-determining, the observed (second-order) rate constant is equal to $K_{act}k_{et}$. If the formation of the precursor complex is rate-determining the reaction becomes diffusion-controlled (k_{diff}). For the intermediate cases ($K_{act}k_{et} \approx k_{diff}$), k_{obs} may be expressed as follows:

$$1/k_{obs} = 1/k_{diff} + 1/K_{act}k_{et} \tag{25}$$

with k_{diff} values usually calculated according to the standard Debye equation:

$$k_{diff} = \frac{8RT}{3\eta} \frac{w_r(r_{12})/RT}{\exp\left[w_r(r_{12})/RT\right] - 1} \tag{26}$$

where η is the macroscopic solvent viscosity and $w_r(r_{12})$ is the energy required to bring the reactants together. The diffusion limitations are the main reason why the "true" rates of the fastest bimolecular electron transfer reactions cannot be directly measured. For this reason ECL may be regarded as a very useful tool for providing direct information on the relative rates of bimolecular electron transfer reaction in both the normal and the inverted Marcus regions.

Two models are frequently used to obtain the values of K_{act}: the "encounter pre-equilibrium" model [90, 91]:

$$K_{act} = 4\pi N_A r_{12}^2 \delta r_{12} \exp\left[-w_r(r_{12})/RT\right] \tag{27}$$

and the Eigen–Fuoss [92, 93] model:

$$K_{act} = (4\pi/3) N_A r_{12}^3 \exp\left[-w_r(r_{12})/RT\right] \tag{28}$$

For homogeneous reactions the K_{act} values provided by Eqs. (27) and (28) are nearly the same (maximal difference does not exceed a factor of 2). Typically δr_{12} is chosen to equal 0.06–0.10 nm. These values arise simply from the distance dependence of the electronic coupling element ($\delta r_{12} \approx 1/\beta$) [32–36]:

$$V_{12}(r_{12}) = V_{12}^0 \exp\left[-\beta(r_{12}^0 - r_{12})/2\right] \tag{29}$$

The separation distance r_{12} for the reactant is typically equal to 0.4–0.6 nm (contact ion pair) [94]; therefore $r_{12}/3 \approx 0.1$–0.15 nm, only somewhat greater than δr_{12}. The electron transfer reaction is also possible for solvent-separated reactants (solvent-separated ion pair) with an r_{12} distance larger by about 0.3–0.4 nm (e.g., [55]). This is the case for bimolecular processes with large values of V_{12} and it may be especially important for reaction occurring in the inverted Marcus region. Sometimes the lowering in the pre-exponential factor in Eq. (12) is overcompensated by an increasing in the outer reorganization energy, resulting in the enhancement of the electron transfer rate [95–97].

3 Formation of Excited States in Electron Transfer Reactions

3.1 Routes of the Excited States Formation

The generation yield ϕ_{es} of excited state is proportional to the electrochemiluminescence efficiency ϕ_{ecl} (in photons emitted per electrons transferred):

$$\phi_{\mathrm{ecl}} = \phi_{\mathrm{es}}\phi_{\mathrm{o}} \tag{30}$$

where ϕ_{o} is the emission quantum yield. Since ϕ_{o} is an intrinsic property of the emitting state, ϕ_{es} is fundamentally descriptive of the efficiency of the ECL process. These values are of considerable interest from a practical point of view and also because they can provide insight into mechanistic features of highly exergonic electron transfer reactions, providing direct information on the relative rates of bimolecular electron transfer in the normal and inverted Marcus regions. In the case of a strongly exergonic electron transfer reaction, the formation of the ground state lies far into the inverted Marcus region. Therefore it may be relatively slow compared with the less exergonic formation of the excited states. The yield of production of the emissive state may be given by the ratio of the rate constants of formation of the excited-state and the ground-state products in the electron transfer reaction.

This simplest route is the most important case, because the experimental values of the ECL efficiencies may be compared with those theoretically predicted. However, it should be noted that the case of only two reaction pathways, i.e., formation of the emissive excited state and the ground state, has been found only for the ECL systems of some coordination compounds of transition metals (e.g., [98, 99]).

Extensive investigations of ECL processes of organic compounds have established a general, more complicated scheme for excited-state formation [7–13]. In electrochemical reactions a neutral molecule R is reduced or oxidized to the corresponding radical anion R^- or cation R^+, respectively:

$$R + e^- \rightleftarrows R^- \tag{31}$$

$$R - e^- \rightleftarrows R^+ \tag{32}$$

These ions form an active complex in the diffusion-controlled reaction. Then tree reaction pathways are possible:

$$R^+ + R^- \xrightarrow{k_0} R + R \tag{33}$$

$$R^+ + R^- \xrightarrow{k_1} R + {}^1R^* \tag{34}$$

$$R^+ + R^- \xrightarrow{k_3} R + {}^3R^* \tag{35}$$

where ${}^1R^*$ and ${}^3R^*$ are the excited singlet and triplet states of the parent molecule R.

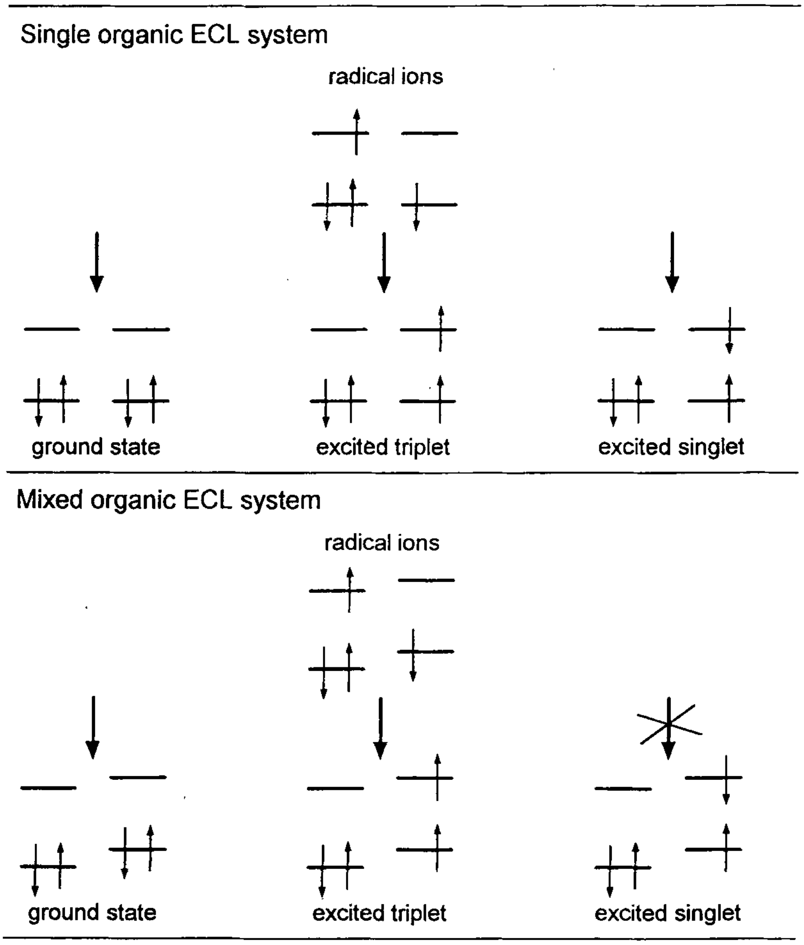
Single organic ECL system
radical ions
ground state
excited triplet
excited singlet
Mixed organic ECL system
radical ions
ground state
excited triplet
excited singlet

Fig. 7. Molecular orbital description of the reactants and products of single and mixed (organic) ECL systems.

The scheme presented above may be rationalized by a simple molecular orbital diagram for the reaction (Fig. 7). This picture is, of course, a very crude representation of what occurs when reaction takes place. Although it is a zero-order approximation, it provides a useful starting point for more detailed consideration. In the electrode processes an electron is removed from the highest occupied molecular orbital (HOMO) to form the radical cation R^+, or placed on the lowest unoccupied molecular orbital (LUMO) to form the radical anion R^-. When the system follows the pathway most favored by thermodynamics predictions – formation of ground state, i.e., the step characterized by the highest driving force – the electron transfers take place from the LUMO of the anion radical to the HOMO of the cation radical. Another, more likely, pathway is an electron transfer between the LUMO of the anion radical and the LUMO of the cation radical. Again, a negative driving force indicates that the triplet pathway may be a spontaneous one. The electron transfer reaction is still extremely rapid, but much less energy needs to be dissipated. The formation of the excited singlet is the least (if at all) exergonic and much less thermodynamically favored. The preference for the given reaction pathway is related to the free-energy difference between the oxidized and reduced precursors. The formation of the excited product requires this difference to be equal to or higher than the energy difference between the excited and ground electronic states. Therefore, only an energy-sufficient system may generate the fluorescent singlet state. The emitting singlet state may be formed directly upon electron transfer from R^- to R^+ (the S-route). The emissive singlet $^1R^*$ undergoes radiative deactivation (with quantum yield ϕ_o):

$$^1R^* \longrightarrow R + hc\tilde{\nu}_f \tag{36}$$

Obviously, if the electron transfer reaction is energetically sufficient to populate the excited singlet directly, formation of lower-lying excited triplets must also take place (T-route). In most cases, organic triplets are nonemissive and their phosphorescence is usually not observed in liquid solutions, at least at room temperature. Nonemissive $^3R^*$ may take part in an up-conversion reaction (bimolecular triplet–triplet annihilation) which yields (with rather low efficiency) the emitting singlet state.

$$^3R^* + {}^3R^* \xrightarrow{k_{\text{upc}}} R + {}^1R^* \longrightarrow R + R + hc\tilde{\nu}_f \tag{37}$$

The efficiency of this up-conversion process is generally very low (typically it does not exceed ca 10^{-3}–10^{-4}). Thus, in the case of organic ECL systems the efficiency of light production is much lower for this process (the T-route) compared with the S-route. Therefore, if the efficiency of the S-route is greater than 0.005, light emission resulting from this reaction pathway becomes dominant. However, light emission from the triplet state (phosphorescence allowed by the spin–orbit coupling induced by the heavy-metal ions) can be observed for the transition-metal complexes. Triplet $^3R^*$ emission in ECL experiments has been also directly observed in organic systems containing benzophenone [100], which has a high triplet phosphorescence quantum yield due to the spin–orbit coupling by its carbonyl group.

If the exothermicity of the annihilation of the given ions is still smaller than the energy of the excited triplet states, the reaction is generally not of interest, although it has been shown that such systems may still produce light. This last case, however, corresponds formally to radiative electron transfer from R^- to R^+ (the E-route). It should be described in terms of the competition between radiative and radiationless transition in the inverted Marcus region.

3.2 Energetics of the Ions Annihilation

The Gibbs energy for the annihilation of ions ΔG_0 (i.e., formation of the ground state in reaction (31)) can be calculated in a straightforward way from the standard electrode potential of oxidation E°_{ox} and reduction E°_{red} of the parent compounds. The magnitude of $E^\circ_{\mathrm{red}} - E^\circ_{\mathrm{ox}}$ corresponds to the difference in energies of the isolated reactants and products. This value should be corrected for work terms because in the electron transfer reaction the reatants are required to be brought together in the precursor complex:

$$\Delta G_0 = F(E^\circ_{\mathrm{red}} - E^\circ_{\mathrm{ox}}) - w_{\mathrm{r}}(r_{12}) + w_{\mathrm{p}}(r_{12}) \tag{38}$$

where F is the Faraday constant. The energy $w_{\mathrm{r}}(r_{12})$ corresponds to the interaction between reactants and it is the energy required to bring the reactants together to the most probable separation distance r_{12} at which the electron transfer takes place, preferably (according to the "encounter pre-equilibrium" model [90, 91]) within a small range of distances δr_{12}. Analogously $w_{\mathrm{p}}(r_{12})$ is the energy required to bring the products into the precursor complex. Both quantities $w_{\mathrm{r}}(r_{12})$ and $w_{\mathrm{p}}(2_{12})$ correspond mainly to electrostatic interactions; thus their values may be calculated using the familiar Coulomb expression. In the case of two oppositely charged ions (i.e., cation and anion radicals) it takes the form:

$$w_{\mathrm{r}}(r_{12}) = -N_{\mathrm{A}}e_0^2/4\pi\varepsilon_0\varepsilon r_{12} \tag{39}$$

In the case of neutral organic ECL systems the $w_{\mathrm{p}}(r_{12})$ value may be neglected, but it should be taken into account in the case of charged transition-metal complexes.

The driving forces ΔG_1 and ΔG_3 for reactions (33) and (34) can be calculated in a similar way, using the corresponding energies E_1 and E_3 of both (singlet and triplet) excited states:

$$\Delta G_1 = F(E^\circ_{\mathrm{red}} - E^\circ_{\mathrm{ox}}) - w_{\mathrm{r}}(r_{12}) + w_{\mathrm{p}}(r_{12}) + E_1 \tag{40}$$

$$\Delta G_3 F = (E^\circ_{\mathrm{red}} - E^\circ_{\mathrm{ox}}) - w_{\mathrm{r}}(r_{12}) + w_{\mathrm{p}}(r_{12}) + E_3 \tag{41}$$

Equations (40) and (41) are not exactly correct because of the mixing of Gibbs energy and energy terms. The entropic contribution ΔS needed to avoid this inconsistency [101] can be evaluated from the following equation:

$$\Delta S = -\partial \Delta G_0/\partial T = -\partial[F(E^\circ_{\mathrm{red}} - E^\circ_{\mathrm{ox}}) - w_{\mathrm{r}}(r_{12}) + w_{\mathrm{p}}(r_{12})]/\partial T \tag{42}$$

It should be noted that the correction for the Coulombic interaction energy terms usually leads to much smaller values of ΔS than those calculated for the isolated ions (at the reaction distance formally equal to infinity) and, at least in the first approximation, the eventual entropic contribution can be neglected. The observed temperature changes of the difference $E^\circ_{\mathrm{red}} - E^\circ_{\mathrm{ox}}$ in the standard redox potentials are compensated by the changes in $(w_{\mathrm{r}}(r_{12}) - w_{\mathrm{r}}(r_{12}))$ because both quantities depend on T in a similar way.

The relative probabilities of the reaction pathways leading to the ground-state product vs. formation of an excited state are directly related to the free energy of the reaction and to the relative energies of activation, as illustrated in Fig. 8. The shapes

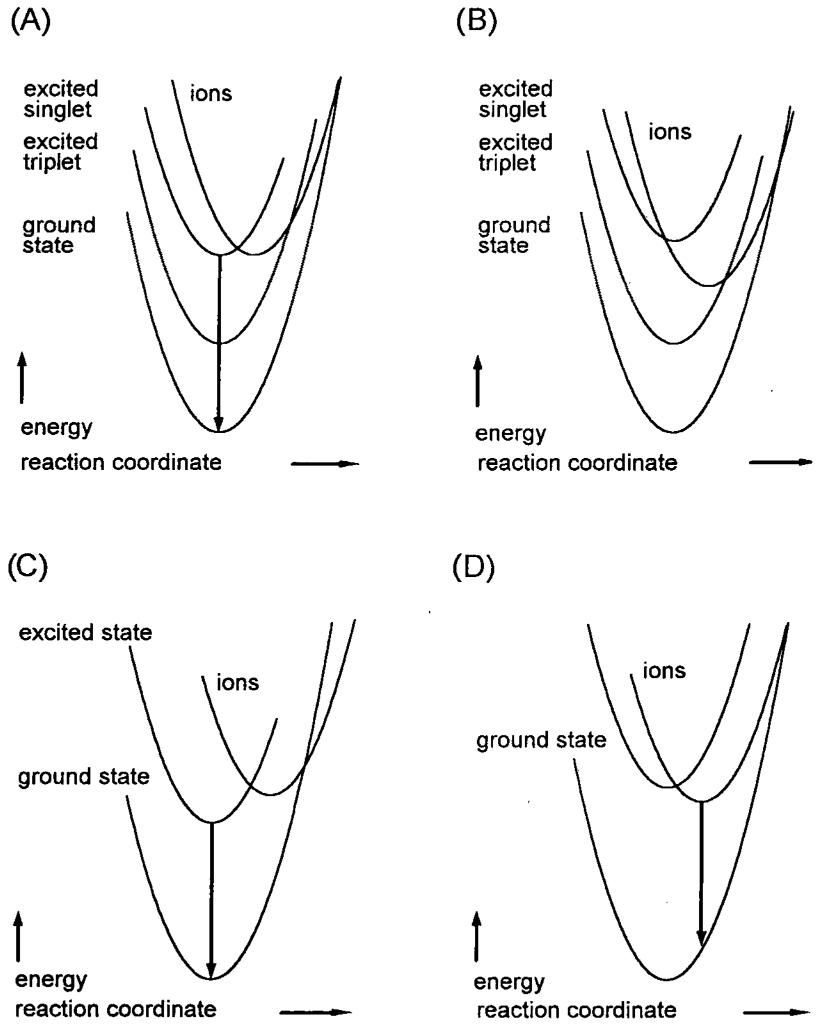
(A)
excited singlet
excited triplet
ground state
ions
energy
reaction coordinate
(B)
excited singlet
excited triplet
ground state
ions
energy
reaction coordinate
(C)
excited state
ions
ground state
energy
reaction coordinate
(D)
ions
ground state
energy
reaction coordinate

Fig. 8. Reaction coordinate diagram for different ECL processes (potential energy curves are presented in the zero-order approximation, without removing the degeneracy at the crossing points of the potential energy curves). (A) Single organic ECL system with direct formation of the excited singlet state (S-route). (B) Mixed organic ECL system without direct formation of the excited singlet state. Formation of the excited triplet may lead to ECL emission through triplet–triplet annihilation (T-route). (C) ECL system involving a transition-metal complex with an emissive excited state (e.g., a triplet) directly formed in the electron transfer reaction. (D) ECL charge-transfer (exciplex) emission by the E-route.

of the given potential energy curves can be predicted in terms of the Marcus theory, taking into account the energies of activation for the organic electron transfer reactions [94] as well as the energies of singlet–triplet splitting [102]. From such a representation it becomes evident that the formation of excited triplets should prevail in most organic ECL systems, especially since this process is also favored by a spin multiplicity statistical factor of 3 [103, 104]. This is especially true for mixed systems in which the radical cation and radical anion are formed from different parent molecules. On the basis of the molecular orbital description it may be simply argued that probably only symmetric (single) ECL systems, in which both cation and anion radicals are formed from the same parent molecule, can follow the S-route.

3.3 Triple-Potential-Step Technique in Electrochemiluminescence

The energetics of an electron transfer reaction provide only a rough indication of the possible ECL mechanism. Essentially, this fails to predict whether the resulting excited state is a singlet or a triplet (or both). Therefore, in order to decide which reaction pathway is dominant, a more detailed analysis must be applied to differentiate between reaction routes.

The most useful diagnosis is based on the relationship between ECL intensities $I(t_r)$ and the square root of the ratio between the times of duration of forward and reverse potential step: this is the triple-potential-step technique. The experiment starts with the working electrode at a potential of no electroactivity (Fig. 9). The electrode potential is changed to value at which the generation of the first reactant occurs and subsequently to values corresponding to the formation of the second reactant. The potential limits of the program sequence should be chosen to ensure production of the electrogenerated intermediates in the mass-controlled region and to minimize the influence of secondary electrochemical reactions. Subsequently, the electrode potential is again changed to the initial value. Light emission is observed during the second reactant generation step in the course of the triple-potential-step sequence.

The appropriate relationship (usually called a Feldberg plot [105, 106]) can be derived after an analytical treatment of diffusion (to and from the electrode) and the overall electron transfer rate. In the case of the simple S-route, the appropriate plots,

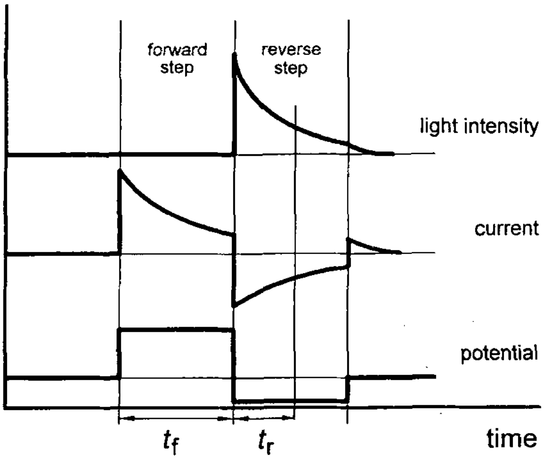

Fig. 9. Variation of potential, current and photon flux vs. time in an ECL experiment performed using the triple-potential-step technique.

according to Eq. (43), should be linear with the slope-to-intercept ratio $a/b = 0.959$ [107, 108].

$$I(t_r) = a\sqrt{t_f/t_r} - b \tag{43}$$

where t_f is the duration of the first (forward) step of the triple-step sequence and t_r is the time span of the second (reverse) step. In the case of the "pure" T-route (treated as a superposition of two bimolecular reactions) as well as for the "mixed" ST-route, plots of the ECL intensities $I(t_r)$ vs. $(t_f/t_r)^{1/2}$ are nonlinear [109]. This criterion may be used to distinguish the S-route from the T- or ST-routes in ECL experiments. However, similar deviations from linearity are also caused by a reactant's instability. An analytical treatment incorporating pseudo-first-order decay rate constants has been presented in [110]. The more unstable the electrogenerated species, the larger are the deviations from linearity that are observed. Therefore it is very important to rule out the instability of radicals when using the Feldberg plot to distinguish between the S- and T-routes. The analysis may be impeded and should be performed very carefully, because other parasitic processes also lead to deviations from the linearity of Feldberg plots [111–113]. Frankly speaking, only in the case of a "pure" S-route with linear Feldberg plots may this analysis be conclusive. For a more complicated ECL system some additional verification, such as the influence of a magnetic field (e.g., [114, 115]) or the triplet interceptors technique (e.g., [116, 117]), may be indispensable.

In the case of charge-transfer emission (formally a bimolecular reation), Feldberg plots are also linear (e.g., [118]). The charge-transfer character of this emission, however, can be demonstrated by a correlation of emission energies of various ECL systems with the standard redox potential (e.g., correlation of the emission maxima with the oxidation potentials of the donor or with the reduction potentials of the acceptors [119]). The associated charge-transfer character can also be demonstrated by the effects of solvent and temperature on the emission energy and intensity (e.g., [120]).

4 Efficiencies of the Formation of Excited States

4.1 Aromatic Hydrocarbons

Aromatic hydrocarbons, with the reaction scheme as described above, play the same key role in ECL studies as in organic electrochemistry and organic UV–VIS spectroscopy. 5,6,11,12-Tetraphenyltetracene (rubrene) and 9,10-diphenylanthracene (DPA) are the most notable examples (Fig. 10). The stability of their radical ions, with the quantum efficiency ϕ_0 of the parent molecules near unity, [121] has fascinated many ECL investigators since the 1960s ([122, 123] and cited references). Taking into account the fact that other aromatic hydrocarbons usually do not form stable

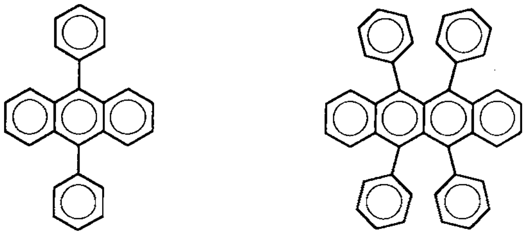

9,10-diphenylanthracene
DPA

5,6,11,12-tetraphenyltetracene
Rubrene

Fig. 10. Examples of the aromatic hydrocarbons mostly used in ECL studies.

radical cations [124], it seems to be understandable that only these ECL systems have been the subject of quantitative studies. Almost all reported results have been obtained in solutions containing 0.1 M tetra-n-butylammonium perchlorate (TBAP) as the supporting electrolyte. In these solutions, however, additional parasitic processes take place [111, 112], leading to perturbation of the ECL efficiencies and transients. The mechanism of these parasitic processes is not exactly known, but the phenomenon seems to be general. In fact the reported ECL efficiency values have shown a wide variation, even under similar conditions. On the other hand, the use of other supporting electrolytes [123] and/or the lowering of electrolyte concentration [122] leads to ECL efficiencies unaffected by any additional processes, and allows quantitative discussion of the reaction mechanism.

The Gibbs energies ΔG_0 released during the annihilation of DPA or rubrene ions (calculated from the difference $E^\circ_{\mathrm{red}} - E^\circ_{\mathrm{ox}}$ corrected for $w_r(r_{12})$) are close to that necessary for the generation of the emitting singlet states, indicating that these reaction channels correspond to nearly isoenergetic resonance electron transfer (with $\Delta G_1 \approx 0$). Formation of the excited triplets and ground states is so exergonic that both processes lie in the inverted Marcus region (Fig.11).

In the case of rubrene, the above mechanistic scheme must be somewhat amended. Taking into account the energies of the rubrene excited states, it becomes clear that an additional process should be added to the reaction scheme. The energy of the lowest rubrene triplet $E_3 = 1.15\,\mathrm{eV}$ [125, 126]. The energy of the lowest rubrene singlet E_1 is equal to 2.29 eV [127] giving $2E_3 \approx E_1$. It can be concluded that the rates of the formation of two neighboring triplets,

$$\mathrm{R}^+ + \mathrm{R}^- \xrightarrow{k_{\mathrm{TT}}} {}^3\mathrm{R}^* + {}^3\mathrm{R}^* \xrightarrow{k_{\mathrm{upc}}} \mathrm{R} + {}^1\mathrm{R}^* \longrightarrow \mathrm{R} + \mathrm{R} + hc\tilde{\nu}_{\mathrm{f}} \tag{44}$$

and the rate of direct formation of the excited singlet (reaction (34)) should be similar. The formation of two geminate triplets leads to an efficient triplet–triplet annihilation (TTA). This process can be also treated as a pseudo-first-order reaction (primary TTA) if the up-conversion takes place before the triplets formed are separated. Of course, the triplets produced directly in reaction (35) or not up-

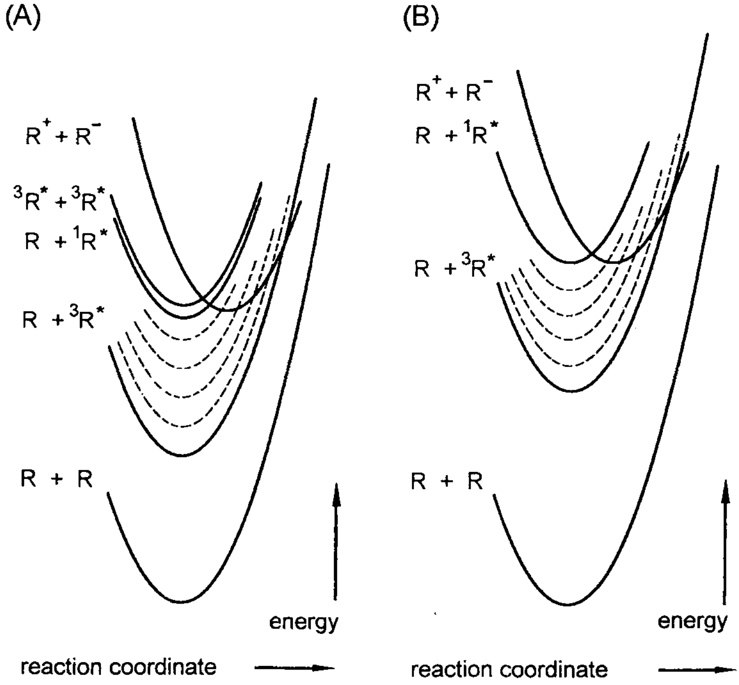

Fig. 11. Reaction coordinate diagram for ECL system involving rubrene (A) and 9,10-diphenylanthracene (B). Potential energy curves are presented in the zero-order approximation, without removing the degeneracy at the crossing points of the potential energy curves. Broken lines represent the vibronically excited triplet state.

converted in primary TTA may also take part in the triplet–triplet annihilation (real bimolecular, secondary TTA according to reaction (37)). Such a process leads, however, to much less efficient formation of the excited singlet states. The ECL efficiencies ϕ_{ecl} reported for both hydrocarbons are fairly large (up to a few percent), at least an order of magnitude greater than those found for ECL processes occurring according to a "pure" T-route. This strongly suggests that the emitting species (excited singlets) are formed directly by electron transfer between R^- and R^+. In the case of rubrene this was additionally supported by analysis of the results from the ECL transient studies [123].

The Gibbs energies released during the annihilation of DPA or rubrene ions (calculated from the difference $E^\circ_{\mathrm{red}} - E^\circ_{\mathrm{ox}}$ with correction for $w_r(r_{12})$) seem to be independent of solvent polarity. Thus, the observed solvent effect on ϕ_{ecl} can hardly be explained by changes in the reaction driving forces. On the other hand, a correlation between ϕ_{ecl} and the solvent polarity parameter (the Pekar factor, $1/n^2 - 1/\varepsilon$) has been found for rubrene and DPA. For example, this relationship in the case of rubrene is shown in Fig. 12. The Pekar factor describes the influence of the medium on the outer (solvent) reorganization energy. The observation mentioned above strongly suggests that the Marcus theory may be useful in the quantitative description of the electrochemiluminescence of rubrene as well as of DPA.

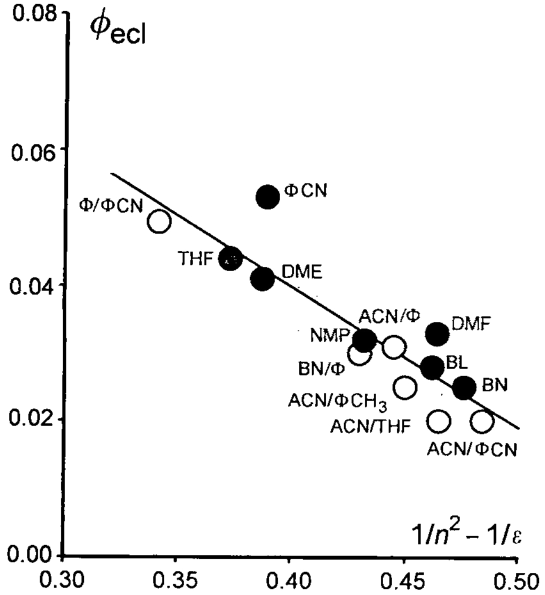

Fig. 12. Rubrene ECL efficiency (ϕ_{ecl}) as a function of the solvent polarity parameter (Pekar factor ($1/n^2 - 1\varepsilon$)) in (•) single and (o) mixed 1:1 solvents. Solvent name abbreviations: ACN, acetonitrile; BL, γ-butyrolactone; BN, butyronitrile; DME, 1,2-dimethoxyethane; DMF, *N,N*-dimethylformamide; NMP, *N*-methylpyrrolidone; THF, tetrahydrofuran; Φ, benzene; ΦCH$_3$ toluene; ΦCN, benzonitrile. Adapted from [123].

As discussed above, the experimental values of the excited-state yields ϕ_{es} are connected to competition between the parallel electron transfer processes. To a first approximation, in the case of DPA the ϕ_{ecl} is given by the ratio of the rate constants of reactions (33), (34) and (35):

$$\phi_{ecl} = \phi_{es}\phi_o = k_1/(k_1 + 3k_3 + k_0) \tag{45}$$

In Eq. (45) unimolecular reaction rates are introduced. They arise from the assumption of similar structures of the precursor complex for all three reaction channels, which seems to be allowed in the view of the minimum energy and maximum orbital overlap rules. The reaction rate, k_3, corresponding to population of the excited triplet, is multiplied by the statistical factor relating to spin multiplicity.

The reaction mechanism of excited singlet formation in rubrene ECL seems to be a superposition of two parallel processes. It is produced directly in the electron transfer reaction and/or in the efficient triplet–triplet annihilation within the geminate triplet pair. Thus, in the rubrene ECL system ϕ_{ecl} is the sum of efficiencies for the separate reaction pathways and it can be described as follows:

$$\phi_{ecl} = \phi_o\phi_s + \phi_o\phi_{TT}\,\phi_{TTA} \tag{46}$$

where ϕ_{TT} and ϕ_{TTA} are the fractions of electron transfer events that produce a triplet pair (via reaction (44)) and a contact triplet-pair-converting efficiency to an excited singlet; ϕ_s is the fraction of electron transfer producing an excited singlet (via reaction (34)). According to Eqs. (47) and (48), both ϕ_s and ϕ_{TT} are given by the ratio of the rate constants for electron transfer processes producing the excited-state and the ground-state products:

$$\phi_s = k_1/(k_1 + 3k_3 + 9k_{TT} + k_0) \tag{47}$$

and

$$\phi_{TT} = 9k_{TT}/(k_1 + 3k_3 + 9k_{TT} + k_0) \tag{48}$$

In Eqs. (47) and (48) the factor 9 connected to the k_{TT} rate may be not exactly correct. For two interacting triplets nine encounter pair spin states (which constitute the sublevels of encounter pairs with quintet, triplet, and singlet multiplicities) are formally possible. However, two from the quintet sublevels (with the spin quantum numbers ± 2) may not be directly accessible because of the spin conservation rule. If so, the factor 9 should be replaced by 7. Use of Eq. (48) with the factor 9 may lead to some overestimation of ϕ_{TT}. Triplet–triplet annihilation can also produce either triplets, singlets, or quintets. With the usual assumption that the formation of rubrene in the excited quintet state is energy-forbidden, the spin statistics predict an average yield of 1/4 singlet per triplet pair. In most cases such a large efficiency cannot be obtained. This is because some of the triplet–triplet pairs are able to dissociate into separate reactants before the up-conversion takes place. The measurements of the temperature dependence of ϕ_{ecl} (described in [123] with the results shown in Fig. 13) support this conclusion. The most important feature of Fig. 13 is that ϕ_{ecl} initially increases as the temperature is reduced, goes through a maximum and then decreases at lower temperatures. The trivial explanation that the rubrene fluorescence quantum yield ϕ_0 increases at lower temperatures can be excluded because ϕ_0 is already almost

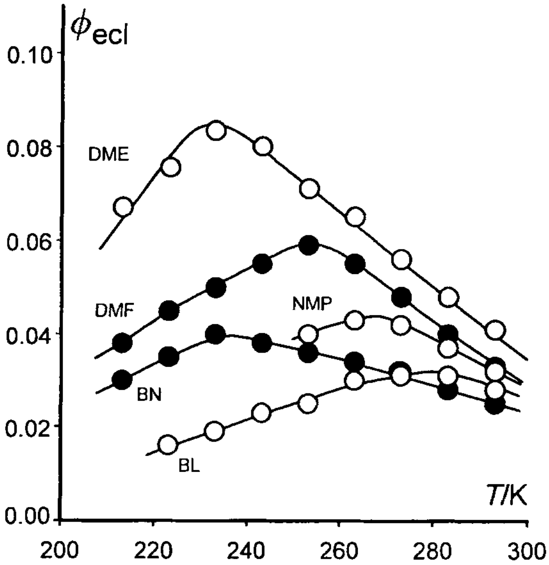

Fig. 13. Rubrene ECL efficiency (ϕ_{ecl}) as a function of the temperature (T) in 1,2-dimethoxyethane (DME) N,N-dimethylformamide (DMF), N-methylpyrrolidone (NMP), butyronitrile (BN) and γ-butyrolactone (BL) solutions. Adapted from [123].

unity at room temperature. The fact that the position of the temperature $T_{\max}$ of the ϕ_{ecl} maxima depends on the solvent viscosity η plays a key role in the understanding of the reaction mechanism. The dissociation of the triplet–triplet pair into separate products is a diffusion-controlled process. Thus the efficiency of the primary TTA will be governed by the ratio of the up-conversion rate k_{upc} to the separation rate k_{sep} and will increase with medium viscosity and/or as the temperature decreases. The temperature dependence of ϕ_{ecl} also becomes understandable. Reduction of the temperature decreases the efficiency of formation of both the excited rubrene singlet formed directly and the contact triplet–triplet pair (reactions (34) and (44) are thermally activated). However, reduction of the temperature increases the efficiency of the triplet–triplet up-conversion (primary TTA). These two effects act in the opposite direction, leading to the appearance of the maximum on the plot of ϕ_{ecl} vs. temperature.

The ECL behavior of rubrene and DPA seems to be qualitatively understood within the context of the Marcus electron transfer model for electrochemiluminescence. The most important question is whether the experimentally obtained results can be interpreted quantitatively in the terms of the Marcus theory. Unfortunately, only some of the parameters (Gibbs energies) in the expression for the electron transfer rate constant may be evaluated straightforwardly from pertinent electrochemical and spectroscopic data. Appropriate values of the other terms are not directly available, but some conclusion can be drawn by taking into account the literature data for other similar systems. Relatively large values of V_{12} are characteristic for aromatic hydrocarbons. For example, values of V_{12} in the range 0.05–0.10 eV were found for the electron exchange between anthracene and the anthracene radical anion [128, 129]. In the alternate hydrocarbon approximation this range of V_{12} values is expected for electron exchange involving other hydrocarbons (between the parent molecule and the corresponding radical anion or the corresponding radical cation). This is also true for electron transfer reactions involving the excited states. Thus, relatively large values of V_{12} are expected for an electron transfer reaction in the DPA and rubrene ECL system, even taking into account that in these particular cases the reaction takes place at a somewhat larger distances because of the steric effects of the phenyl rings almost perpendicular to the anthracene or tetracene kernels.

The rates of direct excited singlet formation, occurring in the normal Marcus region for both the ECL systems discussed with $\Delta G_{\mathrm{l}} \approx 0$, can be expressed as follows:

$$k_{\mathrm{l}} = \frac{1}{\tau_{\mathrm{L}}} \sqrt{\frac{\lambda_{\mathrm{o}}}{16\pi RT}} \exp\left(-\lambda_{\mathrm{o}}/4RT\right) \qquad (49)$$

Equation (49) describes the rate of formation of the rubrene geminate triplet–triplet pair in a similar way. Strongly exergonic formation of the excited triplets and ground states lies in the inverted Marcus region and therefore Eq. (24) must be applied. In both cases, vibronic excitation of the reaction products can take place, leading to an increase in the electron transfer rate. The electron transfer rate constitutes a superposition of a solvent-dynamics-controlled contribution and a nonadiabatic contribution depending on the V_{12} and S values. A detailed discussion of this problem has been presented in [55], with the main conclusion that the electron transfer rate achieves its maximum over a wide range of the reaction exothermicity (for ΔG up to ca. $-1.5\,\text{eV}$ for acetonitrile solutions with the parameters $V_{12} = 0.10\,\text{eV}$, $S = 1$ and $\tau_L = 0.2\,\text{ps}$) and drops sharply for $\Delta G < -1.5\,\text{eV}$. Thus, the less exergonic formation of the excited triplets is expected to occur at the maximum accessible rate:

$$k_3 = \frac{1}{\tau_L}\sqrt{\frac{\lambda_o}{16\pi RT}} \tag{50}$$

The more exergonic formation of the ground states is inhibited and it is expected to occur at the rate $k_0 \ll k_3$. In view of these considerations and taking into account the fact that the ECL efficiency does not exceed a few percent ($k_1 < k_3$), Eq. (47) can be further simplified. Now efficiencies of the direct formation of the excited singlet are expressed as follows:

$$\phi_s = \frac{k_1}{3k_3} = \frac{1}{3}\exp(-\lambda_o/4RT) \tag{51}$$

Equation (51) may be directly applied in the interpretation of ECL efficiency data for DPA. With the ECL efficiencies of this system [122] one can obtain λ_o values in the range 0.13–0.22 eV. Similar values are obtained from the calculation according to Eq. (6). Assuming the effective radii of both DPA radicals $r_1 = r_2 \approx r = 0.48\,\text{nm}$ (from the molar volume of DPA) and reaction distance $r_{12} = 0.55\,\text{nm}$, the following values can be obtained: $\lambda_o = 0.15\,\text{eV}$ in 1,2-dimethoxyethane and 0.20 eV in acetonitrile solutions ($\lambda_o = 0.38\,\text{eV}$ in *N,N*-dimethylformamide solutions has been found in [130] for electron exchange between anthracene and its radical anion). These calculations must be treated only as a semiquantitative approach until the systematic temperature study of ϕ_{ecl} efficiency has been done, especially as the DPA ECL system has been studied only in a limited number of solvents.

As mentioned above, the ECL system containing rubrene is somewhat more complicated, but has been studied in more detail. In the case of rubrene the primary triplet–triplet annihilation cannot be neglected and:

$$\phi_s = \left[\frac{1}{3} + \frac{3}{4}\phi_{TTA}\right]\exp(-\lambda_o/4RT) \tag{52}$$

In the case of full triplet–triplet up-conversion ($\phi_{TTA} = 1$) this leads to:

$$\phi_s = \frac{13}{12}\exp(-\lambda_o/4RT) \tag{53}$$

If no triplet–triplet up-conversion takes place ($\phi_{TTA} = 0$), Eq. (52) is again simplified to Eq. (51). In the intermediate cases (rate of triplet–triplet up-conversion comparable with rate of separation), the final expression is more complicated:

$$\phi_s = \left[\frac{1}{3} + \frac{3}{4}\frac{k_{\mathrm{upc}}}{k_{\mathrm{upc}} + k_{\mathrm{sep}}}\right] \exp(-\lambda_o/4RT) \approx \left[\frac{1}{3} + \frac{3}{4}(1 - k_{\mathrm{sep}}/k_{\mathrm{upc}})\right] \exp(-\lambda_o/4RT) \tag{54}$$

In the case of rubrene Eq. (54) allows for the quantitative analysis of the relation between T and ϕ_{ecl} with more detailed discussion of the parameters λ_o and k_{upc}. The experimental results of the ECL efficiency (at low temperatures, below $T_{\max}$) can be linearized in $\ln(\phi_{\mathrm{ecl}})$ vs. $1/T$ coordinates. The intercept values (in the range 0.88–1.05) lead to the conclusion that at low temperatures the contact triplet–triplet pair is fully converted in the emissive singlet state of rubrene, with the efficiency predicted by simple spin statistics (factor 1/4), also indicating that the up-conversion rate k_{upc} is large compared with the separation rate k_{sep}. Thus, according to Eq. (53) the slopes obtained may be simply attributed to $\lambda_o/4$. The observed sequence agrees well with that expected from the values of the Pekar factor $(1/n^2 - 1/\varepsilon)$. With the assumption that λ_o is constant, the pre-exponential factor (PF) in Eq. (54) may be simply evaluated over the whole temperature range. At room temperature PF values found in 1,2-dimethoxyethane, *N,N*-dimethyformamide and butyronitrile lie in the range 0.30–0.36, which is in agreement with the value of 1/3 expected for the case of a fully dissociative triplet–triplet encounter pair. In very viscous γ-butyrolactone (1.74 cP at 293 K) their larger PF values suggest that in this particular case the triplet–triplet up-conversion has already take place at room temperature. Resuming, the statistical factors evaluated as described above depend on temperature, changing from near unity (at low temperatures) to 1/3 (at room temperature); this indicates that the T dependence of ϕ_{ecl} may be described in the terms of Eq. (54). According to Eq. (54) the "effective" PF value may be approximately described as follows:

$$\mathrm{PF} = \frac{13}{12} - \frac{3}{4}\frac{k_{\mathrm{sep}}}{k_{\mathrm{upc}}} \tag{55}$$

Figure 14 shows the relationship between PF values and the rate of separation calculated from the standard Debye equation ($k_{\mathrm{sep}} = k_{\mathrm{diff}} = 8RT/3$). The slope of the solid line corresponds to the value of $1 \times 10^{10}\,\mathrm{M}^{-1}\,\mathrm{s}^{-1}$, which agrees well with the triplet–triplet up conversion rates found for aromatic hydrocarbons [131]. The k_{upc} estimated on this way seems to be constant in all solvents as well as over the whole range of temperatures studied; possible differences were less than the experimental errors.

The considerations presented above strongly suggest that triplet–triplet up-conversion is almost negligible at room temperature in low-viscosity solvents (with $\eta < 1$ cP). Thus, the ECL efficiencies at 293 K allow for evaluation (using Eq. (51)) of the outer reorganization energies λ_o as shown in Fig. 15, with the solid line passing through the origin of the $(1/n^2 - 1/\varepsilon)$ and λ_o coordinates. The evaluated λ_o values are relatively small (similarly to the DPA ECL system) but comparable with those found for the electron self-exchange between tetracene and the tetracene radical anion [132].

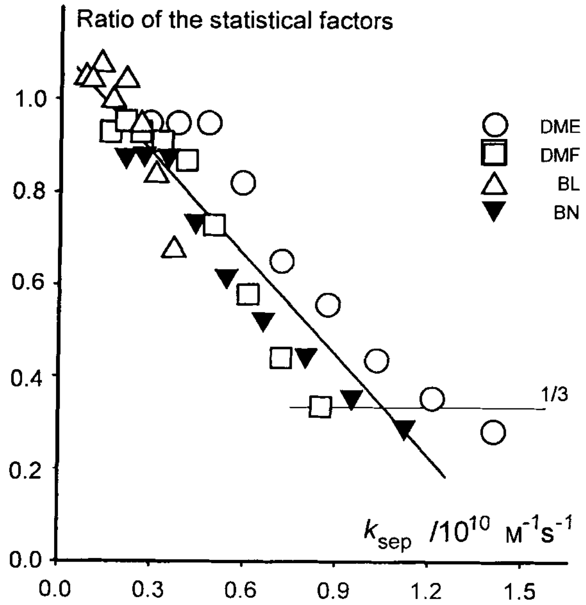

Fig. 14. Ratio of the pre-exponential (statistical) factors in the kinetic description of rubrene ECL efficiency as a function of the separation rate (k_{sep}) in 1,2-dimethoxyethane (DME), *N,N*-dimethylformamide (DMF), butyronitrile (BN) and γ-butyrolactone (BL) solutions. The solid line represents the fit with triplet-triplet up-conversion rate $k_{upc} = 1 \times 10^{10}\,M^{-1}s^{-1}$. Adapted from [123].

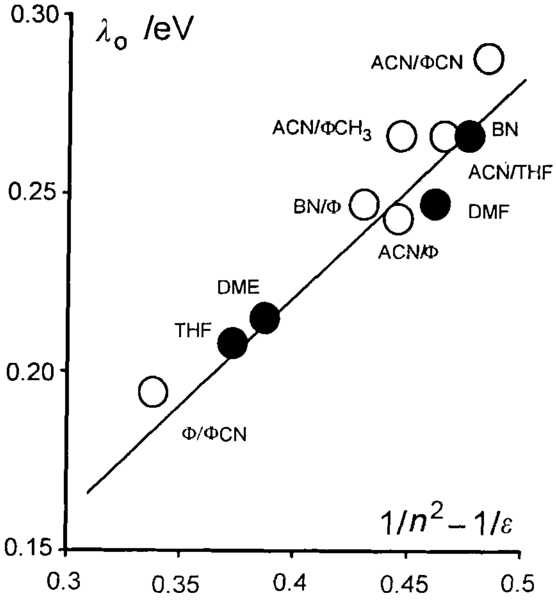

Fig. 15. Outer reorganization energy λ_o for the rubrene ECL system as a function of the solvent polarity parameter (Pekar factor ($1/n^2$–$1/\varepsilon$)), in (•) single and (o) mixed 1:1 solvents. For the solvent name abbreviations, see Fig. 12. Adapted from [123].

The reaction mechanism described above also allows an explanation for the influence of the magnetic field on ECL efficiencies. In the case of DPA, the absence of magnetic field effects [104, 114] in ECL supports the dominance of the S-route. Moreover, results reported in [104, 112, 133] for the rubrene ECL system are not in conflict with the reaction mechanism proposed; it can be explained by assuming that triplet–triplet annihilation (within a triplet encounter pair) is being altered in the magnetic field. In a low-viscosity solvent (e.g., 1,2-dimethoxyethane or tetrahydrofuran) such an alteration should be relatively small because the separation of triplet pairs is very fast. In very viscous media (e.g., *N,N*-dimethylformamide at low temperatures) such an alteration cannot increase the efficiency of the triplet–triplet up-conversion because this process is already fast compared with the separation rate. In the case of intermediate viscosities (e.g., benzonitrile or *N,N*-dimethylformamide at room temperature), application of the magnetic field leads to enhancement of the ECL efficiency because both the up-conversion and separation processes have comparable rates.

4.2 Intramolecular Donor–Acceptor Systems

The S-route for electrochemical generation of the excited states is expected to be favored for a system where the luminescence originates from the low-lying excited states. For organic compounds, it may be expected that some of the systems which exhibit a large Stokes shift should involve the direct formation of the emitting species. A large Stokes shift is observed for those molecules which change their structure greatly after excitation. Intramolecular charge transfer in systems containing large π-aromatic donor (D) and acceptor (A) subunits may be an example. In some cases, when A and D are linked together by a formally single bond, the most favorable conformation of the ground state does not deviate very much from the decoupled, perpendicular one, and the electrochemical behavior corresponds to that expected from the electrochemical properties of A and D alone [134–138]. Thus the possible problems caused by radical-ion instabilities may be ruled out by the appropriate choice of both A and D subunits.

Similarly, the electronic absorption indicates only a weak electronic interaction between A and D [139–142]. Typically the UV–VIS absorption spectra of the molecules studied are a superposition of the bands attributed to the absorption of donor and acceptor subunits alone. In some cases a new band with a charge-transfer character appears [139, 140]. This band can be separated if the parent bands (of both A and D subunits) are subtracted from the spectrum [143]. With the appropriate values of the absorption and emission maxima, the energies of the emitting species can be re-evaluated.

Such excited species are intramolecular charge-transfer states (the electron transfer from D to A occurs after photoexcitation). It has been shown that the primary excited singlet (with excitation localized on the acceptor or donor subunit) undergoes a solvent-assisted femto/picosecond relaxation to a polar charge-transfer state. The intramolecular charge transfer leads to a large Stokes shift in the fluorescent states. These states are very polar, strongly stabilized in polar solvent, and situated energetically lower than the locally excited singlets of both subunits A and D. Their depopulation is a superposition of the radiative and radiationless electron transfer in the inverted Marcus region. The radiationless charge recombination is controlled by two competitive mechanisms: internal conversion to the ground state and intersystem crossing (through a nearly isoenergetic charge-transfer triplet state) to the triplet

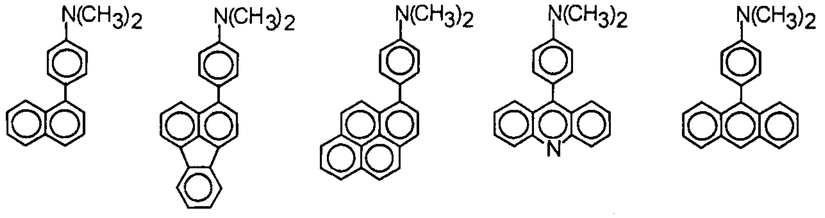

NDMA FDMA PDMA BDMA ADMA

Fig. 16. Examples of the intramolecular donor–acceptor system: aryl derivatives of *N,N*-dimethylaniline. NDMA, 4-(1-naphthyl)-*N,N*-dimethylaniline; FDMA, 4-(3-fluoranthyl)-*N,N*-dimethylaniline; PDMA, 4-(1-pyrenyl)-dimethylaniline; BDMA 4-(9-acridynyl)-*N,N*-dimethylaniline; ADMA, 4-(9-anthryl)-*N,N*-dimethylaniline.

manifold (with the excitation localized on the lowest locally excited triplet of the acceptor or donor subunit). If A and D are large aromatic subunits, the intramolecular electron transfer is associated with the flattening of the molecule in the excited state [68]. The large values of the excited state dipole moments (typically between 15 and 20 D [139–142, 144] as well as transient absorption spectra [145] are consistent with a radical ion pair description of the excited state. Because of the interaction between A and D (in the excited state) many of these A–D systems also exhibit a high fluorescence quantum yield. The observed optical transition moment M corresponds to the contribution involving the high permanent dipole moment of the charge-transfer configuration and the electronic delocalization interaction between both A and D entities [146, 147].

The electrochemical behavior of the A–D compounds (selected structures are shown in Fig. 16) agrees well with that expected on the basis of the electrochemical properties of both the donor and the acceptor moieties [134–138]. That they can be reversibly reduced and oxidized to the corresponding radical cation and anion has been ascertained by cyclic voltammetry. The standard reduction potentials, E°_{red}, are close to the values found for the parent aromatic hydrocarbons or acridine [124]. In a similar way, the standard oxidation potentials, E°_{ox}, are congruent with those found for the corresponding amines [148]. The electrochemical reaction of A–D compounds can be formulated as follows:

$$\text{A-D} + \text{e}^- \rightleftharpoons \text{A}^-\text{-D} \tag{56}$$

$$\text{A-D} - \text{e}^- \rightleftharpoons \text{A-D}^+ \tag{57}$$

After electrochemical reduction an electron is placed in the lowest unoccupied molecular orbital (LUMO) of the acceptor subunits of A–D. In the electrochemical oxidation an electron is removed from the highest occupied molecular orbital (HOMO) of the donor moiety.

In an ECL experiment the application of a triple-potential-step sequence causes very intense and bright emission. The ECL emission bands, exhibiting charge-transfer character, agree well with those observed with photoexcitation. The Feldberg plot analysis indicates that the emissive excited state is formed directly by electron transfer between A^-–D and A^-–D. In most cases, the emitted light intensities were found to be linear vs. $(t_f/t_f)^{1/2}$ according to Eq. (43); thus in the time scale of ECL experiments only the reactions of anion–cation annihilation are dominant:

$$A^-\text{-D} + \text{A-D}^+ \rightarrow \text{products} \tag{58}$$

The ϕ_{ecl} values seem to be unaffected by any additional processes and may be directly related to the yields of generation of excited state ϕ_{es} by Eq. (30). The large ϕ_{es} values (up to 0.21) reveal clearly that formation of the excited charge-transfer state is competitive with the formation of other excited and ground states.

In the present cases, the Gibbs energies ΔG_0 calculated from the difference in the redox potential for oxidation and reduction (according to Eq. (38)) are between −2.31 and −3.23 eV. Thus, of all locally excited states (from molecules constituting an A–D entity), only the locally excited triplets for the given A subunits (with energies $E_3 = 1.80$, 1.94, 2.09, 2.30, and 2.64 eV for anthracene, acridine, pyrene, fluoranthene, and naphthalene, respectively [102]) can be accessed. The other locally excited states cannot be directly populated, because their energy levels are much higher than the Gibbs energies for the annihilation of radical ions. In a similar way ΔG_{CTS} and ΔG_{CTT} for reactions (62) and (63) may be evaluated, if the corresponding energies of both (singlet and triplet) excited intramolecular charge-transfer states are available. The energy of these states can be expressed as follows [149–151]:

$$E_{CTS} \approx E_{CTT} \cong F(E^\circ_{ox} - E^\circ_{red}) + W(r_{in}) \tag{59}$$

where $w(r_{in})$ is the Coulomb energy that is gained when the two ions (A^- and D^+) are brought together (with the separation distance r_{in}). Equation (59) neglects the destabilizing and stabilizing interactions between the intramolecular charge-transfer state and the ground and locally excited states. Theoretical consideration of the electronic structure of exciplexes [60–63] leads to the conclusion that such interactions are really responsible for the observed values of the optical transition moments, but the corrections to the energy of the excited charge-transfer state are negligible. Both stabilizing and destabilizing, rather small, interactions are working in opposite directions. In a similar way it may be concluded that the destabilizing interaction between the intramolecular triplet charge-transfer state and the energetically lower-lying locally excited triplet $^3(A^*\text{–D})$, and the stabilizing interaction with the energetically higher other local triplets, e.g., $^3(\text{A–D}^*)$, do not lead to remarkable changes in the energy of $^3(A^-\text{–D}^+)$. Phosphorescence [152] as well as triplet–triplet absorption [142] studies indicate that the energy levels of local triplets are not markedly affected by any interaction with the intramolecular charge-transfer state. The Coulombic stabilization energy in the radical ion pairs (i.e., the excited charge-transfer state) $w(r_{in})$ is roughly constant for all systems

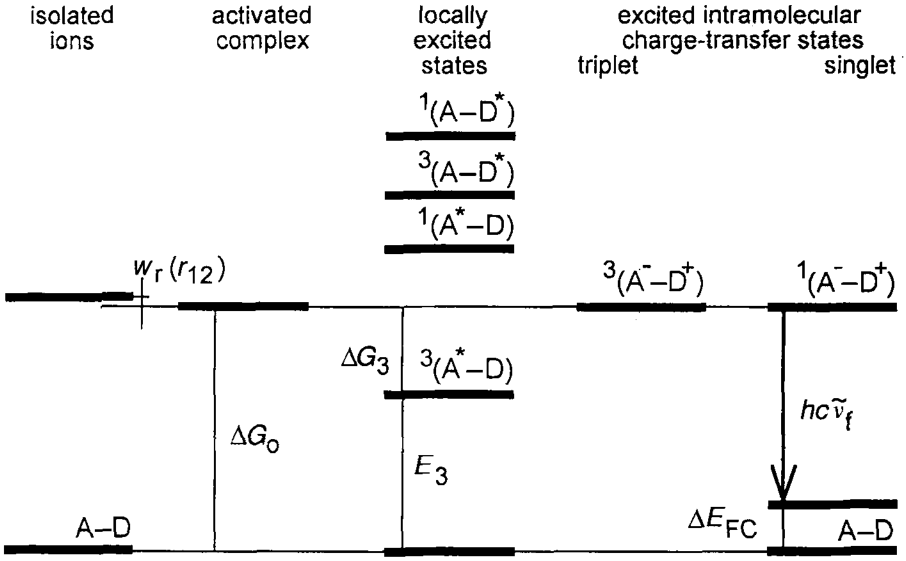

Fig. 17. Schematic representation of the energy levels for the ECL processes of intramolecular donor–acceptor systems.

studied, and according to Eq. (39) nearly equal to $w(r_{12})$ because $r_{in} \approx r_{12}$. Thus the expected values of ΔG_{CTS} and ΔG_{CTT} should be nearly equal to zero ($\Delta G_{CTS} \approx \Delta G_{CTT} \cong \Delta G_{CT} \approx 0$). Analysis of the charge-transfer absorption and emission bands leads to the same conclusion [138]. The energy of the emissive intramolecular charge-transfer state may also be estimated by considering the energy of the Franck–Condon ground state reached in the emission. The nonpolar Franck–Condon state is more energetic than the equilibrated ground state by the energy difference ΔE_{FC}, which is the sum of two contributions, the first associated with nonequilibrium solvation energy, and the second corresponding to the reorganization of intramolecular bonds and angles. E_{CTS} values obtained in this way [68] agree with those calculated according to Eq. (59) within ± 0.05 eV.

The considerations presented above made it possible to construct the energy diagram for the ECL processes studied, as shown in Fig. 17. They also allowed the conclusion that the formation of both $^1(A^-–D^+)$ and $^3(A^-–D^+)$ corresponds to isoenergetic (resonance) electron transfer between A^-–D and A–D^+. The formation of $^3(A^*–D)$ is more exergonic; e.g., for FDMA and BDMA in acetonitrile solutions (with $\Delta G_3 = -0.19$ and -0.37 eV, respectively) it occurs in the normal Marcus region. For other ECL systems studied (with $\Delta G_3 < -0.69$ eV) it belongs to the inverted Marcus region (because the λ term typically lies in the range 0.2–0.6 eV for aromatic molecules [94]).

The mechanism of ECL processes of A–D molecules can be formulated as follows: in the diffusion-controlled reaction A^-–D and A–D^+ form an activated complex $A\text{-}D^{+}\cdots A^{-}\text{-}D$ for which four reaction pathways are possible:

$$A\text{-}D^{+}\cdots A^{-}\text{-}D \xrightarrow{k_0} A\text{-}D + A\text{-}D \tag{60}$$

$$A\text{-}D^{+}\cdots A^{-}\text{-}D \xrightarrow{k_3} A\text{-}D + {}^3(A^{*}\text{-}D) \tag{61}$$

$$A\text{-}D^{+}\cdots A^{-}\text{-}D \xrightarrow{k_{CTS}} A\text{-}D + {}^1(A^{-}\text{-}D^{+}) \tag{62}$$

$$A\text{-}D^{+}\cdots A^{-}\text{-}D \xrightarrow{k_{CTT}} A\text{-}D + {}^3(A^{-}\text{-}D^{+}) \tag{63}$$

where ${}^3(A^{*}\text{–}D)$ represents the locally excited triplets. ${}^1(A^{-}\text{–}D^{+})$ and ${}^3(A^{-}\text{–}D^{+})$ are the excited intramolecular change-transfer states, emissive singlet, and nonemissive triplet, respectively. The emissive ${}^1(A^{-}\text{–}D^{+})$ state is deactivated with light emission, but the nonemissive ${}^3(A^{-}\text{–}D^{+})$ state undergoes nonradiative relaxation to the lower-lying ${}^3(A^{*}\text{–}D)$ and later to A–D [144]:

$${}^1(A^{-}\text{-}D^{+}) \longrightarrow A\text{-}D + hc\tilde{\nu}_f \quad (\text{with efficiency } \phi_o) \tag{64}$$

$${}^3(A^{-}\text{-}D^{+}) \longrightarrow {}^3(A^{*}\text{-}D) \longrightarrow A\text{-}D \tag{65}$$

The very weak emission from ${}^3(A^{*}\text{–}D)$ (phosphorescence $hc\tilde{\nu}_{ph}$) cannot be observed in liquid solutions at room temperature. Similarly, the efficiency of the annihilation of both excited triplets (local and charge-transfer) was too low to be observed.

The yield of production of the emissive excited state is given by the ratio of the rate constants for the electron transfer processes producing the excited-state and the ground-state products, respectively. Thus, at least to a first approximation, the efficiency is given by:

$$\phi_{es} = \frac{k_{CTS}}{k_O + 3k_3 + k_{CTS} + 3k_{CTT}} \tag{66}$$

where k_O, k_3, k_{CTS}, and k_{CTT} are the rate constants of the processes (60), (61), (62), and (63) respectively. In Eq. (66) the statistical factors from the spin multiplicity (of the given reaction product) are introduced again. The formation of the ground state is so highly exergonic that it should lie far into the inverted Marcus region, and therefore it should be relatively slow and negligible. It is expected not to be as slow as predicted by the simple Marcus theory, but surely the rate constant k_O is small in comparison with the sum $(3k_3 + k_{CTS} + 3k_{CTT})$ in Eq. (66). On the other hand, the energy splitting between ${}^1(A^{-}\text{–}D^{+})$ and ${}^3(A^{-}\text{–}D^{+})$ should be small (as discussed above); thus, $k_{CTT} \approx k_{CTS} \equiv k_{CT}$. Consequently Eq. (66) may be further simplified:

$$\phi_{es} = \frac{k_{CT}}{3k_3 + 4k_{CT}} \tag{67}$$

Appropriate values of these rates are not directly available, but a quantitative estimate is possible in view of the experimental values of ECL efficiencies that have

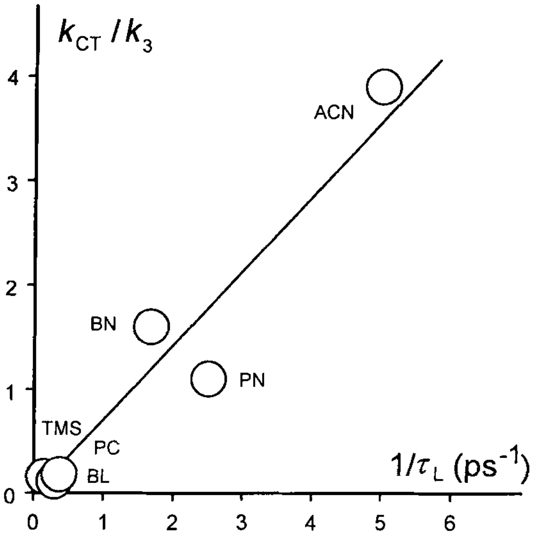

Fig. 18. Values of the k_{CT}/k_3 ratio (evaluated from the experimental efficiencies of formation of the excited state) as a function of the solvent longitudinal relaxation time τ_L. Data for 4-(9-anthryl)-*N*,*N*,3,5-tetramethylaniline in acetonitrile (ACN), propionitrile (PN), butyronitrile (BN), propylene carbonate (PC), sulfolane (TMS) and γ-butyrolactone (BL) solutions. Adapted from [153].

been obtained. A nearly linear correlation between the ratio of the rate constants k_{CT}/k_3 and the reciprocal of the longitudinal relaxation time τ_L of the given solvent was found [153] (according to Eq. (67), $k_{CT}/k_3 = 3\phi_{es}/(1 - 4\phi_{es})$), as shown in Fig. 18. Such a correlation cannot be accidental and cannot be attributed to changes in ΔG_{CT} and ΔG_3 (the driving forces for the formation of $^1(A^- – D^+)$, $^3(A^- – D^+)$ and $^3(A^* – D)$ are nearly constant in all of the solvents used [153]) or to changes in λ_o. Outer reorganization energy dependence on the solvent polarity parameter – the Pekar factor $1/n^2 - 1/\varepsilon$ – which varied from 0.529 for acetonitrile to 0.431 for sulfolane, is only marginal. Moreover, the V and λ_i terms are also expected to be independent of solvent. It may be concluded that the formation of the excited intramolecular charge-transfer state is controlled by the solvent dynamics (with the corresponding value of $V_{CT} > 0.02$ eV), and that the reaction rate k_{CT} may be expressed by Eq. (49) (because $\Delta G_{CT} \approx 0$). It may also be concluded that the formation of $^3(A^* – D)$ is nonadiabatic, and Eq. (12) may be used for the calculation of the reaction rate k_3 (with $j \leq 5$). ECL data for other intramolecular donor–acceptor systems (shown in Fig. 19) indicate that the rate k_3 depends upon the reaction exothermicity ΔG_3 in a manner consistent with the Marcus inverted region [138] (according to Eq. (67) $k_3/k_{CT} = (1 - 4\phi_{es})/3\phi_{es}$).

It was possible [138] to evaluate those rates (and also to predict the experimentally observed ϕ_{es}) from pertinent electrochemical and spectroscopic data. The necessary thermodynamic quantities may be evaluated using the literature data for relatively well-understood electron exchange between the neutral species (A or D) and its own radical anion or cation (A^- or D^+, respectively), but a somewhat different approach seems to be more accurate. The quantities needed (λ_i, λ_o, and V_3) are chosen to obtain the best fit between experimentally found and theoretically predicted ϕ_{es} values. Collection of sufficient experimental data makes it possible to use such a procedure, although the number of parameters introduced into the calculation is still

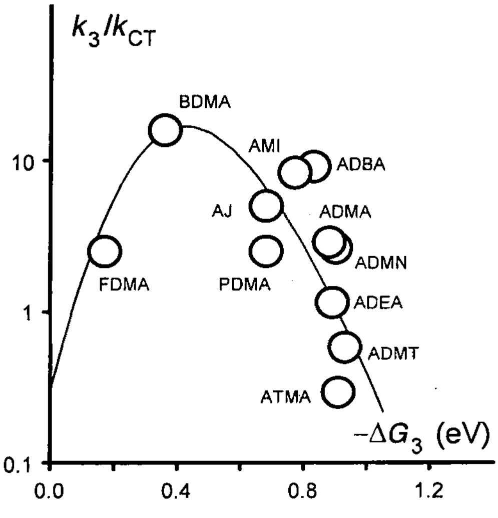

Fig. 19. Values of the k_3/k_{CT} ratio (evaluated from the experimental efficiencies of formation of the excited state in acetonitrile solutions) as a function of the exothermicity of formation ΔG_3 of the localy excited triplet. ADMA, BDMA, FDMA, and PDMA are the A–D compounds with structures presented in Fig. 16. Other A–D system abbreviations denote 4-(9-anthryl) derivatives of *N,N*-diethylaniline (ADEA), *N,N*-di-n-butylaniline (ADBA), *N,N*-dimethyl-1-naphthlamine (ADMN), *N*-methylindoline (AMI), jullolidine (AJ), *N,N*,3-trismethylaniline (ADMT), and *N,N*,3,5-tetramethylaniline (ATMA). Adapted from [138].

rather high. This was done under the following additional assumptions:

- the V_3 and λ_i values are independent of the solvent
- in a given solvent the λ_o values are the same for both reaction channels
- λ_o depends on the solvent according to the Marcus equation
- $h\nu_i = 0.20$ eV (from the vibration frequencies of C–C and C–N bonds)

The best fit was obtained for the following values of the reorganization energies: outer, $\lambda_o = 0.40\,\text{eV}$ in acetonitrile solutions (and proportionally less in other solvents); inner, $\lambda_i = 0.05\,\text{eV}$ (and correspondingly, $S = 0.25$). The corresponding electronic coupling element, $V_3 = 0.007$ eV, was found to be distinctly smaller than V_{CT}.

The obtained results indicate that the matrix elements (V_{CT} and V_3) describing the coupling of the electronic states of the reactants with those of the products are different for both electron transfer processes contributing significantly to the overall reaction rate. This is understandable because different molecular orbitals are involved in the electron transfer reactions leading to excited intramolecular charge-transfer states and to locally excited triplets. In the formation of excited intramolecular charge-transfer states (reaction (62) and (63)) the electron is transferred from A^- in A^-–D to A in A–D^+ or from D in A^-–D to D^+ in A–D^+. The formation of locally excited triplets (reaction (61)) corresponds to electron transfer from A^- in A^-–D to D^+ in A–D^+. In the formation of the ground state (reaction (60)) the electron is also transferred from A^- in A^-–D to D^+ in A–D^+. This is shown in Fig. 20.

Of course, appropriate values of both electronic coupling elements, V_3 for reaction (61) and V_{CT} for reactions (62) and (63), are not directly available. However, semiquantitative discussion is possible in the view of data for other similar systems. For the electron transfer between anthracene and the anthracene radical anion, the corresponding coupling element $V_{AA} = 0.05$–$0.10\,\text{eV}$ [128, 129] is quite large. For

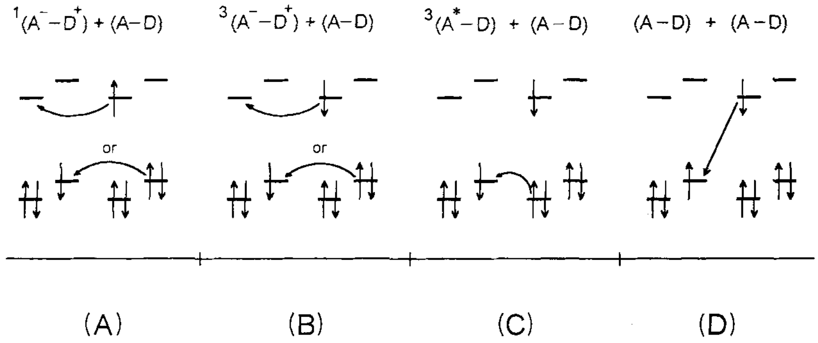

Fig. 20. Molecular orbital description for the electron transfer reactions within ECL processes of intramolecular donor–acceptor systems A–D to give (A) excited singlet intramolecular charge-transfer state; (B) excited triplet intramolecular charge-transfer state; (C) locally excited triplet; and (D) ground state. Adapted from [138].

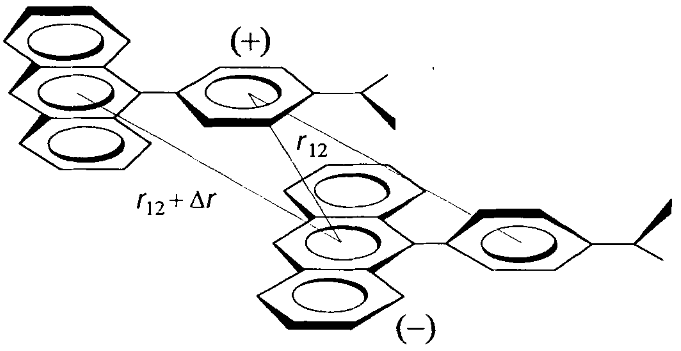

Fig. 21. Assumed structure of the activated complex in ECL processes of intramolecular donor–acceptor A–D systems involving aromatic amines. Adapted from [138].

other acceptor subunits studied (in A–D systems) the corresponding values of V_{AA} are not available in the literature, but are also expected to be high. The homogeneous electron self-exchange for aromatic amines was found to be nonadiabatic, with small values of $V_{DD} = 0.002–0.004\,\text{eV}$ [154]. With those values of V_{AA} and V_{DD}, and with the assumed structure of the activated complex (as in Fig. 21), V_3 and V_{CT} can be evaluated for both cross-reactions using the geometric mean approximation [155] (taking also into account the fact that different molecular orbitals are involved in the given electron transfer process). For the electron transfer producing locally excited triplets (reaction (61)), the electronic coupling element can be expressed as follows:

$$V_3 = (V_{AA}V_{DD})^{1/2} \tag{68}$$

The value of V_3 obtained lies in the range 0.01–0.02 eV. The experimentally found $V_3 = 0.007$ eV agrees well with the lower limit of the above range. The upper limit of V for electron transfer between A^- and D^+ may also be estimated on the basis of the emissive properties of the corresponding exciplex $A^- \cdots D^+$. As previously mentioned, the optical transition moment M of the given exciplex is related to the electronic coupling element V according to Cannon [60]:

$$M = V\mu_{CT}/E_{CT} \qquad (69)$$

where μ_{CT} are the static dipole moment and the energy of the given exciplex. For example, the corresponding values of $E_{CT} = 2.80$ eV, $\mu_{CT} = 25$ D and $M < 0.1$ D for the exciplex between pyrene and *N,N*-dimethylaniline (in polar solutions [61, 62]) lead also to the conclusion that $V < 0.01$ eV.

For the reactions producing the excited intramolecular charge-transfer states (reactions (62) and (63)), the electron transfer processes occur at the greater distance, $r_{12} + \Delta r$ (see Fig. 21). Since the electronic coupling elements decrease exponentially with distance, V_{CT} may be expressed as follows:

$$V_{CT} = (V_{AA} + V_{DD})\exp(-\beta\Delta r/2) \qquad (70)$$

with β equal to 10–12 nm^{-1}. The resulting V_{CT} with $\Delta_r = 0.2$–0.3 nm (from the assumed structure of the activated complex) lies in the range 0.01–0.02 eV. This is very close to the experimentally found $V_{CT} > 0.02$ eV. Only the dependence on the separation distance was considered in the estimation of V_{CT} (according to Eq. (70)), neglecting any effects of molecular orientation. It seems reasonable in the view of Cave and co-workers, and Helms et al. [156,157].

Values of λ_o and λ_i can also be predicted from experimental data concerning the electron exchange reactions between a neutral species (A and D) and its own radical anion or cation (A^- and D^+; respectively). For cross-reactions λ_o as well as λ_i were shown by Marcus to be the averages of the values for the self-exchange reactions between the radical anion or cation from one side, and the corresponding neutral molecule from the other. The λ_o values for aromatic hydrocarbons $\lambda_o(A/A^-)$ and aromatic amines $\lambda_o(D/D^+)$ lie in the ranges 0.32–0.43 eV [94] and 0.48–0.54 eV [158, 159], respectively. Thus, the expected λ_o is equal to 0.45 ± 0.05 eV (in acetonitrile solutions). The comparable range of λ_o is also provided by Eq. (6) (with r_{A^-} and r_{D^+} from the molar volumes of the corresponding A or D and $r_{12} = 0.5$ nm). Values of λ_o in the range 0.38–0.48 eV were also found for the intramolecular electron transfer within $^1(A^-\text{–}D^+)$ of the A–D studied (in acetonitrile solutions) [68].

In the case of aromatic amines, the change in the bond length between the amino group and the benzene ring is the most important. The shortening of this C–N bond (from 0.141 to 0.136 nm) is accompanied by distortion to a quinoid structure with co-planarity of the amino group and the phenyl ring. The energy required for these changes is of the order of 0.07–0.10 eV [159]. On the other hand, the crystallographic data for 1-(*p*-diethylanilino)naphthalene [139] indicate that such a quinoid structure is already present, at least partially, in the compounds studied. The diethylamino group is almost co-planar with the phenylene ring with the C–N bond length only

0.138 nm (in the unsubstituted *N,N*-diethylaniline, the corresponding length has a "normal" value of 0.143 nm [160]). This suggests that the structural changes in the donor subunit of A–D, accompanying oxidation to the radical cation, should be not very significant. The differences between the structures of the parent arenes (A in the A–D molecule) and their radical anion, A$^-$, are expected to be still less pronounced; for example, the changes in bond lengths between anthracene and its radical anion are very small ($\approx$ 0.002 nm) [161]. Similar changes are also expected for other arenes (or acridine) used as the acceptor subunits in the compounds studied. This allows us to conclude that λ_i should be very small, much smaller than λ_o. The experimentally found $\lambda_i = 0.05\,\mathrm{eV}$ agrees very well with the above considerations. The λ_i value $0.07 \pm 0.02\,\mathrm{eV}$ was found for the intramolecular electron transfer within $^1(A^- {-} D^+)$ of the A–D studied [68].

The experimental results presented above indicate also that the intramolecular donor–acceptor compounds offer a unique opportunity to design new ECL systems with extremely high efficiencies. This is expected for the system in which all of the locally excited states are lying above the excited intramolecular charge-transfer state. However, it is very difficult to propose an appropriate system. On the other hand, a system with a large energy gap between the excited intramolecular charge-transfer states and the lower-lying locally excited triplets may also exhibit high values of ECL efficiency. It may be simply argued that the largest possible values of this energy gap are expected for symmetric systems, in which A = D. 9,9′-Bianthryl and its symmetrically substituted derivatives (with structures as shown in Fig. 22) are the most representative examples [162–165]. It has been shown that the primary excited singlet state of anthracene subunits undergoes a solvent-assisted relaxation to a polar charge-transfer state [166, 167], with rotation from the mutually perpendicular conformation to a more planar structure [168] (in the gas phase). ECL behavior of 9,9′-bianthryl (BA) and its 10,10′-dimethoxy derivative (DA) has been reported [169–171].

The electrochemical behavior of BA and DA agrees well with that expected, taking into account the electrochemical properties of 9-methoxyanthracene and

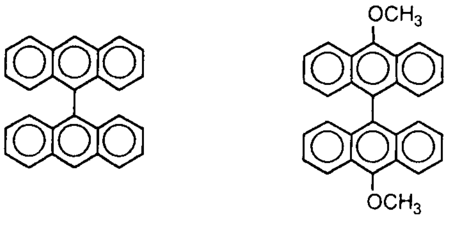

9,9'-bianthryl 10,10'-dimethoxy-9,9'-bianthryl

BA DA

Fig. 22. Examples of the symmetric intramolecular donor–acceptor A–A system.

anthracene alone [124, 172]. The electrochemical reactions can be formulated as follows:

$$\text{A-A} + e^- \rightleftarrows \text{A-A}^- + e^- \rightleftarrows \text{A}^-\text{A}^- \tag{71}$$

$$\text{A-A} - e^- \rightleftarrows \text{A-A}^+ - e^- \longrightarrow \text{unknown products} \tag{72}$$

where A–A^-, $\text{A}^-\text{–A}^-$ and A–A^+ represent the radical anion, the dianion, and the radical cation of the parent molecule A–A. The above formulation implies that the unpaired electron is located within one of the two subunits of the A–A molecule. Such an assumption arises from the electronic absorption spectra [173] and ESR [173, 174] studies of the reduction products. ESR studies indicate that an unpaired electron of the radical anion is localized on one of the subunits with a rather low intramolecular exchange ($\text{A–A}^- \rightleftharpoons \text{A}^-\text{–A}$) rate (ca. $2\text{–}4\times10^7\ \text{s}^{-1}$ [174]). Similarly, the electronic absorption spectra indicate only a small interaction between the two subunits in the anion radicals [173] as well as in the neutral molecules (e.g., [163–165]). The corresponding data are not available for the cation radicals but the picture (at least in the alternate hydrocarbons approximation) should be congruent. The electronic structure of dianions corresponds to the lowest-energy dianion triplet state [173].

The mechanism of the ECL processes of A–A systems has been formulated analogously to that for A–D systems.

$$\text{A-A}^- + \text{A-A}^+ \longrightarrow \text{products} \tag{73}$$

The most important observed difference arises from the different values of the electronic coupling elements and from the exothermicities of the locally excited triplet $^3(\text{A}^*\text{–A})$ formation. The temperature dependence of ϕ_{ecl} for both A–A ECL systems has been studied in acetonitrile solutions [171]. The measurements of temperature dependence on the emission quantum yields, ϕ_{o} (an intrinsic property of the emitting state $^1(\text{A}^-\text{–A}^+)$) indicate that the observed effects are due to the changes in ϕ_{o} as well as to changes in the yields of generation of excited state ϕ_{es}. The experimental rations k_3/k_{CT} have been evaluated from $(1 - 4\phi_{\text{es}})/3\phi_{\text{es}}$. It was found that k_{CT} drops with the decreasing temperature faster than does k_3. The observed behavior has been explained quantitatively using the Marcus theory similarly to the way it was done for the A–D ECL system. From the geometric mean approximation relatively large values of V_3 and V_{CT} are expected. In the formation of the excited intramolecular charge-transfer states the electron is transferred from A^- in $\text{A}^-\text{–A}$ to A in A–A^+ or from A in $\text{A}^-\text{–A}$ to A^+ in A–A^+. The formation of locally excited triplets corresponds to the electron transfer from A^- in $\text{A}^-\text{–A}$ to A^+ in A–A^+. In the formation of the ground state the electron is also transferred from A^- in $\text{A}^-\text{–A}$ to A^+ in A–A^+.

Similarly, as for A–D systems, values of λ_{o} and λ_{i} have been estimated on the basis of the Marcus cross-relation, leading to the conclusion that λ_{i} is very small, probably not exceeding 0.05–0.10 eV. The λ_{o} values for arromatic hydrocarbons lie in the range 0.32–0.43 eV [94] (determined for the A/A^- couple, but similar values

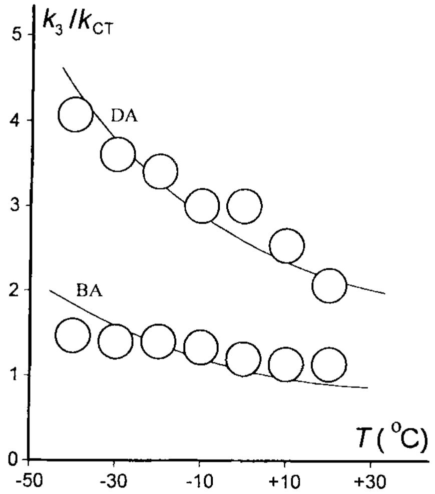

Fig. 23. Values of the k_3/k_{CT} ratio (evaluated from the experimental efficiencies of formation of the excited state) as a function of the temperature (T) for 9,9′-bianthryl and 10,10′-dimethoxy-9,9′-bianthryl in acetonitrile solutions. Adapted from [171].

are expected also for A/A$^+$). Comparable values are also provided by Eq. (6) with $r_{A^+} = r_{A^-} = 0.383\,\text{nm}$ from the molar volume of anthracene and the reaction distance $r_{12} = 0.45$–$0.55\,\text{nm}$.

With an intermediate value of $\lambda_o = 0.40\,\text{eV}$ and $S = \lambda_i/h\nu_i = 0.25$, k_3 and k_{CT} rates have been evaluated at different temperatures, also taking into account the temperature dependence on τ_L. Dielectric relaxation data for acetonitrile are incomplete, but with the available values [175] it is possible to estimate appropriate τ_L [176, 177] (temperature dependence on λ_o and ΔG values may be neglected). Solvent dynamics effects in both normal and inverted Marcus regions have been taken into account because of the expected large values of V_3 and V_{CT} terms, and Eqs. (24) and (49) have been applied for the calculation of k_{CT} and k_3 rates. Electronic coupling elements V_3 have been chosen to obtain the best fit between experimental and theoretical predictions ($V_3 = 0.065$ and $0.030\,\text{eV}$ for BA and DA, respectively). Both V_3 values correspond very well with the expected, e.g., their values agree very closely with those estimated for nonradiative [166, 167] and radiative [178] electron transfer within ^{1}(A$^-$–A$^+$). The results of the above kinetic calculations (k_3/k_{CT} ratios) are shown in Fig. 23. The agreement between theory and experiment can be regarded as satisfactory, indicating that the main set of parameters (which seem to be the most probable from a kinetic point of view) introduced into calculations has been correctly selected.

4.3 Ruthenium(II) Chelates

In view of the results discussed above it becomes clear that the formation of the lowest excited states (namely triplets) prevails in most organic ECL systems. The overall electron transfer rate seems to be determined mostly by this particular channel. Therefore one may expect that ECL system in which the lowest excited state

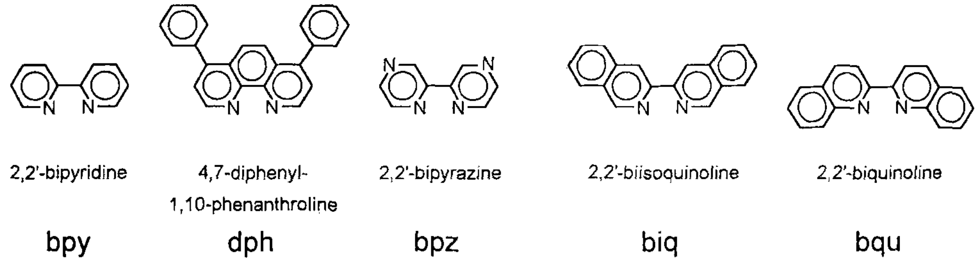

Fig. 24. Examples of the bidentate ligands forming electrochemiluminescent ruthenium(II) complexes.

is the emitter should be much more efficient. In fact, in some ECL systems involving transition-metal complexes (in which phosphorescence is allowed by the spin–orbit coupling) ECL yields approach the luminescence quantum yield, indicating that the emitting state is produced with an efficiency near unity. The most notable and studied example is that concerning Ru(bpy)$_3^{2+}$(bpy = 2,2′-bipyridine) in acetonitrile solutions [179–182]. When a cyclic square potential wave between the reduction and oxidation potential of Ru(bpy)$_3^{2+}$ is applied, the typical orange emission is observed. It continues indefinitely if the potential stepping is maintained. The reaction mechanism can be formulated as follows:

$$\mathrm{RuL}_3^{2+} + \mathrm{e}^- \rightleftharpoons \mathrm{RuL}_3^{+} \tag{74}$$

$$\mathrm{RuL}_3^{2+} - \mathrm{e}^- \rightleftharpoons \mathrm{RuL}_3^{3+} \tag{75}$$

$$\mathrm{RuL}_3^{3+} + \mathrm{RuL}_3^{+} \xrightarrow{k_g} \mathrm{RuL}_3^{2+} + \mathrm{RuL}_3^{2+} \tag{76}$$

$$\mathrm{RuL}_3^{3+} + \mathrm{RuL}_3^{+} \xrightarrow{k_e} \mathrm{RuL}_3^{2+} +{}^{*}\mathrm{RuL}_3^{2+} \tag{77}$$

where L denotes 2,2′-bipyridine (structure shown in Fig. 24). Reversible one-electron oxidation corresponds to the straightforward removal of a metal t_{2g} electron and in one-electron reversible reductions the added electron is localized on individual ligand π^* orbitals [183, 184].

The ECL efficiency ϕ_{ecl} was found to be 0.05 in acetonitrile at 25 °C [180]. This value, obtained from actinometric measurements, is frequently used as the efficiency standard for other ECL processes. Moreover, since ϕ_{ecl} strictly approaches the luminescence efficiency ϕ_0 (especially at lower temperatures; see Fig. 25), it was concluded that the formation efficiency ϕ_{es} of the excited *Ru(bpy)$_3^{2+}$ in reaction (77) is near unity. This strongly suggests that the thermodynamically favored reaction (76), to form the ground-state product directly, is kinetically inhibited. Other ruthenium(II) polypyridines, biquinolines, phenanthrolines or bipyrazine complexes (ligand structures are shown in Fig. 24) exhibit a similar behavior [185–189], but the corresponding ϕ_{ecl} values are found to be strongly dependent on the nature of the ligand. This arises from the differences in the efficiencies ϕ_{es} of formation of the

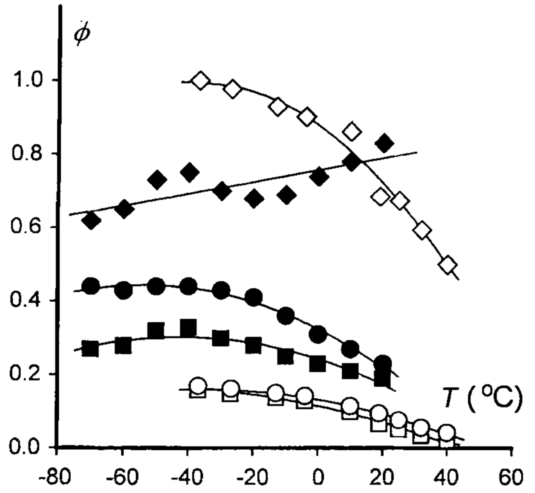

Fig. 25. ECL efficiencies (squares), luminescence quantum yields (circles) and efficiencies of formation of the excited state (diamonds) for $Ru(bpy)_3^{2+}$ in acetonitrile (open symbols) and $Ru(dph)_3^{2+}$ in butyronitrile solutions (solid symbols) as a function of the temperature (T). Data from [180] and [189].

emitting excited-states, as well as from the differences in the quantum efficiencies ϕ_o. Up till now (to our knowledge) the maximum ECL efficiency has been found for the tris(4,7-diphenyl-1,10-phenanthroline)ruthenium(II) complex $Ru(dph)_3^{2+}$, at 0.24 in acetonitrile (ACN) and 0.20 in butyronitrile (BN) solution at room temperature [188, 189]. At decreased temperatures the observed ECL efficiency of this system is still higher (see Fig. 25).

The ECL mechanism for both $Ru(bpy)_3^{2+}$ and $Ru(dph)_3^{2+}$ complexes seems to be parallel, with one important difference. In the case of $Ru(bpy)_3^{2+}$, the efficiency ϕ_{es} increases as temperature decreases. The opposite trend is observed for $Ru(dph)_3^{2+}$. The effects are rather small, but certainly greater than the experimental errors. The trivial explanation that the observed difference is caused by medium effects can be simply excluded. Our unpublished results indicate that the ECL behavior of $Ru(bpy)_3^{2+}$ in both solvents (ACN and BN) is nearly the same. The observed difference can be understood by kinetic analysis in terms of the electron transfer model for ECL processes. According to this model, the yield of the emissive excited state is given by the ratio of the rate constants for the electron transfer processes producing the excited-state and the ground-state products, respectively. Unfortunately, the values of the appropriate parameters, which are necessary for the calculation of these rates, are not available. However, some qualitative conclusions are possible; they are summarized below.

The formation of the ground state (for both ruthenium(II) complexes) is so exergonic ($\Delta G_0 \approx 2.66$ eV from the difference in the standard redox potentials) that it should lie far into the inverted Marcus region, and therefore be relatively slow. The formation of the emissive excited species is much less exergonic. With the energies of both $^*Ru(bpy)_3^{2+}$ and $^*Ru(dph)_3^{2+}$ (ca. 1.96 eV from the emission maxima) it is deduced that their formation occurs with an exothermicity ΔG_e of ca. 0.7 eV. In these estimates the energy contributions the Coulomb repulsion energy required to bring the reactants into the active complex and the Franck–Condon energy of the ground

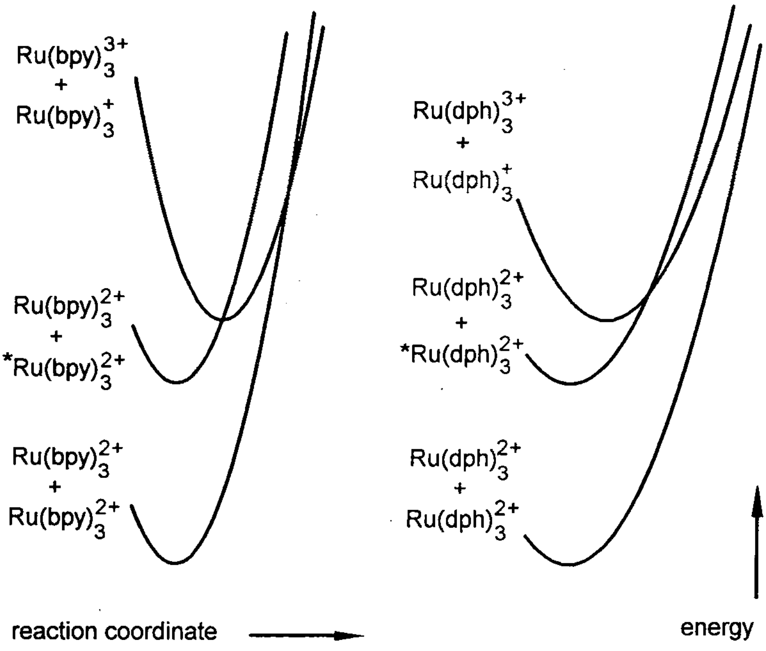

Fig. 26. Reaction coordinate diagrams for ECL systems containing Ru(bpy)$_3^{2+}$ in acetonitrile (left) and Ru(dph)$_3^{2+}$ in butyronitrile (right) solutions. Potential energy curves are presented in the zero-order approximation without removing the degeneracy at the crossing points. Adapted from [189].

state reached in the emission have been neglected. This is justified, at least in the first approximation, because these two rather small quantities are working in opposite directions.

In the case of the Ru(bpy)$_3^{2+}$ complex, the exothermicity ($\approx$ 0.7 eV) is comparable to the outer reorganization energy λ_o calculated according to Eq. (6), strongly suggesting that the formation of *Ru(bpy)$_3^{2+}$ is nearly barrierless. For the octahedral complexes with spherical symmetry that have been studied, one can also assume that $r_1 \approx r_2 = r$ and $r_{12} \approx 2r$. With $r = 0.57$ nm for Ru(bpy)$_3^{2+}$ [190] the corresponding λ_o (in ACN) is estimated to be 0.67 eV. Thus the fact that the efficiency of Ru(bpy)$_3^{2+}$ formation approaches unity seems to be understandable, especially since this process is also favored by the statistical factor 3 from the spin multiplicity. The data for ECL system Ru(bpz)$_3^{2+}$ in ACN [186] can be interpreted in the same way. In contrast, the corresponding λ_o value (0.35 eV with $r = 1.00$ nm) for the ECL system involving Ru(dph)$_3^{2+}$ in BN solutions is evidently smaller, indicating that the formation of *Ru(dph)$_3^{2+}$ (similarly to the formation of Ru(dph)$_3^{2+}$) takes also place in the inverted Marcus region (Fig. 26).

For the electron transfer reaction occurring in the normal Marcus region, the reaction products are principally formed in their vibrational ground states. In the inverted Marcus region the electron transfer reaction leads to the vibrational excitation of the high-frequency modes. It lowers the effective energy gap, which results in the relative enhancement of the reaction rate. These quantum effects are expected not only to modify the free-energy relationship but also to affect the temperature dependence of the electron transfer rate [59], with the essential quantitative difference between systems with small and large λ_o values. For relatively large values of outer reorganization energy the electron transfer rate (in the inverted Marcus region) remains temperature-activated also for large values of the inner reorganization energy λ_i. Taking into account that the electron transfer reaction leading to the excited $^*Ru(bpy)_3^{2+}$ is probably barrierless, the fact that ϕ_{es} increases as the temperature is lowered may be rationalized by a decreases in the rate of ground-state formation.

For systems with relatively small values of the outer reorganization energy, the temperature dependence of the electron transfer rate strongly decreases with increasing inner reorganization energy. The appropriate λ_i values for the reactions (77) and (76) are not directly available. However, from the nature of the metal-to-ligand charge-transfer process, with electron transfer from a metal t_{2g} orbital to one of the ligand π^* orbitals of the given ruthenium(II) complexes [191–194], one may simply argue that the intramolecular changes required in the population of $^*Ru(dph)_3^{2+}$ should be smaller than those for ground-state formation. In the case of ground-state formation an electron is transferred between a ligand π^*-orbital and a metal t_{2g} orbital. During excited-state formation an electron is transferred between ligand π^* orbitals or between metal t_{2g} orbitals. This probably leads to the different values of electron coupling elements but also to the different values of inner reorganization energy. In the case of ground-state formation, intramolecular changes involving the ligands as well as those for the central metal–ligand bonds are required, whereas in excited-state formation only one of these is sufficient. On the basis of low-temperature emission spectra of ruthenium(II) complexes [195, 196] (which are dominated by a single high-frequency vibrational progression with $h\nu_i \approx 1300$–$1400\,\mathrm{cm}^{-}1$), one may conclude that the intramolecular changes within the ligand are much more pronounced. Thus the formation of the excited $^*RuL_3^{2+}$ seems to be preferentially associated with the electron transfer between central metal t_{2g} orbitals in RuL_3^{3+} and RuL_3^{+}, probably with very small values of λ_i (only relatively weak metal–ligand bonds are reorganized). According to considerations presented in [59], the effective activation energy for reaction (76) should be smaller than that of reaction (77), leading to the lowering of the excited-state efficiency at low temperatures, which is indeed observed.

ECL efficiencies for ruthenium(II) mixed complexes in which one or two 2,2′-bipyridine molecules are replaced by 2,2′-biisoquinoline (biq) or 2,2′-biquinoline (bqu) ligands have been found to be distinctly smaller [187] than those of $Ru(bpy)_3^{2+}$ although λ_o and ΔG_e terms are similar in all of the above cases. For the $Ru(bpy)_2(bqu)^{2+}$ or $Ru(bpy)(bqu)_2^{2+}$ complexes (with ϕ_{es} efficiencies of 0.052 and 0.062 in ACN solutions) this probably results from the changes in ΔG_g (reaction (76)) which is ca. 0.4 eV smaller than that for $Ru(bpy)_3^{2+}$, leading to an increase in the rate of the formation of the ground state (probably by a factor 10–100). Efficiencies ϕ_{es} of 0.26 and 0.21, respectively, for $Ru(bpy)_2(biq)^{2+}$ and $Ru(bpy)(biq)_2^{2+}$ complexes in ACN solutions, however, cannot be rationalized in this way, because all of the energy terms (λ_o, ΔG_o and ΔG_e) are comparable with those for $\mathrm{Ru(bpy)_3^{2+}}$. The observed lowering in ϕ_{es} may arise from the different changes in the electronic coupling elements V_{12} for reactions (76) and (77), e.g., caused by the perturbation of the complex symmetry. The other explanation is given by deviation from the Marcus theory in the inverted region. Theoretical predictions [95–97] indicate that electron transfer in the inverted region accelerates with increasing distance, owing to an increase in the solvent reorganization energy λ_o. The rate constants for the production of the ground state may therefore be greater. The scarcity of the experimental data (e.g., lack of information on the temperature and/or the solvent dependence of ϕ_{es}) precludes more detailed discussion.

4.4 Molybdenum(II) and Tungsten(II) Halide Cluster Ions

In the kinetic interpretation of ECL data presented above the closest approach of reactants has been assumed. It seems to be fulfilled in the case of organic ECL systems (because of the Coulombic attraction between oppositely charged ions). In contrast, in ECL systems involving identically charged transition-metal complexes, Coulombic repulsion may lead to an increase in the electron transfer distance. The molybdenum(II) halide cluster ion $\mathrm{Mo_6Cl_{14}^{2-}}$ [197–199] is the one of the best-understood examples. In electrochemical reactions $\mathrm{Mo_6Cl_{14}^{2-}}$ is reversibly reduced or oxidized to stable $\mathrm{Mo_6Cl_{14}^{3-}}$ and $\mathrm{Mo_6Cl_{14}^{-}}$ respectively:

$$\mathrm{Mo_6Cl_{14}^{2-}} + e^- \rightleftarrows \mathrm{Mo_6Cl_{14}^{3-}} \tag{78}$$

$$\mathrm{Mo_6Cl_{14}^{2-}} - e^- \rightleftarrows \mathrm{Mo_6Cl_{14}^{-}} \tag{79}$$

ECL of $\mathrm{Mo_6Cl_{14}^{2-}}$ is produced by the electron transfer reaction between electrochemically generated $\mathrm{Mo_6Cl_{14}^{3-}}$ and $\mathrm{Mo_6Cl_{14}^{-}}$ ions:

$$\mathrm{Mo_6Cl_{14}^{-}} + \mathrm{Mo_6Cl_{14}^{3-}} \xrightarrow{k_g} \mathrm{Mo_6Cl_{14}^{2-}} + \mathrm{Mo_6Cl_{14}^{2-}} \tag{80}$$

$$\mathrm{Mo_6Cl_{14}^{-}} + \mathrm{Mo_6Cl_{14}^{3-}} \xrightarrow{k_e} {}^*\mathrm{Mo_6Cl_{14}^{2-}} + \mathrm{Mo_6Cl_{14}^{2-}} \tag{81}$$

The excellent solubility of $\mathrm{Mo_6Cl_{14}^{2-}}$ tetra-n-butylammonium salt in nonaqueous solutions permits investigations in various organic solvents, with the most important conclusion that the observed ECL efficiency (ϕ_{es} in the range 0.014–0.50) depends strongly on the reaction medium [199]. The ϕ_{es} efficiency obtained is quite small (0.065) in ACN solutions but increases with lowering of the solvent polarity in a similar way to what is observed for organic ECL systems (up to 0.50 in dichloromethane or 1,2-dichloroethane solutions).

The magnitudes of the standard redox potentials (e.g., −1.56 and +1.53 V vs. SCE in acetonitrile) and the relatively low energy of excited $^*\mathrm{Mo_6Cl_{14}^{2-}}$ (1.9 eV) have also made possible observation of ECL from the annihilation of $\mathrm{Mo_6Cl_{14}^{-}}$ and $\mathrm{Mo_6Cl_{14}^{3-}}$ with a variety of electroactive donors D (aromatic amines forming stable radical cations D^+):

$$Mo_6Cl_{14}^{3-} + D^+ \xrightarrow{k_e} {}^*Mo_6Cl_{14}^{2-} + D \tag{82}$$

$$Mo_6Cl_{14}^{3-} + D^+ \xrightarrow{k_g} Mo_6Cl_{14}^{2-} + D \tag{83}$$

and acceptors A (quinones and aromatic nitro compounds forming stable radical anions A^-):

$$Mo_6Cl_{14}^{3-} + A^- \xrightarrow{k_e} {}^*Mo_6Cl_{14}^{2-} + A \tag{84}$$

$$Mo_6Cl_{14}^{-} + A^- \xrightarrow{k_g} {}^*Mo_6Cl_{14}^{2-} + A \tag{85}$$

or *N*-alkylpyridinium cations R^+ (forming stable *N*-alkylpyridinium radicals $R^\bullet$):

$$Mo_6Cl_{14}^{-} + R^\bullet \xrightarrow{k_e} {}^*Mo_6Cl_{14}^{2-} + R^+ \tag{86}$$

$$Mo_6Cl_{14}^{-} + R^\bullet \xrightarrow{k_g} {}^*Mo_6Cl_{14}^{2-} + R^+ \tag{87}$$

These acceptors and donors were chosen such that population of their excited states is an energetically unfavorable process.

As was expected, functional dependence of ϕ_{es} on the driving force for the electron transfer reaction (presented in Fig. 27) has been found. As energies become negative, ϕ_{es} increases rapidly with increasing reaction exothermicity, but in a way depending on the nature of the organic reaction partner. The trivial explanation that the observed behavior arises from the different chemical nature of the given organic reactant may be simply ruled out, in view of the electron transfer quenching data for ${}^*Mo_6Cl_{14}^{2-}$. Reductive quenching of ${}^*Mo_6Cl_{14}^{2-}$ by aromatic amine donors (D) and oxidative quenching by nitroaromatics and quinones (A) or *N*-alkylpyridinium

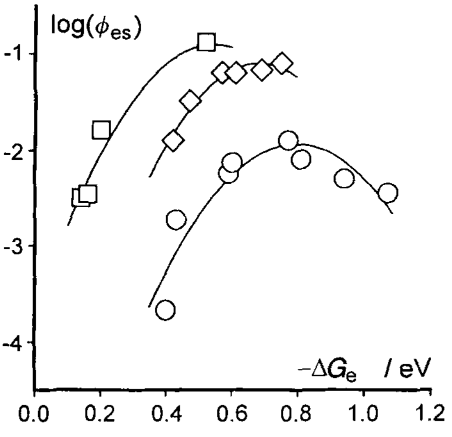

Fig. 27. Efficiency of excited state formation ϕ_{es} (data from [197]) as a function of the reaction exothermicity ΔG_e for the ECL system $Mo_6Cl_{14}^{3-}/D^+$ (□), $Mo_6Cl_{14}^{-}/A^-$ (○) and $Mo_6Cl_{14}^{-}/R^\bullet$ (◇) in acetonitrile solutions. ΔG_e values are calculated from the difference in the standard redox potentials corrected for the Coulombic interactions between reactants and products.

cations (occurring in the presence of an excess of quencher) are processes that occur parallel to the ECL reactions, probably according to schemes (88)–(90):

$$^{*}\mathrm{Mo_6Cl_{14}^{2-}} + \mathrm{D} \underset{k_e}{\overset{k_{-e}}{\rightleftarrows}} \mathrm{Mo_6Cl_{14}^{3-}} + \mathrm{D^+} \overset{k_g}{\rightleftarrows} \mathrm{Mo_6Cl_{14}^{2-}} + \mathrm{D} \qquad (88)$$

$$^{*}\mathrm{Mo_6Cl_{14}^{2-}} + \mathrm{A} \underset{k_e}{\overset{k_{-e}}{\rightleftarrows}} \mathrm{Mo_6Cl_{14}^{-}} + \mathrm{A^-} \overset{k_g}{\rightleftarrows} \mathrm{Mo_6Cl_{14}^{2-}} + \mathrm{A} \qquad (89)$$

$$^{*}\mathrm{Mo_6Cl_{14}^{2-}} + \mathrm{R^+} \underset{k_e}{\overset{k_{-e}}{\rightleftarrows}} \mathrm{Mo_6Cl_{14}^{-}} + \mathrm{R^{\bullet}} \xrightarrow{k_g} \mathrm{Mo_6Cl_{14}^{2-}} + \mathrm{R^+} \qquad (90)$$

Regular dependence (Fig. 28) of quenching rate constants, k_q, on the free-energy driving force $\Delta G_q (\Delta G_q = -\Delta G_e)$ strongly suggests another reason for the observed ECL behavior.

The extrapolated value of the constant k_q (at $\Delta G_q = 0$) is ca. $10^9\,\mathrm{M^{-1}\,s^{-1}}$. Assuming that $k_g \gg k_e$ (very low or no emission for ECL processes with $\Delta G_e = 0$) and that the electron transfer is a solvent-dynamics-controlled process, one can obtain (form Eqs. (23) and (27)) the upper limit of the outer reorganization energy λ_o. The value of ca. 0.7–0.8 eV, corresponding to the closest approach of reactants, agrees well with the calculated 0.85 ± 0.05 eV [197] from Eq. (6). Therefore one could expect that the most exergonic ECL processes involving molybdenum(II) cluster ions (with $-\Delta G_e$ in the range 0.8–1.2 eV) should produce the excited $^{*}\mathrm{Mo_6Cl_{14}^{2-}}$ with very high yields (similarly to ruthenium(II) chelates). This is obviously not the case; the observed ϕ_{es} efficiencies are usually a few orders of magnitude smaller; they are as large as expected only in the reaction set comprising Eqs. (82) and (83), involving aromatic amine radical cations. In this particular case the Coulombic attraction between oppositely charged (3− and 1+) ions facilitates the approach of the reactants, and one may conclude that the electron transfer reaction occurs over the

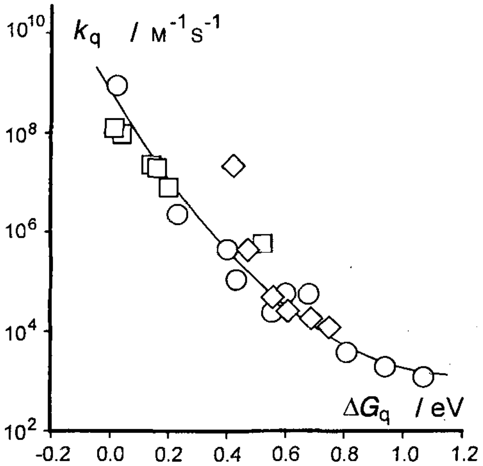

Fig. 28. Quenching rate constant k_q (data from [197, 198]) as a function of the reaction exothermicity ΔG_q for system $\mathrm{Mo_6Cl_{14}^{2-}/D}$ (□), $\mathrm{Mo_6Cl_{14}^{2-}/A}$ (○) and $\mathrm{Mo_6Cl_{14}^{-2}/R^+}$ (◇) in acetonitrile solutions. ΔG_q values are calculated from the difference in the standard redox potentials corrected for the Coulombic interactions between reactants and products.

smaller separation distances. In contrary, for the reaction sets comprising Eqs. (84) and (85), or (80) and (81), because of the Coulombic repulsion between uniformly charged ions (1− and 1−, or 3− and 1−), an increase in the electron transfer distance may be expected. Reactions (86) and (87) without any Coulombic interactions between reagents are probably the intermediate case. Moreover, the sequence of asymptotically limiting values of the excited state yields (at $-\Delta G_e = 0.6\,\mathrm{eV}$) is very similar to the ratio of the respective diffusion rates calculated according to Eq. (26). This strongly suggests that the rate of formation of the activated complex plays an important role in these particular ECL systems. Such behavior is expected in the case where the association and electron transfer rates are comparable and annihilation of

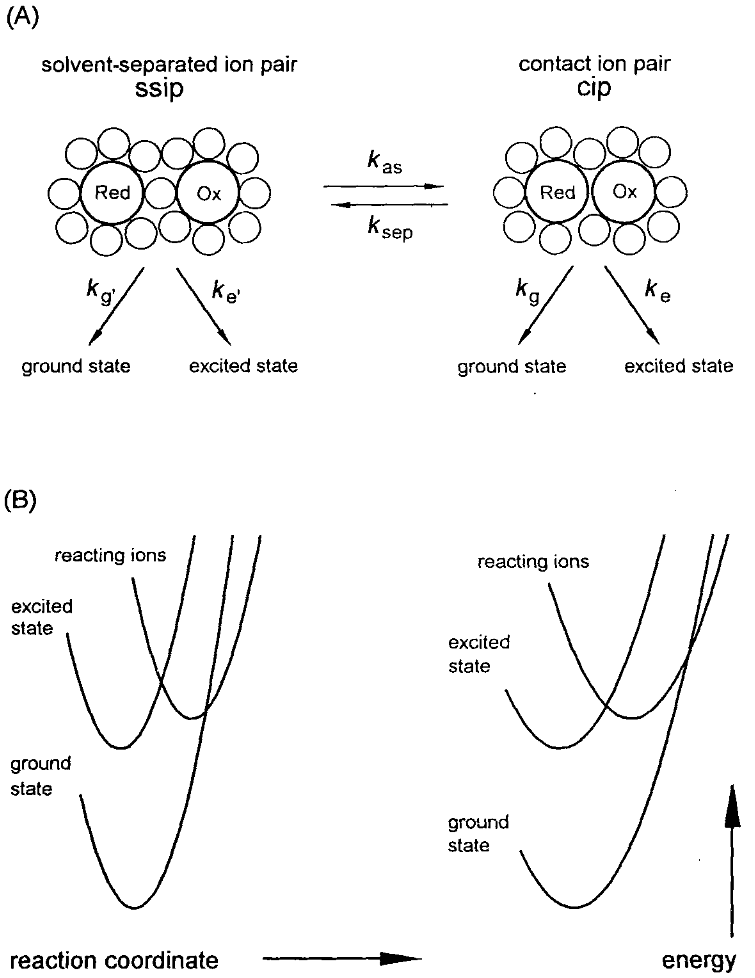
(A)
solvent-separated ion pair
ssip
contact ion pair
cip
Red
Ox
Red
Ox
k_{as}
k_{sep}
$k_{g'}$
$k_{e'}$
k_g
k_e
ground state
excited state
ground state
excited state
(B)
reacting ions
excited state
ground state
reacting ions
excited state
ground state
reaction coordinate
energy

Fig. 29. Schematic representation of a contact ion pair (cip) and a solvent-separated ion pair (ssip) (A) with the corresponding reaction coordinate diagrams (B). Potential energy curves are presented in the zero-order approximation without removing the degeneracy at the crossing points.

ions may occur at larger separation distances. Such a conclusion has been already drawn in the original work, but the assumption that the reaction distance changes monotonically with the reaction exothermicity is somewhat factitious. The concept of equilibrium between contact ion pair (cip) and solvent-separated ion pair (ssip) (Fig. 29) appears to be more adequate. Taking into account the values of the Franck–Condon factors, it may be expected that the formation of the excited state should prevail within the cip configuration. On the other hand, the formation of the ground state should prevail within the ssip configuration. The total yield of the excited state formation is governed by four electron transfer rates (k_e or k_g within the cip and $k_{e'}$ or $k_{g'}$ within the ssip configuration) as well as by the rates of association k_{as} and separation k_{sep}.

It is possible to obtain the exact but rather complex solution of this kinetic problem [200]. However, the number of the parameters in the final equations does not permit quantitative analysis without additional assumptions. Assuming that the excited state is produced mostly within the cip configuration at a rate k_e and the ground state mostly within the ssip configuration at a rate $k_{g'}$, one can simply obtain:

$$\phi_{es} = \frac{k_e}{k_e + k_{sep}} \frac{k_{as}}{k_{g'} + k_{as}} \tag{91}$$

where k_{as} and k_{sep} are the rates of formation and dissociation of the contact ion pair (see Fig. 29). In Eq. (91) first term on the right-hand side describes the free-energy functional dependence of ϕ_{es}; the second one is responsible for the efficiency of cip formation. The rate constants k_{as} and k_{sep} could not be measured directly. However, taking into account their possible values [55, 201, 202] and the expected values of the electron transfer rates (k_e and $k_{g'}$), Eq. (91) may be further simplified to:

$$\phi_{es} \approx \frac{k_e}{k_{sep}} \frac{k_{as}}{k_{g'}} = \frac{k_e}{k_{g'}} K_{as} = \frac{k_e}{k_{g'}} \exp\left[\frac{w_r(r_{ssip} - w_r(r_{cip})}{RT}\right] \tag{92}$$

where $w_r(r_{ssip}) - w_r(r_{cip})$ corresponds to the difference in the Coulomb repulsion (or attraction) energies for the ssip and cip configurations. Equation (92) is probably not exactly correct, but at least in the zero-order approximation may be used for semiquantitative discussion. With the values −0.09, 0, and 0.03 eV for the reactions involving positively charged D^+, neutral $R^\bullet$, and negatively charged A^-, the K_{as} values 37, 1, and 0.3 (respectively) can be calculated. A much more uniform plot of ϕ_{es}/K_{as} vs. ΔG_e (presented in Fig. 30) indirectly supports that the proposed model may be correct. The shape of the parabolic curve (the energy dependence of the Franck–Condon factor) in Fig. 30 corresponds to outer reorganization energy $\lambda_o = 0.8\,\text{eV}$, in agreement with the estimate on the basis of the excited $^*Mo_6Cl_{14}^{2-}$ quenching constant values.

In view of the above considerations, much smaller ϕ_{es} efficiencies (at a given reaction exothermicity) are expected for the reaction between $Mo_6Cl_{14}^-$ and $Mo_6Cl_{14}^{3-}$ ions (ϕ_{es} only 0.065 in ACN solution at $\Delta G_e = -1.2\,\text{eV}$). In this particular case the

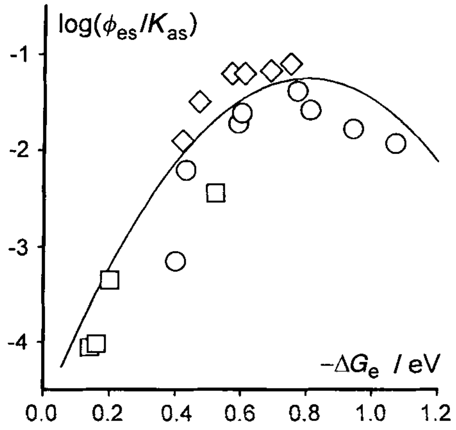

Fig. 30. Corrected (normalized) efficiency of formation of the excited state ϕ_{es}/K_{as} as a function of the reaction exothermicity ΔG_e for ECL system $Mo_6Cl_{14}^{3-}/D^+$ (□), $Mo_6Cl_{14}^-/A^-$(○) and $Mo_6Cl_{14}^-/R^\bullet$(◇) in acetonitrile solutions. ΔG_e values are calculated from the difference in the standard redox potentials corrected for the Coulombic interactions between reactants and product. The shape of the parabolic curve corresponds to the outer reorganization energy $\lambda_0 = 0.8\,eV$.

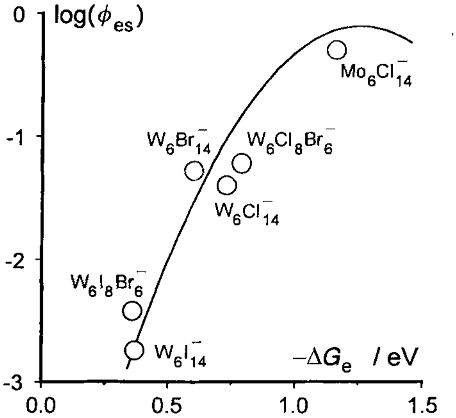

Fig. 31. The excited state efficiency ϕ_{es} as a function of the reaction exothermicity ΔG_e (data from [198, 199]) in the annihilation reactions of $Mo_6Cl_{14}^{3-}$ with the tungsten halide cluster acceptor $WX_8Y_6^-$ and $Mo_6Cl_{14}^-$ in dichloromethane solutions. ΔG_e values are calculated from the differences in the standard redox potentials corrected for the Coulombic interactions between reactions and product. The shape of the parabolic curve corresponds to the outer reorganization energy $\lambda_o = 1.2\,eV$.

Coulombic repulsion between ions with 1− and 3− charges lowers K_{as} as well as k_{as} values, and electron transfer takes place preferentially within the ssip configuration. ECL data for the annihilation reactions between $Mo_6Cl_{14}^{3-}$ and different tungsten halide cluster ions $W_6X_8Y_6^-$ [198] in dichloromethane support this conclusion. For example, $\phi_{es} = 0.5$ for the ECL system involving $Mo_6Cl_{14}^{3-}$ and the 4-cyano-*N*-methylpyridinium radical [199] (with no Coulombic repulsion) is ca. two orders of magnitude larger than ϕ_{es} for $Mo_6Cl_{14}^{3-}/W_6I_{14}^-$ or $Mo_6Cl_{14}^{3-}/W_6I_8Br_6^-$ pairs (with nearly the same exothermicity but with strong Coulombic repulsion). For other ECL reactions involving tungsten halide cluster ions, the efficiency ϕ_{es} increases with reaction exothermicity (Fig. 31) consistently with the Marcus theory. The shape of the parabolic curve (energy dependence of the Franck–Condon factor) in Fig. 31

corresponds to the outer reorganization energy $\lambda_o = 1.2\,\mathrm{eV}$, in agreement with the increased reaction distance.

The reaction mechanism proposed above seems to be the most probable from the kinetic point of view, but must be treated only as a semiquantitative approach until the role of the ion pair dynamics has been exactly recognized. Systematic studies (similar to those performed in acetonitrile solutions) of solvent polarity and viscosity may provide the decisive answer, probably also making possible a more quantitative description with estimates of all the kinetic parameters.

5 Conclusions

The results obtained clearly demonstrate that the Marcus model for ECL processes may be used for qualitative as well as for quantitative descriptions of this kind of electron transfer reactions. The more sophisticated approach, taking into account the vibronic excitation in the reaction products (important in the inverted Marcus region), solvent molecular dynamics (important in the case of large values of the electronic coupling elements), as well as the changes in the electron transfer distance, should be used. The results indicate that the Marcus theory may also be used for predicting the ECL efficiency, provided that some conditions are fulfilled. Especially, during the ECL process, only the annihilation of ions should occur, without any competitive reactions. The necessary rate constants can be evaluated from pertinent electrochemical and spectroscopic data.

The results also indicate the possibility of designing new ECL systems with extremely high efficiencies. Two groups of ECL systems, namely organic intramolecular donor–acceptor compounds and transition-metal complexes, seem to be the most promising.

In the case of donor–acceptor systems, this is expected where all locally excited states (nonemissive triplets) lie above the excited intramolecular charge-transfer states. In such cases the expected efficiency of formation of the emissive (singlet) charge-transfer state is expected to be 0.25 (because of the spin multiplicity). The nonemissive excited charge-transfer state (a triplet populated with an efficiency of 0.75) will probably be deactivated in the form of delayed fluorescence (through the nearly isoenergetic singlet). On the other hand, the quantum yield of the charge-transfer emission from this kind of excited intramolecular charge-transfer state should also be relatively large, because one of the nonradiative deactivation channels (intersystem crossing to the lower-lying locally excited triplet) will be closed. Thus the ECL efficiencies obtained may be fairly large.

In the case of transition-metal complexes, the more efficient formation of the emissive excited state may require annihilation reactions between redox centers over shorter separation distances. Therefore use of neutral parent molecules, forming opositely charged ions in the reduction and oxidation processes, may be advantageous.

6 References

1. R. A. Marcus, J. Chem. Phys. 24, 979 (1956).
2. R. A. Marcus, J. Chem. Phys. 43, 2654 (1965).
3. M. Cornier, D. M. Hercules, J. Lee (eds.), Chemiluminescence and Bioluminescence, Plenum Press, New York (1973).
4. W. Adam, C. Cilento (eds.), Chemical and Biological Generation of Excited States, Academic Press, New York (1982).
5. K.-D. Gundermann, F. McCapra, Chemiluminescence in Organic Chemistry, Springer-Verlag, Berlin (1987).
6. K. A. Zachariasse, PhD Thesis, Amsterdam (1972).
7. A. Zweig, Adv. Photochem. 6, 425 (1968).
8. C. P. Keszthelyi, Acta Phys. Chem. 26, 1731 (1980).
9. L. R. Faulkner, A. J. Bard, Electroanal. Chem. 10, 1 (1977).
10. S.-M. Park, D. A. Tryk, Rev. Chem. Intermed. 4, 43 (1981).
11. A. I. Bykh, R. F. Vasil'ev, N. N. Rozickij, Itogi Nauki i Tiekhniki. 2, 3 (1979).
12. J. G. Valesco, Electroanalysis. 3, 261 (1991).
13. H. Tachikawa, L. R. Faulkner in: Laboratory Techniques in Electroanalytical Chemistry, P. T. Kissinger, W. R. Heineman (eds.), Academic Press, New York (1982), Chapter 6.
14. K. S. Santhanam, A. J. Bard, J. Am. Chem. Soc. 87, 139 (1965).
15. J. T. Maloy, K. B. Prater, A. J. Bard, J. Am. Chem. Soc. 93, 5959 (1971).
16. J. T. Maloy, A. J. Bard, J. Am. Chem. Soc. 93, 5968 (1971).
17. J. E. Bartelt, S. M. Drew, R. M. Wightman, J. Electrochem. Soc. 139, 70 (1992).
18. J. Ouyang, A. J. Bard, J. Phys. Chem. 92, 5201 (1988).
19. R. McIntyre, J. K. Sass, Phys. Rev. Lett. 56, 651 (1986).
20. K. Murakoshi, K. Uosaki, J. Phys. Chem. 96, 4593 (1992).
21. J. D. Lutmer, A. J. Bard, J. Electrochem. Soc. 125, 1423 (1978).
22. R. Dehmlow, P. Janietz, R. Landsberg, J. Electroanal. Chem. 65, 115 (1975).
23. M. Gleria, R. Memming, Z. Phys. Chem. NF 101, 171 (1976).
24. R. M. Measures, Appl. Optics 13, 1121 (1974).
25. M. M. Nicholson, J. Electrochem. Soc. 119, 461 (1972).
26. C. P. Keszthelyi, A. J. Bard, J. Electrochem. Soc. 120, 241 (1973).
27. D. Laser, A. J. Bard, J. Electrochem. Soc. 122, 632 (1975).
28. R. J. Bowling, R. L. McCreery, C. M. Pharr, R. C. Engstrom, Anal. Chem. 55, 1580 (1983).
29. R. C. Engstrom, C. M. Pharr, M. D. Koppang, J. Electroanal. Chem. 221, 251 (1987).
30. J. O'M. Bockris, S. U. M. Khan, Quantum Electrochemistry, Plenum Press, New York (1979).
31. R. R. Dogonadze, A. M. Kuznetsov, T. A. Marsagishvili, Electrochim. Acta 25, 1 (1980).
32. N. Sutin, Acc. Chem. Res. 15, 275 (1982).
33. N. Sutin, Progr. Inorg. Chem. 30, 441 (1983).
34. R. A. Marcus, N. Sutin, Biochim. Biophys. Acta 811, 265 (1985).
35. M. D. Newton, N. Sutin, Annu. Rev. Phys. Chem. 35, 437 (1989).
36. M. D. Newton, Chem. Rev. 91, 767 (1991).
37. S. F. Fischer, R. I. van Duyen, Chem. Phys. 26, 9 (1977).
38. J. Jortner, J. Ulstrup, J. Am. Chem. Soc. 101, 3744 (1979).
39. M. D. Newton, Int. J. Quantum Chem. 14, 364 (1980).
40. I. Webman, N. R. Kestner, J. Chem. Phys. 77, 2387 (1982).
41. P. Siders, R. J. Cave, R. A. Marcus, J. Chem. Phys. 81, 5613 (1984).
42. M. E. Peover, J. D. Davies, J. Electroanal. Chem. 6, 46 (1963).

43. E. D. German, A. M. Kuznetsov, Electrochim. Acta 26, 1595 (1981).
44. W. R. Fawcett, Yu. I. Kharkats, J. Electroanal. Chem. 47, 413 (1973).
45. T. Asahi, N. Mataga, J. Phys. Chem. 95, 1956 (1991).
46. S. Efrima, M. Bixon, Chem. Phys. Lett. 25, 341 (1974).
47. S. Efrima, M. Bixon, Chem. Phys. 13, 447 (1976).
48. D. Rehm, A. Weller, Ber. Bunsenges. Phys. Chem. 73, 834 (1969).
49. D. Rehm, A. Weller, Isr. J. Chem. 8, 259 (1970).
50. J. R. Miller, J. V. Beitz, R. H. Huddleston, J. Am. Chem. Soc. 106 5057 (1984).
51. J. R. Miller, L. T. Calcaterra, G. L. Closs, J. Am. Chem. Soc. 106, 3047 (1984).
52. J. R. Miller, L. T. Calcaterra, G. L. Closs, J. Phys. Chem. 90, 3673 (1986).
53. M. P. Wasielewski, M. P. Niemczyk, W. A. Swec, E. B. Pewitt, J. Am. Chem. Soc. 107, 1080 (1985).
54. M. D. Johnson, J. R. Miller, N. J. Green, G. L. Closs, J. Phys. Chem. 93, 1173 (1989).
55. I. R. Goud, R. H. Young, R. E. Moody, S. Farid, J. Phys. Chem. 95, 2068 (1991).
56. G. Grampp, G. Hetz, Ber. Bunsenges. Phys. Chem. 96, 198 (1992).
57. M. P. Irvine, R. J. Harrison, G. S. Beddard, P. Leighton, J. K. M. Sanders, Chem. Phys. 104, 315 (1986).
58. R. Ohno, A. Yoshimura, H. Shioyama, N. Mataga, J. Phys. Chem. 91, 4365 (1987).
59. M. Bixon, J. Jortner, J. Phys. Chem. 95, 1941 (1991).
60. R. D. Cannon, Electron Transfer Reactions, Butterworths, London (1980).
61. H. Beens, A. Weller in: Organic Molecular Photophysics, J. B. Birks (ed.), Wiley, New York (1975), Vol. 2, p. 159.
62. H. Beens, PhD Thesis, Amsterdam, 1970.
63. B. R. Wegewijs, PhD Thesis, Amsterdam, 1994.
64. N. Mataga in: The Exciplex, M. Gordon, W. R. Ware (eds.), Academic Press, New York (1975), p. 113.
65. R. A. Marcus, J. Phys. Chem. 93, 3078 (1989).
66. J. A. Barltrop, J. D. Coyle, Principles of Photochemistry, Wiley, New York (1978).
67. I. R. Gould, D. Noukakis, L. Gomez-Jahn, R. H. Young, J. L. Goodman, S. Farid, Chem. Phys. 176, 439 (1993).
68. J. Herbich, A. Kapturkiewicz, Chem. Phys. 170, 221 (1993).
69. L. D. Zusman, Chem. Phys. 49, 295 (1980).
70. L. D. Zusman, Chem. Phys. 80, 29 (1983).
71. I. V. Alexandrov, Chem. Phys. 51, 449 (1980).
72. D. F. Calef, P. G. Wolynes, J. Phys. Chem. 87, 3387 (1983).
73. D. F. Calef, P. G. Wolynes, J. Chem. Phys. 78, 470 (1983).
74. A. Kapturkiewicz, B. Behr, J. Electroanal. Chem. 179, 187 (1984).
75. W. Harrer, G. Grampp, W. Jaenicke, Chem. Phys. Lett. 112, 263 (1984).
76. D. Huppert, H. Kanetz, E. M. Kosower, Faraday Discuss. Chem. Soc. 74, 161 (1982).
77. E. M. Kosower, D. Huppert, Chem. Phys. Lett. 96, 433 (1983).
78. D. N. Beratan, J. N. Onuchic, J. Chem. Phys. 89, 6195 (1988).
79. J. N. Onuchic, D. N. Beratan, J. Phys. Chem. 92, 4817 (1988).
80. R. A. Marcus, H. Sumi, J. Chem. Phys. 84, 4247 (1986).
81. I. Rips, J. Jortner, J. Chem. Phys. 87, 2090 (1987).
82. W. R. Fawcett, M. Opatto, Angew. Chem., Int. Ed. Engl. 33, 2131 (1994).
83. J. D. Simon, Acc. Chem. Res. 21, 128 (1988).
84. M. J. Weaver, G. E. McManis III, Acc. Chem. Res. 23, 294 (1990).
85. P. F. Barbara, W. Jarzeba, Adv. Photochem. 15, 1 (1990).
86. H. Fröhlich, Theory of Dielectrics, Oxford University Press, Oxford (1958).
87. A. Kapturkiewicz, W. Jaeniche, J. Chem. Soc. Faraday Trans. 1, 83, 2727 (1987).
88 J. D. Morgan, P. G. Wolynes, J. Phys. Chem. 91, 874 (1987).
89. J. Jortner, M. Bixon, J. Chem. Phys. 88, 167 (1988).

90. D. R. Rosseinsky, Commun. Inorg. Chem. 3, 153 (1984).
91. J. T. Hupp, M. J. Weaver, J. Electroanal. Chem. 152, 1 (1983).
92. M. Eigen, Z. Phys. Chem. NF 1, 176 (1954).
93. M. Fuoss, J. Am. Chem. Soc. 80, 5059 (1958).
94. L. Eberson, Adv. Phys. Org. Chem. 18, 79 (1982).
95. R. A. Marcus, P. Sider, J. Phys. Chem. 86, 622 (1982).
96. B. S. Brunschwig, S. Ehrenson, N. Sutin, J. Am. Chem. Soc. 106, 6858 (1984).
97. S. S. Isied, A. Vassilian, J. F. Wishart, C. Creutz, H. A. Schwarz, N. Sutin, J. Am. Chem. Soc. 110, 635 (1988).
98. A. Vogler, H. Kunkely, S. Schäffl, ACS Symp. Ser. 307, 120 (1986).
99. A. Vogler, H. Kunkely, ACS Symp. Ser. 333, 155 (1987).
100. S.-M. Park, A. J. Bard, Chem. Phys. Lett. 38, 2571 (1976).
101. L. R. Faulkner, H. Tachikawa, A. J. Bard, J. Am. Chem. Soc. 94, 691 (1972).
102. S. L. Murov, I. Carmichael, G. L. Hug, Handbook of Photochemistry, Marcel Dekker, New York (1993).
103. G. J. Hoytink, Discuss. Faraday Soc. 45, 14 (1968).
104. H. Tachikawa, A. J. Bard, Chem. Phys. Lett. 26, 246 (1974).
105. S. W. Feldberg, J. Am. Chem. Soc. 88, 390 (1966).
106. S. W. Feldberg, J. Phys. Chem. 70, 3928 (1966).
107. L. R. Faulkner, J. Electrochem. Soc. 124, 1724 (1977).
108. L. R. Faulkner, J. Electrochem. Soc. 122, 1190 (1975).
109. P. R. Michael, L. R. Faulkner, J. Am. Chem. Soc. 99, 7754 (1977).
110. R. Bezmann, L. R. Faulkner, J. Am. Chem. Soc. 94, 6331 (1972).
111. J. Kim, L. R. Faulkner, J. Electroanal. Chem. 242, 107 (1988).
112. J. Kim, L. R. Faulkner, J. Am. Chem. Soc. 110, 112 (1988).
113. A. Kapturkiewicz, J. Electroanal. Chem. 290, 135 (1990).
114. L. R. Faulkner, A. J. Bard, J. Am. Chem. Soc. 91, 209 (1969).
115. L. R. Faulkner, A. J. Bard, J. Am. Chem. Soc. 91, 6495 (1969).
116. D. J. Freed, L. R. Faulkner, J. Am. Chem. Soc. 93, 3565 (1971).
117. D. J. Freed, L. R. Faulkner, J. Am. Chem. Soc. 94, 4790 (1972).
118. H. A. Sharifian, S.-M. Park, Photochem. Photobiol. 88, 83 (1982).
119. S.-M. Park, M. T. Paffertt, G. H. Daub, J. Am. Chem. Soc. 99, 5393 (1977).
120. S.-M. Park, A. J. Bard, J. Am. Chem. Soc. 95, 2978 (1975).
121. J. Saltiel, B. W. Atwater, Adv. Photochem. 14, 1 (1988).
122. K. M. Maness, J. E. Bartelt, R. M. Wightman, J. Phys. Chem. 98, 3939 (1994).
123. A. Kapturkiewicz, J. Electroanal. Chem. 372, 101 (1994).
124. J. Perichon in: Encyclopedia of the Electrochemistry of the Elements, A. J. Bard, H. Lunds (eds.), Marcel Dekker, New York (1978), Vol. 11, p. 71.
125. W. G. Herkstroeter, P. B. Merkel, J. Photochem. 16, 331 (1981).
126. A. P. Darmanyan, V. A. Kuzmin, Dokl. Akad. Nauk SSSR, 260, 1167 (1982).
127. S. J. Strickler, R. A. Berg, J. Chem. Phys. 37, 814 (1962).
128. J. Jortner, J. Am. Chem. Soc. 102, 6676 (1980).
129. L. D. Zusman, Elektrokhimiya, 25, 957 (1989).
130. A. E. J. Forno, M. E. Peover, R. Wilson, Trans. Faraday Soc. 66, 1322 (1970).
131. A. Yekta, N. J. Turro, Mol. Photochem. 3, 307 (1972).
132. K. Suga, S. Ishikawa, S. Aoyagui, Bull. Chem. Soc. Jpn. 46, 755 (1973).
133. N. Perisamy, S. J. Shah, K. S. V. Santhanam, J. Chem. Phys. 58, 821 (1973).
134. K. Itaya, S. Toshima, Chem. Phys. Lett. 51, 447 (1977).
135. M. Kawai, K. Itaya, S. Toshima, J. Phys. Chem. 84, 2368 (1980).
136. A. Kapturkiewicz, Z. R. Grabowski, J. Jasny, J. Electroanal. Chem. 279, 55 (1990).
137. A. Kapturkiewicz, J. Electroanal. Chem. 302, 131 (1991).
138. A. Kapturkiewicz, Chem. Phys. 166, 259 (1992).

139. J. C.-C. Tseng, S. Huang, L. A. Singer, Chem. Phys. Lett. 153, 401 (1988).
140. J. C.-C. Tseng, L. A. Singer, J. Phys. Chem. 93, 1874 (1989).
141. N. Detzer, W. Baumann, B. Schwager, J.-C. Fröhling, Z. Brittiger, Z. Naturforsch., Teil A. 42, 395 (1987).
142. A. Siemiarczuk, Z. R. Grabowski, A. Krówczynski, M. Asher, M. Ottolenghi, Chem. Phys. Lett. 51, 315 (1977).
143. K. Tominaga, G. C. Walker, W. Jarzeba, P. Barbara, J. Phys. Chem. 95, 10475 (1991).
144. J. Herbich, A. Kapturkiewicz, Chem. Phys. 158, 143 (1991).
145. T. Okada, N. Mataga, W. Baumann, A. Siemiarczuk, J. Phys. Chem. 91, 4490 (1987).
146. S. Masaki, T. Okada, N. Mataga, Y. Sakato, S. Misumi, Bull. Chem. Soc. Jpn. 49, 1277 (1976).
147. N. Mataga, N. Nishikawa, T. Asahi, T. Okada, J. Phys. Chem. 94, 1443 (1990).
148. R. N. Adams, Electrochemistry at Solid Electrodes, Marcel Dekker, New York (1969).
149. Z. R. Grabowski, K. Rotkiewicz, A. Siemiarczuk, D. J. Cowley, W. Baumann, Nouv. J. Chim. 3, 443 (1979).
150. Z. R. Grabowski, J. Dobkowski, Pure Apple. Chem. **55**, 245 (1983).
151. W. Rettig, Angew. Chem. Int. Ed. Engl. 25, 2083 (1986).
152. J. Herbich, A. Kapturkiewicz, unpublished results.
153. A. Kapturkiewicz, Z. Phys. Chem. NF 170, 87 (1991).
154. G. Grampp, W. Jaenicke, Ber. Bunsenges. Phys. Chem. 95, 904 (1991).
155. N. Sutin, Acc. Chem. Res. 1, 225 (1968).
156. R. J. Cave, P. Siders, R. A. Marcus, J. Phys. Chem. 90, 1463 (1986).
157. A. Helms, D. Heiler, G. McLendon, J. Am. Chem. Soc. 113, 4325 (1991).
158. G. Grampp, W. Jaenicke, Ber. Bunsenges. Phys. Chem. 88, 335 (1984).
159. G. Grampp, W. Jaenicke, J. Chem. Soc., Faraday Trans. 2, 81, 265 (1985).
160. L. V. Vilkov, T. P. Timasheva, Dokl. Akad. Nauk. SSSR, 161, 351 (1965).
161. B. Bogdanovic, N. Janke, C Krüger, R. Mynott, K. Schlichte, V. Westeppe, Angew, Chem., Int. Ed. Engl. 97, 972 (1985).
162. S. Müller and J. Heinze Chem. Phys. 157, 231 (1991).
163. F. Schneider, E. Lippert, Ber. Bunsenges. Phys. Chem. 72, 1155 (1968).
164. F. Schneider, E. Lippert, Ber. Bunsenges. Phys. Chem. 74, 624 (1970).
165. W. Rettig, M. Zander, Ber. Bunsenges. Phys. Chem. 87, 1143 (1983).
166. W. Jarzęba, M. Kahlow, P. F. Barbara, J. Imaging Sci. 33, 53 (1989).
167. T. J. Kang, W. Jarzęba, P. F. Barbara, T. Fonseca, Chem. Phys. 149, 81 (1990).
168. A. Subaric-Leitis, Ch. Monte, A. Roggan, W. Rettig, P. Zimmermann, J. Heinze, J. Chem. Phys. 93, 543 (1990).
169. K. Itaya, A. J. Bard, M. Schwarc, Z. Phys. Chem. NF. 112, 1 (1978).
170. A. Zweig, A. H. Maurer, B. G. Roberts, J. Org, Chem. 32, 1322 (1967).
171. A. Kapturkiewicz, J. Electroanal. Chem. 348, 283 (1993).
172. V. D. Parker, G. Sundholm, U. Svanholm, A. Roulan, O. Hammerich in: Encyclopedia of the Electrochemistry of the Elements, A. J. Bard, H. Lunds (eds.), Marcel Dekker, New York (1978), Vol. 11, p. 182.
173. H. Hoshino, K. Kimura, M. Imanura, Chem. Phys. Lett. 20, 193 (1973).
174. G. Grampp, A. Kapturkiewicz, J. Salbeck, Chem. Phys. 187, 391 (1994).
175. K. Krishaji, A. Hausing, J. Chem. Phys. 41, 827 (1964).
176. G. Grampp, A. Kapturkiewicz, W. Jaenicke, Ber. Bunsenges. Phys. Chem. 94, 439 (1990).
177. G. Grampp, W. Jaenicke, Ber. Bunsenges. Phys. Chem. 95, 904 (1991).
178. A. Kapturkiewicz, unpublished results.
179. N. E. Tokel-Takvoryan, A. J. Bard, J. Am. Soc. 95, 6582 (1973).
180. W. L. Wallace, A. J. Bard, J. Phys. Chem. 83, 1350 (1979).
181. J. D. Luttmer, A. J. Bard, J. Phys. Chem. 85, 1155 (1981).

182. R. S. Glass, L. R. Faulkner, J. Phys. Chem. 85, 1180 (1981).
183. H. E. Toma, P. R. Auburn, E. S. Dodsworth, M. N. Golorin, A. B. P. Lever, Inorg. Chem. 26, 4257 (1987).
184. P. A. Mabrouk, M. S. Wrighton, Inorg. Chem. 25, 526 (1986).
185. N. E. Tokel-Takvoryan, R. E. Hemigway, A. J. Bard, J. Am. Chem. Soc. 95, 6582 (1973).
186. J. Gonzales-Velasco, J. Phys. Chem. 92, 2202 (1988).
187. F. Bolletta, M. Vitale, Inorg. Chim. Acta 175, 127 (1990).
188. P. McCord, A. J. Bard, J. Electroanal. Chem. 318, 91 (1991).
189. A. Kapturkiewicz, Chem. Phys. Lett. 236, 389 (1995).
190. M. R. McDevitt, A. W. Addison, Inorg. Chim. Acta 204, 141 (1993).
191. R. F. Dallinger, W. H. Woodruff, J. Am. Chem. Soc. 101, 4391 (1979).
192. M. Forster, R. E. Hester, Chem. Phys. Lett. 81, 42 (1981).
193. S. McClanahan, T. Hayes, J. Kincaid, J. Am. Chem. Soc. 105, 4486 (1983).
194. P. G. Bradley, N. Kress, B. A. Hornberger, R. F. Dallinger, W. H. Woodruff, J. Am. Chem. Soc. 103, 7441 (1981).
195. J. V. Caspar, T. J. Meyer, J. Am. Chem. Soc. 105, 5583 (1983).
196. G. D. Hager, R. J. Watts, G. A. Crosby, J. Am. Chem. Soc. 97, 7037 (1975).
197. R. D. Mussel, D. G. Nocera, J. Am. Chem. Soc. 110, 2764 (1988).
198. R. D. Mussel, D. G. Nocera, Inorg. Chem. 29, 3711 (1990).
199. R. D. Mussel, D. G. Nocera, J. Phys. Chem. 95, 6919 (1991).
200. J. B. Birks, Nouv. J. Chim. 1, 453 (1977).
201. A. Weller, Z. Phys. Chem. NF 130, 129 (1982).
202. R. I. Gould, D. Ege, J. E. Moser, S. Farid, J. Am. Chem. Soc. 112, 4290 (1990).

This work is a part of 3T09A12708 Research Project sponsored by the Committee of Scientific Research.

Advances in Electrochemical Science and Engineering
Edited by Richard C. Alkire, Heinz Gerischer, Dieter M. Kolb and Charles W. Tobias
© WILEY-VCH Verlag GmbH, 1997

Electrochemistry of Oxide High-Temperature Superconductors

Oleg A. Petrii and Galina A. Tsirlina

Department of Electrochemistry, Moscow State University, Vorob'evy Gory V-234,
Moscow GSP-3, 119889 Russia

Contents

1 Introduction 62
2 Peculiarities of Oxide HTSC Materials and the Corresponding Electrodes 64
3 Some Electrochemical Properties of Oxides – Structural Analogs of HTSC 67
4 Charge-Transfer Phenomena on Superconducting Substrates: Electrochemistry in Extreme Conditions 68
5 Electrosynthesis of HTSCs 75
  5.1 Brief Survey of the Methods of HTSC Synthesis and the Possibilities of Electrosynthesis 75
  5.2 Cathodic Codeposition of Alloys and Polymetallic Compositions – the HTSC Precursors 76
  5.3 Electrooxidation of Metals and Aloys 79
  5.4 Electrochemical Variation of HTSC Stoichiometry 81
  5.5 Anodic Electrocrystallization 88
    5.5.1 Characteristics of the Process and the Principal Conditions for its Realization 88
    5.5.2 Anodic Electrocrystallization from Aqueous Solutions: Thallium-Oxide System 90
    5.5.3 Anodic Electrocrystallization in Low-Temperature Alkaline Melts: Norton Method 93
  5.6 Synthesis of Hydroxide Precursors by Varying the pH of the Near-Electrode Layer 75
  5.7 Electrophoresis 96
  5.8 Electrochemical Fabrication of Nanocompositions with HTSC Units 97
6 Electrochemical Properties of HTSC Materials at Ambient Temperatures 99
  6.1 Chemical and Electrochemical Processes that Accompany the Degradation of HTSC Materials 99
  6.2 Electrochemical Coating of HTSC Materials 101
  6.3 Surface Treatment of HTSC Materials: Electrochemical Aspects of Etching and Passivation 103
  6.4 Structure of the Electrical Double Layer on HTSC Oxides 103
7 Electroanalytical Aspects of the HTSC Problem 104
  7.1 Destructive Electroanalysis 104
  7.2 Nondestructive Electroanalysis 105
8 The Prospects for HTSC Photoelectrochemistry 106
9 Conclusions 106
10 References 107

List of Symbols

C_{dl}	double-layer capacitance
D_{Li}	diffusion coefficient of lithium
D_{ox}	diffusion coefficient of oxygen
H_{c}	critical magnetic-field strength
H_{c2}	upper critical field
J_{c}	critical current
T	temperature
T_{c}	temperature of transition to superconducting state
δ	index expressing departure from stoichiometry

Abbreviations

HTSC	high-temperature superconductor
SLC	substituted lanthanum cuprate

Abbreviations for important cuprates and bismuthates are given in Table 1.

1 Introduction

The expression "high-temperature superconductivity" has been used for several decades [1], but it changed from an abstract term to a real one only in 1986 after the famous publication of Bednorz and Müller [2]. Despite the fact that the 20th century has abounded in fundamental discoveries and scientific sensations, the line of inquiry initiated by their work has exceeded all records for the number of specialists involved and, consequently, for the extent of scientific interdisciplinary relationships.

For the first cuprate high-temperature superconductor (HTSC), a substituted lanthanum cuprate (SLC) [2], the temperature of the transition to the superconducting state (T_{c}) is not too high by present standards (Table 1). However, until 1986, the highest known T_{c} was 23.2 K (Nb_3Ge alloy), and the T_{c} values for oxide superconductors known until then were substantially lower. The attention attracted by Bednorz and Müller's result [2] was also significant because theories of superconductivity predicted the existence of a T_{c} upper limit [1, 6]. The corresponding estimates only permitted one to expect on increase of a few Kelvins. All the more revolutionary, both in the fundamental and in the applied aspects, became the subsequent discovery of the oxide HTSC of the YBCO system with a T_{c} higher than the liquid nitrogen temperature, followed by the discovery of other cuprate systems with still higher characteristic values. The main systems are shown in Table 1 (together with the abbreviations used below), and various substituted derivatives are known for each of them. To date, the greatest T_{c} values exceed 130 K [7], and at elevated pressure are about 150 K [8].

The search for new HTSC oxides, which had been very successful in the first two years, then became seemingly less effective in that no new HTSC systems were

Table 1. The main groups of oxide supercondutors (in accordance with [3–5]).

Oxide system	$T_c[\mathrm{K}]^{(a)}$	Year of discovery	Abbreviation
TiO, NbO	1.0	1964	–
$SrTiO_{3-x}$	0.7	1964	–
Ag_7O_8X (X = anion)	1.0	1966	–
Bronzes A_xMO_3 (A = alkali metal; M = Mo, W, Re)	4.0–6.0	1965–1969$^{(b)}$	–
$LiTi_2O_4$	13	1974	
Bismuthates			
$Ba(Pb,Bi)O_3$	17	1975	–
$(Ba,K)BiO_3$	≤ 34	1988–1989$^{(b)}$	BKBO
$(Ba,K,Rb)BiO_3$	37	1989	–
$(La,R)_2CuO_7$ (R = Ba, Sr)	35	1986–1987$^{(b)}$	–
$LaCuO_4$	≤ 45	1987	LCO
$YBa_2Cu_3O_7$	95	1987	YBCO
$LnBa_2Cu_3O_7$ (Ln = rare-earth metals)	≤ 95	1987	–
$Bi_mSr_2Ca_nCu_pO_q$	≤ 110	1987–1988$^{(b)}$	BSCCO
$Tl_mBa_2Ca_nCu_pO_q$	≤ 128	1987–1988$^{(b)}$	TBCCO
$Hg_mBa_2Ca_nCu_pO_q$	≤ 130	1993	HBCCO

(a) The highest known values are given.
(b) Year of discovery–year of achieving the maximum T_c.

discovered in the four years up to 1993 [5]. At the same time, the initial empirical searches have given way to more comprehensive studies of materials, with the composition determined on the basis of various structural predictions [5,9–13]. Therefore, one might expect Table 1 to be supplemented in future.

Most HTSC oxides have the structure of perovskite (though some of them have the spinel-type structure), which pertains to more than 35 structural classes [14], and includes more than a hundred typical unit cells [15]. Along with cuprates, certain bismuthates also exhibit HTSC properties. For fundamental studies of superconductivity in oxides, both the absolute T_c values and the variety of properties and structures are essential. Therefore, the titanium compounds with relatively low T_c values are also actively studied.

Electrochemical studies of HTSC began immediately after their discovery [2]. At present, there are more than 400 publications on this problem, not counting the numerous studies of ionic transport in HTSC solid electrolytes, which are only selectively presented in this review. Hence, the electrochemistry of HTSC can be considered as a new direction in electrochemical science and technology.

The search for approaches to the HTSC problem was largely based on analogies with electrochemical studies of semiconductors [16–19]. Since the majority of HTSC materials exhibit semiconducting properties at ambient temperatures. Moreover, technological problems arising in the practical application of materials of these classes (such as in the electronics field) are similar. The analogy thus stimulates the electrochemical studies on the degradation of HTSC and the deposition of protective coatings, and also the studies of the etching processes.

The potentialities of electrolysis for synthesizing various multicomponent materials, including alloys and semiconductors, has attracted the interest of solid-state chemists for several decades [20–25]. Electrochemical methods for fabricating certain HTSC materials demonstrate significant advantages over alternative conventional methods. It is evident that the possibility of electrosynthesizing a particular material is determined, first of all, by the chemical and electrochemical properties of the elements entering into it. From this viewpoint, it does not matter what is synthesized – the HTSC material or a certain multicomponent oxide. In the text below, studies on the electrochemical synthesis of various oxide materials include data on HTSC electrosynthesis which are represented as fully as possible. In recent years, synthesis investigations have been reported for the electrochemical tailoring of micro- and nanocompositions for electronics, including those with HTSC units.

Attempts have also been made to contribute to the theory of superconductivity in oxide systems by investigating the properties of HTSC electrodes in the common and superconducting states. HTSCs at ambient temperatures are also of interest for traditional electrochemistry as well-characterized novel materials e.g., for the development of the theory and practice of electrocatalysis.

Several attempts to review HTSC electrochemistry have been made fairly recently [26, 27], but the field is developing very rapidly, and more recent work has contributed considerably to its advancement. Taking into account the recent experimental experience and the progress in the chemistry and physics of HTSC, the quality of current studies is considerably higher than those of the early years. Brief reviews published in 1993 and 1994 [28, 29] selectively covered only a fraction of the available publications. In the present review, we intend to accomplish the following tasks.

1. Demonstrate the variety and potentialities of electrochemical methods and approaches for solving various materials-science problems that arise in studies of multicomponent nonstoichiometric oxides.
2. Analyze in detail the analogies between HTSCs and the electrode materials studied earlier, and outline the most interesting properties of the new materials.
3. Systemize the approaches to electrosynthesis and combined synthesis of oxide compositions.
4. Outline the most promising approaches for further research and practical applications.

2 Peculiarities of Oxide HTSC Materials and the Corresponding Electrodes

The value of T_c defines the nature of the cooling agent required to transform the material into its superconducting state. At $T_c > 77$K, the cooling material would be liquid nitrogen, and at $T_c < 77$ K it would be liquid hydrogen or helium. "Low-temperature" superconductors Nb_3Ge and Nb_3AlGe also have a T_c higher than the boiling point of hydrogen, though the difference is minor and requires the use of liquid hydrogen with evacuation; that is essential primarily for the technological applications.

Apart from T_c, the following factors are the most important characteristics of HTSC material [1,6,30].

1. The width of superconducting transition, i.e., the temperature interval between the onset of the sharp resistivity fall and the attainment of the zero resistivity (transitions 0.5 K wide are considered to be sharp).
2. The critical current J_c – the greatest current that can pass in a real material in the superconducting state. In the absence of magnetic field, the greatest J_c values in oxides exceed 10^6 A/cm^2 [30].
3. The critical magnetic-field strength H_c; for the second kind of superconductors, to which oxide HTSCs belong, it is the so-called upper critical field H_{c2}. At $H > H_{c2}$, the superconducting state disappears throughout the material bulk.
4. The differential characteristics $\mathrm{d}J_c/\mathrm{d}T$, $\mathrm{d}H_{c2}/\mathrm{d}T$, $\mathrm{d}T_c/\mathrm{d}H$, and $\mathrm{d}J_c/\mathrm{d}H$ (the derivatives of J_c and H_{c2} on T, and also of T_c and J_c on H, are negative).
5. The anisotropy of J_c and H_{c2}, which for cuprate HTSC is described in terms of dimensionless ratios between the components of these values corresponding to the O–Cu–O planes and planes perpendicular to them.

All the listed values (especially J_c and $\mathrm{d}J_c/\mathrm{d}H$) strongly depend on the structure of the real materials. At the same chemical composition these values can differ by several orders of magnitude.

The main types of HTSC are single crystals, ceramics (pressed and/or sintered disperse HTSCs) and films on foreign substrates which, in turn, may be subdivided into ultrathin (< 0.1 μm), thin (0.1–0.5 μm), and thick (> 5–10 μm) by analogy with the classification accepted in microelectronics [31]. Single crystals often used in fundamental studies are less defective, though for large samples the defectiveness and even the composition can change with depth. Ceramics and especially films are of greater interest for practical applications, and the numerous studies of these materials are at present directed toward the elucidation of the effects of macrostructure, particularly the composition and the structure of grain boundaries [32].

All oxide HTSCs are nonstoichiometric compounds. For example, $YBa_2Cu_3O_{7-\delta}$ (YBCO) has a composition which is formally characterized by the value of $\delta < 1$. (For the sake of brevity, Table 1 shows only integer coefficients.) As a rule, changes in δ unaccompanied by phase destruction can amount to several tenths, although cases are known with $\delta = 1.6{-}1.8$. For many HTSCs, the superconducting/nonsuperconducting oxide phase transition proceeds at a certain value of δ.

Nonstoichiometry can be caused by oxygen deficiency (or excess) or by fractional valences of the metal components. For example, the existence of Cu^{3+} in nonstoichiometric cuprates has been widely discussed [9, 10]. It is essential that in nonstoichiometric oxides the microscopic fluctuations of the composition should proceed (the so-called phase separation). The characteristic size of heterogeneities induced can exceed atomic dimensions by an order of magnitude. This phenomenon is attributable to the fact that the electron-nonuniform state of such chemically single-phase materials appears to be energetically more advantageous.

Phase separation results in the existence of superconductivity only in a part of the oxide volume. For samples of high quality, the content of the superconducting phase can reach 50 percent and more. The additional factor that reduces this characteristic is the crystallographic chemical nonuniformity of the phase, which is caused by the imperfection of the method of synthesis or by certain degradation processes.

It is practically impossible to prepare a stable HTSC material for which all the desired characteristics are present simultaneously. However, in specific applications, only a few of the above-mentioned characteristics are usually important. Moreover, advantage can be taken of certain effects which lead normally to unwanted characteristics of HTSC materials, for special purposes. For example, when the grain boundaries have microscopic areas with low conductivity, it is possible in certain cases to realize the Josephson and related effects.

The application of the most available ceramic specimens of HTSC materials as electrodes is limited, due to incomplete wettability, diffusion limitations in pores, and ohmic losses at the grain boundaries. As a rule, studies of ceramic electrodes should be preceded by optimization of the pressing and sintering conditions, similar to that worked out for physical investigations [33]. Such problems can often be solved by introducing polymer binders and/or carbon fillers, and by using paste electrodes [34–41]. Smooth HTSC electrodes are obtained from ceramics by filling their pores with paraffin [42–45] or by encapsulating ceramics into microelectrodes [46–50] with dimensions of 3–15 μm which exhibit adequate characteristics in redox transformations of various reactants at normal conditions. Techniques have been developed for preparing ceramic disk electrodes with rings of platinum, gold, or glassy carbon [51–58], with which on-line control and quantitative analysis of the products of electrode processes is possible. High-quality HTSC films can usually be obtained only on nonconducting substrates (MgO and $SrTiO_3$ are used most frequently) so that the corresponding electrodes require special techniques which have been previously worked out in connection with thin-film resistive electrodes [59].

Practically all HTSC materials contain chemically active elements with the consequence that various degradation processes are bound to proceed accompanied by the loss of superconducting properties in air, and especially in moist atmospheres and electrolyte solution. Hence, it is essential to carry out electrochemical studies only in media for which degradation does not proceed or is very slow. These are, primarily, aprotic solvents, and also aqueous alkaline solutions of sufficiently high concentration, including those to which have been added salts of the elements of the HTSC components. Thus, in ordinary aqueous solutions, at not too low a pH one can study relatively stable thallium- and bismuth-based HTSCs, and also LCO and certain of its derivatives.

The specifics of the degradation phenomena define the electrode pretreatment. In the case of mechanical treatment, the surface composition can vary due to heating [60], and this can be avoided by polishing in nonaqueous solutions [47] or by slowly cutting the surface layer while it is out of contact with air. Chemical treatment [60, 61] will be discussed below in the context of the HTSC etching problem.

In the electrochemical investigations of HTSC it is of great importance to control the resistive and magnetic properties of materials during synthesis as well as before and after the electrochemical experiments. Only independent measurements of both types can reliably ascertain the transition to the superconducting state. Resistometry of HTSC/metal samples can exhibit errors, due to short-circuiting through the substrate. Problems also arise during physical studies of moist samples. Therefore, it is necessary to develop special methods of physical testing for each specific electrochemical system, and to check the various side-effects in auxiliary test experiments.

Earlier work (1987–1989) took no account of these factors, and thus may contain serious errors. In more recent investigations, improved physical characterization has become more common practice in electrochemical studies on the HTSC problem, and the range of methods used has expanded rapidly, e.g., measurement of critical currents, magnetic-field tests, studies of anisotropy, etc.

3 Some Electrochemical Properties of Oxides – Structural Analogs of HTSCs

Oxides are by no means new materials to electrochemists [63–76] and have been actively studied in connection with electrocatalysis and anodic oxidation of metals. In particular, a great deal of information has accumulated on the electrochemistry of two- (and more-) component perovskites and also of spinels, both of which are structurally similar to HTSC oxides.

The high electrocatalytic activity of perovskites in oxygen reactions [77, 78] greatly depends on the stoichiometry. Numerous electrocatalytic studies performed on perovskites of which several reviews are available [68, 79–83] were chiefly devoted to the oxygen-evolution reaction. These investigations dealt with several tens of systems with the composition $A_{1-x}B_xM_yN_{1-y}O_{3\pm\delta}$ (A = La, Pr, Nd, Sm, Gd; B = Sr, Ni, Pb, Ca, K, Ce, Th; M = Ni, Co, Fe, Mn, Cr; N = Fe, Ni, Co, V, Ti, Mn), i.e., practically all the perovskites with sufficiently high conductivity known in the 1970–1980s.

The use of many of these materials as cathodes was hindered by their reduction, in the course of which, along with the formation of soluble products, the changes in the valence state of M and N components in the solid state apparently take place [84–87]. X-ray diffractometry was used for controlling the homogeneity of the electrodes (see, e.g., [88]). Similar changes were also observed for perovskite anodes [86, 87, 89, 90] and were accompanied by the appearance in the anodic polarization curves of regions with high slopes or a horizontal plateau which preceded the Tafel region of oxygen evolution. During anodic oxidation, anions of the elements M and N in the highest valence states were observed in the solution [91], and passivating films of the highest oxides and hydroxides were found to appear on the surface [92]. Similar trends were also observed for certain spinels [93].

In the majority of publications [79–83] only the correlation of electrocatalytic activity with the composition of various perovskite and spinel materials was considered. For $NiCo_2O_4$ [90, 93, 94] and $LaNiO_3$ [95, 96] extremely high rates of the oxygen reaction were achieved which exceeded those known for platinum by 2–5 orders of magnitude.

Attempts to quantify electrocatalytic activities on the basis of correlation dependences that take into account the volume properties [79–81, 97, 98] made it necessary to obtain well-characterized experimental data, and thus stimulated the improvement of perovskite electrode construction. Methods were developed for determining the real surface area of disperse perovskites in the electrodes with polymer binders [99], and also for measurements on quasi-smooth, highly conductive ceramics [81, 82, 100]. This experience was applied successfully later in the studies of HTSC electrodes.

Determination of stoichiometric effects (mainly controlled by cation substitution [82, 100]) was an important achievement of electrocatalytic studies of perovskites. These served to widen views on the adsorption properties of these materials, and to test assumptions on the composition of adsorption layers on perovskites made on the basis of the analysis of kinetic data of oxygen reactions [85, 101, 102]. The probability of the formation of various oxygen-containing adsorbates in certain sites on perovskite surfaces was estimated by theoretical analysis [83].

The prospect of using perovskite materials of formula $La_{1-x}Sr_xCoO_3$ as reversible oxygen electrodes has been discussed [103–105]. On these electrodes, as well as on spinels [106], equilibrium with respect to oxygen is established between the solution and the oxide bulk. The possibility of reversibly changing the oxygen stoichiometry of HTSCs was considered in context with the search for the new accumulating electrodes [107]. In both cases, the main limitation is caused by the low rate of oxygen transport in the solid phase (see [108–111] and the discussion in Section 5.4). Perovskites find application both as electrolytes [112] and as electrodes [113] in medium-temperature solid electrolyte fuel cells. Spinel oxide electrodes are actively used in carbonate high-temperature fuel cells [114].

Studies of perovskite and other oxide electrocatalysts continue to be of great interest [115–118]. The high activities of perovskite catalysts for the oxidation of organic substances [119, 120] has stimulated related electrocatalytic studies [121–123]. Perovskites are also convenient inactive substrates for electroanalytical purposes [124]. These investigations are intrinsically related to the electrochemistry of HTSC and serve therefore to extend the circle of well-characterized electrode materials.

4 Charge-Transfer Phenomena on Superconducting Substrates: Electrochemistry in Extreme Conditions

Studies of the kinetics of electrode processes on HTSC materials over a wide temperature interval which includes T_c are taking a direction which could advance future understanding of the most fundamental problem of electrochemical kinetics –

the elucidation of the nature of electron and proton tunneling processes. Electrodes of HTSC oxides make it possible not only to change sharply the nature of materials (without changing their composition), but also to realize a principally new type of electrode material.

Before 1986, when the question of studying electrochemical processes on materials in the superconducting state even was not raised, experimental approaches were developed for studying electrochemical systems substantially below room temperature. These formed the basis of cryoelectrochemistry, for the history of which several reviews are available [125, 126]. The approach based on the use of proton-conducting solid electrolytes – hydrates of acids (primarily, $HClO_4 \cdot 5.5H_2O$) – was developed thoroughly [127–130]. In these systems, the double-layer capacitances were measured as well as the kinetic parameters of the hydrogen evolution reaction on certain metals at temperatures as low as 130 K. Measurements with electrolytes were carried out at temperatures as low as 80 K [131] and even 50 K [132].

To interpret data obtained in these systems it is necessary to take into account the changes in the conduction mechanism of acid solid electrolytes in the vicinity of 120 K [133]. At this temperature the activation energy of conduction abruptly decreases, and in the vicinity of 80 K approaches zero. Probably, this corresponds to proton tunneling in the rigid structure of ice. Thus, in the region of still lower temperatures, ohmic losses become essentially temperature-independent in acid solid electrolytes. Therefore the use of acid crystal hydrates makes it possible, in principle, to carry out electrochemical measurements on cuprate HTSC in the superconducting state over a sufficiently wide temperature interval. Bockris and Wass [134] have accomplished such measurements on palladium-doped YBCO ceramics in a cell containing $HClO_4 \cdot 5.5H_2O$ and have attributed the observed currents to the hydrogen evolution reaction. The observed temperature dependence of the current had a maximum at the T_c (Fig. 1(a); Table 2).

Lorenz, Breiter, and co-workers have systematically worked in the same directions by choosing a particular solid electrolyte for low-temperature ($T \geq 10$ K) studies of HTSC electrodes, and by investigating processes uncomplicated by gas evolution on the interface. This group studied in detail the Ag^+ conducting materials: silver-modified glass and β-Al_2O_3, and also $RbAg_4I_5$ [135–148]. They have also found the interval of practical temperature independence (10–100 K) of conductance for these electrolytes which can be attributed to the crystalline/glass-like transition. The electrochemical reactions in the Ag^+/Ag system on the interfaces of various HTSC materials with the chosen electrolytes were studied [135–148] by using mainly open-circuit impedance spectroscopy (with two-, three-, and four-probe schemes). In a number of experiments, silver clusters were preliminarily deposited on the HTSC surface. These authors have solved the principal experimental problems associated with the considerable ohmic losses and the slow establishment of the interface equilibrium in the low-temperature region (for details see [144]). The main result is the interruption of the monotonic temperature dependence of the electrode reaction rate in the vicinity of T_c. Table 2 illustrates this result which consists of an abrupt increase in the rate by a factor of 1.5–2 followed by a subsequent decrease (the so-called hump). In early work, the rate of electrochemical processes was approximately characterized by the impedance value, which at low

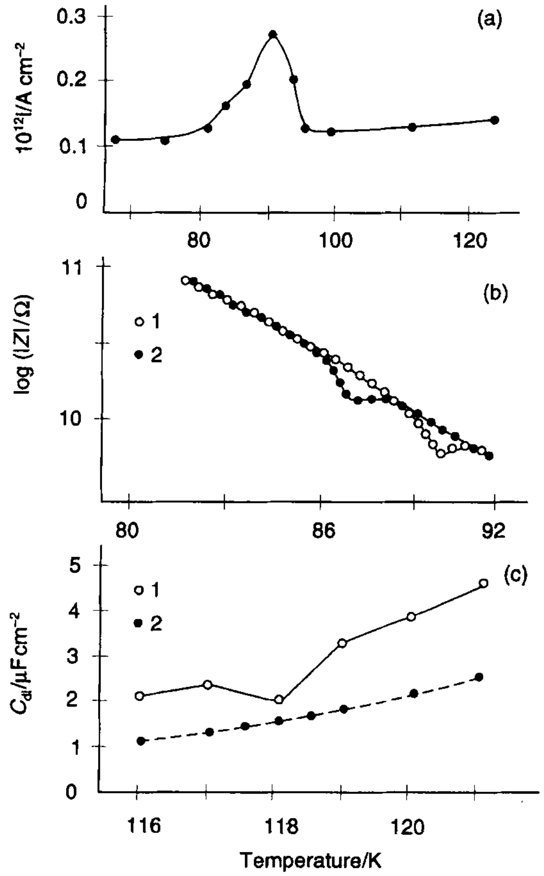

Fig. 1. Examples of anomalies in electrochemical interface characteristics in the vicinity of T_c. (a) Current vs. temperature dependence for proton discharge on $YBa_2(Cu_{0.9}Pd_{0.1})O_{7-x}$($T_c$ = 90 K) in $HClO_4 \cdot 5.5H_2O$ [134]. (b) Shift of impedance minima under magnetic field for Ag/Ag^+ reaction at the YBCO/$RbAg_4I_5$ interface [147]; magnetic field strength: 0 (1), 1 T (2). (c) C_{dl} vs. temperature dependences for TBCCO; T_c = 119 K (1) and glassy carbon (2) measured in a butyronitrile-dichloroethane quasi-liquid solution at potentials −2.5 and −3 V (vs. Ag), respectively. Supporting electrolyte is 0.1 M tributylammonium perchlorate (TBAP) [153].

frequencies (or the order of 10 mHz) was mainly due to polarization resistance. While the current maximum at T_c for the hydrogen evolution reaction could be attributed to certain specific features of the proton tunneling [134], similar data for processes of quite different nature make it possible to consider the current increase near T_c as a universal effect for different charge-transfer processes. According to this view, the current increase is caused by the specific features of the electron tunnelling on a superconducting electrode. It was observed that at $T < 70$ K the charge-transfer rate is practically independent of the temperature for all HTSC systems investigated.

Since the effects listed in Table 2 are small in magnitude, it is very important to check their accuracy by different methods. At present, the fact that the current

Table 2. Experimental data on the parameters of current anomalies [134–147].

TSC	Solid electrolyte type	T_C[K]	$T_{i_{max}}$[K]	Relative value of current at the maximum
TBCCO				
$n = 2$	Ag^+	105	100 ± 5	1.3 ± 0.2
	Ag^+	102	103 ± 2	
$n = 3$	Ag^+	113	124 ± 6	1.6 ± 0.2
Sr-doped	Ag^+	102	102 ± 5	
Pb,Sr-doped	Ag^+	44	44 ± 2	
		74	74 ± 2	
YBCO	Ag^+	92	93 ± 2	2.0 ± 0.2
Pd-doped	H^+	90	90 ± 5	2.1 ± 0.2
Zn-doped	Ag^+	75	75 ± 2	2.0 ± 0.2
		50	50 ± 5	1.8 ± 0.2
		40	32 ± 6	1.6 ± 0.2
$(Nd, Ce)_2CuO_4$	Ag^+	23	23 ± 1	1.6 ± 0.2
NbAlGe	Ag^+	19.3	20 ± 1	1.15 ± 0.05

anomaly is observed precisely near T_c can be considered reliably confirmed by the following factors.

1. The T values at which the effect was observed on various HTSC, and also on the usual type of metal superconductor (Table 2), coincide with the corresponding T_c values with fair accuracy.
2. For nonuniform samples containing different HTSC phases a set of maxima is observed.
3. Under an external magnetic field which reduces the T_c, the anomaly is shifted (Fig. 1(b)) [147].

These results suggest that electrochemical measurements provide a method of determination of T_c for HTSC materials.

The existence of a current hump near T_c is confirmed by several additional facts. In the first place, these are deduced from the results of the quantitative treatment of the impedance spectra of the HTSC/solid electrolyte system [147]. This approach consists of calculating from the experimental complex-plane impedance diagrams the parameters characterizing the solid electrolyte, the polarization resistance of the reaction with the participation of silver, and the double-layer capacitance (C_{dl}) for each T value (measured with an accuracy of up to 0.05°). Temperature dependence of the conductance and capacitance of the solid electrolyte (considered as control parameters) were found to be monotonic, while the similar dependences of two other parameters exhibited anomalies near T_c. The existence of a weakly pronounced minimum of C_{dl} near T_c, which is of great interest in itself, was interpreted by the authors as the result of sharp reconstruction of the interface in the course of superconducting transition [145].

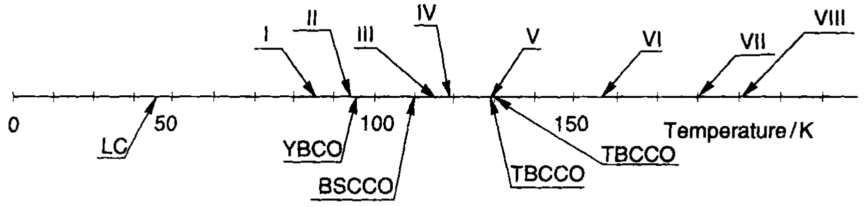

Fig. 2. Relative scale of the T_c of the main HTSC groups and solidification points of different mixed solvents: chloroethane + butyronitrile (I), n-pentane + methylcyclohexane + n-propanol (II), bromoethane + butyronitrile + isopentane + methylcyclopentane (III), chloromethane + dimethyl ether (IV), bromoethane + butyronitrile (V), propionitrile + butyronitrile (VI), methanol + dichloromethane (VII), ammonia + isopropanol + dimethylformamide (VIII). Data are taken from [28, 152].

Another test experiment resulted from comparative studies carried out in cells with a solid electrolyte of HTSC ceramics of YBCO and also the $YBa_2Cu_3O_6$ phase which possesses no superconducting properties. The nonsuperconducting material revealed no anomalies in its electrochemical behavior over a wide temperature interval, and in a number of experiments was used as the reference electrode.

Murray, MacDevitt, et al. have realized using cryoelectrochemical methods, unique measurements in liquid electrolytes with ultra-low (90 K and lower) solidification points [28, 149–151]. This allowed sufficiently simple charge-transfer processes to be carried out under conditions in which both redox forms are in solution. In Fig. 2 the melting points of certain organic mixtures are compared with T_c values of the main HTSCs. Mixtures of butyronitrile and chloroethane (0.2 M) $(C_4H_9)_4NClO_4$ supporting electrolyte) were successfully used in voltammetric studies. Such measurements were carried out on gold microband electrodes at temperatures down to 103 K [151] and 83–153 K [150] for model redox reactions of tetracyanoquinodimethane (TCNQ) and Ru(2 + /3+) mixed complexes , respectively. Curtin et al. [149] carried out a detailed study of the redox transformations of alkanethiols, the ferrocene derivatives being immobilized on silver and gold. The lower limit of the temperature interval in which reliable data were obtained (115 K) was substantially higher than the solvent freezing point. Strictly speaking, when the temperature decreases the transition of the liquid into the quasi-liquid state can precede the solidification. This quasi-liquid state is characterized by sufficiently low conductivities for the problem of ohmic losses in liquid electrolyte to be of no less importance than in solid ones. Voltammograms obtained in such solutions are deformed to a lesser extent when micro- or ultramicroelectrodes are used.

Peck et al. [153] carried out an experiment, which to date remains unique, on electrodes in the superconducting state. Unfortunately, instead of voltammetry, they used the less direct method of impedance measurements in the frequency range 10^{-2}–10^{-4} Hz. They studied two TBCCO microelectrodes (T_c 112 and 119 K) and also (in test experiments) platinum and glassy carbon. All these electrodes were cathodically polarized under potentiostatic conditions (so that the amplitude of potential modulation was substantially lower than its constant component). The equivalent circuit included C_{dl} and the parallel polarization resistance. The nature of the electrochemical reaction was not entirely clear to the authors; probably it was the reduction of chloroethane – the solvent component. Both the C_{dl} (Fig. 1(c)) and the polarization resistance measured on the HTSC exhibited anomalies in the vicinity of T_c, while similar parameters of the test electrodes changed smoothly with T. The effect of the delay on the C_{dl}, T dependence for HTSC electrodes was reproducible, although small, and took place in a narrow (1–2 K) temperature interval. In a number of experiments small C_{dl} minima (not exceeding 10–20 percent of C_{dl}) were observed at T_c. In [153], reproducibility of the capacitance absolute values was not attained (probably due to uncertainty in determination of the TBCCO surface area). The anomalies of the temperature dependences of polarization resistance were even smaller in terms of the absolute values of effects, and their reproducibility was worse.

The detailed interpretation of data on HTSC electrochemistry obtained until now in both liquid and solid electrolytes is essentially complicated by the same problem – the choice of the equivalent circuit adequately describing the impedance for the nonzero overvoltages. Peck et al. [153] carried out the quantitative treatment of the results for low- and high-frequency regions separately. As mentioned previously, a thorough treatment of complex-plane impedance diagrams was performed for data obtained in solid electrolytes, but only for the equilibrium potential.

It is evident that the kinetics of electrochemical processes occurring in experiments on HTSC electrodes is determined (at least in a certain frequency range) not by the charge transfer, but by crystallization, chemical, or other phenomena, and these considerably complicate the impedance behavior. Two methods can be considered for solving this problem in the future.

1. Investigations of processes of a simpler nature in liquid electrolytes with model redox systems, or in solid electrolytes with mobile polyvalent metal ions.
2. Investigations in liquid electrolytes using voltammetry and stationary polarization measurements.

The approaches to these investigations are, in fact, well developed. At least two classes of HTSC (thallium- and mercury-based) make it possible to operate on electrodes in the superconducting state at temperatures higher than 115 K, i.e., in the temperature interval studied with model systems [149–151].

The theory of charge transfer across the superconductor/electrolyte interface which was developed in recent years [154–159] predicts a number of effects which accompany the transition into the superconducting state. Originally [154], the change of the electrode process rate near T_c was assumed to be relate to (1) the fact that the wider the superconducting energy gap, the more the tunneling of individual electrons is suppressed (this mechanism was also developed in [155, 159]), and (2) the appearance of a new route of charge transfer as a result of electron-pair (the so-called correlated charge carriers or Cooper pairs) tunneling to two spatially separated reagent particles near the interface.

A mechanism similar to the latter was also put forward recently [134, 138, 140]. It was noted [138, 140] that in Ag^+-conducting solid electrolytes two-level tunneling is possible which, according to these authors, can enhance the probability of Cooper-pair tunneling. However, it is most difficult to explain the extreme form of the temperature dependences of the current: the appearance of the hump, but not the jump. The following qualitative explanations were put forward for the fact that at $T < T_c$ the acceleration effect is not retained:

- the effect of chemical and crystallization stages which are insensitive to the superconducting transition on the kinetics of the process (and also on the measured impedance);
- a gradual decrease in the contribution of one-electron transfer with the simultaneous transfer of pairs (this explanations does not contradict the considerations of Kuznetsov [154]);
- the self-inhibition of the process as a result of the changes in the interface structure (for example, the crystallization of considerable amounts of metal); estimates [144] show that this effect is of low probability.

Attempts have been made to estimate quantitatively the various effects possible from the theoretical viewpoint on an electrochemical interface for superconductors have been made. For example, it was established [154, 156, 158] that the probability of the electron-pair tunneling is, in principle, always substantially lower than that for usual electrons (all other factors being equal), a result that implies the prediction of inhibition near T_c. Kuznetsov [158] considered in detail the mechanisms of the processes with the participation of Cooper pairs. For instance, the energy barriers were estimated for a variety of mechanisms, including the transfer to one and the same particle (capable of multielectron transformation) to two spatially separated particles, and also the transfer of the pair to one particle with the simultaneous transition of one of the pair's electrons to the normal state. It was found that the properties of the system can vary substantially, depending on the relationship between the band gap, the medium reorganization energy, and the overpotential.

We will only note several qualitative predictions of the theory [154, 156, 158] concerned with the possible special properties of electrode processes on superconductors for the case of tunneling of electron pairs:

1. the second-order dependence of the current density on the reagent concentration (at the transfer of a pair to spatially divided particles);
2. the current density decrease in the magnetic field for paramagnetic reagents and its increase (or the absence of magnetic-field effects) for nonparamagnetic reagents;
3. the existence of a critical value of overpotential and the fact that before this value is attained the process rate is extremely small and independent of potential;
4. the existence of a wide region where the current depends linearly on the overpotential;
5. the possibility of the appearance of a maximum on the polarization curve;
6. photosensitivity of all processes at an incident light energy no less than a certain critical value related to the gap band.

Taking into account the analysis in [158], it was concluded that it is possible for the current maximum to appear near T_c, at least in a certain overpotential region. A situation when the maximum is shifted to temperatures lower than T_c is also theoretically possible. It is noteworthy that a maximum in the rates of chemical reactions near T_c was also observed experimentally [160].

The development of the theory of charge-transfer elementary acts on superconductors on the basis of traditional theories of electrode kinetics [161, 162] is limited by the state-of-the-art of the superconductivity theory as a whole, and particularly the HTSC theory [163]. So far theoreticians preferentially use the concepts of the classical Bardeen–Cooper–Schrieffe (BCS) theory [6] developed in the 1960s for common superconductors. Because the applicability of the BSC theory to HTSC materials is not without dispute, the theory of charge-transfer elementary acts will become transformed as adequate HTSC theory develops.

Investigations to date of the charge distribution on the HTSC/ionic electrolyte and HTSC/semiconductor (p- and n-) interfaces [145, 147], and also similar studies of the HTSC/conducting polymer type of composition [28, 50], relate directly to fundamental aspects that arise in modern electronics technology [164]. Of particular interest is analysis of the so-called proximity effect, a sharp increase in metal conductivity as a result of its contact with a superconductor.

Such studies go beyond the scope of electrochemistry, but certain electrochemical experimental methods are used to investigate high-quality junctions on the boundary of two solid phases. Investigations of superconducting electrodes thus bring the field closer to solid-state physics, the result of which is beneficial for the development of electrochemistry as a whole.

5 Electrosynthesis of HTSCs

5.1 Brief Survey of the Methods of HTSC Synthesis and the Possibilities of Electrosynthesis

Conventional methods for synthesizing HTSC include (at least at one of the stages) a high-temperature treatment in order to achieve sufficient crystallization of the oxides. At incomplete levels of crystallinity, the characteristics of HTSC materials prove to be unsatisfactory.

Single-stage chemical synthesis by annealing stoichiometric mixtures of individual oxides is often used for preparing ceramics. When highly volatile oxides are used (thallium- and mercury-based HTSCs), the process is carried out in hermetically sealed ampoules with an excess of the volatile component. The heating temperatures usually exceed those of the crystallization and can take up to 10 h or more.

Two- and multistage methods are used more frequently (and exclusively for the preparation of HTSC films) [4, 165], and the annealing is always the final stage. In the earlier stages, the HTSC precursors (stoichiometric metals components mixtures or their compounds that decompose at the annealing temperature) are obtained by chemical [166] or physical [4] methods. These methods include vapour phase deposition, decomposition of metal-organic compounds, different types of sputtering, laser ablation, etc. The requirements as to precursors can differ for different purposes, but in any case it is necessary to achieve as uniform a component distribution as possible in order to reduce the annealing temperature and to promote HTSC–substrate interaction.

Stoichiometric oxides can be used as precursors for high-quality ceramics (at the second stage the necessary changes in δ are achieved by carrying out the annealing in vacuum or in an atmosphere of a certain composition). The methods of preparation of HTSC single crystals based on the use of saturated melts [167] differ greatly from that described.

The search for new methods of HTSC synthesis is stimulated by the necessity of combining HTSCs in various devices with certain metals, semiconductors, or dielectrics. In each particular case, the technologies should be based on a method that simultaneously ensures the stability of all the materials in the configuration as well as the optimal characteristics for performance. Therefore, multistage combined methods which have the potential for optimization are finding increased use.

The electrosynthesis of HTSCs began to develop somewhat later than most other approaches and at first could compete with the conventional methods only in specific applications. However, in the last two to three years, interest has grown in certain versions of HTSC electrosynthesis. The main limitation of electrosynthetic methods lies in the need to use conductive substrates or materials covered with thin conductive layers. The most significant potential advantage of all electrochemical methods consists in the possibility of accurately controlling the amount of the resulting product by on-line coulometry, the error of which does not exceed a few percent of the charge consumed in the formation of a monolayer.

The approaches to HTSC electrosynthesis known to data are classified below according to the nature of the corresponding electrochemical processes. It should be emphasized that so far only process (anodic electrocrystallization) allow one to obtain HTSCs directly. The other cases deal with the fabrication of HTSC precursors or their electrochemical processing.

5.2 Cathodic Codeposition of Alloys and Polymetallic Compositions – the HTSC Precursors

Both crystalline [168] and amorphous [169] alloys are considered as precursors in the preparation of HTSC films. Atomic-level uniformity of the component distribution in metallurgical alloys can be achieved. One more type of metal precursor, the oxidation of which gives good results under relatively mild conditions, are multilayer polymetallic coatings with nanometer-thick layers [170]. Similar compositions are also the most frequently used type of precursors in the technology of semiconductors [171].

The codeposition of metals from electrolytes of complex compositions is well established for a large number of systems [172]. In such systems, the chemical and/or

Table 3. Experimental data on the electrodeposition of metal precursors of HTSCs.

HTSC Synthesized	Solvent[a]	Substrate	Reference
YBCO	DMSO		[174]
	DMF, DMSO	$SrTiO_3$,$CaTiO_3$/Ag; Zr	[175, 176]
	DMSO+H_2O	Ag	[177]
	DMSO	F^--doped SnO_2; Cu; brass; stainless steel	[178]
	DMSO	MgO/Ag; ZrO_2/Ag	[179]
	DMSO	Cu; Cu–Ag	[180]
Dy-substituted	H_2O	Stainless steel; F^--doped SnO_2/MgO	[181]
Eu-substituted	DMF	$SrTiO_3$,$CaTiO_3$/Ag; Zr	[175]
BSCCO	DMSO		[182]
	H_2O	Stainless steel; Cu; Ti; F^--doped SnO_2/MgO; brass	[183, 184]
	DMSO+H_2O	Ag	[177]
	acetone, H_2O	F^--doped SnO_2/MgO	[185, 186]
	H_2O	Ag	[187]
	DMSO	MgO/Cu; Ag	[188]
	DMSO	YSZ; Ag; MgO/Ag	[189]
Pb-substituted	DMSO	Ni; Pt; Cu; Ti; MgO; quartz; mica/Ag; Cu	[188, 190, 191]
Tl,Pb-substituted	DMSO, DMF	Au; Ag; Ni; Cu; Ta; Mo	[192, 193]
TBCCO	DMSO	Ag	[194–196]
		MgO/Ag/Ni–Ag	[197]
		ZrO_2; MgO; $SrTiO_3$/Ag	[198]
Ag-doped	DMSO	Ag	[194, 199]
HBCCO	DMSO	Ag	[200]

[a] Abbreviations: DMSO, dimethyl sulfoxide; DMF, dimethylformamide.

phase composition of the deposit is achieved by varying two parameters: the ratio of concentrations of discharging ions and the deposition potential. Pulsed multistep potentiostatic modes are widely used for the deposition of alternate nanometer layers. Such processes form the basis of the modern technology of magnetic Cu–Ni films [173].

The main features of studies on this topic are summarized in Table 3. Because deposition of active metals in protic media is always accompanied by the hydrogen evolution, it is common to use substrates with a high hydrogen overpotential, to optimize solution pH, or to operate in aprotic solvents. Thus precursors of bismuth and thallium-based HTSCs are prepared most advantageously in aqueous media, while it is preferable to deposit Y–Ba–Cu and related compositions from organic media. In the latter case, traces of water can substantially spoil the coating quality [174]. Deposition at sufficiently high negative potentials causes reduction of the organic solvent [174, 176, 201] with the formation of carbon and sulfur, which drastically deteriorate the characteristics of HTSC materials.

In most work on deposition of precursors from aqueous solutions, the products were analyzed only after annealing. The possibility cannot be excluded of the presence in the deposits not only of metals (and even instead of them) but also of the corresponding hydroxides which are deposited on the surface as a result of a local pH increase in the course of hydrogen evolution (see below). Such effects were reported in [191].

Prior to their electrodeposition on dielectric substrates, the surfaces of the precursors are metallized by sputtering. This procedure is also sometimes used in the non-electrochemical synthesis of HTSCs [202] to optimize the precursor microstructure.

If the solubility of inorganic salts in the chosen medium is low, complexing additives are used [174, 185] which apparently also exert a brightening effect.

It is not always possible to anticipate the specific features of the process in solutions of complex composition on the basis of data for single-component solutions [178, 185, 186]. Therefore, one has to use empirical methods to attain optimal conditions for the precursor cathodic deposition. The oxygen stoichiometry, the morphology, and the texture of the resulting product are to a large extent determined by the mode of the precursor thermal oxidation, and only in special cases by its deposition regime [182]. As a rule, the deposit composition is defined by the salt concentrations, the deposition potential, the interactions in the multicomponent adatomic layers formed on the cathode surface in the initial deposition stages, and a number of other factors. In the general form, this problem might be considered, at some approximation, for a two-component system [203]. The simplest relationships between the composition of the deposit and that of the solution are observed when all the components are deposited in the potential region of the limiting diffusion current [189, 190, 194]. In this case the cation concentration ratio is close to the HTSC stoichiometry (sometimes such solutions are obtained by the dissolution of HTSC ceramics in acid [187]).

In the majority of cases, potentiostatic regimes were used. In [189, 197], a method was developed to obtain layer-by-layer metallic precursors. This allows one to avoid the semiempirical procedure of solution composition optimization. Moreover, it makes possible deposition under kinetic or mixed control, which improves the deposit morphology. Two- or three-step potentiostatic [177] and pulsed [175] modes which ensure the optimal deposit compositions have also been developed.

Not only compositions containing all the HTSC metal components, but also simpler subsets, may be considered as the precursors. Thus, by a combined technique [189], Ba–Ca–Cu films were obtained by electrodeposition and then thallium was introduced from the vapor phase in the course of simultaneous oxidation. In [190, 191], it was shown that reproducible preparation of Bi–Pb cuprates can be achieved when three-component precursors are deposited and the alkaline earth cations are then introduced before annealing. It is practically impossible to provide reproducible deposition of five-component precursors. Two-stage electrosynthesis of HBCCO [200] included the intermediate annealing of a Ba–Ca–Cu deposit followed by mercury electrodeposition on the resulting oxide substrate.

The most important aspect is to make the complex electrodeposit composition reproducible from one experiment to another and invariant across the surface. The solution of this problem, which consists of selecting the appropriate cell configuration [194, 195, 199], makes it possible to obtain high-quality HTSCs from electrodeposited precursors. Critical currents in the absence of a magnetic field were increased to 10^5 A/cm^2 [194], which may be compared with typical values for conventionally synthesized films which do not exceed 10^3–10^4 A/cm^2. The use of high-quality electrodeposited precursors also ensure high anisotropy of the physical properties of the HTSC [195].

Heating in the course of annealing precursors that were cathodically deposited on metal substrates can cause cracking of deposits [204] as a result of different thermal expansion coefficients. However, as a result of the high uniformity of component distribution, the time and, sometimes also, the temperature of the thermal treatment can be substantially reduced. The last factor is particularly essential for thallium systems because it allows one to carry out annealing without any additional sources of thallium oxide vapor [194, 195, 199].

The approach to HTSC electrosynthesis described in this section is entirely analogous to that used for the production of semiconductive films such as $Cu_xIn_yS(Se)_z$ [205, 206]. The thermal treatment of electrodeposited metallic precursors carried out in an $H_2S(Se)$ atmosphere in some cases proved more successful than the cathodic codeposition of sulfur or selenium with the metals [207]. There is also an analogy with other combined methods of selenide preparation: the sputtering of copper or indium followed by cathodic deposition of selenium [208], and the chemical reaction of selenium with metals. In this case, as in the deposition of "incomplete" HTSC precursors [189], the use of the deposition mode is much easier.

Semiconductor–telluride mixtures are frequently codeposited cathodically [209–212], and the advantages of the method are by and large similar to those of cathodic deposition of HTSC precursors. For two-component systems it has been found possible to control the composition at the submonolayer level [213–216].

In conclusion, we note that deposition of submono- and monolayers of adatoms is the most controllable and reliably predictable method of obtaining metallic nanodimension compositions. At least two or three kinds of adatoms can be deposited in a strictly layer-by-layer fashion on single-crystal substrates [217], and mixed adlayers can also be obtained. The combined deposition of adatoms and phase deposits of metals [217] is even more promising. Among the metals, HTSC components such as lead, thallium, bismuth, and copper rank among the most thoroughly studied adatomic systems. Electrodeposition methods are also applied to the technological preparation of conventional superconductors based on Nb–Sn alloys [218].

5.3 Electrooxidation of Metals and Alloys

The anodic electrooxidation of the surface layers of metallurgical alloys has been used for the electrosynthesis of semiconductive sulfides which are formed in the presence of sulfide in the solution [219]. Analogous methods are used for HTSC film fabrication, although the approach has not provide major advantages to date.

Most metals entering the cuprate HTSC (with the exception of copper) during anodic polarization in aqueous solutions over a wide pH interval form either soluble products or loose oxide-hydroxide films with a poor adhesion. The passivation of such chemically active metals in electrolyte solutions has been incompletely studied. However, for bismuth, cadmium, antimony, and also for the corresponding chalcogenides and certain binary alloys, methods are well developed for obtaining compact oxide films in solutions of special composition [220, 221].

In the context of superconductor electrosynthesis, such an electrolyte (salicylic acid in acetonitrile) was used [222] for the surface oxidation of a single crystal of Bi–Sn alloy. For the films obtained on its surface the authors observed a T_c of up to 28 K, but they did not carry out an analysis of the film or a thickness determination.

Aqueous solutions are used frequently for the oxidizing electrosynthesis of cuprate HTSCs, because it is assumed that the properties of the oxide films formed on the copper-containing alloys are mainly determined by the nature of the copper passivation.

The electrochemistry of copper anodes in neutral and alkaline media has been studied in detail [223–226]. This complicated process includes, as a rule, the growth of ultrathin (several nanometers thick) films of Cu_2O, CuO, and also mixed and nonstoichiometric oxides. Until recently, it was assumed that cations do not affect the dissolution and passivation of copper. However, the first attempts to synthesize HTSCs and (or) their precursors showed that copper oxide films, formed when the potential of a copper electrode is cycled in a $Ba(OH)_2$ solution, incorporate substantial amounts of barium [227]. This result was subsequently confirmed not only for potentiodynamic [228] but also for potentiostatic [229] oxidation modes. It has been suggested that $Ba[Cu(OH)_4]$ or $Ba[Cu_2(OH)_6]$ forms in the supersaturated near-electrode layer [229]. Similar studies with other alkaline-earth cations at high pH are difficult to conduct due to the poor solubility of the corresponding hydroxides.

Potentiodynamic experiments on a copper electrode in a solution with pH 6.5 simultaneously containing salts of yttrium and barium gave an Y–Ba–Cu oxide film which exhibited superconducting properties after a thermal treatment [227]. The pursuit of these experiments [230] led to studies in solutions of even more complicated composition which included the cations of barium, yttrium, and copper. On analyzing the technique and results [227, 230], it can be concluded that the formation of a multicomponent film under potentiodynamic conditions is induced not only by the substrate oxidation, but also by the partial reduction of the copper oxide film. Film formation is accompanied by the surface deposition of hydroxides of all the elements present in the solution. The formation of hydroxides is the result of cathodic alkalinization (see below) and represents the main contribution to the accumulation of barium and yttrium in the film. The authors reporting this technique suggest that to change the composition of the products one has to vary the properties of the hydroxy complexes in the solution, for example by using water–organic media.

Galvanostatic electrosynthesis of an Y–Ba–Cu oxide precursor was accomplished [231]. The incorporation of yttrium into the oxide from the solution did not take place, so a YCu_4 alloy was used as the substrate. In a saturated $Ba(OH)_2$ solution, and also in 7.2 M KOH with Ba^{2+} additives, a loose black layer of amorphous deposit was formed on the anode surface. The layer spontaneously detached and fell to the bottom of the cell. Being annealed in air, it was transformed into a mixture of the YBCO, CuO, and Ba_2CuO_3 phases.

The anodic oxidation of metals and alloys can also be performed in certian melts. For instance, a KCl–NaCl–CuCl–$LaCl_3$ melt was used in which the additional copper and lanthanum ions were generated by the simultaneous galvanostatic dissolution of two anodes, Cu and LaB_6 [232]. Solid $LaCu_2O_4$, Cu_2O, CuO, and CuCl were deposited on a ZrO_2–Y_2O_3 cathode, and readily soluble LaOCl was formed in a melt. Under certain conditions, the preferential deposition of LCO was achieved.

In contrast to the processes described above, the electrooxidation of metals and alloys still cannot be considered as an accepted electrosynthetic method; as yet only its principal possibilities have been demonstrated. At the same time, the anodic oxidation of transition metals, which forms the basis for a number of semiconductor technologies, is extremely effective and convenient for varying and controlling the thickness, morphology, and stoichiometry of oxide films [233]. It therefore cannot be ruled out that, as the concepts concerning the anodic behavior of metal components of HTSCs in various media are developed, new approaches will be found. The development of combined methods that include anodic oxidation can also be expected, by analogy with hydrothermal–electrochemical methods used for obtaining perovskites based on titanium [234, 235], even at room temperature [236].

Recently, HTSC properties were found for certain new complex cuprates of alkaline-earth and rare-earth metals [237, 238]. Electrosynthesis of these compounds by analogy with the formation of barium cuprate films [228, 229] appears to be possible.

5.4 Electrochemical Variation of HTSC Stoichiometry

Often called electrochemical doping, this method is based on electrochemical processing of oxide precursors prepared by usual high-temperature methods. It was carried out for the first time in an aqueous alkaline solution on lanthanum cuprate ceramics by Grenier, Wattiaux and co-workers [239, 240]. This group earlier accomplished a number of electrochemical studies on perovskites as well as detailed studies of solid ferrites [241–244], including those under anodic polarization conditions [100]. By this method, they obtained compounds of tetravalent iron ($SrFeO_{2.68}$ [245]) and cobalt ($SrCoO_3$ [2461]) at room temperature. The results are significant not only because they demonstrate the possibilities of electrooxidation in changing the lattice type under ordinary conditions, but also because analogous chemical methods allow one to achieve similar structural transformations only under extremely severe conditions. Electrochemical transformations of solid compounds with the formation of phases with different structures were known previously for cases in which the resulting products was easily crystallized under ordinary conditions (for example, the oxidation of $Mn(OH)_2$ to MnO_2 [247]). In this connection, the analogy is noteworthy between the oxidation of ferrite and cobaltite and the anodic oxidation of thallium oxide with the formation of peroxide described more recently [248, 249].

La_2CuO_4 (LCO) is a dielectric, the doping of which with oxygen leads to metallization accompanied by transition to the superconducting state at sufficiently low temperatures [250]. The value of T_c achieved by this method of synthesis correlates with the value of δ (the greatest observed T_c values are 40–45 K).

LCO has been actively studied as a model system for elucidating the nature of the superconduction phenomenon in cuprate systems because of the relative simplicity of its chemical composition and structure. The HTSC studies of the effects of oxygen

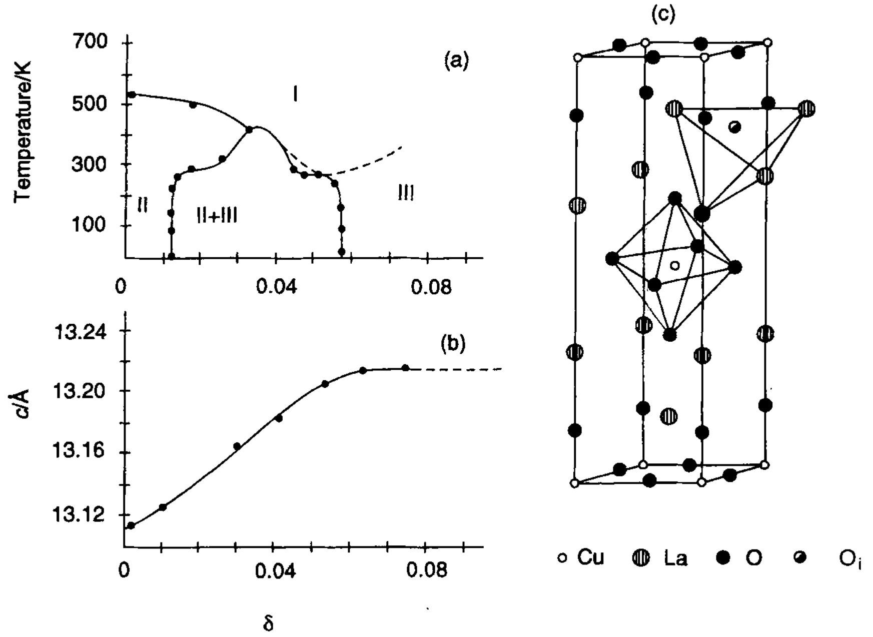

Fig. 3. Structural features of oxygen incorporation into the LCO lattice. (a) Phase diagram of LCO determined partially in electrochemical doping experiments [251]: tetragonal phase (I), oxygen-poor (II) and oxygen-rich (III) orthorhombic phases. (b) Lattice parameters vs. δ dependence measured in situ in the course of electrochemical doping [267]. (c) Schematic representation of LCO structure [266]; O_i = incorporated excess oxygen species.

stoichiometry and the resulting phenomenon of phase separation represent a good example of the achievements of modern electrochemistry of HTSCs [239, 240].

Both stoichiometric and oxygen-doped ($La_2CuO_{4+\delta}$) LCO are characterized by the tetragonal/orthorhombic phase transition, and the transition temperature depends on the value of δ (Fig. 3(a)). It has been reliably shown by various diffractometric methods that orthorhombic phases pertaining to $\delta < 0.01$–0.02 and $\delta > 0.06$–0.08 are not identical (the latter exhibits the higher symmetry [250–252]). It is the highly symmetric orthorhombic phase of variable composition that is superconducting according to modern concepts. The fact that the samples with $\delta < 0.08$ consist of two phases is responsible for their superconducting state. A similar phase separation with different oxygen stoichiometry is inherent to all cuprate HTSCs, but the corresponding phase diagrams of HTSCs containing three or more cations are very complicated. As δ increases, the lattice parameter also increases (Fig. 3(b)).

At the outset, quantitative studies of the LCO phase diagram in the low-temperature region led to contradictory results. It should be borne in mind that oxygen doping from the gas phase succeeded only at $T \geq 600$–700 K, i.e., in the region of the existence of the LCO tetragonal phase. Apparently, in these experiments, it took a long time for the equilibrium oxygen distribution in the lattice to be established in the course of the phase transition. Special investigations of non-equilibrium oxygen-doped LCO (see, e.g., [250, 253]) were mainly concerned with their physical properties. The diffusion coefficient of oxygen D_{ox} in the cuprate lattice is not reliably known to date [254]. On extrapolation to room temperature, the most contradictory data of various experiments carried out at $T \geq 300\,^{\circ}\mathrm{C}$ led to values on the order of 10^{-14} cm^2/s}. Were D_{ox} actually so small, the oxygen doping of 0.1–1 mm thick samples at room temperature would require (independently of the way the reactant is brought to the sarface) a time at least by five to six orders of magnitude greater than that of electrochemical experiments [239, 240, 255].

Turning to the experience gained from perovskite studies, it should be concluded that the procedure of extrapolation over a wide temperature interval is hardly correct for the determination of D_{ox}. According to Kudo et al. [108], for $Nd_{1-x}Sr_xCoO_3$ at room temperature the lattice D_{ox} values are equal to 1.4×10^{-11} and 7.6×10^{-14} cm^2/s for $x = 0.2$ and 0.5, respectively, while the extrapolated values for these materials are about 10^{-19} and 10^{-22} cm^2/s. For $La_{0.5}Sr_{0.5}CoO_{3-\delta}$ [109, 110] the D_{ox} in solid phase at room temperature was about 5×10^{-15} cm^2/s, probably underestimated due to the passivation of the surface by ultrathin oxide–hydroxide films [256]. The result of Kudo et al. [108] demonstrates, above all, a sharp change in the oxygen ion mobility with the stoichiometry. A similar effect consisting of the acceleration of diffusion with an increase in the degree of nonstoichiometry in the high-temperature interval was described for LCO [257] and YBCO [258, 259].

The value of D_{ox} for a wider group of perovskite materials can be estimated from the quasiequilibrium (stationary) values of open-circuit potentials. From [84], we can obtain the values of 10^{-11}–10^{-10} cm^2/s for $LaNiO_{2.84}$. For many systems, as mentioned above, the estimates are probably highly inaccurate due to the absence of data on the dimensions of the oxide species. However, even using dimensions that are *a fortiori* too small, we can obtain $D_{ox} \geq 10^{-14}$–10^{-13} cm^2/s, and, as a rule, they are actually greater by several orders of magnitude. Apparently, LCO pertains to oxides with a high oxygen mobility.

It is from experiments on electrochemical doping that the LCO phase diagram was obtained. The problem of equilibrium establishment in the oxygen sublattice of nonstoichiometric cuprates is closely related to the nature of excess oxygen species in the solid phase and, in turn, the preferential diffusion paths in the lattice, and the diffusion kinetics.

It is most probable that oxygen-containing species are formed under electrochemical conditions which have a different nature from those formed during oxygen adsorption from the gas phase. From the point of view of Grenier et al. a monolayer of oxygen adatoms with the residual charge close to -1 is formed on the surface at the doping potentials [260–262]:

$$OH^- \Rightarrow (OH^-)_{ad} \Rightarrow (O^-)_{ad} \tag{1}$$

These authors assume that lattice incorporation occurs with the participation of metal ions

$$Cu^{2+} + (O^-)_{ad} \Rightarrow Cu^{3+} + O^{2-} \tag{2}$$

In the low-temperature oxidation of LCO in a liquid phase by permanganate [263, 264] or hypobromite [265] the characteristic times of doping prove to be close to those known for electrochemical experiments. This observation probably indicates that mobile oxygen species are identical in these cases. The formation of a charged adsorbate in the gas phase is clearly unlikely.

The present scheme, however, does not entirely correspond to current concepts of the properties of the oxygen adlayers on perovskites. In [85], it has been suggested that OH^- adsorption is unlikely and that the residual charge of adsorbate is close to zero. The supposition that hydroxyl participates in the O_2-evolution limiting stage was considered in view of the correlation between the electrocatalytic activity and the metal–hydroxide bond energy [81]. However, qualitatively similar correlations [100] can also be obtained for other oxygen-containing species as well as for oxygen vacancies on the surface. Calculations in [83] show that hydroxide adsorption on perovskites is possible, but as deprotonated species (oxygen adatoms are only stable at low residual charges). Also, the surface coverage by adsorbed oxygen was estimated as no more than 1 percent [101].

An alternative hypothesis [267] has been advanced according to which LCO prepared in air initially contains, in the anion sites, not only oxygen atoms but also hydroxide particles (10 percent and more, not unlike the bronzes that are formed by transition-metal oxides). The hypothesis has not gained acceptance, nor has there been any independent experimental confirmation. The suggestion that deprotonation occurs in the course of the electrochemical oxidation was put forward as one explanation of the mobility of species in the cuprate bulk [267]. Protonation–deprotonation was also considered to be a possible explanation for the nature of the reversible electrochemical transformations of LCO during anodic and cathodic processing of this material in a 0.5 M H_2SO_4 solution in methanol [268]. In that work, degradation processes did not take place at small concentrations of acid, and the reversibility of the charging in acid media was more pronounced than that at higher pH.

The earliest results on electrochemical oxygen doping were obtained with the use of a strict potentiostatic regime at the simultaneous oxygen evolution [239, 240]. Voltammetry [240] showed that this process was highly irreversible. In the subsequent works [255, 260], the oxidation conditions were optimized and the potentail region preceding the onset of oxygen evolution was chosen. Detailed investigations were carried out of the structural properties of doped samples [251, 252, 269], including studies by in situ X-ray [267] and neutron [267, 270] diffractometry. The state of oxygen in the LCO after processing and the characteristic physical behavior of electrochemically doped samples [251, 255, 269, 271–273] were also studied. It was found that the dependence of T_c on δ at $\delta > 0.08$ was not identical for cuprates doped by electrolyte and gas-phase methods. For the latter, it is accepted reliably that the excess oxygen is uniformly localized in the lattice between the La_2O_2 planes (Fig. 3(c)). At the same time, electrochemical doping at high δ reveals the oxygen superstructure [269], the parameters of which are substantially greater than the characteristic dimensions of the LCO unit cell.

The method of Grenier et al. [239, 240] has been extended to other materials with the composition $La_{2-x}A_xMO_{4+\delta}$ (A = Nd, Sr; M = Ni, Cu), i.e., the structural LCO analogs [261, 262, 274, 275]. The quasireversible values of δ achieved in these are, as a rule, 0.1–0.2 and the greatest value ($\delta = 0.25$) was obtained for $La_2NiO_{4+\delta}$. Similar experiments were carried out on cuprates with partial substitution of lanthanum by alkaline-earth metals [276, 277] and lithium [278]. In [273], an electrode of $La_2Cu_{0.98}Fe_{0.02}O_{4+\delta}$ was doped with oxygen, which made it possible to use Mössbauer spectroscopy for studying the effect of δ on the state of the cationic sublattice.

The electrochemical doping provides $T_c \simeq 45\,K$ (Fig. 4(a)), which is the record value for LCO, and, simultaneously, a high content of the superconducting phase. Another noteworthy result concerns the electrosynthesis of a new HTSC material, $La_{2-x}Nd_xCuO_{4+\delta}$ [261], the superconducting state of which is attained at $x \leq 0.60$ and $\delta \geq 0.07$ by oxygen doping.

The advantage of the electrochemical method of varying the stoichiometry is that it is possible to control quantitatively the degree of doping by coulometry. This advantage has been used only relatively recently [260]. The majority of studies [251, 269, 279] to date have used the galvanostatic mode at relatively high current densities, in which case the coulometrically determined δ values were *a fortiori* too great, due to the charge consumed in the evolution of O_2.

The disagreement between the values of δ determined by the methods of coulometry, potentiometric titration, and thermogravimetry has led to the suggestion that oxygen is incorporated into LCO in the form of hydroxy-like particles (see, e.g., [269] for details). At sufficiently high δ, the mass spectrometry of products withdrawn in the course of thermogravimetric experiments points to the presence of anions of a different nature, including hydroxide and carbonate ions, in the electrooxidized LCO [277, 280, 281]. The presence of admixture species in the lattice after electrochemical doping is evident, according to [279], by the character of the temperature dependences of the Hall effect. At the same time, no such species were observed in thorough studies [260, 261] at $\delta < 0.1$. Evidently, the disagreement among the analytical results of different authors may be due, to a great extent, to the difficulties associated with the removal of traces of electrolyte from the pores of ceramic samples. This problem was mentioned earlier [240] and was solved by improving the procedure of repeated washing of the samples with ethanol and drying them. Modern methods of chemical and physical structural analysis [282] ensure high sensitivity in the determination of light-weight elements, and, based on the data indicated above, one can consider the suggestion [267, 268] that hydrogen is the main dopant as disputable.

Until recently electrochemical studies of LCO were mainly limited to experiments on preparative electrolysis. There are several examples of the usual and quasi-equilibrium charging-curve measurements [260, 266, 267]. The corresponding results (Fig. 4(b)) demonstrate essential differences in the plateau position for different current modes, but it can be concluded that bulk LCO oxidation occurs at potentials more negative than the equilibrium potential of the OH^-/O_2 system. An interesting feature is observed for the quasi-equilibrium cathodic discharge of doped LCO (Fig. 4(c)). The pronounced shift of open-circuit potentials to more negative values confirms the strong irreversibility of the deep doping and probably testifies to the difference in the nature of species that diffuse in the bulk in the course of doping and oxygen removal (de-doping).

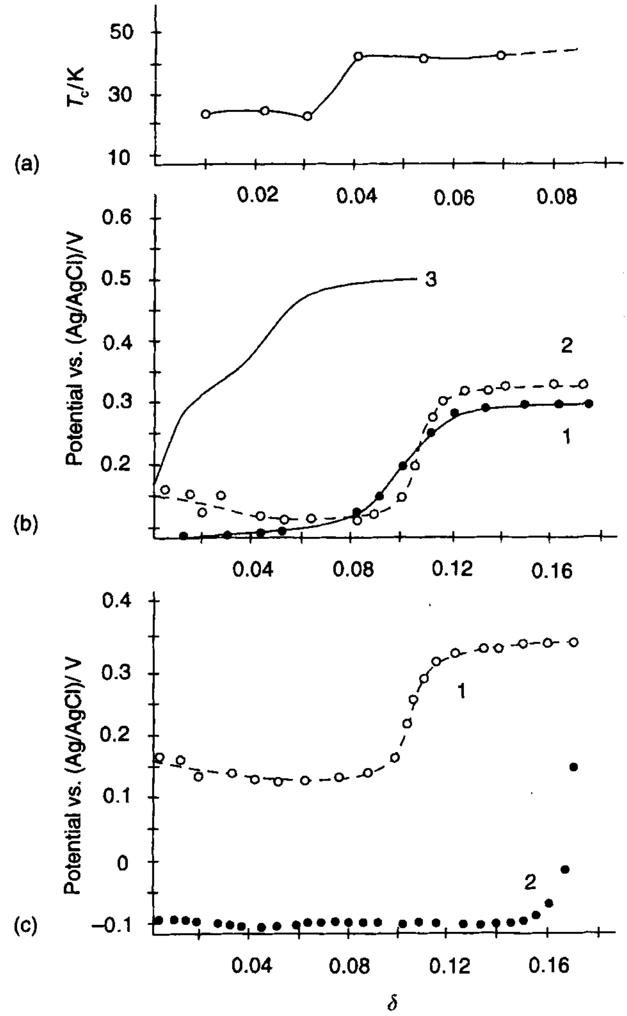

Fig. 4. Changes of properties of LCO with δ: (a) T_c vs. δ dependence for electrochemically doped LCO [267]; (b) anodic charging curves for LCO in 1 M KOH solutions: quasi-equilibrium data (open-circuit potentials measured after the interruption of current from [162] (1) and [266] (2) and a common galvanostatic curve [267] (3); (c) comparison of quasi-equilibrium anodic (1) and cathodic (2) charging curves [266].

The first electrochemical reduction of LCO was studied by chronoamperometry [283]. This method serves as an effective instrument for studying the phase composition and oxide properties [84]. The cathodic current maximum was attributed [283] to the process of lattice reconstruction in the near-surface cuprate layers in the course of de-doping (the process similar to nucleation). Of prime interest for the development of LCO electrochemistry is the more efficient measurement of equilibrium charging curves. Experience of equilibrium measurements on perovskite electrodes [84, 90, 108], and also the existence of plateaus which precede oxygen evolution [87, 89] indicate that it is possible to analyze the phase composition of ceramic oxide materials.

For instance [90], three plateaus could be reproducibly obtained in the equilibrium charging curves and they correspond to the formation of different nonstoichiometric products. The observation of two or three certain δ limits resulting in the chemical oxidation at different $KMnO_4$ concentrations [264] can be considered as a sign of the existence of several plateaus on the charging curves.

For more detailed electrochemical studies of LCO it is also expedient to carry out potentiostatic extraction of oxygen. Such experiments permit quantitative determination of the effective D_{ox} of oxygen-containing species, including their dependence on δ, by analogy with corresponding studies in the Pd–H system [284]. The similarity between the systems is also revealed by common features of their phase diagrams. Although oxygen diffusion in bulk cuprate proceeds more slowly than hydrogen diffusion in palladium, the difference appears not to exceed an order of magnitude (based on the characteristic times of doping the bulk of LCO ceramic samples [240]). For single crystals, diffusion was observed to be slower [285].

The dependence of the electrochemical doping rate of LCO on macrostructure [285] suggests that the initial incorporation of oxygen proceeds precisely into the deficient sites of the cuprate lattice and then to the usual interplanar sites. A similar situation takes place upon formation of the palladium hydride α-phase in defective palladium materials [284].

The high efficiency of electrochemical doping of LCO and related materials is caused by their high stability in aqueous solutions. It is also possible to change the YBCO stoichiometry electrolytically [286–288], despite simultaneous partial degradation. In certain conditions the electroreduction of YBCO in aqueous alkaline [289] or propylene carbonate [290] solutions, and also in nitrate melts [291], led to an increase in T_c. The nature of the corresponding processes was not studied by independent methods. In protic media, hybridization, which in the case of HTSC also leads to an increase in T_c, cannot be ruled out [292]. The reversible oxidation of $YBa_2Cu_3O_{6.5}$ is apparently possible at potentials more negative that the oxygen evolution potential within the region of several tenths of δ [293]. Such a process was carried out under simultaneous O_2 evolution in acetonitrile solutions with water additives [294]. The authors noted that the greater the initial value of δ in YBCO, the more rapid is the saturation with oxygen. This result can also be a consequence of the dependence of D_{ox} on the stoichiometry [258, 259]. According to [295, 296], the room-temperature D_{ox} for YBCO at $\delta = 0.1$–0.2 is equal to 10^{-12}–10^{-11} cm^2/s, i.e. lower than D_{ox} for LCO.

Thallium, bismuth, and lead based HTSCs are relatively degradation-resistant and are therefore convenient systems for conducting electrochemical changes in the oxygen stoichiometry. At the same time, physical properties of these materials are less exactly related to δ because of the more complicated phase compositions of the corresponding systems. The electrochemical treatment of Bi–Pb cuprates in nitrate melts [297] makes it possible to vary δ within the region of ± 0.1.

Along with electrochemical doping–de-doping of HTSC phases by hydrogen and oxygen, the electrochemical intercalation of cations [298, 299] should also be considered as a promising direction. For example, the cathodic intercalation of lithium proceeds reversibly in many systems at a high rate owing to the small size of the dopant atom. Oxide spinel superconductors ($Li_{1-x}Ti_2O_4$) are highly nonstoichiometric with respect to lithium (for the electrosynthesis of these materials, see below) and appear to be obvious candidates for electrochemical doping. According to [300], it is possible for Li–Ti spinels in solid-electrolyte cells to change their stoichiometry within several tenths of x without any destruction.

The cathodic incorporation of lithium from a solution of $LiAsF_6$ in propylene carbonate was used in the attempt [301] to obtain HTSC materials based on calcium and lanthanum niobates. The incorporation of lithium into YBCO from a similar electrolyte proceeds reversibly and ensures a discharging capacitance of the HTSC cathode high enough for application in lithium batteries [302–307]. The possibility was also reported [308–310] of incorporating lithium into BSCCO, but the capacitance values obtained are very contradictory.

It was found recently that for a lithium-doped YBCO the dependence of T_c on the lithium content has a maximum corresponding to one Li atom per molecule [311]. Unusual properties of the lithium-doped LCO are described [278]. It is evident that a wide range of these materials can be obtained by electrochemical methods. Diffusion coefficients D_{Li} in solid cuprate phases demonstrate the same tendencies as D_{ox}: for single crystals, D_{Li} is lower than for powders [308], strongly depending on stoichiometry [304, 305]. The highest room-temperature D_{Li} values described are close to 10^{-7} cm^2/s.

The controlled changes in the YBCO stoichiometry can also be realized in cells with solid electrolytes [312–319]. For the F^--doping of HTSC, ZrO_2-fluoridized solid electrolytes can be used [320]. A combined technique [321] was based on laser sputtering of Y–Ba cuprate on a polarizable layer of a solid electrolyte with oxygen conduction, and this resulted in the variation of the stoichiometry of an HTSC film in the course of its growth. However, a detailed consideration of these studies goes beyond the scope of this review, because they are being developed independently of the electrochemistry of HTSC. We will only note that for oxygen doping–de-doping in solid electrolyte–ceramic materials one can achieve considerably smaller changes in δ than those reported in electrolyte solutions on similar electrodes. More substantial changes in the stoichiometry are accompanied by a number of side-processes which change the grain morphology and the state of phase boundaries. Their rates increase with temperature; therefore, the degradation phenomena in solid electrolytes can be even more pronounced than those in solutions.

5.5 Anodic Electrocrystallization

5.5.1 Characteristics of the Process and the Principal Conditions for its Realization

The kinetics of anodic electrocrystallization has been studied in detail only for a limited group of systems. Oxides, hydroxides, and simple and complex salts can be the products of this process. The electrochemical synthesis of crystalline oxides as the alternative method to other preparation techniques is particularly attractive because i can be performed under low-temperature conditions so that subsequent annealin steps may be eliminated.

Well-known anodic crystallization reactions include the electrodeposition of PbO [73, 322, 323] and MnO_2 [324]. By varying deposition conditions, one can obtai various crystalline modifications [325, 326] as well as doping the deposit with foreig metal cations [327–331].

The anodic crystallization of thallium oxide (Tl_2O_3) has been investigated fo over a century, and has also attracted attention during the recent decade [332], owin to prospects for the wide use of thallium oxide films [333–336] having varie composition, structure, and texture. In the case of thallium compound synthesis because of the environmental aspects of this problem the development of low temperature electrochemical methods is of special importance.

For other oxide systems, the processes in electrolyte solutions have been studie in less detail. In salt melts at not too high an acidity, interesting results have bee obtained by electrocrystallization of various transition-metal compounds [20–25 which, however, cannot be directly used in HTSC electrosynthesis.

We can formulate three conditions that make it possible to accomplish anodi crystallization:

1. the electroactive element should have at least two stable valence states;
2. a considerable difference between the solubilities of oxides (hydroxides, salts) i these valence states is necessary (the reduced form should have the highe solubility);
3. the reaction product conductivity should not be too low.

For oxide electrocrystallization, the last condition is the most strenuous, sinc many oxides are insulating; non-stoichiometric compounds, however, are sufficientl conductive. When two (or more) substances are codeposited, certain specific feature of the crystallization can be expressed for both cathodic and anodic processes on th basis of the thermodynamics of binary (or more complex) systems. If stabl multicomponent phases exist, then it is their deposition (not the deposition of mixture of simpler products) that preferentially proceeds in a certain potential regio In such cases, intermetallic compounds are deposited in cathodic processes, and th deposition of mixed oxides takes place in anodic processes. These products ca represent both chemical compounds and solid solutions.

In recent years the electrocrystallization of mixed oxides became one of th leading methods for fabricating materials for electronics; Pb–Bi [337, 338] and Pb– [339–347] mixed oxides were studied the most thoroughly. Of the basic componen of HTSC, the best candidates for developing anodic crystallization are thalliun bismuth, and lead. Condition 2 can be satisfied for the majority of polyvale elements, if an appropriate electrolyte is chosen. But the problem of cuprate HTS preparation is complicated because it is precisely copper (as well as mercury) th belongs to that group of a few elements for which condition 2 is not fulfilled common media. Indirect methods of copper oxide electrocrystallization are therefo used.

5.5.2 Anodic Electrocrystallization from Aqueous Solutions: Thallium Oxide System

An example of indirect oxide electrocrystallization is the method of preparing crystalline Ba–Tl–Cu–O films with HTSC properties put forward in [348]. This complicated process of copper substrate oxidation in aqueous alkaline solutions containing Tl^- and Ba^{2+} ions led to the formation of previously unknown thallium cuprate (Fig. 5(a)) doped in the surface layer by barium. Freshly prepared $TlCuO(OH) \cdot nH_2O$ was characterized by $T_c = 40–45\,K$ and its dehydration in air with heating only to 100–150 °C ensured $T_c = 80–85\,K$ (i.e., the maximum possible values for thallium HTSC containing no calcium [3, 4]) (Fig. 5(b)). At the same time, the structure of the electrosynthesized cuprate determined by X-ray analysis of its crystal [348] differed significantly from the structure of common thallium-based HTSCs (Fig. 5(a)). Attempts to introduce calcium as the dopant in thallium cuprate failed, probably because of the considerable difference in the crystallographic radii of Ca and Tl, while thallium and barium cations are closer in size. The introduction of solution cations into oxide lattice vacancies was described for oxides of lead [338] and manganese [349].

It should be emphasized that thallium is present in its univalent state in the cuprate system. This fact, in principle, means that no electrochemical process involving thallium takes place in the course of synthesis, and only copper undergoes

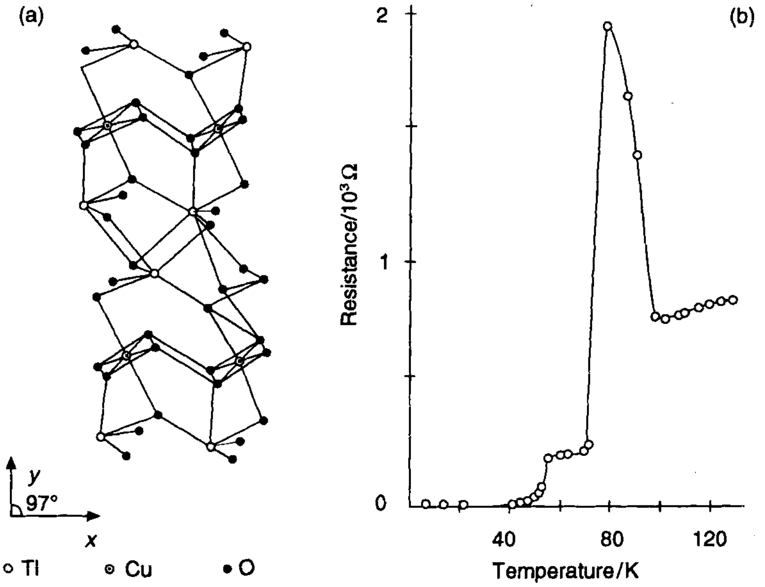

Fig. 5. Characteristics of thallium cuprate TlCuO(OH) electrosynthesized by anodic electrocrystallization [348]: (a) structure calculated on the basis of X-ray crystal analysis; (b) resistivity vs. temperature of the deposit on a copper substrate measured by the two-probe technique.

electrooxidation. However, in a Tl^+-containing solution, the deposition of copper oxide from the supersaturated near-electrode layer differs from the usual deposition [224–226] not only by introduction of solution cations into the solid product but more importantly by the presence of clear evidence of crystallization processes. Common copper oxide films can only reach relatively small thicknesses even after a period of steady growth and, as a rule, do not exhibit any phase properties. Thicker films, formed under certain conditions, are not entirely crystalline. As for thallium cuprate, it forms crystals with characteristic sizes up to 150 μm. In this situation, HTSC electrosynthesis is a special case of anodic electrocrystallization in which the reactant is generated in the course of the anodic dissolution of the substrate. The validity of such an interpretation is confirmed by recent experimental studies on thallium adatom deposition on a copper substrate [350, 351]. According to these studies, the formation of thallium monolayers in an alkaline medium does not inhibit dissolution of copper and oxide films on its surface. In this case, the usual electrocrystallization processes occurring in the thallium oxide system are competitive. The successful electrosynthesis of HTSC films [348] has stimulated studies of these side-processes and this in turn has led to a number of interesting results.

It was found that at $pH > 11$ in the region of low anodic overpotentials the product of thallium oxidation on an inert substrate represents the individual phase of a mixed-valence oxide which was previously unknown [352, 253]. On a copper substrate, this same phase can be formed simultaneously with thallium cuprate, while at the higher overpotentials the amounts of both products in the deposit prove to be small due to the preferential formation of Tl_2O_3 which proceeds at a high rate. At anodic overpotentials that are not too high, the rations of the amount of thallium cuprate to that of the mixed oxide in the deposits grown on copper correlates with the rate of active dissolution of copper [354], i.e., cuprate is preferentially formed at the higher pH.

The lack of information on the Gibbs energies of new oxide phases makes it difficult to calculate their regions of stability in aqueous solutions. For thallium oxide of a mixed valence, this problem was solved with high accuracy in a model approach [355], and it was shown that in the potential–pH diagram the region of the existence of such an oxide represented by a triangle which widens as the pH increases, and which separates the regions of Tl^+ and Tl_2O_3 stability (Fig. 6).

A similar model for the case of thallium cuprate is complicated by the large number of parameters that affect the state of the system, and also by the necessity to introduce two experimentally unknown quantities simultaneously into the model. However, taking into account the character of the pH dependences of all the processes that occur with the participation of thallium and copper, one can suppose that the shape of the thallium cuprate stability region would be close to that for the mixed oxide. That is, its width would increase with increasing concentration of copper ions (hydroxo complexes) within the crystallization zone. Although the crystallization process took place under *a fortiori* non equilibrium conditions, the results of the preparative analysis agree qualitatively with the concept of stability of the products. The interval over which formation of thallium cuprate on copper substrates occurs and the formation of the mixed oxide on platinum and carbon substrates can be observed is wider for higher values of the pH [352–354].

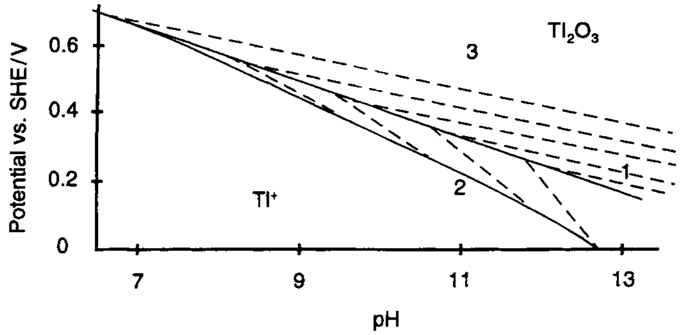

Fig. 6. Model pH-potential diagram calculated for the thallium oxide–water system with consideration of the existence of the mixed-valence oxide. Equilibrium potentials for the redox systems Tl^+/Tl_2O_3 (1), Tl^+/mixed oxide (2) and mixed oxide/Tl_2O_3 (3) are given for 1 mM Tl_2SO_4 solution.

In fact, the effect of pH can be observed within the framework of these models only in a very narrow interval up to pH 13–13.5, because upon further increase of pH the state of the thallium ions in aqueous solutions undergoes drastic changes owing to the association of ions of both valences with hydroxide ion. The possibility of formation of mixed-valence oxide at base concentrations up to 10 M (pH 15–16) was noted for thallium oxide passivating films on a thallium anode [356]. At the same time, in a recent study [357] on deposition of thin (several tens of nanometers thick) thallium oxide films on glassy carbon from a 5 M base, the result was the codeposition of an amorphous product. After a certain induction period dependent on the overpotential, Tl_2O_3 begins to deposit on top of this amorphous product. The amorphous deposit can result from the deposition of a metastable hydroxide $Tl(OH)_3$ from the near-electrode layer supersaturated by $Tl(OH)_4^-$. The possibility of $Tl(OH)_4^-$ formation was not taken into account in [357]. At the same time, certain experimental effects observed in [357] can be interpreted under the assumption that the mixed oxide is formed at higher pH. Microscopic data [358, 359] for mixed thallium–oxygen adlayers confirm the possibility that the deposit is a phase of mixed valence.

Studies at "superhigh" pH for electrosynthesizing complex cuprate systems are of interest. In strong bases it is possible to obtain Cu^{3+}-containing oxygen compounds that are unstable in water at common pH values, such as the respective barium salts [241, 360]. This possibility of HTSC electrosynthesis has not yet been studied.

The anodic electrocrystallization [348] is carried out at a lower temperature than any other known method for the electrosynthesis (and synthesis in general) of any HTSC to date, and it is undoubtly of interest to develop it further and to extend it to other materials. In this regard, the possibility of formation of mixed-valence oxide [332, 353] merits notice because in common thallium HTSCs the effective valence of thallium is less than three [361, 362] (the corresponding Tl(I) content is about 10%, i.e., close to the composition of the mixed-valence oxide).

One more interesting prospect for anodic electrocrystallization for HTSC synthesis is the possibility of electrosynthesizing Tl_2O_3–TlOF compositions [363].

Oxyfluorocuprates of rare-earth metals with low concentrations of fluorine exhibit the properties of HTSCs [364]. By slightly fluorinating certain HTSC materials, one can enhance T_c, and the content of the superconducting phase [365], and reduce ΔT_c [366, 367]. Apparently, attempts are being made to synthesize the simplest HTSC oxyfluorides of the $Sr_2CuO_{3-x}F_x$ type [368] using the simpler method of anodic oxidation of copper in certain solutions.

5.5.3 Anodic Electrocrystallization in Low-Temperature Alkaline Melts: Norton Method

The most frequently used electrochemical method for synthesizing HTSC materials by anodic electrocrystallization is the so-called Norton method [369]. The technique is used for obtaining copper-free bismuth-based HTSCs. In moist alkaline melts o KOH + $Ba(OH)_2$ + Bi_2O_3 at temperatures of 180–400 °C (the higher temperature corresponds to a lower water content) $Ba_{1-x}K_xBiO_3$ (BKBO) is deposited on the iner anode surface, and upon addition of RbOH its rubidium-containing analog is formed [370]. Bismuthates are characterized by rather low T_c (less than 35 K), but, like lanthanum cuprates, they are of considerable interest as model systems; moreover, i is electrosynthesis that, as in the case of LCO, makes it possible to study the system's phase diagram over the widest ranges [371]. The method allows one to obtain single crystals with the greatest attainable face dimensions, close to the dimensions of the biggest crystals grown by the usual methods from high-temperature melts [372–373 and sometimes even greater [374–376]. The problem of localizing the crystal growth to obtain large individual samples [377] is solved by optimizing the geometry of the substrate.

The electrosynthesized BKBO samples, as do those grown by cooling the oxide melts [378], contain substantial amounts of admixed Na in the K sites [373, 375, 378 379], and thus have the composition $Ba_{1-x-z}K_xNa_zBiO_{3-y}$. The value of x varies between the surface (where it is typically equal to 0.36) and greater depth (it is typically 0.22 at 100 μm; upon further movement toward the center of the crystal, the composition changes are less) [378]. The addition to the melt of small amounts o NaOH has practically no effect on the incorporation of sodium into the BKBO crysta (i.e., the amount of admixed sodium is sufficiently large under the usual mode o synthesis). Sodium incorporation has been studied in detail, because this phenomenon drastically reduces the HTSC characteristics of BKBO. The analogs of BKBO with potassium completely substituted by sodium or cesium (obtained electrochemically from the corresponding melts [370]) have no HTSC properties at all.

One way to improve on the Norton method with the aim of obtaining les defective crystals has been to use the potentiostatic mode [374, 380] since, in the majority of studies reported in the literature, the crystals were grown galvanostatically. However, this factor, although essential when electrochemical side-processe can occur in the operating potential region, is not the key one with respect to the Norton method. At the same time, one cannot claim the total absence of any side processes, because the experimentally determined current efficiencies [377, 379 differ from the theoretical ones by 10–15 percent. The most probable parallel reaction is the oxidation to the soluble bismuthate of the highest valence. It was noted [381] that the best reproducibility could be obtained at deposition in the region of the Bi^{3+}/Bi^{4+} transition, and the limits of this region were determined voltammetrically. The nature and the kinetics of individual stages of the process that provides the basis of the Norton method were studied only incompletely. The activation energy estimates carried out by Shiryaev et al. [379] point to the fact that, along with electrochemical stages, this process also includes chemical and diffusion stages, one of which could be the intercalation of potassium into a barium-enriched crystal [382].

The strongest effect on the properties of electrolysis products is exerted by the composition of moist alkaline melts. The moisture level is difficult to control and, in addition, can change in the course of sufficiently long electrolyses. Along with the $KOH/Ba(OH)_2$ ratio, the water content in the melt is also essential for the product composition. Its variation over a wide range affects the melting point of the alkaline mixture, and this makes it rather difficult to compare melts of various compositions at a constant and sufficiently low temperature. The complex effects of the melt composition on the electrolysis characteristics in the Norton method have been studied with special attention [370, 379], but, as yet, one can speak only of the tendencies observed (Fig. 7). On the basis of Norton method, a low-temperature technique has been developed for synthesizing $KBiO_3$ [377, 383], a substance which otherwise can be synthesized chemically only at high temperatures and oxygen pressures.

Attempts has been made to extend the Norton method to cuprate systems. $La_{2-x}Na_xCuO_4$ was obtained by anodically polarizing a NaOH melt with addition of

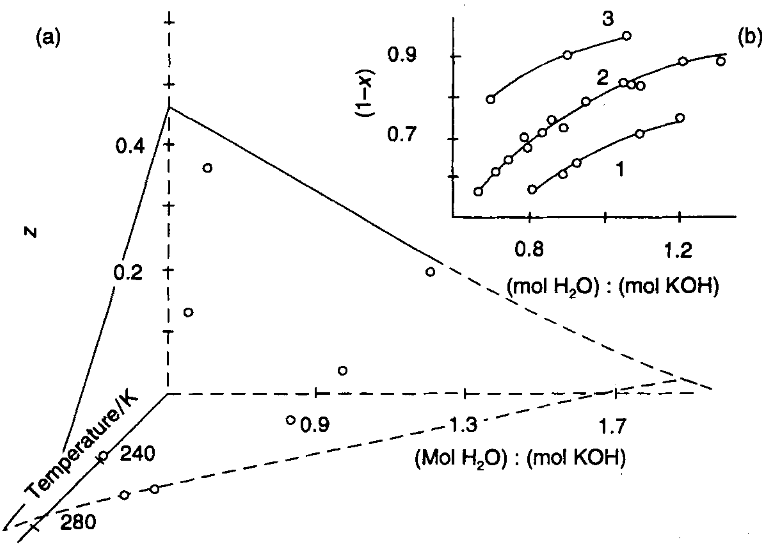

Fig. 7. Influence of the water content in an alkaline melt on the composition of $Ba_{1-x-z}K_xNa_zBiO_3$ electrosynthesized by the Norton method [379]: (a) ternary diagram showing water content-melting temperature-z for a constant [KOH]/[BaO] ratio in the melt; (b) binary diagrams showing water content vs $(1-x)$ for [BaO]/[KOH] molar ratios in the melt of 0.0076 (1), 0.0127 (2), and 0.0254 (3).

La_2O_3 and CuO [384, 385]. In this case, the charge consumed per molecule *a fortiori* amounts to less than one electron and corresponds formally to partial oxidation of the copper. This process is extremely sensitive to the melt composition and leads to the desired product only in the complete absence of water. The kinetics of the process is determined, according to the authors, by the diffusion of lanthanum hydroxo complexes. In acid (moist) melts, the oxygen evolution is apparently accelerated on the anode, and this enhances the acidity locally in the near-electrode layer and causes the precipitation of CuO.

Electrochemical studies in alkaline melts are complicated by the absence of detailed information on the chemistry of corresponding systems, and in particular on solvation processes. Moist melts generally represent the limiting case of strong base solutions. It would undoubtedly useful to study the changes in the kinetics and the composition of the products of anodic electrocrystallization in a model system upon the gradual transition from common alkaline solutions to concentrated bases, and then to alkaline melts with different water contents.

A certain similarity to the Norton method can be recognized in the combined technique for growing YBCO crystals from a high-temperature melt [386], where electrolysis is used for locally increasing the oxygen concentration and thus for promoting nucleation in melts saturated with respect to CuO.

The processes of electrocrystallization form the basis of methods for synthesizing the spinel superconductors $Li_{1-x}NbO_2$ [387] and $Li_{1-x}Ti_2O_4$ [388–390]. The stoichiometric forms are obtained by the electrolysis of borate melts followed by lithium extraction with HCl solution.

Electrochemical methods in fused salts and oxides (by and large, based on cathodic electrocrystallization [20–25]) do not display any important advantages attention is therefore directed to electrolysis in solutions and melts of moist bases The latter give the opportunity to reduce the HTSC synthesis temperature significantly. At the same time, from the standpoint of kinetic studies of the electrochemical formation of oxide phases, high-temperature melts are undoubtedly of grea interest since many of them are characterized in detail chemically and thermodynamically, and the experimental techniques for such systems ensure the invariance of the melt composition.

In conclusion, it should be emphasized that anodic electrocrystallization is so far the only method for single-stage synthesis of HTSC at low temperatures. It has no analogs among the numerous alternative methods. Generally, there is no major obstacle to widening the range of systems which can be synthesized by anodic electrocrystallization, although the difficulties can be quite great. Nevertheless, one can expect that new methods of this kind will appear in future for synthesizing multicomponent oxide systems.

5.6 Synthesis of Hydroxide Precursors by Varying the pH of the Near-Electrode Layer

The method of cathodic alkalization, the use of which is not accompanied by any electrode reactions of the components of the solid products, is often considered to be an electrochemical process. The deposition on the cathode surface of various oxide–hydroxide compositions that form as the result of a local pH increase accompanying hydrogen evolution forms the basis of the technologies of nickel oxide and certain other electrode materials [391]. This method is used for obtaining precursors for radiochemical metal targets [392]. In recent years, cathodic alkalization is also used for special electrosyntheses such as deposition of oxides of rare-earth elements [334], tungsten (molybdenum) oxide films [393, 394], and also heteropolytungstates (molybdates) [395, 396]. These substances, with extremely peculiar chemical properties, offer great possibilities for the redox modification of their stoichiometry, composition, and physical properties and also for the realization of electrochromic transitions [397, 398]. Using the processes of cathodic alkalization, one can synthesize materals with different structures [399, 400], but a thermal post-treatment is necessary to obtain crystalline multicomponent oxides.

The method of cathodic alkalization is undoubtedly promising for synthesizing perovskite compounds [400]. By this method, a distribution of components in the deposit-precursor can be obtained that allows the subsequent annealing to be carried out at lower temperatures and for shorter periods. The disadvantage of the method is the spatial variation of the pH and, consequently, the difficulty of controlling product composition (especially when simultaneously several hydroxides with different dissociation constants are deposited locally).

Nevertheless cathodic alkalization has been found successful for preparing YBCO precursors [401]. In the isopropanol solutions that were used, hydrogen evolution was apparently inhibited as compared with aqueous solutions, and the pH variations were more uniform. Abolmaali and Talbot [401], rightly noted that in work on the preparation of metallic precursors from protic (and even more so from aqueous) solutions (see Section 5.2), it is most reasonable to expect the deposition not of metal but of hydroxide compositions. We should add that this refers even to those experiments in which complexing additives were used, because at sharp changes of pH even very stable EDTA complexes can be transformed into less stable, poorly soluble hydroxo complexes (hydroxides, in the limiting case). Inhibition of hydrogen evolution in the presence of organic ligands weakens the effects of cathodic alkalization. However, considerable rates of electrodeposition of chemically active metals can be attained at moderate cathodic potentials, at which the hydrogen-evolution rate is extremely high even in the presence of inhibitors. Therefore, in aqueous and other protic media, the deposition of hydroxides in the course of cathodic alkalization apparently starts earlier than the electrodeposition of alloys.

5.7 Electrophoresis

The electrophoretic deposition of HTSC films on conductive substrates, which was probably first described by Koura [402], is not a case of electrosynthesis [26], but a procedure for forming the product from the previously synthesized material. Since, in the course of electrophoretic deposition, the HSTC oxide contacts the liquid phase (most frequently the electrolyte solution) a number of experimental problems inherent to electrosynthesis are also present.

Suspensions of HTSC for the electrophoretic deposition of bismuth [403–409] and thallium [403] HTSC, various cuprates of rare-earth metals and barium [204, 407, 410–414], and also silver HTSC [415, 416] and PbO–HTSC [417] compositions have been used. These are prepared in acetone, acetonitrile, toluene, butanol, methylethylketone, or mixed solvents. They contain chemically pure materials (silver is introduced as Ag_2O) dispersed thoroughly, first mechanically and then in liquid) by ultrasonic treatment (in which case the particles became charged). The choice of solvent is by and large determined by its effect on the stability of the deposited oxide [417].

The main advantage of electrophoretic deposition is that it ensures film uniformity even for large thicknesses (5 μm and more). Freshly deposited films, as a rule, exhibit unsatisfactory characteristics, but after a short annealing their T_c and especially their J_c increase (mostly due to the removal of traces of solvent). In this case, the cracking of deposits on metal substrates is significantly less than usual and can even be completely eliminated by using lower rates of deposition [408]. The electrophoretic method allows one to deposit films on substrates of a complex geometry and large dimensions [406, 418, 419]. Most impressive, for instance, is the electrophoretic preparation of a superconducting cable up to 1000 m long on a nickel substrate [412]. The possibility of significantly deforming the samples with electrophoretic coatings without cracking is also attractive [410].

Electrophoretic methods may be improved by fundamental colloidochemical studies of oxides. For example, additives are introduced that promote the particles optimal surface state [420, 421] as a rule, I_2 is used since it does not react chemically with HTSC oxides [422], the purity of the solvent is controlled [419]. ζ-potential measurements are used to select the measurement conditions [402, 423], and the milling procedure is optimized [424]. By varying the particle charge it is, in fact, possible to influence the deposition rate and make the electrophoretic method more controllable.

The texture of deposits formed under a magnetic field [413, 414] is a characteristic of films which depends primarily on conditions of deposition, not annealing.

Studies of the electrophoresis and sedimentation [425] processes in HTSC suspensions serve also to advance the understanding of adsorption phenomena on HTSC surfaces.

5.8 Prospects for the Electrochemical Fabrication of Nanocompositions with HTSC Units

The direction of modern device fabrication, is toward production of complex structures (including those with the elements of HTSC) with characteristic dimensions in the micro and nano ranges [426–428]. These include superlattices [429, 430], and other nanocompositions [431, 432], particularly those which contain HTSC/HTSC junctions (two HTSC materials with different properties), as well as HTSC/metal, HTSC/semiconductor, and HTSC/dielectric junctions. These structures form the basis of modern electronics, and exhibit different size-dependent quantum effects.

The electrochemical design of special nanocompositions can be achieved both by creating the multilayer structures and by locally modifying the surfaces. These common approaches are used for both the HTSC and or their precursors.

The more traditional approach has already been used in anodic electrocrystallization processes to produce nanocompositions and superlattices of mixed Ti–Pb oxides [341–347]. With HTSC materials, initial steps have been made in this direction in studies on the electrochemical deposition of conductive polymers on the surface of microband YBCO electrodes [28, 50, 433]. In the resulting composition, the reversible transition from the HTSC/metal junction (at the high doping degree of the polymer) to the HTSC/semiconductor junction has been achieved. The properties of these compositions allow one to control the T_c shift over a wide interval.

Compositions of HTSC and ultrathin layers of dyes also exhibit interesting properties [434]. The potentiality of electrosynthesis for fabrication of such structures with specific optical transitions is excellent, particularly as a result of experience gained in studies and applications of the electrochromism phenomenon [435] such as forming films of poorly soluble cyanide complexes [436–441]. These compounds provide the opportunity to carry out electrochemical fabrication of linked and sandwich structures. The region of potential during deposition corresponds to the stability regions of HTSC surfaces.

Various multilayer compositions can also be obtained, in principle, on the basis of most of the techniques described above for synthesizing HTSCs precursors, as well as by the combination of these techniques with other electrochemical methods of fabrication. The potentialities of nanoelectrosynthesis have yet to be recognized. It is well known that HTSC oxides doped with oxygen-containing anions exhibit certain pecular properties [442, 443]. The incorporation of large anions into the oxide bulk at room temperature seems to be impossible. At the same time, the creation of anion-containing regions in the near-surface layers of grains in electrolyte solutions is quite feasible, and may be put forward as one of the methods for creating nanostructures. Studies in this direction will require investigation of ionic adsorption on HTSC oxides.

The problem of lateral modification of HTSC surface layers, and the local electrosynthesis of HTSCs on the surface of patterned substrates including the precursors is very interesting. Such processes can occur, for example, during electro-oxidation of metals when the process in its initial stages takes place only on isolated microscopic regions. Thus, Josephon junctions on the surface of Bi–Sn alloys [222] and on ceramic YBCO samples [295, 444] were obtained by using electrochemical oxidation without any special local techniques. But it is hard to control such oxidation processes, and sufficient reproducibility cannot be ensured for most systems. Josephson tunnel junctions based on electrochemically synthesized BKBO crystals have been described [445].

Electrochemical nanotechnologies using ultramicroelectrodes such as the tips of electrochemical scanning tunneling microscopes and related devices [446, 447] are of special interest both, for conducting local electrosynthesis and for electrochemical modification. The tip nanotechnique in electrolyte solutions ensures the optimal level of surface purity, offers additional possibilities in governing the processes by varying the potentails of the tip electrode and the substrate, and may also be used for stabilizing the resulting nanostructures. To date, local electrochemical etching [448, 449] and local electrodeposition of metals [448, 450, 451] have already been realized, including cases when the photosensitive modified surfaces were illuminated by pulsed light [449]. The process of removal of regions of insulating polymer films followed by electropolymerization on the free regions of the substrates of polymers of a different nature has also been demonstrated [452].

Developments in techniques of fabrication of multicomponent oxide materials stimulated by the problem of HTSC electrosynthesis thus demonstrate numerous possibilities for special electrosynthesis. These are beneficial for its development as an independent direction of fundamental and technological investigation.

6 Electrochemical Properties of HTSC materials at Ambient Temperatures

It is by now evident that there is nothing unusual in the electrochemical behavior of HTSC oxides at ambient temperatures [49, 453]. The kinetics of electrode reactions on HTSC materials can be complicated by numerous side-processes. HTSC investigations under ordinary conditions are complicated by the low stability of cuprates to solvents and/or electrolyte ions, which is closely related to the principal problem of HTSC chemistry: the problem of degradation.

6.1 Chemical and Electrochemical Processes that Accompany the Degradation of HTSC Materials

The chemistry of degradation phenomena in HTSC oxide systems has been investigated in detail. Current studies are predominantly directed toward elucidation of the initial stages of degradation, primarily the properties of ultrathin layers of degradation products that do not exibit any definite phase properties [454–456]. In parallel, the vital problem of protection against degradation is studied by developing methods for electrodeposition of protective coatings and electrochemical processing of the HTSC surfaces.

Attention is usually focused on degradation phenomena that are caused by interaction with water (including atmospheric moisture) and carbon dioxide. Regarding interactions with water, YBCO and its substituted derivatives are the most active [457–460]. Their hydrolysis leads to the formation of a number of ions, including unstable aquacomplexes of Cu^{3+} which react with water evolving oxygen. In a small volume of water or a moist atmosphere solid products are accumulated, and the process as a whole is usually represented as

$$2YBa_2Cu_3O_7 + 3H_2O \Rightarrow Y_2BaCuO_5 + 5CuO + 3Ba(OH)_2 + \tfrac{1}{2}O_2 \qquad (3)$$

Y_2BaCuO_5 can be subsequently hydrolyzed with the formation of $Y(OH)_3$ [461]. In the presence of CO_2 or CO (which is also oxidized by Cu^{3+}, Ba_2CO_3 is formed [462].

These reactions are observed even at the temparature of liquid nitrogen [458]. They lead to a gradual decrease in T_c, in superconducting phase content, and (most rapidly) in J_c [463]. At a certain stage, the superconducting properties disappear entirely. This takes place even before the complete deterioration of bulk cuprate, because the low-conductivity degradation products preferentially block the grain boundaries [464]. The slow reaction with dry CO_2 [465] involves only certain regions of grain boundaries [466], while in a moist atmosphere and aqueous solutions it is strongly accelerated [465]. It was reported that minor amounts of water react reversibly with YBCO, thus protonating Cu^{2+} in the lattice [467], and the cuprate remains superconducting.

The rate of degradation of YBCO depends substantially on the impurity content and the sample's prehistory, as well as on the porosity, grain size, and other macrostructural factors [468]. Surface contamination by carbon-containing particles substantially accelerates intractions with water [469]. Inner stresses in the samples also have a certain effect on these processes [470]. As a rule, high-quality HTSC films are more stable to degradation than the corresponding ceramics [453].

The degradation processes of other HTSCs are by and large similar, even if slower, and are generally characterized by their preferential depletion of alkaline-earth components with the formation of the corresponding hydroxides and carbonates [468, 471]. The stability rows discussed sometimes [28] are, as a rule, of a limited application, and the position of HTSC oxides in them depends substantially on the nature of the medium and the interaction conditions [417].

These tendencies are also observed in the kinetics of the hydrolysis processes of HTSC oxides in aqueous electrolyte solutions. The leaching of alkaline earth cations proceeds most rapidly [52, 472, 473] and can be inhibited by introducing additives of corresponding salts into the solution. For example, in the presence of only 0.01 M $BaCl_2$ in aqueous solutions, YBCO retains the chracteristics of the superconducting phase [473], although the degradation is not entirely suppressed [52]. According to [474], carbonate films formed on the grain surfaces under certain conditions exhibit protective properties and thus prevent further degradation. The other HTSC components also pass into solution as a result of hydrolysis, but due to their low solubility, the concentrations attained in neutral solutions, as a rule, do not exceed 10 μM [472]. In chloride and sulfate solutions, the kinetics of degradation is defined by the formation of poorly soluble CuCl and $BaSO_4$ [475]. It is significant that the O_2 concentration in solution hardly affects the rate of such degradation processes [476].

As the solution pH increases, the rate of degradation is sharply reduced. For instance, no degradation-phase products were observed in a 10 M base at room temperature [473]. However, this does not mean that degradation does not affect the near-surface layers of HTSC oxide. The chemistry of the HTSC surface in concentrated alkaline solutions is practically unknown. But it has been observed that in an alkaline melt which contained water, YBCO rapidly decomposed to the individual oxides at 500 °C while in a dry base it remained sufficiently stable [477].

As is evident the dissolution of HTSC in most proceeds selectively. That is, one or more elements accumulate on the surface as the products of degradation. The possibilities of selective dissolution will be considered with reference to the etching problem.

The products of degradation during polarization of HTSC electrodes have not been studied in much detail [44, 287, 293, 476, 478]. Upon cathodic polarization of cuprates, the reduced forms of copper oxides [44, 476], and sometimes metallic copper [293], are formed at considerable rates; these processes are photosensitive [453]. During anodic polarization, the formation of alkaline-earth compounds on the HTSC surface is accelerated [287, 476].

Electrochemical techniques allow one to estimate qualitatively, and even quantitatively for certain groups of related materials, the degree and the rate of oxide degradation. For this purpose, use is made of sufficiently simple measurements of impedance [474, 476], voltammograms [49, 293, 479], and open-circuit potentials [287, 480, 481]. For example, the dependence of the slope of YBCO open-circuit chronopotentiograms on δ was found [40, 482, 483], which was probably due to the acceleration of degradation with the increase in δ.

The most sensitive techniques are based on the reversibility degree of the redox reactions of certain reactants present in solution. The reactions of TCNQ [60] and ferrocene derivatives [47, 53] can be carried out quite reversibly on the freshly formed surfaces of encapsulated ceramic HTSC electrodes and high-quality films in dry acetonitrile. On addition of water, the reversibility is upset due to the formation of low-conductivity degradation products on the surface. The increase in the potential difference between anodic and cathodic peaks correlates with the degradation rate. According to [484] reversible responses to similar reactants can also be obtained on electrodes made of high-quality ceramics.

Degradation processes cannot also be avoided in electrochemical systems with solid electrolytes [316]. It is therefore necessary to consider the specific features of these processes at high temperatures within the framework of the problem of the interaction between HTSC oxides and their substrates, junctions and other interfaces.

6.2 Electrochemical Coating of HTSC Materials

The development of methods for metallizing HTSC ceramics and films is the technological problem that is perhaps the most important for realizing practical applications of these materials. There are a great variety of structures of HTSC–metal compositions which are of practical interest. Continuous metal coatings that prevent contact of HTSC oxides with the atmosphere are used primarily for protection. Silver coatings are most frequently used [485]; it should be noted that ceramic HTSC–silver compositions, as well as having high resistance to degradation, are also characterized by lower resistivity on the grain boundaries. Good results can be achieved with small silver clusters [486] even if coating is not continuous.

The metallization of local regions of HTSC surfaces is being studied in connection with the problem of junction fabrication. In this case, the adhesion that determines the ohmic resistance on the HTSC/metal interface is of greatest importance.

Table 4. Experimental data on the electrochemical metallization of HTSCs.

HTSC	Solvent	Deposited metal	Reference
YBCO	AN	Cu; Ag; Pb	[61, 491]
YBCO	H_2O	Cu	[492]
YBCO	H_2O	Cu; Ag	[493]
YBCO	H_2O	Cu	[53]
YBCO	H_2O	Pb; Tl; Ag; Hg	[494]
BSCCO	Glycerol; methanol	Ag; Cu	[495]
Tl,Pb-substituted BSCCO	H_2O	Cu	[496]

[a] Abbreviation: AN, acetonitrile.

Another important problem is the elimination of the chemical interactions between contacting phases and also of the diffusion of metal atoms into the oxide bulk [487–489]. One example is the operation of commonly used indium junctions, which are convenient because films of this soft metal and its alloys can be applied mechanically [490]. This fact stimulates the quest for low-temperature techniques for junction fabrication. It is known that silver, gold, and copper, and also probably platinum [202] and palladium [487], are most suitable because of their weak interaction with HTSCs.

Unfortunately, the electrodeposition of metals summarized in Table 4 is accompanied by increased HTSC degradation under cathodic polarization [53, 55]. In nonaqueous media, electrocrystallization processes can be inhibited due to the peculiarities of the intermediate Cu^+ species solvation [286]. Moreover, the surface morphology of deposits can be adversely affected by the formation of dendrites; this can be overcome by the addition of a brightening agent [497].

Special studies with ring-disk electrodes showed that only metals with relatively positive deposition potentials silver and mercury [53, 494] and also probably copper can be cathodically deposited on HTSC substrates without partial reduction of the oxide surface. HTSC–silver composites are fabricated by multistage techniques that include an electrodeposition stage [498, 499]. It has been noted during deposition of silver and copper that their incorporation into the BSCCO lattice is possible (0.01 and 0.4 atom per molecule, respectively) with the formation of substituted phases [495].

In recent years, electrochemical metallization of semiconductors [500–502], including photoassisted processes [503, 504], has been investigated extensively. The experience gained in these experiments on the controlled deposition of ultrathin films is yet to be applied to HTSCs.

Oxide, flouride, and polymeric films, as well as certain others, are used as protective coatings for HTSC materials (for example, see [505]). The electrodeposition of conducting polymers such as polypyrrole [433, 491, 493, 506], polythiophene and its derivatives [493, 507], and polyaniline [478] is the most effective process. Anodic electropolymerization in acetonitrile solutions proceeds without any degradation of the HTSC substrate and ensures continuous and uniform coatings. Apparently, this method is promising not only for the fabrication of compositions with special properties based on HTSC [50, 28, 295] as mentioned above, but also for the creation of junctions with special characteristics [507].

6.3 Surface Treatment of HTSC materials: Electrochemical Aspects of Etching and Passivation

Two methods of chemical etching are used for obtaining pure surfaces of HTSC oxides: dissolution in alcohol solutions of bromine [508–510], and in aqueous solutions (as a rule, concentrated) of acids [510–513]. The first method ensures atomic-level surface purity for most oxides [422, 510]. Electrochemical methods of etching were also proposed [514], including cathodic reduction of oxide surface layers to metals with subsequent dissolution of the latter in dilute acids [515], and anodic dissolution in $HClO_4$ solutions in 2-butoxyethanol [516, 517].

As in the case of semiconductors, electrochemical methods can provide sufficient information on the characteristics of certain stages of complicated processes of HTSC etching. This was convincingly demostrated in a number of studies by Miller and co-workers [51–55], who carried out measurements in aqueous solutions of different composition on rotating ring-disk HTSC electrodes. The use of platinum or gold rings made possible the determination of dissolution products under polarization and also in open circuit. The conditions were thereby in which HTSC dissolution proceeds via the mechanism of initial protonation and is accompanied by stoichiometric transition of the components into solution [51, 52, 56]. Effects of the anion composition of the solution were also revealed. In particular, it was shown that in the presence of Cl^-, ClO_4^-, and PO_4^{3-}, preferential dissolution of the alkaline-earth metal takes place, and the other components form films of poorly soluble salts [52]. On the basis of these experiments, etching solution compositions containing EDTA were proposed [518]. The kinetics of cuprate dissolution was also found to depend on the solution composition when no poorly soluble compounds are formed. This result is attributed to the effect of the potentail shift in the electrical double layer on the protonation rate of the oxide species [519, 520].

Another way to stabilize the HTSC surface state is to passivate it by the formation of thin, compact, chemically inactive films. Chemical methods of passivation in solution [521] generally consist in the formation of poorly soluble salts (sulfides, iodides, oxalates, etc.) of the metal components. The oxidation of the thin surface layers accepted for the passivation of semiconductors [220, 221] apparently cannot be directly applied for oxide materials, and requires further development. The insoluble compounds that form on HTSC surfaces do not display pronounced passivating properties.

6.4 Structure of the Electrical Double Layer on HTSC Oxides

The adsorption properties of oxides in electrolyte solutions have been studied in less detail than those of metals. The explanation of these phenomena is based on the model of binding sites which assumes that ions are bound to the hydrated centers which are characterized by acidic- or basic-type dissociation [64, 66, 71], and also on the electrostatic approach based on the Grahame–Parsons theory [522].

The capacitances of the HTSC solution interface cited in the literature [153, 523] apparently pertain to the total polarization capacitance. To estimate the double-layer capacitance and more correctly describe the equilibria in the surface layer, the results of ζ-potential measurements can, in principle, be used [423]. However, these data correspond to the surfaces which have undergone the degradation.

Studies of the electrical double-layer structure on HTSC oxides are of significance for analyzing the degradation processes. In the case of dispersed oxides, changes in the solution composition can occur not only as the result of degradation but also due to ionic adsorption that accompanies the formation of the double layer on the interface [524]. To take into account this factor is particularly important for neutral solutions. Moreover, ion-exchange methods including those which stabilize the surface composition, can be developed for modifying the HTSC material surface.

7 Electroanalytical Aspects of the HTSC Problem

Electroanalytical methods have been used repeatedly in HTSC studies for the quantitative determination of the chemical composition of ceramics and films, their precursors, and also the degradation products. To analyze a multicomponent non-stoichiometric oxide it is necessary to determine independently with sufficient accuracy, the content of individual components that are simultaneously present in the samples [282]. The independent quantitative determination of oxygen is most essential (difference analysis introduces noticeable errors in the values of the important parameter δ). Also important is the determination of the valence of copper. Certain theories of superconductivity of cuprate systems consider Cu^{3+} as the principal essential component of HTSCs [9, 10], which attracts special attention to this problem.

Highly sensitive electroanalytical methods are sufficiently efficient. Their main limitation is the lack of reliable procedures for determination of alkaline-earth metals.

7.1 Destructive Electroanalysis

The simplest methods of HTSC analysis are based on the determination of the products of sample dissolution in acidic media. Potentiometric, amperometric, or coulometric titrations are frequently used (mainly for YBCO ceramics [525–527] and their analogs with other rare-earth elements [528, 529], and also for BSCCO [530]). We note particularly the method of potentiostatic coulometric analysis [531], which allows one to analyze thallium cuprate samples over a wide range of the Tl/Cu ratio, and also the method of flow-through coulometry for determining the effective valence of copper [532]. The polarographic determination of Cu^{3+} content in the samples obtained by dissolving HTSCs in concentrated alkaline solutions with special complexing additives [533] is also of interest. In combination with independent methods of chemical analysis of the cation composition of the original materials, these techniques can be used for determining δ with an accuracy that significantly exceeds that of the widely used iodometric titration [505].

7.2 Nondestructive Electroanalysis

Nondestructive analysis of solid HTSC oxides is based on voltammetric [42, 45, 62, 534] and chronopotentiometric [62] investigations of specially designed electrodes which contain microquantities of HTSC (paraffined graphite with the oxide powder pressed on the top [43–45] and carbon paste electrodes [34–41]). Analytical details are thoroughly documented for such systems (including HTSCs and other multicomponent materials) [535–537].

Similar studies on bulk ceramic electrodes make it possible to analyze the samples qualitatively. As a rule, such methods are directed to the determination of the copper valence. From the appearance of an additional peak in the cathodic run of voltammograms [37, 44, 46, 476, 534, 538, 539] or the shift of the Cu^{2+} reduction peak [534, 540], it is assumed that Cu^{3+} is present in solid cuprates along with Cu^{2+}.

The fine features of the voltammogram are defined to a large extent by the potential scan limits and scanning rate [293], and also by the details of electrode design related to ohmic losses in pores and grain boundaries. The shape of voltammograms in chloride solutions differs substantially from that observed in other electrolytes because, in the former, the reduction of copper corresponds to the formation of CuCl [35]. The most informative data can be obtained by using slow scanning rates, so that each current peak is the set corresponds to a definite stages of the multielectron reactions. Such a technique also enhances the possibilities of qualitative analysis. Examples of such a measurements can be found in [36–38].

Cyclic voltammetry at high anodic potentials overestimates the Cu^{3+} content because of the partial oxidation of copper in the near-surface HTSC layers in the course of the anodic run [293]. Measurements of voltammograms starting from the open-circuit potential appear to be more correct [39, 483]. Differential pulse voltammetry has been used for estimating the proportions of tetragonal and orthorhombic (superconducting) phases in YBCO from the difference in the ratio between the currents of the two respective reduction peaks [39]. A high accuracy is also exhibited by coulometry on a ring-disk electrode [56–58], which eliminates the superposition of signals corresponding to different redox transformations of copper.

To refer the electrochemical responses to certain redox transitions in the solid state, they are usually compared with the data for model systems of individual oxides [37, 38, 51, 56, 494]. In a number of studies, the authors also modeled the HTSC voltammograms by fabricating the electrodes from mixtures of individual oxides [35, 37, 38, 541] and cuprates of the simpler composition [36, 43]. Such efforts make it possible to check the correctness of the correspondence of a certain peak (plateau) to a proper redox transition. The modeling of Cu^{3+} reduction was carried out in a solution of chemically synthesized periodate complexes [483, 533].

In analytical investigations in nonaqueous media and aqueous solutions of optimal composition (high concentrations of bases and/or alkaline-earth cations), the electroanalysis provides sufficiently reproducible results, even for relatively unstable YBCO [34]. However, voltammetry in degradation-active media also gives valuable characteristics of the products of the oxide reactions with the medium.

Potentiometric [319,541] and coulometric [312,318,542] methods were put forward to determine δ in cells with a solid electrolyte and Cu_2O/Cu counter-electrode.

8 The Prospects of HTSC Photoelectrochemistry

Only a few studies [453,543–547] have been carried but on the photoelectrochemical behaviour of YBCO ceramics and single crystals. In nonaqueous media, in the absence of degradation, the data show that the usual concepts of photoelectrochemistry of p-type semiconductors apply to those systems. Such studies have not yet been actively developed, probably because of the high sensitivily of photoelectrochemical processes to the nature of materials. Reproducibility of data for such complex systems as HTSC oxides is an issue. At the same time, the photoassisted electrochemical processes on HTSC electrodes can lay the basis for certain effective technologies. This is especially true for the photoelectrochemical etching and metallization which prove to be extremely effective as applied to semiconductors [503,504].

9 Conclusions

The infusions of electrochemistry into the HTSC arena has been beneficial for the latter, and also fruitful for both fields. The role of electrochemistry has undeniably led to development of alternative methods for synthesizing HTSCs and their precursors, to methods of HTSC protection and modification of HTSC surfaces (including micro- and nanostructuring), to the fabrication of new hybrid devices that include the HTSC units, and also to new types of junctions. Highly sensitive, relatively simple, and reliable methods of the electrochemical analysis of both the volume and the surface of HTSC materials make it possible to quantitatively characterize the interaction of multicomponent oxides with the environment. In turn, electrochemical experimental methodologies have been enriched by new techniques for controlling the state of complicated and unusual objects under conditions unfamiliar to classical electrochemistry.

The investigation of HTSC materials has allowed electrochemists to make a breakthrough into the new fields of extremely low temperatures. The area has opened up new possibilities for elucidating the interface structure, understanding charge-transfer kinetics, and also probably, the nature of high-temperature superconduttivity itself. The phenomena that have come to light in these studies were quite unexpected, they are still not entirely clear, but they are worthy of further detailed investigation. In particular, the Tafel relationships for the electrode processes in the region of ultra-low temperatures have still not been obtained. Their analysis could become one of the directions of fundamental electrochemistry in the future. Of great interest are the unique quasi-liquid electrolytes with ultra-low freezing temperatures, which have to date been incompletely studied.

Electrochemical studies of HTSC materials have also led to progress in methods for measuring ultra-low currents and for solving special problems of impedance under unconventional conditions.

High-temperature superconducting oxides are of interest for electrocatalysis since they represent materials that are comprehensively characterized by various physical methods. They therefore hold promise for obtaining new correlative relationships between catalytic activity and the bulk properties of materials.

Recently, non-oxide HTSCs such as derivatives of fullerenes [549, 550] were discovered, as well as certain high-melting compounds of transition metals [551, 552]. The electrochemistry of fullerenes has already been transformed into an actively developed independent field [550, 553, 554]. The electrosynthesis of a number of carbides, sulfides, borides, and their analogs represents a well-known method for their production [23, 555]. Hence, electrochemistry also plays an active role in the new directions of the HTSC chemistry.

Acknowledgments. We will be always grateful to Professor H. Gerischer, who in his letter dated August 1994 approved the project of this review and made brief but expert remarks, drawing attention to those aspects of HTSC electrochemistry that could be of greatest interest for a wide circle of electrochemists.

We are also grateful to T. Ya. Safonova for her invaluable assistance in the preparation of the manuscript, and to Yu. G. Metlin and S. T. Koretskaya for their help in the quest for information which is of special importance for this rapidly developing fields.

This work was financially supported by the Russian State Program of HTSC Research (Project No. 92127).

10 References

1. V. L. Ginzburg, Annu. Rev. Mater. Sci. 2, 663 (1972).
2. J. G. Bednorz, K. A. Müller, Z. Phys B 64, 189 (1986).
3. A. W. Sleight, Thermochim. Acta 174, 1 (1991).
4. C. H. Stoessel, R. F. Bunshah, S. Prakash, H. R. Fetterman, J. Supercond. 6, 1 (1993).
5. S. Putilin, E. Antipov, O. Chmaissem, M. Marezio, Nature (London) 362, 204 (1993).
6. J. R. Schrieffer, Theory of Superconductivity, W. A. Benjamin, New York (1964).
7. N. Hur, N. Kim, K. Lee, Y. Park, J. Park, Mater. Res. Bull. 29, 959 (1994).
8. C. Chu, L. Gao, F. Chen, Z. Huang, R. Meng, X. Xue, Nature (London) 365, 323 (1993).

9. T. V. Ramakrishnan, C. N. R. Rao, J. Phys. Chem. 93, 4414 (1989).
10. S. Uchida, Jap. J. Appl. Phys. Pt. I 32, 3784 (1993).
11. C. J. Jou, J. Washburn, Appl. Phys. Lett. A 53, 87 (1991).
12. G. D. Ilyushin, L. N. Dem'yanets, Sverkhprovodimost': Fiz. Khim. Tekhn. 4, 245 (1991).
13. S. L. M. Volkova, S. A. Polishuk, S. A. Magarill, Sverkhprovodimost': Fiz. Khim. Tekhn. 6, 2112 (1993).
14. R. J. Cava, Nature (London) 362, 204 (1993).
15. J. Hauck, K. Mika, Physica C 175, 386 (1991).
16. A. K. Vijh, Electrochemistry of Metals and Semiconductors, Marcel Dekker, New York (1973).
17. W. Kern, G. L. Schnable in: The Chemistry of the Semiconductor Industry, S. J. Moss, A. Ledwith (eds.), Chapman and Hall, New York (1987), p. 225.
18. A. Hamnett, in: Comprehensive Chemical Kinetics, Elsevier, Amsterdam (1987), Vol. 27, p. 61.
19. Yu. V. Pleskov, Yu. Ya. Gurevich, Semiconductor Photoelectrochemistry, Consultants Bureau, New York (1986).
20. D. Inman, S. H. White, J. Appl. Electrochem. 8, 375 (1978).
21. K. Ravindran Nair, E. Wang, M. Greenblatt, J. Solid State Chem. 55, 193 (1984).
22. J. D. Corbett in: Solid State Chemistry Techniques, A. K. Cheetham, P. Day (eds.), Clarendon Press, Oxford (1987) p.1.
23. S. Crouch-Backer, R. A. Huggins, J. Mater. Res. 4, 1495 (1989).
24. P. Searson, Sol. Energy Mater. Sol. Cells 27, 377 (1992).
25. T. Wade, R. M. Crooks, E. G. Garza, Chem. Mater. 6, 87 (1994).
26. A. M. Kraitsberg, Sverkhprovodimost': Fiz. Khim. Tekhn. 4, 414 (1991).
27. O. A. Petrii, G. A. Tsirlina, Rossiiskii Khim. Zh. 37, 116 (1993).
28. J. T. McDevitt, D. R. Riley, S. G. Haupt, Anal. Chem. 65, 535A (1993).
29. T. N. Kol'tsova, I. S. Shaplygin, Neorganich. Mater. 30, 1067 (1994).
30. V. M. Pan, J. Alloys Compds. 195, 387 (1993).
31. U. Rao, J. Kumar, K. Reddy, Progr. Cryst. Growth Charact. 15, 187 (1987).
32. D. Shi, J. Electron. Mater. 22, 1211 (1993).
33. Yu. A. Kirichenko, S. M. Kozlov, K. V. Rusanov, E. G. Tyurina, S. G. Titova, V. A. Fotiev, Sverkhprovodimost': Fiz., Khim. Tekhn. 4, 2357 (1991).
34. W. Gruner, A. Drescher, Fresenius Z. Anal. Chem. 335, 304 (1989).
35. W. Gruner, R. Stablberg, Kh. Z. Brainina, N. Akselrod, V. M. Kamyshov, Electroanalysis 2, 397 (1990).
36. N. A. Zakharchuk, V. S. Kravchenko, A. I. Romanenko, V. E. Fedorov, S. A. Gromilov, Izv. Sibir. Otdel. AN SSSR 1, 50 (1990).
37. M. T. San Jose, A. M. Espinosa, M. L. Tascon, M. D. Vazquez, P. S. Batanero, Electrochim. Acta 36, 1209 (1991).
38. A. M. Espinosa, M. T. San Jose, M. L. Tascon, M. D. Vazquez, P. Sanchez Batanero, Electrochim. Acta 36, 1561 (1991).
39. A. A. Kaplin, N. M. Svishenko, N. M. Dubova, G. B. Slepchenko, Yu. A. Karbainov, G. F. Ivanov, Zh. Anal. Khim. 46, 976 (1991).
40. N. A. Bondarenko, T. N. Kol'tsova, V. V. Sergievskii, T. N. Adrianova, A. I. Khol'kin, Dokl. Akad. Nauk SSSR 325, 84 (1992).
41. A. G. Rebeko, N. A. Vedernikov, T. E. Nikiforova, I. S. Shaplygin, E. V. Lunina, Yu. N. Barinov, Neorganich. Mater. 29, 1271 (1993).
42. S. Rochani, D. B. Hibbert, S. X. Dou, A. J. Bourdilon, H. K. Liu, J. P. Zhou, C. C. Sorrel, J. Electroanal. Chem. 248, 461 (1988).
43. F. Scholz, L. Nitschke, E. Kemnitz, T. Olesch, G. Henrion, D. Hass, R. Bagchi, R. Herrmann, N. Pruss, W. Wilde, Fresenius Z. Anal. Chem. 335, 571 (1989).
44. S. Scheurell, F. Scholz, T. Olesch, E. Kemnitz, Supercond. Sci. Technol. 5, 303 (1992).

45. I. Zezula, I. Sargankova in: Abstr. 4th Int. Conf. HTSC, Grenoble, (1994), p. 227.
46. J. T. McDevitt, R. McCarley, E. F. Dalton, R. Gollmar, R. W. Murray, J. Collman, G. T. Yee, W. A. Little in: ACS Symp. Ser. 377, 207 (1988).
47. R. O. Gollmar, J. T. McDevitt, R. W. Murray, J. P. Collman, G. T. Yee, W. A. Little, J. Electrochem. Soc. 136, 3696 (1989).
48. S. I. Shah, J. T. McDevitt, R. W. Murray, J. Electrochem. Soc. 138, 1346 (1991).
49. D. R. Riley, A. Manthiram, J. T. McDevitt, Chem. Mater. 4, 1176 (1992).
50. S. G. Haupt, D. R. Riley, C. T. Jones, J. Zhao, J. T. McDevitt, J. Am. Chem. Soc. 115, 1196 (1993).
51. J. M. Rosamilia, B. Miller, L. F. Schneemeyer, J. V. Waszczak, H. M. O'Bryan, J. Electrochem. Soc. 134, 1863 (1987).
52. V. M. Magee, J. M. Rosamilia, T. Y. Kometani, L. F. Schneemeyer, J. V. Waszczak, B. Miller, J. Electrochem. Soc. 135, 3026 (1988).
53. J. M. Rosamilia, B. Miller, J. Electrochem. Soc. 135, 3030 (1988).
54. B. Miller, J. M. Rosamilia, J. Electrochem. Soc. 136, 234C (1989).
55. J. M. Rosamilia, B. Miller, J. Electrochem. Soc. 136, 1053 (1989).
56. J. Rosamilia, B. Miller, Anal. Chem. 61, 1497 (1989).
57. J. M. Rosamilia, B. Miller, J. Electrochem. Soc. 137, 226C (1990).
58. J. M. Rosamilia, B. Miller, J. Electroanal. Chem. 291, 163 (1990).
59. N. D. Sverdlova, W. Schafer, G. M. Mansurov, O. A. Petrii, Russ. J. Electrochem. 31, 227 (1995).
60. D. R. Riley, J. T. McDevitt, J. Electroanal. Chem. 295, 373 (1990).
61. H. D. Rubin, J. M. Rosamilia, H. M. O'Bryan, B. Miller, Appl. Phys. Lett. 54, 2151 (1989).
62. S. Salkalachen, E. Salkalachen, P. K. John, H. R. Froelich, Appl. Phys. Lett. 53, 2707 (1988).
63. V. Brusic in: Oxides and Oxide Films, Marcel Dekker, New York (1972), Vol. 1, p. 2.
64. S. M. Ahmed in: Oxides and Oxide Films, Marcel Dekker, New York (1972), Vol. 1, p. 320.
65. A. K. Vijh in: Oxides and Oxide Films, Marcel Dekker, New York (1973), Vol. 2, p. 1.
66. P. Mark, S.-C. Chang in: Oxides and Oxide Films, Marcel Dekker, New York (1976), Vol. 3, p. 273.
67. G. Belanger, A. K. Vijh in: Oxides and Oxide Films, Marcel Dekker, New York (1977), Vol. 5, p. 1.
68. H. Tamura, H. Yoneyama, Y. Matsumoto in: Electrodes of Conductive Metallic Oxides, S. Trasatti (ed.), Elsevier, Amsterdam (1980), Part A, p. 261.
69. A. Cimino, S. Carra in: Electrodes of Conductive Metallic Oxides, S. Trasatti (ed.), Elsevier, Amsterdam (1980), Part A, p. 97.
70. M. R. Tarasevich, B. N. Efremov in: Electrodes of Conductive Metallic Oxides, S. Trasatti (ed.), Elsevier, Amsterdam (1980), Part A, p. 221.
71. D. N. Furlong, D. E. Yates, T. W. Healy in: Electrodes of Conductive Metallic Oxides, S. Trasatti (ed.), Elsevier, Amsterdam, 1981, Part B, p. 367.
72. S. Trasatti, G. Lodi in: Electrodes of Conductive Metallic Oxides, S. Trasatti (ed.), Elsevier, Amsterdam (1981) Part B, p. 522.
73. J. Pohl, H. Rickert in: Electrodes of Conductive Metallic Oxides, S. Trasatti (ed.), Elsevier, Amsterdam (1980), Part A, p. 183.
74. H. L. Hartnnagel in: Oxides and Oxide Films, Marcel Dekker, New York (1981), Vol. 6, p. 147.
75. E. O'Sullivan, E. Calvo in: Comprehensive Chemical Kinetics, Elsevier, Amsterdam (1987), Vol. 27, p. 243.
76. J. Desilvestro, O. Haas, J. Electrochem. Soc. 137, 5C (1990).
77. D. B. Meadowcroft, Nature (London) 226, 847 (1970).

78. A. C. C. Tseung, B. Hobbs, A. Tantram, Electrochim. Acta 15, 473 (1970).
79. J. Balej, Int. J. Hydrogen Energy 10, 89 (1982).
80. J. O'M. Bockris, T. Otagawa, V. Young, J. Electroanal. Chem. 150, 633 (1983).
81. J. O'M. Bockris, T. Otagawa, J. Electrochem. Soc. 131, 290 (1984).
82. A. Wattiaux, J. Grenier, M. Pouchard, P. Hagenmuller, J. Electrochem. Soc. 134, 1714 (1987).
83. S. P. Mehandru, A. B. Anderson, J. Electrochem. Soc. 136, 158 (1989).
84. Y. Matsumoto, H. Yoneyama, H. Tamura, J. Electroanal. Chem. 80, 115 (1977).
85. Y. Matsumoto, H. Yoneyama, H. Tamura, J. Electroanal. Chem. 79, 319 (1977).
86. G. Bronoel, J. C. Grenier, J. Reby, Electrochim. Acta 25, 1015 (1980).
87. Y. Matsumoto, E. Sato, Electrochim. Acta 25, 585 (1980).
88. Y. Matsumoto, H. Yoneyama, H. Tamura, J. Electroanal. Chem. 83, 167 (1977).
89. Y. Matsumoto, E. Sato, Electrochim. Acta 24, 421 (1979).
90. P. Rasiyan, A. C. C. Tseung, D. B. Hibbert, J. Electrochem. Soc. 129, 1724 (1982).
91. Y. Matsumoto, J. Kurimoto, E. Sato, J. Electroanal. Chem. 102, 77 (1979).
92. A. G. C. Kobussen, H. Willems, G. H. J. Broers, J. Electroanal. Chem. 142, 85 (1982).
93. S. M. Jasem, A. C. C. Tseung, J. Electrochem. Soc. 126, 1353 (1979).
94. A. C. C. Tseung, S. Jasem, Electrochim. Acta 22, 31 (1977).
95. Y. Matsumoto, H. Yoneyama, H. Tamura, Chem. Lett., 7, 661 (1975).
96. T. Otagawa, J. O'M. Bockris, J. Electrochem. Soc. 129, 2391 (1982).
97. Y. Matsumoto, H. Yoneyama, H. Tamura, J. Electroanal. Chem. 83, 237 (1977).
98. Y. Matsumoto, H. Yoneyama, H. Tamura, J. Electroanal. Chem. 83, 245 (1977).
99. T. Kudo, H. Obayashi, M. Yoshida, J. Electrochem. Soc. 124, 321 (1977).
100. A. Wattiaux, J. Grenier, M. Pouchard, P. Hagenmuller, J. Electrochem. Soc. 134, 1718 (1987).
101. K. L. K. Yeung, A. C. C. Tseung, J. Electrochem. Soc. 125, 878 (1978).
102. Y. Matsumoto, H. Manabe, E. Sato, J. Electrochem. Soc. 127, 811 (1980).
103. A. C. C. Tseung, H. L. Bevan, J. Electroanal. Chem. 45, 429 (1973).
104. F. R. van Buren, G. H. J. Broers, C. Boesveld, A. J. Bouman, J. Electroanal. Chem. 87, 381 (1978).
105. F. R. van Buren, G. H. J. Broers, A. J. Bouman, C. Boesveld, J. Electroanal. Chem. 87, 389 (1978).
106. J. L. Gautier, J. Brenet, E. Trollund, Electrochim. Acta 28, 1153 (1983).
107. T. Nakamura, M. Misono, Y. Yoneda, J. Catal. 83, 151 (1983).
108. T. Kudo, H. Obayashi, T. Gejo, J. Electrochem. Soc. 122, 159 (1975).
109. F. R. van Buren, G. H. J. Broers, A. J. Bouman, C. Boesveld, J. Electroanal. Chem. 88, 353 (1978).
110. A. G. C. Kobussen, F. R. van Buren, G. H. J. Broers, J. Electroanal. Chem. 91, 211 (1978).
111. Y. Matsumoto, J. Kurimoto, E. Sato, Electrochim. Acta 25, 539 (1980).
112. R. L. Cook, A. F. Sammells, Solid State Ionics 45, 311 (1991)
113. T. Inoue, K. Equchi, T. Setoguchi, H. Arai, Solid State Ionics 40/41 (1), 407 (1990).
114. C. Lagergren, A. Lundblad, B. Bergman, J. Electrochem. Soc. 141, 2959 (1994).
115. J. L. Gautier in: Abstr. 45th Meet. ISE, Porto (1994), Vol. 1, p. KV–12.
116. A. Restovic, G. Poillerat, P. Chartier, J. Gautier in: Abstr. 45th Meet. ISE, Porto (1994), Vol. 2, p. V–65.
117. A. Tavares, M. Da Silva-Pereira, F. da Costa in Abstr. 45th Meet. ISE, Porto (1994), Vol. 2, p. V–79.
118. R. C. Rosim, E. R. Gonzalez, G. Tremiliosi-Filho in Abstr. 45th Meet. ISE, Porto (1994), Vol. 2, p. IV–75.
119. J. M. D. Tascon, L. G. Tejuca, React. Kinet. Catal. Lett. 15, 185 (1980).
120. T. Nitadori, M. Muramatsu, M. Misono, Chem. Mater. 1, 215 (1989).

121. A. Bandi, H. Meininger, M. Spechtin in: Abstr. 45th Meet. ISE, Porto (1994), Vol. 2, p. VII–6.
122. J. H. White, A. F. Sammells, J. Electrochem. Soc. 140, 2167 (1993).
123. M. Schwartz, R. L. Cook, V. M. Kehoe, R. C. MacDuff, J. Patel, F. Sammells, J. Electrochem. Soc., 140, 614 (1993).
124. M. I. Silva Pereira, M. J. B. Melo, F. M. A. Costa, M. R. Nunes, L. M. Peter, Electrochim. Acta 34, 663 (1989).
125. B. E. Conway, in Modern Aspects of Electrochemistry, B. E. Conway, R. E. White, J. O'M. Bockris (eds.), Plenum Press, New York (1985), Vol. 16, p. 103.
126. Z. Borkowska, U. Stimming in: Frontiers of Electrochemistry, J. Lipkowski, P. N. Ross (eds.), Verlag Chemie, Weinheim (1993), Vol. 2, p. 277.
127. U. Stimming, W. Schmickler, J. Electroanal. Chem. 150, 125 (1983).
128. U. Frese, U. Stimming, J. Electroanal. Chem. 198, 409 (1986).
129. U. Frese, U. Stimming, Ber. Bunsenges. Phys. Chem. 92, 1412 (1988).
130. U. Frese, T. Iwasita, W. Schmickler, U. Stimming, J. Phys. Chem. 89, 1059 (1985).
131. A. Matsunaga, K. Itoh, A. Fujishima, K. Honda, J. Electroanal. Chem. 205, 343 (1986).
132. J. O'M. Bockris, J. Wass, J. Electroanal. Chem. 267, 325 (1989).
133. M. Cappandonia, U. Stimming, J. Electroanal. Chem. 300, 235 (1991).
134. J. O'M. Bockris, J. Wass, J. Electroanal. Chem. 267, 329 (1989).
135. A. Pinkowski, J. Doneit, K. Jüttner, W. J. Lorenz, G. Saemann-Ishenko, T. Zeitterer, M. W. Breiter, Physica C, 162/164, 1039 (1989).
136. A. Pinkowski, J. Doneit, K. Jüttner, W. J. Lorenz, Electrochim. Acta 34, 1113 (1989).
137. A. Pinkowski, J. Doneit, K. Jüttner, W. J. Lorenz, G. Saemann-Ishenko, M. W. Breiter, Europhys. Lett. 9, 269 (1989).
138. A. Pinkowski, K. Jüttner, W. J. Lorenz, G. Saemann-Ishenko, M. W. Breiter, J. Electroanal. Chem. 286, 253 (1990).
139. A. Pinkowski, J. Doneit, K. Jüttner, W. J. Lorenz, G. Saemann–Ishenko, T. Zetterer, M. W. Breiter, J. Electrochem. Soc. 137, 226C (1990).
140. A. Pinkowski, K. Jüttner, W. J. Lorenz, J. Electroanal. Chem. 287, 203 (1990).
141. M. W. Breiter, W. J. Lorenz, G. Saemann-Ishenko, Surface Sci. 230, 213 (1990).
142. A. Pinkowki, W. J. Lorenz, G. Saemann-Ishenko, M. W. Breiter, Solid State Ionics 40/41, 822 (1990).
143. W. J. Lorenz, G. Saemann-Ishenko, M. W. Breiter, Ber. Bunsenges. Phys. Chem. 95, 1055 (1991).
144. I. Engelhardt, R. Speck, J. Inche, H. Khalil, M. Ebert, W. J. Lorenz, G. Saemann-Ishenko, M. W. Breiter, Electrochim. Acta 37, 2129 (1992).
145. R. Speck, D. Kurzeja, G. Staikov, W. J. Lorenz, M. W. Breiter, G. Saemann-Ishenko in: Abstr. 45th Meet. ISE, Porto (1994), Vol. 2, p. IV–83.
146. H. S. Zaghloul, M. H. Zayan, T. M. Nazmy, M. A. Abdel Raouf, Chem. Phys. Lett. 221, 23 (1994).
147. W. J. Lorenz, G. Saemann-Ishenko, M. W. Breiter Russian J. Electrochem. 31, 873 (1995).
148. A. Pinkowski, J. Doneit, K. Jüttner, W. J. Lorenz, G. Saemann-Ishenko, T. Zetterer, M. W. Breiter, DECHEMA Monogr. 121, 247 (1989).
149. S. Curtin, S. Peck, L. Tender, R. Murray, Anal. Chem. 65, 386 (1993).
150. J. T. McDevitt, S. Ching, M. Sullivan, R. W. Murray, J. Am. Chem. Soc. 111, 4528 (1989).
151. S. Ching, J. T. McDevitt, S. R. Peck, R. W. Murray, J. Electrochem. Soc. 138, 2308 (1991).
152. A. J. Gordon, R. A. Ford, The Chemist's Companion, Wiley-Interscience, New York (1972).

153. S. R. Peck, S. Curtin, J. T. McDevitt, R. W. Murray, J. P. Collman, W. A. Little, T. Zetterer, H. M. Duan, C. Dong, A. M. Hermann, J. Am. Chem. Soc. 114, 6771 (1992).
154. A. M. Kuznetsov, J. Electroanal. Chem. 278, 1 (1990).
155. L. Zusmann, A. B. Gelman, B. Shapiro, Chem. Phys. Lett. 167, 457 (1990).
156. A. M. Kuznetsov, Elektrokhimiya 27, 430 (1991).
157. A. M. Kuznetsov in Condensed Matter Physics Aspects of Electrochemistry, M. P. Tosi, A. A. Kornyshev (eds.), World Scientific, Singapore (1991), p. 474.
158. A. M. Kuznetsov, Electrochim. Acta 37, 2123 (1992).
159. L. Zusmann, Chem. Phys. Lett. 200, 379 (1992).
160. Y. Takasu, K. Hanyu, K. Takeda, Y. Matsuda, K. Yahikozawa in: Abstr. 40th Meet. ISE, Kyoto (1989), Vol. 1, p. 98.
161. R. R. Dogonadze, A. M. Kuznetsov in: Comprehensive Treatise of Electrochemistry, B. E. Conway, J. O'M. Bockris, E. M. Yeager, S. U. M. Khan, R. E. White (eds.), Plenum Press, New York (1983), Vol. 7, p.1.
162. A. M. Kuznetsov in Modern Aspects of Electrochemistry, B. E. Conway, R. E. White, J. O'M. Bockris (eds.), Plenum Press, New York (1989), Vol. 20, p. 95.
163. A. S. Alexandrov, N. F. Mott, Supercond. Sci. Technol. 6, 215 (1993).
164. C.-S. Hsi, G. Haertling, E. Furman, Appl. Phys. Lett. 64, 1050 (1994).
165. M. Leskela, H. Molsa, L. Niinisto, Supercond. Sci. Technol. 6, 627 (1993).
166. Yu. G. Metlin, Yu. D. Tretyakov, J. Mater. Chem. 4, 1659 (1994).
167. W. Assmus, W. Schmidbauer, Supercond. Sci. Technol. 6, 555 (1993).
168. D. Gruen, W. F. Calaway, V. A. Maroni, B. S. Tani, A. R. Krauss, J. Electrochem. Soc. 134, 1588 (1987).
169. J. Luo, D. Michel, J. Chevalier, Rev. Phys. Appl. 25, 3 (1990).
170. B. Tsaur, M. S. Dilorio, A. J. Strauss, Appl. Phys. Lett. 51, 858 (1987).
171. F. J. Bachner, P. H. Nguyen, Metal Finishing 86, 23 (1988).
172. V. V. Bondar', V. V. Grinina, V. N. Pavlov in: Itogi Nauki i Tekhniki, Viniti, Moscow (1980), Vol. 16, p. 3.
173. R. D. Shull, L. H. Bennett, Nanostruct. Mater. 1, 83 (1992).
174. S. Ondono-Castillo, A. Fuertes, P. Gomez-Romero, N. Casan-Pastor in: Abstr. 4th Int. Conf. HTSC, Grenoble (1994), p. 119.
175. A. Weston, S. Lalvani, F. Willis, N. Ali, J. Alloys Compds. 181, 233 (1992).
176. A. Weston, S. Lalvani, N. Ali, J. Mater. Sci. Mater. Electron. 2, 129 (1991).
177. H. Minoura, K. Naruto, H. Takano, E. Haseo, Ya. Ueno, T. Endo, Chem. Lett. 3, 379 (1991).
178. S. Pawar, M. Tonape, V. Shinde, Indian J. Pure Appl. Phys. 31, 350 (1993).
179. R. Bhattacharya, R. Noufi, U. Roybal, R. Ahrenkiel, J. Electrochem. Soc. 138, 1643 (1991).
180. A. Weston, S. Lalvani, N. Ali, J. Electrochem. Soc. 137, 226C (1990).
181. S. Pawar, M. Pendse, Mater. Res. Bull. 26, 641 (1991).
182. P. Gendre, L. Schmirgeld, P. Regnier, S. Senoussi, A. Marquet in: Abstr. 4th Int. Conf. HTSC, Grenoble (1994) p. 22.
183. S. Pawar, H. Mujawar, Mater. Chem. Phys. 28, 259 (1991).
184 S. Pawar, H. Mujawar, B. Todkar, M. Rendse, P. Patil, Bull. Electrochem. 6, 315 (1990).
185. S. Pawar, H. Mujawar, Mater. Res. Bull. 25, 1443 (1990).
186. S. Pawar, H. Mujawar, Mater. Lett. 10, 355 (1991).
187. C. Kim, H. You, S. Han, M. Jang, P. Hur, Physica C 185–189, 2303 (1991).
188. M. Maxfield, H. Eckhardt, Z. Iqbal, F. Reidinger, R. H. Baughman, Appl. Phys. Lett. 54, 1932 (1989).
189. L. Su, C. Grovenor, M. Goringe, Supercond. Sci. Technol. 7, 133 (1994).

190. A. M. Molchadskii, R.-D. Yankauskene, A. Sharkis, S. Yuktonis, B. Vengalis, Sverkhprovodimost': Fiz., Khim. Tekhn. 6, 1896 (1992).
191. A. M. Molchadskii, R.-D. Yankauskene, A. Sharkis, R. Yushkenas, B. Vengalis, Sverkhprovodimost': Fiz., Khim. Tekhn. 6, 1903 (1992).
192. F. Pern, C. Schwerdtfeger, A. Nelson, R. Noufi, J. Electrochem. Soc. 136, 234C (1989).
193. M. Maxfield, H. Eckhardt, Z. Iqbal, F. Reidinger, R. Baughman, J. Electrochem. Soc. 136, 234C (1989).
194. R. Bhattacharya, R. Blangher, Physica C. 229, 244 (1994).
195. R. N. Bhattacharya, A. Duda, D. S. Ginley, J. A. De Luca, Z. F. Ren, C. A. Wang, J. H. Wang, Physica C. 229, 145 (1994).
196. R. N. Bhattacharya, P. Parilla, R. Blaugher, Physica C. 211, 475 (1993).
197. M. Maxfield, M. Behi, H. Reidinger, H. Eckhardt, R. H. Baughman, J. Electrochem. Soc. 137, 225C (1990).
198. R. N. Bhattacharya, P. A. Parilla, R. Noufi, P. Arendt, N. Elliott, J. Electrochem. Soc. 139, 67 (1992).
199. R. Bhattacharya, R. Blangher, Physica C. 225, 269 (1994).
200. S. H. Pawar, M. J. Ubale, S. B. Kulkarni, Mater. Lett. 20, 279 (1994).
201. N. V. Moseev, Sverkhprovodimost': Fiz., Khim. Tekhn. 7, 22 (1994).
202. S. Hatta, H. Higashino, K. Hirochi, H. Adachi, K. Wasa, Appl. Phys. Lett. 53, 148 (1988).
203. B. Bhattacharya, S. Rangarajan, J. Electroanal. Chem. 366, 271 (1994).
204. F. J. Mizuguchi, M. Suzuki, H. Yamato, M. Matsumura. J. Electrochem. Soc. 138, 2942 (1991).
205. R. N. Bhattacharya, D. Cahen, G. Hodes, Sol. Energy Mater. 10, 41 (1984).
206. G. Hodes, T. Engelhard, C. R. Harrington, L. L. Kazmerski, D. Cahen, Progr. Cryst. Growth Charact. 10, 345 (1985).
207. S. Jundale, C. Lokhande, Indian J. Pure Appl. Phys. 30, 215 (1992).
208. A. Gard, K. Balakrishnan, A. C. Rastogi, J. Electrochem. Soc. 141, 1566 (1994).
209. K. Mishra, K. Rajeshwar, A. Weiss, J. Electrochem. Soc. 136, 1915 (1989).
210. L. Thouin, S. Massaccesi, S. Sanchez, J. Vedel, J. Electroanal. Chem. 374, 81 (1994).
211. E. Mori, K. Rajeshwar, J. Electroanal. Chem. 258, 415 (1989).
212. M. Takahashi, Y. Oda, T. Ogino, S. Furuta, J. Electrochem. Soc. 140, 2550 (1993).
213. M. Hepel, E. Seymour, D. Yogev, J. Fendler, Chem. Mater. 4, 209 (1992).
214. B. W. Gregory, J. L. Stickney, J. Electroanal. Chem. 300, 543 (1991).
215. A. Kressin, V. Doan, J. Klein, M. Sailor, Chem. Mater. 3, 1015 (1991).
216. B. Gregory, D. Suggs, J. Stickney, J. Electrochem. Soc. 138, 1279 (1991).
217. H. J. Pauling, G. Staikov, K. Juttner, J. Electroanal. Chem. 376, 179 (1994).
218. V. D. Kalugin, E. B. Pereverzeva, V. V. Kozinets, I. A. Kovalev, D. B. Pavin, Sverkhprovodimost': Fiz., Khim. Tekhn. 5, 1543 (1992).
219. N. Tacconi, O. Medvedco, K. Rajeshwar, J. Electroanal. Chem. 379, 545 (1994).
220. S. A. Kachusov, S. Ya. Vasina, A. M. Gas'kov, O. A. Petrii, V. P. Zlomanov, Izv. AN SSSR, Ser. Neorganich. Mater. 1, 60 (1990).
221. S. A. Kachusov, S. Ya Vasina, A. M. Gas'kov, O. A. Petrii, V. P. Zlomanov in: Sintez i Issledovanie Hal'kogenidnykh Plenok, Sverdlovsk, Russia (1988), p. 14.
222. V. N. Alfeev, B. A. Aminov, N. B. Brandt, S. Ya. Vasina, B. B. Damaskin, O. A. Petrii, Ya. G. Ponomarev, E. G. Frank, Fiz. Nizkikh Temper. 15, 1099 (1989).
223. D. Shoesmith, S. Sunder, M. Bailey, G. Wallace, F. Stanchell, J. Electroanal. Chem. 143, 153 (1983).
224. H. Strehblow, H. Speckmann, Werkst. Korr. 35, 512 (1984).
225. H. Speckmann, M. Lohrengel, J. Schultze, H. Strehblow, Ber. Bunsenges. Phys. Chem. 89, 392 (1985).
226. U. Collisi, H. Strehblow, J. Electroanal. Chem. 210, 213 (1986).

227. D. J. Zurawski, P. J. Kulesza, A. Wieckowski, J. Electrochem. Soc. 135, 1607 (1988).
228. I. I. Astakhov, I. Barbasheva, G. Teplitskaya, Russ. J. Electrochem. 30, 821 (1994).
229. S. Yu. Vassiliev, G. A. Tsirlina, O. A. Petrii, Russ. J. Electrochem. 30, 738 (1994).
230. P. Slezak, A. Wieckowski, J. Electrochem. Soc. 138, 1038 (1991).
231. A. M. Kraitsberg, I. I. Astakhov, G. L. Teptitskaya, private communication.
232. T. Nakamura, M. Natsuhara, H. Kawaji, M. Itoh, Jap. J. Appl. Phys. 30, L1 465 (1991).
233. E. M. Patrito, V. A. Macagno, J. Electroanal. Chem. 371, 59 (1994).
234. S. E. Yoo, M. Hayashi, N. Ishizawa, M. Yoshimura, J. Am. Ceram. Soc. 73, 2561 (1990).
235. N. Ishizawa, H. Banno, M. Hayashi, S. E. Yoo, M. Yoshimura, Jap. J. Appl. Phys. 29, 2467 (1990).
236. P. Bendale, S. Venigalla, J. R. Ambrose, E. D. Verink, H. Adair, J. Am. Ceram. Soc. 76, 2619 (1993).
237. B. Dabrowski, J. Electron. Mater. 22, 1183 (1993).
238. H. Ihara, K. Tokiwa, H. Ozawa, M. Hirabayashi, A. Negishi, H. Matuhata, Y. S. Song, Jap. J. Appl. Phys. 33, L503 (1994).
239. J.-C. Grenier, A. Wattiaux, J.-C. Park, M. Pouchard, Acta Crystallogr. Ser. C. 46, 316 (1990).
240. A. Watiaux, J.-C. Park, J.-C. Grenier, M. Pouchard, C. R. Acad. Sci., Ser. 2, 310, 1047 (1990).
241. M. A. Alario-Franco, M. Henche, M. Vallet, J. M. G. Calbet, J.-C. Grenier, A. Wattiaux, P. Hagenmuller, J. Solid State Chem. 46, 23 (1983).
242. M. A. Alario-Franco, J. M. G. Calbet, M. Vallet-Regi, J.-C. Grenier, J. Solid State Chem. 49, 219 (1983).
243. J.-C. Grenier, N. Ea, M. Pouchard, M. M. Abou-Sekkina, Mater. Res. Bull. 19, 1301 (1984).
244. J.-C. Grenier, A. Wattiaux, J.-P. Doumerc, P. Dordor, L. Fournes, J.-P. Chaminade, M. Pouchard, J. Solid State Chem. 96, 20 (1992).
245. A. Wattiaux, L. Fournes, A. Demourgues, Solid state Commun. 77, 489 (1991).
246. P. Bezdicka, A. Wattiauk, J.-C. Grenier, M. Pouchard, P. Hagenmuller, Z. Anorg. Allg. Chem. 619, 7 (1993).
247. W. D. Briggs, D. F. Davies, Electrochim. Acta. 24, 439 (1979).
248. G. A. Tsirlina, F. M. Spiridonov, O. A. Petrii, Russ. J. Electrochem. 31, 55 (1995).
249. G. A. Tsirlina, Russ. J. Electrochem. 31, 219 (1995).
250. E. Sigmund, V. Hizhnyakov in: Springer Sec. Solid-State Sci. Springer-Verlag, Berlin (1993), Vol. 114, p. 402.
251. P. G. Radaelli, J. D. Jorgensen, R. Kleb, B. Hunter, F. Chou, D. Johnston, Phys. Rev. B 49, 6239 (1994).
252. J.-C. Grenier, A Wattiaux, M. Pouchard in: Proc. 3rd Workshop on Phase Separation in Cuprate Superconductors, K. A. Muller, G. Benede (eds.), World Scientific, Singafore (1993).
253. A. A. Zakharov, A. A. Nikonov, Pis'ma ZhETF 60, 340 (1994).
254. Yu. M. Boikov, E. K. Shalkova, T. A. Ushakova, Sverkhprovodimost': Fiz. Khim. Tekhn. 6, 449 (1993).
255. J.-C. Grenier, A. Wattiaux, N. Lagueyte, J.-C. Park, E. Marquestaut, J. Etourneau, M. Pouchard, Physica C 173, 139 (1991).
256. I. Nikolov, R. Darkaoui, E. Zhecheva, R. Stoyanova, N. Doimitrov, T. Vitanov, J. Electroanal. Chem. 362, 119 (1993).
257. A. T. Matveev, V. P. Novikov, Sverkhprovodimost': Fiz. Khim. Tekhn. 6, 387 (1993).
258. J. MacManus. D. Fray, J. Evetts, Physica C 169, 193 (1990).
259. V. I. Tsidilkovskii, A. K. Demin, M. V. Patrakeev, I. A. Leonidov, V. L. Kozhevnikov, Physica C 210, 213 (1993).

260. J. Grenier, C. Monroux, A. Wattiaux, J. Etourneau, M. Pouchard in: Superconducting Materials J. Etourneau, B. Torrance, H. Yamauchi (eds.), IITT-International, Gournay-sur-Marne (1993), p. 107.
261. J. Grenier, A. Wattiaux, M. Pouchard, J. Locquet in: Abstr. 4th Int. Conf. HTSC, Grenoble (1994), p. 15.
262. J.-C. Grenier, A. Wattiaux, M. Pouchard in: Abstr. 45th ISE, Porto (1994), Vol. 1, p. KV-10.
263. E. Takayama-Muromachi, T. Sasaki, Y. Matsui, Physica C 207, 97 (1993).
264. Izumi, Y.-I. Kim, E. Takayama-Muromachi, T. Kamiyama in: Abstr. 4th Int. Conf. HTSC, Grenoble (1994), p. 143.
265. P. Rudolf, R. Schollhorn, J. Chem. Soc., Chem. Commun. 16, 1168 (1992).
266. F. C. Chou, J. H. Cho, D. C. Johnston, Physica C 197, 303 (1992).
267. P. Rudolf, W. Paulus, R. Scholhorn, Adv. Mater. 3, 438 (1991).
268. J. C. Bennett, M. Olfert, G. A. Scholz, F. W. Boswell, Phys. Rev. B 44, 2727 (1992).
269. P. G. Radaelli, J. D. Jorgensen, A. J. Schultz, B. A. Hunter, J. L. Wagner, F. C. Chou, D. C. Johnston, Phys. Rev. B 48, 499 (1993).
270. W. Paulus, G. Heger, P. Rudolf, R. Schollhorn in: Abstr. 4th Int. Conf. HTSC, Grenoble (1994), p. 322.
271. J. C. Park, P. V. Huong, M. Rey-Lafon, J.-C. Grenier, A. Wattiaux, M. Pouchard, Physica C 177, 487 (1991).
272. F. Arrouy, A. Wattiaux, C. Cros, G. Demazeau, J.-C. Grenier, M. Pouchard, J. Etourneau, Physica C 175, 342 (1991).
273. N. Lagueyte, A. Wattiaux, J. C. Park, J. C. Grenier, L. Fournes, M. Pouchard, J. Phys. III Fr. 1, 1755 (1991).
274. I. Yazdi, S. Bhavaraju, J. F. DiCarlo, D. P. Scarfe, A. J. Jacobson, Chem. Mater. 6, 2078 (1994).
275. R. Suryanarayanan, M. S. R. Rao, O. Gorochov, L. Ouhammou, W. Paulus, G. Heger, Supercond. Sci. Technol. 3, 82 (1992).
276. Z. Zhao, 4th Int. Conf. HTSC, Grenoble (1994), pp. 14–15.
277. M. Itoh, Y.-J. Shan, S. Sakamoto, Y. Inaguma, T. Nakamura, Physica C, 223, 75 (1994).
278. J.-C. Park, S.-G. Kang, D.-H. Kim, C.-H. Park, G. Demazeau, J.-H. Choy in Superconducting Materials, J. Etourneau, B. Torrance, H. Yamauchi (eds.), IITT-International, Gournay-sur-Marne (1993), p. 115.
279. R. Suryanarayanan, O. Gorochov, M. S. R. Rao, L. Ouhammou, W. Paulus, G. Heger, Physica C 185–189, 573 (1991).
280. J.-C. Park, S.-G. Kang, J.-H. Choy, A. Wattiaux, J.-C. Grenier, Physica C 185–189, 567 (1991).
281. S. Ondono-Castillo, C. R. Michel, A. Seffar, J. Fontcuberta, N. Casan-Pastor in: Abstr. 4th Int. Conf. HTSC, Grenoble (1994), p. 227.
282. S. S. Grazhulene, Yu. A. Karpov, Zh. Vsesoyus. Khim. Obsh. Mendeleeva 34, 537 (1989).
283. S. Bhavaraju, J. F. DiCarlo. I. Yazdi, A. J. Jacobson, H. H. Feng, Z. G. Li, P. H. Hor, Mater. Res. Bull. 29, 735 (1994).
284. F. A. Lewis, The Palladium Hydrogen System, Academic Press, New York (1967).
285. F. Chou, D. Johuston, S. Cheong, P. Canfield, Physica C 216, 66 (1993).
286. N. A. Fleisher, J. Manassen, J. Electrochem. Soc. 135, 3174 (1988).
287. K. Borowiec, J. Przybuski, K. Kolbruka in: Abstr. 41st Meet, ISE, Praga (1990), Vol. 2, p. Fr-7.
288. M. Schartz, M. Rappoport, G. Hodes, D. Kahen, Physica C 153/155, 1457 (1988).
289. F. Celani, M. Boutet, D. DiGioacchino, A. Spallone, P. Tripodi, S. Pace, M. Polichetti, P. Marini, Rapp. Lab. Naz. Frascati 94/021, 1 (1994).

290. M. Schwartz, D. Cahen, M. Rappoport, G. Hodes, Solid State Ionics 32/33 (Pt. 2), 1137 (1989).
291. V. M. Koshkin, I. V. Lyubomirskii, E. E. Ovechkin, V. D. Zaporozhskii, A. P. Mul'ner, Fiz. Niz. Temperatur 17, 118 (1991).
292. H. Drulis, A. Zygmunt, J. Klamut, N. Suleimanov, J. Alloys Compds. 195, 471 (1993).
293. U. Barsch, F. Beck, Electrochim. Acta 35, 759 (1990).
294. V. D. Kalugin, V. N. Yas'ko, N. S. Opaleva, L. Yu. Voronko, Sverkhprovodtmost': Fiz., Khim. Tekhn. 6, 144 (1993).
295. N. Hass, U. Dai, Y. Scolnik, M. Rappaport, D. Cahen, Physica C 209, 305 (1993).
296. Y. Scolnik, E. Sabatani, D. Cahen, Physica C 174, 273 (1991).
297. A. L. Pergament, G. B. Stefanovich, F. A. Chudnovskii, Sverkhprovodimost': Fiz., Khim. Tekhn. 5, 2368 (1992).
298. P. G. Brucke, Philos. Mag. 64, 1101 (1991).
299. G. E. Murch, J. C. Dyre, CRC Crit. Rev. Solid State Mater. 15, 345 (1989).
300. T. Jacobsen, B. Zachau-Christiansen, K. West, S. Atlung, Electrochim. Acta 34, 1473 (1989).
301. R. Jones, W. R. McKinnon, Solid State Ionics 45, 173 (1991).
302. T. A. Whitney, W. L. Bowden, A. N. Dey, Electrochim. Acta 36, 381 (1991).
303. Y. Morikawa, K. Satoh, S. Ozawa, K. Nakamura, H. Yamamoto, M. Tanaka, Physica C 185–189, 431 (1991).
304. J. Vondrak, I. Jakubec, J. Bludska, Electrochim. Acta 35, 995 (1990).
305. L. Chen, A. Zomeren, J. Schoonman, Solid State Ionics 50, 55 (1992).
306. A. Stoklosa, J. Molenda, T. Bak, Physica C 207, 147 (1993).
307. Y. Xia, F. Li Z. Zeng, B. Wang, Chin. Chem. Lett. 3, 577 (1992).
308. J. B. Schlenoff, W. J. Rink, L. Seger, Physica C 180, 387 (1991).
309. N. A. Fleischer, J. Manassen, P. Coppens, P. Lee, Y. Gao in: AIP Conf. Proc. (1992), Vol. 251, p. 366.
310. N. A. Fleischer, J. Manassen, P. Coppens, P. Lee, Y. Gao, S. G. Greenbaum, Physica C 190, 367 (1991).
311. A. M. Andersson, C. G. Granqvist, Z. G. Ivanov, J. Alloys Compds. 195, 343 (1993).
312. Q. Zhang, T. Atake, Y. Saito, Solid State Ionics 50, 209 (1992).
313. K. Govinda Rajan, P. Parmeswaran, J. Janaki, T. S. Radhakrishnan, J. Phys. D 23, 694 (1990).
314. V. I. Nefedov, M. D. Val'kovskii, A. N. Sokolov, Sverkhprovodimost': Fiz., Khim. Tekhn. 5, 1081 (1992).
315. D. J. Vischjager, A. A. van Zomeren, J. Schoonman, I. Kontoulis, B. C. H. Steele, Solid State Ionics 40/41 (Pt. 2), 810 (1990).
316. D. J. Vischiager, J. Schram, A. Mackor, J. Schoonman, Silicates Industriels, 54, 153 (1989).
317. R. V. Kumar, D. J. Fray, J. E. Evetts, H. W. Williams, A. Misson, J. Electrochem. Soc. 140, 2895 (1993).
318. H. Huang, C. R. M. Grovenor, Physica C 210, 87 (1993).
319. J. MacManus, D. Fray, J. Evetts, Supercond. Sci. Technol. 1, 291 (1989).
320. J. L. MacManus, D. J. Fray, J. E. Evetts, Physica C 184, 172 (1991).
321. A. T. Matveev, V. P. Novikov, V. F. Gremenok, I. A. Viktorov, Sverkhprovodimost': Fiz., Khim. Tekhn. 5, 1903 (1992).
322. M. Fleischmann, H. Thirsk, Trans. Faraday Soc. 51, 71 (1955).
323. N. A. Hampson in: The Electrochemistry of Lead, A. T. Khun (ed.), Academic Press, London (1979), p. 29.
324. M. Fleischmann, H. Thirsk, I. Tordesillas, Trans. Faraday Soc. 58, 1865 (1962).
325. H. Chang, D. Johnson, J. Electrochem. Soc. 136, 23 (1989).
326. S. Campbell, L. Peter, Electrochim. Acta 34, 943 (1989).

327. I. Yeo, Y. Lee, D. Johnson, Electrochim. Acta 37, 1811 (1992).
328. I. Yeo, D. Johnson, J. Electrochem. Soc. 134, 1973 (1987).
329. C. Ho, B. Hwang, Electrochim. Acta. 38, 2749 (1993).
330. H. Laitinen, N. Vatkins. J. Electrochem. Soc. 123, 804 (1976).
331. A. Babak, R. Amadelli, A. Battisti, V. Fateev, Electrochim. Acta 39, 1597 (1994).
332. G. A. Tsirlina, O. A. Petrii, J. Electroanal. Chem. 402, 33 (1996).
333. J. Switzer, J. Electrochem. Soc. 133 (4), 722 (1986).
334. J. Switzer, Am. Ceram. Soc. Bull. 66, 1521 (1987).
335. R. Phillips, M. Shane, J. Switzer, J. Mater. Res. 4, 923 (1989).
336. G. A. Tsirlina, S. N. Pron'kin, F. M. Spiridonov, S. Yu. Vassiliev, O. A. Petrii, Russ. J. Electrochem. 30, 236 (1994).
337. I. Yeo, S. Kim, R. Jacobson, D. Johnson, J. Electrochem. Soc. 136, 1395 (1989).
338. J. Feng, D. C. Johnson, S. N. Lowery, J. J. Carey, J. Electrochem. Soc. 141, 2708 (1994).
339. M. Sakai, T. Sekine, Y. Yamazaki, J. Electrochem. Soc. 130, 1631 (1983).
340. T. Werner, W. Dietrich, Z. Naturforsch. Teil B 39, 594 (1984).
341. R. Phillips, J. Electrochem. Soc. 137, 259C (1990).
342. B. Voos, W. Plieth, R. Borner, R. Schollhorn, Electrochim. Acta 38, 2551 (1993).
343. J. Switzer, Nanostruct. Mater. 1, 43 (1992).
344. J. Switzer, M. Shane, R. Phillips, Science 247, 444 (1990).
345. J. Switzer in: Chemistry of Electronic Ceramic Materials, P. K. Davies, R. S. Roth (eds.), Lauasler, Pennsylvania and Basel, Suitzerland (1990), pp. 185–192.
346. J. Switzer, R. Phillips, R. Raffaelle in: ACS Symp. Ser. 244, 499 (1990).
347. J. Switzer, T. Golden, Adv. Mater. 5, 474 (1993).
348. G. A. Tsirlina, S. N. Putilin, O. A. Petrii, E. V. Antipov, Ya. G. Ponomarev, K. T. Rakhimov, Sverkhprovodimost': Fiz. Khim. Tekhn. 4, 1580 (1991).
349. T. Sasaki, Y. Matsumoto, J. Hombo, M. Nagata, J. Electroanal. Chem. 371, 241 (1994).
350. D. A. Berg, V. A. VanderNoot, R. G. Barradas, E. P. C. Lai, J. Electroanal. Chem. 369, 33 (1994).
351. D. A. Berg, D. Nedezdin, R. D. Barradas, J. Electroanal. Chem. 355, 165 (1993).
352. G. A. Tsirlina, S. Yu. Vassiliev, N. S. Korzakova, O. A. Petrii, Russ. J. Electrochem. 30, 162 (1994).
353. G. A. Tsirlina, S. Yu. Vassiliev, A. I. Danilov, O. A. Petrii, Russ. J. Electrochem. 30, 114 (1994).
354. O. A. Petrii, G. A. Tsirlina, T. V. Rakova, S. Yu. Vassiliev, J. Appl. Electrochem. 23, 583 (1993).
355. G. A. Tsirlina, A. A. Moskovskii, S. N. Pron'kin, O. A. Petrii, Russ. J. Electrochem., submitted.
356. O. A. Petrii, G. A. Tsirlina, S. Yu, Vassiliev, Mater. Sci. Forum 285–289, 687 (1995).
357. R. J. Phillips, T. D. Golden, M. G. Shumsky, J. A. Switzer, J. Electrochem. Soc. 141, 2391 (1994).
358. W. Polewska, J. X. Wang, B. M. Ocko, R. R. Adzic, J. Electroanal. Chem. 376, 41 (1994).
359. J. Wang, R. Adzic, B. Ocko, J. Phys. Chem. 98, 7182 (1994).
360. G. I. Rozovskii, A. Yu. Prokopchik, Lietovus TSR Mokslu Akademija, Ser. B 3 (26), 181 (1961).
361. T. Jondo, C. Opagiste, J. Jorda, M. Cohen-Adad, F. Sibieude, M. Couach, A. Khoder, Physica C 195, 53 (1992).
362. B. Raveau, C. Martin, M. Hervieu, D. Bourgault, C. Michel, J. Provost, Solid State Ionics 39, 49 (1990).
363. G. A. Tsirlina, F. M. Spiridonov, O. A. Petrii, Russ. J. Electrochem. 31, 222 (1995).
364. A. A. Tighjezza, J. Rehspringer, J. Alloys Compds. 195, 69 (1993).

365. B. M. Tissue, K. M. Cirillo, J. C. Wright, M. Daeumilling, D. Larbalestier, Solid State Commun. 65, 51 (1988).
366. M. Cassart, E. Grivei, J.-P. Issi, J. Hejtmanek, C. Robin-Brisson, E. Ben Salem, B. Chevalier, A.Tressaud, J. Etourneau, J. Alloys Compds. 195, 335 (1993).
367. C. Perrin, O. Pena, M. Mokhtari, C. Thivet, M. Guilloux-Viry, A. Perrin, M. Sergent, J. Alloys Compds. 195, 339 (1993).
368. M. Al-Mamouri, P. Edwards, C. Greaves, M. Slaski, Nature (London) 369, 382 (1994).
369. M. L. Norton, Mater. Res. Bull. 24, 1391 (1989).
370. J. M. Rosamilia, S. H. Glarum, R. J. Cava, B. Batlogg, B. Miller, Physica C, 182, 285 (1991).
371. Y. Tang, W.-L. Chen, T.-R. Chien, M. L. Norton, M.-K. Wu, Jap. J. Appl. Phys. 32, L312 (1993).
372. Y. Hidaka, M. Suzuki, Nature (London) 338, 635 (1989).
373. S. N. Barilo, J. Alloys Compds. 195, 1(1993).
374. W. Schmidbauer, B. M. Wanklyn, J. W. Hodby in: Abstr. 4th Int. Conf. HTSC, Grenoble (1994), p. 236.
375. J. Marcus, C. Escribe-Filippini, S. Agarwal, C. Chaillout, J. Durr, T. Fournier, J. Tholence, Solid State Commun. 78, 967 (1991).
376. Y. Nagata, N. Suzuki, T. Uchida, W. D. Mosley, P. Klavins, R. N. Shelton, Physica C 195, 195 (1992).
377. S. N. Barilo, D. I. Zhigunov, L. A. Kurochkin, A. V. Pushkarev, S. N. Shiryaev, Sverkhprovodimost': Fiz. Khim. Tekhn. 5, 1084 (1992).
378. J. Marcus, C. Escribe-Filippini, S. K. Agarwal, C. Chaillout, J. Durr, T. Fournier. Physica C 185–189, 707 (1991).
379. S. V. Shiryaev, D. I. Zhigunov, S. N. Barilo, A. V. Pushkarev, A. A. Zakharov, L. A. Igolkina in Superconducting Materials, J. Etourneau, B. Torrance, H. Yamauchi (eds.), IITT-International, Gournay-sur-Marne (1993), p. 137.
380. M. L. Norton, H. -Y. Tang, Chem. Mater. 3, 431 (1991).
381. G. L. Roberts, S. M. Kauzlarich, R. S . Glass, J. C. Estill, Chem. Mater. 5, 1645 (1993).
382. L. A. Klinkova, M. V. Filatova, O. A. Volegova, Sverkhprovodimost': Fiz. Khim. Tekhn. 6, 1917 (1993).
383. T. N. Nguen, D. M. Giaquinta, W. M. Davis, H. -C. Loye, Chem. Mater. 5, 1273 (1993).
384. H. Y. Tang, C. S. Lee, M. K. Wu in: Abstr. 4th Int. Conf. HTSC, Grenoble (1994), p. 226.
385. H. Y. Tang, C. S. Lee, M. K. Wu, Physica C 231, 325 (1994).
386. F. Garzon, I. Raistrick, J. Electrochem. Soc. 136, 2753 (1989).
387. E. Moshopoulou, P. Bordet, J. Capponi in: Abstr. 4th Int. Conf. HTSC, Grenoble (1994), p. 234.
388. E. Moshopoulou P. Bordet, J. Capponi, C. Chaillout, B. Souletie, A. Sulpice, J. Alloys Compds. 195, 81 (1993).
389. E. Moshopoulou, P. Bordet, A. Sulpice, J. Capponi in: Abstr. 4th Int. Conf. HTSC, Grenoble (1994), p. 234.
390. J. Compa, M. Velez, C. Cascales, E. Gutierrez-Puebla, M. Monge, I. Rasines, C. Ruiz Valero in: Abstr. 4th Int. Conf. HTSC, Grenoble (1994), p. 234.
391. M. Ya. Fioshin, Uspekhi v Oblasti Elektrosinteza Neorganicheskikh Soedinenii, Khimiya, Moscow (1974).
392. P. Armbruster in: NATO ASI Series Ser. B (1986), Vol. 143, p. 1.
393. J. Roland, F. Anson, J. Electroanal. Chem. 336, 245 (1992).
394. J. Yao, B. Loo, K. Hashimoto, A. Fujushima, J Electroanal. Chem. 290, 263 (1990).
395. B. Keita, L. Nadjo, J. Electroanal. Chem. 243, 87 (1988).
396. B. Keita, L. Nadjo, R. Parsons, J. Electroanal. Chem. 258, 207 (1989).
397. A. Weser, E. Pungor, Acta Chim. Acad. Sci. Hung. 59, 319 (1969).
398. J. E. Toth, F. C. Anson, J. Electroanal. Chem. 256, 361 (1988).

399. Y. Matsumoto, H. Adachi, J. Hombo, J. Am. Ceram. Soc. 76, 769 (1993).
400. H. Konno, M. Tokita, R. Furuichi, J. Electrochem. Soc. 137, 361 (1990).
401. S. B. Abolmaali, J. B. Talbot, J. Electrochem. Soc. 140, 443 (1993).
402. N. Koura, Denki Kagaku, 56, 208 (1988).
403. S. K. Remillard, P. N. Arendt, N. E. Elliott, Physica C 177, 345 (1991).
404. M. Yang, M. J. Goringe, C. R. M. Grovenor, R. Jenkins, H. Jones, Supercond. Sci. Technol. 7, 378 (1994).
405. P. Sazkas, S. Mathur, P. S. Nicholson, C. V. Stager, J. Appl. Phys. 69, 1775 (1991).
406. A. D. Nikulin, A. K. Shikov, N. B. Kalinin, T. P. Gorshkov, Sverkhprovodimost' Fiz. Khim. Tekhn. 5, 748(1992).
407. N. Koura, H. Shoji, Physica C 190, 163(1991).
408. J. C. Yj, H. B. Liu, C. Y. Wu, P. G. Wahlbeck, D. L. Myers, S. He, F. J. Schmidt, IEEE Trans. Magnet. 27, 1438 (1991).
409. J. C. Ho, C. Y. Wu, X. W. Cao, F. J. Schmidt, Supercond. Sci. Technol. 4, 507 (1991).
410. H. S. Maiti, S. Datta, R. N. Basu, J. Am. Ceram. Soc. 72, 1733 (1989).
411. C. T. Chu, B. Dunn, Appl. Phys. Lett. 55, 492 (1989).
412. L. D. Woolf, W. A. Raggio, F. E. Elsner, M. Fishez, Appl. Phys. Lett. 58, 534(1991).
413. G. Hofer, W. Kleinlein, in: Proc. ISMAC'92, Paris (1992), p. 87.
414. M. Hein, F. Hill, G. Muller, H. Piel, H. P. Schneider, M. Strupp, IEEE Trans. Appl. Supercond. 3, 1745 (1993).
415. H. Nojima, H. Shintaku, M. Nagata, M. Koba, Jap. J. Appl. Phys. 30, L1166 (1991).
416. M. Fujimoto, H. Nojima, H. Shintaku, H. Taniguchi, M. Nagata, M. Koba, Jap. J. Appl. Phys. 32, L576 (1993).
417. N. Koura, H. Shoji, Physica C 200, 50 (1992).
418. H. Nojima, M. Nagata, H. Shintaku, M. Koba, Jap. J. Appl. Phys. 29, L1655 (1990).
419. H. Hein, S. Kraut, E. Machner, G. Muller, D. Opie, D. Piel, L. Ponto, D. Wehler, M. Becks, U. Klein, M. Peiniger, J. Supercond. 3, 323 (1990).
420. H. Niu, H. Shinkawata, Y. Hagiwara, S. Kashino, Supercond. Sci. Technol. 4, 229 (1991).
421. N. Minami, N. Koura, H. Shoji, Jap. J. Appl. Phys. 31, L784 (1992).
422. R. P. Vasquez, M. C. Foote, B. D. Hunt, J. Appl. Phys. 66, 4866 (1989).
423. A. Q. Wang, T. R. Hart, Appl. Phys. Lett. 60, 1750 (1992).
424. B. Zhang, P. Fabbricatore, G. Gemme, R. Musenich, R. Parodi, L. Risso, Physica C 193, 1 (1992).
425. J. P. Traverse, P. Roux, J. C. Bressolles, E. Snoeck, C. Roucau, Supercond. Sci. Technol. 6, 573 (1993).
426. N. Newman, W. G. Lyons, J. Supercond., 6, 119 (1993).
427. R. T. Bate, Nanotechnology 1, 1 (1990).
428. R. Notzel, K. Ploog, Adv. Mater. 5, 22 (1993).
429. I. Trofimov, H.-U. Habermeier, A. Litvinchuk, D. Leach, K. Kamaras, C. Thomsen, M. Cardona, J. Alloys Compds. 195, 187 (1993).
430. C. Fu, V. Moshalkov, E. Rossel, M. Baert, W. Boon, Y. Bruynseraede, G. Jakob, T. Hahn, H. Adrian, J. Alloys Compds. 195, 191 (1993).
431. J. Schneider, R. Wordenweber in: Abstr. 4th Int. Conf. HTSC, Grenoble (1994), p. 124.
432. I. Bozovic, J. N. Eckstein, G. F. Virshup in: Abstr. 4th Int. Conf. HTSC, Grenoble (1994), p. 20.
433. S. G. Haupt, D. R. Riley, J. Grassi, R.-K. Lo, J. Zhao, J.-P. Zhou, J. T. McDevitt, J. Am. Chem. Soc. 116, 9976 (1994).
434. J. Zhao, D. Jurbergs, B. Yamazi, J. T. McDevitt, J. Am. Chem. Soc. 114, 2737 (1992).
435. H. Freller, K. Mund, DECHEMA Monogr. 90, 107 (1980).
436. S. Moon, A. Xidis, V. Neft, J. Phys. Chem. 97, 1634 (1993).
437. J. Joseph, H. Gomathi, G. Prabhakara Rao, Bull. Electrochem. 8, 86 (1992).

438. A. Xidis, D. Neff, J. Electrochem. Soc. 138. 3637 (1991).
439. M. Jiang, Z. Zhao, J. Electroanal. Chem. 292, 281 (1990).
440. M. Jiang, X. Zhou, Z. Zhao, J. Electroanal. Chem. 292, 289 (1990).
441. S. Dong, Z. Jin, Electrochim. Acta 34, 963 (1989).
442. A. B. Domingues, R. B. Scorzelli, E. Baggio-Saitovitch, B. Giordanengo, M. Elmassalami in: Abstr. 4th Int. Conf. HTSC, Grenoble (1994), p. 140.
443. A. Veneva, I. Nedkov, V. Lovchinov in: Abstr. 4th Int. Conf. HTSC, Grenoble (1994), p. 140.
444. D. Cahen, Y. Scolnik, J. Electron. Mater. 20, 12 (1991).
445. A. N. Pargellis, F. Sharifi, R. C. Dynes, B. Miller, E. S. Hellman, J. M. Rosamilia, E. H. Hartford, Appl. Phys. Lett. 58, 95 (1991).
446. U. Staufer in: Scanning Tunnelling Microscopy II: Further Applications and Related Scanning Techniques, H.-J. Guntherdt, R. Wiesendanger (eds.), Springer-Verlag, Berlin (1992), pp. 273–302.
447. A. M. Dykhne, O. A. Petrii, G. A. Tsirlina, Rossiiskii Khim. Zh. 38, 24 (1994).
448. J. Schneir, P. Hansma, V. Elings in: Scanning Microscopy Technologies and Applications, E. Clayton (ed.) Billingham, WA SPIE, p.16 (1988).
449. C. Lin. F. Fan., A. Bard, J. Electrochem. Soc. 134, 1038 (1987).
450. O. Husser, D. Craston, A. Bard, J. Vac. Sci. Techn. B 6, 1873 (1988).
451. D. M. Kolb in: Abstr. 45th Meet. ISE, Porto (1994), p. KVI-1.
452. J. C. Brumfield, C. A. Goss, E. A. Irene, R. W. Murray, Langmuir 8, 2810 (1992).
453. S. Srivastava, B. Roas, K. Juttner, Electrochim. Acta 35, 1219 (1990).
454. W. Zhao, W. Y. Liang in: Abstr. 4th Int. Conf. HTSC, Grenoble (1994). P. 139.
455. P. Salvador, J. L. G. Fierro, J. Amador, C. Cascales, I. Rasines, J. Solid State Chem. 81, 240 (1989).
456. S. Myhra, P. C. Healy, C. F. Jones, Mater. Chem. Phys. 25, 135 (1990).
457. M. F. Yan, R. L. Barns, H. M. O'Bryan, P. K. Gallagher, R. C. Sherwood, S. Jin, Appl. Phys. Lett. 51, 532 (1987).
458. H. R. Khamn, C. J. Raub, J. Less-Common Met. 146, L1 (1989).
459. S. G. Jin, L. G. Lin, Z. Z. Zhu, J. Y. L. Huang, Solid State Commun. 69, 179 (1989).
460. P. G. Egdell, W. R. Flavell, P. C. Hollanby, J. Solid State Chem. 79, 238 (1989).
461. D. Zhuang, M. Xiao, Z. Zhang, S. Yue, H. Zhao, S. Shang, Solid State Commun. 65, 339 (1988).
462. P. Gallagher, G. Grader, H. O'Bryan, Mater. Res. Bull. 23, 1491 (1988).
463. Y. Gao, Y. Li, K. L. Merkle, J. N. Mundy, G. Zhang, U. Balachandran, R. B. Poeppel, Mater. Lett. 9, 347 (1990).
464. L. D. Fitch V. L. Burdick, J. Am. Ceram. Soc. 72, 2020 (1989).
465. T. E. Os'kina, Yu. D. Tret'yakov, E. A. Soldatov, Sverkhprovodimost': Fiz. Khim. Tekhn. 4, 1032 (1991).
466. E. A. Cooper, A. K. Gangopadhyay, T. O. Mason, U. Balachandran, J. Mater. Res. 6, 1393 (1991).
467. A. V. Dmitriev, L. V. Zolotukhina, T. A. Denisova, V. L. Kozhevnikov, Sverkhprovodimost': Fiz. Khim. Tekhnika 4, 1202 (1991).
468. J.-P. Zhou, J. T. McDevitt, Chem. Mater., 4, 953 (1992).
469. E. A. Eremina, N. N. Oleinikov, N. G. Lisina, A. M. Gas'kov, Yu. D. Tret'yakov, Sverkhprovodimost': Fiz. Khim. Tekhn. 4, 2374 (1991).
470. J.-P. Zhou. D. R. Riley, J. T. McDevitt, Chem. Mater. 5, 361 (1993).
471. K. Yoshikawa, M. Yoshida, M. Nakano, Jap. J. Appl. Phys. Pt. 2, 27, L2324 (1988).
472. A. N. Turanov, G. K. Strukova, I. I. Zver'kova, Sverkhprovodimost' Fiz. Khim. Tekhn. 5, 1116 (1992).
473. R. L. Barns, R. A. Laudise, Appl. Phys. Lett. 51, 1373 (1987).
474. V. H. Desai, K. B. Sundaram, Phys. Stat. Solidi A 143, 109 (1994).

475. A. H. Morrish, K. Z. Zhou, M. Raudsepp, I. Maartense, J. A. Eaton, Y. L. Luo, Canad. J. Phys. 65, 808 (1987).
476. Bachtler, W. J. Lorenz, W. Schindler, G. Saemann-Ischenko, J. Electrochem. Soc. 135, 2284 (1988).
477. L. A. Klinkova, N. V. Barkovskii, S. S. Khasanov, K. V. Van, Sverkhprovodimost': Fiz. Khim. Tekhn. 7, 375 (1994).
478. S. N. Slusar', I. A. Borovoi, N. V. Pogorelova, I. P. Krainov, Elektrokhimiya 25, 1326 (1989).
479. L. E. Sparling, V. Desai, J. Electrochem. Soc. 137, 226C (1989).
480. Z. Stankovic, P. Uskovic, M. Susic, M. Pjescic, L. Mancic in: Abstr. 45th Meet. ISE, Porto (1994), Vol. 2, p. V-76.
481. Z. D. Stankovic, M. Susic, M. Pjescic, 40th Meet. ISE, Kyoto (1989). Vol. 1, p. 132.
482. J. H. Choy, S.-G. Kang, D.-H. Kim, J.-C. Park, Jap. J. Appl. Phys. 32, L400 (1993).
483. E. M. Roizenblat, S. I. Ermolina, N. N. Saiko, A. A. Kosogov, K. P. Ivanova, V. V. Prisedskii, L. G. Gusakova, Zavod. Labor. 56, 44 (1990).
484. M. Mohammad, A. Y. Khan, M. S. Subhani, A. Naseer, S. Malik, A. Maqsood, B. Suleman, Izhar-ul-Haq, Bull. Electrochem. 5, 893 (1989).
485. C. -A. Chang, J. A. Tsai, Appl. Phys. Lett. 53, 1976 (1988).
486. D. Kumar, P. R. Apte, R. Pinto, M. Sharon, L. C. Gupta, J. Electrochem. Soc. 141, 1611 (1994).
487. A. Balzarotti, F. Patella, F. Arciprete, N. Motta, M. De Crescenzi, Physica C. 196, 79 (1992).
488. K. Oka, T. Ira, Jap. J. Appl. Phys. 31, 2689 (1992).
489. S. F. Wang, W. Huebner, J. Am. Ceram. Soc. 76, 474 (1993).
490. M. Grajcar, A. Plecenik, M. Darula, S. Benacko, Solid State Commun. 81, 191 (1992).
491. J. G. Osteryoung, L. J. Magee, R. T. Carlin, J. Electrochem. Soc. 135, 2653 (1988).
492. Y. S. Chang, S. M. Ma, F. L. Yang, C. S. Li, Mater. Chem. Phys. 28, 121 (1991).
493. K. Kaneto, K. Yoshino, Jap. J. Appl. Phys. 26, L1842 (1987).
494. J. M. Rosamilia, B. Miller, J. Electroanal. Chem. 249, 205 (1988).
495. G. A. Scholz, F. W. Boswell, Solid State Commun. 74, 959 (1990).
496. F. I. Yang, Y. S. Chang, C. S. Li, S. M. Ma, Y. T. Huang, W. H. Lee, J. Mater. Sci. 27. 5739 (1992).
497. J. M. Rosamilia, B. Miller, J. Mater. Res. 5, 1612 (1990).
498. Z. D. Stankovic, M. Rajcic-Vujasinovic, L. Mancic, in Abstr. 43th Meet. ISE, Cordoba (1992), p. 489.
499. M. Pjescic, Z. D. Stankovic, in Abstr. 43th Meet. ISE, Cordoba (1992), p. 490.
500. P. Allongue, E. Souteyrand, J. Electroanal. Chem. 286, 217 (1990).
501. P. Allongue, E. Souteyrand, J. Electroanal. Chem. 362, 79 (1993).
502. P. Allongue, E. Souteyrand, L. Allemand, J. Electroanal. Chem. 362, 89 (1993).
503. N.-J. Wu, T. Hashizume, H. Hasegawa, Jap. J. Appl. Phys. 33, 936 (1994).
504. T. Okumura, S. Yamamoto, M. Shimara, Jap. J. Appl. Phys. 32, 2626 (1993).
505. V. L. Arbuzov, O. M. Bakunin, S. E. Dailov, A. D. Levin, I. Sh. Trakhtenberg, Sverkhprovodimost': Fiz. Khim. Tekhn. 7, 553 (1994).
506. J. G. Osteryoung, L. J. Magee, R. T. Carlin, J. Electrochem. Soc. 136, 292 (1989).
507. S. G. Haupt, D. R. Riley, J. Zhao, J. T. McDevitt, J. Phys. Chem. 97, 7796 (1993).
508. B. D. Hunt, M. C. Foote, R. P. Vasquez, Appl. Phys.Lett. 56, 2678 (1990).
509. R. P. Vasquez, R. M. Housley, Physica C. 175, 233 (1991).
510. R. P. Vasquez, M. C. Foote, B. D. Hunt, Appl. Phys. Lett. 54, 1060 (1989).
511. G. K. Baranova, N. V. Abrosimov, A. N. Malyuk, Sverkhprovodimost': Fiz. Khim. Tekhn. 7, 365 (1994).

512. G. K. Baranova, S. A. Zver'kov, L. V. Ovchinnikova, Svekhprovodimost': Fiz. Khim. Tekhn. 2, 30 (1989).
513. G. K. Baranova, L. A. Dorosinskii, Physica C 194, 425 (1992).
514. K. B. Sundaram, V. H. Desai, S. M. Arora, J. Electrochem. Soc. 137, 226C (1990).
515. K. B. Sundaram, S. S. Seshan, V. H. Desai, S. M. Arora, J. Mater. Sci. Mater. Electron. 3, 26 (1992).
516. G. Lacayo, R. Herrmann, G. Kastner, Phys. Stat. Solidi A 127, K105 (1991).
517. G. V. S. Sastry, R. Wordenweber, H. C. Freyhardt, J. Appl. Phys. 65, 3975 (1989).
518. J.M. Rosamilia, L. F. Schneemeyer, T. Y. Kometani, J. V. Waszczak, B. Miller, J. Electrochem. Soc. 136, 2300 (1989).
519. I. G. Gorichev, B. E. Zaitsev, I. S. Shaplygin, V. I. Yashkichev, O. A. Egorova, Neorganich. Mater. 30, 74 (1994).
520. I. G. Gorichev, V. V. Batrakov, M. V. Dorofeev, Russ. J. Electrochem. 31, 292 (1995).
521. R. P. Vasquez, M. C. Foote, B. D. Hunt, Appl. Phys. Lett. 55, 1801 (1989).
522. B. B. Damaskin, Elektrokhimiya 25, 1641 (1989).
523. B. Das, D. Behera, M. D. Srichandan, N. C. Mishra, K. Patnaik, B. B. Deo, U. N. Dash, Bull. Electrochem. 5, 242 (1989).
524. B. B. Damaskin, A. Vitin'sh, O. A. Petrii, Elektrokhimiya 27, 435 (1991).
525. A. I. Kamenev, I. P. Viter, Otkrytiya, Izobreteniya, 43, 176 (1991).
526. G. O. Kawamura, M. Hiratani, J. Electrochem. Soc. 134, 3211 (1987).
527. N. A. Ezerskaya, M. V. Afanas'eva, N. K. Bel'skii, L. I. Ochertyanova, Zavod. Labor. 57(8), 14 (1991).
528. N. A. Ezerskaya, I. N. Kiseleva, N. K. Bel'skii, L. I. Ochertyanova, N. A. Kulysov, Zavod. Labor. 57(11), 11(1991).
529. M. Kato, N. Saga, T. Sawamura, K. Yoshimura, K. Kosuge in: Abstr. 4th Int. Conf. HTSC, Grenoble (1994), p. 141.
530. M. Kato, K. Yoshimura, K. Kosuge in: Abstr. 4th Int. Conf. HTSC, Grenoble (1994), p. 228.
531. I. V. Markova, Zh. Anal. Khim. 48, 1690 (1993).
532. Y. Sasaki, H. Aoyagi, H. Takeishi, Z. Yoshida, Physica C 191, 347 (1992).
533. F. P. Dousek, Physica C 171, 156 (1990).
534. L. Q. Chen, Y. Z. Huang, L. Z. Xin, X. J. Huang, T. E. Hui, Bull. Electrochem. 5, 483(1989).
535. P. Encinas, L. Lorenzo, M. L. Tascon, M. D. Vazquez, P. Sanchez-Batanero, J. Electroanal. Chem. 371, 161 (1994).
536. P. Encinas, M. L. Tascon, M. D. Vazquez, P. Sanchez-Batanero, J. Electroanal. Chem. 367, 99 (1994).
537. Kh. Brainina, E. Neyman, Electroanalytical Stripping Methods, Wiley, New York (1993).
538. M. Bachtler, W. J. Lorenz, W. Schindler, G. Saemann-Ischenko, Modern Phys. Lett. B 2, 819 (1988).
539. F. Beck, U. Barsch, J. Electroanal. Chem. 282, 175 (1990).
540. K. Kaneko, H. Kaneko, H. Ihara, S. Waki, K. Murata, K. Oka, Y. Nishihara, M. Hirabayashi, N. Terada, S. Ishibashi, A. Negishi in: Abstr. 45th Meet. ISE, Porto (1994), Vol. 2, p. V-31.
541. N. A. Zakharchuk, T. P. Fedina, N. S. Borisova, Izv. Sibir. Otdel. AN SSSR, 1, 61 (1990)
542. M. Tetenbaum, B. Tani, B. Czech, M. Blander, Physica C 158, 377 (1989).
543. M. Rekas, W. Weppner, J. Nowatny, J. Am. Chem. Soc. 73, 1040 (1990).
544. M. Hampel, E. W. Grabner, M. Bachtler, W. J. Lorenz, Int. J. Modern Phys. B 3, 303 (1989).
545. M. Hampel, E. W. Grabner, J. Electrochem. Soc. 137, 226C (1990).
546. S. K. Srivastava, K. Jutner, W. J. Lorenz, J. Electrochem. Soc. 137, 226C (1990).
547. M. Hampel, E. W. Grabner, R. Schneider, Electrochim. Acta 35, 1977 (1990).

548. E. W. Grabner, M. Hampel, M. Mitzlaff, DECHEMA Monogr. 121, 71 (1989).
549. A. Penicaud, A. Perez-Benitez, R. Gleason, E. Munoz, R. Escudero, J. Am. Chem. Soc. 115, 10392 (1993).
550. H. Araki, Y. Nobuo, T. Kawai, A. A. Zakhidov, R. Yoshino, Jap. J. Appl. Phys., Pt. II 32, L498 (1993).
551. R. J. Cava, H. Takagi, B. Batlogg, H. W. Zandbergem, J. J. Krajewski, Nature (London) 367, 146 (1994).
552. A. Gupta, R. Chevrel, M. Decroux, P. Selvam, D. Cattani, R. Flukiger, T. C. Willis, O. Fisher in: Superconducting Materials, J. Etourneau, B. Torrance, H. Yamauchi (eds.), IITT-International, Gournay-sur-Marne (1993), p. 397.
553. S. I. Cordoba de Torresi, R. M. Torresi, G. Ciampi, C. A. Luengo, J. Electroanal. Chem. 377, 283 (1994).
554. K. Chen, W. Caldwell, C. Mirrkin, J. Am. Chem. Soc. 115, 1193 (1993).
555. C. R. Ross, T. Wade, R. M. Crooks, Chem. Mater. 3, 768 (1991).

Advances in Electrochemical Science and Engineering
Edited by Richard C. Alkire, Heinz Gerischer, Dieter M. Kolb and Charles W. Tobias
© WILEY-VCH Verlag GmbH, 1997

Flow Rate Dependence of Localized Corrosion in Thermal Power Plant Materials

Digby D. Macdonald and Leo B. Kriksunov

Center for Advanced Materials, The Pennsylvania State University,
517 Deike Building, University Park, PA 16802, USA

Contents

1 Introduction 127
2 Stages in the Development of Damage 130
3 Hydrodynamic and Mass-Transfer Theory 131
  3.1 Navier–Stokes Equation 132
4 Mass-Transfer Correlations 133
5 High-Temperature Aqueous Systems 139
6 Electrochemical Corrosion Potential 142
  6.1 The Critical Potential 142
  6.2 Calculation of the ECP 151
  6.3 Effect of Fluid Flow on the ECP 152
  6.4 Effect of Fluid Flow on E_{IGSCC} 156
7 Stress Corrosion Cracking and Corrosion Fatigue 157
  7.1 Initiation and Passivity Breakdown 157
  7.2 Modeling of the Passivity Breakdown 163
  7.3 Effect of Fluid Flow on Passivity Breakdown 168
  7.4 Growth of the Critical Nucleus 171
  7.5 Modeling Effect of Fluid Flow on the Properties of Pits 180
  7.6 Effect of Fluid Flow on Short Cracks 183
  7.7 Effect of Fluid Flow on Long Cracks 186
8 References 190

List of Symbols

a	crack length
b/c	factor defining crack geometry
$\hat{B}$	
C_i	concentration of species i
CR	corrosion rate
D_i	diffusivity of species i
E	potential
E_{SCC}	critical potential for SCC
f	friction factor
F	Faraday constant
i_{corr}	corrosion current density
$i_{\mathrm{O/R}j}$	current density of jth redox couple
J_i	flux of species i

k	mass-transfer coefficient
k^0	standard rate constant
K_I	Mode I loading stress intensity
K_{IC}	critical stress intensity
K_{ISCC}	(lower) critical stress intensity for slow crack growth
l	crack length
L_{SS}	steady-state thickness of barrier layer
N	number of breakdown sites
p	pressure
g	local acceleration due to gravity
L	specimen length; layer thickness
Pe	Peclet number
r	radius
Re	Reynolds number
RPM	speed of rotation
Sc	Schmidt number
Sh	Sherwood number
St	Stanton number
t^{c}_{init}	crack initiation (or induction) time
t^{f}_{init}	flaw initiation time
$\vec{u}$	velocity of flowing liquid
V	flow velocity
z_i	charge on species i

α	function describing dependence of potential drop across film/solution interface on applied voltage
δ	valence
ϵ	dielectric constant; electric field in barrier layer
ϵ_0	permittivity of free space
κ	conductivity
ν	kinematic viscosity of flowing liquid
ξ'	number related to critical areal concentration of condensed vacancies
ρ	electrical potential
σ	stress
σ_D	standard deviation in normal distribution
τ	shear stress at surface; time for dissolution of barrier layer (relaxation time)
ϕ	electrical potential
χ	stoichiometry
ω	angular velocity

Abbreviations

AMPM	advanced mixed-potential model
BWR	boiling-water reactor
CEFM	coupled environment fracture model
CERT	constant extension rate
CF	corrosion fatigue
CGR	crack growth rate
CT	compact toughness
DFA	damage function analysis
DOS	degree of sensitization
ECP	electrochemical potential
FRASTA	fracture reconstruction by surface topographical analysis
IGA	intergranular attack

IGSCC	intergranular stress corrosion cracking
LEFM	linear elastic fracture mechanics
LWR	light-water reactor
MPM	mixed-potential model
PDM	point defect model
PWR	pressurized-water reactor
RCE	
RHE	reversible hydrogen electrode
SCC	stress corrosion cracking
SSRT	
TGSCC	transgranular stress corrosion cracking
WOL	

1 Introduction

Localized corrosion of metals and alloys represents one of the most dangerous and widely occurring forms of environmentally-induced damage to metallic structures. Although numerous studies dealing with the various aspects of localized corrosion have been reported, relatively little attention has been paid to the effect of fluid flow upon either the initiation or propagation of the localized attack. Because of the complex effects that fluid flow has on the electrochemical and chemical conditions that exist within crevices (e. g., pits and cracks) it is not surprising to find a wide range of reported dependencies, ranging from an increase in propagation rate, through no effect at all, to inhibition of localized corrosion, depending on the nature of the metal, solution composition, fluid flow, and environmental parameters. Some of these complex interrelationships between the fluid flow and localized corrosion phenomena are illustrated in Fig. 1 as a means of bringing some order to this complex, but important, subject.

Even for a single metal, the experimental results on flow effects reported in the literature are sometimes ambiguous or even contradictory because of differences in the experimental conditions and/or geometries studied. Some of the earlier work dealing with flow effects on pitting, especially at ambient temperatures, have been reviewed by Szklarska-Smialowska [1] and the reader is referred to this monograph for background material. In this review, we address flow effects on pitting in more detail, with emphasis on the high-temperature aqueous systems that are of particular practical interest in the thermal power industry. We also review the available data on fluid flow effects on stress corrosion cracking (SCC) and corrosion fatigue (CF) that remain principal threats to the integrity of many industrial systems, including the heat-transport circuits of light-water reactors (LWRs) [2–6]. In particular, life extension issues depend critically upon our ability to estimate the development of damage due to SCC and CF during operation on a component-by-component basis, so that appropriate inspection and maintenance schedules may be devised. Indeed, the quantity that is ultimately required is the damage function [7], an example of which for pitting corrosion is shown in Fig. 2. In this example, pit depth distributions (i.e., damage functions) for Type 403 stainless steel are plotted for two exposure times. As

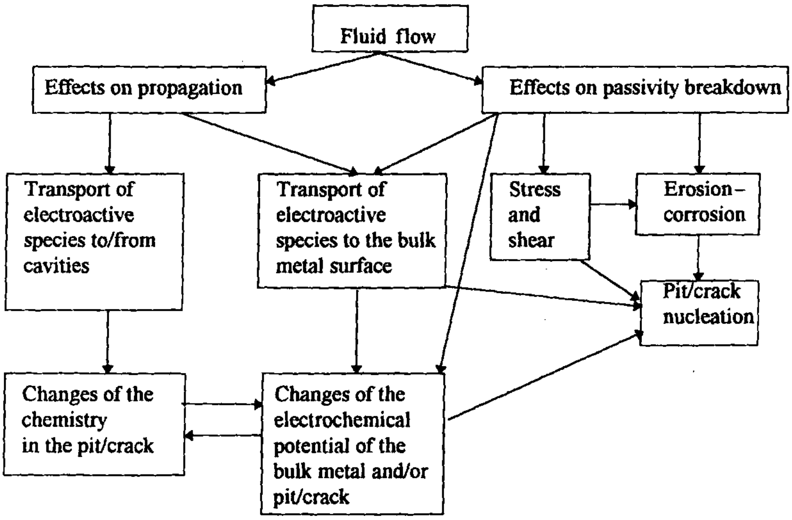
Fluid flow
Effects on propagation
Effects on passivity breakdown
Transport of electroactive species to/from cavities
Transport of electroactive species to the bulk metal surface
Stress and shear
Erosion-corrosion
Pit/crack nucleation
Changes of the chemistry in the pit/crack
Changes of the electrochemical potential of the bulk metal and/or pit/crack

Fig. 1. Interrelationships between the fluid flow and localized corrosion phenomena.

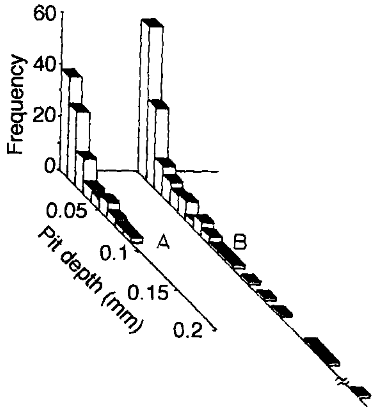

Fig. 2. Pit depth distributions for Type 403 stainless steel. (A) Initial distribution; (B) after five years. Frequency is in number/unit area. After [8]. Originally published in Trans. ISIJ, 22 (1982), p. 978, Fig. 2.

can be seen, the distribution for the longer exposure time extends to a greater depth. Therefore, the properties of the distribution function at the high pit-depth extreme are of greatest interest because the deepest pit (in this case) causes failure. Thus, the component lifetime is readily defined as the time at which the upper extreme of the damage function exceeds a critical dimension (e.g., the thickness of the pipe wall). A number of models, with varying degrees of determinism, are currently being developed to compute damage functions. In our own case, we have successfully applied damage function analysis (DFA) to explore the development of pitting damage in gas-fired condensing heat exchangers [9].

In calculating the damage function, it is necessary to differentiate between the initiation, growth, and (possibly) death phases in the development of the damaging process. While this feature will be discussed at some length later in this chapter, it is worthwhile pointing out at the outset that, for a single event (e.g., a single crack), these three phases occur in series, but for an ensemble of events the processes tend to occur in parallel. We refer to this phenomenon as progressive nucleation/growth/death, a term that reflects the fact that new damage nucleates as existing damage continues to grow or die ("death," in this context, refers to the repassivation of the localized corrosion events, not to failure of the component). At one extreme, when all of the damage nucleates within a very short time from exposure of the component to the environment, the damage function takes the form of a vertical line that moves to greater depths with increasing observation time. This case is referred to as "instantaneous nucleation/growth/death" and is best viewed as a particular case of the more general progressive nucleation/growth/death phenomenon. The available evidence for LWR heat-transport circuits is that progressive nucleation and growth prevail. Thus, any predictive algorithm or model that is developed to explore life extension issues must necessarily address the initiation, growth, and possibly death phases in the development of damage.

That each of the phases in the development of damage from a single event depends in a complex way on various system parameters comes as no surprise to those who have examined the problem of predicting damage. Thus, in the case of austenitic stainless steels (e.g., Type 304SS), the three phases depend in a rather complex manner on metallurgical, microstructural, mechanical, and environmental parameters, such as the degree of sensitization, grain size, presence of cold work, inclusion density, oxygen concentration, temperature, flow rate, and so forth. In particular, extensive research that has been carried out over the past two decades has demonstrated the importance of environmental parameters, such as solution conductivity and corrosion potential. Indeed, this latter parameter is of prime importance because it acts as an electrochemical "switch" that can determine when damage nucleates, how rapidly it develops, and when it dies.

As was noted above, one parameter that has received relatively little attention is fluid flow rate. This situation no doubt reflects the difficulties inherent in carrying out SCC and CF studies in aqueous systems under well-controlled hydrodynamic conditions. Intuitively, we expect fluid flow to affect all phases of the development of damage (particularly the initiation and growth phases) because of the known sensitivities of many corrosion processes to mass transport. These effects may be direct, as in the case of the transport of oxygen to the metal surface, or they may be indirect, through the effect of flow rate on the corrosion potential.

The purpose of this chapter is to review our state of knowledge with respect to the effects of fluid flow on the failure of materials in industrially important environments. Accordingly, emphasis will be placed on high-temperture aqueous systems but, where necessary, work performed at ambient temperature will be discussed to illustrate key concepts. Particular attention is placed on identifying critical shortcomings in our experimental database and theoretical understanding, so that well-designed experiments may be devised and carried out to address issues that are important in the development of predictive technologies.

2 Stages in the Development of Damage

Before the hydrodynamic and mass-transport properties of the systems of interest are discussed, it is advantageous to outline first the sequence of events that occur at the metal/solution interface that leads to the development of damage. This is done so that the reader will have a greater appreciation of the role that fluid flow plays in each phase and how those parameters that are affected by fluid flow impact the nucleation, growth, and death phases of the damaging processes.

In developing the arguments that are presented later in this review, it is necessary to keep in mind the relative scales (dimensions) at which each phase occurs. This is important because the effect of flow on localized corrosion is largely (though not totally) a question of the relative dimensions of the nucleus and the velocity profile in the fluid close to the surface. However, the velocity profile is a sensitive function of the kinematic viscosity, which in turn depends on the density and the dynamic viscosity. Because the kinematic viscosity of water drops by a factor of more than 100 on increasing the temperature from 25 °C to 300 °C, the conclusions drawn from ambient temperature studies of the effect of flow on localized corrosion must be used with great care when describing flow effects at elevated temperatures.

We illustrate the various phases in the development of damage in Fig. 3, in the form of a cartoon. In all instances, regardless of the existence of any pre-existing geometry, the initial event that must occur is the breakdown of passivity, in which the normally protective barrier oxide films that exist on all reactive metals in contact with oxidizing environments are ruptured. The scale of this event is of the order of 2–20 nm normal to the surface. Assuming that the breakdown event survives, localized corrosion results in the growth of a nucleus until the critical conditions necessary for self-sustained growth and/or the nucleation of a crack are achieved. Numerous observations have shown that the critical dimension of the nucleus for the nucleation of a crack is of the order of 1–5 times the grain size, which, for most materials of interest, corresponds to 30–150 μm. This dimension is of the same order as the thickness of the laminar sublayer, so that, at the lower end of the range, the defect is effectively embedded in a laminar flow field, whereas at the upper end the hydrodynamic and mass-transport properties of the system are dominated by the induced or prevailing turbulence. Once a crack has nucleated, and has grown to a depth of a few grain diameters, the crack tip is probably isolated from the flow field at the external surface, particularly for cracks of high aspect ratio [10]. Of course, a flow field may be induced within a crack under fatigue loading conditions by the pumping action of the crack flanks but, in this case, the flow field within the crack is effectively decoupled from that external to the crack, provided that the aspect ratio is sufficiently large. Although the flow fields that are induced in fatigue cracks, due to the relative motion of the crack flanks, can have a great impact on fatigue crack growth, our primary emphasis in this report is on pitting corrosion and stress corrosion cracking, where minimal motion of the crack flanks occurs. The case of fatigue loading has been dealt with Turnbull and Ferriss [11].

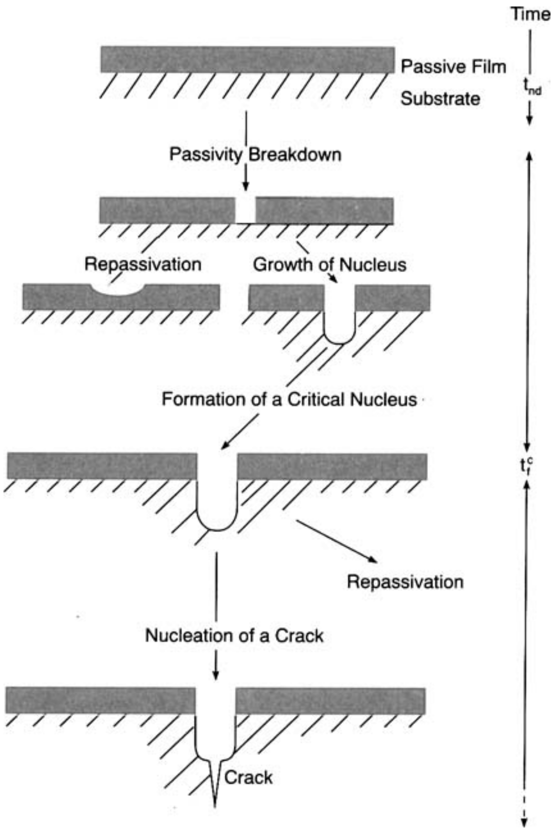
Time
Passive Film
Substrate
t_nd
Passivity Breakdown
Repassivation
Growth of Nucleus
Formation of a Critical Nucleus
t_f^c
Repassivation
Nucleation of a Crack
Crack

Fig. 3. Schematic history of the nucleation of a crack on a smooth metal surface.

3 Hydrodynamic and Mass-Transfer Theory

As noted above, the nucleation of damage due to localized corrosion occurs at dimensions at which hydrodynamic effects are expected (and found) to be of great importance. Accordingly, any quantitative discussion of the issues involved requires a reasonably comprehensive knowledge of those hydrodynamic and mass-transport principles that apply to the relevant geometries and dimensions. Our purpose is not to provide a comprehensive review of the subject, which has been done elsewhere [12–14], but rather to concentrate only on those issues that will assist the reader to understand the material that is presented later in this review.

3.1 Navier-Stokes Equation

By assuming incompressible flow, the conservation of momentum and mass for a flowing fluid can be described by the Navier–Stokes equation,

$$\frac{\mathrm{d}\vec{u}}{\mathrm{d}t} = -\frac{1}{\rho}\nabla p + \mathrm{v}\nabla 2\vec{u} + \vec{g} \tag{1}$$

where $\vec{u}$ is the velocity, p is the pressure, ν is the kinematic viscosity, ρ is the density, and $\vec{g}$ is the local gravitational acceleration. For dilute solutions, the transport of species within the fluid is described by Fick's first law,

$$\vec{J}_i = -D_i\nabla C_i - z_iFD_iC_i\nabla\phi/RT + \vec{u}C_i \tag{2}$$

The corresponding continuity condition for circumstances where there are no homogeneous reactions is

$$\frac{\partial C_i}{\partial t} = -\nabla\vec{J} \tag{3}$$

where $\vec{J}_i$ is the flux, z_i is the charge, D_i is the diffusivity, C_i is the concentration of species i, and ϕ is the electrical potential. The distribution in potential is given by the solution to Poisson's equation

$$\nabla^2\phi = -\sum_{i=1}^{M} z_tC_i/\epsilon\epsilon_0 \tag{4}$$

where ϵ_0 is the permittivity of free space and ϵ is the dielectric constant. The solution of Eqs. (1), (3), and (4) ($i = 1, 2, ..., M$ species), using the appropriate boundary conditions, yields the local velocity vector, $\vec{u}$, the local concentrations, C_i, the local potential, ϕ, and hence the local fluxes, $\vec{J}_i$. Finally, the local current density in regions of uniform concentration is given by

$$\vec{i} = \sum_{i=1}^{M} z_i\vec{J}_i = -\nabla\phi/\kappa \tag{5}$$

where κ is the conductivity. Note that for a noncharged species, or for the case of a charged species (i.e., ions) in the presence of a large excess of inert "background" electrolyte, the flux becomes independent of potential. This greatly simplifies the problem of solving for C_i and $\vec{J}_i$.

The great difficulties that have been experienced in solving these equations analytically has led to a myriad of approximate solutions, which are normally obtained by assuming some analytical form for the velocity profile close to the surface, and to the development of powerful numerical algorithms. An excellent example of how the Navier–Stokes and continuity equations can be solved for a particular geometry is that of the rotating-disk electrode, the solution for which has been developed by Levich [12]. In deriving the solution for laminar flow conditions, it was found that the polar coordinate velocities of the fluid close to the disk surface can be expressed as infinite series of the nondimensional parameter

$$\gamma = (\omega/\nu)^{1/2} y \tag{6}$$

where y is the distance normal to the disk. Solution of the convective diffusion equation (Eq. (3)) for this velocity field yields the well-known expression for the mass-transfer coefficient, k (= rate of reaction/concentration driving force) under laminar flow conditions as

$$k = 0.6205 D^{2/3} \nu^{-1/6} \omega^{1/2} \tag{7}$$

where ω is the angular velocity. The validity of this equation has been confirmed by innumerable studies.

While Eqs. (1) to (5) may be difficult to solve analytically, various methods have been developed to solve the equations numerically. Perhaps the most practical methods are the finite element, finite difference, and boundary element techniques. With these techniques, the velocity (hydrodynamic) and potential fields, and the concentration gradients (mass transport), are readily calculated for complicated geometries using commercially available software. These techniques have been used extensively by Alkire and co-workers [15], and by others [16], to explore the hydrodynamic properties of pits and crevices. These studies will be discussed in some detail in Section 7.5.

4 Mass Transfer Correlations

Because of the difficulties inherent in solving the Navier–Stokes and continuity equations, as discussed above, the mass-transfer properties of any given geometry are commonly expressed in the form of empirical correlations between dimensionless groups. These correlations commonly (but not always) take the form

$$\mathrm{Sh} = \hat{A}\,\mathrm{Re}^{\mathrm{a}}\mathrm{Sc}^{\mathrm{b}} \tag{8}$$

and

$$\mathrm{St} = \hat{B}\,\mathrm{Re}^{\mathrm{a}'}\mathrm{Sc}^{\mathrm{b}'} \tag{9}$$

where the Sherwood (Sh) and Stanton (St) numbers are defined by

$$\mathrm{Sh} = kd/D \tag{10}$$

and

$$\mathrm{St} = k/V = \mathrm{Sh}/\mathrm{ReSc} \tag{11}$$

respectively, and the Reynolds (Re) and Schmidt (Sc) numbers are given by

$$\mathrm{Re} = Vd/\nu \tag{12}$$

and

$$\mathrm{Sc} = \nu/D \tag{13}$$

In these expressions, V is the linear velocity, d is the characteristic dimension, D is the species diffusivity, and ν is the kinematic viscosity (dynamic viscosity/density). Thus, the rate of reaction becomes

$$\mathrm{Rate} = k\Delta C = D\hat{A}\,\mathrm{Re}^{\mathrm{a}}\mathrm{Sc}^{\mathrm{b}}\Delta C/d(\mathrm{mol/cm^2 s}) \tag{14}$$

$$\mathrm{Rate} = V\hat{B}\,\mathrm{Re}^{\mathrm{a}'}\mathrm{Sc}^{\mathrm{b}'}\Delta C(\mathrm{mol/cm^2\,s}) \tag{15}$$

where ΔC is the difference between the concentration of the species in the bulk fluid (C^{b}) and at the surface (C^{s}). That is, $\Delta C = C^{\mathrm{b}} - C^{\mathrm{s}}$ for a discharge reaction, but it is the reverse ($C^{\mathrm{s}} - C^{\mathrm{b}}$) for a dissolution reaction. Thus, for a discharge reaction under complete mass-transfer control, $C^{\mathrm{s}} = 0$ and hence $\Delta C = C^{\mathrm{b}}$. For electrochemical reactions, which are of prime interest in this work, the mass-transfer-limited current density can be expressed as

$$i_l = nF \cdot \mathrm{Rate} = nFD\hat{A}\,\mathrm{Re}^{\mathrm{a}}\mathrm{Sc}^{\mathrm{b}}C^{\mathrm{b}}/d\,(\mathrm{A/cm^2}) \tag{16}$$

or

$$i_l = nFV\hat{B}\,\mathrm{Re}^{\mathrm{a}'}\mathrm{Sc}^{\mathrm{b}'}C^{\mathrm{b}}\,(\mathrm{A/cm^2}) \tag{17}$$

where n is the electron number for the reaction

$$\mathrm{R} \leftrightarrow \mathrm{O} + ne^- \tag{18}$$

and F is Faraday's constant (96 487 C/equiv.). By convention, the current is positive in the forward direction of Reaction (18) (i.e., in the anodic direction), and negative in the reverse (reduction) direction.

Table 1. Representative mass-transfer correlations for different hydrodynamic geometries (after Selman and Tobias [14]).

Geometry	Flow characteristics	Reynolds number	Correlation(a)
Pipe	Laminar	<2100	$\mathrm{Sh} = 1.85\ (\mathrm{ReSc}d_e/L)^{1/1}f(g)$
	Turbulent	$8000 < \mathrm{Re} < 200\ 000$	$\mathrm{Sh} = 0.0165\ \mathrm{Re}^{0.68}\mathrm{Sc}^{0.33}$
Rotating disk	Laminar	$\mathrm{Re} < 2.7 \times 10^5$	$\mathrm{Sh} = 0.621\ \mathrm{Re}^{1/2}\mathrm{Sc}^{1/3}$
	Turbulent	$8.95 \times 10^5 < \mathrm{Re} < 1.18 \times 10^7$	$\mathrm{Sh} = 0.0117\ \mathrm{Re}^{0.896}\mathrm{Sc}^{0.249}$
Rotating cylinder	Laminar	$\mathrm{Re} < 10$	$\mathrm{Sh} = 3.5$
	Turbulent	$600 < \mathrm{Re} < 2.5 \times 10^5$	$\mathrm{Sh} = \mathrm{ReSc}^{0.356}/[1.25+5.76\log(d_i/2h)^2]$
Annulus	Laminar	$1.7\times10^4 < \mathrm{ReSc}d_e/L < 9 \times 10^7$	$\mathrm{Sh} = 1.94(\mathrm{ReSc}d_e/L)^{1/3}$
	Turbulent	$2100 < \mathrm{Re} < 30\ 000$	$\mathrm{Sh} = 0.023\mathrm{Re}^{0.8}\mathrm{Sc}^{1/3}$

(a) Definitions of Sh and Re and other parameters are given in [14].

Dimensionless group correlations are available for a large number of hydrodynamic geometries under laminar, transitionary, and turbulent flow conditions [12–14]. These correlations are frequently determined by measuring the mass-transfer-limited current for a reversible electrochemical reaction (e.g., $\mathrm{Fe(CN)}_6^{4-}/\mathrm{Fe(CN)}_6^{3-}$) as a function of flow velocity and viscosity. The latter is normally changed by adding a "viscosity modifier", such as glycol or glycerol, to the solution. These components also change the density of the solution and diffusivity of the reactant [e.g., $\mathrm{Fe(CN)}_6^{3-}$], which must be measured independently. The Reynolds and Schmidt numbers are calculated using Eqs. (12) and (13), and the correlations (Eqs. (8) and (9)) are then determined by regression. In determining these correlations, when using a charged reactant (such as $\mathrm{Fe(CN)}_6^{3-}$), it is necessary to use a sufficiently high concentration of inert electrolyte (e.g., KCl or KOH) to render migration negligible (since the migration term is seldom included in the continuity equation or allowed for in the dimensionless group correlations).

A number of excellent compilations of dimensionless group correlations are available in the literature (see Levich [12], Selman and Tobias [14], and Poulson [17]). These compilations are not reproduced here, but the correlations for a number of common hydrodynamic geometries are listed in Table 1. Because these equations are empirical in nature, they are valid only for the employed ranges in Re and Sc.

Most surfaces in systems of technological interest are rough, and this roughness enhances the rate of mass transfer to the interface. In the empirical correlations, the effect of roughness is normally taken into account by a "roughness factor," which is a function of the Reynolds number and the roughness height. For corroding interfaces, surface roughness poses a particularly difficult problem because the roughness may change over the course of the exposure. The reader is referred to an excellent discussion of this subject by Poulson [17].

For systems operating under transitionary and turbulent conditions, it is frequently necessary to introduce a "friction factor," which arises from the fact that the fluid velocity is not zero at the surface, as assumed in an ideal hydrodynamic model. The friction factor (f) is a function of the velocity of the fluid in the bulk (V), the shear stress at the surface (τ), and the density. For example, in the case of a rotating-cylinder electrode [14, 17], the mass-transfer coefficient may be written as

$$k = (\tau/\rho U_r)\mathrm{Sc}^{-0.644} \tag{19}$$

where

$$\frac{1}{f/2} = -1.71 + 5.76\log_{10}(\mathrm{Re}\, f^{1/2}/2) \tag{20}$$

The importance of surface shear in passivity breakdown and the nucleation of damage on steel surfaces in high-temperature aqueous environments is discussed in Section 7 of this chapter.

The final issue that we wish to address here concerns the correlations that have been developed between different hydrodynamic geometries. This issue is of great practical significance because it is frequently necessary to compare information obtained in studies that often differ greatly in geometry, scale, and velocity. This problem has been considered by several authors [18–23] for ambient-temperature systems, but little has been reported for systems at elevated tempertures.

Heitz [22] employed the mass-transfer-controlled reaction between zinc and iodine to explore the correlations between mass transport in a pipe, to a rotating disk, and to a rotating cylinder. The correlations were expressed in terms of the equivalent velocity through the tube as (quoted by Poulson [17])

$$V_{\mathrm{tube}}(\mathrm{m/s}) = 6.6 \times \mathrm{RPM}_{\mathrm{disk}} \times [\text{disk radius (cm)}]^{0.3} \tag{21}$$

$$= 37 \times (\mathrm{RPM}_{\mathrm{cyl}})^{0.9} \times [\text{cylinder radius (cm)}]^{0.7} \tag{22}$$

where RPM is the speed of rotation of the disk or cylinder. To our knowledge, these expressions have not been extensively tested, particularly under conditions where complete mass transfer control does not occur.

Ellison and Schmeal [19] explored a similar approach by using the corrosion of carbon steel in concentrated sulfuric acid as the mass-transport/corrosion probe. A model was proposed to reconcile corrosion rate data from pipe and rotating cylinder geometries based on the premise that the corrosion rate is controlled by the transport of Fe^{2+} from the interface. The data were subsequently used by Silverman [21] to construct a more precise model for correlating mass-transfer effects between pipe flow and a rotating cylinder.

Silverman [21] derived velocity correlations between a rotating cylinder (u_1), pipe flow (u_2), annulus flow (u_3), and an impinging jet (wall jet region only, u_4), as listed in Table 2. These equations assume that the appropriate transformations are to be made on the basis of equal mass-transfer rates for the different geometries. Silverman [21] also explored the case where the equality of surface shear stress is the appropriate criterion, on the basis that the equality of the shear stress will ensure the same corrosion processes for the various geometries. We stress that the equations listed in Table 2 must be used with great caution because they are based on the

Table 2. Velocity of a rotating cylinder that yields the same mass-transfer coefficients for the indicated geometries (after Silverman [21]).

Geometry	Relationship[(a)]
Pipe	$u_1 = 0.11845[n^{-1/4}x(d_1^{3/7}/d_2^{5.28})\mathrm{Sc}^{-0.0857}]u_2^{5/4}$
Annulus	$u_1 = 0.11845[n^{-1/4}x(d_1^{3/7}/d_3^{5.28})\mathrm{Sc}^{-0.0857}]u_3^{5/4}$
Impinging jet	$u_1 = 2.959[n^{-0.162}x(d_1^{3/7}/d_4^{0.26})\mathrm{Sc}^{-0.329}]u_4^{1.17}$

Symbols are defined as follows:

(a) d_i is the hydrodynamic diameter for geometry i. Thus, d_2 = pipe diameter, $d_3 = 2(d_o - d_1)$, where d_o is the diameter of the outer boundary of the annulus and d_1 is the inner diameter of the annulus, d_4 = diameter of the jet; u_1 (rotating cylinder), u_2 (pipe), u_3 (annulus), and u_4 (impinging jet) are the linear velocities of the fluid relative to the surface.

questionable assumption that the mass-transfer coefficient should be matched. Thus, this approach does not recognize the possibility that the mass-transfer rate is limited by the presence of a corrosion product film on the surface, which is almost certainly the case for most alloys of engineering interest.

The problem of transferring corrosion rate data from one hydrodynamic system to another has also been considered in some depth by Chen et al. [18], by using the corrosion of 90:10 Cu:Ni alloy in aerated 1 M NaCl solution at 25 °C in pipe-flow, annular-flow, and rotating-cylinder systems. The authors recognized that two mass-transfer processes should be distinguished: transfer through the diffusion boundary layer in the solution (mass-transfer coefficient, k_h), and transfer through the corrosion product film (k_f). The overall mass-transfer coefficient was defined as

$$k_1 = (1/k_h + 1/k_f)^{-1} \tag{23}$$

and it was found that all geometric systems gave the same log (corrosion rate) vs. log (k_1) correlation (Fig. 4). The k_1 expressions for the three systems are as follows.

1. Pipe flow:

$$k_1 = [1.04 \times 10^2\,\mathrm{Re}^{-0.913}\mathrm{Sc}^{-1/3}(X/D) + 1.29 \times 10^{10}\,\mathrm{Re}^{-1.62}]^{-1} \tag{24}$$

2. Annular flow:

$$k_1 = [4.21\,\mathrm{Re}^{-0.6}\mathrm{Sc}^{-1/3}\,(X/L)^{-1/3}\,(D/X)^{-1} + 3.23 \times 10^9\,\mathrm{Re}^{-1.62}]^{-1} \tag{25}$$

3. Rotating cylinder:

$$k_1 = [12.6\,\mathrm{Re}^{-0.7}\mathrm{Sc}^{-0.356}(X/D) + 6.45 \times 10^9\,\mathrm{Re}^{-1.62}]^{-1} \tag{26}$$

where X is the characteristic dimension of the hydrodynamic system with

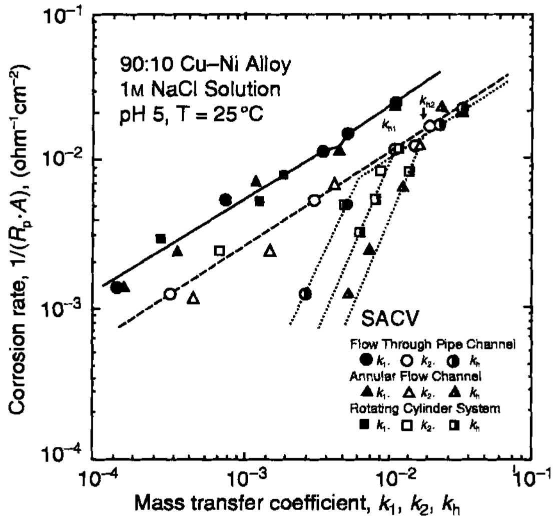

Fig. 4. Correlation of corrosion rate with mass-transfer coefficient, k_1, k_2, and k_h for Alloy 706 (90Cu10Ni) in 1 M NaCl solution at 25 °C [18]. Reproduced from Corrosion J. 48, 239 (1992) by permission of the Editor.

1. X = inside diameter of tube (pipe flow),
2. X = effective diameter of annulus (annular flow),
3. X = diameter of cylinder (rotating cylinder),

L is the specimen length, D is the diffusion coefficient of oxygen, $\mathrm{Re} = XV/\nu$, and $\mathrm{Sc} = \nu/D$. The equation correlating the corrosion rates for the three hydrodynamic geometries is given as

$$\log(CR) = 0.66\log(k_1) - 0.33 \tag{27}$$

where the corrosion rate is given terms of the specific polarization resistance, $1/(\mathrm{Rp}{\cdot}A)(\Omega^{-1}\ \mathrm{cm}^{-2})$ and A is the specimen area. The correlations expressed by Eqs. (24) to (27) for pipe flow, annular flow, and the rotating cylinder geometry are capable of yielding corrosion rates to within ±10% when used under the specified conditions. An important difference between this [18] and previous work is that the model of Chen et al. [18] allows for mass transfer through a corrosion product film on the alloy surface as being rate-controlling. Because most metals and alloys of interest passivate, the inclusion of a mass-transfer term for the corrosion product film would seem to be most appropriate.

In summary, while a number of dimensionless group correlations have been proposed to transfer mass-transfer and corrosion-rate data from one hydrodynamic geometry to another, all of these correlations are system-specific and are not generally valid for use outside of the ranges of conditions (Re, Sc, T) for which they have been derived. Clearly, a universal correlation is lacking (and is perhaps unattainable), particularly one that can be used to correlate mass-transfer geometries at elevated temperatures. Again, we emphasize that the development of correlations of this type is vitally important for the quantitative comparison of different series of experimental data.

5 High Temperature Aqueous Systems

We have stressed, in the above discussion, that the dimensionless group mass-transfer correlations are strictly valid only for the ranges in Re and Sc from which they were derived. Typically Sc is of the order of 180–1000 for aqueous solutions at ambient temperature (depending on the nature of the solute and the solution), but due to the rapid decrease in the kinematic viscosity and increase in species diffusivity with increasing temperature, Sc falls to a little over 1 at 300 °C (Table 3) [24]. Thus, from a fluid dynamics viewpoint, water at high temperatures is quite different from water at ambient temperature, for which almost all dimensionless group mass-transfer correlations have been derived. However, few attempts have been made to qualify mass-transfer correlations specifically for application to high-temperature water, so that a quantitative (including an empirical) basis is currently lacking for the transfer of mass-transfer information from ambient-temperature systems to those at elevated temperatures.

Two approaches have been employed to address this problem.

1. The assumption has been made that the form of the mass-transfer correlation is independent of temperature, and that the effect of temperature may be expressed through the values for D and ν.
2. New correlations that incorporate temperature-dependent exponents (and even different forms of the correlation) may be derived by analyzing data for the appropriate ranges for Re and Sc at the temperatures of interest.

As an example of the first case, an annular flow channel was calibrated using the mass-transfer limited oxidation of H_2 on platinized Alloy 600 in 0.1 M NaOH as a function of the rotational velocity of a flow-activating impeller [24]. By assuming, a priori, the form of the mass-transfer correlation (corresponding to that for ambient temperature), it was possible to calculate the equivalent linear flow velocity as shown in Fig. 5. These data were then used to establish correlations between the Sherwood and Stanton numbers and the Reynolds number corresponding to the temperature of interest (Fig. 6). We note that at the highest temperature (250 °C), and for the highest

Table 3. Variation of the kinematic viscosity of water and the Schmidt number for hydrogen in water as a function of temperature.

T [°C]	ν [cm^2/s]	Sc
25	8.98×10^{-3}	187.1
50	5.61×10^{-3}	66.2
100	3.03×10^{-3}	15.9
150	2.01×10^{-3}	6.09
200	1.62×10^{-3}	3.34
250	1.41×10^{-3}	2.12
300	1.26×10^{-3}	1.52

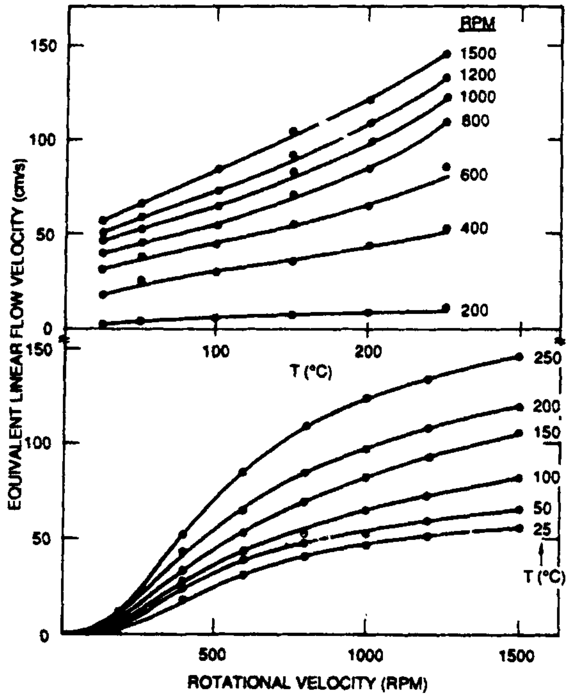

Fig. 5. Dependence of equivalent linear flow velocity in the annular channel on temperature and flow-activating impeller rotational velocity [24]. Reproduced from Corrosion J. 44, 186 (1988) by permission of the Editor.

rotational velocity employed (1500 rpm), the equivalent linear flow velocity is of the order of 1.5 m/s and Re $\simeq 10^5$. Evidence of the high linear flow velocity in this system was obtained from the accumulation of extensive cavitation damage at the exit end of the Alloy 600 outer boundary of the annulus. This apparatus was subsequently used to investigate the effect of flow velocity on the pitting of Alloy 600 and Type 304SS in high-temperature aqueous systems.

On the other hand, Stein [25, 26] synthesized a heat-transfer (and hence mass-transfer) correlation for pipe flow, which spans the relevant ranges in Re and Sc, from various correlations for partial ranges in these parameters that have appeared in the literature. We summarize in Table 4 a comparison of limiting currents for oxygen reduction calculated using this correlation and those estimated from an ambient-temperature correlation for pipe flow (Table 1), in which we have substituted elevated-temperature values for D and ν (Table 4). The calculated limiting current densities summarized in Table 4 imply that little quantitative difference exists between the two correlations, with the difference being at a maximum of ~ 10 percent at the highest flow velocity. The level of agreement between the two approaches should be regarded as being remarkable, given their tenuous foundations.

The most common approach, by far, in devising mass-transfer correlations for a high-temperature system is to simply adopt the correlation that has been established at ambient temperature and pressure and substitute the appropriate values for ν and D

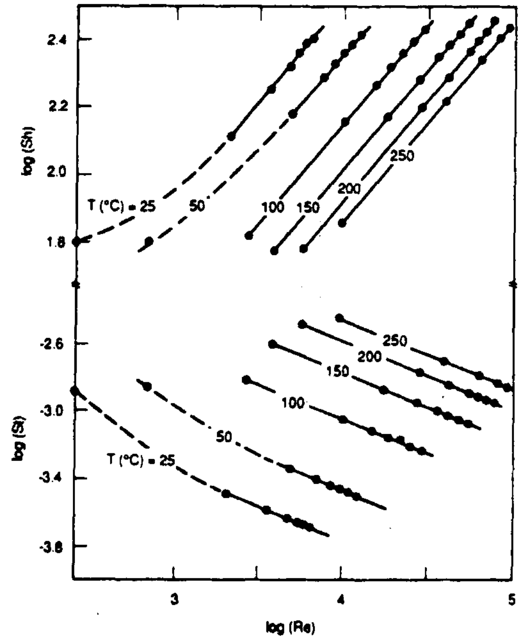

Fig. 6. Variation of the Sherwood (Sh) and Stanton (St) numbers for the oxidation of hydrogen in 0.1 M NaOH on the inner radius of the annular flow channel as a function of the Reynolds (Re) number [24]. Reproduced from Corrosion J. 44, 186 (1988) by permission of the Editor.

Table 4. Comparison of limiting current densities for oxygen reduction in turbulent pipe flow as a function of flow velocity at 288 °C.

Flow velocity [m/s]	Re	i_l [A/cm^2]	
		Stein's correlation	Correlation in Table 1
200	1.24×10^7	-1.19×10^{-5}	-1.25×10^{-5}
400	2.49×10^7	-2.11×10^{-5}	-2.27×10^{-5}
600	3.73×10^7	-2.96×10^{-5}	-3.22×10^{-5}
700	4.35×10^7	-3.36×10^{-5}	-3.67×10^{-5}
800	4.97×10^7	-3.75×10^{-5}	-4.12×10^{-5}
900	5.59×10^7	-4.13×10^{-5}	-4.56×10^{-5}

[a] Pipe diameter = 80 cm, CO_2 = 0.1 ppm (3.125×10^{-7} m)

for the system at elevated temperatures and pressures. Notwithstanding the data summarized in Table 4, it is important to keep in mind that such correlations generally have not been demonstrated to hold for the range of Schmidt numbers that characterize the majority of industrially important systems, including the heat-transport circuits of thermal power plants.

6 Electrochemical Corrosion Potential

Perhaps the most important parameter in determining the onset of localized corrosion is the electrochemical potential (ECP)[27]. While the importance of the ECP in determining the susceptibility of a subrate metal or alloy to pitting attack had long been known, its importance in the stress corrosion cracking of steels in high-temperature aqueous systems became apparent only in the late 1970s when CERTs (constant extension rate tests), carried out under potentiostatic control, showed that the failure time and fracture morphology are strong functions of the imposed potential. These studies defined a critical potential for SCC (E_{SCC}), which provides the basis of one of the promising methods for controlling SCC in some power plant heat-transport circuits. Clearly, any analysis of the effect of flow on SCC must consider the effect of flow on the critical potential. However, before embracing this issue, it is worthwhile to summarize first what is known about the critical potential for stress corrosion cracking in high-temperature aqueous solutions.

6.1 The Critical Potential

The existence of critical potentials for certain corrosion processes has been known for many decades (e.g., the critical potential for pitting). However, the importance of electrochemistry (and in particular, critical potentials) in the failure of power plant materials was not appreciated until in-depth studies on the intergranular stress corrosion cracking (IGSCC) of sensitized Type 304SS were carried out in the late 1970s and early 1980s. This subject has been extensively reviewed [28, 29], so that only the principal findings will be summarized here.

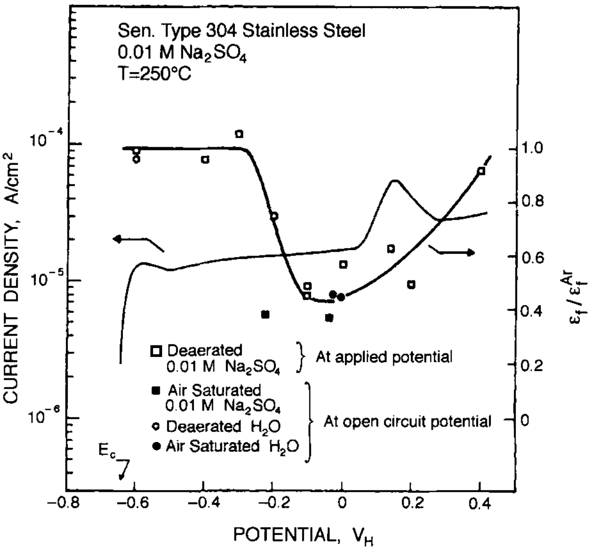

Fig. 7. Stress corrosion cracking susceptibility of sensitized Type 304SS in 0.01 M Na_2SO_4 at 250 °C as a function of potential [29]. Reproduced from Proc. 9th Int. Congr. Met. Corros. Vol. 2, pp. 185–201 (1984) by permission of the National Research Council of Canada.

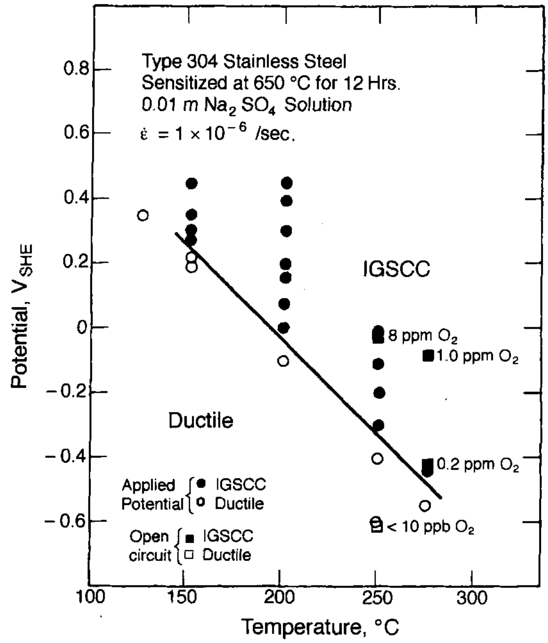

Fig. 8. Potential–temperature diagram showing domains of IGSCC and ductile failure in sensitized Type 304SS in 0.01 M Na_2SO_4 as determined using CERTs at an extension rate of 10^{-6} s^{-1} [29]. Reproduced from Proc. 9th Int. Congr. Met. Corros., Vol. 2, pp. 185–201 (1984) by permission of the National Research Council of Canada.

Critical potentials for IGSCC in sensitized Type 304SS are commonly (although not exclusively) measured by using the constant extension rate test (CERT), and the data are normally presented as fracture "mode diagrams" of the type shown in Figs. 7 to 9. Thus, the critical potential versus temperature correlation divides regions of ductile and brittle (IGSCC) behavior. In some cases (Fig. 9), regions of other forms of corrosion damage are identified on the diagrams as well. Additionally, it should be noted that:

1. The same critical potential (within experimental precision) is observed regardless of whether the potential is established chemically (by controlling the oxygen concentration) or electrochemically (by using a potentiostat) [28, 29].
2. The value of E_{SCC} for any given temperature shifts in the negative direction as the degree of sensitization (DOS) of the steel is increased [28].
3. E_{SCC} does not appear to be a strong function of pH, but as the medium is made acidic, sensitized Type 304SS may fail in an intergranular mode at $E < E_{SCC}$ (Fig. 10), probably due to the occurrence of a hydrogen-induced fracture process.
4. Significant anion effects are observed in the value of E_{SCC} for certain electrolytes. For example, phosphate inhibits fracture (moves E_{SCC} to a more positive value) compared with sulfate and chloride solutions [28, 29].
5. The same value for E_{SCC} is observed using fracture mechanics specimens under constant load or in CERTs, provided that similarly sensitized material is used (cf. Figs. 8 and 11).

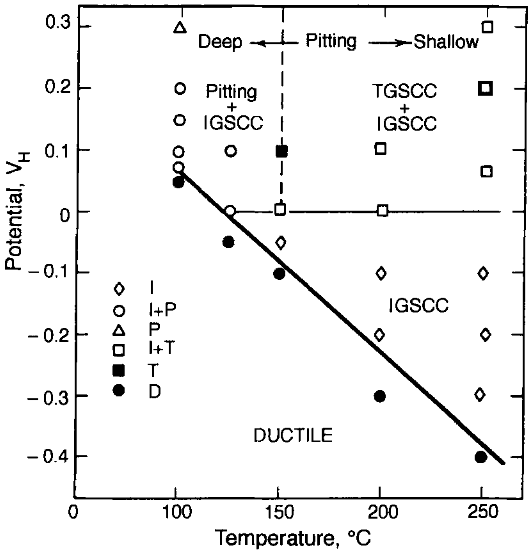

Fig. 9. Potential–temperature diagram for sensitized Type 304SS in 0.01 m NaCl solution showing regions of different failure modes [29]. TGSCC, transgranular stress corrosion cracking. Reproduced from Proc. 9th Int. Congr. Met. Corros., Vol. 2, pp. 185–201 (1984) by permission of the National Research Council of Canada.

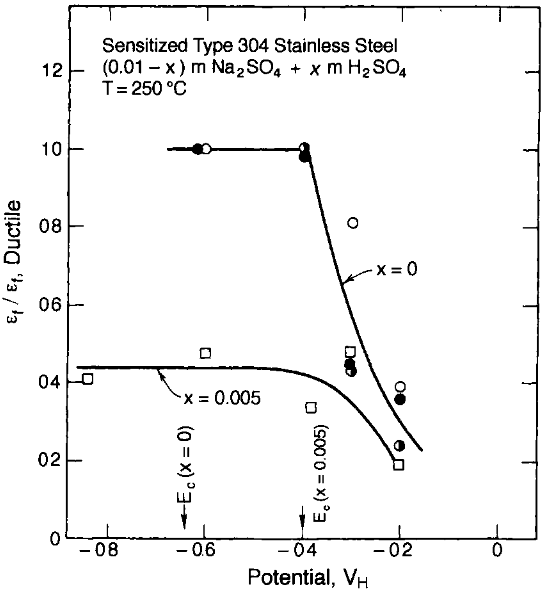

Fig. 10. Effect of potential on the IGSCC susceptibility of sensitized Type 304SS in $(0.01-x)$ m Na_2SO_4 + x m H_2SO_4 at 250 °C [29]. Reproduced from Proc. 9th Int. Congr. Met. Corros., Vol. 2, pp. 185–201 (1984) by permission of the National Research Council of Canada.

6. The same critical potential is observed for intergranular fracture under fatigue conditions as for monotonic loading (SCC), provided that the loading frequency in fatigue is sufficiently low ($f < 0.1$ Hz for $R = 0.5, \Delta K = 20\,\mathrm{MPa\,m^{1/2}}$) [28].

The fact that E_{SCC} is truly a "critical" potential may be seen from the data plotted in Figs. 11 and 12. In Fig. 11, we show crack growth rate versus potential data for

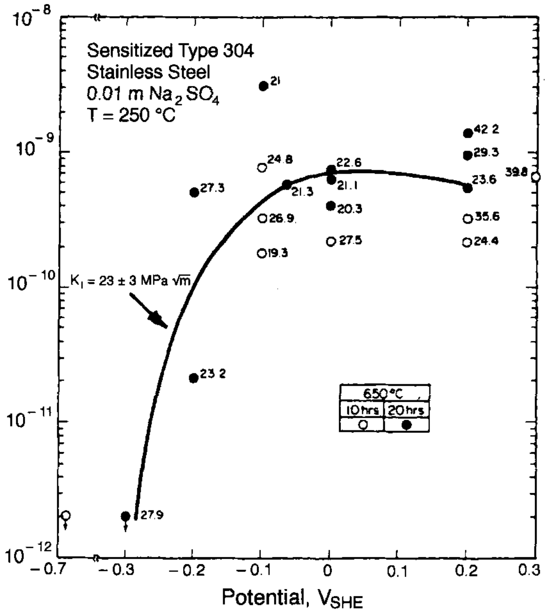

Fig. 11. Effect of potential on the maximum crack growth rate for sensitized Type 304SS in 0.01 m Na_2SO_4 at 250 °C. Numbers denote K_I values [29]. Reproduced from Proc. 9th Int. Congr. Met. Corros., Vol. 2, pp. 185–201 (1984) by permissioin of the National Research Council of Canada.

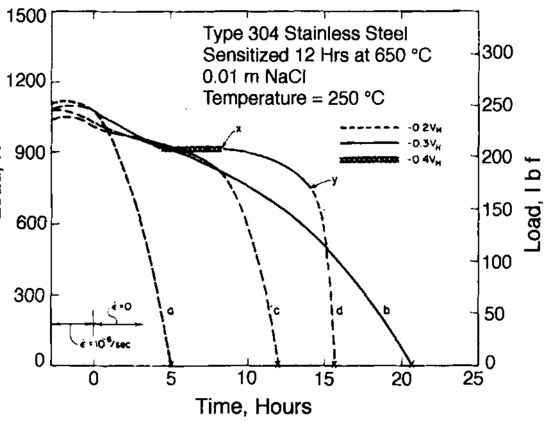

Fig. 12. Effect of potential on load vs. time plots during propagation of intergranular cracks in sensitized Type 304SS in 0.01 m Na_2SO_4 solution at 250 °C [29]. Reproduced from Proc. 9th Int. Congr. Met. Corros., Vol. 2, pp. 185–201 (1984) by permission of the National Research Council of Canada.

sensitized Type 304SS measured in dilute Na_2SO_4 (0.01 m) solutions at 250 °C using wedge opening loading fracture mechanics specimens. At potentials below −0.3 V_{SHE}, crack growth rates were found to be lower than the minimum detectable limit of ~ 10^{-11} m/s, but on increasing the potential by as little as 0.1 V in the positive direction, the crack growth rate increases by a factor of more than 100. In a second set of experiments, crack growth could be "switched off" in CERT specimens under continuous strain by changing the potential in the negative direction by 500 mV (−0.20 V_{SHE} to −0.70 V_{SHE}). By switching the potential back in the positive direction by 500 mV (to −0.20 V), it was possible to "restart" the crack, resulting in a relaxation of the load, even though the specimen was being continuously strained [28, 29]. In a third set of experiments, straining was stopped once a crack had initiated in a CERT specimen at the maximum stress (Fig. 12). Provided that the potential was maintained at $-0.2\ V_{SHE}$ (for a sensitized Type 304SS specimen in 0.01 M NaCl solution), the load relaxed rapidly as the crack propagated through the matrix. If the potential was changed to $-0.3V_{SHE}$, the load still relaxed, but at a much slower rate. However, on switching the potential to $-0.40\ V_{SHE}$, the relaxation in the load stopped and the load remained constant for at least 4 h (indicating that if cracking occurs during this period, the crack growth rate is less than 10^{-11} m/s). On switching the potential back to $-0.3\ V_{SHE}$, the crack was observed to reactivate and, on further increasing the potential to $-0.20\ V_{SHE}$, crack extension accelerated [28, 29]. Accepting that a crack growth rate of 10^{-11} m/s represents "no crack growth" (i.e., the crack grows less than 0.3 mm in one year), the experiments described above clearly demonstrate that the critical potential is indeed an "electrochemical switch."

Practical use of this phenomenon is now being made in the control of IGSCC in the heat-affected zones adjacent to welds in Type 304SS recirculation piping in commercial nuclear boiling-water reactors (BWRs). The criterion for protection is that the potential should be displaced to a value more negative than $-0.23\ V_{SHE}$; indeed, this value has been accepted by the Nuclear Regulatory Commission based upon short-term in-reactor tests [30].

Other metal and alloy systems exhibit critical potentials for specific corrosion processes. For example, pressure-vessel steels (A533B and A508-II and -III) have been shown to crack in pure water, and also in simulated pressurized-water reactor (PWR) primary environments at 288 °C only at potentials above approximately $-400\ mV_{SHE}$, which is about 300 mV more positive than the normal corrosion potential in a fully deaerated environment [31, 32]. Transgranular cracks on round CERT specimens are found to nucleate at pits, some of which form by dissolution of emergent MnS inclusions, and apparent crack growth rates of the order of 10^{-7} cm/s are calculated from the dimension of the deepest crack and the failure time. Of course, because no measure of the initiation time is available, the true crack growth rate could be as much as an order of magnitude higher under these severe straining conditions.

It has long been known that the corrosion behavior of Alloy-600 is considerably more complex than that of the austenitic stainless steels, with different forms of attack (pitting, intergranular attack, IGSCC) occurring within more-or-less well-defined potential regions across the entire potential range that is accessible for this alloy. Different forms of attack occur in different environments, including those that are characteristic of the primary and secondary sides of PWRs. This subject also has been extensively reviewed elsewhere, so that this account will be restricted to a discussion of the critical potentials for specific forms of attack.

The pitting behavior of Alloy-600 in high-temperature aqueous environments has been investigated by Karaminezhaad-Ranjbar et al. [33], Jeon and co-workers [34], and Park and Szklarska-Smialowska [35]. The results of these studies, where comparisons can be made, are only in fair agreement, most probably due to the wide variability in the properties of the alloy. For example, Karaminezhaad-Ranjbar et al. [33] found that the pitting potential of mill-annealed Alloy-600 in buffered sodium

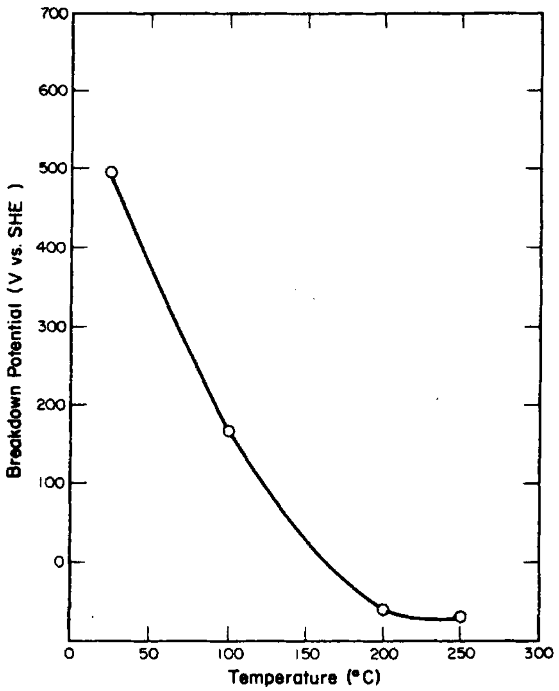

Fig. 13. Plot of breakdown potential vs. temperature for Alloy 600 in buffered 0.1 M NaCl solution. Flow velocity = 0 cm/s [33]. Reproduced from Corrosion J. 41, 197 (1985) by permission of the Editor.

chloride solution (0.1 M NaCl + 0.001 M H_3BO_3 + 0.001 M LiOH) drops precipitously from approx. 500 mV_{SHE} at 25 °C, to approx. −100 mV_{SHE} at 200 °C, but then remains constant at higher temperatures (Fig. 13). Similar findings were made by Jeon et al. [34] (Fig. 14) and by Park and Szklarska-Smialowska [35] (Fig. 15), although the latter report pitting potentials at 250 °C that are almost 200 mV more negative than those of the other workers [33, 34]. On the other hand, the data Karaminezhaad-Ranjbar et al. [33] and Park and Szklarska-Smialowska [35] do not compare well with those of Jeon and co-workers [34] at lower temperatures at comparable chloride concentrations. This is not surprising, given the complex nature of the substrate and the differences in the environments employed in these studies. Most importantly, copper salts are found to have a profound impact on the susceptibility of Alloy 600 to pitting attack, as shown by the "pitting susceptibility diagram" of Park and Szklarska-Smialowska [35] (Fig. 16). However, these observations are accounted for by the observed effect of Cu^{2+} on the corrosion potential, as noted by the authors [35], and pitting in the copper-containing solutions occurs only when the corrosion potential exceeds (i.e., is more positive than) the pitting potential measured in the copper-free (but chloride-containing) system. Accordingly, the role of copper is that of a "chemical potentiostat," and the fundamental reason for the nucleation and growth of pits remains the same (i.e., the corrosion potential exceeds a critical value for the nucleation of damage).

A considerable amount of work has also been reported on cracking and intergranular attack (IGA) in Alloy 600 in simulated PWR steam-generator secondary

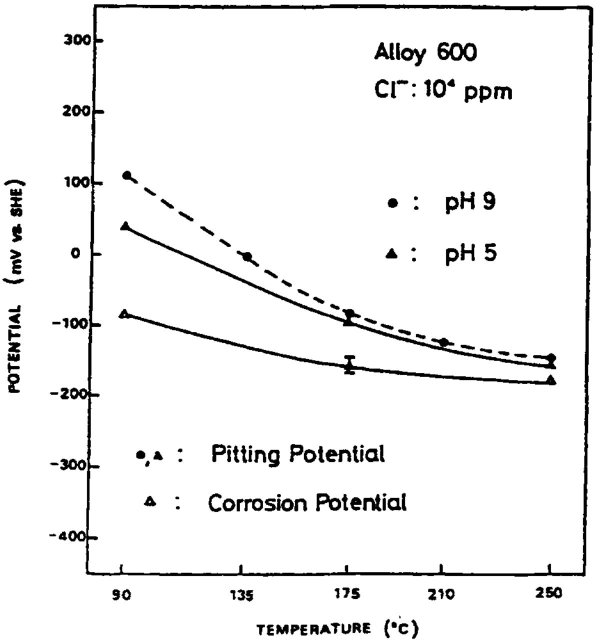

Fig. 14. Effect of the temperature on the pitting potential of Alloy 600 in 10^4 ppm Cl^- solution of pH 5 and 9 [34]. Reproduced with permission.

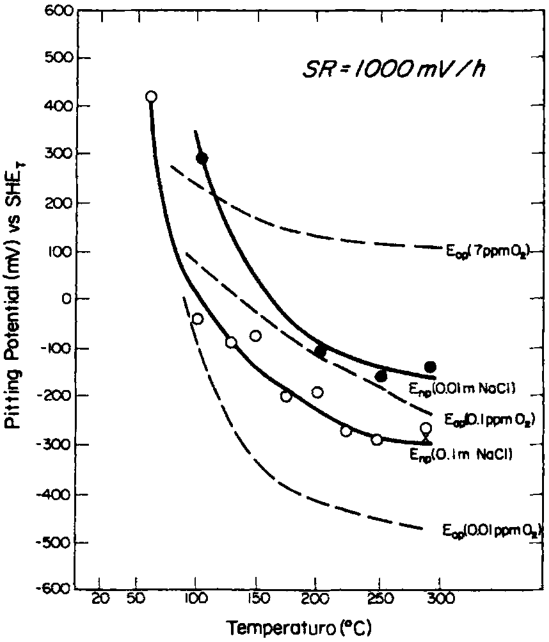

Fig. 15. The pit nucleation potential (E_{np}) of a clean surface of alloy 600 in deaerated NaCl solutions as a function of chloride concentration and temperature, and the open-circuit potential (E_{op}) of Alloy 600 in water as a function of dissolved oxygen concentration and temperature [35]. Reproduced with permission. Copyright 1985 by the American Nuclear Society, La Grange Park, Illinois.

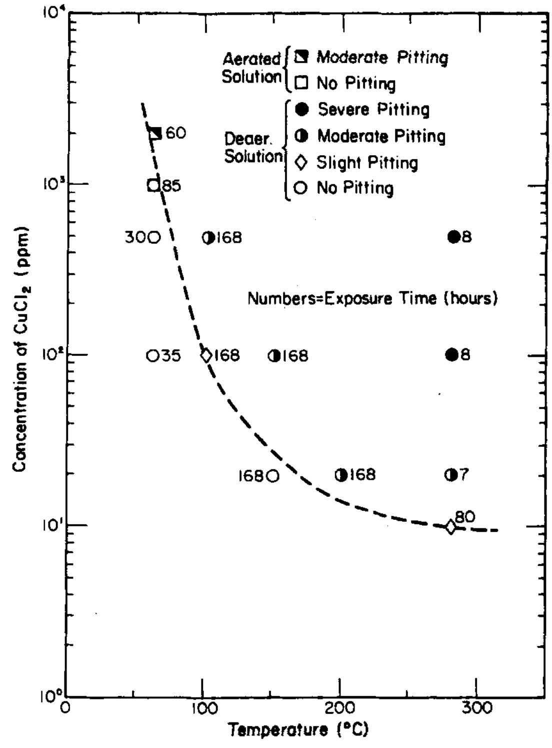

Fig. 16. Pitting susceptibility diagram for a clean surface of Alloy 600 tubing in recirculating $CuCl_2$ solutions as a function of $CuCl_2$ concentration and temperature [35]. Reproduced with permission. Copyright 1985 by the American Nuclear Society, La Grange Park, Illinois.

side solutions. Much of this work has been carried out in concentrated alkaline solutions (e.g., 25 M NaOH) at relatively low temperatures (e.g., 140 °C), so that the direct relevance to secondary side cracking in PWRs is debatable. Nevertheless, the complex nature of the fracture behavior of Alloy 600 in concentrated alkaline solution is well illustrated by the data shown in Fig. 17 where, for mill-annealed material, at least three zones of environment-enhanced fracture are evident with both intergranular and transgranular cracking being observed. Even the solution-annealed alloy exhibits susceptibility to IGSCC at potentials just positive to the open-circuit value, although this may simply reflect the difficulty in completely redissolving grain boundary carbides because of the low solubility of carbon in the predominantly nickel matrix.

Work on caustic cracking of Alloy 600 at steam generator operating temperatures has also been reported. For example, Bandy and VanRooyen [37], using C-ring specimens under potentiostatic control with a nickel wire as reference, found that intergranular crack growth in Alloy 600 in 10% NaOH + 0.1% Na_2CO_3 solution at 300 °C occurs at potentials from 100 to 300 mV more positive than the open-circuit value. On the other hand, IGA was observed even at the open-circuit potential, but the extent of attack becomes more pronounced as the potential is made more positive.

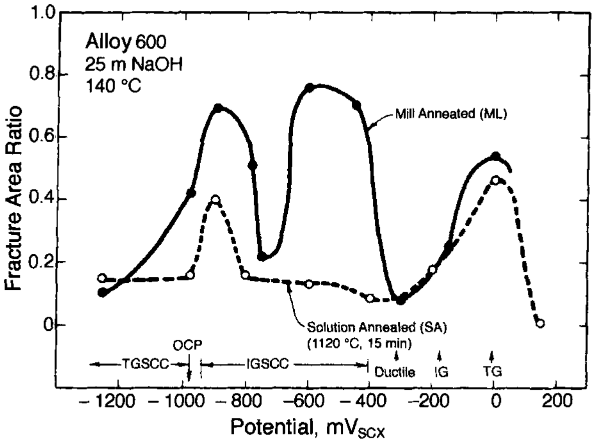

Fig. 17. Fracture area ratio (IG/ductile) vs potential for mill annealed and solution annealed Alloy 600 in 25 m NaOH at 140 °C. Regions of intergranular, transgranular and ductile fracture are marked [36]. Reproduced from Corrosion J. 41, 540 (1985) by permission of the Editor.

The conditions under which IGA occurs in Alloy 600 in high-temperature caustic solutions (20–25% NaOH, 290–320 °C) have been somewhat better defined, from an electrochemical viewpoint, in the work of Cayla et al. [38]. These workers employed an external Hg/HgO reference electrode that was calibrated to the "reversible hydrogen electrode (RHE)" scale at the pH and temperature of interest. However, even in this case, it is not clear to which hydrogen partial pressure this scale refers (presumably $f_{H_2} = 1$), which again emphasizes the need for the nuclear corrosion community to settle on a single potential scale that is understood by everyone involved in this type of work. Nevertheless, Cayla et al. [38] found that IGA occurs in a limited range of potential close to (within 100 mV of) the reversible hydrogen potential.

The situation is somewhat better with respect to primary side cracking because the environment can be more closely defined due to the known composition of the coolant and to the lack of boiling, and because some work has begun to appear in which the electrochemical conditions are clearly stated. Thus, Totsuka and Szklarska-Smialowska [39, 40] found that annealed Alloy 600 in 0.01 m H_3BO_3 + 0.001 m LiOH suffers intergranular fracture at potentials more negative than a critical value of about -0.8 V_{SHE}. This critical potential is about 150 mV more positive than the open-circuit value in the presence of about 0.1 MPa (~ 1 atm) of hydrogen (Fig. 18). The susceptibility of the material to fracture, and the locations of the cracks, were found to be strongly correlated with the (local) hydrogen content, leading to a strong case that hydrogen embrittlement is the primary cause of failure. Szklarska-Smialowska [40] also reports that IGSCC occurs in Alloy 600 in this environment at anodic potentials in the active-to-passive region (Fig. 18) and in the transpassive potential region. The data of Szklarska-Smialowska and co-workers [40] enable us to

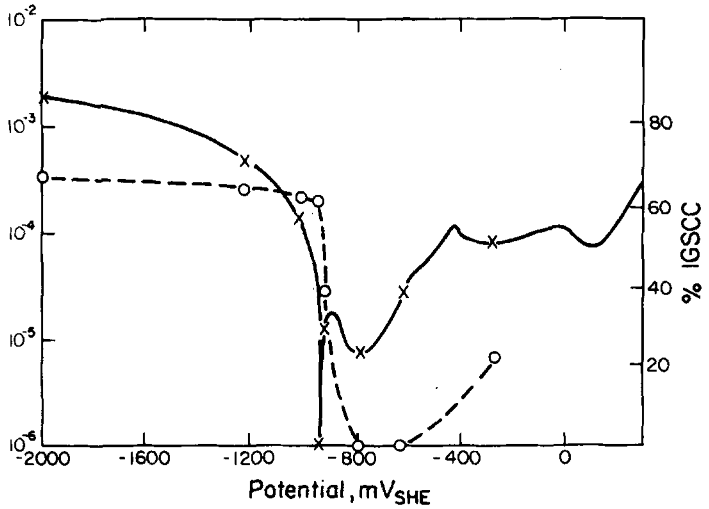

Fig. 18. Polarization curves measured for Alloy 600 in lithiated water at 350 °C and percentages of IGSCC fracture in slow strain rate test specimens with humps [40]. Reproduced with permission.

establish with some confidence the fracture behavior of Alloy 600 in the neighborhood of the open-circuit potential in primary-side heat-transport media.

6.2 Calculation of the ECP

The direct measurement of the ECP in thermal power plant heat-transport circuits is now being made on a regular basis, and considerable data have been accumulated (see Indig et al. [30, 44], for example). However, some regions in heat-transport circuits, particularly those in nuclear reactors, are virtually and practically inaccessible, so that the direct measurement of the ECP is impossible. The alternative to direct measurement is to calculate corrosion potentials using a physically viable model. This approach has been adopted by Macdonald [43], who developed a mixed-potential model (MPM) to calculate the corrosion potential under various chemical conditions in high-temperature water. The MPM is based on the Wagner–Traud hypothesis that the anodic and cathodic partial reactions that occur on a freely corroding metal surface under conditions of uniform attack are separable and that charge must be conserved. In this case, the corrosion potential is given by the solution to the equation

$$\sum_j i_{\mathrm{O/R},j}(E) + i_{\mathrm{corr}}(E) = 0 \tag{28}$$

where $i_{\mathrm{O/R},j}$ is the current density for the jth redox couple, and i_{corr} is the corrosion current density, both of which are functions of the potential E.

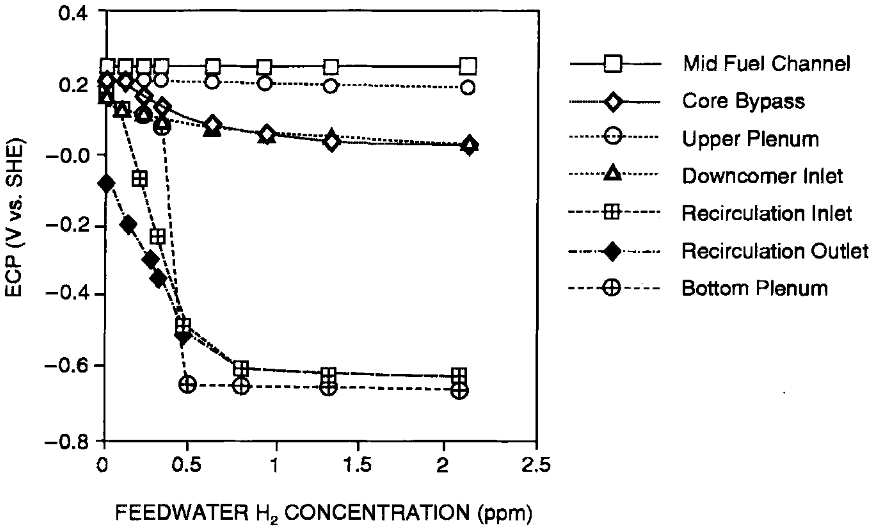

Fig. 19. Calculated corrosion potentials for various in-vessel components of a boiling-water reactor.

Using this approach, corrosion potentials have been calculated for various components in the heat-transport circuit of a BWR, as shown in Fig. 19, as a function of the concentration of hydrogen added to the feedwater. The calculations predict that the lower plenums and recirculation systems of many BWRs can be protected by hydrogen water chemistry, but that those components that are exposed to high radiation fields and/or high concentration of radiolysis products cannot be protected, at least under full-power operating conditions. Similar calculations have been carried out [46] for in-vessel materials in PWRs, in order to explore the susceptibility of various components to intergranular fracture.

The two cases described above were chosen to demonstrate that useful predictions can be made of the behavior of the materials on the basis of mixed-potential models. These calculations also highlight the critical role played by the electrochemical potential in determining whether failure will or will not occur, and they demonstrate the promising methods for calculating the ECP in various environments that are practically important.

6.3 Effect of Fluid Flow on the ECP

Only a few systematic studies have been made of the effect of fluid flow on the ECP of power plant alloys in high-temperature water, even though theory suggests that the effect should be substantial under certain conditions [43]. Because the theoretical predictions, from the mixed-potential model (MPM) [43] and more recently the advanced mixed-potential model (AMPM) [47], preceded systematic experimental studies, it is appropriate to discuss the theoretical predictions first.

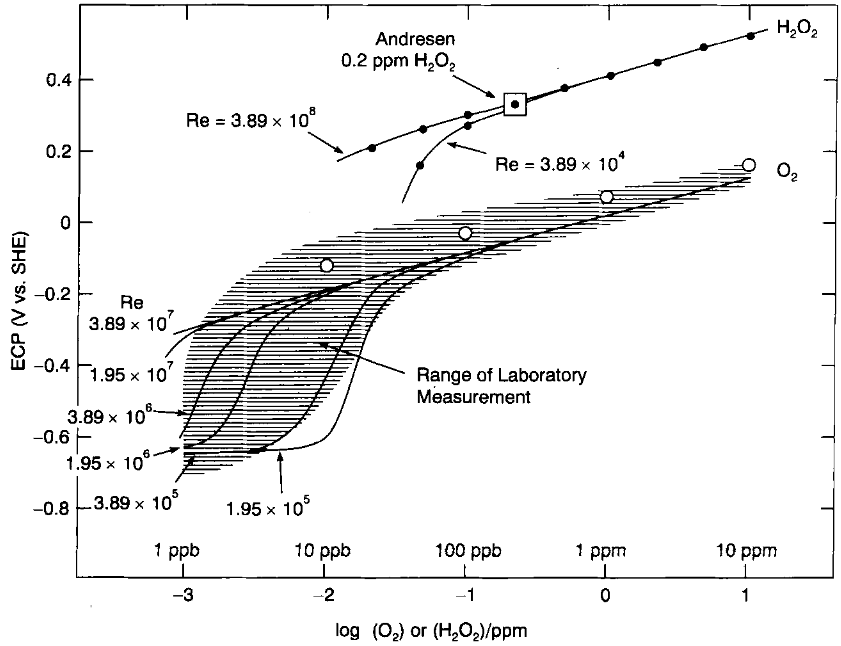

Fig. 20. ECP vs. oxygen (lower curves) and hydrogen peroxide (upper curves) concentration. Calculated for $SF(O_2) = 0.44$ and $SF(H_2O_2) = 1.0$, respectively; O, $SF(O_2) = 1.0$ SF(X) corresponds to the factor used to scale the exchange current density for species X. [43]. Reproduced from Corrosion J. 48, 194 (1992) by permission of the Editor.

Predicted plots of ECP for Type 304SS versus oxidant concentration (oxygen or hydrogen peroxide) at several flow rates (Reynolds numbers) are shown in Fig. 20. Also plotted in this figure is a compilation of experimental data (laboratory and plant) for oxygenated solutions (shaded area) and one experimental datum for 0.2 ppm H_2O_2. The values for the kinetic parameters (reduction of oxygen) were taken from the work of Lee (see [43]), and were assumed to hold also for the reduction of hydrogen peroxide. Good agreement is obtained between the calculated ECP and that observed experimentally. Of particular interest is the low oxygen concentration regime where the significant effects of flow rate are predicted. Thus, the MPM indicates that increasing Reynolds number shifts the ECP in the positive direction by 3–400 mV, even though the oxygen concentration is held constant at 1–10 ppb. This sensitivity to flow rate probably accounts for the large scatter in the experimental results (shaded area) at low oxygen concentrations. (Few experimental studies have employed controlled, or even known, hydrodynamic conditions.) The electrochemical explanation for the sensitivity of the ECP to fluid flow rate at low oxygen concentrations is simply that the concentration of the cathodic depolarizer (oxygen) at the steel surface is affected by mass transport. As the concentration of oxygen is increased, the supply of oxygen to the surface that is required to consume the electronic current being released by the dissolution of the steel becomes insensitive to mass transport, and the ECP is predicted to be independent of the hydrodynamic properties of the system, as observed. The calculations for oxygenated solutions

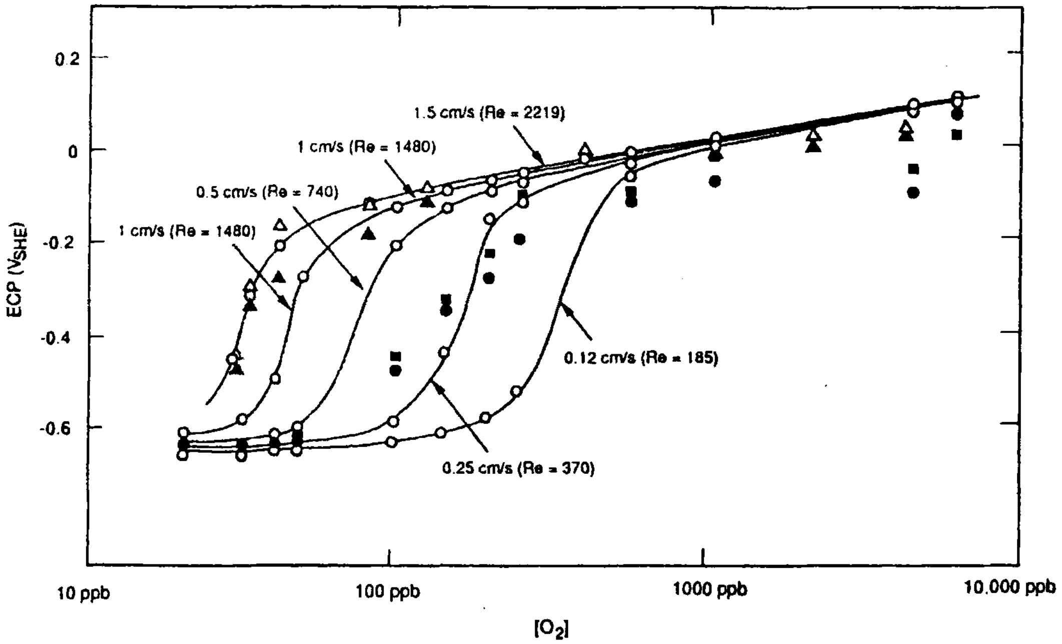

Fig. 21. Plots of ECP vs. oxygen concentration at low Reynolds numbers. Experimental: (●) type 304SS and (■) alloy 182 at 0.12 cm/s; (△) type 304SS and (▲) alloy 182 at 0.216 cm/s. Calculated: (○) for various flow velocities (Reynolds numbers). $T = 288°C$ [51]. Reproduced from Corrosion J. 49, 8 (1993) by permission of the Editor.

represented by the solid lines in Fig. 20 were carried out using an oxygen electrode reaction exchange current density that was optimized (by multiplying that from Lee by the factor 0.44) to yield better agreement of the model with ECP data from an operating BWR. If this correction is not applied, the ECP values for the highest Reynolds number represented by the open circles result. For our present purposes, they are negligibly different from the original calculations. Finally, it is appropriate to note that Niedrach and Stoddard [48] and Ullberg [50] have proposed similar models, but they do not appear to have been developed beyond a qualitative diagrammatic stage (i.e., Evans diagrams), and hence are not capable of providing analytical results of the type shown in Fig. 20. Also, an empirical model has been proposed by Ramp et al. [49] that correlates a very large database for ECP as a function of [H_2], [O_2], [H_2O_2], and flow velocity.

Experimental studies of the effect of flow rate on the ECP of Types 304SS and Alloy 182 in high-temperature water have been reported by Macdonald et al. [51], on Type 316SS under simulated BWR chemistry conditions by Kim et al. [52, 53], and on Type 304SS by Prein and Molander [54]. In the work of Macdonald et al. [51] tubular flow at low flow rates was employed which, while not simulating the exact conditions in BWR coolant circuits did provide a sensitive test of the MPM. A comparison between experiment and theory is shown in Fig. 21. The experimental data do indeed confirm, in a semiquantitative manner, the high sensitivity of the ECP to Reynolds number at low oxygen concentrations. The lack of quantitative agreement between the experimental data and the MPM is due to the fact that the hydrodynamic/mass transport correlation incorporated in the algorithm (which is strictly valid for much higher Reynolds numbers) is not the most appropriate one that could have been used to simulate the experimental data.

Kim et al. [53] obtained the experimental data for Type 316SS in oxygenated solutions at 288 °C as a function of flow rate, as determined by using a rotating-cylinder electrode. Unfortunately, Kim et al. [53] chose not to interpret their data in terms of the MPM, but offered only a qualitative explanation in terms of schematic Evans diagrams. These workers also found that the ECP of stainless steel is shifted in the positive direction with increasing flow rate, although the shift with peripheral velocity of the cylinder is relatively small (100 mV for an increase in the peripheral velocity from 0.665 m/s to 7.32 m/s corresponding to rotational velocities of 200 rpm and 2200 rpm, respectively, for a 2.5-inch (6.35 cm) diameter cylinder). However, their data are in good agreement with the predictions of the MPM shown in Fig. 20, if one notes that they fall within the high mass-transfer rate regime for tubular flow. Under these conditions, the ECP is not a strong function of flow velocity. In this regard, it is important to note that fluid dynamics are fundamentally different for a rotating-cylinder electrode (RCE) than for pipe flow, which is typified by the wide disparity between the critical Reynolds numbers for transition from laminar to turbulent flow ($\mathrm{Re}_{\mathrm{cr}} < 10$ for an RCE, but $\mathrm{Re}_{\mathrm{cr}} > 2000$ for a pipe at ambient temperature). Furthermore, while mass-transfer effects are demonstrably important in determining the ECP, they do not scale in the simple manner obtained by equating the mass-transfer coefficients for the two geometries, as proposed by Kim et al. [52, 53]. The reason for this is that the mass-transfer effects are incorporated in terms that are (approximately) linearly related to the partial currents, which must be summed to zero at the interface, whereas the ECP is incorporated into exponential terms. Thus, the mass-transfer effects and the ECP are related in a highly nonlinear manner.

Recently, Prein and Molander [54], also using a rotating-cylinder electrode, explored the effect of flow velocity (i.e., rotational velocity) on the ECP of Type 304SS in oxygenated water at 288 °C. These workers found that the ECP at low oxygen concentrations is quite sensitive to flow rate, and their data are in semi-quantitative agreement with the MPM.

Although considerable work remains to be done to quantify the effect of flow rate on ECP, the experimental findings to date strongly support the initial predictions of the MPM that the ECP of stainless steel is shifted in the positive direction with increasing flow rate, particularly at low oxygen concentrations. Because the nucleation of localized corrosion occurs only if the ECP is more positive than the critical potential (E_{crit}) for that corrosion process, and since the rate of development of damage increases with increasing [ECP$-E_{\mathrm{crit}}$], it is clear that flow velocity can have a very important impact on the nucleation and development of damage in LWR coolant circuits. However, we refer to this effect as an "indirect" effect, so as to distinguish it from the "direct" effect of oxidizing agents such as oxygen and hydrogen peroxide. The reason for this division will become evident later in this chapter.

6.4 Effect of Fluid Flow on E_{IGSCC}

Work has also been reported on the effect of flow velocity on the critical potential for IGSCC in sensitized water at elevated temperatures. Thus, Fuller and Macdonald [55], using CERTs in an annular flow channel, found that for sensitized Type 304SS in 0.01 M Na_2SO_4 at 288 °C, E_{IGSCC} was independent of flow rate at flow rates ranging from 0 cm to 8 cm/s (Figs. 22 and 23). Note that the same value for E_{IGSCC} (approx. −400 mV) is obtained using the elongation-to-failure (Fig. 22) and the maximum stress (Fig. 23) as the measure of IGSCC susceptibility. In both cases, E_{IGSCC} is not a

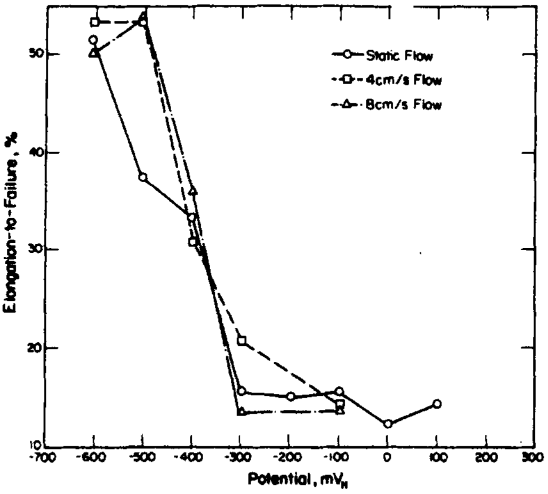

Fig. 22. Elongation-to-failure of sensitized AISI 304SS in 0.01 M Na_2SO_4 solution at 280 °C as a function of applied potential and flow velocity [55]. Reproduced from Corrosion J. 40, 474 (1984) by permission of the Editor.

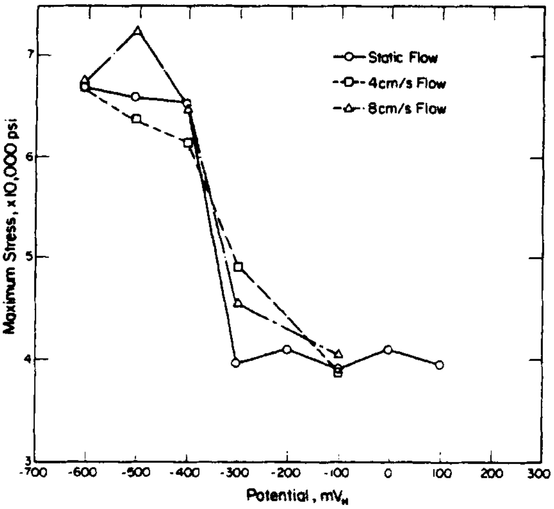

Fig. 23. Maximum stress (10^6 psi = 6.89× 10^6 k) vs. applied potential for sensitized AISI 304SS in 0.01 M Na_2SO_4 at 280 °C as a function of flow velocity [55]. Reproduction from Corrosion J. 40, 474 (1984) by permission of the Editor.

function of fluid flow rate. This finding was later confirmed by Kim and Szklarska-Smialowska.

7 Stress Corrosion Cracking and Corrosion Fatigue

Although fluid flow has been recognized for many years as having an important impact upon corrosion processes, relatively little systematic work has been reported on the effect of hydrodynamic factors on the stress corrosion cracking of steels. Over the past decade, however, considerable advancements have been made in development of experimental techniques for studying the effect of fluid flow on corrosion processes under reactor heat-transport system environmental conditions, as described elsewhere in this chapter. Furthermore, significant theoretical advances are now being made with the development of models for the growth of pits and cracks that incorporate hydrodynamic and mass-transport effects in a deterministic manner.

In this section, we review the literature with respect to the effect of fluid flow on the initiation and growth of cracks in steels, mostly in high-temperature aqueous systems. Our purpose is to identify the important factors that lead to flow-induced effects, as deduced from laboratory experiments and theory, for systems under well-controlled experimental conditions.

7.1 Initiation and Passivity Breakdown

The events that lead to the initiation of stress corrosion (and corrosion fatigue) cracks in high-temperature aqueous systems is a matter of great debate, and has been the subject of a number of recent workshops [56, 57]. Almost all treatments of this problem invoke the concept of a "critical" nucleus, which serves to (1) concentrate the local stress, and (2) establish a local environment that is conducive to the propagation of a crack. The critical nucleus is envisaged as developing from a corrosion pit, from emergent grain boundaries at the surface, from emergent slip bands, or from preexisting flaws, such as grinding damage or machine marks. Regardless of the exact mechanism, the postulate is that a flaw grows to a critical size, at which point it transforms into a crack. The time that transpires from exposure of the surface to the corrosive environment to the transition of the nucleus into a crack is defined as the "crack initiation (or induction) time" ($t^{\mathrm{c}}_{\mathrm{init}}$). This quantity must be distinguished from the "flaw initiation time" ($t^{\mathrm{f}}_{\mathrm{init}}$), which may be very short for surfaces that contain preexisting crevices or very long for microscopically smooth surfaces. In any event, we may write

$$t^{\mathrm{c}}_{\mathrm{init}} = t^{\mathrm{f}}_{\mathrm{init}} + t^{\mathrm{c}}_{\mathrm{f}} \tag{29}$$

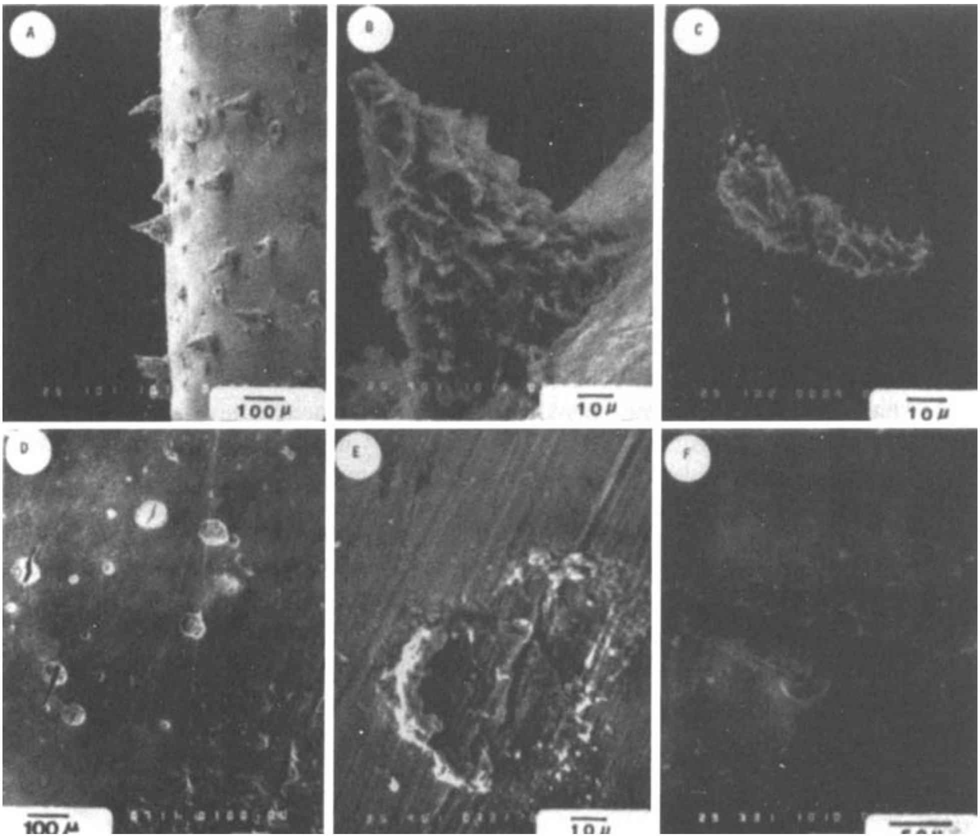

Fig. 24. SEMs of the side surfaces of A508Cl.2 CERT specimens tested in high-purity water containing 8 ppm of oxygen at 250 °C. (**A**) As-tested surface appearance; (**B**) high magnification of the cone-shaped hematite in (**A**); (**C**) hematite crystal straddling crack in steel; (**D**) after descaling of (**A**) in Clark's solution; (**E**) the depression observed after 12.5 h; (**F**) the depression across a crack after 28 h [58]. The bars indicate the scale (μm). Reproduction from Corrosion J. 38, 136 (1982) by permission of the Editor.

where t_f^c is the time required for the growth of a viable flaw into a viable crack. Equation (29) defines the crack initiation time.

The fact that cracks can nucleate at pits, at least in the case of carbon and low alloy steels, is shown in Fig. 24. In this particular case [58], smooth steel (A508–Cl.2) round tensile specimens, loaded under constant strain rate conditions, had been exposed to oxygenated pure water (8 ppm O_2) at 25 °C for 28 h. Numerous pits were observed on the surface, many of which led to cracks. The susceptibility of this steel to various forms of localized corrosion in oxygenated, high-temperature, pure water is summarized in Fig. 25, which displays the combinations of temperature and oxygen concentration at which pitting and stress corrosion cracking occur. Plotted in Fig. 26 is the failure time versus temperature, illustrating that the cracking susceptibility, as determined by a CERT, is greatest at highest $[O_2]$ (and hence potential) at 250 °C.

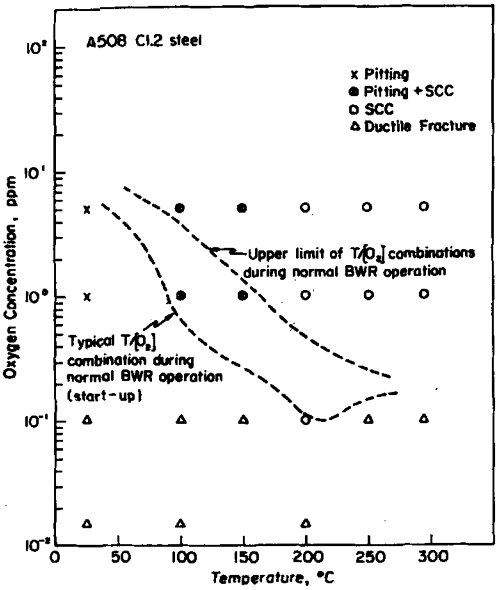

Fig. 25. Crack morphology and failure modes of A508Cl.2 CERT specimens as a function of temperature and oxygen concentration [58]. Reproduced from Corrosion J. 38, 136 (1982) by permission.

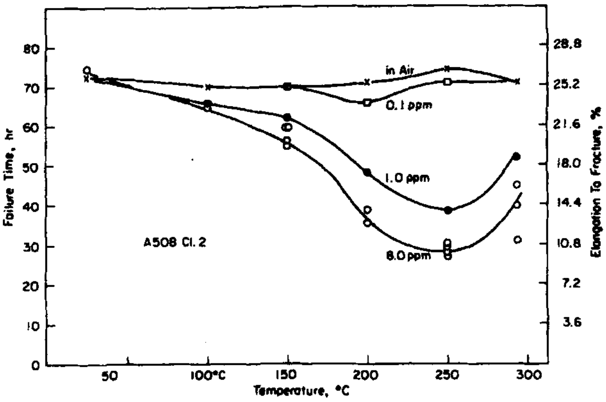

Fig. 26. Elongation to fracture of A508Cl.2 as a function of temperature and oxygen concentration [58]. Reproduced from Corrosion J. 38, 136 (1982) by permission of the Editor.

As a second example, we show in Fig. 27 the nucleation of intergranular stress corrosion cracks in sensitized Type 304SS as observed by Diercks and Dragel at the Argonne National Laboratory (see [56]). The cracks were found to nucleate from pits or at intergranular penetrations (e.g., intergranular attack, IGA). In other cases, cracks are found to nucleate from MnS inclusion but, in this case too, the primary event is probably the formation of a pit which acts as a stress riser. Examination of many micrographs indicates that the critical nucleus is of the order of 30–100 μm deep.

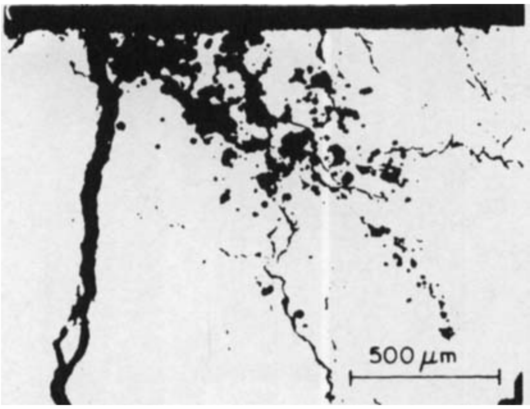

Fig. 27. Surface pitting and cracking on outer surface of stainless steel piping [56]. Copyright © 1988. Electric Power Research Institute EPRI NP-5828. Proceedings: Workshop on Initiation of Stress Corrosion Cracking under LWR Conditions. Reprinted with permission.

The possibility that cracks nucleate at emergent slip planes (at the surface) has been noted in various studies. This also appears to be a viable mechanism for the initiation of cracks in Type 304SS in high-temperature oxygenated water. We cite, as an example of this phenomenon, recent micrographs of constant-extension-rate specimens of sensitized Type 304SS in oxygenated water (1 ppm O_2) at 288 °C (Fig. 28) [57]. Slip bands are clearly visible on the surface, and while the large central crack appears to nucleate at an emergent grain boundary, smaller microcracks appear to nucleate at emergent slip bands. In this mechanism of initiation, each of the N slip steps are characterized by a Burgers vector, $\tilde{b}$, with the band intersecting the surface to form a local crevice. The dimensions of this crevice are readily calculated by assuming a geometrical model (in this case a 45° intersection of the slip planes with the surface) and the number of slip planes (N). As a reasonable estimate, we take $N = 1000$ and $\tilde{b} = 3$ Å to yield a crevice of the order of 0.3 μm under conditions of local yielding.

The final case that we wish to cite is the very intriguing one that arises from the work of Kobayashi et al. [41]. In this case, two identical Type 304SS (sensitized) SSRT specimens were stained to failure in two aqueous environments at 288 °C. One environment simulated BWR-grade water (ambient-temperature conductivity of < 0.1 mS/cm), and the other environment was contaminated with 1 ppm ($\sim 10^{-5}$ m) H_2SO_4. The pH of the pure-water environment is estimated from the dissociation product of water (K_w) to be ~ 5.6, whereas that of the environment contaminated with sulfuric acid is estimated to be ~ 5. The fracture behaviors in the two cases were characterized using FRASTA (fracture reconstruction by surface topographical analysis), as shown in Figs. 29 and 30. It was found that, in the case of the H_2SO_4-contaminated environment, the fractures nucleated inside the specimen, whereas in the pure-water environment the cracks nucleated at the periphery of the sample in contact with the external environment. The latter is clearly a case of stress corrosion cracking, but the former raises the very real (and interesting) possibility that cracks nucleate by a hydrogen-induced fracture mechanism in this alloy in slightly acidic environments.

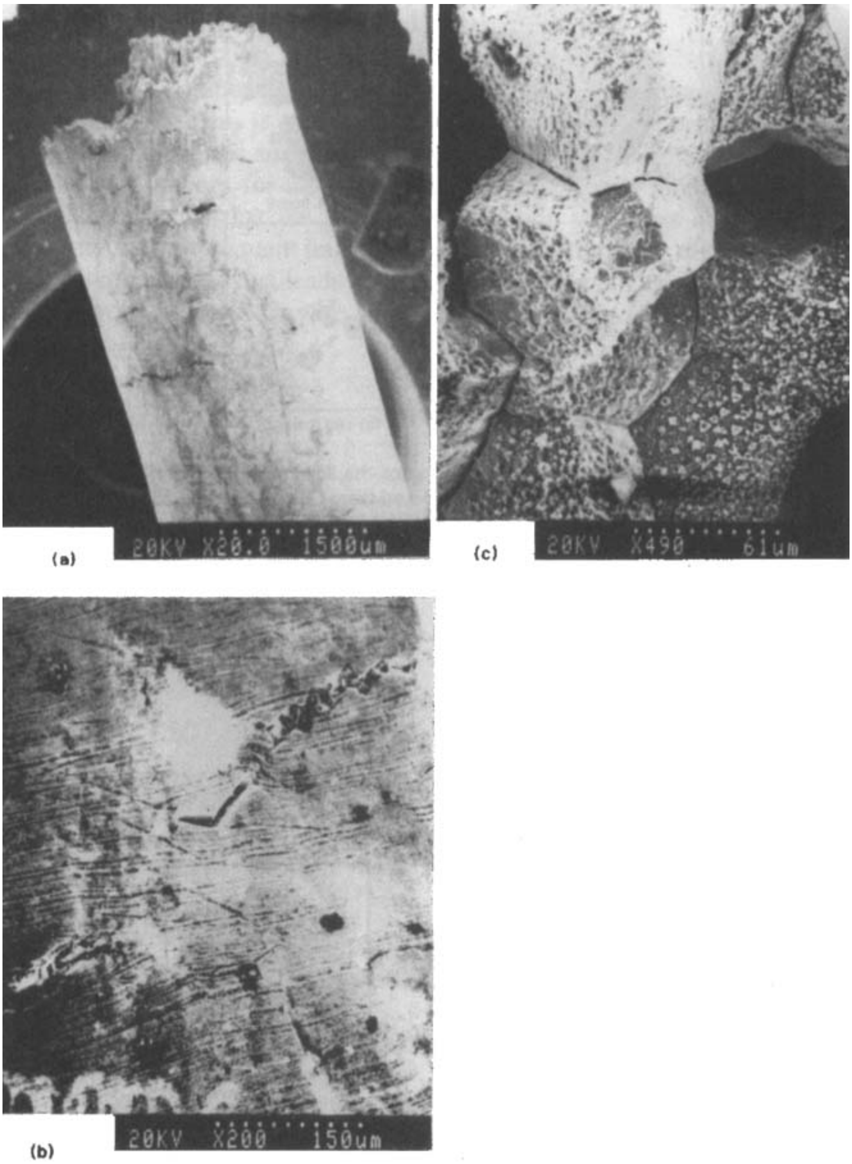
(a)
20KV X20.0 1500um
(c)
20KV X490 61um
(b)
20KV X200 150um

Fig. 28. Micrographs of a fractured specimen, showing numerous small cracks on the gauge length (enlarged in (b)), and intergranular fracture; (c) enlargement of fracture surface [57]. Copyright © 1991. Electric Power Research Institute/EPRI ER-7247. Intergranular Corrosion of Stainless Steel. Vol. 1: Mechanism of Crack Initiation. Reprinted with permission.

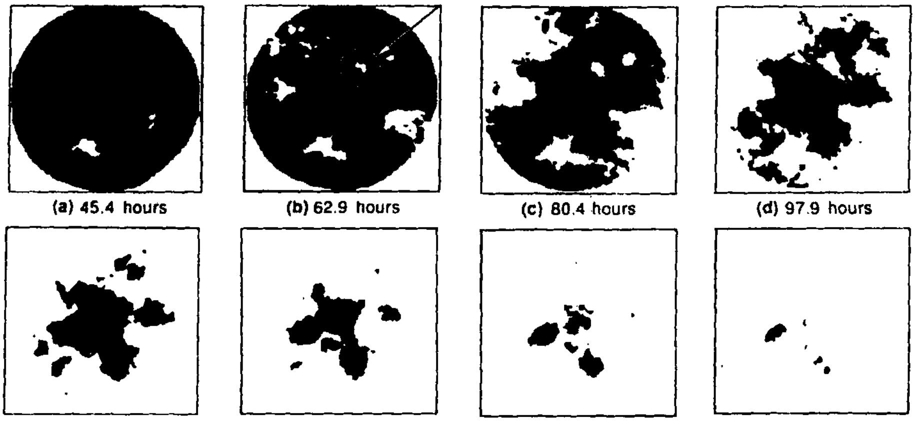

(a) 45.4 hours (b) 62.9 hours (c) 80.4 hours (d) 97.9 hours

(e) 115.4 hours (f) 132.8 hours (g) 150.3 hours (h) 167.8 hours

Fig. 29. A series of fractured area projection plots for the sensitized Type 304SS specimen tested in water contaminated with 1 ppm H_2SO_4 [47]. Reproduced from Corrosion J. 47, 528 (1991) by permission of the Editor.

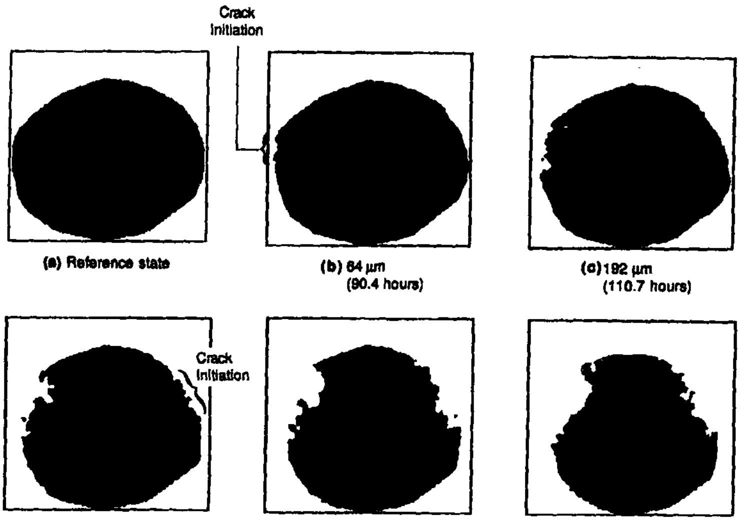

(a) Reference state

(b) 64 µm (90.4 hours)

(c) 192 µm (110.7 hours)

(d) 321 µm (131.1 hours)

(e) 449 µm (151.4 hours)

(f) 577 µm (171.8 hours) (test interruption)

Fig. 30. A series of fractured area projection plots for the sensitized Type 304SS specimen tested in clean water [41]. Reproduced from Corrosion J. 47, 528 (1991) by permission of the Editor.

7.2 Modeling of the Passivity Breakdown

Even if the surface is not perfectly smooth, the initial event that must occur in the development of a nucleus is passivity breakdown, in which the protective oxide layer is ruptured to expose the underlying metal to the aqueous environment. The most highly developed theory for this process is the point defect model (PDM) [59–65]. This model postulates that the generation of cation vacancies at the film/solution interface, and their subsequent transport across the barrier layer of the passive film, is the fundamental process that leads to passivity breakdown. Once a vacancy arrives at the metal/film interface, it may be annihilated by reaction (i) in Fig. 31:

$$m + V_M^{\chi'} \xrightarrow{k_1} M_M + V_m + \chi e' \tag{30}$$

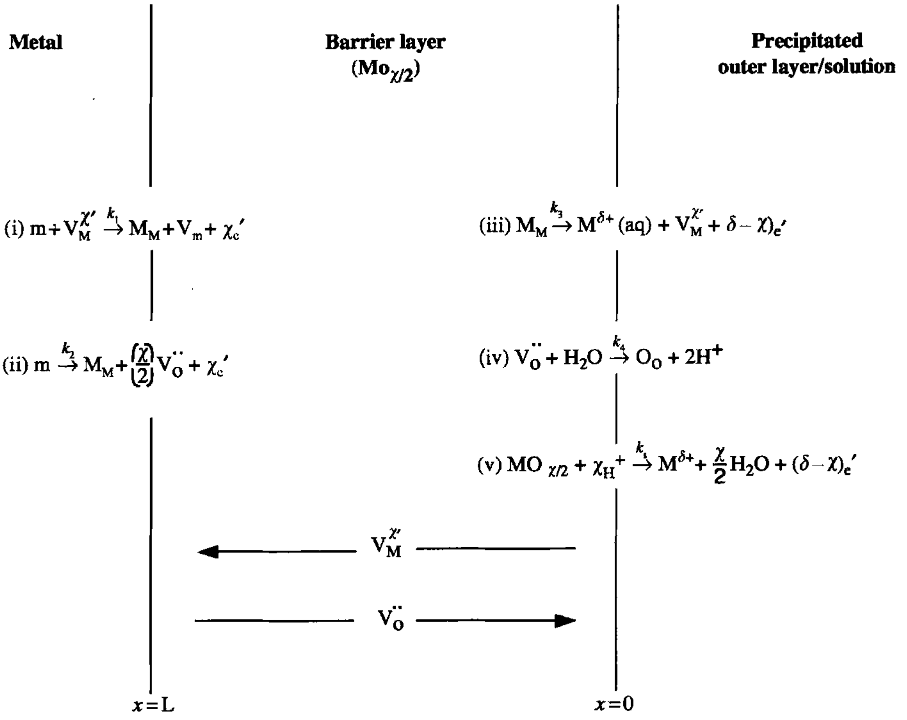
Metal
Barrier layer (Mo$_{\chi/2}$)
Precipitated outer layer/solution
(i) $m+V_M^{\chi'} \xrightarrow{k_1} M_M+V_m+\chi_e'$
(ii) $m \xrightarrow{k_2} M_M+\left(\frac{\chi}{2}\right)V_O^{\cdot\cdot}+\chi_e'$
(iii) $M_M \xrightarrow{k_3} M^{\delta+}(aq) + V_M^{\chi'} + (\delta-\chi)_e'$
(iv) $V_O^{\cdot\cdot} + H_2O \xrightarrow{k_4} O_O + 2H^+$
(v) $MO_{\chi/2} + \chi_H^+ \xrightarrow{k_5} M^{\delta+} + \frac{\chi}{2}H_2O + (\delta-\chi)_e'$
$V_M^{\chi'}$
$V_O^{\cdot\cdot}$
$x=L$
$x=0$

Fig. 31. Schematic of physicochemical processes that occur within a passive film according to the point defect model: m = metal atom; M_M = metal cation in cation site; O_O = oxygen ion in anion site; $V_M^{\chi'}$ = cation vacancy; $V_O^{\cdot\cdot}$ = anion vaccancy; V_m = vacancy in metal phase. During film growth, cation vacancies are produced at the film/solution interface, but are consumed at the metal/film interface. Likewise, anion vacancies are formed at the metal/film interface, but are consumed at the film/solution interface. Consequently, the fluxes of cation vacancies and anion vacancies are in the directions indicated. Note that reactions (i), (iii), and (iv) are lattice-conservative processes, whereas reactions (ii) and (v) are not. Reproduced from J. Electrochem, Sec. 139, 3434 (1992) by permission of the Electrochemical Society.

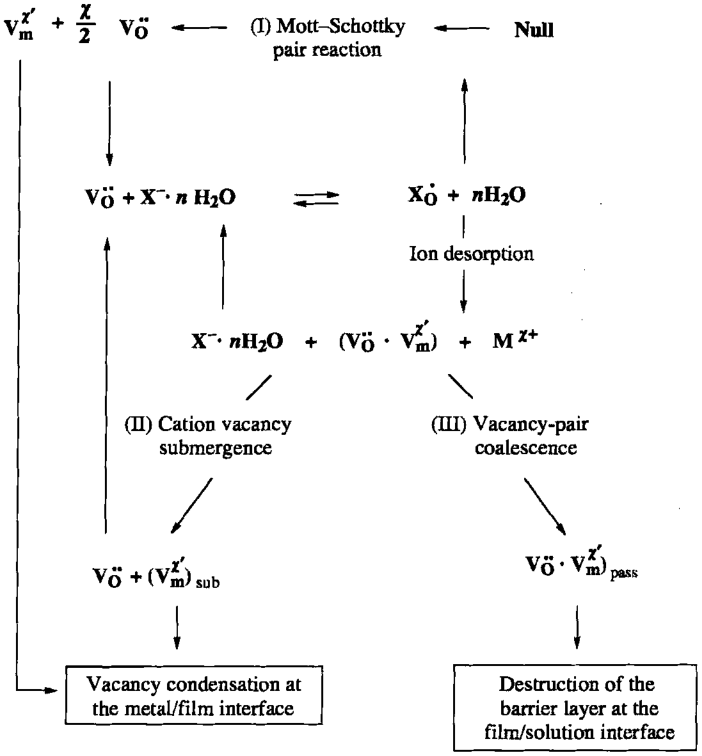
$V_m^{\chi'} + \frac{\chi}{2} V_O^{\cdot\cdot}$
(I) Mott–Schottky pair reaction
Null
$V_O^{\cdot\cdot} + X^{-} \cdot nH_2O$
$X_O^{\cdot} + nH_2O$
Ion desorption
$X^{-} \cdot nH_2O + (V_O^{\cdot\cdot} \cdot V_m^{\chi'}) + M^{\chi+}$
(II) Cation vacancy submergence
(III) Vacancy-pair coalescence
$V_O^{\cdot\cdot} + (V_m^{\chi'})_{sub}$
$V_O^{\cdot\cdot} \cdot V_m^{\chi'})_{pass}$
Vacancy condensation at the metal/film interface
Destruction of the barrier layer at the film/solution interface

Fig. 32. Summary of proposed reactions leading to passivity breakdown. Reproduced from J. Electrochem, Sec. 139, 3434 (1992) by permission of the Electrochemical Society.

where m is a metal atom on the metal side of the metal/film interface, V_m is a vacancy in the metal, and M_M is a cation in the film. However, if the vacancy flux is sufficiently high for complete annihilation not to occur, the excess vacancies may condense at the metal/film interface to cause local decohesion of the barrier layer from the metal substrate. The film thins locally because film growth (at the metal/film interface) can only occur if the barrier layer is in intimate contact with the substrate (Fig. 32). We note that the process described above will tend to occur at localities on the surface that are characterized by high cation vacancy diffusivities (i.e., at the so-called "weak spots," such as ghost grain boundaries, intersections of the barrier layer with precipitates (e.g., MnS or Cr_2O_3 inclusions), and emergent slip planes).

The processes that we invoked in the past [65] to explain passivity breakdown that is induced by an aggressive anion (e.g., Cl^-) are shown in Fig. 33. However, passivity breakdown also occurs in environments that are "free" of aggressive anions, with notable examples being passivity breakdown on steels and stainless steels in high-temperature pure water. Experimentally, it is found that breakdown occurs only when the corrosion potential is more positive than some critical value. Accordingly, it is reasonable to invoke a charge-transfer reaction as the process that generates cation

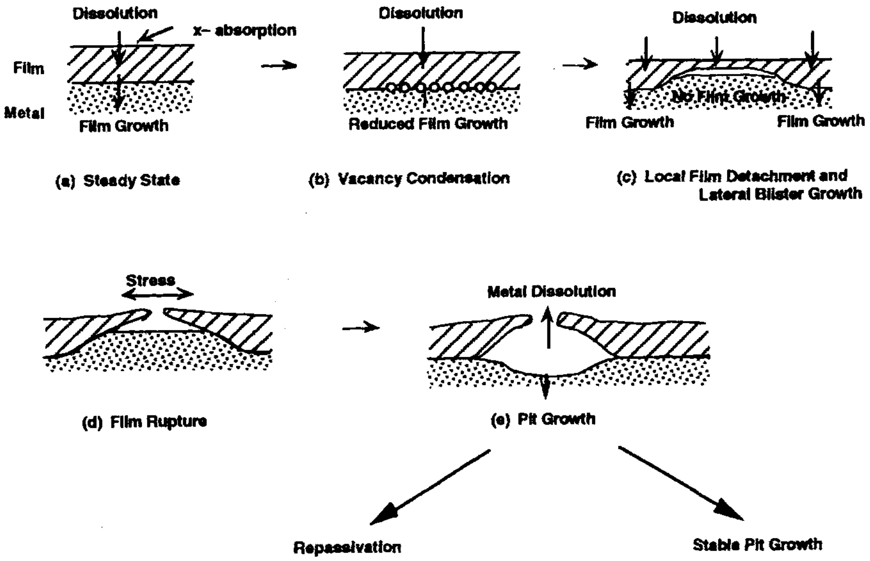
Dissolution
x- absorption
Film
Metal
Film Growth
(a) Steady State
Dissolution
Reduced Film Growth
(b) Vacancy Condensation
Dissolution
No Film Growth
Film Growth
Film Growth
(c) Local Film Detachment and Lateral Blister Growth
Stress
(d) Film Rupture
Metal Dissolution
(e) Pit Growth
Repassivation
Stable Pit Growth

Fig. 33. Cartoon outlining various stages of pit nucleation according to the point defect model. Reproduced from J. Electrochem, Sec. 139, 3434 (1992) by permission of the Electrochemical Society.

vacancies at the film/solution interface. Following our previous work [65], we suggest the following reaction,

$$\mathrm{Cr_{Cr}} + 4\mathrm{H_2O} \rightarrow \mathrm{CrO_4^{2-}} + \mathrm{V_{Cr}^{3'}} + 8\mathrm{H^+} + 3\mathrm{e'} \tag{31}$$

for the breakdown of stainless steels and possibly

$$\mathrm{Fe_{Fe}} \rightarrow \mathrm{Fe^{3+}} + \mathrm{V_{Fe}^{2'}} + \mathrm{e'} \tag{32}$$

for carbon and low alloy steels, where $\mathrm{Cr_{Cr}}$ is a Cr(III) cation in a normal chromium site in the barrier layer, and $\mathrm{Fe_{Fe}}$ is an Fe(II) cation in the iron oxide film on iron. For example, if the barrier layer on stainless steel is $\mathrm{FeCr_2O_4}$, reaction (31) could be written as

$$[\mathrm{FeCr_2O_4}] + 4\mathrm{H_2O} \rightarrow [\mathrm{FeV_{Cr}^{3'}CrO_4}] + \mathrm{CrO_4^{2-}} + 8\mathrm{H^+} + 3\mathrm{e'} \tag{33}$$

Likewise, for a magnetite film on iron

$$[\mathrm{Fe_3O_4}] \rightarrow [\mathrm{Fe_2V_{Fe}^{2'}O_4}] + \mathrm{Fe^{3+}} + \mathrm{e'} \tag{34}$$

where the entities in square brackets represent solid surface phases. Note that the solid phases (quantities in square brackets) remain electrically neutral because the charge is transferred to the solution is balanced by an equal (positive) charge being transferred to the solid by the cathodic partial reaction. The PDM has been developed in considerable detail for the case of anion-induced passivity breakdown, leading to the following equations for the pitting potential V_c and induction time t_{ind} for a single breakdown site on a surface:

$$V_c = [4.606RT/\chi\alpha F] \log [J_m/J^\circ \chi^{-\chi/2}] - [2.303RT/\alpha F] \log (a_x) \tag{35}$$

$$t_{ind} = \xi'[\exp(\chi F\alpha\Delta V/2RT) - 1]^{-1} + \tau \tag{36}$$

where $\Delta V = V - V_c, V$ is the applied voltage, χ is the oxide stoichiometry $(MO_{\chi/2}), J_m$ is the rate of annihilation of cation vacancies at the metal/film interface, α describes the dependence of the potential drop across the film/solution interface on the applied voltage, τ is the time for dissolution of the barrier layer over the breakdown site once vacancy condensation has occurred, ξ' is related to the critical areal (number per cm^2) concentration of condensed vacancies, and J° is a function of various thermodynamic parameters. By assuming that the breakdown sites on a real surface are normally distributed with respect to the cation vacancy diffusivity, i.e.,

$$\frac{dN}{dD} = \frac{1}{\sqrt{2\pi}\sigma_D} \exp\left[-\frac{(D-\bar{D})^2}{2\sigma_D^2}\right] \tag{37}$$

where N is the number of breakdown sites, $\bar{D}$ is the mean cation vacancy diffusivity, and σ_D is the standard deviation in the normal distribution, the following distribution functions have been derived for the number of breakdown sites with respect to the breakdown voltage and induction time:

$$\frac{dN}{dV_c} = \frac{1}{\sqrt{2\pi}\sigma_D \gamma D} \exp\left[-\frac{(D-\bar{D})^2}{2\sigma_D^2}\right] \tag{38}$$

$$\frac{dN}{dt_{ind}} = \left[\frac{\xi u^{\chi/2}}{\sqrt{2\pi}\sigma_D \hat{a}}\right] e^{-(D-\bar{D})^2/2\sigma_D^2} \cdot \frac{e^{-\gamma V}}{a_x^{\chi/2}(t_{ind} - \tau)^2} \tag{39}$$

where u is a thermodynamic function and $\hat{a} = J^\circ D$. These distribution functions are found to provide an accurate account of the experimentally-measured distributions of the breakdown sites on Fe17Cr in 3.6% NaCl solution, as reported by Shibata et al. (Figs. 34 and 35) and as discussed in Refs. [59–65].

In deriving Eq. (36), and hence Eq. (38), it was assumed that the induction time is dominated by the time required to accumulate a critical areal concentration of cation vacancies (i.e., the formation time of the vacancy condensate). However, as evident from Fig. 33, the induction time may exceed the vacancy condensation time by the amount required for the film to dissolve locally and rupture. We previously lumped these effects into the "relaxation time," τ, and for the pitting of metals such as iron, copper, nickel, and stainless steels, which form very thin barrier layers, this approximation appears to be reasonable, in that Eq. (36) accounts for the experimental data very well. It is possible, however, to envision a case where the time

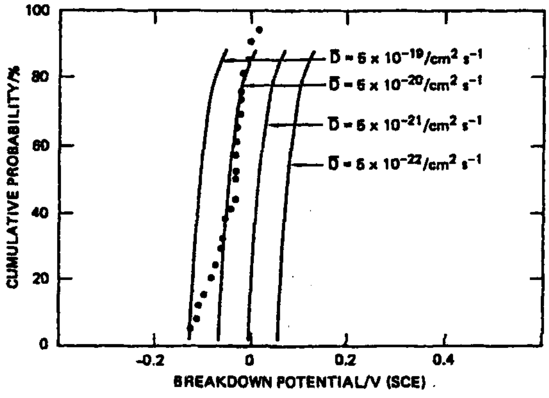

Fig. 34. Cumulative probabilities for the breakdown voltage as a function of $\bar{D}$ for normal distributions in the diffusivity $D \cdot \sigma_D = 0.75$.•, Data for Fe17Cr in 3.5% NaCl solution at 30 °C. $\bar{V}_c = -0.046\,\mathrm{V}$ (SCE). After Shibata (see [65]). Reproduced from J. Electrochem. Soc. 139, 3434 (1992) by permission of the Electrochemical Society.

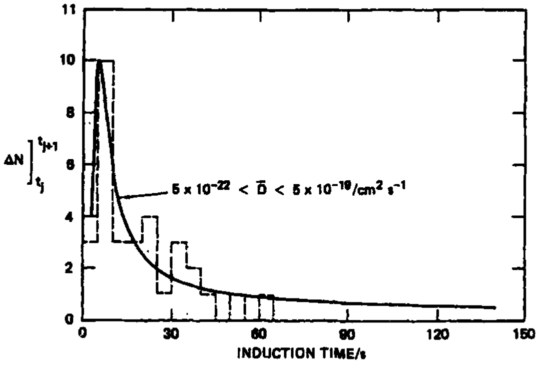

Fig. 35. Differential cumulative probabilities for the induction time as a function of $\bar{D}$ for normal distributions in $D \cdot \sigma_D = 0.75$. $\bar{D}$. - - - - Data for Fe17Cr in 3.5% NaCl solution at 30 °C. $\bar{V}_c = -0.046\,\mathrm{V}$ (SCE), $V = 0.0220\,\mathrm{V}$ (SCE), $\bar{t} = 7.5\,\mathrm{s}$, $\tau = 0$. After Shibata (see [65]). Reproduced from J. Electrochem. Soc. 139, 3434 (1992) by permission of the Electrochemical Society.

required to thin the film above the vacancy condensate is comparable with or greater than the time to form the vacancy condensate. In this case, Eq. (36) should be modified to read

$$t_{\mathrm{ind}} \lesssim \xi'[\exp(\chi F\alpha\Delta V/2RT) - 1]^{-1} + L_{\mathrm{ss}}/k_{\mathrm{s}}C_{\mathrm{H^+}}{}^{n} \tag{40}$$

where L_{ss} is the steady-state thickness of the barrier layer,

$$\begin{aligned} L_{\mathrm{ss}} &= \frac{1}{\varepsilon}\left[1 - \alpha - \frac{\alpha\alpha_{\mathrm{d}}}{\alpha_2}\left(\frac{\delta}{\chi} - 1\right)V\right. \\ &\quad \left. + \frac{1}{\varepsilon}\left\{\frac{2.303n}{\alpha_2\chi\gamma} - \beta\left[\frac{\alpha_{\mathrm{d}}}{\alpha_2}\left(\frac{\delta}{\chi} - 1\right) + 1\right]\right\}\mathrm{pH} + \frac{1}{\alpha_2\chi K}\ln\left(\frac{k_2^{\circ}}{k_{\mathrm{s}}^{\circ}}\right)\right. \end{aligned} \tag{41}$$

ε is the electric field strength in the barrier layer, k_2° is the standard rate constant for film formation [reaction (ii), Fig. 31], k_{s}° is the standard rate constant for film dissolution [reaction (v), Fig. 31], $C_{\mathrm{H^+}}$ is the concentration of hydrogen ions at the film/

solution interface, and n is the kinetic order of the dissolution reaction with respect to C_{H^+}. The inequality in Eq. (40) reflects the possibility that the barrier layer cap over the vacancy condensate may rupture due to stresses in the film prior to complete dissolution. In the limit, where the second term on the right-hand side of Eq. (40) is very much greater than the first term, and noting that k_2° is potential-dependent,

$$k_s = k_2^\circ \exp\left[\alpha\alpha_d(\delta - \chi)\gamma V + \beta\alpha_d(\delta - \chi)\gamma \cdot \mathrm{pH}\right] \tag{42}$$

where α_d is the dissolution transfer coefficient, δ is the valence of the ion ejected from the film, and k_2° is the standard rate constant, we obtain

$$t_{\mathrm{ind}} \rightarrow (L_{\mathrm{ss}}^{\mathrm{vc}} - L_{\mathrm{ss}}^{\mathrm{c}})/k_s C_{H^+}{}^{n} \tag{43}$$

where $L_{\mathrm{ss}}^{\mathrm{vc}}$ is the thickness of the barrier layer over the defect when vacancy condensation occurs, and $L_{\mathrm{ss}}^{\mathrm{c}}$ is the corresponding thickness when rupture of the barrier layer takes place (i.e., when the breakdown event occurs). For $\delta = \chi$ (i.e., no change in oxidation state on ejection of the cation from the film), the rate of dissolution is constant so that the induction time is governed by the magnitude of the numerator, and Eq. (43) predicts that the induction time will increase with increasing applied voltage V, because of the (experimentally demonstrated) increase in L_{ss}, provided that the film is formed before conditions become conducive to vacancy condensation (e.g., before exposure to chloride ion). To our knowledge, this behavior has not been observed in the studies reported to date. However, the experimental data for iron, chromium, nickel, and Fe–Cr–Ni alloys are well represented by Eq. (40) without the last term, indicating that vacancy condensate growth is the dominant process. This is important because one may argue that, at a constant voltage V, the rate of dissolution of the barrier layer at the film/solution interface might increase with increasing fluid flow velocity and hence that the induction time will decrease accordingly.

Examination of Eqs. (35) to (41) does not reveal any parameter that is obviously dependent on flow rate, provided that the applied voltage is maintained constant and vacancy condensation dominates the induction time. Thus, neither the thermodynamics of absorption of X^- into a surface oxygen vacancy nor the ejection of a cation from the film is expected to depend on flow velocity, nor are the events (e.g., vacancy condensation) that occur at the metal/film interface expected to be sensitive to fluid motion. Thus, the PDM predicts that the breakdown ("pitting") potential for passive alloys that are of interest to the thermal power industry should not be sensitive to flow rate. The PDM also predicts that the induction time should be insensitive to fluid flow velocity, provided that the induction period is dominated by vacancy condensation at the metal/film interface.

7.3 Effect of Fluid Flow on Passivity Breakdown

A number of studies have explored the effects of fluid flow on passivity breakdown (pit nucleation) in aqueous solutions at ambient and elevated temperatures [33, 66–

75]. The findings from the studies at ambient temperature are ambiguous, with some finding no dependence of the pitting potential on fluid flow, whereas others report a shift in the pitting potential in the noble direction. One of these studies [69] employed conditions (200 Hz vibrations) under which cavitation may have occurred; this case should be discounted because of the possibility of physical rupture of the film (although this might be expected to shift the pitting potential in the opposite direction to that found). Perhaps the most significant study in this regard is that reported by Williams et al. for the pitting of Type 304L stainless steel in sodium chloride solutions at ambient temperature as a function of flow velocity [74]. These workers analyzed the electrochemical current noise that is generated by passivity breakdown/repassivation events and found that the event frequency did not depend on the flow rate. However, they did find that the probability of a nucleus developing into a stable pit was lower at higher flow rate, an observation that is discussed in greater depth elsewhere in this chapter. In this regard, it is important to note that the point defect model addresses events only up to breakdown. Thus, the experimental findings of Williams et al. [74] summarized above are consistent with the prediction of the PDM that fluid flow should have little effect on passivity breakdown.

Not surprisingly, less work has been reported on passivity breakdown in aqueous solutions at elevated temperatures. Only two systematic studies of passivity breakdown in high-temperature aqueous solutions could be found in the literature. Thus, Karaminezhaad-Ranjbar et al. [33] explored the pitting of mill-annealed Alloy 600 in 0.1 M NaCl solutions at temperatures ranging from 25 °C to 250 °C at flow rates from 0 to ~ 1.6 m/s in an annular flow geometry. While the pitting potential was found to be a strong function of temperature (decreasing from ~ 0.5 V_{SHE} at 25 °C to ~ 0.1 V_{SHE} at 250 °C; see Fig. 13), no dependence on flow rate was noted at any temperature over the range studied (Fig. 36). At all studied flow rates (0–1.6 m/s) and temperatures (25–250 °C), no definitive relationship between flow velocity and pit morphology or distribution could be established. In many cases it was evident that the distribution of pits on the surface was determined by microstructural features (e.g.,

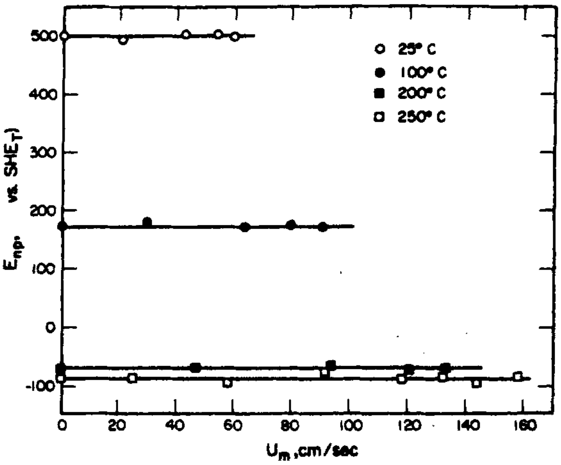

Fig. 36. Plot of breakdown potential vs. flow velocity for Alloy-600 in buffered 0.1 m NaCl solution at 250, 200, 100, and 25 °C [33]. Reproduced from Corrosion J. 41, 197 (1985) by permission of the Editor.

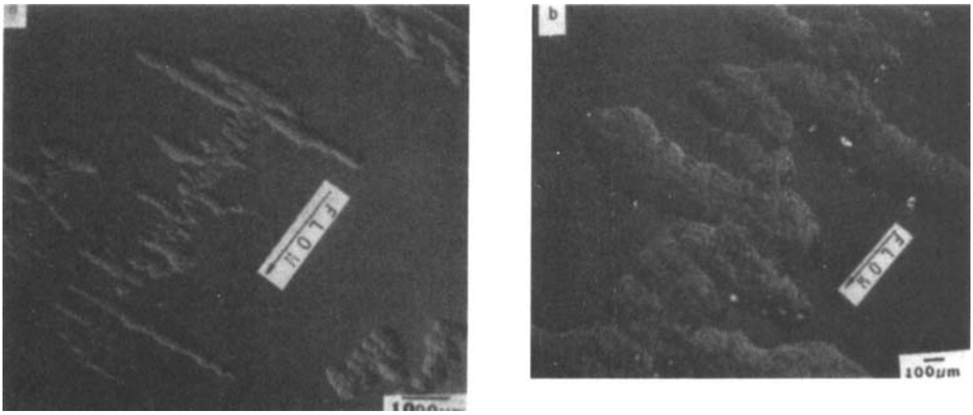

Fig. 37. Effect of flow velocity on the surface morphology of Alloy-600 after exposure to 0.1 M NaCl at 200 °C; flow velocity 132 cm/s [33]. Reproduced from Corrosion J. 41, 197 (1985) by permission of the Editor.

polishing marks; Fig. 37) rather than by hydrodynamic factors. These observations suggest that fluid flow does not affect the dynamics of passivity breakdown on Alloy 600 in high-temperature solutions.

The situation with solution-annealed and sensitized Type 304 stainless steel in 0.01 M NaCl at temperatures ranging from 25 °C to 275 °C is quite different [75]. Although the breakdown potential is insensitive to flow rate, the location of the breakdown sites and the morphology of attack is highly dependent on fluid flow. Thus, in the case of solution-annealed Type 304SS at all temperatures studied, the pits are randomly distributed across the surface under quiescent conditions, but at high flow rates (i.e., high rotation speeds of the flow-activating impeller) the pits are aligned in the flow direction. Indeed, pits were found to nucleate downstream from existing pits at distances that appear to be only weakly (if at all) dependent on the flow velocity. In the case of sensitized Type 304SS under quiescent conditions, the pits nucleate at emergent grain boundaries, presumably at the intersections between the passive film and chromium carbide particles. As the fluid velocity increases, a competition develops between the tendency of pits to nucleate at emergent grain boundaries and the hydrodynamic effect that causes them to nucleate along flow lines. These observations clearly indicate subtle interplay metallurgical/microchemical effects and hydrodynamic factors in determining the location of breakdown sites on the surface. For example, the progressive nucleation of pits at regular distances downstream of existing pits strongly suggests that the location of the breakdown points is determined by the dimensions of a standing pressure wave that emanates from the nearest upstream pit.

In summary, the existing work suggests that fluid has little effect upon the critical potential for passivity breakdown on aluminium, iron, Type 304SS, and Type 304LSS at ambient temperature, as well as on solution-annealed Type 304SS, sensitized Type 304SS, and mill-annealed Alloy 600 in chloride-containing solutions at elevated temperatures. However, fluid flow may affect the location of pit nucleation (in some systems) in a manner that is consistent with the formation of a standing pressure wave emanating from an upstream pit. The lack of dependence of V_c on flow velocity is consistent with the point defect model, assuming that the induction time is dominated by vacancy condensation at the metal/film interface. Furthermore, electrochemical noise studies of passivity breakdown on Type 304L SS in chloride solutions at elevated temperature show that the frequency of the breakdown events is insensitive to flow rate, which is again consistent with the prediction of the PDM that the induction time should be independent of fluid flow, provided that the induction time is dominated by the condensation of cation vacancies at the metal/film interface. However, this same study found that the probability of a nucleus developing into a stable pit decreases with increasing flow rate, which can be attributed to rinsing of the incipient crevice, as discussed in the following section.

It is important to note that, in the above analysis, we have assumed that the potential of the specimen is constant. However, for freely corroding systems, the ECP may vary with flow rate, and the resulting change in potential may have a substantial *indirect* effect on the dynamics of passivity breakdown. Thus, because the ECP of stainless steel increases with increasing flow rate (see above), at least for solutions containing moderate oxygen concentrations (< 100 ppb), this indirect effect of flow should lead to an increased rate of passivity breakdown at the higher flow rates. However, for environments that are characteristic of BWR pressure vessel internals under normal water chemistry (and under hydrogen water chemistry), where the ECP is more positive than $-0.1\,V_{SHE}$, little dependence of the ECP on flow rate is expected and, hence, one would expect flow to have little indirect effect. Finally, we emphasize that the available literature on the effect of fluid flow on passivity breakdown is very meager, particularly for systems at elevated temperatures. Although the theory of passivity breakdown, in the form of the point defect model, is relatively well developed, a much greater database on the effect of flow on V_c and t_{ind} is required to provide a quantitative assessment of the effect of flow on pit (and hence crack) nucleation.

7.4 Growth of the Critical Nucleus

The second stage of the crack nucleation process is the growth of a surviving passivity breakdown event into a critical nucleus, from which a crack may propagate. In examining this problem, it becomes apparent that the criteria for the size of the critical nucleus may depend on both mechanical and environmental factors. Some theoretical and experimental work exists on defining the critical nucleus, although much of the work is so qualitative that it lacks the necessary predictive nature to be included in this review. However, from examination of the literature, it is clear that the following factors must be considered in defining the properties of the critical nucleus:

1. the stress intensity ratio for the particular geometry of interest;
2. the aspect ratio;

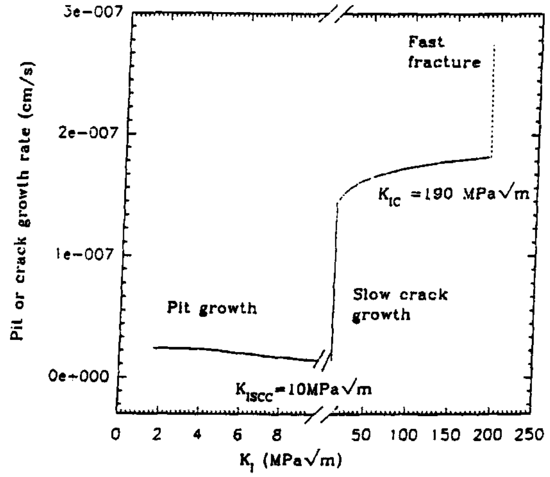

Fig. 38. Stages of development of a pit in low pressure steam turbine steel into a crack ultimately resulting in fast fracture, presented as a plot of growth rate vs. stress intensity. ($T = 453\,\mathrm{K}$, $[\mathrm{NaCl}] = 1.0\times10^{-3}\,\mathrm{mol/cm^3}$, $[\mathrm{HCl}] = 1.08\times10^{-6}\,\mathrm{mol/cm^3}$, $[\mathrm{O_2}] = 1.0\,\mathrm{ppm}$, $\sigma = 3.0\times10^{2}\,\mathrm{MPa}$, $h = 1.0\times10^{-3}\,\mathrm{cm}$, $a_O = 5.0\times10^{-5}\,\mathrm{cm}$, $L_O = 1.0\times10^{-3}\,\mathrm{cm}$). C. Liu and D. D. Macdonald, unpublished data.

3. the rinsing of the crevice, which depends on the hydrodynamics of the system and the geometry, including the aspect ratio.

A purely mechanical criterion for the existence of a critical nucleus is that $K_I > K_{ISCC}$, where K_I is the Mode I loading stress intensity ratio and K_{ISCC} is the (lower) critical stress intensity ratio for slow (environment-assisted) crack growth (Fig. 38). Because the stress intensity can be defined in terms of crack length (a) and stress (σ) as (assuming linear elastic fracture mechanics, LEFM)

$$K_I = \sigma Y \sqrt{a} \tag{44}$$

where Y is a geometrical factor, we may define a critical nucleus dimension as

$$a_{Cr} = K^2_{ISCC}/\sigma^2 Y^2 \tag{45}$$

More refined mechanical criteria may be defined on the basis of treatments that consider small-scale yielding, and hence an energy integral (e.g., the "J" integral), as the criterion for the nucleation of a crack. Regardless of the mechanical treatment that is employed, K_{ISCC} is essentially an environmentally determined parameter because its value is normally much less than K_{IC}, and it may depend on the applied potential and the composition of the environment. For example, for Type 304SS at 288 °C, $K_{IC} \simeq 60\,\mathrm{MPa\,m^{1/2}}$, whereas $K_{ISCC} \simeq 10\,\mathrm{MPa\,m^{1/2}}$ in oxygenated water at the same

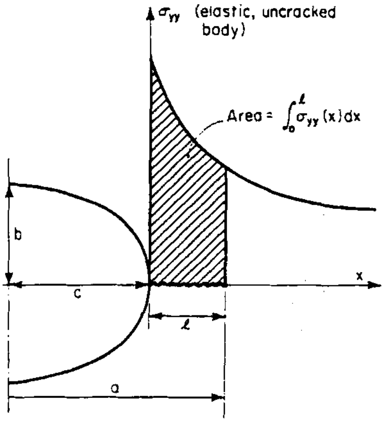
σ_{yy} (elastic, uncracked body)
Area = $\int_0^l \sigma_{yy}(x)dx$
b
c
x
l
a

Fig. 39. Nomenclature for the empirical expression for K at a notch [76]. Reproduced with permission.

temperature. Thus, Eq. (45) is more appropriately written as

$$a_{\mathrm{Cr}} = [K_{\mathrm{ISCC}}(\mathrm{ECP}, \kappa, v, \ldots)]^2/\sigma^2 Y^2 \tag{46}$$

where ECP (corrosion or applied potential), κ (solution conductivity), v (flow velocity), and ... (other factors) are environmental parameters that determine the susceptibility of the material to environment-induced fracture.

In the above simplistic theory, we have assumed that LEFM, as embodied in Eq. (44), can be used to describe the local stress state at a notch simulating a corrosion pit from which a crack may nucleate. This problem has been addressed by many authors, so reasonably accurate solutions are available provided that LEFM is strictly applicable. The stress states of long cracks (i.e., cracks that have grown well beyond the influence of the notch) may be accurately described by conventional LEFM even though small-scale yielding occurs. However, this is not the case for short cracks, which have considerably higher measured crack growth rates than those predicted by the models for long cracks.

Consider a crack emanating from a blunt notch (Fig. 39), as defined by McClung [76], where l is the crack length and b/c defines the notch geometry ($b/c = 1$ for a circular notch; $b/c < 1$ for an elliptical notch). Fatigue crack growth rate measurements in 1026 carbon steel by McClung [76] are summarized in Fig. 40 as a function of l/c, which is the parameter that was used to differentiate short and long cracks. Also plotted on this figure is the expected growth rate according to a long-crack model, where the stress intensity is given by Eq. (44). McClung, citing previous work by Newman [77], Ibrahim et al. [78], Marriott and Knott [79], Lukas [80], and Glinka [81], among others, proposes that the true stress intensity for Mode I loading can be written as

$$K_{\mathrm{I}} = 1.12\left\{0.77\sigma_{yy}(l) + \frac{0.23}{l}\int_0^l \sigma_{yy}(x)\mathrm{d}x\right\}\sqrt{\pi l} \tag{47}$$

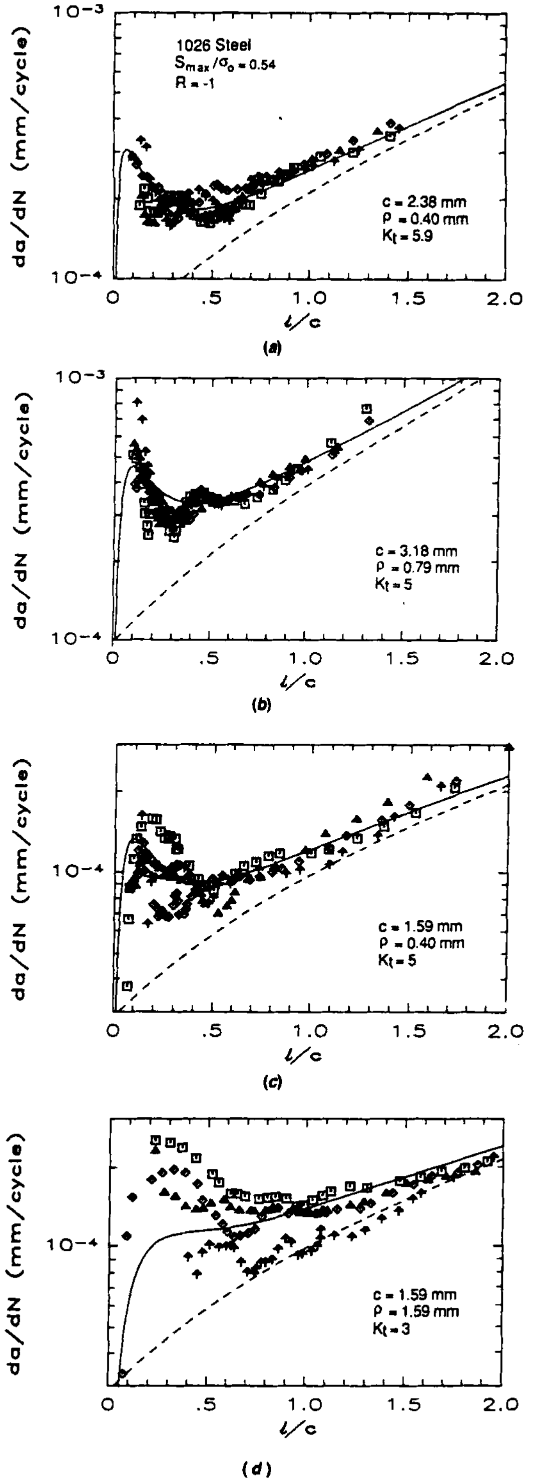

Fig. 40. Experimental data for cracks growing from notches in a 1026 steel, compared with the predictions of a simple short-crack model (solid line) and a long-crack model (broken line) [76]. Reproduced with permission.

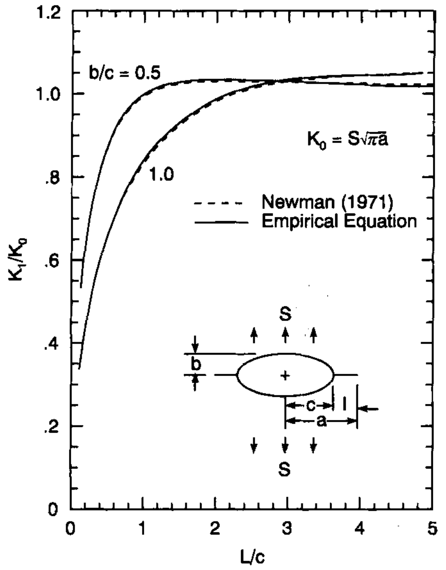

Fig. 41. Comparison of the result of Newman [77] and the present empirical equation for the stress intensity factory of a crack growing from a notch [76]. Reproduced with permission.

where the various parameters are as defined in Fig. 39. Provided $\sigma_{yy}(x)$ is known (from the calculated elastic stress distribution), Eq. (47) may be used to estimate the effective K_I value for any value of l/c. The effect of the l/c ratio on K_I is illustrated in Fig. 41. The match between Eq. (47) and Newman's exact solution is excellent (to within 0.5 for $l/c \leq 0.5$). However, for large l/c, Eq. (47) overestimates K_I for long cracks by about 12%, but that is of little consequence because various "long-crack" LEFM solutions for K_I are available. Returning now to Fig. 40, we see that Eq. (47) provides for an excellent correlation between crack growth rate and l/c. Finally, note that for a very long crack, $l \simeq a$, so that Eq. (47) transforms into Eq. (44).

As will become apparent later in this review, complete descriptions of crack nuclei, short cracks, and long cracks require estimates of the aspect ratios (crevice length/crevice mouth opening). The crevice length is estimated from a suitable crevice growth model, but the crevice mouth opening displacement must be calculated from the mechanical properties of the system. This is because little corrosion occurs on the crevice walls (at least at distance remote from the crack tip) for short and long cracks. This is not true, however, for a corrosion pit, where the aspect ratio is almost totally determined by corrosion processes. The problem of estimating crack mouth opening displacement is described extensively in standard texts in fracture mechanics. Therefore, this subject matter will not be reviewed here.

Let us return to consider the properties of the critical stress intensity for environmentally induced crack growth (K_{ISCC}). The fact that K_{ISCC} for sensitized Type 304SS apparently depends on the applied potential can be gleaned from the data shown in Fig. 42. Furthermore, both experiment and theory have established that the crack growth rate for $K_{ISCC} < K_I < K_{IC}$ depends on the solution conductivity, temperature, ECP, flow rate, and possible ion type (e.g., sulfate versus nitrate). The most comprehensive database for the effect of conductivity on crack growth rate is probably that of Kassner et al. [82] at the Argonne National Laboratory. Their data

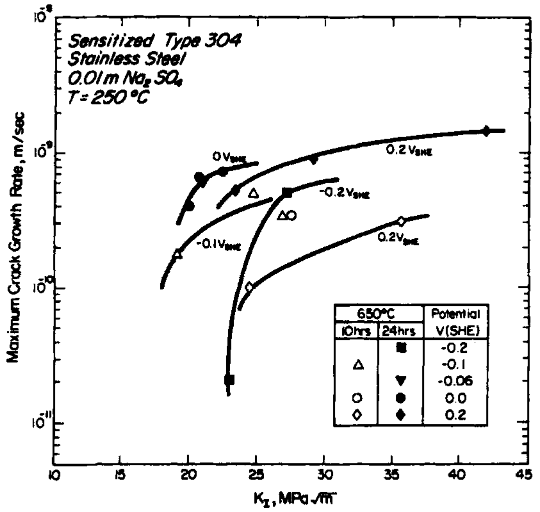

Fig. 42. Maximum crack growth rate as a function of stress intensity and potential for sensitized Type 304SS in 0.01 m Na_2SO_4 at 250 °C. [29]. Reproduced from Proc. 9th Int. Congr. Met. Corros., Vol. 2, pp. 185–201 (1984) by permission of the National Research Council of Canada.

show a somewhat lower dependence of the crack growth rate on conductivity than has been claimed by other workers, or than is indicated by theory (see later). Likewise, crack growth rate is a sensitive function of the ECP, provided ECP > E_{IGSCC}, but the dependencies on the other parameters noted above are (in the authors' opinion) much less well established. However, K_{ISCC} is normally taken as the stress intensity at which the lowest crack growth rate can be detected, which is usually determined by the sensitivity of the experiment. The important point is that the apparent K_{ISCC} value may simply reflect the measurement conditions and, in the limit, K_{ISCC} may approach zero as the methods for measuring crack growth rate become more sensitive. In the limit of $K_{ISCC} \rightarrow 0$, IGSCC becomes indistinguishable from intergranular attack (IGA).

From a practical viewpoint, K_{ISCC} may be defined in terms of the limit of sensitivity of crack growth rate measurements, which typically is of the order of 1×10^{-10} cm/s, under the best circumstances. However, recognizing that the growth rate at the lower limit is controlled by creep, an argument can be made that the concept of a K_{ISCC} is inappropriate because creep crack growth gradually transitions into environment-assisted crack growth as the environmental conditions become more conducive to the latter.

Returning now to the definition of the critical nucleus, we note that fluid flow velocity must be recognized as a key parameter in determining the properties of the critical nucleus. Many workers have recognized, in a qualitative manner, the unique properties of a short crack, or they have proposed that small crevices may respond to hydrodynamic factors differently from long cracks. Intuitively, the role of fluid flow in the case of a crack nucleus or a short crack is to "rinse" the crevice, and hence to counteract the effects of the establishment of an "aggressive" environment within the crack due to differential aeration. Such arguments are commonly devoid of physical detail, and hence they cannot form the basis of a quantitative theory that relates crack nucleation to hydrodynamic effects. This can only be done by exploring in detail the role of hydrodynamic and mass-transfer effects on the properties of the nucleus or short-crack enclave.

The growth of the crack nucleus may be described in terms of the differential aeration hypothesis, which recognizes that the driving force for localized attack is the potential difference between the nucleus enclave and the external environment. This potential difference gives rise to segregation of anious (typically Cl^-, SO_4^{2-}, HSO_4^{2-}, CO_3^{2-}, HCO_3^-) into the crevice, thereby producing locally aggressive conditions. If the crevice is open (i.e., has a low aspect ratio), the establishment and maintenance of the aggressive conditions will be counteracted by flow, due to the hydrodynamically induced exchange of the crevice solution with the external environment. Intutively, one would expect that fluid flow could exert a significant influence over the kinetics of growth of a nucleus, but this specific question has not yet been addressed in any depth. However, a number of studies have been reported on the hydrodynamics of flow within crevices that is induced by flow past the orifice [83–98]. These studies provide a detailed outline of the nature of the problem but they do not exactly address the question that we wish to explore.

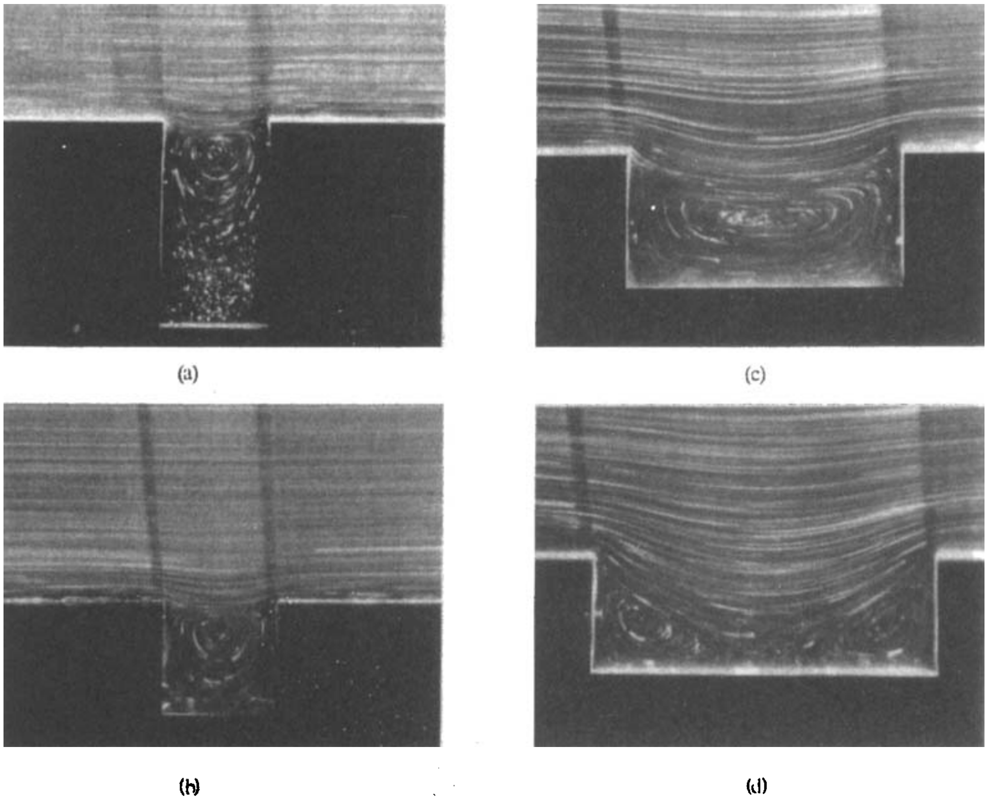

Fig. 43. Streamline patterns of the flow past a cavity (Reynolds number 1.0×10^{-2}) [83]. (a) b/h = 0.5, (b) 1, (c) 2, (d) 3, where b is the cavity width and h is the cavity depth. Reproduced with permission.

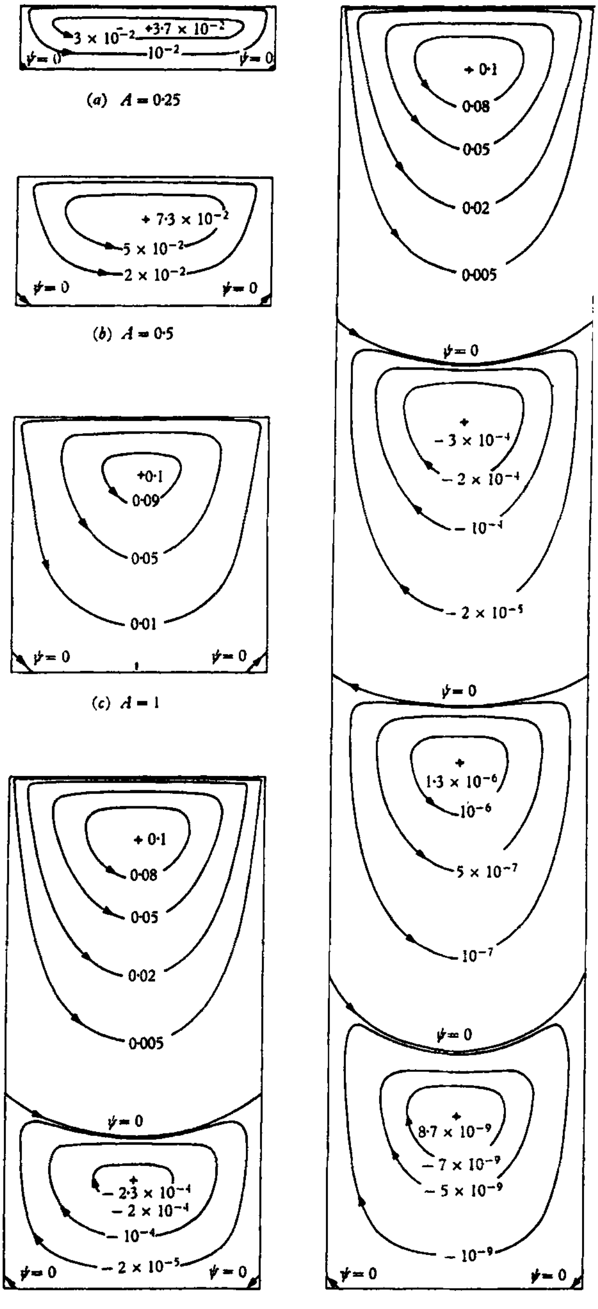

3 × 10⁻²
+3·7 × 10⁻²
10⁻²
ψ = 0
ψ = 0
+ 7·3 × 10⁻²
5 × 10⁻²
2 × 10⁻²
ψ = 0
ψ = 0
+0·1
0·09
0·05
0·01
ψ = 0
ψ = 0
+ 0·1
0·08
0·05
0·02
0·005
ψ = 0
− 2·3 × 10⁻⁴
− 2 × 10⁻⁴
− 10⁻⁴
− 2 × 10⁻⁵
ψ = 0
ψ = 0
+ 0·1
0·08
0·05
0·02
0·005
ψ = 0
− 3 × 10⁻⁴
− 2 × 10⁻⁴
− 10⁻⁴
− 2 × 10⁻⁵
ψ = 0
1·3 × 10⁻⁶
10⁻⁶
5 × 10⁻⁷
10⁻⁷
ψ = 0
8·7 × 10⁻⁹
− 7 × 10⁻⁹
− 5 × 10⁻⁹
− 10⁻⁹
ψ = 0
ψ = 0

(a) $A = 0{\cdot}25$

(b) $A = 0{\cdot}5$

(c) $A = 1$

(d) $A = 2$

(e) $A = 5$

Fig. 44. Creeping-flow streamline patterns in rectangular cavities [84]. (a) A = 0.25; (b) A = 0.5; (c) A = 1.0, (d) A = 2.0, (e) A = 5.0. Reproduced with permission. (A = aspect ratio = $\frac{\text{depth}}{\text{width}}$).

The problem of flow within crevices has been addressed in two ways:

1. by the use of dyes to permit direct visualization;
2. by solving the Navier–Stokes equations to yield the vector velocity field.

As a typical example of the first approach, we cite the work of Taneda [83], who visualized the flow past rectangular cavities as shown in Fig. 43. The most important feature of this study is the establishment of rotational eddies, particularly for the crevice with the higher aspect ratio (Fig. 43(a)). For deep crevices, multiple eddies are established, with each one rotating in the opposite direction, as shown in Fig. 44 [84]. These eddy contours were obtained by solving the Navier–Stokes equation for the crevice as a function of the crevice aspect ratio. The calculations show that the dimension of the eddy in the vertical direction (i.e., down the crevice) is about 1.3 times the crevice width. The most important fact is that the intensity of the eddy decreases exponentially with distance, so that the intensity at the core decreases by a factor of almost 10^7 over a depth of five eddy dimensions. This issue has also been explored by Taneda [83] for a wedge-shaped crevice (Fig. 45). In this particular case, the crevice was formed between a rotating cylinder and a wall, so that it does not exactly correspond to a stationary crevice. However, it does demonstrate the principal issue. That is, for a triangular crevice, each successive crevice cross-sectional dimension becomes smaller with respect to crevice length (from the mouth). As compared with that of a rectangular crevice, the exponential drop in intensity is

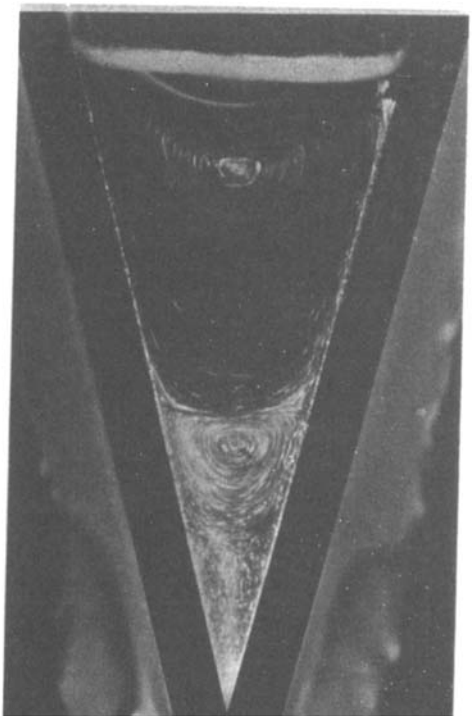

Fig. 45. Streamline pattern in a wedge-shaped region (Reynolds number 1.7×10^{-1}) [83]. Reproduced with permission.

stronger. Taking the rectangular crevice as a model, the fluid in the crevice essentially becomes quiescent at an aspect ratio of 5.

7.5 Modeling Effects of Fluid Flow on the Properties of Pits

Various authors have attempted to model the influence of fluid flow on the properties of crevices, including cracks and corrosion pits. For example, Schmitt et al. [85] have modeled the flow characteristics of crevices (Fig. 46), with particular emphasis on

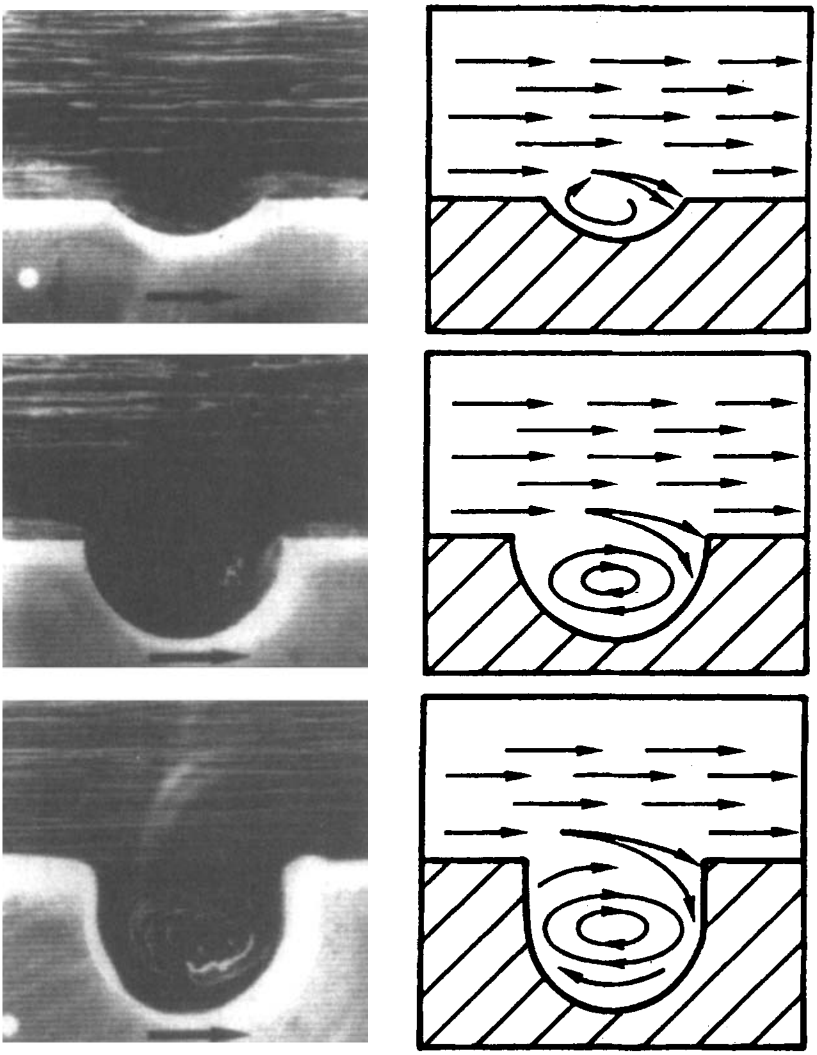

Fig. 46. Real and schematic flow patterns at grooves in a flow channel, visualized by injection of small air bubbles (flow rate: 2 m/s) [85]. Reproduced from Corrosion J. 48, 431 (1992) by permission of the Editor.

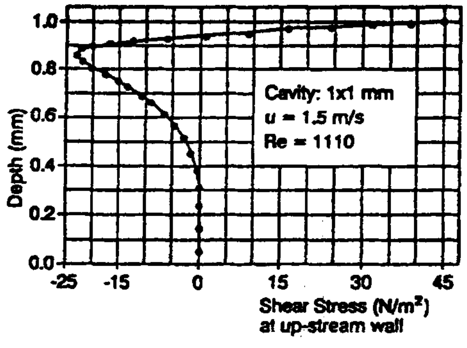

Fig. 47. Wall shear stress downstream of wall no. 1 [85]. Reproduced from Corrosion J. 48, 431 (1992) by permission of the Editor. Wall no. 1 = wall facing against flow direction.

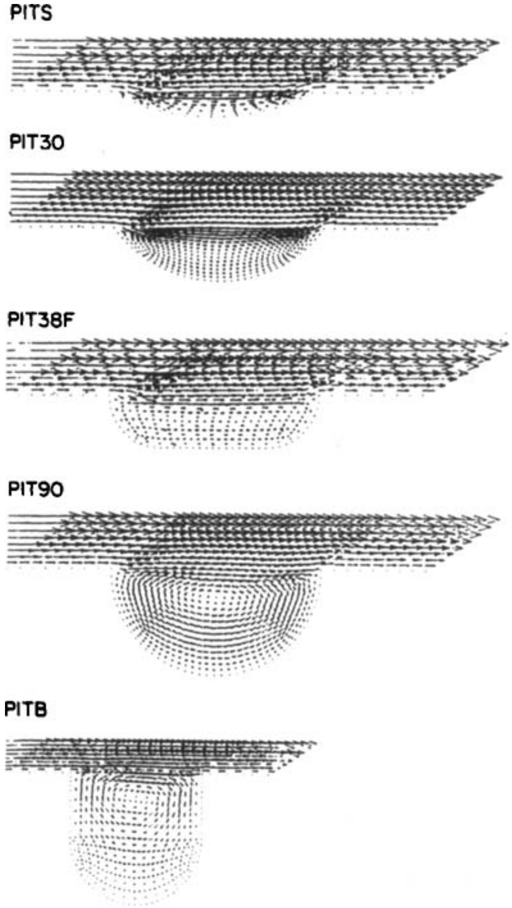

Fig. 48. Velocity vector flow field within various cavities. The arrow length is proportional to velocity [94]. Reproduced from J. Electrochem. Soc. 131, 2795 (1984) by permission of the Electrochemical Society.

determining the distribution in shear stress within the crevice. Their calculations (Fig. 47) demonstrate that the most intense shear exists just downstream of the crevice. In fact, these calculations provide a convincing explanation of the data reported by Choi et al. [75] where pits were found to nucleate at regular distances downstream of existing pits.

The most extensive calculations of this type have been reported by Alkire et al. [91–98] using a commercial finite element program, FIDAP. Typical velocity vector flow fields for pits of increasing depth are shown in Fig. 48. The maximum pit depth explored was not sufficiently large to give rise to multiple eddies, but the establishment of an eddy within the crevice is clearly indicated. These calculations also included solutions to the convective diffusion equations for the transport of corrosion products from the crevice. They were done because it was assumed that at some velocity (i.e., corresponding to a given Peclet number $\mathrm{Pe} = \mathrm{ReSc} = u_0 r_0 / D$, which is the ratio of convective to diffusive transport, where u_0 is the characteristic flow velocity within the crevice, r_0 is the radius of the crevice, and D is the species diffusivity), flow within the crevice would prevent the formation of a salt film, which is thought to be necessary to sustain pit growth. This effect of flow is clearly demonstrated in Fig. 49, in which the current produced by the growth of a single pit in Type 304SS is switched off by activating flow with $\mathrm{Pe} = 17$, whereas pitting continues if $\mathrm{Pe} = 0.44$. Measurements of this type as a function of pit diameter (Fig. 50) allowed Harb and Alkire [98] to evaluate the critical Peclet number for sustained pit growth (in this case $\mathrm{Pe} \simeq 10$). Thus, for a pit radius of 10 μm, and assuming $D = 10^{-5}\,\mathrm{cm}^2/\mathrm{s}$, we estimate a critical velocity of 0.1 cm/s.

In a recent series of studies, Shibata et al. [99, 100] successfully applied stochastic analysis to the investigation of the flow velocity effects on pitting of titanium. The authors have shown that the pitting potential shifts in the noble direction with increasing flow velocity, and the pit generation is suppressed at higher flow rates. Accordingly, the pit repassivation rate was also found to increase with increasing flow velocity. Shibata and Zhu [99] conclude that the flow velocity affects the mass transport from the pit to the bulk solution, and that this mass transport is a rate-determining process for the pit repassivation.

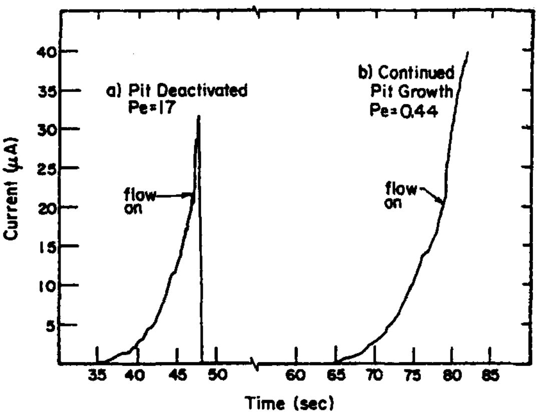

Fig. 49. Current vs. time curves for two different experiments in which a single pit growing under potentiostatic control [9.8 V (Ag/AgCl)] was subjected to flow. Electrode, 304 stainless steel; electrolyte, 0.1 M Na_2SO_4, 0.2 M NaCl (pH = 3.5) [98]. Pe = Peclet number. Reproduced from Corros. Sci. 29, 31 (1989) by permission of the Editor.

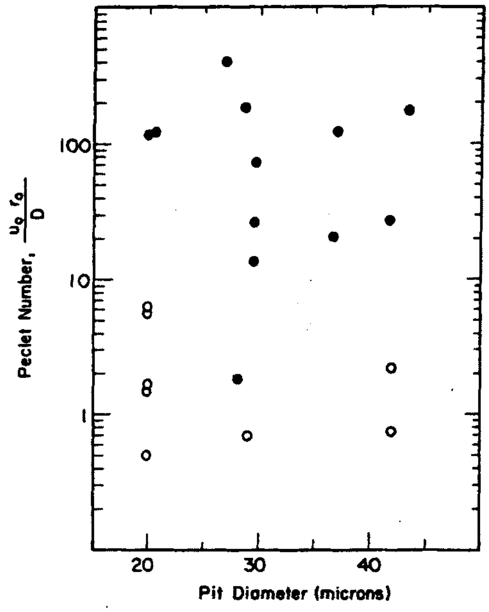

Fig. 50. Deactivation of pitting due to initiation of flow over a pit growing under potentiostatic control in a previously stagnant medium: (•) pit repassivated; (o) pit growth continued. Results are expressed in terms of the Peclet number for the pit [98]. Reproduced from Corros. Sci. 29, 31 (1989) by permission of the Editor.

The issue of the role of hydrodynamic phenomena in the propagation of small cavities is far from settled, even for ambient-temperature systems. Any calculations of this type must be checked by carefully conceived experiments that are capable of providing quantitative data on the growth of pits as a function of aspect ratio and flow velocity. The key question appears to be: to what depth do flow-induced eddies penetrate in a crevice, and how do these eddies affect the aggressive conditions that are established within the crevice due to the differential aeration?

7.6 Effect of Fluid Flow on Short Cracks

The problem of defining the effect of flow on short cracks is similar to that presented above for the critical nucleus, in that the aspect ratio is the key parameter of interest. However, a short crack differs from a crack nucleus in that $K_I > K_{ISCC}$, but it is not so long that a substantial fraction of the enclave is not subject to rinsing induced by flow past the crack mouth. From the discussion presented in Section 7.4, an aspect ratio of 5–10 would seem to be appropriate, but of course the exact length will depend on many factors, including the flow velocity, kinematic viscosity, stress, and geometry. The theoretical factors that must be considered in describing short cracks are therefore similar to those outlined above for crack nuclei, except that the rate of growth of a short crack is stress-dependent.

Few experimental studies have been reported on the behavior of short cracks. However, in one study, Prater et al. [101] used an electrical potential drop method to monitor the growth of surface cracks in carbon steel in oxygenated (8 ppm O_2) high-temperature (288 °C) water. The cracks were semielliptical in shape and the crack

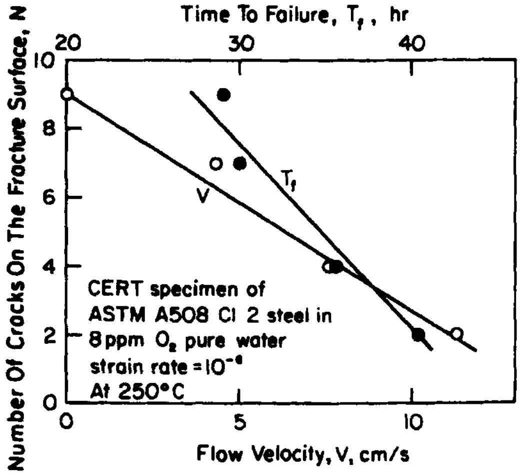

Fig. 51. Number of cracks on the fracture surface as a function of flow velocity and time to failure for ASTM A508 Cl.2 steel in high-temperature water [102]. Reproduced from Corrosion J. 38, 761 (1982) by permission of the Editor.

growth tests were carried out using trapezoidal loading with a one-hour hold period. The cracks grew from thumbnail defects that had been cut into the surface by electrical discharge machining. The defect size was typically less than 1 mm deep × 2.5 mm long. These data clearly define the Stage I region of the crack growth rate versus stress intensity correlation. The data also clearly indicate a K_{ISCC} value of 10 ksi $\mathrm{in}^{1/2}$ (11 MPa $\mathrm{m}^{1/2}$). Unfortunately, no flow rate effects were explored.

Perhaps the most thorough analyses of the effect of flow on short cracks are those published by Choi et al. [102], and by Easthope and Turnbull [103]. Choi et al. carried out constant-extension-rate tests on round tensile specimens of Type 304SS and A508 carbon steel in oxygenated (8 ppm O_2) pure water within an annular flow channel at a temperature of 250 °C. By delineating the crack initiation time from the total failure time, it was possible to explore the effect of flow on the initiation versus propagation stages. For example, the effect of flow velocity on total time to failure for A508 steel is shown in Fig. 51. These data clearly illustrate that increasing flow rate inhibits stress corrosion cracking of the alloy. Furthermore, the number of cracks that were found on the surface of A508 decreased with increasing flow velocity. Analysis of the data indicated that the maximum dimension of a short crack, in this case, was $\sim$ 0.1 mm. This permitted the calculation of the initiation time versus flow velocity (Fig. 52), and also the crack propagation rate versus crack length as a function of flow velocity (Fig. 53). Clearly, fluid flow is found to have a strong effect on the initiation time and on the number of cracks that eventually nucleate. However, an increasing flow rate decreases the growth rate of short cracks (length < 0.1 mm).

The relationship between increasing flow rate and decreasing short crack growth rate is consistent with the concept of flow-induced "rinsing" of the crack enclave. Assuming an aspect ratio of $\sim$ 10, a crack opening of 10 μm is indicated, which would seem to be a reasonable value. While the studies of Choi et al. [102] were carried out under some conditions that closely resemble those that exist in BWR primary circuits and in PWR secondary circuits, the flow rates and Reynolds numbers

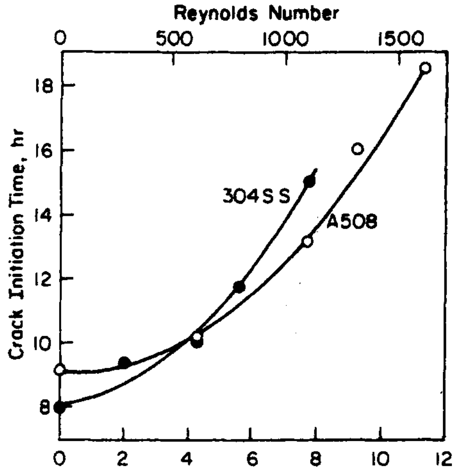

Fig. 52. Crack initiation time as a function of flow velocity for sensitized Type 304 stainless steel and ASTM A508 Cl.2 steel in oxygenated water ($[O_2]$ = 8 ppm) at 250 °C [102]. Reproduced from Corrosion J. 38, 76 (1982) by permission of the Editor.

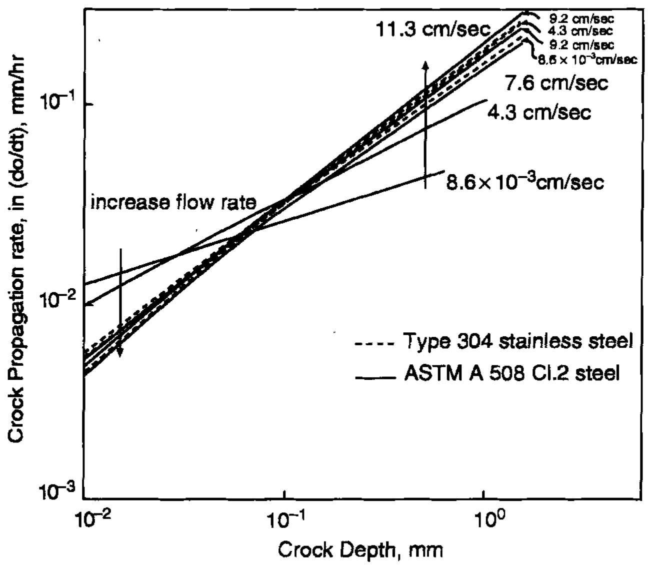

Fig. 53. Crack propagation rate as a function of crack depth for sensitized Type 304 stainless steel (broken lines) and ASTM A508 Cl.2 steel (solid lines) in oxygenated water ($[O_2]$ = 8 ppm) at 250 °C at various flow velocities [102]. Reproduced from Corrosion J. 38, 76 (1982) by permission of the Editor.

employed were very low. Furthermore, the use of constant-extension-rate specimens is not without controversy (see the next section). Accordingly, we strongly recommend conducting well-conceived experiments, using surface cracks and/or fracture mechanics specimens, to expand further the database on the effect of flow on the growth of short cracks.

On the other hand, Easthope and Turnbull [103], using analytical models, explored the expected effects of flow velocity on crack propagation for a number of scenarios, including: (1) flow along or across the crack mouth; (2) flow through the crack; (3) flow directed into a surface crack; and (4) flow induced by cyclic displacement of the crack walls as in corrosion fatigue. They concluded that flow in the bulk solution is likely to have a significant effect only for shallow cracks or where the flow is directed into the crevice. This theoretical result is in good agreement with the experimental work of Choi et al. [102] and with the concept of enclave rinsing as posited by the hydrodynamic analysis discussed above. However, Easthorpe and Turnbull [103] did not consider the effect that flow may have on the transport of a cathodic depolarizer (e.g., oxygen) to the external surface, where it might consume electrons released by anodic processes occurring within the crack.

7.7 Effect of Fluid Flow on Long Cracks

A review of the literature revealed a dearth of information on the effect of fluid flow on the rates of propagation of long cracks in reactor materials in high-temperature water. Indeed, little information is available on this subject for systems at *ambient* temperature, even though the experimental difficulties are greatly eased as compared with those at higher reactor temperatures. This situation is not surprising, however, because few corrosion scientists have backgrounds in hydrodynamics and mass-transport theory, even though the effect of fluid motion on many types of corrosion processes is well recognized. In Sections 7.5 and 7.6, we discussed the role of hydrodynamics in the growth of pits and other cavities that may serve as nuclei for cracks. We concluded, on the basis of theory and experiment, that hydrodynamic and mass-transport processes may exert strong influences over cavity growth. However, the experimental data are contradictory, and insufficient theoretical work has been reported to settle the issue. Still, the theory does insist that any rinsing effects will decrease rapidly with increasing aspect ratio, so that a substantial difference is expected between short (low aspect ratio) and long (large aspect ratio) cavities and cracks.

From a theoretical viewpoint, three cases may be identified:

1. corrosion fatigue, in which the relative motion of the crack flanks (due to periodic mechanical loading) causes exchange of the crack enclave solution with the external environment;
2. long cracks, in which the eddy intensity within the crack is never sufficiently large to exchange the solution in the neighborhood of the crack tip with the external environment;
3. experiments in which solution is forced through the crack enclave, in contradiction to the situation that exists for a naturally occurring surface crack.

In case 3, the geometry employed (i.e., the solution being forced through the crack in the vicinity of the crack tip by external pressurization) does not represent the situation that occurs in freely growing cracks and crevices in industrial environments. Thus, experiments that have employed this technique arrive at the predictable result that if the aggressive conditions (which are established within the crevice by differential aeration, for example) are destroyed, crevice (and hence crack) growth will cease. This case will not be considered further in this review.

As is the case for short cracks, few experimental studies have been reported on the effect of flow velocity on the propagation rates of long cracks. Thus, while Rippstein and Kaesche [104] studied the initiation and propagation of cracks in SA508 Cl.2 steel in high-temperature water at very high Reynolds numbers, flow velocity was not employed as an independent variable. On the other hand, Cullen et al. [105] explored the effect of flow rate on the fatigue cracking of low-, medium-, and high-sulfur steels in high-temperature water under typical PWR operating conditions. However, these are conditions where flow rate is not expected to affect the crack growth rate, for reasons that are discussed later in this section. Apparently, the work of Choi et al. [102] is the only study that has attempted to address experimentally the effect of flow rate on the kinetics of crack growth under conditions that are relevant to thermal power technology, and under conditions where an effect might be expected to exist (due to mass transfer of a cathodic depolarizer to the external surface). Thus, with reference to Fig. 53, Choi et al. [102] found that the rate of growth of long cracks (crack lengths > 0.1 mm) increased with increasing flow velocity, but that the effect quickly saturated at flow velocities above 9 cm/s. The corrosion potential was also found to increase by $\sim$ 20 mV on increasing the flow rate from 0 to 11.3 cm/s. These observations are consistent with the crack growth rate being controlled by the transport of the cathodic depolarizer (O_2) to the steel surface. Finally, we note that the interpretation of these data by Choi et al. [102] has not gone unchallenged, and the reader is referred to the comments of Hickling [106] and the response of Choi et al. [107] for a discussion of the controversy. In our opinion the original interpretation is correct, particularly when viewed in the light of subsequent theoretical developments.

The coupled environment fracture model (CEFM) [108–110] is possibly the only currently available crack growth model that indicates an influence of hydrodynamic phenomena in the external (crack) environment on crack growth rate (CGR) in a quantitative manner. The CEFM predicts that in the absence of crack-enclave rinsing, the CGR will increase with increasing flow rate, particularly at low oxygen concentrations. This behavior may be rationalized by noting that at high oxygen concentrations, or for high flow rates, sufficient oxygen is present at the external surface to consume any current that may be ejected from the crack. The fact that current is ejected from the mouth of a crack growing in sensitized Type 304SS in high-temperature water is shown unequivocally by the work of Manahan et al. [111, 112]. In these experiments, electrically isolated compact toughness (CT) specimens coupled to side cathodes (stainless steel, titanium, or lightly platinized nickel) were used to test the basic pretext of the CEFM. The coupling current, which was measured with a zero-resistance ammeter connected to the specimen and the cathode, responded to load in the manner expected for crack propagation. It was also demonstrated that current does flow from the crack enclave to the external surfaces. To our knowledge, no corresponding experiments as a function of flow rate have been reported.

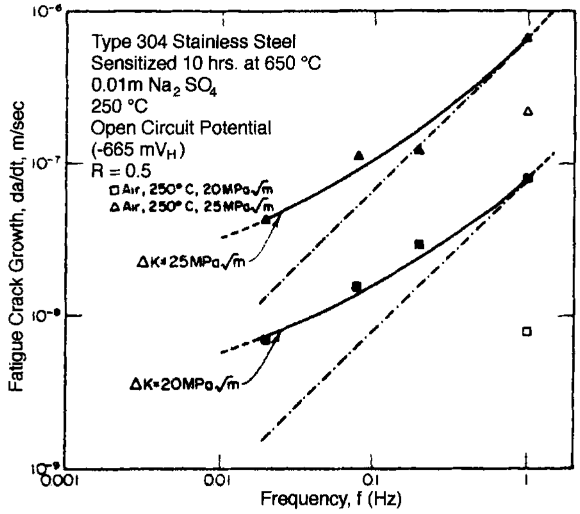

Fig. 54. Effect of frequency on the time-based crack growth rate in sensitized Type 304Ss in 0.01 m Na_2SO_4 solution at 250 °C and at $\Delta K = 20\,MPa\,m^{1/2}$ and $25\,MPa\,m^{1/2}$ [114]. Reproduced from Corrosion J. 40, 573 (1984) by permission of the Editor.

Another way of looking at this problem is to note that increased flow rate is predicted (and found experimentally) to shift the ECP in the positive direction, particularly at low oxygen concentration and low flow velocities. Because the crack growth rate for long cracks increases with increasing ECP (as predicted by the CEFM and experimental findings), it is therefore expected that increased flow rate will result in an increase in the CGR for IGSCC in sensitized stainless steels. Claims to the contrary are difficult to reconcile with the known dependencies of the ECP on flow rate, as well as with the known dependency of the crack growth rate on the ECP.

At this point, we should note that the effect of fluid flow velocity on the CGR of long cracks in sensitized stainless steel is predicted to disappear as conditions are changed so that the ECP becomes very negative. In this case, the crack growth rate approaches the creep limit, in which the CGR is insensitive to environmental effects [113]. This prediction clearly explains the finding of Cullen et al. []105], who showed that flow rate has little effect on CGR in pressure vessel steel under PWR primary environmental conditions (i.e., high hydrogen concentration and hence very negative ECP).

Case 1, the case of corrosion fatigue, is most interesting. This is because it illustrates the delicate interplay between crack-enclave hydrodynamics and mass transport, and also the kinetics of establishment of conditions that are conducive to crack propagation. Thus, Tsai et al. [114], and others, have found that intergranular fracture occurs in sensitized Type 304SS in high-temperature aqueous systems under cyclic loading only at low frequencies (e.g., 0.1 Hz; Figs. 54 and 55). At lower frequencies, it is probable that the rate of exchange of the crack-enclave solution with the external environment, due to the pumping action of the crack flanks, is slow

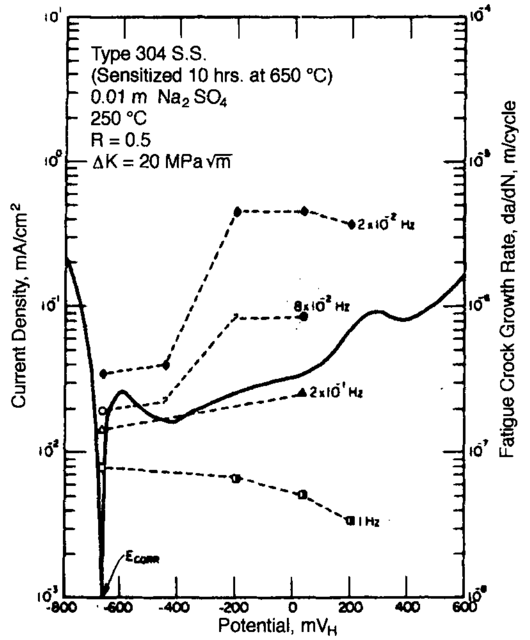

Fig. 55. Corrosion fatigue crack growth rate in sensitized Type 304SS as a function of potential and frequency in 0.01 m Na_2SO_4 solution at $\Delta K = 20 MPa\,m^{1/2}$. 250 °C. Open symbols denote transgranular mode of cracking, half-symbols denote mixed transgranular/intergranular mode of cracking, and closed symbols denote intergranular mode of cracking [114]. Reproduced from Corrosion J. 40, 573 (1984) by permission of the Editor.

enough for it to be possible for the conditions required for intergranular fracture to be maintained at the crack tip, and to be sustained by coupling of the crack internal and external environments. However, at higher frequencies, the exchange of the crack-enclave solution with the external environment is so rapid that the necessary conditions for crack growth cannot be maintained at the crack tip, regardless of coupling with the external environment.

In summary, a consistent picture has emerged for the effect of flow rate on the rate of crack growth of long cracks in LWR coolant environments. Based on the experimental data that are currently available, we conclude that the dominant effect of increasing flow rate is to increase the flux of cathodic depolarizer to the external surface, therby increasing the CGR, except in those instances where the aspect ratio is sufficiently low (short crack, or very large crack opening displacement due to excessive plastic deformation), where rinsing of the crack enclave is possible. Experimentally it is found that, for a crack of high aspect ratio, the effect of flow rate on the crack growth rate appears to saturate with increasing flow rate, particularly at higher oxygen concentration. This observation is consistent with the view that a primary effect of fluid flow in localized corrosion is to transport a cathodic depolarizer to the surface from the bulk environment, where charge transfer occurs in accordance with the differential aeration hypothesis.

8 References

1. Z. Szklarska-Smialowska, Pitting Corrosion of Metals, NACE, Texas (1986).
2. P. M. Scott, Corros. Sci. 25, 583 (1985).
3. D. D. Macdonald, G. Cragnolino In: Corrosion of Steam Cycle Materials, in: ASME Handbook on Water Technology for Thermal Power Systems, P. Cohen (ed.), ASME, New York (1989).
4. F. P. Ford, D. F. Taylor, P. L. Andresen, R. G. Ballinger, Corrosion-Assisted Cracking of Stainless and Low Alloy Steels in LWR Environments, EPRI Report NP-5064 (1987).
5. D. R. Tice, Corros. Sci. 25, 705 (1985).
6. S. H. Bush, J. Press. Vess. Technol. 114, 389 (1992).
7. D. D. Macdonald, Corrosion J. 48, 354 (1992).
8. Y. Ishikawa, T. Ozaki, N. Hosaka, O. Nishida, Trans. ISIJ 22, 977 (1982).
9. D. D. Macdonald, C. Liu, M. Urquidi-Macdonald, G. H. Stickford, B. Hindin, A. K. Agrawal, K. Krist, Corrosion J. 50, 761 (1994).
10. K. S. Brown, G. M. Gordon in: Environmental Degradation of Materials Nuclear Power Systems – Water Reactors, G. J. Theus, J. R. Weeks (eds.), The Metallurgical Society, Metals Park, OH (1988), p. 243.
11. A. Turnbull, D. H. Ferriss, Corros. Sci. 27, 1323 (1987).
12. V. G. Levich, Physicochemical Hydrodynamics, Prentice-Hall, Englewood Cliffs, NJ (1962).
13. J. Newman, Electrochemical Systems, Prentice-Hall, Englewood Cliffs, NJ (1973).
14. J. R. Selman, C. W. Tobias, Adv. Chem. Eng. 10, 211 (1978).
15. J. N. Harb, R. C. Alkire, Int. J. Number. Meth. Fluids 8, 1513 (1988).
16. G. A. Schmitt, W. Bucken, R. Fanebust, Corrosion J. 48, 431 (1992).
17. B. Poulson, Corros. Sci. 23, 391 (1983).
18. T. Y. Chen, A. A. Moccari, D. D. Macdonald, Corrosion J. 48, 239 (1992).
19. B. T. Ellison, W. R. Schmeal, J. Electrochem. Soc. 125, 524 (1978).
20. K. Denpo, H. Ogawa, Corros. Eng. 41, 293 (1992).
21. D. C. Silverman, Corrosion J. 41, 679 (1985).
22. E. Heitz, Werkstoff Korros. 15, 63 (1964).
23. L. A. Poluboyartseva, P. I. Zarubin, V. M. Nouakovskii, J. Appl. Chem. USSR 36, 1210 (1963).
24. D. D. Macdonald, J. Mankowski, M. Karaminezhaad-Ranjbar, Y.-H. Hu, Corrosion J. 44, 186 (1988).
25. W. A. Stein, Int. Chem. Eng. 32, 431 (1992).
26. W. A. Stein, Int. Chem. Eng. 32, 439 (1992).
27. R. L. Jones, Corrosion Experience in US Light Water Reactors – A NACE 50th Anniversary Perspective, presented as CORROSION 93, New Orleans, LA, March 8–12, 1993, Paper 168.
28. D. D. Macdonald, G. Cragnolino, The Critical Potential for the IGSCC of Sensitized Type 304SS in High Temperature Aqueous Systems, in: Proc. 2nd Int. Symp. Environ. Degr. Mater. Nucl. Power Systs. – Water Reactors, Monterey, CA, Sept. 9–12, 1985, American Nuclear Society, LaGrange Park, IL (1986).
29. G. Cragnolino, D. D. Macdonald, Proc. 9th Int. Congr. Met. Corros., National Research Council, Ottawa, Canada (1984), Vol. 2, p. 185.
30. M. E. Indig, B. M. Gordon, R. B. Davis, J. E. Weber, Evaluation of In-Reactor Intergranular Stress Corrosion Cracking via Electrochemical Measurements, in: Proc. 2nd Int. Symp. Environ. Degr. Mater. Nucl. Power Systs. – Water reactors, Monterey, CA, Sept. 9–12, 1985, American Nuclear Society, LaGrange Park, IL (1986).

31. D. D. Macdonald, S. Smialowska, S. Pednekar, The General and Localized Corrosion of Carbon and Low Alloy Steels in Oxygenated High Temperature Water, EPRI NP-2853, Ohio State University, Columbus, OH (1983).
32. P. Hurst, P. Banks, G. Pemberton, A. S. Raffel in: Proc. 2nd Int. Symp. Environ. Degr. Mat. Nucl. Power Systs. – Water Reactors, Monterey, CA, Sept. 9–12, 1985, American Nuclear Society, LaGrange Park, IL (1986).
33. M. Karaminezhaad-Ranjbar, J. Mankowski, D. D. Macdonald, Corrosion J. 41, 197 (1985).
34. K. S. Jeon, M. H. Song, S. H. Park, J. S. Kim, U. C. Kim, S. K. Chae in: Proc. 4th Int. Symp. Env. Degr. Mat. Nucl. Power Systems – Water Reactors, Jekyll Island, GA, Aug. 6–10, 1989. NACE, Houston, TX (1990).
35. J. R. Park, Z. Szklarska-Smialowska in: Proc. 2nd Int. Symp. Environ. Degr. Nucl. Power Systems – Water Reactors, Monterey, CA, Sept. 9–12, 1985, American Nuclear Society, LaGrange Park, IL (1986).
36. K. H. Lee, G. Cragnolino, D. D. Macdonald, Corrosion J. 41, 540 (1985).
37. R. Bandy, D. VanRooyen, J. Mat. Energy Systs. 7, 237 (1985).
38. O. Cayla, P. Combrade, G. Slama in: Proc. 2nd Int. Symp. Environ. Degr. Mat. Nucl. Power Systs. – Water Reactors, Monterey, CA, Sept. 9–12, 1985, American Nuclear Society, LaGrange Park, IL (1986).
39. N. Totsuka, Z. Szklarska-Smialowska, Corrosion J. 43, 734 (1987).
40. Z. Szklarska-Smialowska in: Proc. 4th Int. Symp. Env. Degr. Mat. Nucl. Power Systems – Water Reactors, Jekyll Island, GA, Aug. 6–10, 1989, NACE, Houston, TX (1990).
41. T. Kobayashi, D. A. Shockey, R. L. Jones, Corrosion J. 47, 528 (1991).
42. S. Govindarajan, G. Cragnolino, J. Electrochem. Soc. 134, 2986 (1987).
43. D. D. Macdonald, Corrosion J. 48, 194 (1992).
44. M. E. Indig, J. L. Nelson, Corrosion 47, 202 (1991).
45. W. E. Ruther, T. F. Kassner, F. A. Nichols in: Proc. 2nd Int. Symp. Environ. Degrad. Mat. Nucl. Power Systs. – Water Reactors, Monterey, CA, Sept. 9–12, 1985, American Nuclear Society, LaGrange Park, IL (1986).
46. A. Bertuch, J. Pang, D. D. Macdonald, The Argument for Low Hydrogen and Lithium Operation in PWR Primary Circuits, in the Seventh International Symposium on Environmental Degradation of Materials in Nuclear Power Systems-Water Reactors, Breckenridge, CO, August 6–10, 1995.
47. D. D. Macdonald, unpublished work (1994).
48. L. W. Niedrach, W. H. Stoddard, Corrosion 41, 45 (1985).
49. K. S. Ramp, C. C. Liu, G. Remeo, R. P. Kruger, Y. J. Kim, Proc. Int. Symp. Plant Aging Life Prediction Corrod. Structures, Sapporo, Japan, May 15–18, 1995, NACE, Houston, TX (1995).
50. M. Ullberg, On Corrosion Potential Measurements in BWRs, in: Proc. 4th Int. Symp. Environ. Degrad. Mat. Nucl. Power Systs. – Water Reactors, Jekyll Island, August 6–10, 1989, NACE, Houston, TX (1990).
51. D. D. Macdonald, H. Song, K. Makela, K. Yoshida, Corrosion J. 49, 8 (1993).
52. Y.-J. Kim, C. C. Lin, R. Pathania, Effect of Water Flow Velocity on Electrochemical Corrosion Potential of Stainless Steel in 288 °C Water, presented at CORROSION 93, New Orecans, LA, March 8–12, 1993, Paper 621.
53. Y.-J. Kim, C. C. Lin, R. Pathania, Water Chem. Nucl. React. Systs. 6, 139 (1992).
54. K. Prein, A. Molander, Corrosion Potentials of Stainless Steel in High Temperature Water, in: Chemistry in Water Reactors: Operating Experience and New Developments, Nice, France, April 24–27, 1994, French Nuclear Energy Society, Paris, France (1994), p. 299.
55. G. A. Fuller, D. D. Macdonald, Corrosion J. 40, 474 (1984).
56. Proceedings of the Workshop on Initiation of Stress Corrosion Cracking Under LWR Conditions, EPRI NP-5828, Electric Power Research Institute, Palo Alto, CA (May 1988).

57. Intergranular Corrosion of Stainless Steel, Vol. 1: Mechanism of Crack Initiation, EPRI ER-7247, Electric Power Research Institute, Palo Alto, CA (March 1991).
58. H. Choi, F. H. Beck, Z. Szklarska-Smialowska, D. D. Macdonald, Corrosion J. 38, 136 (1982).
59. C.-Y. Chao, L. F. Lin, D. D. Macdonald, J. Electrochem. Soc. 128, 1187 (1981).
60. L. F. Lin, C.-Y. Chao, D. D. Macdonald, J. Electrochem. Soc. 128, 1194 (1981).
61. C.-Y. Chao, L. F. Lin, D. D. Macdonald, J. Electrochem. Soc. 129, 1874 (1982).
62. D. D. Macdonald, M. Urquidi-Macdonald, J. Electrochem. Soc. 137, 2395 (1990).
63. D. D. Macdonald, S. Biaggio, H. Song, J. Electrochem. Soc. 138, 170 (1991).
64. M. Urquidi-Macdonald, D. D. Macdonald, J. Electrochem. Soc. 136, 961 (1989).
65. D. D. Macdonald, J. Electrochem. Soc. 139, 3434 (1992).
66. F. Mansfeld, J. V. Kenkel, Corrosion J. 35, 43 (1979).
67. F. Franz, P. Novak in: Proc. Conf. Localized Corrosion, NACE, Houston, TX (1974), p. 576.
68. N. Sato, T. Nakagawa, K. Kudo, M. Sakashita, in: Proc. Conf. Localized Corrosion, NACE, Houston, TX (1974), p. 447.
69. T. Nakayama, K. Sasa, Corrosion J. 32, 283 (1976).
70. M. A. C. de Castro, B. E. Wilde, Corrosion J. 35, 560 (1979).
71. T. R. Beck, S. G. Chan, Corrosion J. 37, 665 (1981).
72. T. R. Beck, Corrosion J. 33, 9 (1977).
73. B. E. Brown, H. H. Lu, D. J. Duquette, Corrosion J. 48, 970 (1992).
74. D. E. Williams, M. Fleischmann, J. Stewart, T. Brooks, Electrochemical Methods in Corrosion Research, Mater. Sci. Forum, Vol. 8, M. Duprat (ed.), Trans Tech. Publications, Switzerland (1986), p. 151.
75. H. J. Choi, Y.-H. Hu, M. Karaminezhaad-Ranjbar, J. Mankowski, F. H. Beck, S. Smialowska, D. D. Macdonald in: Proc. Int. Symp. Environ. Degrad. Mat. Nucl. Power Syst. – Water Reactors, Myrtle Beach, SC, August 22–23, 1983, NACE/Met. Soc./ANS, Houston, TX (1984), p. 532.
76. R. C. McClung, Trans. ASME 113, 542 (1991).
77. J. C. Newman, AGARD Conf. Proc. No. 328 (1982), pp. 6.1–6.26.
78. F. K. Ibrahim, J. C. Thomson, T. H. Topper, Int. J. Fatigue, 8, 135 (1986).
79. D. L. Marriott, B. Knott, Innovative Approaches to Irradiation Damage and Fracture Analysis,. PVP Vol. 170, ASMR (1989), pp. 1–8.
80. P. Lukas, Eng. Fract. Mech. 36, 471 (1987).
81. G. Glinka, Eng. Fract. Mech. 22, 839 (1985).
82. W. J. Shack, T. F. Kassner, Review of environmental effects of fatigue crack growth of austenitic stainless steels, Office of Nuclear Reactor Regulation, U.S. Nuclear Regulatory Commission, Supt. of Docs, U.S. G.P.O. [distributor], Washington, DC, 1994.
83. T. Taneda, J. Phys. Soc. J. 46, 1935 (1979).
84. F. Pan, A. Acrivos, J. Fluid Mech. 28, 643 (1967).
85. G. A. Schmitt, W. Bücken, R. Fanebust, Corrosion J. 48, 431 (1992).
86. V. O'Brien, Phys. Fluids 15, 2089 (1972).
87. R. T.-S. Chen, Phys. Fluids 15, 2098 (1972).
88. M-.U. Kim, J. Phys. Soc. J. 46, 1929 (1979).
89. H. K. Kuiken, J. Eng. Math. 12, 129 (1978).
90. J. J. L. Higdon, J. Fluid Mech. 159, 195 (1985).
91. R. C. Alkire, T. Bergh, R. L. Sani, J. Electrochem. Soc. 125, 1981 (1978).
92. T. R. Beck, R. C. Alkire, J. Electrochem. Soc. 126, 1662 (1979).
93. R. C. Alkire, A. Cangellari, J. Electrochem. Soc. 130, 1252 (1983).
94. R. C. Alkire, D. B. Reiser, R. L. Sani, J. Electrochem. Soc. 131, 2795 (1984).
95. Y. H. Huang, R. C. Alkire, J. Electrochem. Soc. 136, 2763 (1989).

96. R. C. Alkire, H. Deligianni, J.-B. Ju, J. Electrochem. Soc. 137, 818 (1990).
97. J. N. Harb, R. C. Alkire, J. Electrochem. Soc. 138, 3568 (1991).
98. J. N. Harb, R. C. Alkire, Corros. Sci. 29, 31 (1989).
99. T. Shibata, Y.-C. Zhu, Corrosion Sci. 37, 853 (1995).
100. T. Shibata, Y.-C. Zhu, Corrosion Sci. 37, 343 (1995).
101. T. A. Prater, W. R. Catlin, L. F. Coffin in: Proc. Int. Symp. Environ. Degrad. Mat. Nucl. Power Systs. – Water Reactors, Myrtle Beach, SC, August 22–25, 1983, NACE/Met. Soc./ANS, Houston, TX (1984), p. 746.
102. H. Choi, F. H. Beck, Z. Szklarska-Smialowska, D. D. Macdonald, Corrosion J. 38. 76 (1982).
103. P. F. Easthope, A. Turnbull, Aspects of Fluid Flow of Relevance to Corrosion Fatigue and Stress Corrosion Cracks, UK National Physical Laboratory, Division of Material Applications, Teddington, Report DMA (A) 105 (1985).
104. K. Rippstein, H. Kaesche, Corros. Sci. 29, 517 (1989).
105. W. Cullen, M. Kemppainen, H. Hanninen, K. Torronen, Report NUREG/CR-4121, MEA-2053 (1985). (Available from NTIS.) (National Technical Information Service).
106. J. Hickling, Corrosion J. 40, 36 (1984).
107. H. Choi, F. H. Beck, Z. Szklarska-Smialowska, D. D. Macdonald, Corrosion J. 40, 37 (1984).
108. D. D. Macdonald, M. Urquidi-Macdonald, Corros. Sci. 39, 51 (1991).
109. D. D. Macdonald, M. Urquidi-Macdonald, An Advanced Couple Environment Fracture Model for Predicting Crack Growth Rates, in: Proc. Parkins Symp. Fundam. Aspects Stress Corros. Crack, Cincinnati, OH, October 20–24, 1991.
110. D. D. Macdonald, M. Urquidi-Macdonald, P.-C. Lu, The Coupled Environment fracture Model – A Deterministic Method for Calculating Crack Growth Rates, presented at CORROSION 94, Baltimore, MD, February 28–March 4, 1994, Paper 246.
111. M. P. Manahan, K. E. Newman, D. D. Macdonald, A. J. Peterson, Experimental Validation of the Basis for the Coupled Environment Fracture Model, in: Proc. EPRI Workshop on Secondary-Side Initiated IGA/IGSCC, Minneapolis, MN, October 14–15, 1993. EPRI, Published while at the Center for Advanced Materials, The Pennsylvania State University, University Park, PA 16802; in cooperation with MPM Research and Consulting, 915 Pike St. PO Box 840, Lemont, PA; in cooperation with Global Technical Consultants, Inc., Centre Hall, PA 16828; and in cooperation with Niagara Mohawk Power Corp. Research and Development, 300 Erie Blvd. W. Syracuse, NY 13202, 1993.
112. M. P. Manahan, D. D. Macdonald, A. J. Peterson, Corrosion Sci. in press (1995).
113. P.-C. Lu, M. Urquidi-Macdonald, D. D. Macdonald, in preparation (1994).
114. W.-T. Tsai, A. Moccari, Z. Szklarska-Smialowska, D. D. Macdonald, Corrosion J. 40, 573 (1984).

Advances in Electrochemical Science and Engineering
Edited by Richard C. Alkire, Heinz Gerischer, Dieter M. Kolb and Charles W. Tobias
© WILEY-VCH Verlag GmbH, 1997

Polymer Electrolyte Fuel Cells

Shimshon Gottesfeld and Tom A. Zawodzinski*

Materials Science and Technology Division, Electronic and Electrochemical Materials and Devices Group, Los Alamos National Laboratory, Los Alamos, NM 87545, USA
*Co-author of Section 5 on "The Ionomeric Membrane"

Contents

1 Introduction ... 197
2 The Polymer Electrolyte Fuel Cell: A General Description ... 198
3 Electrocatalysis in the Polymer Electrolyte Fuel Cell ... 202
  3.1 The Kinetics of the ORR at the Pt/Ionomer Interface ... 203
  3.2 Electrocatalysis at the Hydrogen Anode ... 217
  3.3 Impurity Effects on Anode Electrocatalysis ... 219
    3.3.1 Poisoning of the PEFC Anode Catalyst by Low Levels of CO ... 219
    3.3.2 Poisoning of the PEFC Anode Catalyst in the Presence of CO_2 ... 225
    3.3.3 A CO_2-Tolerant PEFC Anode ... 227
    3.3.4 Electrocatalysis Issues at the PEFC Anode: Summary ... 228
4 Practical Aspects of Electrocatalysis: The Membrane/Electrode Assembly ... 229
  4.1 Platinum Black Catalysts Bonded to Membrane ... 230
  4.2 Pt/C Catalysts Applied as Part of a Gas-Diffusion Electrode ... 231
  4.3 Pt/C Catalysts Applied to the Membrane ... 235
  4.4 Long-Term Testing of Membrane/Electrode Assemblies ... 241
    4.4.1 Ionomeric Membrane Integrity and Maintenance of Protonic Conductivity ... 241
    4.4.2 Catalyst Ripening ... 242
    4.4.3 Long-Term Anode Poisoning and Recovery ... 243
    4.4.4 Freeze–Thaw Cycles ... 244
  4.5 Membrane/Electrode Assemblies for PEFCs: Summary ... 244
5 The Ionomeric Membrane ... 245
  5.1 PEFC Membranes: Significance, Sources, and General Properties ... 245
  5.2 Structural Aspects of Ionomeric Membrane Materials ... 247
  5.3 Water in PEFC Membranes ... 249
    5.3.1 Water Content and Protonic Conductivity in Ionomeric Membranes ... 250
    5.3.2 Water Transport Properties ... 265
  5.4 The Ionomeric Membrane of the Polymeric Electrolyte Fuel Cell: Summary ... 270
6 Modeling and Diagnostics of the Polymer Electrolyte Fuel Cell ... 271
  6.1 Modeling of Processes in the Ionomeric Membrane ... 272
  6.2 Modeling of Electrode Losses ... 278
    6.2.1 Modeling of Steady-State Polarization ... 278
    6.2.2 Modeling and Diagnostics Based on Impedance Spectra Measurements ... 284
7 PEFC Stack and Complete Power Systems ... 285
  7.1 Earlier History – Efforts at General Electric ... 286
  7.2 Further Developments During the 1980s and Early 1990s ... 287

8 The Polymer Electrolyte Direct Methanol Fuel Cell (DMFC) 291
9 References 297

List of Symbols

a_w	water activity
A_r	effective platinum surface area per unit geometric surface area
c	concentration
C	concentration
D	diffusion coefficient
D_{wH}	binary water/hydrogen gas-phase diffusion coefficient
$E^{\#}$	apparent activation energy
EW	equivalent weight
F	Faraday constant
I	current; current density
$k_{hyd}(\lambda)$	membrane hydraulic permeability
l_X	thickness of X
M_m	equivalent weight of membrane
N	flux
p_{ox}, P_{ox}	partial pressure of oxygen
P	pressure
P_A	overall anode pressure
P_X	partial pressure of X
R	gas constant; resistance
σ	effective protonic conductivity
t_A	anode thickness
T	temperature
V	potential
V_p	volume fraction of polymer
x_X	mole fraction of X
x_{wn}	mole fraction of water in gas stream of n
z	membrane thickness
α	ratio of water flux to molar flux of hydrogen I (see Eq. (20))
$\varepsilon(J)$	effective porosity of catalyst layer backing
η	overpotential
θ_X	fraction of surface area covered by X
κ	conductivity
λ	degree of hydration or water content of membrane (H_2O/SO_3^-)
$\xi(\lambda)$	electroosmotic drag coefficient
ρ_{dry}	density of dry membrane
$\Delta\Phi$	difference in potential
$\mathscr{D}_{SON}$	D_{ON} at standard conditions
$\mathscr{V}$	standard molar volume of an ideal gas

Abbreviations

DMFC	direct methanol fuel cell
DVB	divinylbenzene
EW	equivalent weight
HOR	hydrogen oxidation reaction
LANL	Los Alamos National Laboratory
M&E	membrane/electrode
ORR	oxygen reduction reaction

PBI	polybenzimidazole
PEFC	polymer electrolyte fuel cell
PEM	polymer electrolyte membrane
PESA	poly(ethylenesulfonic acid)
PFSA	perfluorocarbon sulfonate; perfluorosulfonic acid
poly-AMPS	poly(2-acrylamido-2-methylpropanesulfonic acid)
PSSA	poly(styrenesulfonic acid)
PTFE	polytetrafluoroethylene
RDE	rotating disk electrode
scfh	standard cubic feet per hour
RHE	reference hydrogen electrode
SAXS	smal-angle X-ray scattering
SPE^{TM}	solid polymer electrolyte
TBA$^+$	tetrabutylammonium cation
TFMSA	trifluoromethanesulfonic acid
TMPP	tetramethylphenylporphyrin

1 Introduction

Polymer electrolyte fuel cells (PEFCs) have attracted much interest recently. The need for an efficient, nonpolluting power source for vehicles in urban environments, emphasized by recent legislative initiatives, has resulted in increased attention to the option of fuel-cell-powered vehicles of high efficiency and low tail-pipe emissions. Of various fuel cell systems considered, the polymer electrolyte fuel cell technology seems to be the most suitable for terrestrial transportation applications. This is thanks to low temperature of operation, perfect CO_2 tolerance by the electrolyte and a combination of high power density and high energy conversion efficiency. Key barriers for the development of this fuel cell technology for terrestrial applications, considered very high just 5–10 years ago, have been successfully overcome, as described in detail in this chapter. As a result, automotive and fuel cell manufacturing industries have initiated significant technology validation programs and demonstrations which include fuel-cell-powered vehicles, stationary power generation systems and battery replacement devices. Market entry of PEFCs through the latter applications may actually precede implementation of such fuel cells in vehicular power systems, in large part because of less stringent demands on system costs.

At present, PEFC R&D is being inspired by the technology needs of PEFC power sources for transportation. Central technology needs of low cost, high performance, and high reliability that have to be met simultaneously to make such an electric vehicle a reality are translated into R&D targets which include lowering of platinum electrocatalyst loading while maintaining high cell performance, provision of solutions for anode electrocatalyst performance loss caused by practical fuel feed streams, evaluation and improvement of gas distributor configurations to increase air cathode performance at low air pressures, and definition of ionomeric membrane characteristics required to achieve optimized water profiles along the cell thickness dimension and, consequently, high protonic conductivity. These R&D activities cover a range of fundamental subjects in interfacial electrochemistry and materials science as well as more applied aspects which belong mostly to the areas of chemical and electrochemical engineering.

In this chapter, we will focus our discussion on the single polymer electrolyte fuel cell and will describe only briefly fuel cell stacks and complete power systems based on such cells. We will show how R&D efforts at the cell level enhanced the understanding of key factors which determine PEFC performance, cost, and reliability and, consequently, enabled significant recent advancements in this fuel cell technology.

2 The Polymer Electrolyte Fuel Cell: a General Description

Figure 1 is a schematic presentation of the cross-section of a single polymer electrolyte fuel cell (PEFC). This scheme will be used to discuss the key materials and processes in the PEFCs. The "heart" of the cell, which is magnified in the

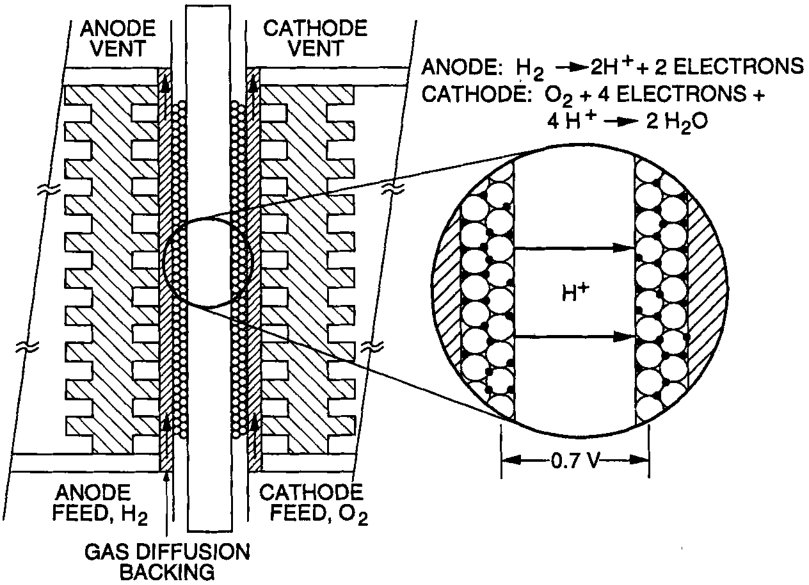
ANODE VENT
CATHODE VENT
ANODE: $H_2 \rightarrow 2H^+ + 2$ ELECTRONS
CATHODE: $O_2 + 4$ ELECTRONS + $4H^+ \rightarrow 2H_2O$
H^+
0.7 V
ANODE FEED, H_2
CATHODE FEED, O_2
GAS DIFFUSION BACKING

Fig. 1. Schematic presentation of a PEFC cross-section. The cell (left) consists of a membrane catalyzed on both sides (referred to as a "membrane/electrode (M&E) assembly"), gas-diffusion backing layers and current collectors with flow fields for gas distribution. The latter become bipolar plates in a fuel cell stack. The M&E assembly described schematically here (right) shows catalyst layers made of Pt/C catalyst intermixed with ionomer and bonded to the membrane (large circles in the scheme correspond to 10 nm dia. carbon particles and small circles to 2 nm dia. platinum particles).

scheme, is the so-called membrane/electrode (M&E) assembly. In its simplest form, the "electrode" component of the M&E assembly would consist of a thin film (5–50 μm thick) containing a dispersed platinum catalyst. This catalyst layer is in good contact with the ionomeric membrane (the central slab in the scheme in Fig. 1) which serves as electrolyte and gas separator in this cell. The membrane electrolyte is typically 50–175 μm thick. The M&E assembly then simply consists of an ionomeric membrane with thin catalyst layers bonded onto each of its two major surfaces. The "gas-diffuser" (or "backing") layers in immediate contact with the catalyzed membrane (see Fig.1) are made of hydrophobized porous carbon paper, or carbon cloth. These layers are typically 100–300 μm thick and are wet-proofed by treatment with polytetrafluoroethylene (PTFE).

In other modes of PEFC fabrication, the catalyst layer is applied to the porous carbon backing layer and this catalyzed carbon paper is subsequently hot-pressed onto the membrane. For this mode of fabrication, the term "electrode" usually refers to the carbon paper (or carbon cloth) with the catalyst layer on one of its surfaces, i.e., the surface to be bonded to the membrane. In this case, the "M&E assembly" includes the membrane and the carbon electrode, i.e., it includes the backing layer as well. Irrespective, however, of how the catalyst layer is bonded, first to the membrane or first to the porous carbon backing, the complete single PEFC will always have the following structure observed along the cross-section of the cell from the center to each side: ionomeric membrane/catalyst layer/porous wet-proofed carbon backing (Fig.1). The single cell is completed by current collector plates which usually contain machined flow fields, as required for effective distribution of reactant gases along the surfaces of the electrodes. These plates become bipolar plates in the fuel cell stack, in which case they would have gas flow fields on both sides, as shown schematically in Fig. 1. A general view of a single cell hardware is presented in Fig. 2. The Teflon

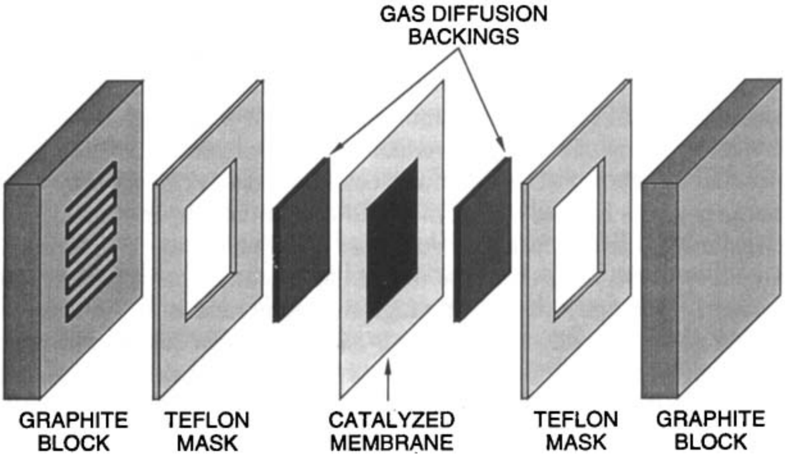

Fig. 2. Components of a single polymer electrolyte fuel cell used for laboratory investigations. In a stack, relatively thinner current collectors will become bipolar plates with the flow fields machined on both sides.

masks shown are gaskets that confine the gas flow to the active area and provide, together with the periphery of the ionomeric membrane, an effective seal.

The magnified part in Fig. 1 highlights the components of the M&E assembly, the central element of the PEFC which consists of a proton-conducting membrane electrolyte with a composite catalyst layer adjacent to each of its surfaces. The scheme shows the catalyst layer as platinum (small circles) supported on carbon (larger circles). This type of catalyst has been used in more recent developments of PEFCs, mainly at the R&D level. The Pt/C powder, prepared mostly by established procedures based on colloid chemistry, has to be intimately intermixed with recast ionomer to provide sufficient ionic conductivity within the catalyst layer. Thus, the catalyst layer can be described as a Pt/C// ionomer composite, where each of the three components are uniformly distributed within the volume of the layer. The scheme in Fig. 1 highlights the recently demonstrated PEFC catalyst layers employing Pt/C. Industrial implementation of this newer catalyst technology in PEFC stacks has begun, but, at the time of writing, there is still significant use in PEFC stacks fabricated to date of PTFE-bonded platinum black catalysts applied by hot-press to the ionomeric membrane, typically requiring a platinum loading 20–40 times higher (4 mg Pt/cm^2 vs. 0.1 mg Pt/cm^2) to obtain a similar cell performance. The Pt/C catalysts have been preferred in the basic scheme of Fig. 1, assuming that they will be adapted sooner or later in commercial PEFCs because of their much lower cost and their intrinsic good performance and reliability.

The proton-conducting polymeric membrane is the most distinctive element of the polymer electrolyte fuel cell, as is indeed reflected by any of the three names used for this type of cell: PEM fuel cell ("polymer electrolyte membrane" fuel cell), SPE^{TM} fuel cell ("solid polymer electrolyte" fuel cell), or PEFC ("polymer electrolyte fuel cell"). We use the last of those acronyms in this chapter. The membrane commonly employed in most recent PEFC technology developments is made of a perfluorocarbon sulfonic acid ionomer. Nafion^{TM} made by DuPont is the best-known material of this type. Similar materials are produced as either commercial or developmental products by W. L. Gore and by Asahi Chemical and Asahi Glass. The combined chemical and physical properties of perfluorocarbon sulfonate (PFSA) membranes give them significant superiority over any other membrane material as electrolytic separators in PEFCs. These membranes exhibit very high long-term chemical stability under both oxidative and reductive environments, thanks to their Teflon-like molecular backbone. The protonic conductivities achieved in well-humidified membranes are as high as 0.1 S/cm at cell operation temperatures, which translates to an areal resistance as low as 0.05 ohm cm^2 for a membrane 50 μm thick. Such a thin membrane can serve at the same time as an effective gas separator: the permeability of both oxygen and hydrogen through the membrane is of the order of 10^{-11}–10^{-10} mol/cm s atm, which translates to a gas crossover equivalent current density of 1–10 mA/cm^2 through a membrane 100 μm thick in an operating fuel cell. This leakage current is at or below 1% of the operating current of a PEFC – typically 1 A/cm^2 or higher.

The two important drawbacks of PFSA membranes are the limited range of temperatures in which they can be effectively employed and their high cost at present. The first limitation typically forces operation of PEFCs at temperatures below 100 °C, although some increase of the temperature of operation, e.g., to 120 °C, may be possible at the expense of operation under pressurized steam. The upper limit on the temperature is dictated by the need for effective humidification of the membrane, a prerequisite for maximizing its protonic conductivity. This need also dictates, in turn, operation in a temperature/pressure domain corresponding to a dual-phase (liquid–vapor) water system, which results in liquid water removal and/or liquid water recirculation requirements. The cost of the membrane is an issue outside the scope of our discussion. However, it can be predicted with reasonable certainty that this cost may come down significantly as the market for the membrane will significantly increase, e.g., as a result of large-scale application in electric vehicles.

Adjacent the ionomeric membrane on both sides are the catalyst layers (Fig. 1). As described above, these are platinum black/PTFE composites with high platinum loadings (typically 4 mg Pt/cm^2 on each electrode) or composites of carbon-supported platinum and recast ionomer, with or without added PTFE, of much lower platinum loading (as low as 0.1 mg Pt/cm^2 on each electrode). The electrochemical processes in the fuel cell take place at these electrocatalysts. In the hydrogen (or methanol reformate)/air fuel cell, the processes at the anode and cathode, respectively, are:

$$H_2 \longrightarrow 2H^+ + 2e \tag{1}$$

and

$$O_2 + 4e + 4H^+ \longrightarrow 2H_2O \tag{2}$$

The porous backing layer which is placed behind the catalyst layer (Fig. 1) fulfills important tasks in the PEFC. In this layer, combined requirements of effective reactant gas supply to the catalyst layer and effective water supply and removal in either vapor or liquid form have to be simultaneously fulfilled. Wet-proofing by PTFE is required to ensure that at least part of the pore volume in the cathode backing remains free of liquid water in an operating cell, so as to enable rapid gas-phase transport. The scale of the porosity and the amount of PTFE added are two important parameters that determine the success of the backing layer in fulfilling the combined tasks of gas and water transport. Obviously, the backing layer has to be made of a material of high and stable electronic conductivity in a wet environment. Although some expanded metal structures have been suggested, most of PEFC backings to date have been based on porous carbon paper or cloth.

The final element on the outer side of the unit cell (Figs. 1 and 2) is the current collector plate, which typically contains the machined gas flow field. These two functions of current collector and gas flow field may be fulfilled, in principle, by two separate components but, in most of the cells and and stacks tested so far, the flow field is machined in the current collector plate using a range of geometries, e.g., a single serpentine channel, parallel channel flow and series–parallel combinations. The specific flow-field geometry may be critical in fulfilling the requirements of effective water supply and effective liquid water removal from the cathode.

The current collector plate becomes the bipolar plate in a PEFC stack. It should therefore exhibit high electronic conductivity and be impermeable to oxygen and hydrogen gas. Both carbon and metals like stainless steel or titanium have been considered as potential materials for the current collector, or the bipolar plate as it would be called in the context of a stack.

The very general description provided above for the component parts of a PEFC should clarify the diversity of R&D elements involved in the development of a PEFC and PEFC stack. These R&D elements span fields of research in interfacial electrochemistry (electrocatalysis); electrochemical and materials science aspects of membranes, carbon, and metals; and mass/heat-transport engineering. This chapter covers recent R&D work devoted to the establishment and advancement of PEFC technology. The work described here has been devoted primarily to electrochemical and materials aspects of the PEFC and to the building and testing of single cells based on improved materials and electrocatalysts. In the most general terms, the target of these efforts has been to achieve the combined properties of high PEFC performance, long-term performance stability, and low intrinsic cost.

3 Electrocatalysis in the Polymer Electrolyte Fuel Cell

The overall electrode processes in a hydrogen/air PEFC, oxidation of molecular hydrogen to protons ("HOR") at the anode, and reduction of molecular oxygen to water (4e process) at the cathode ("ORR"), are described by Eqs. (1) and (2), respectively. Both electrode processes are electrocatalytic in nature, essentially because they both require active catalyst sites to break the bond in the diatomic gaseous reactant molecule. There is, however, a big difference between the rates of the two processes: the oxygen reduction process requires an overpotential of around 400 mV to reach a rate of 1 mA/cm^2 (Pt) at the Pt/ionomer interface, whereas the hydrogen oxidation process requires only around 20–30 mV to reach the same current density at the same type of interface. As a result, in a PEFC which employs highly dispersed platinum catalysts, with a surface area equal to or exceeding 100 cm^2 Pt per cm^2, of membrane, the anodic overpotential could be negligible even at cell currents of 1 A/cm^2. This is not always the case in practice, however, because of two sources of anode performance limitation in PEFCs: local loss of water on the anode side of the cell and poisoning of the anode catalyst in the presence of impurities in the fuel feed stream, particularly ppm levels of CO. We discuss below, in some detail, these three important subjects of electrocatalysis in PEFCs: the low specific rate of the oxygen reduction process and the possible limitations of anodic electrocatalytic activity associated with either catalyst poisoning or local drying of the ionomer.

Platinum and platinum alloy electrocatalysts are by far the most studied in the PEFC and in model, bulk, metal catalyst/ionomer interfacial systems devised to study the electrocatalytic process in a PEFC environment. The reason is that, to date, no other electrocatalyst has been demonstrated to approach the specific activity exhibited by platinum (or platinum alloys) in PEFCs, particularly in the more demanding process of oxygen electroreduction. This is not too surprising. The PEFC employs essentially an aqueous acidic (polymeric) electrolyte, typically a humidified poly(perfluorosulfonic acid) (PFSA), in which the four-electron oxygen reduction process is expected to be inherently slow, as is generally the case for acid aqueous media. Platinum and platinum alloys seem to be the only catalysts capable of generating high rates of ORR under these relatively adverse interfacial kinetics conditions. Furthermore, alternative electrocatalysts developed quite successfully in the past for the cathodic oxygen reduction process in alkaline fuel cells, for example different types of metal porphyrins, may have limited chemical stability in the acid environment of the PEFC. In the following, we therefore focus our discussion on electrocatalysis of the ORR and HOR processes at the platinum (or platinum alloy)/ ionomer interface.

3.1 The Kinetics of the ORR at the Platinum/Ionomer Interface

The high overpotential at the PEFC cathode is the single most important source of loss in the PEFC, as in all other low-temperature fuel cells. This is directly reflected in the polarization curve of the PEFC by the open-circuit voltage being close to 1.0 V, to be compared with a thermodynamically expected value of 1.23 V (at room temperature) for a H_2/O_2 fuel cell. This discrepancy is caused by the sluggish kinetics of the ORR process, resulting in an open-circuit mixed potential, determined by a cathodic ORR component current and a parasitic anodic component current of several possible origins. The sluggish kinetics of the ORR contributes significantly to losses in a PEFC under current. A cathode potential as low as 0.70–0.80 V is required to reach an ORR current density of 1 A/cm^2 in a PEFC air cathode at 80 °C, corresponding to a cell voltage loss of 400–500 mV. Evaluation of the kinetics of the ORR at the Pt/ionomer or, in the context of more recent PEFC structures, at the Pt/*recast* ionomer interface, is thus most important for cell diagnostic as well as any planned improvement in PEFC performance.

From the schematic structure of the catalyst layer shown in Fig. 1, it can be seen that the reduction of O_2 occurs in the PEFC at the interface between dispersed platinum particles and a recast ionomeric electrolyte. The ionomeric PFSA electrolyte provides the interfacial environment for reaction (2). This means that the hydrated ionomer is the medium of solvation for both reactants in this interfacial process, i.e., dioxygen molecules and protons. The unique nature of the PFSA electrolyte has generated in the past some hope for particularly high ORR rates at the Pt/PFSA interface. Some special features of this electrolyte in the context of the ORR are: the high solubility of oxygen in it (10 times the solubility of O_2 in water); its mixed hydrophilic/hydrophobic nature; and immobilization of anions. The benefit of the higher solubility of the reactant is obvious since the ORR process is typically first-order in oxygen partial pressure. Molecular-scale hydrophilic and hydrophobic domains could be beneficially involved in different steps of the ORR process, whereas site-blocking effects of adsorbed anions at the platinum catalyst could be minimized by anion immobilization. The systematic measurements of the rate of the interfacial ORR process at the Pt/ionomer interface, carried out since the late 1980s, have revealed ORR rates that are comparable with the highest obtained at Pt/aqueous acid interfaces, but are less unusual than was hoped.

The overall voltage loss in the fuel cell cathode itself is a complex combination of interfacial (ORR), mass-transport and charge-transport losses (see Sections 4 below). Correction for mass-transport and/or charge-transport losses within a fuel cell cathode, as required to derive ORR interfacial kinetics within the PEFC itself, is complicated. Parameters of the interfacial ORR process can be derived from measurements of the performance of a fuel cell cathode only as part of a fit of the overall cell polarization curve, using in the process several additional adjustable parameters to solve for various transport and ohmic barriers (see Sections 4 and 6). Unfortunately, at low cell polarization, where the cathode currents are least affected by further cathode transport limitations, the net measured cathode current in the PEFC is also not purely determined by interfacial ORR rates. This time the reason is the effect of hydrogen "crossover" through the membrane separator which becomes significant in the analysis at (fuel cell) current densities significantly below 100 mA/cm^2. For these reasons, model interfacial systems are required to study the ORR at the Pt/ionomer interface. Such model systems require properties of:

1. simple, well-defined geometry which enables accurate mass-transport corrections, and
2. an interfacial composition which mimics as well as possible the interfacial environment within the PEFC cathode, i.e., platinum in contact with hydrated ionomer with no added liquid electrolyte.

Model systems of this type recently described in the literature have been based on two general schemes. In one of these schemes, a smooth platinum electrode, or microelectrode, is coated by a film of recast ionomer to generate a Pt/recast ionomer interface. In the other approach, a platinum microelectrode is pressed onto an ionomeric membrane to generate a Pt/membrane interface. To complete the electrochemical cell, counter- and reference electrodes have to be in contact with the same ionic medium; this can be achieved by direct contact of these other electrodes with the ionomeric phase, or by contacting the reference electrode to the ionomeric phase through a "salt bridge" containing a dilute acid solution. The latter involves a negligible perturbation of the hydrous ionomer system.

In the earliest attempt to study the ORR at the Pt/ionomer interface [1], Gottesfeld et al. used a classical rotating disk electrode (RDE) configuration to control oxygen transport to a smooth platinum electrode coated by a recast film of Nafion. However, this configuration requires the circuit to be completed by immersing the RDE in an aqueous electrolyte in which the other two electrodes are inserted, leaving some questions as to the possible effect of the liquid electrolyte on the measured interfacial rates. The correction for the combined mass-transport limitations in the Levich layer and in the recast ionomeric film could be evaluated with good precision for the coated RDE geometry, based on measurements of the limiting currents at the coated and at the bare electrode at the same rotational

Table 1. Measured ORR current densities for "bare" and ionomer-coated RDEs.

Potential vs. RHE [V]	Current density in 0.5 M H_2SO_4 at 25 °C [mA/cm^2]	
	Bare RDE	Filmed RDE
0.90	0.056	0.11
0.95	0.27	0.34
0.85	0.74	0.71
0.80	1.8	1.1

frequency ω. The detailed equations are given in [1]. Results of mass-transport-corrected ORR currents at the "bare" platinum electrode and at the same RDE coated with a recast film of Nafion are given in Table 1.

No attempt was made to analyze these results further in terms of an apparent exchange current density or Tafel slope. The similarity of the ORR activity at the bare and the filmed electrode is quite obvious from Table 1. A question which Gottesfeld et al. tried to address was why the reported higher solubility of oxygen in bulk Nafion (an order of magnitude higher than in water) did not result in stronger relative enhancement of the rate of interfacial ORR at the Pt/Nafion interface. Part of the answer came from analysis of the actual concentration and diffusion coefficient of oxygen in the *recast* film. Resolution of the two elements of gas permeability – concentration and diffusion coefficient – could be achieved by combining measurements of steady-state (filmed) RDE current and currents measured at the same filmed RDE under conditions of linear potential scan in the scan-rate range 10 to 500 mV/s [1]. The steady-state RDE currents yield the product $D_{\text{film}}C_{\text{film}}$, whereas the linear potential scanning experiments yield the product $D_{\text{film}}^{1/2}C_{\text{film}}$, enabling solution of D_{film} and of C_{film} [1]. The results of these combined measurements are given in Table 2, which shows also D and C values reported for oxygen in a 0.5 M H_2SO_4 solution and in bulk Nafion.

Table 2 demonstrates that the concentration and diffusion coefficient of dioxygen in the recast film are quite different than those in the bulk ionomer, both parameters showing values which fall between aqueous solution and bulk ionomer levels. Table 2 shows why measurements of ORR kinetics should preferably be performed at model Pt/*recast* ionomer interfaces in order to evaluate the ORR process in fuel cell cathodes which employ recast films of the ionomer. Gottesfeld et al. interpreted the ORR results shown in Table 1 in light of the parameters shown in Table 2, suggesting

Table 2. Oxygen concentrations and oxygen diffusion coefficients in aqueous acid, recast ionomer, and bulk ionomer phases [1].

	0.5 m H_2SO_4	Recast film	Bulk Nafion
$10^6 \times C$ [mol cm^{-3}]	1.13	3.1	9–16
$10^6 \times D$ [cm^{2}S^{-1}]	18.0	4.0	0.1–0.4

two reasons why a more significant enhancement in ORR rate is not seen at the filmed platinum electrode:

1. the local oxygen enrichment is less than expected from bulk ionomer properties;
2. the composition of the interface in this experiment is apparently only partly Pt/recast ionomer, the other part being Pt/aq. H_2SO_4.

Penetration of the acid through the recast film all the way to the platinum surface was supported by voltammetric evidence and was apparently assisted by the potential multicycling routine employed to maintain an impurity-free platinum surface [1]. Such a study of a filmed platinum electrode immersed in aqueous acid solution is, therefore, less than perfect for providing good data on the rate of ORR at the interface between platinum and hydrated ionomer in a fuel cell cathode, where the only interfacial liquid is distilled water.

In the first attempt to measure the rate of the ORR at a Pt/recast Nafion interface with no added electrolyte, Paik et al. employed a platinum gauze coated by recast ionomer which was pressed onto a Nafion membrane [2]. A dynamic hydrogen reference electrode was pressed, together with the counter platinum wire, onto the same side of the membrane and the working platinum- gauze electrode was pressed onto the other side of the membrane. The authors faced difficulties in correcting for ohmic losses in the case of thinner recast films around the wires of the gauze, and in correcting for mass-transport losses in the case of thicker recast films. An important, practically unknown, factor was the contact resistance at the interface between the coated gauze and the membrane.

Parthasarathy et al. subsequently described [3–6] investigations of the ORR at the better-defined interface between a platinum microelectrode and a humidified Nafion membrane. The contact between the microelectrode and the membrane was achieved by mechanical pressure. The system employed by these authors is shown in Fig. 3. In this case, the interface studied is Pt/bulk ionomer, rather than Pt/recast ionomer and, therefore, does not mimic precisely the interfacial composition in PEFC cathode structures based on Pt/C//recast ionomer composites (see Table 2). Nevertheless, this arrangement enables preparation of a Pt/ionomer interface and completion of the cell by other electrodes in direct contact with the membrane, all achieved in a relatively simple configuration of well-defined geometry: a microelectrode of known diameter in direct contact with an ionomeric membrane. The complete cell was bathed in humidified oxygen. This geometry has also enabled studies at elevated pressures and temperatures. The authors derived the apparent roughness factor of the platinum microelectrode from cyclic voltammetry. Prolonged cycling was required to achieve a steady-state, well-behaved interfacial system, explained by significant interfacial contamination. The results in the first paper in the series describe ORR measurements at 25 °C [3]. For room-temperature measurements, the oxygen supply was humidified by passing it through a bubbler. Mass-transport-corrected results, derived from slow scan (2mV/s) measurements of ORR currents, are shown in Fig. 4. They are fitted with two linear Tafel domains, as is traditional in the description of such ORR data. From plots of this kind, the authors concluded by extrapolation an exchange current density, J_0, of 2.1×10^{-9} A/cm^2 associated with the domain of low Tafel slope (low

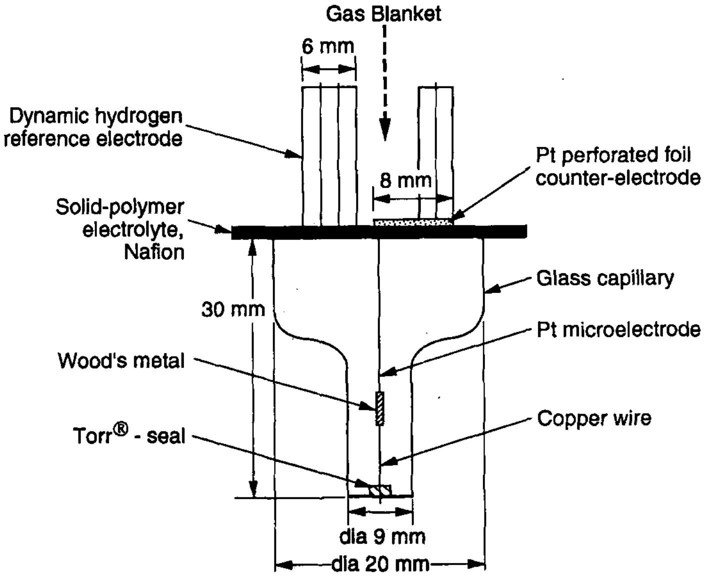
Gas Blanket
6 mm
Dynamic hydrogen reference electrode
8 mm
Pt perforated foil counter-electrode
Solid-polymer electrolyte, Nafion
Glass capillary
30 mm
Pt microelectrode
Wood's metal
Copper wire
Torr® - seal
dia 9 mm
dia 20 mm

Fig. 3. A simplified schematic of a cell used for ORR measurements at the platinum microelectrode/ Nafion membrane interface [4]. (Reprinted by permission of the Electrochenical Society).

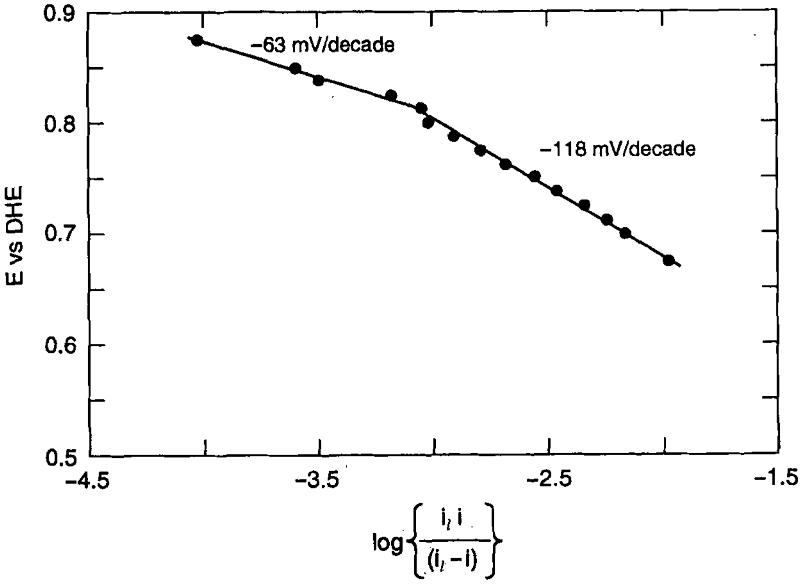

Fig. 4. Mass-transport-corrected Tafel plot for oxygen reduction at the Pt/Nafion interface measured with the system described in [4]. (Reprinted by permission of the Electrochemical Society).

polarization) and $J_0 = 7.8 \times 10^{-7}$ A/cm^2 associated with the domain of high Tafel slope (high polarization). The authors claimed that the latter is "the highest exchange current density reported for the ORR at room temperature at any Pt/electrolyte interface".

While the high apparent exchange current density may look interesting, it should be realized that a direct comparison of *measured* ORR rates at the Pt/ionomer interface and at other Pt/dilute aqueous acid solution interfaces does not reveal a higher rate at the Pt/ionomer interface [7]. The value of exchange current densities obtained by extrapolation of data such as that presented in Fig. 2 has been subsequently questioned by Uribe et al. [7], who suggested that such comparative evaluations of ORR rates should rely only on (mass-transport-corrected) *measured*, rather than extrapolated, current densities. Parthasarathy et al. also derived [3] the diffusion coefficient and concentration of oxygen in the bulk ionomer, according to chronoamperometric measurements performed in a potential-step experiment. The diffusion coefficient of oxygen derived was $7.4\ (\pm 0.3) \times 10^{-7}$ cm^2/s and the concentration reported for oxygen in the ionomer was 26 mM. This oxygen concentration is 2–3 times higher than that reported before by Ogumi et al. for a fully immersed Nafion membrane [8]; this was explained as the result of the lower water content in the membrane which was exposed only to water vapor. The diffusion coefficient derived by Parthasarathy et al. is also three times higher than the value reported by Ogumi et al. (A possible reason for these discrepancies is that the fast chronoamperometric transients which were the basis for the derivation of D and C for oxygen in [3] could have contained significant contributions of platinum oxide reduction currents.)

Parthasarathy et al. subsequently described [6] a detailed investigation of the temperature dependence of the ORR kinetic parameters at the Pt/bulk Nafion interface. The cell employed was similar but a pressure vessel was added to enable measurements at 5 atm O_2. In order to ensure effective humidification at the higher temperatures, a (liquid) water-retaining Teflon cup was constructed around the working electrode to keep the membrane wet. This element of the experiment is important because, as will be shown later in this section, increase of the temperature in the presence of water vapor alone is ineffective in maintaining a high level of ionomeric membrane humidification. Plots of the log of mass-transport-corrected current density vs. the potential of the platinum microelectrode showed an increase by a factor of about five in the rate of ORR at 0.90 V and about three at 0.85 V as the temperature is increased from 30 °C to 90 °C. Parthasarathy et al. analyzed their results in detail by evaluating the apparent Tafel slopes and exchange current densities in the two domains of oxide-covered and oxide-free platinum. The Tafel slope in the first domain showed a systematic increase with temperature (T) from 65 to 75 mV/decade between 30 °C and 90 °C, whereas the Tafel slope in the domain of higher current density showed no clear trend with increase in T. The apparent activation energies for the two regions (low and high Tafel slope) were calculated from the dependence of the apparent exchange current density on T according to:

$$E^{\#} = -2.303 R [\mathrm{d} \log J_0 / \mathrm{d}(1/T)] \quad (3)$$

yielding values of 17.5 ± 0.4 kcal/mol (73.2 ± 1.7 kJ/mol) for the low-current-density domain and 6.6 ± 0.3 kcal/mol (27.6 ± 1.3 kJ/mol) for the high-current-density domain. These are quite similar to activation energies of the ORR reported for platinum in contact with solutions of trifluoromethanesulfonic acid (TFMSA), or in contact with TFMSA hydrate.

In another investigation of the same microelectrode/bulk Nafion interface by Parthasarathy et al. [5], the pressure dependence of the rate of the ORR was determined by analyzing the mass-transfer-corrected Tafel plots and examining the resulting slope of log J_0 vs. log P_{O_2}. A slope of unity was obtained for both neat oxygen and for oxygen in air, in both the low and high current density domains. This result is shown in Fig. 5. A first-order ORR rate with respect to oxygen partial pressure is common to all Pt/aqueous acid systems and confirms that the rate-determining step is a one-electron charge-transfer step, usually written (although never rigorously proven) as:

$$O_{2,ads} + H^+ + e \rightarrow (O_2H)_{ads} \qquad (4)$$

Parthasarathy et al. also performed ac impedance measurements in the frequency range 0.05 Hz–100 kHz for the same platinum microelectrode/bulk ionomer interface

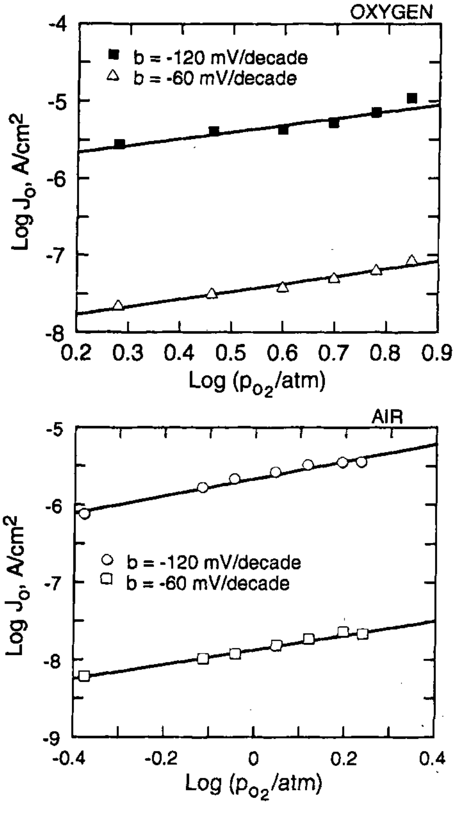

Fig. 5. Reaction-order plots for the ORR process at the Pt/Nafion membrane interface. A unity reaction order is evaluated from the dependence of the apparent J_0 on oxygen partial pressure [5]. (Reprinted by permission of the Electrochemical Society).

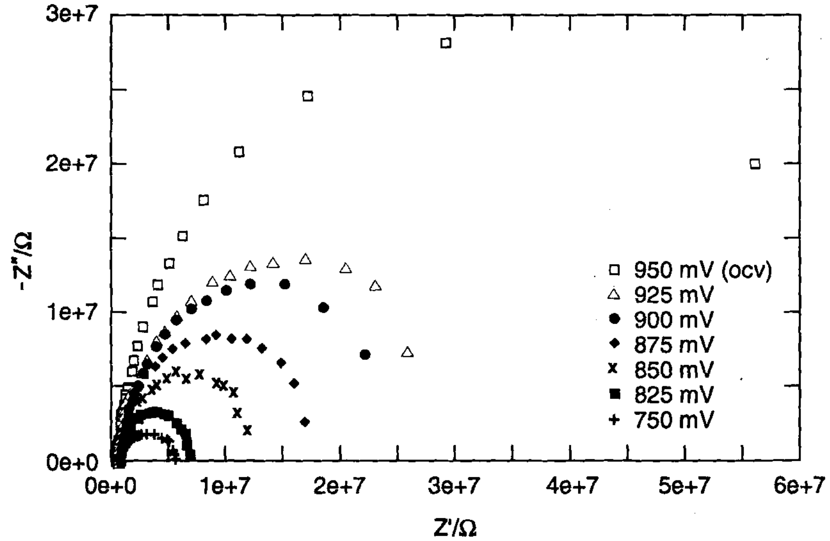

Fig. 6. Interfacial impedance spectra recorded for the ORR at the Pt/Nafion membrane interface with the cell described in Fig. 3 [4]. (Reprinted by permission of the Electrochemical Society).

[4]. In this frequency domain, the authors observed two major features in the complex impedance plot: a lower-frequency feature is associated with the charge-transfer resistance in parallel with the interfacial double layer capacitance. A higher-frequency feature, measured typically in the 10–100 kHz frequency domain, was assigned by the authors to "grain boundaries" in the ionomeric membrane electrolyte, i.e., to a bulk ionomeric electrolyte phenomenon. At higher cathode polarizations, the kinetic semicircle in the complex impedance plot approached the real Z axis at the high-frequency end with an angle of 45°, corresponding to a Warburg element from which oxygen concentration and diffusion coefficients in the Nafion membrane could be extracted. The ORR interfacial kinetics parameters and the oxygen transport parameters evaluated from the impedance spectra were quite similar to the ones collected from steady-state measurements [3]. The variation with potential of the lower-frequency impedance feature (0.05 Hz–1 kHz), associated with ORR interfacial kinetics at this platinum microelectrode/bulk ionomer interface, is given in Fig. 6. It shows a well-behaved pattern of a monotonic decrease in the charge-transfer resistance (diameter of the semicircle) with increase in cathode overpotential. This is to be contrasted with the more complex pattern of impedance spectra measured for Pt/H_2 anodes in contact with Nafion membranes, as described below in Section (3.2).

In an attempt to mimic as closely as possible the composition and structure within the fuel cell cathode, Uribe and co-workers applied a recast Nafion film to a platinum microelectrode in order to study the rate of the ORR as a function of temperature and humidification conditions [9]. The cell employed by Uribe et al. is shown in Fig. 7.

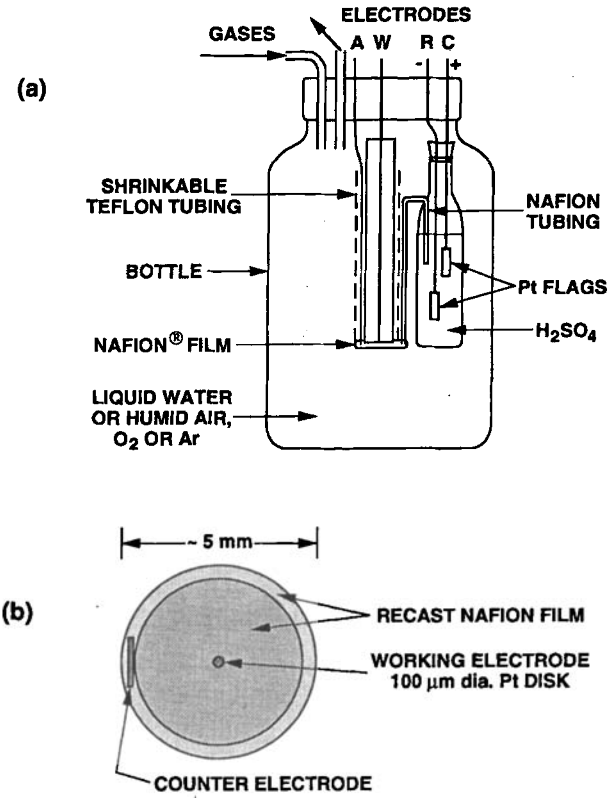
(a)
GASES
ELECTRODES
A W R C
-
+
SHRINKABLE TEFLON TUBING
BOTTLE
NAFION® FILM
LIQUID WATER OR HUMID AIR, O_2 OR Ar
NAFION TUBING
Pt FLAGS
H_2SO_4
(b)
~ 5 mm
RECAST NAFION FILM
WORKING ELECTRODE 100 μm dia. Pt DISK
COUNTER ELECTRODE

Fig. 7. Cell employed for measurements of ORR kinetics at the platinum microelectrode/recast ionomer interface [9]. (a) Side view; (b) cross.section of cathode. W–working electrode, A–anode, R–dynamic hydrogen reference (DHE), and C–counter electrode for hydrogen electrode in DHE. (Reprinted by permission of the Electrochemical Society).

This configuration comes closest to PEFC cathode conditions, in that the platinum surface is in contact with the recast ionomer, rather than bulk ionomer as in [3–6], and the atmosphere is humidified oxygen with no liquid electrolyte and with only water vapor added. The voltammograms obtained for this filmed platinum microelectrode (in a humidified inert atmosphere) is compared in Fig. 8 with the voltammogram recorded with the same electrode in aqueous sulfuric acid solution. For the filmed electrode, effects of site blocking are clearly seen in the Pt–H domain and some anodic oxidation of surface impurities is apparent in the anodic half-cycle above 1 V. The voltammogram did not change following several hours of cycling, suggesting site blocking by impurities or by the ionomer itself. This must have an effect on the apparent ORR kinetic parameters derived, particularly at lower temperatures where impurity adsorption is more pronounced, but it reflects, most probably, the real interfacial condition in fuel cell cathodes based on platinum catalyst/recast ionomer composites.

Current potential dependencies for the ORR process at such a platinum microelectrode coated with a recast Nafion film are shown in Fig. 9 for a range of

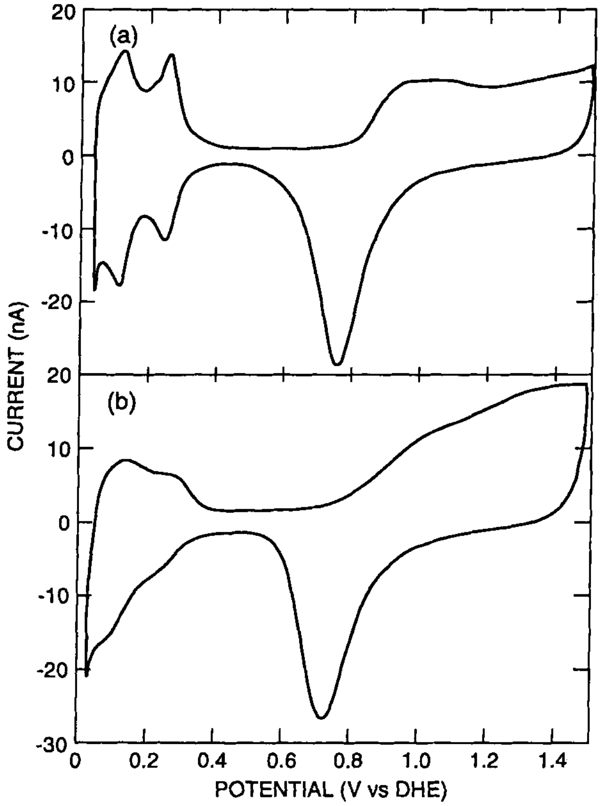

Fig. 8. Voltammogram obtained with the cell in Fig. 7 and for the same electrode immersed in 0.5 M sulfuric acid, recorded in both cases in an argon atmosphere [9]. (Reprinted by permission of the Electrochemical Society).

temperatures. At each temperature the gaseous atmosphere maintained around the microelectrode was saturated with water *vapor* by passing the oxygen gas stream into the cell through a temperature-controlled bottle equipped with a gas bubbler. The cell itself was also carefully temperature-controlled. The result shown in this figure demonstrate the complex effect of temperature on the rate of the ORR at the Pt/recast ionomer in contact with water vapor. In spite of an expected beneficial effect of the temperature on the rate of the interfacial ORR process, a severe loss of ORR activity is seen above 40 °C for a filmed electrode in contact with saturated water vapor. The authors ascribed this behavior to loss of water from the recast film which takes place at elevated temperatures, although the water activity in the gas phase in contact with the film is maintained at unity (saturated vapor). To prove that drying of the ionomer caused this loss of ORR activity, the authors [9] immersed the filmed electrode temporarily in liquid water at 80 °C and showed that the ORR activity could be temporarily restored in this way. This was followed, however, by renewed loss of

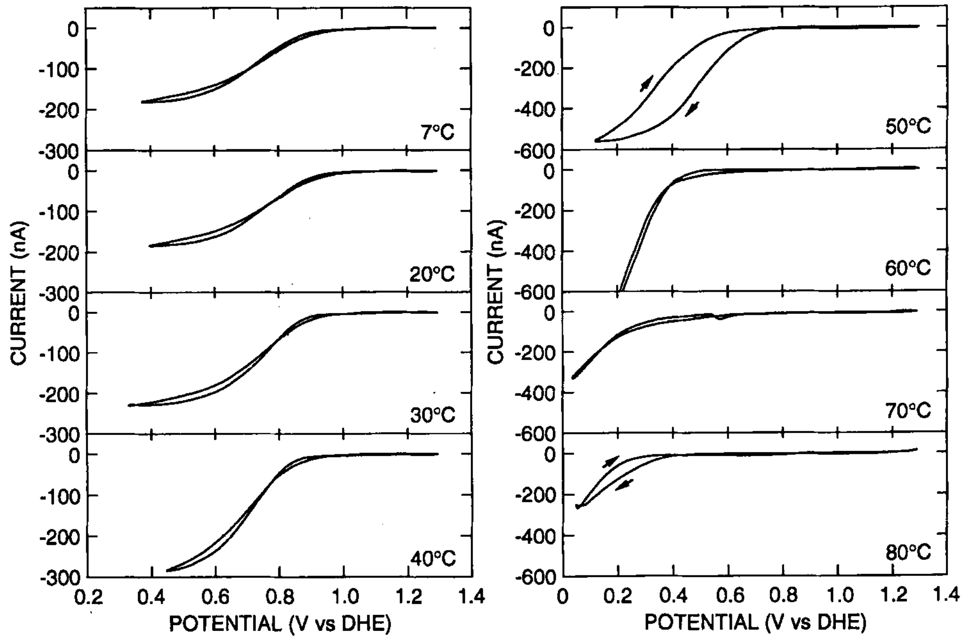

Fig. 9. Current potential characteristics obtained with the cell in Fig. 7 at several temperatures in a water-vapor-saturated oxygen atmosphere [9]. (Reprinted by permission of the Electrochemical Society).

ORR activity as the recast ionomer film gradually dried again while in contact with saturated water vapor at 80 °C. These observations are important in the context of ORR catalytic activity in PEFC cathodes. The sensitivity of the rate of ORR to interfacial water content (Fig. 9) and the tendency of the ionomer to dry up at elevated temperatures when in contact with saturated water vapor, clearly suggest that the level of humidification at the PEFC cathode catalyst should be kept high by maintaining some water in *liquid* state in contact with the cathode catalyst layer.

Uribe et al. went on to treat the ORR kinetic currents at the Pt/recast ionomer interface by correcting raw results collected at 30 °C for the mass-transport limitations in the thin recast film. Measured ORR currents, net kinetic current densities, and the value of $dV/d \log J$ as computer-calculated directly from the plot of $\log J_{\mathrm{orr}}$ vs. V, are presented as a function of potential in Fig. 10. Results are shown for a cathodic and an anodic slow scan of the potential. Each triangular scan of the potential had to start from 1.2 V to remove surface impurities before the onset of ORR measurement. Figure 10 shows that a gradually varying Tafel slope was found in a wide potential domain of significance to the PEFC (0.8–0.6 V). Consequently, the authors suggested that there is no good basis to "force" two constant Tafel slopes upon these data, and no good basis to derive two apparent exchange current densities corresponding to each of these slopes, as has been done before [10] and in other analyses of ORR kinetics at Pt/aqueous acid interfaces. Uribe et al. [7, 9] argued that extrapolation to the thermodynamic potential for the O_2/H_2O couple (1.23 V at

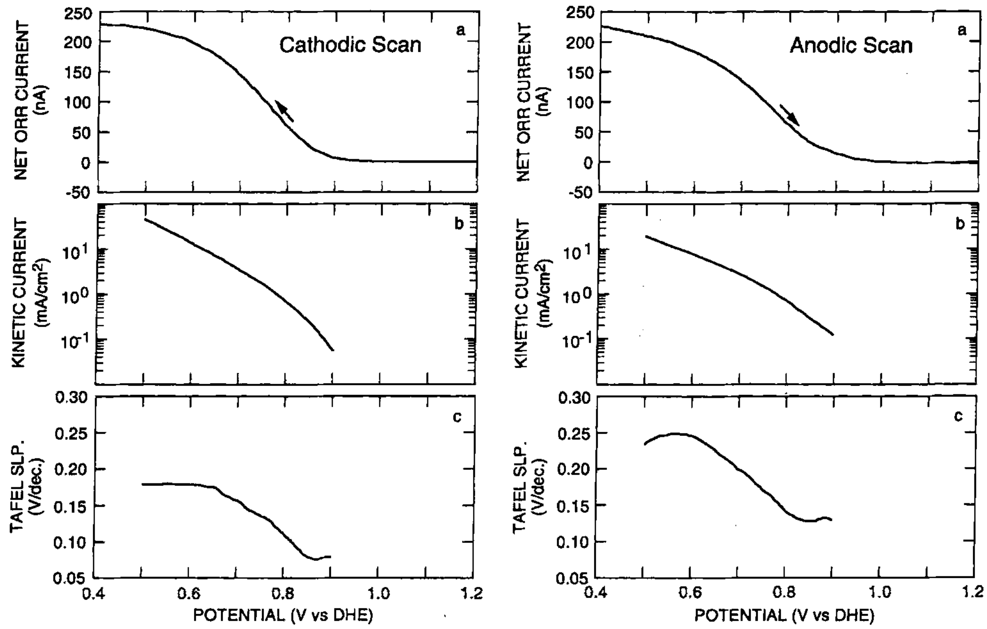

Fig. 10. ORR current (a), kinetic (mass-transport-controlled) ORR current (b) and the apparent slope dV/d log J (c) as functions of cathode potential, obtained with the cell in Fig. 7 at 30 °C [9]. (Reprinted by permission of the Electrochemical Society).

ambient temperature), using a constant Tafel slope, in fact yields misleading exchange current densities for the ORR. This would be particularly true for the domain of low polarization which is most relevant for the evaluation of cathode kinetic losses in the PEFC. The reason why this traditional routine of extrapolation may lead to physically meaningless exchange current densities is the complex dependence of ORR rate at a platinum electrode on cathodic applied potential. The variation of the apparent ORR rate with potential is determined not just by the (usually considered) effect on the electron transfer element of the ORR (see Eq. (4)), but, in addition, by the cathodic removal of the OH_{ads} species derived from water which attenuates the rate of the ORR. How this combined effect of cathodic potential results in a small and variable apparent Tafel slope in ORR measurements which is not characteristic of the ORR process proper, and therefore cannot be used in extrapolations to derive the ORR exchange current density, has been discussed in detail [7].

Uribe et al. suggested that the only meaningful comparison between ORR rates obtained at various interfacial systems should be based on mass-transport-corrected ORR currents *measured* at a given cathode potential (as distinct from extrapolated). Such a comparison is shown in Table 3 for Pt/ionomer and Pt/aqueous acid solution interfaces.

These results indicate an ORR activity at the Pt/ionomer interface near room temperature which is quite similar to that measured at interfaces of platinum with dilute aqueous acid solutions which contain no strongly adsorbed anions. The activity

Table 3. Measured ORR rates and apparent Tafel slopes (*b*) at various Pt/acid electrolyte interfaces at 25 °C [9].

Interface	Measured ORR rate mA/cm^2 Pt		*b* at 0.85 V [mV/decade]
	At 0.9V	At 0.85V	
Pt/recast Nafion	0.1	0.4	80
Pt/bulk ionomer	–	0.2	63
Pt/0.5 M H_2SO_4	0.2	0.6	–
Pt/9.5 M TFMSA	0.2	0.4	118
Pt/6 M TFMSA	0.4	–	61

at the Pt/recast ionomer interface is somewhat higher than that measured at the Pt/bulk ionomer interface at the same ambient temperature. This is in spite of the lower concentration of oxygen in the former (Table 2). The reason may be the higher state of hydration of the recast film, which is apparently very beneficial for the enhancement of the rate of the ORR process at the Pt/ionomer interface (see Fig. 9).

Before summarizing this discussion of ORR kinetics at the electrocatalyst/ionomer interface, it would be appropriate to comment on possible replacements for, or improvements on performance of, platinum cathode catalyst employed in PEFCs. Some nonprecious metal ORR electrocatalysts, for example macrocyclics of the type FeTMPP (iron tetramethylphenylporphyrin) or CoTMPP, have been considered as alternative cathode catalysts for PEFCs. However, their specific ORR activity in the best cases is significantly lower than that of platinum catalysts in the acidic PFSA medium [11]. Their long-term stability also seems to be significantly inferior to that of platinum electrocatalysts in the PFSA electrolyte environment [11b]. Based on these observations, and in light of the ultra-low loadings of platinum required in newly developed, highly performing catalysts for PEFCs, no advantage can so far be seen from the use of such alternative PEFC cathode catalysts.

In contrast, recent work by Mukerjee et al. [12] has demonstrated enhanced ORR activities achieved in PEFC cathodes with some supported platinum-alloy catalysts. These platinum alloy catalysts have been reported to exhibit good stability under PEFC conditions. Mukerjee et al. have demonstrated that a range of Pt–Ni, Pt–Co and Pt–Cr alloys supported on carbon exhibited a higher PEFC cathode activity per mg Pt in the catalyst layer [12]. The PtCr/C alloy exhibited the highest activity per mg Pt, about five times higher than that of Pt/C for a neat oxygen cathode in a PEFC operating at 90 °C, corresponding to a voltage gain at constant current density of about 40 mV. The interpretation given by Mukerjee et al. for the enhanced activity was an increased Pt *d*-orbital vacancy and a resulting lower surface affinity for adsorbed OH intermediates that tend to block Pt sites required for the ORR process [12]. However, previous work has shown that this advantage of (supported) platinum-alloy catalysts over (supported) platinum catalysts cannot be observed for bulk platinum alloys in acid electrolytes [13]. Therefore, the advantage of dispersed platinum alloys as ORR electrocatalysts in PEFC (or in phosphoric acid fuel cell) cathodes may not be simply explained by a higher intrinsic ORR activity of the alloy catalyst surface. Rather, it could be to do with the overall complex composition and structure of the fuel cell catalyst layer, and their variation with time of cell operation [13].

To summarize this section on studies of the ORR at the Pt/ionomer interface, let us examine the important conclusions and the implications concerning the performance of the oxygen cathode, or air cathode, in the PEFC. Examination of Table 3 reveals that the Pt/recast ionomer interface is relatively favorable for reaching significant ORR rates in an acidic electrolyte but it is by no means unusual in this regard. This is probably the result of combined favorable effects – enhanced oxygen concentration in the ionomer and immobilization of anions – and unfavorable effects – site blocking by impurities and perfluorocarbon moieties, and the high sensitivity of the rate of ORR to the interfacial water content in the ionomer in contact with water vapor. The intrinsic ORR activity achievable at the Pt/ionomer interface, as measured with appropriate model systems described in this section, is a sufficient basis for high-performance fuel cell cathodes, provided good catalyst utilization could be secured (see Section 4 below). The platinum catalyst in the fuel cell is highly dispersed, making it possible to attain a platinum surface area of 100 cm^2 per geometric cm^2 of the membrane, with a total cathode loading of only 0.15 mg Pt/cm^2 [14]. Considering the gain of about a factor of 5 in the ORR rate between room temperature and 80 °C if the ionomer is kept well humidified [6, 9], it can be seen from the intrinsic room-temperature activity per cm^2 Pt (Table 3) that a current density of 50 mA/cm^2 is expected from a PEFC cathode of 100 cm^2 Pt at a cathode potential of 0.9 V at 80 °C and 1 atm O_2. Very similar PEFC cathode performances are indeed obtained under such conditions in reality, demonstrating good agreement between ORR studies of model Pt/ionomer systems and "real-life" fuel cell cathodes. This agreement obviously depends on high catalyst utilization (typically above 70%), achieved with advanced PEFC catalyst layer fabrication [14].

According to an expected cathode performance of this kind at 0.90 V and an apparent "Tafel slope" of 80 mV/decade at 80 °C [6, 9], it can be seen that a cathode kinetic current density of 1 A/cm^2 can be reached with low platinum loadings (0.1–0.2 mg Pt/cm^2) at a cathode potential of 0.80 V. Further enhancement in cathode activity is apparently possible by using carbon-supported platinum-alloy ORR catalysts, such as PtCr/C [12]. A PEFC voltage of 0.70 V is usually considered a reasonable target from an energy conversion efficiency viewpoint (this cell voltage corresponds to 57% conversion efficiency based on the low heat value, and 47% based on the high heat value of hydrogen). A cathode potential of 0.80 V at 1 A/cm^2, as calculated above for low-loading Pt/C cathodes, would thus allow 100 mV for all other remaining PEFC losses. The overall target of a cell voltage of 0.70 V at 1 A/cm^2 is indeed quite readily achievable in PEFCs employing such low loadings of Pt/C ORR electrocatalysts, particularly for H_2/O_2 operation. H_2/air PEFCs employing the same Pt/C ORR catalysts typically reach only 0.60–0.65 V at 1 A/cm^2, because of the additional transport limitations in the air cathode (see Sections 4 and 6).

From such basic calculations, it becomes clear that the intrinsic ORR activity at the Pt/recast ionomer interface is sufficient to achieve quite high performances in PEFCs in terms of desired combinations of high energy conversion efficiency and high power density, employing low platinum-catalyst loadings. At the same time, however, it is also true that, as in all other low-temperature fuel cells, the air cathode losses are the highest by far compared with other sources of voltage loss in the PEFC; the limited rate of the electrocatalytic ORR process is the fundamental reason for these losses.

3.2 Electrocatalysis at the Hydrogen Anode

The rate of the hydrogen oxidation process at the Pt/ionomer interface at 80 °C is very high, as long as the catalyst surface is not contaminated by adsorbed impurities. Probably as a result of the high performance of (pure) hydrogen platinum anodes in PEFCs, relatively little work has been done on the rate and mechanism of the hydrogen oxidation process at an impurity-free Pt/ionomer interface. One exception is the impedance work performed by Raistrick [15] which revealed details of the mechanism of hydrogen oxidation at the Pt/ionomer interface at room temperature. An example of an impedance spectrum measured by Raistrick for the H_2/H^+ couple at the smooth platinum electrode/hydrated Nafion^{TM} membrane interface at room temperature is given in Fig. 11. The spectrum includes three features which correspond, in order of increasing frequency, to

1. mass-transport limited supply of H_2 gas to the planar platinum electrode pressed against the membrane,

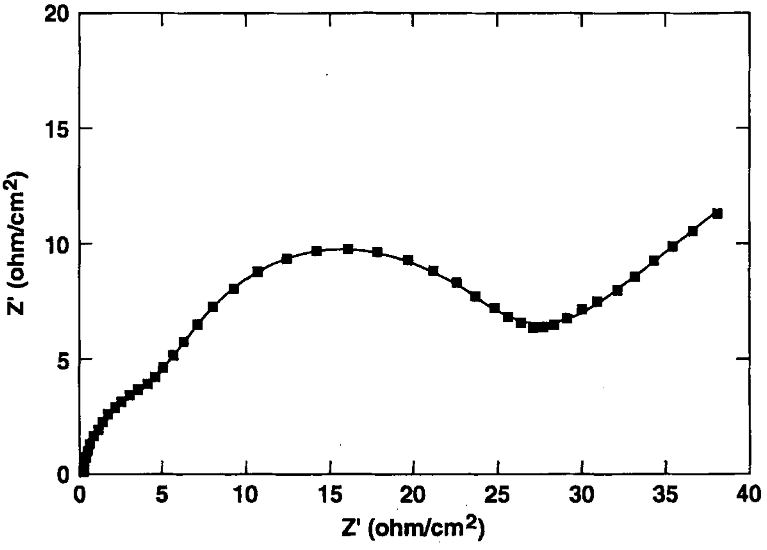

Fig. 11. Impedance spectrum (imaginary component vs. real component of the impedence) measured for a bulk, smooth Pt/Nafion membrane interface in a hydrogen atmosphere at the H_2/H^+ equilibrium potential [15].

2. the dissociative chemisorption of H_2 molecules on platinum-catalyst sites to form adsorbed hydrogen atoms and
3. electrooxidation of adsorbed hydrogen atoms.

The resolution of the latter two steps in the overall interfacial process of hydrogen electrooxidation should be contrasted with the impedance spectrum for the ORR at a smooth Pt/Nafion membrane interface (see Fig. 6), that includes only a single feature associated with a single rate-limiting interfacial charge-transfer step. Figure 12 shows an equivalent circuit for the H_2/H^+ process at the smooth Pt/Nafion™ membrane interface, based on the experimental results in Fig. 11 [15]. The interfacial process of H_2 electrooxidation seems to be controlled at higher current densities by the rate of the dissociative chemisorption step [15], and this impedance spectral feature is also most strongly affected by the introduction of traces of carbon monooxide into the hydrogen gas [15]. The total impedance associated with the interfacial hydrogen oxidation process at the Pt/hydrated Nafion membrane interface is indeed much smaller than that of the ORR process in the same electrolyte. The total faradaic impedance at the equilibrium potential for the H_2/H^+ couple is seen in Fig. 11 to be around 25 Ω cm^2, corresponding to an exchange current density of the order of 1 mA/cm^2 for the H_2/H^+ couple at the Pt/Nafion membrane interface at room temperature. (A similar net rate for the ORR at this interface is achieved only at cathodic overpotentials exceeding 400 mV.)

As a result of the high rate of the hydrogen oxidation process at platinum in contact with this ionomeric medium, the interfacial potential drop at a well-humidified H_2 anode in a PEFC operating at 80 °C at 1 A/cm^2 has been usually considered negligible. It should be remembered, however, that this would not be the case when:

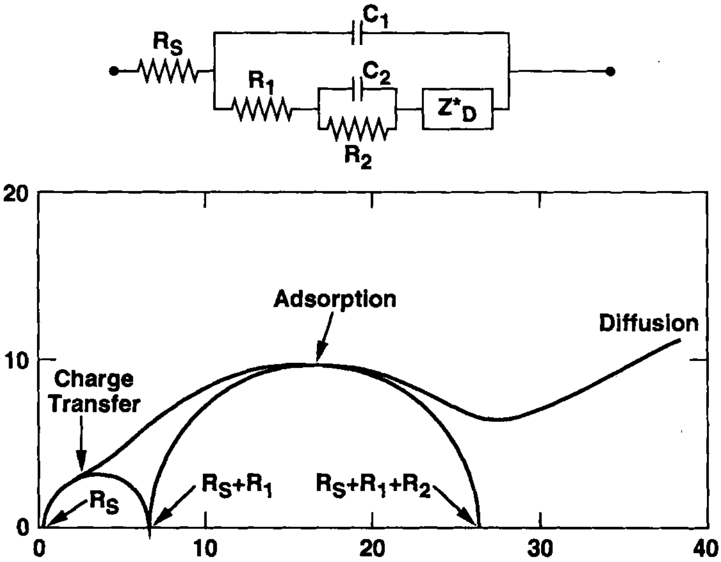

Fig. 12. Equivalent circuit for the H_2/H^+ process at the smooth Pt/Nafion membrane interface, based on the experimental results in Fig. 11 [15].

1. the anode side of the membrane becomes dehydrated, and/or
2. the hydrogen feed stream to the cell is less than perfectly pure.

The latter point is discussed in detail in the next section.

3.3 Impurity Effects on Anode Electrocatalysis

3.3.1 Poisoning of the PEFC Anode Catalyst by Low Levels of CO

Cell Performance in the Presence of CO

Significant PEFC losses could arise because of two anode-related problems: local loss of water caused by electroosmotic drag of water (see Section 5), and, most importantly, anode catalyst poisoning. The problem of local loss of water at the PEFC anode is discussed in detail in Section 5. It has now been practically resolved by the use of thinner ionomeric membranes and membranes of higher water permeability. Poisoning of the anode catalyst is caused primarily by carbon monoxide, either brought into the cell with the fuel feed stream or generated in situ by the reduction of CO_2. This problem is therefore particularly severe with fuel feed streams derived from the steam reforming of methanol or other liquid fuels, and is of lesser concern when the PEFC operates on neat hydrogen. Nevertheless, the level of CO which brings about significant poisoning at the hydrogen anode in a PEFC is so small (several parts per million) that even in the case of relatively pure hydrogen feeds, e.g., bottled hydrogen of nominal 99.99% purity, some long-term platinum anode performance loss has been observed.

The option of carrying methanol or other liquid fuel on a fuel-cell-powered vehicle, and steam reforming it on-board the vehicle to a mixture of hydrogen and CO_2, is considered attractive because of the high energy density of the liquid fuel, particularly when compared with the options of carrying hydrogen on-board the vehicle in either pressurized gas or metal hydride forms. However, the impure hydrogen fuel which results from the reforming of liquid fuels presents significant problems for the PEFC anode. Methanol reformate is typically 75% H_2 + 25% CO_2 with about 1% CO. This CO level can be further minimized by a shift process and by a subsequent catalytic oxidizer, reducing the CO level to the 1–100 ppm level, depending on the design and the precise operation conditions of the oxidizer [16]. When fueled by (oxidatively-treated) methanol reformate, the PEFC has to operate on hydrogen which contains this final level of CO, without significant loss of performance.

The effect of low levels of carbon monoxide on the performance of PEFCs was first documented by Gottesfeld and Pafford [17], who described the effects of CO levels in a H_2 feed stream ranging between 5 and 100 ppm, measured in PEFCs employing impregnated gas-diffusion electrodes with a platinum loading in the anode of 0.45 mg/cm^2. The results obtained are summarized in Fig. 13. It is clear from this Figure that such very small levels of carbon monoxide can generate severe

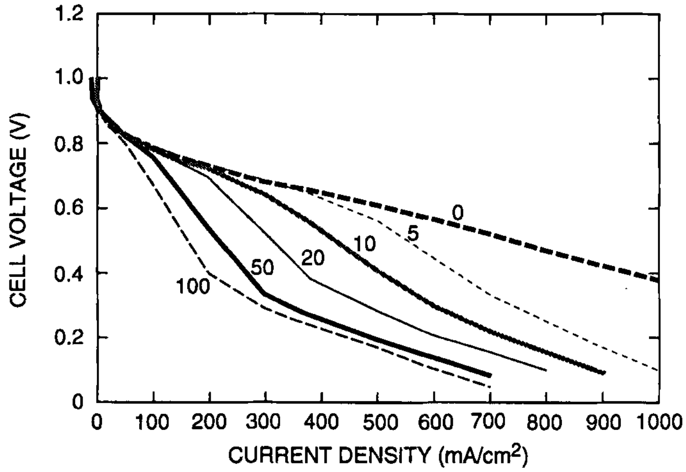

Fig. 13. Effects of CO level (ppm) in the hydrogen feed stream on the performance of a PEFC at 80 °C. Both electrodes were based on an ionomer-impregnated Pt/C catalyst and thin sputtered platinum film, of total loading 0.45 mg Pt/cm^2 [17].

performance losses in PEFCs at the optimized PEFC operation temperature of 80 °C. The reason is the very high affinity of the CO molecule to the platinum surface at the relatively low temperature of 80 °C, resulting in a high platinum surface coverages by CO even in contact with a CO partial pressure as low as 10^{-6} atm.

The form of fuel cell polarization curves observed in the presence of part-per-million levels of CO in the anode feed stream (Fig. 13) has not been fully interpreted until very recently, although important aspects of the relevant surface processes have been described before [18a,b]. The fuel cell polarization characteristic in Fig. 13 shows very small loss in performance up to some critical cell current (100–300 mA/cm^2 for platinum anode catalysts), whereas beyond that "threshold" there is a much sharper drop in cell voltage. Voltage losses of the magnitude seen in Fig. 13 at higher current densities are unacceptable because the fuel cell is typically expected to maintain high power density and high energy conversion efficiency in the complete dynamic range. The viable domain of operation is therefore confined to the maximum current density at which CO-free cell performance can be approached, to within 20–50 mV.

A recent evaluation [18c] of the behavior shown in Fig. 13 is based on the processes at a fuel cell platinum anode catalyst, listed below in Eqs. (5).

$$\mathrm{Pt} + \mathrm{CO} \longrightarrow \mathrm{CO/Pt} \tag{5a}$$

$$\mathrm{H_2} + 2\mathrm{Pt} \longrightarrow 2\,\mathrm{H/Pt} \tag{5b}$$

$$\mathrm{H/Pt} \longrightarrow \mathrm{Pt} + \mathrm{H^+} + \mathrm{e^-} \tag{5c}$$

$$\mathrm{CO/Pt} + \mathrm{OH_{ads}} \longrightarrow \mathrm{Pt} + \mathrm{CO_2} + \mathrm{H^+} + \mathrm{e^-} \tag{5d}$$

Adsorption of carbon monoxide (Eq.(5a)) is assumed to occur in parallel with the dissociative chemisorption of hydrogen (Eq. (5b)) (M is a catalyst site), hydrogen oxidation current is assumed to be generated by process (5c), and adsorbed carbon monoxide would oxidize electrochemically to CO_2 according to Eq. (5d), reacting with a water-derived adsorbed oxygen species.

The technically desirable conditions of anode potentials smaller than 100 mV vs. RHE, imply very small rates of process (5d) at either platinum or platinum-alloy PEFC anode catalysts, as can be seen, for example, from the RDE results reported in [18d,e]. The PEFC anode catalyst is thus required to electro-oxidize hydrogen in the presence of significant coverage by CO. The rate of sequence (5b) + (5c) can be enhanced by anodic overpotential as long as process (5c) significantly limits the rate of this sequence. Since reaction (5c) is a fast and potential-driven process, at relatively low anodic overpotentials the rate of sequence (5b) + (5c) could become fully controlled by the rate of chemisorption of H atoms (Eq. (5b)) on a catalyst surface with few CO-free sites.

This scenario is expressed mathematically as follows. Surface coverages by the adsorbed species (θ) reach a steady state at any anode overpotential, i.e.,

$$d\theta_H/dt = d\theta_{CO}/dt = 0 \tag{6}$$

As explained above, the requirement of low anodic overpotential implies that $\theta_H << 1$, $\theta_H << \theta_{CO}$, and thus the steady-state coverage by hydrogen atoms under such conditions will be given by (see Eqs. (5b), (5c)):

$$\theta_H = k_{ads}P_{H_2cat.}(1-\theta_{CO})^2/k_{e,H}[\exp(\eta/b) - \exp(-\eta/b)] \tag{7}$$

where k_{ads} is a rate constant for process (5b)(forward), $P_{H_2,cat.}$ is the partial pressure of hydrogen at the catalyst site, $k_{e,H}$ is the rate constant for process (5c) and overpotential η is measured vs. the equilibrium potential for the H_{ads}/H^+ couple. The anode current density under such conditions is obtained from Eqs. (5c) and (7) by

$$J = F\,k_{ads}P_{H_2,cat.}(1-\theta_{CO})^2 \tag{8}$$

As explained above, θ_{CO} which appears in Eq. (8) would be determined by the energetics of the CO/catalyst surface system, only slightly modified at the relevant low anodic potentials by any marginal electrochemical reactivity.

Equation (8) gives the limiting, potential-independent current density predicted for complete control of sequence (5b) + (5c) by the dissociative chemisorption of H_2 (process (5b)) at a catalyst surface with a small number of CO-free sites (see 18a). Such a limiting rate of hydrogen electro-oxidation at low anodic overpotentials has been observed recently in RDE experiments with H_2/CO mixtures, performed with platinum and PtRu RDEs [18d,e]. This limiting current density (Eq. (8)) explains the PEFC characteristic observed with low CO levels in the fuel feed stream, depicted in Fig. 13. Under such conditions, the fuel cell will exhibit ordinary anode losses up to the current density defined by Eq. (8), but higher current demands would require a significant increase in anodic overpotentials, i.e., excessive cell voltage losses, to allow removal of adsorbed CO by electro-oxidation (Eq. (5d)).

In summary, effective "CO tolerance" has to be achieved by PEFC anodes operating at low anodic overpotentials which do not allow significant CO electro-oxidation rates at either platinum or platinum-alloy catalyst surfaces. Therefore, CO tolerance of PEFC anodes requires maintenance of the full range of required cell current densities in the presence of significant site coverage by CO. The technical challenge seems to be lowering of θ_{CO} without resorting to significant rates of CO electro-oxidation. This can be achieved by either chemical (rather than electrochemical) oxidation of adsorbed CO or, in part, by alloying platinum with ruthenium and/or raising cell temperature. These options are described below in the next two sections.

Anode Catalyst Cleansing by Oxygen Bleeding

Gottesfeld and Pafford showed in their paper [17] that one possible approach to the serious problem of CO poisoning at the PEFC anode catalyst is to bleed low levels of oxygen, or air, into the CO-contaminated anode feed stream. They demonstrated for Nafion-impregnated gas-diffusion anodes (0.4 mg Pt/cm^2) that bleeding of 0.4–2% oxygen into the CO-contaminated H_2 feed stream can completely correct for deleterious effects of 5–100 ppm CO. Two experimental issues should be noticed in the context of such experiments:

1. Establishment of a steady-state cell voltage at some demanded current density may take a significant fraction of an hour in the presence of very low levels of CO, and the same is true for reestablishment of CO-free cell performance following bleeding of oxygen or air into the H_2 feed stream.
2. It is important that the levels of oxygen employed be well below the explosion threshold for O_2/H_2 mixtures (5% O_2 in hydrogen). Because of this limitation, the maximum level of CO which can be treated effectively by this in-situ oxygen (or air) bleeding approach at 80 °C is around 100 ppm.

The success of the in-situ bleeding of oxygen in removing deleterious effects of CO in PEFC anodes can be understood from the following apparent scenario, starting from a PEFC platinum anode catalyst exposed to a H_2/CO mixture. As mentioned above, the affinity of CO for platinum surfaces at 80 °C is so great that the catalyst surface coverage by CO is very high in the presence of just 10–100 ppm CO. A significant CO surface coverage is already obtained even at 1 ppm CO in the anode feed stream. Schematically describing the anode processes for a case of, e.g., 10 ppm CO in H_2, one can write the platinum catalyst deactivation process as:

$$(10\,\text{ppm})\ CO_{(1\ \text{atm}\ H_2)} + Pt \longrightarrow CO/Pt \tag{9a}$$

Also,

$$(10\,\text{ppm})\ CO_{(1\ \text{atm}\ H_2)} + H/Pt \longrightarrow CO/Pt + \tfrac{1}{2}H_2 \tag{9b}$$

"Cleansing" of the catalyst site by bleeding of dioxygen can be described by:

$$CO/Pt + (2\%)O_{2\,(1\,\mathrm{atm}\,H_2;10\,\mathrm{ppm}\,CO)} + Pt \rightarrow O/Pt + CO/Pt \tag{10a}$$

$$O/Pt + CO/Pt \longrightarrow CO_2 + 2Pt \tag{10b}$$

$$\tfrac{1}{2}O_2 + H_2 \longrightarrow H_2O \qquad (O_2/H_2 \text{ recombination at } CO^- \text{ free Pt sites}) \tag{10c}$$

As Eqs. (10) suggest, the strong preferential adsorption of CO at the Pt site is also the basis for its catalytic oxidation by the O_2 molecules introduced into the anode feed stream. The chemical oxidation of CO by dioxygen at the platinum anode catalyst most probably takes place by dissociative chemisorption of oxygen followed by a bimolecular surface reaction between adsorbed CO and adsorbed O atoms (Eq. (10a), (10b)) [19]. As described in the schematic reaction sequence, following oxidation of CO off the platinum surface, the remaining (i.e., most) of the oxygen in the anode feed stream would recombine at freed Pt sites with hydrogen which is present in large excess in the anode compartment (Eq. (10c)). This recombination process results in a loss of fuel (hydrogen) at a percentage which is twice the oxygen level in the anode (Eq. (10c)).

Continuous bleeding of low levels of oxygen prevents anode poisoning from taking place altogether [17], as the CO in the fuel feed stream continuously reacts at anode Pt sites with the oxygen added to the fuel feed stream, according to:

$$CO_{gas} + O_{2,gas}\,(+Pt) \rightarrow O/Pt + CO/Pt \rightarrow CO_2 + Pt \tag{11}$$

thus maintaining a CO level of zero in the gas phase within the anode compartment. This has been demonstrated experimentally by analyzing the anode exhaust stream when the anode feed stream contained 100 ppm CO and 2% O_2 was continuously added [20].

The scheme in Eqs. (10) is based on the well-documented process of CO catalytic oxidation at a platinum catalyst [19]. Under ordinary circumstances in CO oxidation, i.e., at much higher CO, the threshold temperature for significant CO oxidation rates at a supported platinum catalyst is above 100 °C. The higher temperature is required to have some Pt sites free of CO enabling dissociative chemisorption of oxygen. Under the operation conditions of PEFC discussed here, the CO level is very low, however; (10–100 ppm) CO coverage is thus incomplete in spite of the lower temperature of 80 °C, making it possible to carry out chemical oxidation of CO at the PEFC anode platinum catalyst at 80 °C. This explanation is fully supported by the reported turnover rates for CO oxidation and their dependence on CO and oxygen partial pressures and on temperature, as documented, e.g., by Berlowitz et al. [19]. The presence of water or of hydrogen in the anode compartment apparently has no significant effect on the rate of chemical oxidation of CO by O_2 at the anode catalyst.

This mode of anode catalyst cleansing was recently reexamined by Wilson and others in PEFCs utilizing thin-film catalysts of ultra-low catalyst loading (0.10–0.15 mg/cm) [21]. As shown in Fig. 14, a thin-film anode catalyst of ultra-low platinum

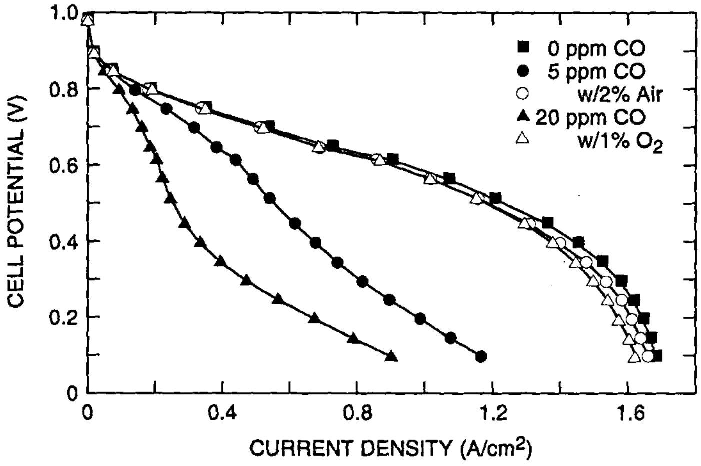

Fig. 14. Cleansing by oxygen bleeding of a platinum anode catalyst in the presence of 5–20 ppm CO in the hydrogen fuel, demonstrated for a platinum anode catalyst of ultra-low loading (0.14 mg Pt/cm^2), consisting of a Pt/C//ionomer thin film composite bonded to the membrane [21]. (Reprinted by permission of the American Chemical Society).

loading exposed to CO concentrations of 20 ppm is fairly well cleaned up by air and/or O_2 injection, following the same routine as has been described [17] for electrodes of four times higher platinum loading. However, the levels of oxygen required to achieve effective cleansing at a given level of CO in the gas stream are higher (cf. Fig. 13). Apparently, an excess of unutilized catalyst in the impregnated gas-diffusion electrodes provides additional CO oxidation sites for reactions (10), absent in a well-

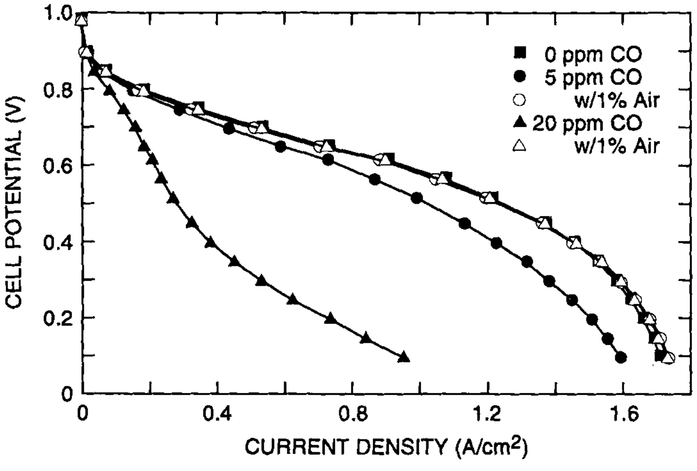

Fig. 15. 1% (see Fig. 14) can be replaced by just 1% air, to achieve the complete elimination of anode poisoning at 20 ppm CO, when a "prefilter" with Pt/C catalyst (dry, unimpregnated gas-diffusion electrode) is placed upstream of the anode. The anode catalyst was a thin-film containing 0.14 mg Pt/cm^2 [21]. (Reprinted by permission of the American Chemical Society).

intermixed Pt/C//Nafion thin-film catalyst [21]. To prove this point, a "prefilter", consisting of a dry unimpregnated gas-diffusion electrode, was introduced on the anode feed stream between the air-bleed injection point and the fuel cell, thus adding more Pt sites in direct contact with the anode feed stream. As shown in Fig. 15, with the prefilter in line, 1% air was sufficient for complete performance recovery at the level of 20 ppm CO in the H_2 feed stream (compared with 1% O_2 necessary without the prefilter to take care of the same CO level). The dry catalyst in the prefilter thus provides additional CO oxidation sites, allowing a decrease in the level of oxygen required for effective anode catalyst cleansing. Interestingly, it can be seen in Fig. 15 that the poisoning effect of 5 ppm CO (with no air bleeding) is less severe when the prefilter is introduced, possibly because the platinum in the prefilter is also serving as a "getter" for the limited duration of the experiment [21].

CO-Tolerant Platinum Alloy Anode Catalysts

Although demonstrated successfully in PEFC stacks with CO-contaminated feed streams [24], air bleeding into the anode is not considered a problem-free approach. Mixtures of hydrogen and oxygen are of some concern even in well-controlled systems. Therefore, the search for a PEFC anode catalyst of better CO tolerance has been pursued by several groups. At such an anode catalyst, the hope is that a larger number of "free" Pt sites could be maintained at steady state in the presence in the presence of a given level of CO in the feed stream, while maintaining minimal anode overpotentials. Recent reports [22, 23] have demonstrated significant PEFC anode tolerance to CO levels of 100–200 ppm exhibited by higher loadings (1–2 mg/cm^2) of PtRu anode catalysts. Such improved tolerance was demonstrated particularly at lower cell current densities of, typically, <300 mA/cm^3, whereas more significant losses are still observed at higher current densities [22]. There is a significant spread in the degrees of CO tolerance reported for different PtRu anode catalysts employed in PEFCs (compare [21], [22], and [23]). Such a spread suggests special significance of the exact PtRu catalyst formulation and structure, as well as significance of PEFC operation/testing conditions, in achieving a certain degree of CO tolerance with this kind of anode catalysts. Whereas such PtRu catalysts have usually been reported to be less effective at current densities exceeding 0.5 A/cm^2 (the only exception is the recent report in [23]), the oxidative cleansing of the anode catalyst by bleeding of dioxygen into the anode chamber [17, 21] has been reported to be effective, up to the highest PEFC current density. This suggests a more complete removal of surface CO at minimal anode overpotentials with the latter approach.

3.3.2 Poisoning of the PEFC Anode Catalyst in the Presence of CO_2

It has been reported [24] that PEFC stacks with anodes of high platinum loading (typically 4 mg Pt/cm^2, in the form of a platinum black/PTFE mixture), when operating on a mixture of 75% $H_2 + 25\%$ CO_2, have suffered performance losses significantly greater than expected from hydrogen dilution effects alone. Figure 16

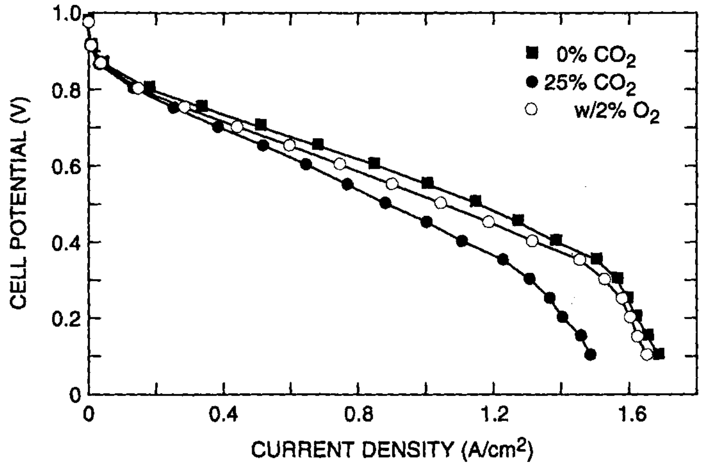

Fig. 16. Effects of CO_2 at the level expected in amethanol reformate, and of subsequent oxygen addition to the anode, in the case of a H_2/air PEFC with a 0.12 mg Pt/cm^2 thin-film anode [21]. (Reprinted by permission of the American Chemical Society).

shows the performance of a PEFC with a thin-film anode catalyst (0.12 mgPt/cm^2) operating on 75% H_2 + 25% CO_2 [21]. While less dramatic than reported in [24], the deleterious CO_2 effect shown here is appreciable. CO, apparently generated by the reduction of CO_2 at the anode platinum catalyst [see, e.g., 25], adsorbs at anode Pt sites, bringing about the loss in cell performance seen in Fig. 16. In-situ CO generation within the PEFC anode can take place at low rates by either the reverse water-gas shift reaction,

$$CO_2 + H_2 \longrightarrow CO + H_2O \tag{12}$$

or by the direct electroreduction of carbon dioxide,

$$CO_2 + 2H^+ + 2e^- \longrightarrow CO + H_2O \tag{13}$$

As Fig. 16 shows, catalytic oxidation of such internally generated CO takes place as oxygen, or air, is bled into the anode feed stream, according to the same sequence described by Eqs. (10).

Once again, introduction of a "prefilter" upstream of the cell anode helped in elucidating the nature of the process that takes place at the PEFC anode [21]. As shown in Fig. 17, cell performance on 75% H_2 + 25% CO_2 was significantly worse after introduction of the prefilter. Evidently, the additional (uncoated) platinum catalyst in the "prefilter" enhances the reduction of CO_2 via reaction (12), much as an electrode rich in unutilized platinum black [24] would. Having less anode catalyst and all of it being tied up within an electroactive structure, as in a thin-film catalyst layer, is apparently beneficial in lowering the rate of reaction (12) and minimizing the effect of CO_2 at a platinum anode catalyst. Air bleeding upstream of the prefilter recovered the cell performance, as shown in Fig. 17.

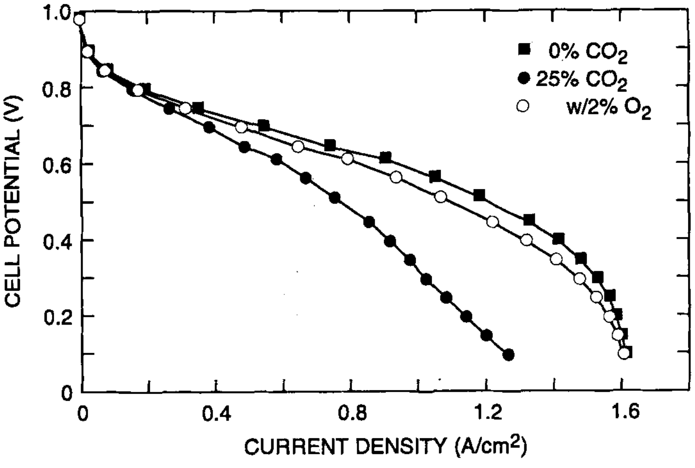

Fig. 17. The conditions of Fig. 16 are replicated on a 0.14 mg Pt/cm^2 thin-film anode with "prefilter" (dry, unimpregnated, gas-diffusion electrode) upstream of the anode [21]. (Reprinted by permission of the American Chemical Society).

3.3.3 A CO_2-tolerant PEFC Anode

Recent reports [22, 23] have demonstrated better CO tolerance with higher loadings (1–2 mg/cm^2) PtRu catalysts in PEFC anodes, particularly at cell current densities lower than 200 mA/cm^2. In contrast, a thin-film anode catalyst of very low PtRu loading, prepared as a composite of carbon-supported PtRu (0.15 mg/cm^2) and recast ionomer [14], did not exhibit lower losses when 5–20 ppm CO was introduced into the hydrogen feed stream [21]. The same PtRu catalyst was successful, however, in

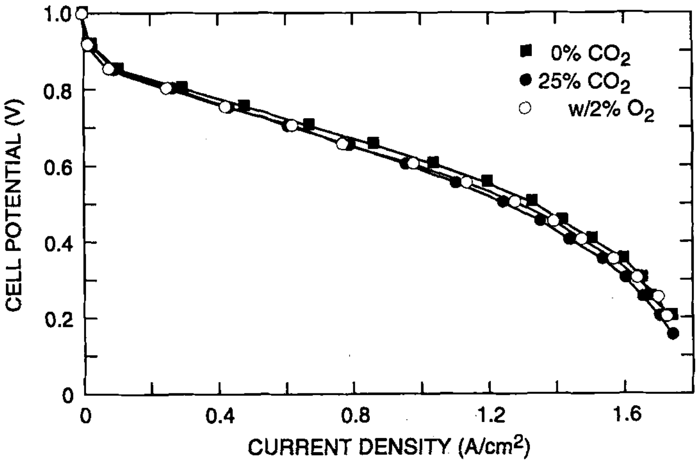

Fig. 18. Effect of CO_2 and anode oxygen bleeding on the performance of a Pt–Ru PEFC anode. A 0.19 mg Pt–Ru/cm^2, carbon-supported Johnson–Matthey FCA-6X catalyst was used in the thin-film anode [21]. (Reprinted by permission of the American Chemical Society).

reducing the in-situ generation of CO from CO_2. When the anode feed stream contained 25% CO_2, but was free of CO(< 2 ppm), the performance loss of fuel cells with PtRu anodes was found to be very small, as depicted in Fig. 18 [21]. This is to be compared to the loss experienced at a platinum anode catalyst of similar loading, shown in Fig. 17. Since CO electro-oxidation did not take place effectively at this thin-film PtRu catalyst, the negligible sensitivity to CO_2 is apparently because reduction of CO_2 to CO (Eq. (12) and/or (13)) is suppressed at this catalyst. PtRu anode catalysts of low loadings thus seem effective in preventing anode losses associated with the presence of high levels of CO_2 in the gas feed stream.

3.3.4 Electrocatalysis issues at the PEFC anode: Summary

Our discussion of PEFC anode electrocatalysis can be summarized as follows. The rate of hydrogen oxidation at an impurity-free, well-humidified Pt/ionomer interface is sufficiently high to generate negligible anode voltage losses in PEFCs. At most, losses of the order of 30–50 mV at 1 A/cm^2 are expected under such conditions.

However, anode catalyst poisoning by CO is a serious problem that needs to be addressed in each PEFC-based power system according to the expected composition of the fuel feed stream. Levels of CO up to 100 ppm in the anode feed can be taken care of by in-situ bleeding of oxygen, without or with an additional prefilter as described above. Recent experiments have established that this oxygen bleeding approach can be effective not only in single-cell testing but also in the operation of PEFC stacks with methanol reformate as fuel feed stream [24]. Alternatives to air bleeding will undoubtedly be further pursued. Such alternatives include effective CO-tolerant catalysts for PEFC anodes, as well as changes in cell operation conditions. Regarding the former, recent reports described above [22, 23] suggest that, with further optimization of PtRu anode catalysts, CO tolerance in PEFCs could be improved for the 100 ppm CO level, although such results still require further confirmation and long-term testing. Regarding cell operation conditions, earlier work [26] suggested advantages of a somewhat elevated PEFC temperature (e.g., 104 °C [26]), which in conjunction with advanced PEFC anode catalysts could assist in achieving higher CO tolerance. To the extent that stable PEFC stack performance can be established under such elevated temperatures, better CO tolerance may be achieved. Another significant aspect of cell behavior in the presence of low CO levels is the "threshold" current densities that can apparently be maintained at small cell losses (see Fig. 13 and its discussion, as well as [22]). To the extent that only lower current densities (e.g., < 300 mA/cm^2) are required in a given PEFC application (this is typically true for stationary power generation or other high-efficiency/lower-power-density applications), higher anode catalyst loading (probably PtRu) could enable smooth operation of a PEFC stack with minimal losses at CO levels of around 100 ppm.

The additional problem identified recently, of in-situ generation of CO by reduction of CO_2 within the PEFC cathode, can be minimized by the use of a PtRu anode catalyst. Low PtRu loading (0.1 mg/cm^2) seems to be effective in maintaining the anodic hydrogen oxidation activity while minimizing the rate of CO_2 reduction.

Furthermore, designing the anode catalyst, so that inactive dry catalyst (uncoated by ionomer) is practically eliminated, significantly reduces the CO generation at a platinum anode catalyst in a PEFC.

Finally, it should be realized that CO is not the only fuel (or fuel-derived) contaminant expected to affect anode performance in the PEFC. In a test of other possible contaminants that could result, in principle, from methanol reforming, Seymour et al. [27] reported strong and irreversible effects of formic acid at a PEFC platinum (high-loading) anode, whereas methanol, formaldehyde, and methyl formate were found to have much smaller and reversible effects. The fuel impurity aspects of coupling between natural gas (or gasoline) reformers of various types and a PEFC stack are even wider, and make it essential to probe and address, either by removal upstream or by use of modified catalysts, the possible detrimental effects of low levels of sulfur, H_2S, COS, and NH_3 [28].

4 Practical Aspects of Electrocatalysis: The Membrane/Electrode Assembly

In Section 3, the slow rate of the ORR at the Pt/ionomer interface was described as a central performance limitation in PEFCs. The most effective solution to this limitation is to employ dispersed platinum catalysts and to maximize catalyst utilization by an effective design of the cathode catalyst layer and by the effective mode of incorporation of the catalyst layer between the polymeric membrane electrolyte and the gas distributor/current collector. The combination of catalyst layer and polymeric membrane has been referred to as the membrane/electrode (M&E) assembly. However, in several recent modes of preparation of the catalyst layer in PEFCs, the catalyst layer is deposited onto the carbon cloth, or paper, in much the same way as in phosphoric acid fuel cell electrodes, and this catalyzed carbon paper is hot-pressed, in turn, to the polymeric membrane. Thus, two modes of application of the catalyst layer – to the polymeric membrane or to a carbon support – can be distinguished and the specific mode of preparation of the catalyst layer could further vary within these two general application approaches, as summarized in Table 4.

Table 4. Modes of catalyst layer preparation and application.

(A) Bonding to the membrane		(B) Bonding to carbon cloth/paper	
Mode	Application	Mode	Application
A1	Hot-pressed Pt black/PTFE layers	B1	Ionomer – impregnated Pt/C//PTFE
A2	Electroless deposition of Pt on membrane	B2	B1 + sputtered Pt layer
A3	Hot-pressed Pt/C//ionomer layers	B3	Pt catalyst electrodeposited at carbon/ ionomer interface

We will describe in this section the variety of techniques for the preparation of catalyst layers in polymer electrolyte fuel cells, in chronological order of development.

4.1 Platinum Black Catalysts Bonded to the Membrane

The earliest method of preparation of membrane/electrode assesmblies (M&Es) was based on bonding of a black of platinum to the polymeric membrane. A US Patent [29] described catalytically active layers prepared from finely divided metal powders (blacks) mixed with a binder such as polytetrafluoroethylene (PTFE). The active layer comprised a structure formed from the Pt/PTFE mixture bonded upon the two major surfaces of a membrane electrolyte. The PTFE and metal (or metal alloy) powder mix is formed into active layer by forming a film from an emulsion and directly applying it to the membrane, using appropriate combinations of temperature and pressure. This technique, corresponding to case A1 in Table 4, has been the first approach to the preparation of the M&E assembly, and has apparently remained to date the method of choice in the preparation of M&E assemblies in semicommercial PEFC stacks. This choice is explained by the high reliability of these M&Es, as demonstrated in various tests at GE (later Hamilton Standard), where this technology was originally developed in the 1960s for the Gemini space program. The drawback of this mode of preparation of catalyst layers is the low catalyst utilization, which originates from lack of efficient access of protons to a large fraction of catalyst particles (those located away from the membrane electrolyte) and lack of efficient gas access to another fraction of catalyst sites (those deeply embedded into the membrane). Also, the degree of platinum dispersion in this approach is limited to what can be achieved with platinum black, i.e., platinum particle sizes not smaller than 10 nm in diameter. The combined result of limited dispersion and low utilization in such Pt/PTFE mixtures is the requirement of a high platinum loading, typically 4 mg Pt/cm^2, to obtain satisfactory cathode performance, particularly for operation on air. Consequently, this remains a reasonable approach to M&E fabrication for space and military applications, or for demonstration of technical feasibility of PEFCs, i.e., where cost considerations are relatively insignificant. Further developments of this technology are described in several additional patents; several earlier patents describing this approach have been reviewed [30]. The last patent deals, for example, with pretreatment of the membrane surface by abrasion which enables some reduction in the catalyst loading. Similar membrane/electrode assemblies, based on Pt/PTFE catalyst layers applied to an ionomeric membrane, were used at GE for polymer electrolyte water electrolyzer technology.

Another approach to the direct deposition of platinum onto the membrane surface has been adopted by several workers in exploratory studies of electrochemical processes at the Pt/ionomer membrane interface. Takenaka and Torikai [31] and later Fedkiw and Her [32] and Aldebert and others [33] developed various electroless deposition techniques for the application of a film of platinum to the surface of an ionomeric membrane. The original method suggested by Takenaka and Torikai [31] was based on exposure of one side of the membrane to an anionic salt of the metal

($PtCl_6^{2-}$) and the other side to a reducing agent (e.g., N_2H_4). The latter diffuses through the membrane to react at the surface adjacent the metal salt solution and form a platinum film. Fedkiw, Aldebert and co-workers modified this approach by a two-step process where initially the ionomer is charged with Pt cation ($Pt(NH_3)_6^{4+}$) and subsequently one surface is exposed to an anionic reductant, $NaBH_4$. This last approach results in reaction of the Pt cations at the surface adjacent to the reductant sustained by diffusion of the Pt cations from the bulk of the membrane to that surface. The result is typically a dense film of particles of diameter 10–50 nm (i.e., of a typical particle size for blacks) embedded within the first few microns of the surface. Fedkiw and Her reported also on the deposition by this technique of films of palladium, copper, and nickel on Nafion membranes. While simple and effective in exploratory studies, this approach yields relatively large platinum particles and cannot provide good simultaneous access of gas, electrons, and protons to a majority of the platinum particles deposited.

4.2 Pt/C Catalysts Applied as Part of a Gas-Diffusion Electrode

The first move toward substantial lowering of platinum loading employed in PEFCs, while maintaining comparable cell performance, was described by Raistrick [34]. Raistrick experimented with gas-diffusion electrodes developed for phosphoric acid fuel cells. In such electrodes, the catalyst layer is a mixture of carbon-supported platinum (Pt/C) and PTFE and is deposited onto a carbon cloth or paper. The porous carbon cloth/paper is pretreated with PTFE, usually by filling the macropores with a mixture of (uncatalyzed) carbon powder and PTFE. The catalyst layer is subsequently deposited onto one surface of the pretreated carbon cloth/paper. The catalyst layer in such a gas diffusion electrode is typically based on 10% Pt/C and is 100 μm thick. Compared with catalysts based on platinum black, an important advantage of the carbon-supported platinum catalyst is the higher degree of dispersion. Particle diameters of 2 nm are easily obtained in carbon-supported form by various protocols described in the patent literature. This is to be compared with a minimum particle size of about 10 nm obtainable in blacks. Transmission electron microscopy (TEM) images of a typical carbon support (Vulcan X-72) and of a carbon (Vulcan X-72)-supported platinum catalyst of 20 wt% Pt is given in Figs. 19(a) and (b), respectively.

Raistrick started his investigation by hot-pressing gas-diffusion electrodes of this type directly to an ionomeric membrane, and realized that the poor cell performance obtained was caused by lack of protonic access to the majority of catalyst sites not in intimate contact with the membrane. This understanding of limitations in M&E assemblies for PEFCs was important. In order for a Pt site to be effective in the process of oxygen reduction, it has to be effectively accessed simultaneously by all three reactants: oxygen gas molecules, electrons, and protons. In a catalyst layer comprising Pt/C (or platinum black) mixed with PTFE, the two first requirements are effectively met – thanks, respectively, to the good connectivity within the carbon support/carbon powder (or platinum black) and the hydrophobic pores generated by

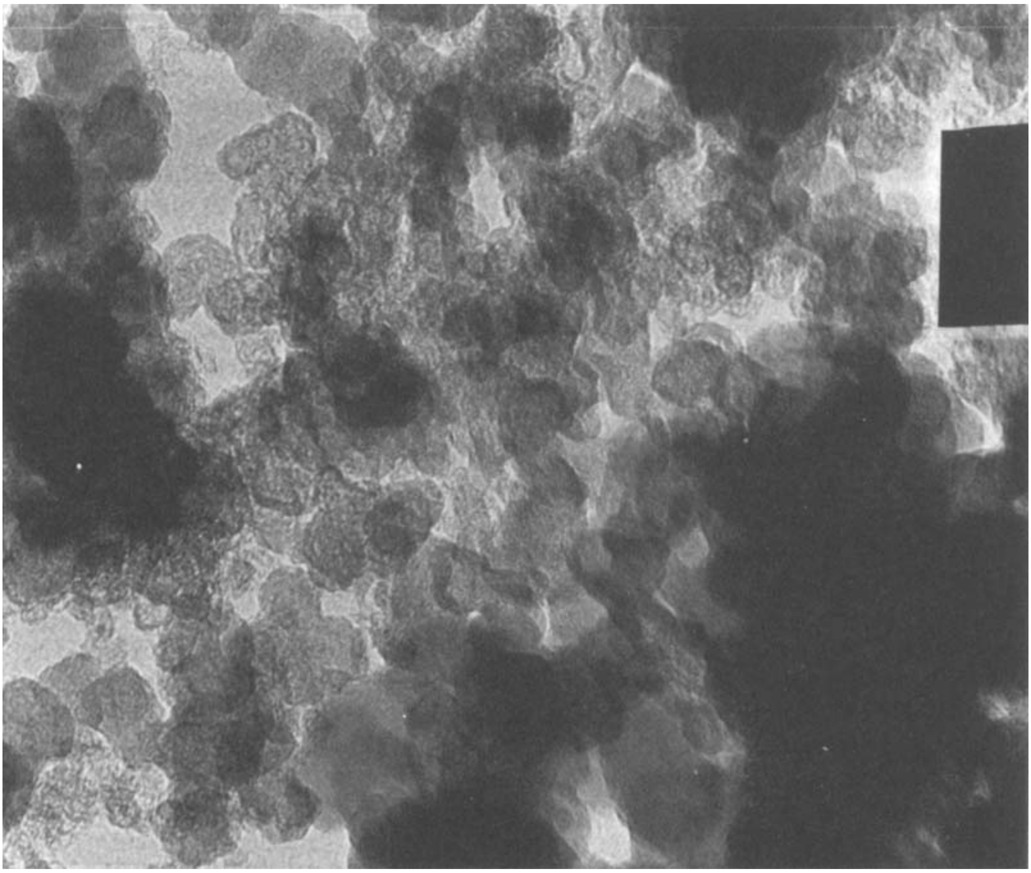

Fig. 19. TEM image of (a) a typical carbon support (Vulcan-XC 72) and (b) a carbon-supported platinum catalyst (10% Pt/Vulcan-XC 72). The particle size of platinum crystallites in such catalysts is typically in the range 1.5–2.5 nm.

the PTFE component. The third requirement, effective protonic access, cannot be met adequately, however, because most of the Pt sites distributed in a 100 μm-thick catalyst layer are removed by (much) more than the Debye length (about 1 nm) from the ionomeric membrane. To overcome this critical limitation, Raistrick impregnated the Pt/C//PTFE catalyst layer on the carbon cloth with a solution of Nafion, in order to fill it, or at least a significant part of it, with recast ionomer prior to hot-pressing the impregnated electrode onto the membrane [34]. This step of catalyst layer impregnation with recast ionomer resulted in a very significant increase in performance and demonstrated, for the first time, significant PEFC performance with platinum loading as low as 0.4 mg/cm^2, i.e., an order of magnitude lower than that employed in the GE/Hamilton Standard technology. This first result of Raistrick with impregnated gas-diffusion electrodes [34] was a breakthrough in PEFC

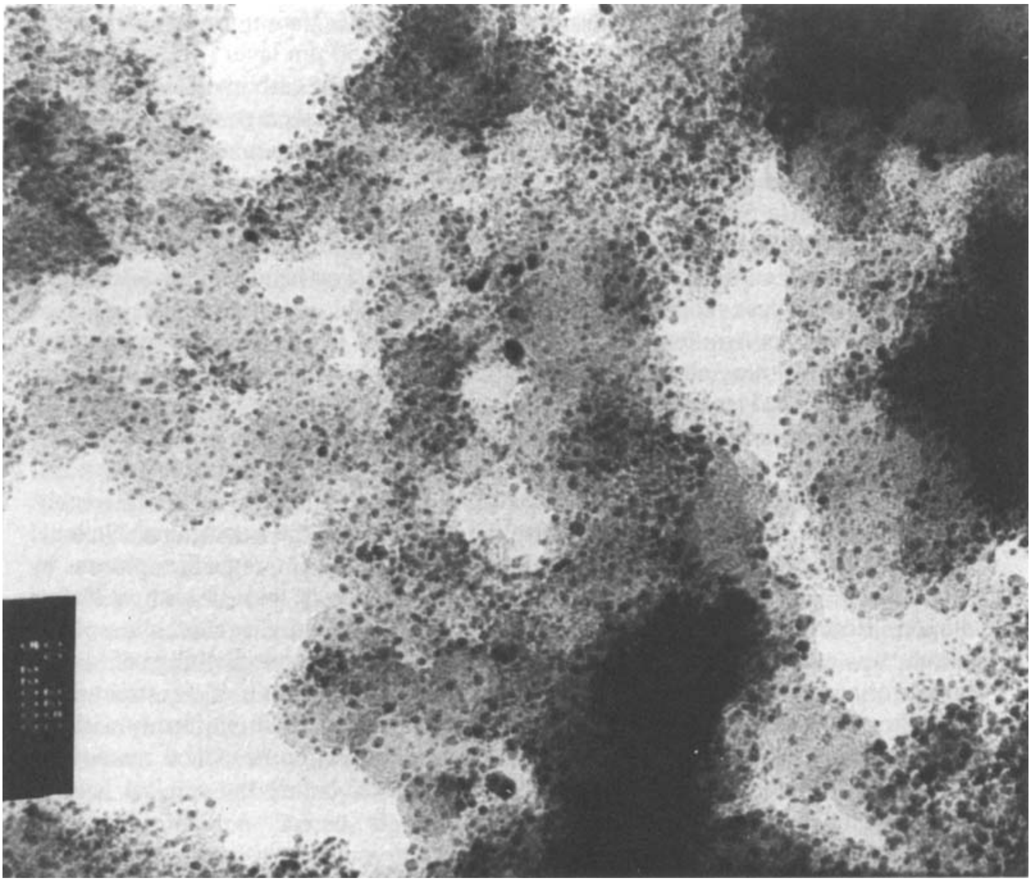

Fig. 19. (*continued*)

technology in two senses. Firstly, it demonstrated that PEFCs could be effectively operated with Pt/C catalysts of loading similar to the ones employed in phosphoric acid fuel cells, thus bringing the loading and cost of precious metal catalyst down by an order of magnitude. In addition, and perhaps even more importantly for further developments to follow, this innovative experiment revealed the great importance of "triple access" (gas, electrons, protons) to each active catalyst site and with that it opened the way to further optimization of catalyst layers in PEFCs with the desired combination of low loadings and high performance.

Further significant improvements of the initial idea described by Raistrick were achieved by Srinivasan, Ticianelli and their co-workers. They described, in a series of contributions, successful attempts to increase the performance of impregnated Pt/C layers on carbon support hot-pressed to the membrane by increasing the temperature and gas pressure [35]; optimizing the percentage of Nafion impregnant [36]; replacing the 10% Pt/C 100 μm layer with a 20% Pt/C 50 μm layer [37]; and adding a thin film of sputtered platinum on the front surface of the carbon elecrode prior to impregnation [38]. The last two modifications shorten the average distance traveled by protons to access a platinum catalyst site and generate, particularly in the case of the sputtered film, a significant number of active Pt sites very close to the membrane. As shown below in Section 6, minimization of protonic transport losses within the catalyst layer is a very important target toward the optimization of electrode performance. Optimization of the PTFE content in the catalyst layer was also described [39]. With all of these modifications completed, a typical cell performance reported by Srinivasan and co-workers is shown in Fig. 20. It has to be noted that the smallest catalyst layer thickness employed in such preparations is still not less than 50 μm. This substantial catalyst layer thickness prevents maximization of catalyst utilization, as explained further in Section 6.

Problems with the fabrication of catalyzed, impregnated carbon cloth or paper electrodes in PEFCs include the reproducibility and the durability of the assembly. Significant effort has been invested during the late 1980s at the Los Alamos National Laboratory (LANL) in the optimization and control of the impregnation process by which the Pt/C//PTFE layer on a carbon cloth/paper is treated with a Nafion solution. Both brushing and spraying were attempted and the alcoholic solvent mixture was evaporated at different rates. However, good reproducibility of single-cell performance could not be achieved. This is probably a result of the structure of the hydrophobic Pt/C//PTFE layer which is hard to impregnate uniformly with the alcoholic Nafion solution. As described below in this section, a radical remedy for this problem is premixing of the catalyst and ionomer before the catalyst layer is

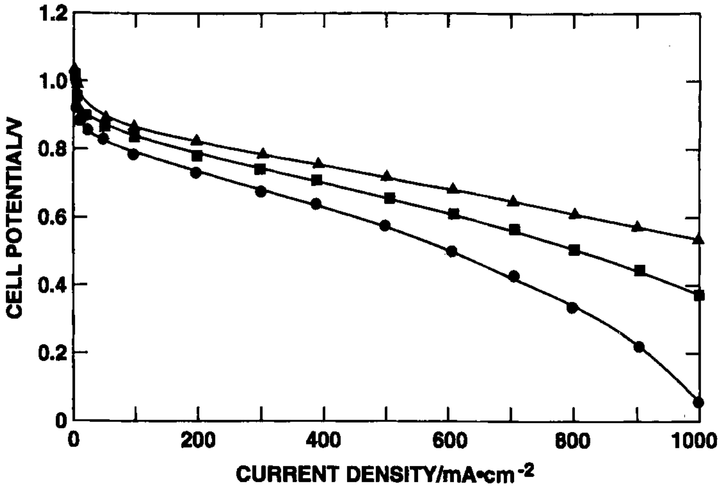

Fig. 20. Single PEFC H_2/air performance with catalyzed carbon cloth electrodes of 0.45 mgPt/cm^2, including catalyst layer with 20 wt% Pt/C catalyst and 50 nm thick film of sputtered Pt: lower curve – 50°C, 1/1 atm; middle curve – 50°C, 3/5 atm; upper curve – 80°C, 3/5 atm [37]. (Reprinted by permission of Elsevier Science)

deposited (onto the membrane), rather than ionomer impregnation of a Pt/C//PTFE layer.

Another factor which apparently prevents good reproducibility in single PEFCs prepared with such impregnated gas-diffusion electrodes is the nature of the hot-press bonding between the carbon electrode and the membrane. The conditions of hot-pressing in terms of the temperature, pressure, and duration have to be optimized for each ionomeric membrane. During hot-press, the glass transition temperature of the ionomer (typically, 130–160 °C) has to be exceeded, or at least approached, to enable partial penetration of the fibers of the carbon cloth (or paper) into the softened polymer. Such hot-press can produce initially a very satisfactory bond between the carbon cloth/paper and the membrane. However, as the complete cell is assembled and humidified, the membrane swells significantly on rehumidification whereas the carbon does not change its dimensions on exposure to water. Therefore, the probability of partial delamination at the porous carbon/membrane contact on rehumidification is substantial, with consequences of loss of active surface area and/or increased cell resistance. (Recall that the liquid layer between the partly delaminated carbon electrode and membrane will be distilled water.)

Another mode of application of platinum catalyst to a porous carbon structure has been described by Taylor et al. [40]. This special mode involves impregnation of the porous carbon structure with ionomer, exhange of the cations in the ionomer by a cationic complex of platinum, Pt $(NH_3)_4^{4+}$ and electrodeposition of platinum from this complex onto the carbon support. The result of such a procedure is the deposition of platinum only at sites which are accessed effectively by both the electronic conductor (carbon) and the ionic conductor (recast Nafion). In this regard, this mode of catalyst preparation seems to offer an important advantage of catalyst utilization. Indeed, significant PEFC performances can be obtained with cathodes prepared in this way with loading as low as 0.05 mg Pt/cm^2, as reported by Taylor and co-workers [40]. From experiments conducted in our laboratory, it seems that a drawback of this approach is the larger platinum crystallites which tend to grow at some of the original sites of crystalization when the electrodeposition is continued in an attempt to increase the platinum loading to the level of 0.1–0.2 mg/cm^2. The large platinum particles thus formed lead to smaller surface area per unit mass of platinum as compared with the Pt/C catalysts formed by chemical reduction/colloidal techniques. The approach described by Taylor and others could somehow be more advantageous if a higher dispersion of platinum crystallites could be maintained at somewhat higher catalyst loading than those reported [40], say 0.1–0.2 mg/cm^2.

4.3 Pt/C Catalysts Applied to the Membrane

Most recently, an alternative low-platinum-loading catalyst layer structure has been developed by Wilson at LANL. In this structure, recast ionomer is used instead of PTFE to bind the catalyst layer structure together, and the low-loading catalyst layer is applied to the membrane, rather than to the gas-diffusion structure (mode A3)

[14, 41–43]. Such (PTFE-free) layers have been described as "thin-film" catalyst layers, because the high performance is obtained with a very low catalyst loading (0.12–0.16 mg Pt/cm^2) in a thin layer (< 10 μm thick). By virtue of their thinness and the high ionomer contents achievable with these catalyst layers, high catalyst utilizations are obtained and the continuity and integrity of the catalyst layer/membrane interface is greatly improved compared with the structures prepared by modes B2 or B3. Although no hydrophobic component is introduced into this structure, the gas permeabilities through it are sufficient to achieve good catalyst utilization at high current density in layers 5–7 μm thick which provide high cell performance [14, 41–43].

The thin-film catalyst layers are cast from "inks" consisting of the supported platinum catalyst and solubilized ionomer [14]. Because the ionomer must bind the thin-film structure together, special treatments of the recast films are necessary during fabrication to impart robustness to the ionomer in the catalyst layer. Initially, the robustness of the composite film with the ionomer in protonic form was improved by heat-treating the catalyst layer [14]. Later, higher ionic conductivities in the catalyst layer and a moderate degree of robustness were achieved with an electrode fabrication process based on a high-temperature casting technique that utilizes the ionomer in the Na$^+$ form [41]. However, the long-term performances still indicated that further improvement was necessary. A thermoplastic form of the ionomer was contemplated eventually as the best solution for the film robustness problem. Use was made [42] of a recent report that Nafion (and other perfluorinated ionomers) can be converted to a thermoplastic form by the ion-exchange inclusion of large, "hydrophobic" counterions such as tetrabutylammonium (TBA$^+$). The large counterions effectively cloak the anionic sites in the ionomer, thus minimizing the ionic interactions between polymer sidechains. The material is, consequently, moderately melt-processable and can be molded or extruded at sufficiently high temperatures and pressures. Thus, in the updated version of the original fabrication process [42], thin-film catalyst layers are cast from an ink that consists of supported platinum catalyst and solubilized ionomer in TBA$^+$ form. A general scheme describing the preparation of a catalyzed membrane employing thin-film catalyst layers is given in Fig. 21.

Details of the preparation of a thin-film catalyst layer based a mixture of recast ionomer in TBA$^+$ form and a Pt/C catalyst and the application of such a catalyst layer to the ionomeric membrane are as follows [43]. Inks from which the thin-film electrodes are cast are prepared by first thoroughly mixing together the catalyst (typically 20 wt% platinum on carbon supplied by E-TEK, Natick, MA) and an appropriate amount of 5 wt% solubilized Nafion (Solution Technology, Inc., Mendenhall, PA). The ratio of supported platinum catalyst to Nafion for the cathode catalyst layer is typically in the range of 5:2 to 3:1 (weight of solids); the anode ratio may be as low as 1:1. The protonated form of Nafion within the ink is next converted to the TBA$^+$ form by the addition of 1 m TBAOH in methanol to a catalyst and Nafion solution which has been well mixed for a few hours. The paintability of the ink (and also the stability of the suspension) can be improved by the addition of glycerol, in the approximate ratio of 1:1 (w/w) with the Nafion solution. Membranes can be catalyzed using a number of application techniques. The majority of membrane/electrode assemblies prepared to date, based on such thin-film catalyst

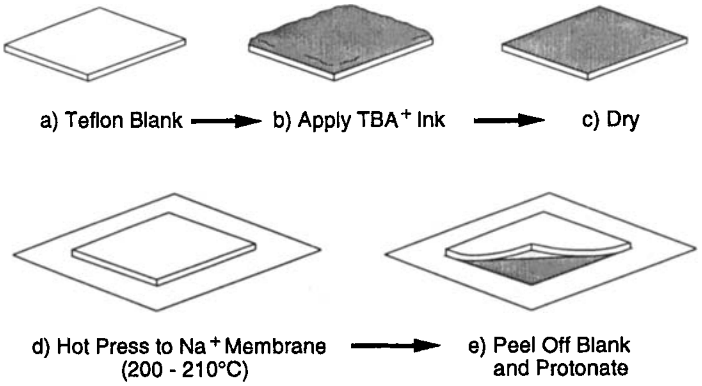
a) Teflon Blank
b) Apply TBA+ Ink
c) Dry
d) Hot Press to Na+ Membrane (200 - 210°C)
e) Peel Off Blank and Protonate

Fig. 21. Scheme describing the preparation of catalyzed membranes for PEFCs by a decal application of thin films (5–7 μm) of a Pt/C//ionomer composite to the ionomeric membrane. Platinum catalyst loading is 0.10–0.15 mg Pt/cm^2.

layers, were constructed using a "decal" process, in which the ink is cast onto Teflon blanks for transfer to the membrane by hot-pressing (Fig. 21). The decals thus formed are hot-pressed to membranes maintained in the Na^+ or K^+ forms at about 200–210 °C and 30 atm for five minutes. If the membrane is damp, the press is started at about 100 °C with a light load to prevent the membrane from shrinking unevenly within the electrode area. Slightly compressible materials are typically used to back the transfer blanks, to distribute the pressure more uniformly, and the hot-press platens are carefully aligned parallel when the force is applied.

The second method for catalyzing the membranes is to cast the same type of ink (TBA^+ form of the ionomer) directly onto the membrane [44]. This process may have an advantage over the decal process in the formation of a more intimate membrane/electrode interface. It may also be more amenable to scale-up. Indeed, initial attempts at laboratory-scale automated application of thin-film Pt/C//ionomer catalyst layers to ionomeric membranes have been quite successful. In this work, a computer-controlled mechanism of an *X–Y* recorder was applied to "paint" catalyst ink by the controlled repetitive motion of the pen of the recorder onto each of the membrane major surfaces. In this way, 100 cm^2 areas of catalyzed membranes were reproducibly generated, yielding performances per cm^2 of a similar level to that achieved previously with catalyzed membrane of 5 cm^2 active area [44]. The laboratory-scale automation equipment is shown in Fig. 22.

In the last step, the catalyzed membranes are rehydrated and ion-exchanged to the H^+ form by immersing them in lightly boiling 0.5 M sulfuric acid for several hours, followed by rinsing in deionized water. This protonation process is more rigorous than in the previous preparations described for the thin-film catalyzed membranes [14, 41], because the hydrophobic TBA^+ cation is relatively difficult to ion-exchange. It is for this reason that the membranes are used in the Na^+ or K^+ (and not the TBA^+) form in the earlier steps of the preparation process described above. PEFC membrane/electrode assemblies prepared by this technique have achieved the

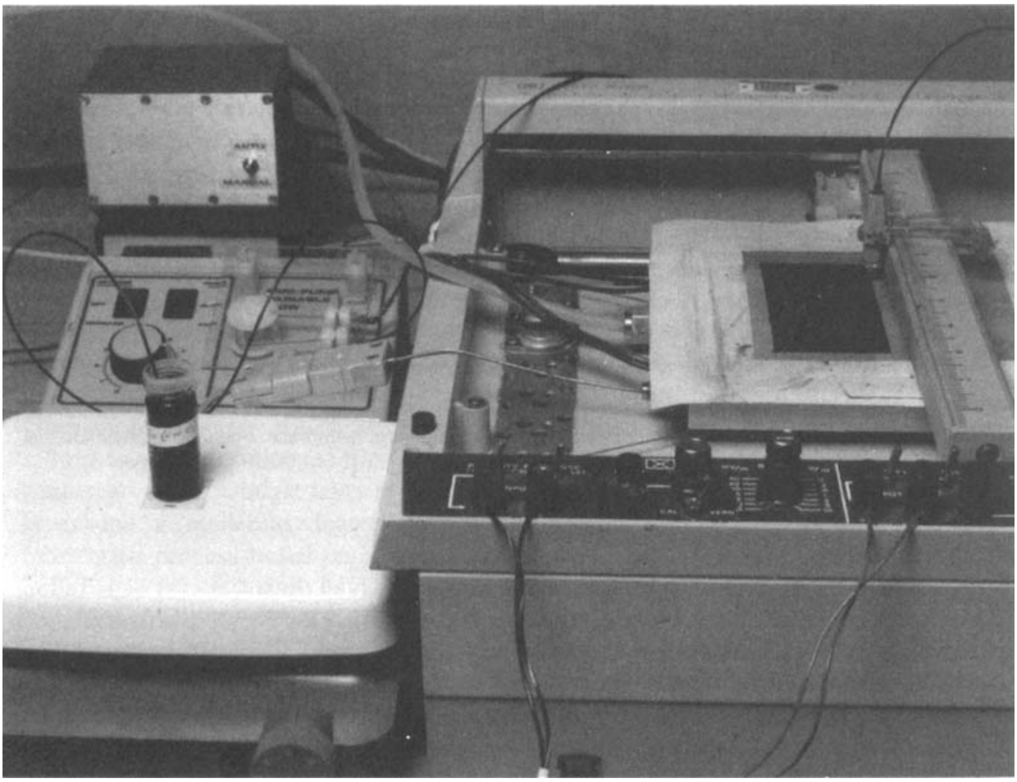

Fig. 22. Equipment for automated application of a Pt/C//ionomer "ink" directly onto an ionomeric membrane, developed by M. Wilson at Los Alamos National Laboratory. Membrane–electrode assemblies of areas exceeding 100 cm^2 could be prepared using this computer-controlled X–Y recorder mechanism.

combined properties of very high catalyst utilization, extremely good durability and stable long-term performance (4000–5000 h) with several shut-off/restart steps and perfect recovery after the cell has been exposed to several freeze/thaw cycles.

Typical PEFC polarization curves obtained with thin-film catalyst layers of this type, applied to Nafion 117 and 105 (DuPont), Membrane "C" (Chlorine Engineers Ltd., Japan) and developmental XUS-13204.10 Dow (Dow Chemical) membranes by decal transfer, are shown in Fig. 23 for H_2/air and for H_2/O_2 operation. The platinum loading of the cathodes for the four membrane/electrode assemblies are 0.13, 0.14, 0.16, and 0.13 mg Pt/cm^2, respectively. Anode loading is somewhat lower. Also shown in these figures are the high-frequency resistances of the cells. This figure shows that high PEFC performance can be obtained with ultra-low loading of platinum applied by this technique, reaching current densities as high as 3 A/cm^2 with oxygen cathodes, and 1 A/cm^2 at 0.6 V with air cathodes in PEFCs based on the more advanced ionomeric membranes. With highly purified H_2 as the anode feed

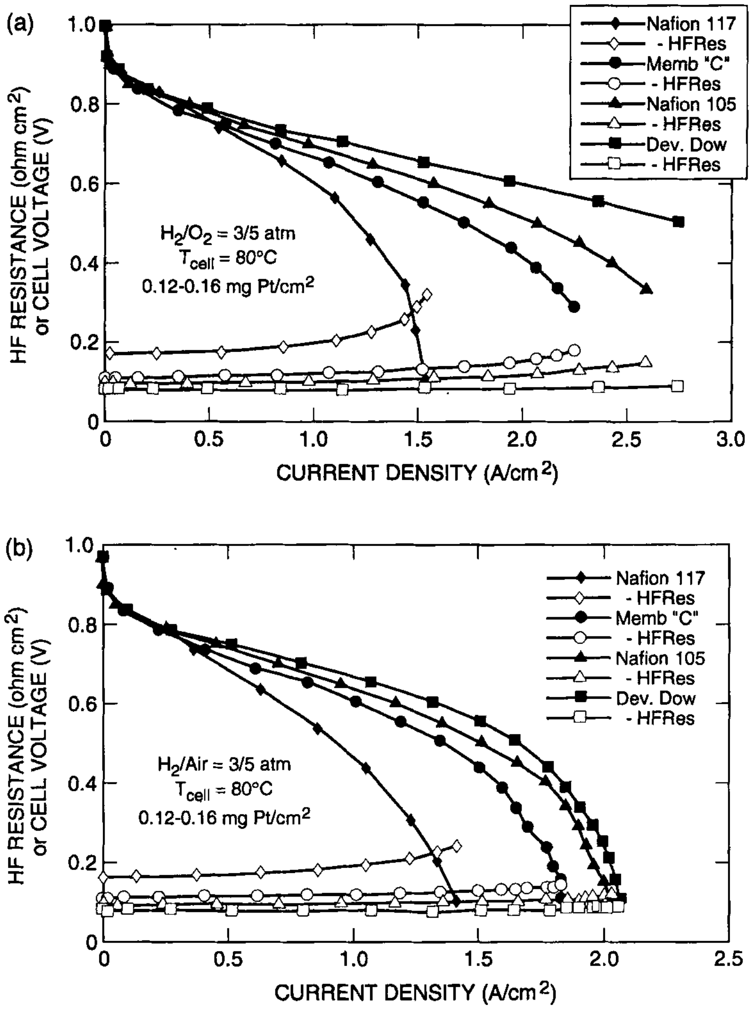

Fig. 23. Performance of thin-film catalysts in (a) oxygen and (b) air cathodes [42]. (Reprinted by permission of the Electrochemical Society).

stream, the total loss in cell power measured for PEFCs based on such catalyzed membranes after 3000 h of continues operation at 0.5 V was only 10% [42].

Figure 24 describes schematically the three recent modes of preparation of membrane/electrode assemblies based on commercially available dispersed platinum catalysts. Comparison of catalyst utilization obtained with the different PEFC catalyzation techniques is given in Fig. 25. The advantage in catalyst utilization of the thin-layer approach is clearly seen, increasing at the higher cell currents (lower cell voltage) thanks to minimized mass-transport limitations in the thin catalyst layer.

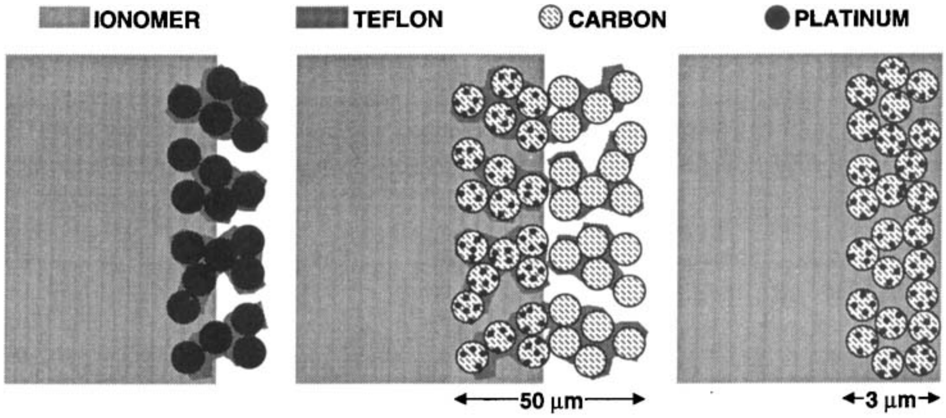

Pt Black/Teflon Bonded to Membrane 4 mg/cm^2

Pt/C/Teflon Catalyst Layer on Carbon Cloth Electrode; Hot Pressed to Membrane 0.5 mg/cm^2

Pt/C Catalyst Bonded to Membrane 0.15 mg/cm^2

Fig. 24. Scheme comparing three modes of application of dispersed platinum catalysts to ionomeric membranes.

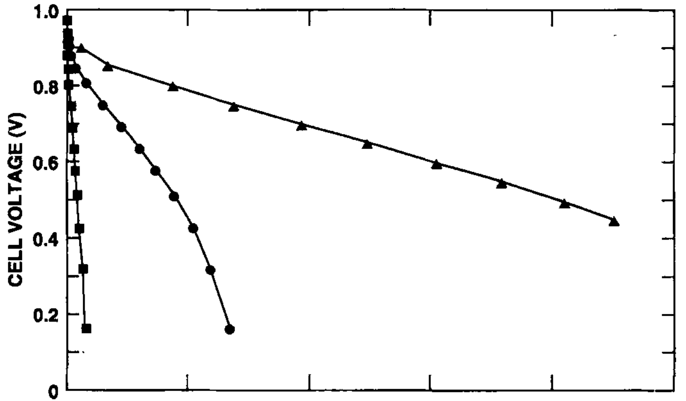

Fig. 25. Air cathode catalyst utilization for different types of catalyst layers in contact with ionomeric membranes. ■, Platinum black/PTFE (4 mg/cm^2); ● ionomer-impregnated gas-diffusion electrodes (0.45 mg Pt/cm^2); △, thin film of Pt/C//ionomer composite (0.13 mg Pt/cm^2). The advantage of thin-film catalyst layers increases particularly at high current density (lower cell voltage) because transport limitations within the catalyst layer are minimized.

4.4 Long-Term Testing of Membrane/Electrode Assemblies

A fuel cell stack developed for transportation applications has to maintain a stable performance for thousands of hours while operating on realistic fuel feed streams. Several critical questions raised in this regard have been:

1. Is the integrity of the membrane sufficient to prevent significant damage during prolonged operation, leading to catastrophic fuel/oxidant intermixing?
2. Will the electrocatalytic activity be maintained in spite of (a) catalyst poisoning phenomena, particularly on the anode side, and (b) catalyst agglomeration phenomena, particularly on the cathode?
3. Will the protonic conductivity of the membrane be maintained for thousands of hours in spite of trace ionic contaminants?

Quite satisfactory answers have been provided to all the above questions, as described below.

Life testing of highly pressurized PEFC stacks developed for space application at GE, later Hamilton Standard, first demonstrated thousands of hours of operation without failure [45]. This was the first series of tests which showed clearly the intrinsically high longevity of such power sources. Particularly, such life tests demonstrated the excellent integrity and longevity of PFSA membranes under fuel cell operation conditions. While such tests provided a good basis for confidence, they were run with high platinum loading of typically 4 mg/cm^2 per electrode, very pure hydrogen probably derived from a liquid hydrogen tank, a relatively thick ionomeric membranes (Nafion^{TM} 117) and testing at relatively low current densities of the order of 100–200 mA/cm^2, seeking maximum energy-conversion efficiency rather than maximized power. This still left, therefore, open questions regarding the longevity of the PEFC under conditions of lower platinum loading, less than ultra-pure hydrogen, thinner ionomeric membranes and higher specific powers. In a series of life tests run recently at LANL, a number of single cells were evaluated with low platinum loading of the order of 0.1 mg/cm^2/electrode, thinner membranes ranging in thickness between 125 μm and 50 μm, areal power densities equal to or higher than 0.5 W/cm^2 and hydrogen fuel from commercial tanks as well as $H_2/CO_2/CO$ mixtures with compositions that mimic methanol reformate cleaned up by preferential oxidation (PROX). Results of such test are described below.

4.4.1 Ionomeric Membrane Integrity and Maintenance of Protonic Conductivity

In all the tests performed, the PFSA membrane integrity was found to be excellent through life tests lasting, 4000–5000 h including the integrity of membranes as thin as 50 μm (Nafion^{TM} 112). Another encouraging observation has been that partial drying-out of the cell, resulting from occasional accidental termination of external water supply with the gas streams, has not caused a significant lasting performance loss once the gas stream has been rehumidified. The long-term integrity of thinner membranes is particularly important, based on their strong advantages for enhanced cell performance, as described in Section 5. It seems that better integrity, especially of thinner membranes, can be achieved by hot-press bonding to the membrane of a thin-film catalyst (mode A3, Table 4), rather than the hot-press bonding of a carbon cloth electrode (mode B1, Table 4). The improved longevity of cells with membranes catalyzed according to mode A3 is apparently achieved thanks to avoidance of damage to the membrane caused by hot-pressing a carbon cloth, or carbon paper electrode onto (and partly into) the membrane. A short life (less than a week) has been observed for cells prepared by hot-pressing catalyzated carbon cloth electrodes onto thin, Nafion 112 membranes, with catastrophic failure typically brought about by a hole through the membrane.

Excellent membrane integrity observed in such laboratory tests does not indicate, however, that catastrophic membrane failure cannot take place if a PEFC stack is not well designed to ensure sufficient humidification over the whole area of the membrane and under the complete range of operating conditions. The possibility of a local thermal run-away cannot be ruled out if local dehydration brings about increased membrane resistivity and, in turn, increased heat generation in a highly resistive part of the membrane. A mechanism that would correct for such a problem would rely on dropping the power dissipated in a dried-out, resistive membrane, and this could happen under voltage, or load control. Having mentioned the possibility, in principle, of such a membrane failure mode, it should be stressed again that, in the large majority of single-cell life tests performed at LANL with poly(perfluorosulfonic acid) (PFSA) membranes, termination of the test, typically after more than 3000 h, had to do with failure of some peripheral equipment or a problem with house plumbing, rather than failure of the cell itself.

As to the membrane conductivity, only small losses of protonic conductivity, of the order of 5–10% after 4000 h, have been observed in well-humidified cells during PEFC life tests according to measurements of cell impedance at 5 kHz [42]. The deionized water employed in the humidification scheme [42] had very low levels of metal ions (e.g., $Fe^{2+/3+}$, Ca^{2+} or Mg^{2+}). Such multivalent ions could exchange irreversibly with protons in the PFSA membrane, causing a drop in membrane conductivity. Deionizing the water used for PEFC humidification is therefore required, and appropriate plumbing should also be used in the humidification loop to avoid generation of ionic contaminants by corrosion processes.

4.4.2 Catalyst Ripening

Wilson and co-workers have measured platinum catalyst ripening in PEFC cathodes of ultra-low platinum loading which operated continuously for 2500 h at a cell voltage of 0.5 V, on pressurized hydrogen and air [46]. Results obtained for the cathode catalyst show that slow catalyst ripening takes place in these PEFC cathodes. The typical degree of ripening for Pt/C catalysts can be summarized as a decrease of platinum surface area from an initial value of 100 m^2/g to 70 m^2/g after 1000 h and to 40 m^2/g after 2500 h. The results of particle size distribution analyses for as-supplied

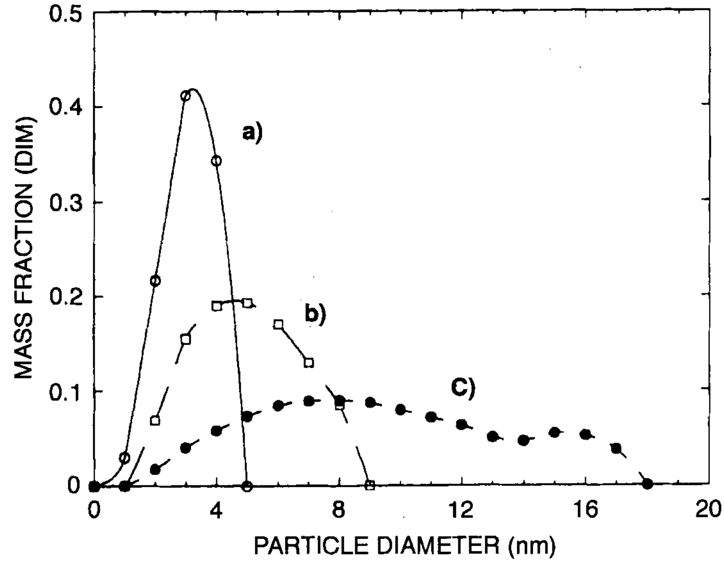

Fig. 26. Mass distributions of Pt/C (a) as cast catalyst, (b) PEFC cathode catalyst after 1320 of operation, and (c) PEFC cathode catalyst after 2200 h of operation [46]. (Reprinted by permission of the Electrochemical Society).

Pt/C catalysts and for such catalysts after prolonged use in the PEFC cathode are shown in Fig. 26. (Somewhat smaller surface area losses were observed for the anode Pt/C catalyst, where the effect of such loss in catalyst surface area would have only marginal impact on cell performance.) Such a surface area loss (Fig. 26) suggests that the cathode catalytic activity should decline by about 60% between the beginning and the end of the life test. However, long-term current losses observed around 0.8 V between beginning and end of the life test (2500 h) were negligible. A likely explanation is that the loss of platinum surface area is compensated by a higher specific activity per unit surface area of the larger platinum catalyst particles formed in the agglomeration process. Further detailed discussion of this point is given in [46]. Wilson and co-workers have concluded that the platinum catalyst ripening phenomenon does not contribute significantly to long-term performance losses in PEFCs based on ultra-low platinum loading.

4.4.3 Long-Term Anode Poisoning and Recovery

In some earlier life tests performed by Wilson and co-workers, PEFCs utilizing thin-film platinum catalyst layers typically experienced a gradual performance loss over the first 500 to 1000 h of operation and then stabilized at about 70% of the original performance (here, performance is described in terms of the current density measured at 0.50 V, i.e., close to the maximum power output of the cell). In such life tests, intermittent anode air bleeding was later applied in conjunction with temporary operation on feed streams containing predetermined, low levels of CO (see Section 3.3). It was found that, following such air bleeding, not only was any effect of intentionally introduced CO completely removed, but most of the gradual performance loss of the PEFC during the first 1000 h of operation on "99.99% pure" bottled hydrogen was also recovered [42]. Evidently, the oxygen bled into the anode had removed a persistent contaminant that had slowly accumulated on the anode catalyst. Levels of CO of the order of a few ppm are likely to be found in H_2 bottles because the origin of this hydrogen is, most probably, a natural-gas reforming process. Wilson and co-workers have subsequently installed a palladium tube purifier on their hydrogen supply. Ever since, the fuel cells tested by them have consistently lost only 5–10% of their original performance after several thousand hours of continuous operation [42]. Clearly, the anode contaminant originated from the (99.99% pure) bottled hydrogen used. These observations suggest that poisoning of the anode catalyst may be the one most important source of performance losses in PEFCs. This problem can be addressed by either air bleeding or the use of Pt–Ru anode catalysts, as described in Section 3.3.

4.4.4 Freeze–Thaw Cycles

Several single cells prepared with thin-film catalyst layers in the TBA^+ form were subjected to a freeze–thaw cycle to see if any performance loss or damage resulted [42]. The complete cell was placed in the freezer and then rethawed. After the first freeze, the performance actually increased slightly and dropped only a very a small net amount over the next two freezes [42]. Performance maintenance after repeated freeze–thaw cycles has important practical significance, particularly in transportation applications of PEFCs, and is apparently achievable in such PEFCs thanks to the intermixing of the ionomeric components of catalyst layer and membrane during the application of the thin film. Such good "ionomeric fusing" is achieved thanks to the composition, structure and mode of application of the ionomer-rich thin-film catalyst to the ionomeric membrane.

4.5 Membrane/Electrode Assemblies for PEFCs: Summary

Several different modes of preparation of membrane/electrode assemblies for PEFCs have been described. Recent developments have demonstrated a breakthrough in platinum catalyst utilization, enabling high PEFC performance with ultra-low platinum loading of 0.10–0.15 mg Pt/cm^2 at the cathode and even lower loading at the anode. PEFCs with such low platinum loading have exhibited long life (5000 h) and high performance stability under adverse conditions of several shut-off/start-up and freeze–thaw cycles. Since the membrane/electrode assembly is the "heart" of the PEFC, these achievements provide a good basis for the development of low-cost PEFC stacks of high performance and reliability.

The PEFC has very good potential for longevity, thanks to an excellent electrolyte (the PFSA membrane) and to advanced techniques for producing such membranes with well-adhering and robust catalyst layers. Additional prerequisites for stable performance are the sustained activity of the anode catalyst with less than perfectly pure hydrogen fuel and the maintenance of sufficient humidification levels for the complete range of cell operation conditions. Both targets seem to be achievable. The anode can apparently be kept fully active by the combined application of Pt–Ru catalysts and ex-situ and in-situ oxidative cleansing techniques for CO levels up to about 100 ppm (Section 3.3), whereas water management is facilitated by the use of thinner membranes and by the optimized design of backing layers and flow fields, and does not seem to present a severe barrier to stable, long-term performance. Having said that, long-term operation of a PEFC stack in the environment of a real system, i.e., a PEFC stack fueled from a methanol reformer on-board a vehicle, will require very effective control of the feed stream, particularly at the anode, and effective and reliable humidification schemes employing well-deionized water.

5 The Ionomeric Membrane

5.1 PEFC Membranes: Significance, Sources, and General Properties

PEFCs are defined as a class of fuel cells by the fact that the sole electrolyte used is polymeric. This confers on the PEFC some unique properties of a pseudo solid-state device (only distilled water needs to be added and managed) operating at relatively low temperatures, while making the properties of the polymeric membrane the key to achieving high performance and long-term stability. Historically, a variety of membrane materials have been employed. Initially, poly(styrenesulfonic acid) (PSSA) and sulfonated phenol–formaldehyde membranes were used, but the useful life of these materials was limited because of their tendency to degrade under fuel cell operating conditions. A critical breakthrough was achieved with the introduction of Nafion^{TM}, a perfluorinated polymer with sidechains terminating in sulfonic acid moieties. This material and its close perfluorosulfonic acid (PFSA) relatives are currently the state-of-the-art in membranes for PEFCs, satisfying in impressive fashion an array of requirements for effective, long-term use in fuel cells. They combine well the important requirements for a membrane in a PEFC, namely high protonic conductivity, high chemical stability under typical operating conditions, and low gas permeabilities. Typically, thicknesses of PFSA membranes for PEFCs range between 50 and 175 μm. The main source of PFSA membranes is DuPont (USA), where these membranes were invented in the 1960s and made into a commercial product for the chlor-alkali industry. Other source of developmental PFSA membranes have been Dow Chemical (USA), Asahi Glass (Japan), and Asahi Chemicals (Japan). A very recent source of developmental microcomposite membranes for fuel cells based on PFSA as the proton-conducting material has been W. L. Gore (USA). The latter membrane has a component providing mechanical strength in addition to the PFSA component which provides protonic conductivity. In spite of their superior characteristics for PEFCs, PFSA membranes do have some weak points. Their relatively high cost (about US $ 100/sq. ft.) has inspired continued work on lower-cost alternatives which could meet the requirements of the fuel cell environment. It is unclear how much the cost of existing PFSA membranes could drop if the demand for them increases, although it has been repeatedly speculated that a two-orders-of-magnitude increase in market for such membranes (their market is now limited to the chlor-alkali application) will bring about an order-of-magnitude decrease in their price. Another drawback of these membranes is presented by fairly strong limits to the range of temperature over which they can be reliably used. The upper operation limit is usually considered to be somewhat above 100 °C because of low membrane water contents above that temperature (and hence lower protonic conductivity) and because of accelerated oxidative degradation, whereas below the freezing point of water the protonic mobility falls precipitously in the hydrated PFSA membrane. In spite of these limitations of present-day high cost and the limited temperature window, PFSA membranes are certainly considered a strong and viable basis for the technology of polymer electrolyte fuel cells.

For optimal use in fuel cells, the membranes empolyed in PEFCs must be chemically and mechanically stable in the fuel cell environment, must present an adequate barrier to mixing of fuel and oxidant gases, and must generate as little ohmic loss as possible at the high current densities used in the PEFC. The chemical stability requirement has been an important issue since the intial development of PEFCs. The acidic nature of the membrane together with the oxidizing environment to which it is exposed on the cathode side of the PEFC, lead to quite aggressive conditions, tending to degrade various polymeric membranes. This is typically the case for membranes prepared from poly(styrenesulfomic acid) (PSSA), or for grafted membranes with oxidizable C–H bonds. The degradation of PSSA membranes under conditions significantly milder than those encountered in an operating fuel cell has been documented. For example, Reddy and Marinsky [47] have shown that PSSA degrades in aqueous solution under ambient conditions. Randin [48] compared the chemical stability of several membrane materials, including PSSA, poly(ethylenesulfonic acid) (PESA), poly(2-acrylamido-2-methylpropanesulfonic acid) (poly-AMPS), and Nafion^{TM} 120. PSSA exhibited chemical instability over a period of 49 days, even at room temperature. PESA degraded at temperatures below 70 °C, while poly-AMPS and Nafion^{TM} were stable under the same conditions even at temperatures over 100 °C. Clearly, the conditions employed [48] were less harsh than in an operating PEFC. LaConti and others [49] have compared the degradation of 6% divinylbenzene-crosslinked poly(styrenesulfonic acid) (DVB-PSSA), poly(trifluorostyrenesulfonic acid), and Nafion^{TM} 120 membranes in peroxide/Fe(II) media and found that, whereas the Nafion^{TM} membrane was quite stable, substantial degradation of the former two membranes occurred over the course of 24 h.

Scherer and co-workers [50] have tried to circumvent this problem by fluorinating at the α and β positions on the vinylbenzene monomer and grafting the α,β,β-trifluorostyrene onto PTFE/ethylene copolymers followed by sulfonation. These workers have also investigated the degradation of PSSA and grafted poly(styrenesulfonic acid) membranes by various techniques. They show very good stability f or both Nafion^{TM} 117 and the α,β,β-trifluorostyrenesulfonic acid/PTFE/ethylene material – up to 10000 h under rather demanding water electrolysis cell conditions. Furthermore, the resistance of the latter membrane material was on the order of 0.08 Ω cm^2. This is very promising behavior. Ballard (BC, Canada) has recently announced the development of a relatively inexpensive PEFC membrane material based on a poly(aromatic) backbone with fluorinated, sulfonic acid terminated sidechains. This membrane has exhibited good performance and stability in the fuel cell, reputedly at a lower cost. Little detail is yet available regarding this material.

5.2 Structural Aspects of Ionomeric Membrane Materials

The basic chemical structures of a variety of membrane materials which have been used in PEFCs are shown in Table 5. The three-dimensional structure of some of these membrane materials has been extensively studied and reviewed [51, 52]. Each of the membrane materials used in PEFCs is ionomeric in nature. Eisenberg and coworkers [53] showed that ion aggregates form in PFSAs. The energetics of cluster formation have been discussed at length by Mauritz and Rogers [54]. These aggregates effectively act to crosslink the membrane, imparting mechanical integrity to these polymeric materials which are otherwise not crosslinked. Evidence for the formation of these ionic aggregates has been derived from small-angle X-ray scattering (SAXS) studies (most recently by Wu [56]). A great deal of work has been carried out to develop structural models to further interpret scattering studies. The membranes discussed here, with their high loading of sulfonic acid moieties, probably have two or more phase-separated regions. Yeager and Steck [55] have suggested that three regions are important in defining polymer transport properties: the fluorocarbon, the ion cluster, and a third, interfacial, region. Most of the polar groups are associated with the large ionic cluster (inverted micelle-like) regions. The existence of these clusters is generally agreed upon, but the details of their arrangement and connectivity, and the importance of fluorocarbon instrusions and interfacial regions, are still topics of debate.

Recent SAXS work by Wu [56] has demonstrated that the ionic domains in Nafion membranes are most probably spherical and exhibit a size distribution and spacing that does not vary much with equivalent weight (EW). The latter work suggested that strings of smaller spherical aggregates could be sufficiently close to coalesce upon swelling with water uptake by the membrane, and thus could provide percolation pathways for ionic transport. This picture could replace the nanoscale (1.2 nm-wide) channels suggested in earlier models for Nafion^{TM} to explain transport phenomena.

Membrane structural properties may depend strongly on the thermal history of the material, affecting, in turn, the transport properties. Following exposure of the ionomeric membrane to different thermal/hydration conditions, a range of metastable structures could arise, each associated with a different water content, cluster size, and cluster connectivity. Consequently, as discussed below, thermal pretreatment effects

Table 5. Chemical structures of some membrane materials

Membrane	Structures
PSSA	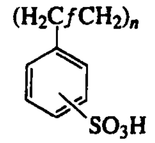
Nafion,^{TM} Membrane C	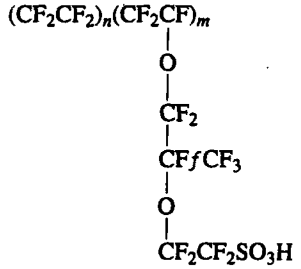 $(CF_2CF_2)_n(CF_2CF)_m$–O–CF_2–$CFfCF_3$–O–$CF_2CF_2SO_3H$
Dow	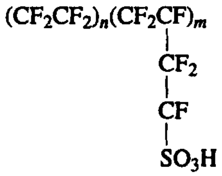 $(CF_2CF_2)_n(CF_2CF)_m$–CF_2–CF–SO_3H
PESA	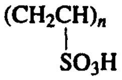 $(CH_2CH)_n$–SO_3H
α,β,β-Trifluorostyrene grafted onto poly(tetrafluoroethylene-ethylene) with post-sulfonation	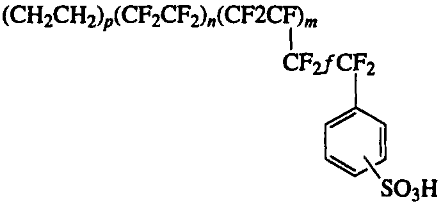
Poly – AMPS	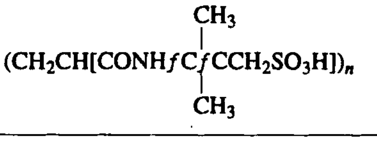 $(CH_2CH[CONHfC(CH_3)_2fCCH_2SO_3H])_n$

are important determinants of water uptake by the membrane as well as of membrane transport properties, and their specification is therefore critical. For the same reason, some form of treatment of "as-received" membranes is preferable to no pretreatment because the state of the membrane can be readily set by, for example, boiling it in water and/or dilute acid. This is in addition to the obvious importance of cleaning up the membrane from impurities by such immersion/boiling treatments.

5.3 Water in PEFC Membranes

The protonic conductivity of a polymeric membrane is strongly dependent on membrane structure and membrane water content. A central challenge in the evaluation of ionomeric membranes for fuel cell applications has thus been the analysis of combined structural and water uptake characteristics required to achieve the highest protonic conductivity in an operating PEFC. Section 5.3.1 will address water uptake by ionomeric membranes employed in PEFCs, the state of water in such membranes and the resulting protonic conductivities obtained.

Having established water uptake by a given membrane, and the protonic conductivity associated with a given water content, an additional requirement for cell diagnostics is to be able to evaluate the water profile in a PEFC membrane of given thickness and properties under given cell current and cell humidification conditions [87]. This water profile could be quite uneven along the membrane thickness dimension and would depend critically on water transport in the membrane and on cell current density. Sources of water and the various flux components which redistribute water in an operating PEFC are shown schematically in Fig. 27. Water is produced at the cathode by the cell process and can enter the cell via humidified reactant gases. Water is transported through the membrane from anode to cathode by electroosmotic drag, i.e., by a water flux associated with the protonic current. The flux of water due to electroosmotic drag ($\mathrm{mol/cm^2\,s}$) is:

$$N_{\mathrm{w,drag}} = I\xi(\lambda)/F \tag{14}$$

where I is the cell current, $\xi(\lambda)$ is the electroosmotic drag coefficient at a given state of membrane hydration $\lambda(= N(\mathrm{H_2O})/N(\mathrm{SO_3H}))$ and F is the Faraday constant. This water migratory flux tends to dry out the anode side of a cell under current and adds to the faradaic production of water at the cathode, to produce an excess of water at the cathode. This buildup of water at the cathode is relieved, in turn, by diffusion down the resulting water concentration gradient and by hydraulic permeation of water in differentially pressurized cells where the cathode is held at higher overall pressure. The fluxes ($\mathrm{mol/cm^2\,s}$) brought about by the latter two mechanisms within the membrane are:

$$N_{\mathrm{w,diff}} = -D(\lambda)\Delta c/\Delta z \tag{15}$$

$$N_{\mathrm{w,hyd}} = k_{\mathrm{hyd}}(\lambda)\Delta P/\Delta z \tag{16}$$

where D is the diffusion coefficient in ionomer of water content λ, $\Delta c/\Delta z$ is a water concentration gradient along the z-direction of membrane thickness, k_{hyd} is the hydraulic permeability of the membrane, and $\Delta P/\Delta z$ is a pressure gradient along z.

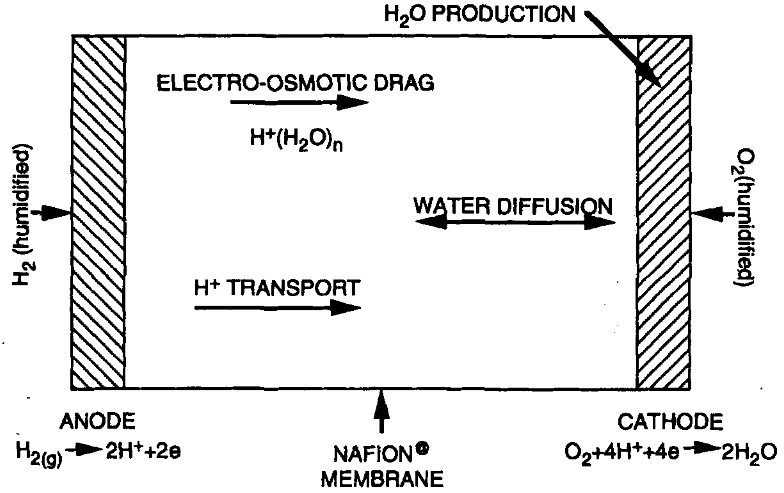

Fig. 27. Schematic representation of water sources and water fluxes that determine the water distribution profile within an operating polymer electrolyte fuel cell.

The steady-state water profile across the ionomeric membrane for given cell current density, external humidification conditions, and differential pressurization, is the resultant of these electroosmotic, diffusive, and hydraulic fluxes.

In order to evaluate the steady-state water profile in the membrane of a PEFC under given operating conditions, the necessary membrane transport properties required thus include water uptake by the membrane as function of water activity and membrane pretreatment conditions, $\lambda(a_w)$ (covered in Section 5.3.1); the diffusion coefficient of water in the membrane as a function of membrane water content, $D(\lambda)$; the electroosmotic drag coefficient as a function of membrane water content, $\xi(\lambda)$ and the membrane hydraulic permeability, $k_{\text{hyd}}(\lambda)$. Section 5.3.2 includes a discussion of water transport modes in ionomeric membranes.

5.3.1 Water Content and Protonic Conductivity in Ionomeric Membranes

Water Uptake by Ionomeric Membranes

Water uptake in ionomeric membranes has been studied intensively. There are significant differences in water uptake by such membranes from liquid and vapor phases. We will first discuss some data on water uptake from the liquid phase by various membranes and the effect of the thermal history of the membrane on such uptake. We will then concentrate on the uptake of water from the vapor phase. Both modes of water uptake could be important under PEFC operating conditions.

Equilibration with liquid water The behavior of the ionomeric membrane in liquid water is an experimentally convenient starting point. Some principal determinants of water uptake by a given sulfonic acid membrane material are its equivalent weight, its mechanical resistance to swelling, and the counterion present in the membrane. Steck and Yeager [99] reported on water sorption by Nafion^{TM} 120 membranes at room temperature, showing that 16.5 water molecules per sulfonate group are taken up by the protonic form of the membrane in water. They also showed a substantial decrease in the water content of the membrane caused by exchanging the proton for alkali or alkaline-earth metal ions. For the alkali metal ions, the water uptake decreased with increasing size of ion, with Li^+-form membranes taking up 14.3 H_2O/SO_3H but Cs^+-form membranes only 6.6 H_2O/SO_3H. For membranes with divalent counter-cations, the water uptake was only weakly dependent on the cation, ranging from 11.6 for the Ba^{2+} form to 14.1 H_2O/SO_3H for the Zn^{2+} form.

The dependence of water uptake from the liquid phase on membrane thermal pretreatment was mentioned in the earliest descriptions of Nafion properties. As Grot et al. have pointed out [57], Nafion membranes take up dramatically more water from liquid water at very high temperatures–up to 100% of the polymer dry weight in the case of Nafion^{TM} 120 when the membrane is in contact with liquid water at 180 °C. Such expanded ("E-form") membranes maintain a constant, high water content when in contact with liquid water at temperatures at or below the pretreatment temperature. In contrast, "S"-form (S for shrunken) membranes are prepared by drying the membranes completely at elevated temperatures. Such membranes imbibe less water than as-received ("normal", N-form) membranes.

The origin of these phenomena lies in the combined effect of temperature and hydration on polymer structure. As temperature increases, the ionomer undergoes successive transitions to a rubbery, then a viscous state. The bulk modulus of the polymer, and therefore its resistance to swelling, are substantially decreased. If water, or another polar swelling solvent, is taken up from the liquid at this high temperature and the polymer is subsequently cooled, the polymer maintains its swollen state brought about by high water uptake into the ionic cluster phase. In contrast, if the polymer is kept dry at an elevated temperature, the ionic clusters can shrink and freeze into that shrunken state upon cooling. Steck and Yeager found that, in each case and regardless of the cation present, significantly more water was taken up for E-form Nafion^{TM} membranes. For example, in membranes containing protons as the counterion, 22.3 H_2O/SO_3H were imbibed, compared with 16.5 H_2O/SO_3H for N-form. Within the E-form membranes, similar trends for water uptake with the nature of the counterion were observed as for N-form membranes.

Zawodzinski et al. [58, 59] have reported on the amount of water taken up by immersed protonic PFSA membranes after different thermal treatments. After complete drying at 105 °C, the water uptake upon immersion of membranes is relatively small and increases with the temperature of the water bath in which the membrane is immersed. In contrast, the water content of well-swollen membranes dried at room temperature and then re-immersed in liquid water is independent of the temperature of the re-immersion bath between room temperature and boiling water. This phenomenon was referred to earlier qualitatively by LaConti et al. [49]. The results of Zawodzinski et al. are summarized in Table 6 for three membranes, Nafion^{TM} (EW= 1100), Membrane C (Chlorine Engineers, EW= 900), and Dow XUS (EW= 800). As seen in Table 6, the uptake expressed as a percentage by weight

Table 6. Water uptake by various membranes from liquid water.[a]

		Water uptake [moles H_2O/moles SO_3H]			
		No thermal treatment	Dried at 105 °C [b]		
		Rehydration temp.	Rehydration temp.		
Membrane	EW	27 °C < T < 94 °C	27 °C	65 °C	80 °C
Nafion117	1100	21 (34%)[c]	12 (20%)	14 (23%)	16 (26%)
Membrane C	900	21 (42%)	11 (22%)	15 (30%)	15 (30%)
Dow	800	25 (56%)	16 (36%)	23 (52%)	25 (56%)

[a] Adapted from [58]

[b] Membrane dehydrated completely at this temperature; incompletely dried membranes behave as in the "No thermal treatment" column.

[c] Percentage of dry weight, in parentheses.

indicates a substantial increase in water uptake with decreasing equivalent weight. This is an important advantage of lower-EW ionomeric membranes for PEFC applications (still lower EWs are difficult to achieve because of ionomer stability limitations). Also, after exhaustive drying at 105 °C, the Dow developmental membrane samples take up a somewhat larger amount of water upon re-immersion in liquid water at a given temperature. This accords with the somewhat higher glass transition temperature reported for this material by (Eisman [60] in that, during the dehydration step, substantially less shrinkage may have taken place.

Following Heaney and Glugla [65], Zawodzinski et al. [58] have investigated the behavior of membranes aggressively swollen at elevated temperatures. Swelling of the PFSA membranes at elevated temperatures in glycerol leads to marked dimensional changes as well as a substantial degradation of the mechanical strength of the membrane. As shown in Fig. 28, the water content of PFSA membranes (Na^+ form) treated by swelling in glycerol increases dramatically as the glycerol treatment temperature is raised. Whereas a Nafion™ 117 membrane boiled in water takes up roughly 22 water molecules per sulfonate group, after treatment of the Nafion 117 membrane in the swelling agent at 225 °C, the membrane weight gain on immersion in water at room temperature corresponds to 80 water molecules per solfonate group. A substantial increase in swelling takes place after treatment above 135 °C. This temperature can be described as an effective glass transition temperature for the sodium-form Nafion™ membrane.

Swelling can be even more dramatic in the case of some other membrane samples: in the case of the glycerol-treated Dow membrane, several times the dry weight of the membrane is imbibed from liquid water in contact with the membrane. Under these extreme swelling conditions, the membrane has lost much of its mechanical integrity and is best regarded as a hydrogel. There is a rough correspondence between the equivalent weight of the membrane and its extent of swelling, with increasing equivalent weight apparently conferring a greater resistance to swelling of the material.

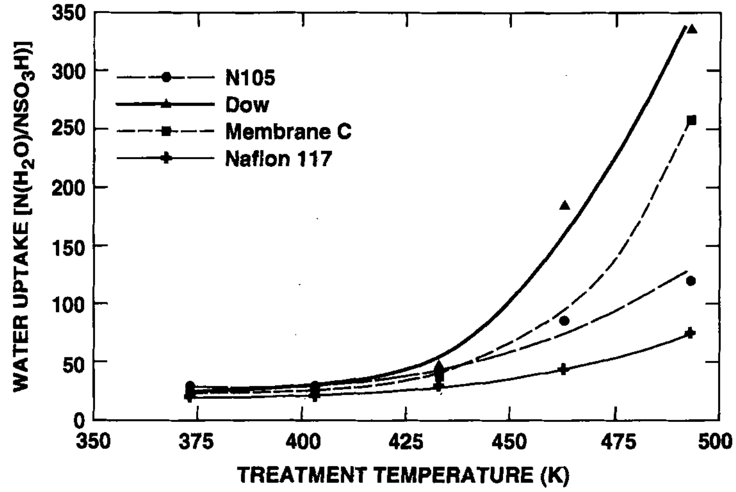

Fig. 28. Water uptake by a Nafion membrane immersed in liquid water at 28 °C as a function of the temperature of membrane pretreatment in a hot glycerol bath.

Eisman [60] has reported water sorption by immersed Dow membranes of various equivalent weights. The water uptake was found to be strongly dependent on EW. At the lowest EW (597), the membrane is doubtless on the verge of dissolution, taking up water at a level of nearly 550% of polymer dry weight! For EW= 850 and EW= 950, the water uptake is more modest, approximately 40 and 25% of dry weight, respectively.

Equilibration with water vapor Substantially less work was done in this area in the early phase of research on PFSAs because of previous emphasis on membranes which would be in contact with liquid water or aqueous solutions (e.g., for chlor-alkali technology). However, water supplied from the vapor phase could be a principal mode of external hydration of the membrane in a PEFC, particularly hydration of the anode side, and thus it is an important focus of study in fuel cell R&D. The shape of the sorption isotherms shown in Fig. 29 (a) and (b) is generic for ion-exchange polymers. With increasing P_{H_2O}, water is sorbed in two steps as evidenced by the sorption isotherm:

1. a low vapor activity region, $a_{H_2O} = 0.15$–0.75, characterized by a relatively small increase in water content with water vapor activity and by enthalpy of sorption of about 12.5 kcal/mol (52 kJ/mol) (greater than the enthalpy of water liquefaction), and
2. a high vapor activity region, $a_{H_2O} = 0.75$–1.0, characterized by steeper increase of water content with water activity and by sorption enthalpies as low as 5 kcal/mol (21 kJ/mol) at $a_{H_2O} = 1.0$ (lower than the enthalpy of water liquefaction).

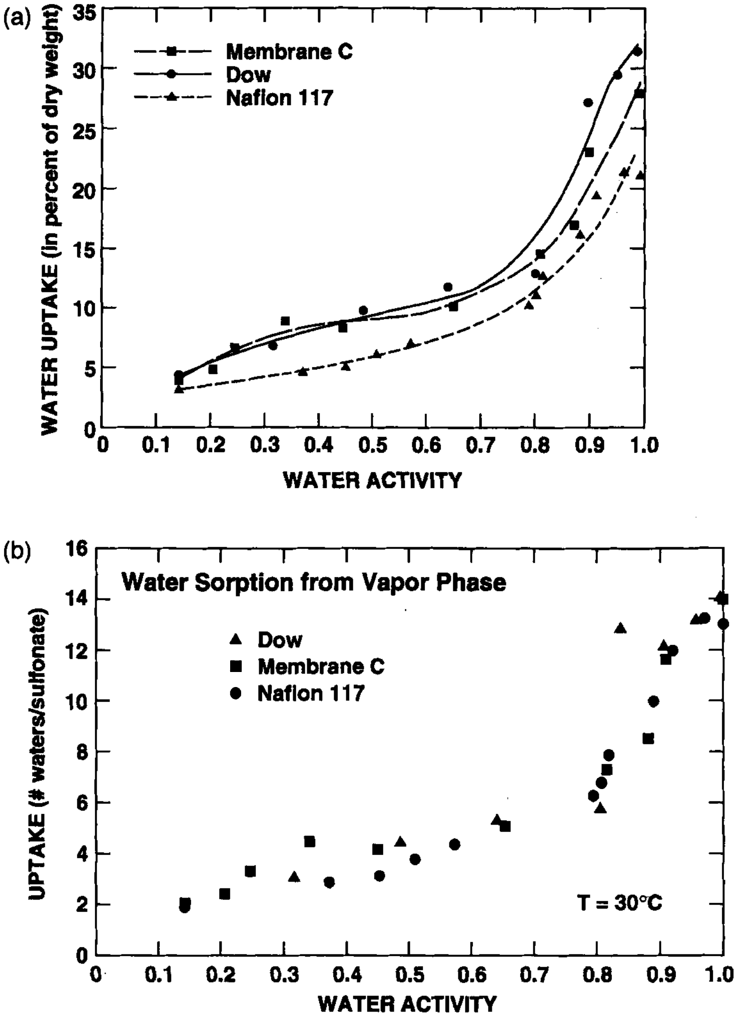

Fig. 29. Measured water uptake by three PFSA membranes from the vapor phase at 30 °C as a function of water vapor activity: (a) in terms of weight %; (b) as the ratio (λ) of no. of water molecules/no. of sulfonate groups.

Region 1 corresponds to uptake of water of solvation by the ions in the membrane, while region 2 corresponds to water which fills the (submicro)pores and swells the polymer. The lower enthalpy for the second step is caused by a weaker water–ion interaction, by endothermic deformation of the polymer matrix on swelling, and by a decrease in the degree of hydrogen bonding in the polymer matrix relative to the state of pure liquid water. The swelling of the membrane at higher water vapor activities is thus driven significantly by increase in entropy.

Randin [48] reported water sorption from the vapor as a function of relative humidity for PSSA, PESA, poly-AMPS, and Nafion 120. The last membrane took up substantially more water per equivalent than did the other membranes, for which only limited data were presented 11 H_2O/SO_3H ($\lambda = 11$) at 90% relative humidity. Escoubes and Pineri [61] have reported water sorption at 22 °C for Nafion and other ionomeric membranes with various counterions. They reported uptake by membranes exposed to a flowing gas stream of given relative humidity in a gravimetric apparatus. They also have determined the enthalpy of sorption of water from the vapor phase for Nafion 120 and other membranes in the protonic and other ionic forms. Compared with other reports [58,63], the results presented in [61] show significantly less water uptake by Nafion from the vapor phase. Since equilibration with the vapor phase is a very slow process and the final water uptake level is also a function of membrane pretreatment, the exact experimental conditions could have a significant effect on the level of sorption measured. Pushpa et al. [63] described water uptake from the vapor phase under isopiestic conditions for $\text{Nafion}^{\text{TM}}$ 117 as well as for Dowex resins with different crosslink densities. The dependence of water uptake on the counterion was explored in this work. These workers have shown that, in general, significantly less water is sorbed by Cs^+ and $N(CH_3)_4^+$ forms of the membranes compared with the Li^+ and H^+ forms. Furthermore, they have shown that crosslinking results in dramatically decreased water sorption; they calculated from the sorption isotherms the free energy of swelling and swelling pressures for the polymers studied. The swelling pressure calculated for protonic $\text{Nafion}^{\text{TM}}$, 194 atm, is substantially larger than the corresponding quantities for the crosslinked resins (143 atm for the 8% crosslinked PSSA was the highest observed for the PSSA materials studied).

Rieke and Vanderborgh [62] focused on the temperature dependence of water sorption from saturated water vapor. They monitored water uptake by infrared spectroscopy and showed that the water content in a membrane in contact with saturated water vapor decreases with increasing temperature above roughly 70 °C. This phenomenon is further discussed below, and is apparently caused by a slow rate of water uptake from the vapor phase at higher temperatures. This is caused, in turn, by very slow water condensation at higher temperatures at a hydrophobic membrane surface [67].

Zawodzinski et al. [58, 59, 64] have investigated the sorption of water vapor of controlled activity by various PFSA membranes at 30 °C. The results shown in Fig. 29 (a) and 29 (b) are quantitatively similar to those reported for Nafion by Pushpa et al. [63] and qualitatively similar to those reported by Escoubes and Pineri [61]. From Fig. 29 it can be seen that differences in water uptake between different PFSA membranes, expressed in terms of percentage of dry weight taken up, are almost completely explained by differences in equivalent weight. When water uptake is expressed in terms of the ratio λ, no. of water molecules/no. of sulfonate groups, the uptake curves look essentially identical for the different PFSA membranes (Fig. 29 (b)). Over the entire range of water activity, the activity coefficient of water in the membrane is greater than unity if one assumes as ideal a Raoult's law relationship between water activity and membrane water content, with $\lambda = \lambda_{\text{immersed},30\,^\circ\text{C}}$ assumed to correspond to unit water activity in the membrane ($\lambda_{\text{immersed},30\,^\circ\text{C}}$ ranges between 21 and 25). The high activity coefficient for water in the membrane reflects the hydrophobic nature of the ionomer. Because the water sorption isotherms for $\text{Nafion}^{\text{TM}}$, Membrane C, and Dow membranes are essentially identical when the water uptake is expressed in units of λ, i.e., moles of water per mole of sulfonate, Membrane C and Dow membranes, which have lower equivalent weights, both take up more water from the vapor than Nafion™ membranes on a percentage by weight basis (Fig 29a).

Comparison of water uptake by PFSA membranes from the liquid and from the vapor phase reveals an interesting apparent paradox: the water content of the membrane in equilibrium with saturated water vapor ($a_w = 1$) is not the same as the water content of a similarly prepared membrane in contact with liquid water ($a_w = 1$). Under the conditions used by Pushpa et al. [63] and by Zawodzinski et al. [58, 59, 64], 14 water molecules per sulfonate group were sorbed from vapor phase at unit activity (saturated vapor) versus 22 from liquid water. A difference in water uptake by polymers exposed to liquid versus saturated vapor phases has been observed for several polymer/solvent systems. The phenomenon was first reported in 1903 by Schroeder [66], and is therefore called Schroeder's paradox. One explanation of this difference in uptake is that sorption from the vapor phase involves condensation of water on the strongly hydrophobic, Teflon-like surface of the polymer, and thus is less favorable than the imbibition of liquid water. This hydrophobic character of vapor-equilibrated membrane surfaces has been demonstrated by contact angle measurements at the air/liquid water/membrane interface [67], summarized in Table 7. Even for saturated water vapor, an advancing contact angle of nearly 100° is observed. The droplet advancing/droplet receding hysteresis of the contact angle observed is substantial. This has been interpreted as shown in Fig. 30. As the droplet advances and the polymer surface contacts liquid water, a segmental flipping of hydrophilic moieties initially buried in the interfacial region occurs, rendering the polymer surface substantially more hydrophilic as reflected by the lower receding angle measured. The surface of the PFSA membrane is, thus, hydrophobic in contact with water vapor (even saturated vapor) and becomes hydrophilic only in contact with liquid water. This may provide some explanation for the significantly different water uptake levels by ionomeric membranes from saturated water vapor and from the liquid. Recent work [69] has shown that a new material, Nafion™ 105, exhibits larger water uptake than usual from the vapor at high water vapor activities. Indeed, for Nafion™ 105 at 30 °C, there is apparently little discernible difference in sorption from the saturated water vapor and from liquid water. The details of membrane properties which bring about this behavior have not been clarified.

Table 7. Contact angles (30 °C) for water on Nafion™ 117 membranes of controlled water content.

Water content	$P_{H_2O}/P^{\circ}_{H_2O}$	Contact angle (advancing/receding) [deg]
0 H_2O/SO_3H	0	116/30
2 H_2O/SO_3H	0.14	115/0
4 H_2O/SO_3H	0.58	114/0
9 H_2O/SO_3H	0.82	107/0
14 H_2O/SO_3H	1.00 (vapor)	98/14

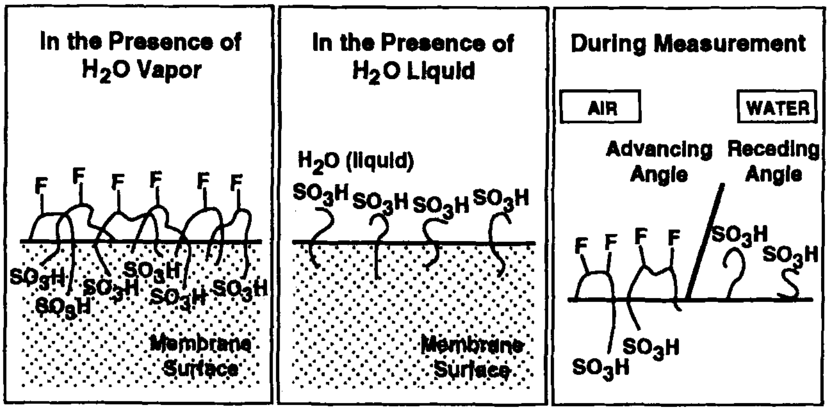
In the Presence of H_2O Vapor
F F F F F F
SO_3H SO_3H SO_3H SO_3H SO_3H SO_3H
Membrane Surface
In the Presence of H_2O Liquid
H_2O (liquid)
SO_3H SO_3H SO_3H SO_3H
Membrane Surface
During Measurement
AIR
WATER
Advancing Angle
Receding Angle
F F F F
SO_3H SO_3H SO_3H SO_3H

Fig. 30. Schematic description of PFSA membrane surface composition in contact with water vapor and with liquid water, as deduced from contact angle measurements. The scheme on the right-hand side describes the change in membrane surface composition during contact angle measurement which results in the large difference between 'advancing' and 'receding' contact angle readings (see Table 7).

More recently, Zawodzinski et al. [68] reported isopiestic sorption data for PFSA membranes at the higher equilibration temperature of 80 °C, corresponding to the typical operating temperature of a PEFC. These data are presented in Fig. 31, together with reference data for the same membrane (Nafion™ 117) at 30 °C. Clearly, a Nafion membrane equilibrated with saturated water vapor takes up less water as the temperature is raised. This finding is in general agreement with the earlier results of Rieke and Vanderborgh [62]. All membranes tested thus far (Nafion 117 and 105, Membrane C, Dow) behave similarly. Sen et al. [98] have used near-

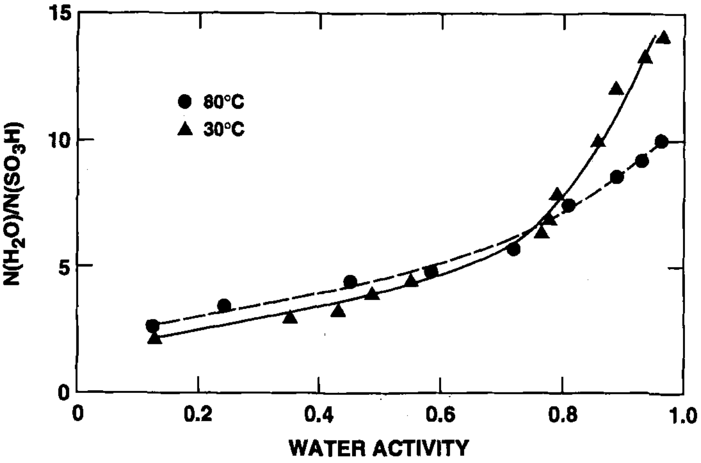

Fig. 31. Water sorption curves measured for Nafion™ 117 membranes equilibrated with water vapor at 30 °C and at 80 °C.

infrared spectroscopy to determine the uptake of water by PFSA membranes exposed to saturated water vapor as a function of temperature in the range 20 °C < T < 100 °C. They confirmed that the water content indeed decreases as the temperature increases [62, 68], leveling off, however, at 70–80 °C. Consequently, membrane conductivity should increase above this temperature when the membrane is kept in equilibrium with saturated water vapor.

State of Water in the Membrane

A substantial amount of work has been carried out to study the state of water in swollen sulfonic acid membranes. Randin [48] carried out differential thermal analysis studies to determine the "nonfreezing" fraction of water in ionomeric membrane materials. He suggested that each of the polymers studied (poly-AMPs, PSSA, PESA, and Nafion^{TM} 1100) has "non-freezing" water at a level of 6 H_2O/SO_3H. From the data, he also deduced an enthalpy of fusion of 5.65 kJ/mol for water in all above membranes beyond the "nonfreezing" fraction, a value similar to that of liquid water–6.01 kJ/mol. He also found that below roughly six water molecules per sulfonate, no enthalpy change due to freezing is observed down to −40 °C, the lower temperature limit of his measurement. This behavior is identified with water adsorbed on pore walls, i.e., strongly associated with ions in the membrane.

Sivashinsky and Tanny [70] reported proton NMR relaxation measurements on water in Nafion^{TM} 125 and several other sulfonated ion-exchange membranes. Spin lattice relaxation times on the order of 0.1 s at room temperature were observed. They concluded that the confinement of water in Nafion to narrow pores, 12 Å in diameter, is reflected in the observed relaxation behavior, which suggests rapid exchange of water molecules from bulk and adsorbed environments. They also found that only part of the water undergoes freezing at temperatures down to −60 °C. Similar behavior was observed for sulfonated polysulfone and chlorosulfonated polyethylene. MacBrierty and co-workers [71] also performed proton NMR studies of water in Nafion membranes. In their case, the presence of trace levels of Fe(III) in the membrane resulted in quite short T_1 values and made the results difficult to interpret. Slade et al. [72] also reported proton relaxation studies for a limited set of water contents in Nafion^{TM} 117 membranes. They concluded that a distribution of translational correlation times could account for the observed behavior. Pineri and co-workers [73] reported quasielastic neutron scattering studies of hydrated Nafion samples which indicate essentially unimpeded water motion within very small structures, typical diameter 8 Å, in the membrane. They suggested that this is a manifestation of either a substructure within the ionic phase of an intermediate structure between ion clusters. Falk [74] reported infrared studies or water in these membranes at 30 °C and relative humidities 3–100% which proved particularly revealing. From the observed vibrational bands associated with water in the membrane, he concluded that:

1. water exists in two distinct environments in the membrane, a bulk-like network and a non-associated water environment; and

2. even the bulk-like network of associated water molecules has weakend hydrogen bonding in comparison with liquid water.

Zawodzinski et al. [58] have reported ^{2}H NMR relaxation measurements on water in Nafion membranes. In contrast with proton NMR relaxation studies, which are difficult to interpret because of various inseparable contributions to the observed relaxation rates, a direct relationship often exists between the observed ^{2}H relaxation rate and rotational dynamics of the deuteron-bearing species. The time scale probed by such measurements is in the pico- to nanosecond range, and thus very short-range motions are probed. In a membrane equilibrated with saturated water vapor, a ^{2}H T_1 on the order of 0.2s was observed. This ^{2}H relaxation rate for D_2O in the membrane is only higher by a factor of two than that in liquid D_2O, indicating a bulk water-like mobility within the pore at high membrane hydration levels. The ^{2}H relaxation rate increases (i.e., local water motion in the membrane becomes slower) as the water to ion-exchange site ratio decreases.

Chen et al. [75] have reported ^{2}H and ^{17}O NMR relaxation measurements for water in Nafion membranes. On the basis of their ^{2}H relaxation measurements, they observed an increase in activation energy for local water mobility with increasing water content, suggesting that water in the membranes does not behave like free water in large voids. The activation energy for water motion varies from 0.20 eV for a membrane with 4.7% ($\lambda = 3$) water to 0.27 eV for a membrane with 18% ($\lambda = 11$) water over the temperature range 220–300 K. This value is high compared with the activation energy for free rotation of D_2O in the liquid. (This result [75] seems to contrast with most other observations concerning the relative hindrance of water motion at high and low water contents in Nafion.) The same workers also observed apparent anisotropy in the membranes via the NMR spectra of water in as-received and stretched films. Pak and Xu [76] have suggested that there appear to be two separate water peaks observable in NMR spectra of Dow membranes. These are ascribed to ion-solvating and bulk water. The relative intensity of the two peaks changes dramatically with changing water content in the polymer. This is somewhat surprising since the water in these two environments would be expected to be in rapid exchange on the NMR time scale. Other possible explanations for the second peak are water in non-cluster regions (and thus in slow exchange with water in clusters) or impurities in the polymer. It is unclear how or if the membranes were treated from their as-received state. Pak and Xu also suggest a distribution of correlation times for water in the polymer. This would indicate that a range of water rotation rates exists in the membrane, suggesting structural heterogeneities (e.g., a distribution of pore sizes).

In summary, it appears from spectroscopic studies such as neutron scattering or NMR relaxation measurements which probe rotational water motions on a short time scale, 10^{-2}–10^{-9} s, and thus over a short distance range that, at the highest water contents, water mobility within the pore of an ionomeric membrane is not drastically different than bulk water mobility. However, as the water content of the membrane decreases, its mobility is increasingly hindered. The nanopore liquid in the membrane is essentially a concentrated acid solution and ion–water (as well as ion–ion) interactions will have significant influences on water motion. Intrusions of sidechains of dynamic orientation must also result in significant perturbation of water mobility within the nanopore.

Proton Conduction in Ionomeric Membranes

The most important property of ionomeric membranes employed in polymer electrolyte fuel cells is the high protonic conductivity they provide under humidification conditions and at current densities typically required in PEFCs. As in any other conducting medium, the magnitude of the specific conductivity is determined by the product of charge carrier density and charge carrier mobility. The charge (proton) carrier density in an ionomeric membrane of EW 1100 is similar to that in 1 M aqueous sulfuric acid solution. Remarkably, proton mobility in a fully hydrated ionomeric membrane is only one order of magnitude lower than the proton mobility in the aqueous solution. As a result, the specific conductivity of fully hydrated PFSA (immersed) membranes is about 0.1 S/cm at room temperature and about 0.15 S/cm at the typical cell operation temperature of 80 °C. These levels of specific ionic conductivity are at least three to four orders of magnitude higher than specific ionic conductivities achieved for solvent-free, ionically conducting polymers at similar temperatures. These high protonic conductivities provide the basis for the high power densities achievable in PEFCs. The dependence of proton mobility in PFSA membranes on water content is, however, quite critical, and demands effective cell and stack design to maintain a high level of water through the thickness of the membrane for the complete range of dynamic operation.

Several recent publications have discussed the methodology in measuring the ionic conductivity of PFSA membranes. Care must be taken to ensure that the membrane conductivity measurement is free of electrode polarization effects. This can be done either with a four-point probe in measurements across the membrane thickness dimension [81] or with two electrodes placed on the same major surface of the membrane, where much larger interelectrode spacings can be employed [58, 59, 80]. The quality of the electrode/membrane surface contact is ensured in the latter experiments by a high interfacial surface area and a sufficiently high measurement frequency which ensures effective capacitive coupling at this interface, indicated by a negligible imaginary component of the impedance.

The conductivity of Nafion$^{\text{TM}}$ 117 (EW 1100), Membrane C (EW 900), and Dow membranes (EW 800) at 30 °C was measured by Zawodzinski et al. [58–60] for membranes immersed in liquid water and for partially hydrated membranes in contact with water vapor. The conductivity of Nafion$^{\text{TM}}$ 117 decreases roughly linearly with decreasing water content, as shown in Fig. 32. The value of the conductivity measured at $\lambda = 14$ (saturated vapor), 0.06 ± 0.01 S/cm, agrees with the value previously reported by Rieke and Vanderborgh [62]. The dependence of conductivity on water content for Membrane C and Dow membranes is somewhat more complicated. In both cases, the conductivity decreases roughly linearly with decreasing water content until an apparent threshold is reached, at which point the conductivity drops substantially (Fig. 32). Above the water content where the steep drop occurs, the specific conductivity of both membranes is substantially higher than

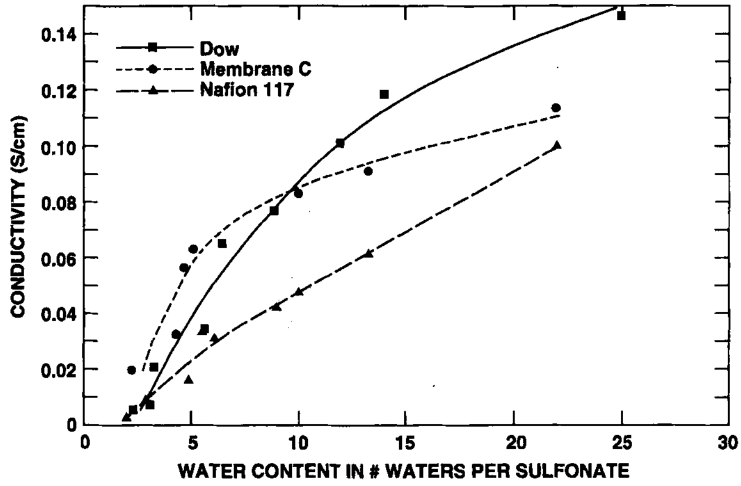

Fig. 32. Protonic conductivity versus water content for several PFSA membranes exposed to water vapor of varying activity at 30 °C.

that of Nafion^{TM} 117. This is expected on the basis of the larger concentrations of charge carriers (lower EW) in Membrane C and Dow relative to Nafion^{TM} 117. However, the enhancement of conductivity is larger than the ratio of ionic concentrations, suggesting that proton mobility in Membrane C and Dow membranes is higher than in Nafion^{TM} 117 at a given H_2O/SO_3H ratio. This finding agrees with a Bruggeman model based formula, suggested by Yeo and Eisenberg for dependence of the conductivity in ionomeric membranes on average water volume fraction [52]. The steep drop in protonic conductivity observed in Membrane C and in the Dow membrane occurs at around $\lambda = 5$, and results in protonic conductivity similar to that in Nafion^{TM} 117 below $\lambda = 5$. This sharp drop in conductivity may be due to the sequestering of protons by sulfonate groups (undissociated sulfonic acid groups) at low water contents. That this occurs is suggested by the infrared results of Rieke and Vanderbrogh [62]. It could also indicate some change in the mechanism of protonic transport at this lowest content level.

A Bruggeman-type relation has been reported by Yeo and Yeager [52] to approximate the dependence of ionic conductivity on water content in a Nafion membrane:

$$\kappa = 0.54\kappa_e(1 - V_p)^{1.5} \qquad (17)$$

where κ is the membrane conductivity, κ_e is the conductivity of a sulfuric acid solution of equal concentration to that of the sulfonic acid, and V_p is the volume fraction of polymer in the "water–polymer composite." At the water contents reported [52], up to $\lambda = 22$, the lowered polymer volume fraction explained the observed increase in conductivity as the water level was increased.

Verbrugge and Hill [77] have compared protonic conductivities of several different Nafion and Dow samples immersed in sulfuric acid solutions at various temperatures. Conductivities on the order of 0.06–0.085 S/cm were reported for the acid-immersed Nafion samples at 22 °C. The immersed Dow membrane samples exhibited somewhat higher conductivity (0.13–0.14 S/cm) at this temperature. These data were reported for membranes in contact with a minimum concentration of 0.3 M H_2SO_4 and are dependent on the sulfuric acid concentration. This study [77] presents a model of water and ion distribution based on properties of pores in the ionomer. The model, which uses Poisson's equation to describe electric potential variation in the pore, is successful in describing experimental acid partitioning results. Other earlier reports of protonic conductivity in ionomeric membranes have been given by Slade et al. [72] and by Eisman [60].

In a separate study, Verbrugge et al. [78] reported the temperature dependence of the resistance of Nafion™ 117 immersed in acid solutions of various concentrations, showing that it decreased over the temperature range 20–80 °C from 0.26 Ω cm^2 to 0.10 Ω cm^2. An activation energy for proton motion of 4.5 kcal/mol (18.8 kJ/mol) is reported from these data. This activation energy is somewhat high compared with that for protonic conduction in either aqueous acid solutions or that reported in membrane conductivity studies (see below). Rieke and Vanderborgh [62] reported a maximum in the membrane protonic conductivity with temperature when a Nafion™ 117 sample is exposed to saturated water vapor. This is a result of the tradeoff of thermal activation of the conduction process with decreased water content under the conditions of their experiment (see Fig. 31). The temperature dependence of the conductivity over the temperature range 25–90 °C of Nafion, Membrane C, and Dow samples immersed in distilled water was also measured Zawodzinski et al [59]. Note that the water content of immersed membranes preequilibrated in boiling water is constant over this temperature range (see Table 6). The specific conductivity of immersed Membrane C and Dow membranes was found to be larger by about 10% and 50%, respectively, than that of immersed Nafion™ 1100.

Fontanella, Greenbaum, and co-workers [79] have reported an interesting study of the pressure dependence of membrane conductivity. A significant increase is observed in the activation volume for proton transport as water content drops below 5 H_2O/SO_3H. This accords well with the expectation of a change in the mechanism for proton conduction when the water in the membrane is essentially only water of ionic solvation.

Kreuer et al. [95] have recently suggested an interesting analogy between the ratios measured for water and for proton mobilities in Nafion membranes and in concentrated aqueous acid solutions. They suggest that proton mobility in the hydrophilic nanopores of Nafion is very similar to the mobility of water. This is expected from observations made on concentrated acid solutions, where the hydrogen-bonded water structure is strongly biased in the electric field of anions, disturbing the solvent symmetry required for fast proton hopping. The result is proton mobility in Nafion which is strongly tied to the mobility of water at values of λ smaller that 12. Kreuer and co-workers further stress the significance of phase separation in Nafion, providing a better-connected and hydrophilic network within the ionomer. This advantage of Nafion can be realized by comparing the protonic

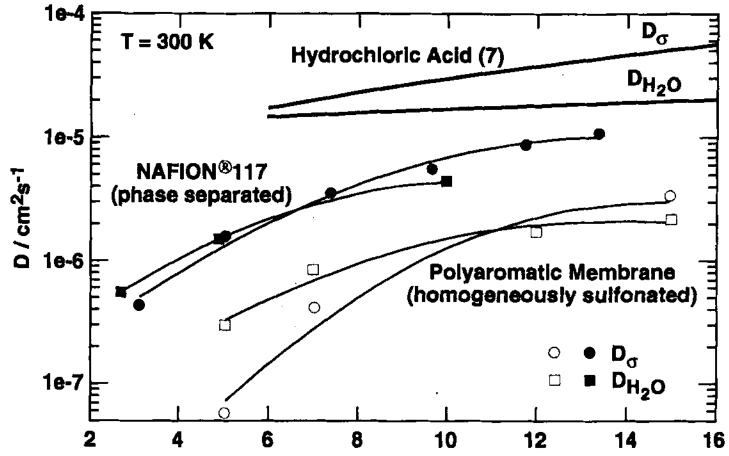

Fig. 33. Intradiffusion coefficients of water and of protons in concentrated aqueous acid solution, homogeneously sulfonated polyaromatic ionomer, and phase-separated PFSA ionomer [95]. (Reprinted by permission of the Electrochemical Society).

conductivity in the PFSA membrane with that measured in a homogeneously sulfonated, polyaromatic ionomer. Comparison of mobilities and relative mobilities of protons and of water in the two types of ionomers and in concentrated HCl solutions is given in Figs. 33 and 34 [95]. In examining the results presented in these figures it should be noted, however, that they are confined to water contents of $\lambda < 14$. The ratio of proton to water mobility in Nafion does increase above unity, up to 2.5 at $\lambda = 22$ [64,49], indicating significant proton hopping in fully swollen membranes (for comparison, in bulk aqueous acid, a ratio of 4 is observed between D_{H^+} and D_{H_2O}). Based on the comparison with a sulfonated polyaromatic homogeneous ionomer, phase separation in the PFSA membrane is indeed seen (Figs. 33 and 34) to enable an order of magnitude enhancement in both water and proton mobilities.

The protonic conductivity of Nafion membranes shows interesting behavior following membrane overswelling in hot glycerol. In Fig. 34, a plot of the protonic conductivity versus water content is given for Nafion membranes immersed in water at 30 °C, including Nafion membranes pretreated in hot glycerol to achieve superswelling. The water content of the latter, overswollen, membranes exceeds 22 H_2O/SO_3H. The membrane protonic conductivity is seen to go through a maximum at roughly $\lambda = 22$ and then decreases with further increase in water content (further swelling). This result is of interest in the context of the magnitude and mechanism of protonic conductivity in PFSA membranes. In previous descriptions of the protonic conductivity mechanism, the similarity of activation energies measured for protonic conductivity in bulk aqueous acid solutions and in well-hydrated Nafion membranes has led to the conclusion that the well-hydrated PFSA membrane serves as not more than a "molecular sponge" hosting a porous H^+/H_2O network [52]. The result demonstrated in Fig. 35 shows that there is an apparent limit to that model because

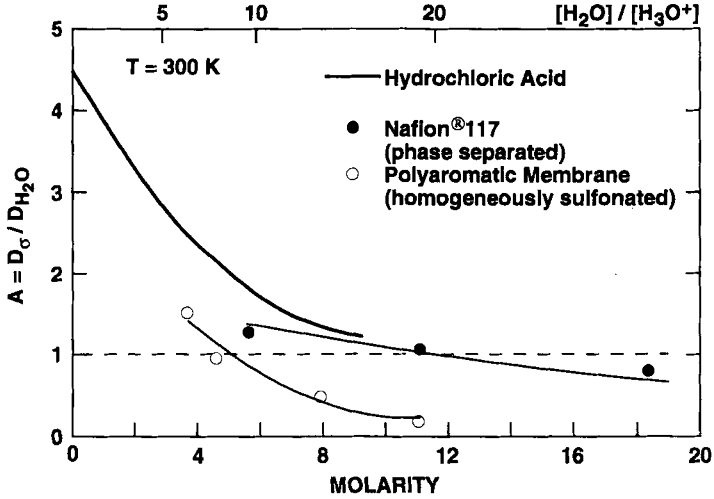

Fig. 34. The ratio of proton/water small-scale mobility in the three media described in the caption for Fig. 33 [95]. (Reprinted by permission of the Electrochemical Society).

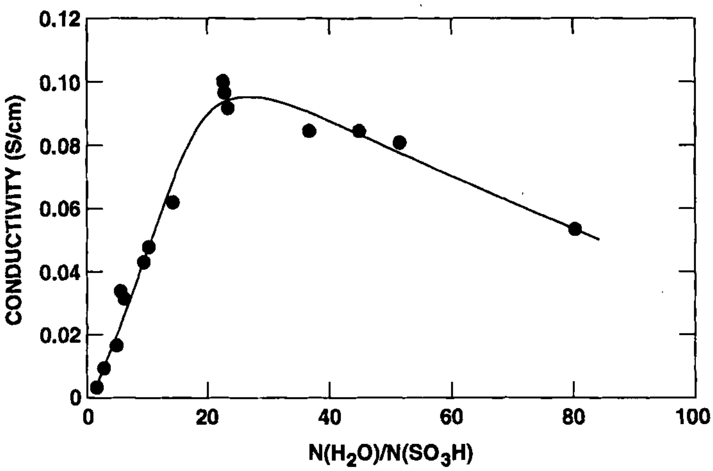

Fig. 35. Protonic conductivity versus water content for Nafion™ 117 membranes at 30 °C, including data for membranes preswollen in glycerol.

the fundamental step of protonic motion in the membrane does differ from its counterpart in aqueous acid solutions by the need of the proton to be stabilized by an immobilized anionic site following each fundamental "jump." Apparently, at water levels up to 22 H_2O/H^+ the requirement for stabilization at an anionic site is easily fulfilled, thanks to the relatively high concentration of sulfonic acid groups and the mobility of sidechains carrying them. However, as the membrane is swollen beyond that level, the combination of ionic concentrations and sidechain mobilities available in the membrane is insufficient to correct for the increased separation between the energy minima along the elementary proton trajectory. From a practical point of view, this result means that "superswollen" ionomeric membranes are not likely to provide further increase in protonic conductivities beyond what is achieved by treatment of the membrane in boiling water.

5.3.2 Water Transport Properties

Diffusion of Water in PFSA Membranes

The diffusion coefficient of water in Nafion and related membranes and its dependence on water content are necessary inputs for the analysis of the performance of cells based on such membranes. The "back-diffusion" of water from cathode to anode (Fig. 27) an important factor in determining water balance. Clarification of the water profile across the ionomeric membrane in a cell under current thus requires knowledge of water diffusion coefficients as a function of water content. Diffusion coefficient measurements will be discussed below.

To describe diffusion of water through the membrane in the presence of water activity gradient, an appropriate interdiffusion coefficient must be determined. Experimental methods used to study diffusion of water in these polymers, such as radiotracer and pulsed gradient spin–echo NMR techniques, probe instead intradiffusion coefficients often referred to as tracer of self-diffusion coefficients. Intradiffusion coefficients are determined in the absence of a chemical potential grading force, representing randomizing of mixtures of species of insignificantly different chemical energies. Intradiffusion and interdiffusion coefficients are related for the case of diffusion of a small molecule in a polymeric matrix as follows:

$$D_{\text{inter}} = D_{\text{intra}}\{\mathrm{d}(\log a)/\mathrm{d}(\log C)\} \tag{18}$$

Care should be taken to ensure that the correct diffusion coefficient is used in applying experimental data, e.g., in modeling efforts.

Diffusion coefficients for sorbed solvent and ions in Nafion have been estimated using several techniques. Yeo and Eisenberg [53] studied the sorption of water by a dry slab of Nafion (EW 1155) and estimated the interdiffusion coefficient of water in the membrane over the temperature range 0–99 °C from the water uptake dynamics. Diffusion coefficients from these measurements increased with increasing temperature over the range $(1\text{–}10)\times10^{-6}$ cm^2/s with a reported activation energy of 4.5 kcal/mol (18.8 kJ/mol). The method used to estimate the diffusion coefficients by Yeo and Eisenberg [53] was based on the $t^{1/2}$ dependence of the uptake in the initial portion of the uptake curve and is probably not fully appropriate [82]).

Yeager et al. [00] reported diffusion coefficients of water in Nafion 120 membranes containing various alkali-metal cations, determined by radiotracer measurements. In these studies, the diffusion coefficient of water was measured for fully hydrated (i.e., immersed) membranes. The water diffusion coefficient was found to be only slightly dependent on the cation present in the immersed membrane, with a value in Na^+ form Nafion of 2.65×10^{-6} cm^2/s at 25 °C and in K^+ and Cs^+ forms 2.15×10^{-6} cm^2/s and 1.32×10^{-6} cm^2/s, respectively.

As part of comprehensive analysis of transport in Nafion membrane, Verbrugge and co-workers [83–85] have described studies of the transport of water, protons, and other ions through Nafion membranes by radiotracer and electrochemical techniques. These experiments were carried out with the membrane exposed to a bulk aqueous acid solution. This situation is not identical to that found in a PEFC. However, at low acid concentration the acid is not partitioned in large amounts into the membrane. Tracer (i.e., intra) diffusion coefficients of water in the range 6×10^{-6} to 1×10^{-5} cm^2/s ($T = 22$ °C) are reported for fully hydrated Nafion membranes. Verbrugge et al. have compared water diffusion rates in various membranes and have calculated the net water flux through membranes using the Nernst–Planck equation modified to include convective flow. They have also derived conclusions regarding the relative pore size and structure in the PFSA membrane (e.g., no narrow interconnections) based on effective porosities derived from their modeling of experimental transport data. Eisman [60] reported approximate water interdiffusion coefficients for the Dow membrane by analyzing the time dependence of water uptake Water diffusion coefficients in the range 10^{-6}–10^{-5} cm^2/s were reported for temperatures ranging from 25 to 100 °C, similar to those measured by Yeo and Eisenberg for Nafion^{TM} as mentioned above. Slade et al. [86] have reported pulsed field gradient NMR studies of water motion in Nafion^{TM} samples, yielding intradiffusion coefficients close to 1×10^{-5} cm^2/s for fully hydrated samples.

Zawodzinski et al. [64] have reported self-diffusion coefficients of water in Nafion^{TM} 117 (EW 1100), Membrane C (EW 900), and Dow membranes (EW 800) equilibrated with water vapor at 303 K, and obtained results summarized in Fig. 36. The self-diffusion coefficients were determined by pulsed field gradient NMR methods. These studies probe water motion over a distance scale on the order of microns. The general conclusion was the PFSA membranes with similar water contents, λ, had similar water self-diffusion coefficients. The measured self-diffusion coefficients in Nafion^{TM} 117 equilibrated with water vapor decreased by more than an order of magnitude, from roughly 8×10^{-6} cm^2/s down to 5×10^{-7} cm^2/s as water content in the membrane decreased from $\lambda = 14$ to $\lambda = 2$. For a Nafion membrane equilibrated with water *vapor* at unit activity, the water self-diffusion coefficient drops to a level roughly four times lower than that in bulk liquid water whereas a difference of only a factor of two in *local* mobility is deduced from NMR relaxation measurements. This is reasonably ascribed to the additional effect of tortuosity of the diffusion path on the value of the macrodiffusion coefficient. For immersed Nafion membranes, NMR diffusion imaging studies showed that water diffusion coefficients similar to those measured in liquid water (2.2×10^{-5} cm^2/s) could be attained in a highly hydrated membrane (1.7×10^{-5} cm^2/s) [69].

To convert the intra(self-)diffusion coefficients (D_{self}) to inter(Fickian)diffusion coefficients (D_{chem}), Zawodzinski and co-workers [64] have corrected the self-diffusion coefficients they measured for water activity coefficient variations along the membrane thickness dimension and for the effects of swelling of the polymer [87]. The resulting D_{chem} for water in the Nafion membrane was 2×10^{-6} cm^2/s at 30 °C and did not exhibit a strong dependence on water content (however, recent reevalua-

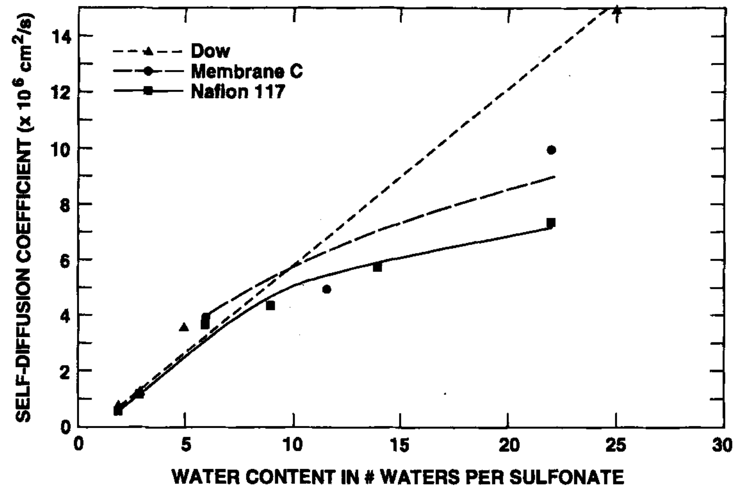

Fig. 36. ^{1}H diffusion coefficients for several PFSA membranes as a function of water content, measured with NMR (PGSE) at 30 °C [59]. (Reprinted by permission of the Electrochemical Society).

tion of these NMR results suggests that D_{self} values reported for the lowest water contents in the membrane were too high by a factor of about two). Zawodzinski et al. have also recently carried out measurements on various membranes at 80 °C, the results of which are summarized in Fig. 37.

Zelsmann and co-workers [88] have reported tracer diffusion coefficients for water in Nafion membranes exposed to water vapor of controlled activity. These were determined by various techniques, including isotopic exchange across the membrane. They reported apparent self-diffusion coefficients of water much lower than those determined by Zawodzinski et al. [64], with a weaker dependence on water content, varying from 0.5×10^{-7} cm^2 to 3×10^{-7} cm^2/s as the relative humidity is varied from 20 to 100%. It is likely that a different measurement method generates these large differences. In the experiments of Zelsmann et al., water must permeate into and through the membrane from vapor phase on one side to vapor phase on the other. Since the membrane surface in contact with water vapor is extremely hydrophobic (see Table 7), there is apparently a surface barrier to water uptake from the vapor which dominates the overall rate of water transport in this type of experiment.

Kreuer et al. [89] have reported an activation energy for water transport in Nafion on the order of 0.17 eV (3.9 kcal/mol; 16 kJ/mol), constant for water contents ranging from $\lambda = 8$ to 14. At the lowest water content examined, $\lambda = 3.5$, an activation energy of 0.22 eV (5.1 kcal/mol; 21 kJ/mol) is reported over the temperature range 20 to 90 °C. These values agree roughly in magnitude with those reported by Chen et al. [75] from relaxation measurements, although their reported trends in activation energy with water content are different. The increase in activation energy for water motion with decreasing water content [89] accords well with the notion that water mobility is increasingly hindered at low water contents by shrunken pores and strong electrostatic interactions. Kreuer et al. have suggested that the selfdiffusion coefficients reported by Zawodzinski et al. are somewhat high. The error is particularly

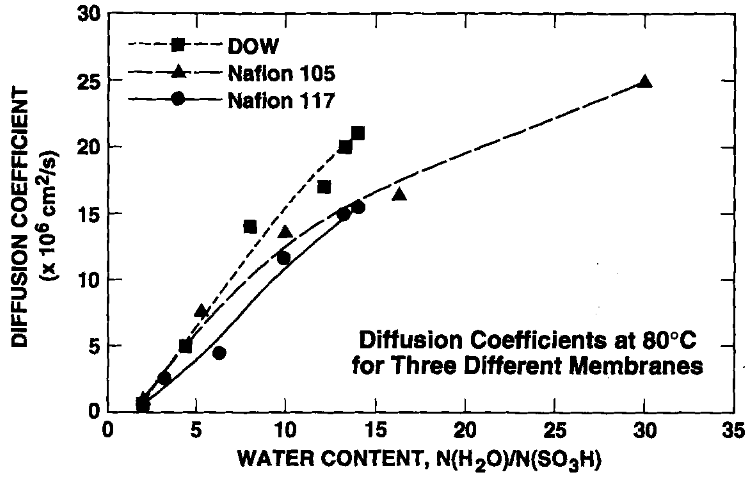

Fig. 37. ^{1}H diffusion coefficients for PFSA membranes vs. water content at 80 °C.

Table 8. Self-diffusion coefficients of water in Nafion 117 (T = 30 °C) as a function of glycerol pre-treatment temperature.

Treatment temperature [K]	Water diffusion coefficient [cm^2/s]
373	0.7×10^{-5}
409	1.0×10^{-5}
498	1.7×10^{-5}

high at lower water contents. Recent work by Zawodzinski et al. suggest that this is indeed true, and the origin of the error is instrumental.

As shown by Zawodzinski et al., the dramatic uptake of water upon preswelling the membrane in glycerol at elevated temperatures (Fig. 27) substantially affects the transport properties in the membrane. In Table 8, the ^{1}H intradiffusion coefficient is given for several different water contents. The water self-diffusion coefficient increases to 1.7×10^{-5} cm^2/s as the water content reaches the exceptionally high level of $\lambda = 80$ (liquid water has a self-diffusion coefficient of 2.2×10^{-5} cm^2/s at the same temperature).

Electroosmosis

The number of water molecules carried through the membrane per proton when a protonic current flows through the membrane is a central factor in the determination of the water profiles in the membrane of an operating PEFC. This number has been reported over the years with considerable variation. There is an important difference between the electroosmotic drag coefficient, $\xi(\lambda)$, a characteristic of an ionomeric membrane with fixed water content and flat water profile, and the net water flux through an operating fuel cell. The latter is the resultant of several water transport modes in the cell (see Fig. 27).

Breslau and Miller [90] measured water drag coefficients for various anions and cations moving through ionomeric membranes. They have compared these experimentally derived drag data with those predicted from a hydrodynamic continuum model which considers the effects of ion size (with hydration sheaths) relative to membrane pore size. The main assumptions were that the membrane consists of parallel-plate pores or cylindrical pores and ions are partially stripped of their hydration sheaths within the membrane pores. Using the pore size in either the cylindrical or parallel-plate structure as an adjustable parameter, this model predicts satisfactorily the drag coefficient in the case of every ion except protons. They derived very small pore sizes – on the order of 8 Å for a parallel-plate model and 4 Å for the cylindrical pore model – from their simple hydrodynamic model. Breslau and Miller refer to proton hopping to justify the lower water drag which they measured, 2.6 H_2O/H^+, in PSSA. The electroosmotic drag coefficient of water measured for the protonic form of an immersed PSSA membrane [90] is very similar to that measured for an immersed Nafion membrane (see below).

LaConti and co-workers [49] have determined the electroosmotic drag in proton-form Nafion membranes with several different equivalent weights. The electroosmotic drag measurement cell was essentially that described by Helferrich [91]. A current is passed through the membrane and the height of a water column is monitored to determine the amount of water transferred per coloumb of charge passed. In this work, membrane water content in contact with liquid water could be varied by exploiting the water content dependence on temperature of rehydration after drying at elevated temperature (see Table 6). These workers [49] reported drag coefficients in the range 2–3 water molecules per proton for water content in the range $15 \leq \lambda \leq 25$. They concluded that the drag coefficient decreases linearly with water content for immersed membranes, and that the electroosmotic drag drops slightly with a drop in EW.

Zawodzinski et al. [59] have reported drag coefficients for various immersed membranes, measured by the same method used by LaConti et al. [49]. However, Pd(H) electrodes were used to pass the protonic current so that no gas evolution takes place complicating volume change measurements. For fully hydrated and (immersed) Nafion 1100 membranes, a drag coefficient of 2.5 $H_2O/SO3_3H$ was measured. A single measurement was also taken for immersed Nafion 117 at the low water content of $\lambda = 11$, and the drag coefficient was determined to be 0.9 H_2O/SO_3H. Bernardi and Verbugge [92] pointed out that electrokinetic permeabilities determined from their modeling of transport in sulfuric-acid-loaded membranes fit quite well with the drag data reported in [59].

Okada et al. [93] have reported water transport numbers based on a measurement of the potential developed when a differential pressure is applied across a membrane contacting dilute electrolytes. For a crosslinked, sulfonated vinyl copolymer, cation-selective membrane designated CR61 AZL 386, they report a water transference number of 2.3 for the protonic form of the immersed membrane.

Fuller and Newman [96] reported an elegant solution to the problem of obtaining electroosmotic drag coefficients ("transport numbers of water" in their parlance) in ionomeric membranes under conditions of vapor phase equilibration. Their EMF method is based on the membrane potential which arises across a membrane sample exposed at each end to different water activities. The potential difference $\Delta\Phi$ is determined by $\xi(\lambda)$ according to [96]:

$$F\Delta\Phi = \xi(\lambda)\{RT \log (a_{\text{water,right}}/a_{\text{water,left}})\} \tag{19}$$

These workers reported a drag coefficient of protons in hydrated Nafion 117 membrane which is essentially constant, 1.4 H_2O/H^+, in the range $5 \leq \lambda \leq 14$, and gradually drops to zero between $\lambda = 5$ and $\lambda = 0$. Zawodzinski et al. subsequently adopted the Fuller–Newman EMF technique and concluded from their data a constant water drag of roughly 1.0 H_2O/H^+ over a large range of water contents in vapor-equilibrated membranes, from $\lambda = 14$ down to $\lambda = 1.4$. A principal reason for the difference between the two results for $\xi(\lambda)$ based on identical EMF measurements [96, 97] is data fitting. Zawodzinski et al. [69] have used a wider range of water activities and showed that the drag coefficient is not decreasing under 1.0 H_2O/H^+ for water contents as low as $\lambda = 1.4$.

Recent results by Zawodzinski et al. [97] show that several PFSA membranes exhibit similar electroosmotic behavior, i.e., a drag coefficient of close to 1.0 H_2O/H^+ over a wide range of water contents for a membrane equilibrated with vapor-phase water. The lack of dependence of the drag coefficient on membrane nanostructure suggests that the drag coefficient is determined by basic elements of the proton transport process which are similar for all membranes, such as proton solvation and local water structure.

5.4 The Ionomeric Membrane of the Polymer Electrolyte Fuel Cell. Summary

The discussion given above of transport properties of ionomeric membranes employed in PEFCs provides insight into some remarkable characteristics of such membranes, particularly the PFSA family. The latter type of membranes exhibit an attractive combination of high protonic conductivity (typically, 0.2 S/cm in the fully hydrated membrane at cell operation temperature) and high water transport rates (diffusion coefficients of 2×10^5 cm^2/s for the fully hydrated membrane), required for minimized losses in the membrane. A PFSA membrane 100 μm thick used in a PEFC should thus contribute only 0.05 Ω cm^2 to cell resistance (voltage loss of only 50 mV at 1 A/cm^2) if the water level is sustained at full hydration through the thickness of the membrane. The latter requirement is facilitated by the high rate of water transport and, indeed, the overall series resistance measured in PEFCs with such PFSA membranes is as low as 0.08 Ω cm^2, the difference being contributed by various contact resistances in the cell. An interesting approach, which may pave the way for PEFC operation without external humidification, has been described recently by Watanabe et al. [120]: to enhance PEFC humidification intensity, the membrane is seeded with platinum nuclei to achieve water generation by oxygen/hydrogen recombination. The excellent conductivities and water transport characteristics of PFSA membranes are complemented by two other important properties: low rates of gas crossover even through membranes below 100 µm in thickness (on the order of 10 mA/cm^2 equivalent hydrogen or oxygen fluxes), and excellent long-term stability (thousands of hours) under fuel cell operating conditions while maintaining initial protonic conductivity. Indeed, it has been the ionomeric membrane which has provided the most important technical basis for the recent fast development of the PEFC.

Are there, nevertheless, some needs for improvement? One feature concerning PFSA membranes has been their cost, as well as their availability. Most probably, the cost will come down significantly if and when the demand for these membranes increases. Therefore, it is not clear that alternative which compromise the remarkable properties of PFSA membranes to achieve lower cost could be competitive in the longer run. Such membranes could, however, accelerate the drop in cost of PFSA membranes if they become commercially available for fuel cell applications. Indications of recent efforts in various laboratories to generate non-perfluorinated fuel cell membranes of intrinsically lower cost but of sufficient long-term stability constitute advancement in this direction. Another recent example of possible improvement is the composite membrane introduced at a developmental level by W. L. Gore, providing improved mechanical properties to very thin (20 µm and less) perfluorinated membranes of high protonic conductivity. The question of electroosmotic drag in PFSA membranes was raised earlier in the history of PEFCs as a significant drawback. There does not seem to be an exception to the rule that, near room temperature, 2.5 water molecules are dragged per proton moving through a liquid-water-equilibrated PFSA membrane and 1.0 water molecule is dragged per proton moving through a PFSA membrane in contact with water vapor. Thus, the hope of minimizing drag by tailoring of molecular details in the structure of the PFSA membrane does not appear to be strongly justified. The overall question of "water management," including the issue of the drag as a central component, has been solved, however, to a very significant extent by the application of sufficiently thin PFSA membranes (< 100 µm thick) in PEFCs and by various modes of external supply of water with the anode and cathode gas feed streams (see also [120]). This is not to say, however, that the sensitivity of membrane conductivity to water level does not remain a fundamental weakness of the PFSA membrane which causes, in turn, another weakness of at PEFC: at upper limit on cell operation, at or below 100 °C.

6 Modelling and Diagnostics of the Polymer Electrolyte Fuel Cell

The PEFC has attracted significant interest among experts in modeling of electrochemical cells. The central targets of such modeling efforts have been the modeling of the water profile in the PEFC, particularly in the membrane [e.g., 87], modeling of air cathodes losses [100], and integrated modeling of the combined losses in the cell [92, 101–106]. Other PEFC elements which have been modeled are temperature profiles and their effects on membrane hydration/conductivity [104,107] and the ac impedance spectrum of the PEFC [108]. In this section, we will describe first the specific modeling of the water profile in the ionomeric membrane and in the complete cell, followed by modeling of PEFC cathode losses. We will also describe experimental diagnostics which can be used to probe the validity of such models and to evaluate quantitatively the critical cell parameters.

6.1 Modeling of Processes in the Ionomeric Membrane

The initial emphasis on evaluation and modeling of losses in the membrane electrolyte was required because this unique component of the PEFC is quite different from the electrolytes employed in other, low-temperature, fuel cell systems. One very important element which determines the performance of the PEFC is the water-content dependence of the protonic conductivity in the ionomeric membrane. The water profile established across and along [106]) the membrane at steady state is thus an important performance-determining element. The water profile in the membrane is determined, in turn, by the combined effects of several flux elements presented schematically in Fig. 27. Under some conditions (typically, $P_{\text{cath}} > P_{\text{an}}$), an additional flux component due to hydraulic permeability has to be considered (see Eq. (16)). A mathematical description of water transport in the membrane requires knowledge of the detailed dependencies on water content of (1) the electroosmotic drag coefficient (water transport coupled to proton transport) and (2) the water diffusion coefficient. Experimental evaluation of these parameters is described in detail in Section 5.3.2.

The water distribution within a polymer electrolyte fuel cell (PEFC) has been modeled at various levels of sophistication by several groups. Verbrugge and coworkers [83–85] have carried out extensive modeling of transport properties in immersed perfluorosulfonate ionomers based on dilute-solution theory. Fales et al. [109] reported an isothermal water map based on hydraulic permeability and electroosmotic drag data. Though the model was relatively simple, some broad conclusions concerning membrane humidification conditions were reached. Fuller and Newman [104] applied concentrated-solution theory and employed limited earlier literature data on transport properties to produce a general description of water transport in fuel cell membranes. The last contribution emphasizes water distribution within the membrane. Boundary values were set rather arbitrarily.

Springer and others were the first to use detailed, experimentally derived diffusion and electroosmotic drag coefficients of water in Nafion in a model for steady-state water profile and the resulting protonic conductivity in the membrane of an operating PEFC [87]. The distribution of water in a PEFC at steady state (at constant current and reactant/water fluxes) was calculated in this model by considering water flow through five regions of unit cross-sectional area within the fuel cell: two inlet channels, two gas-diffusion electrodes, and the Nafion membrane. The cell was considered isothermal. The water flow into the inlet channels was set in the model by the temperatures of external gas humidifiers and that of the cell. Interdiffusion of gases through the porous backing layer was calculated from tabulated data using the Stefan–Maxwell equations with a Bruggeman correction applied to take account of the electrode porosity. (It has to be noted, however, that in [87] the electrodes were treated in much less detail than required for evaluation of losses other than that in the membrane. A much more detailed description of transport within the electrodes, including effects of liquid water, is given elsewhere [100, 105].) Water flux through the electrodes was assumed in the model to take place in the gas phase (water vapor) only. With the added consideration of transport of the reactant gases and their consumption by reaction, this enabled solution of the water mole fraction at the electrode/membrane interface, as required for defining a boundary condition for the water profile in the membrane.

Consideration of the gas inlet streams saturated by water vapor, which pass in part through the gas-diffusion electrode to reach the electrode/membrane interface and in part exhaust the electrode gas channel, yielded the following expression for the mole fraction of water in the gas mixture at the anode/membrane interface (designated as interface 2 [87]):

$$x_{\mathrm{w2}} = \left(x_{\mathrm{w1}} - \frac{\alpha}{1+\alpha}\right) \exp\left(\frac{RTIt_{\mathrm{A}}}{P_{\mathrm{A}} D_{\mathrm{wH}}}\right) + \frac{\alpha}{1+\alpha} \tag{20}$$

In this equation, x_{w1} is the mole fraction of water in the gas stream entering the anode; α is the ratio of the water flux crossing into the membrane from the anode to the molar flux, I, of hydrogen entering the anode; P_{A} is the overall anode pressure; t_{A} is the anode thickness; D_{wH} is the binary water/hydrogen gas-phase diffusion coefficient; and R and T have their usual meanings (gas constant and temperature). Note that α is an unknown parameter at this point, and is to be evaluated in the iterative calculation that establishes eventually the water profile in the membrane. The value of x_{w1} is given by gas inlet parameters, including the mole fraction of water in the gas entering the inlet channel and the stoichiometry of the flow. Equation (20) provides a parameter which is a basis for the boundary condition on the anode side of the membrane. The experimentally determined isotherm for water sorption into the membrane (see Fig. 29) is used to convert from water vapor activity in the gas phase at the interface to water content in the membrane at the interface. A similar evaluation on the cathode side yields x_{w3}, the water vapor activity at the cathode/membrane interface, and thus the boundary condition at the cathode side of the membrane. Because of the generation of liquid water at the cathode, the water level in the membrane surface adjacent to the cathode will be high, corresponding typically to H_2O/SO_3H ratios λ of 14–22 (see Section 5.3).

Having established the boundary conditions for the membrane by expressions for x_{w2} and x_{w3}, the next step is to consider the components of water flow within the membrane. As stated above, they include electroosmotic drag, diffusion, and hydraulic permeability. Hydraulic flux has not been considered in this work, and so the basic equation describing the flux within the membrane is:

$$N_w = \alpha I = \xi^* \cdot (2I) \cdot \frac{\lambda}{22} - \frac{\rho_{\text{dry}}}{M_m} D_\lambda \frac{d\lambda}{dz} \tag{21}$$

where N is the net steady-state flux of water through the membrane when the current density is $2I$ and ξ^* is the average number of water molecules carried per proton migrating through a fully hydrated membrane, ρ_{dry} is the density of the dry membrane and M_m its equivalent weight. D_λ is the diffusion coefficient which provides the diffusional flux of water in conjunction with a gradient of λ (water/sulfonate ratio) across the membrane thickness. Hence,

$$\frac{d\lambda}{dz} = \left[2\xi^* \cdot \frac{\lambda}{22} - \alpha\right] \frac{IM_m}{\rho_{\text{dry}} D(\lambda)} \tag{22}$$

and Eq. (22) can be integrated numerically from interface 2, where λ_2 is determined by x_{w2} through Eq. (20). This allows one to calculate a profile of λ and solve λ_3 and x'_{w3} (the water level in the membrane next to the cathode). Both profile and the water level at the cathode will be, however, a function of the value of α chosen in Eqs. (20) and (21). An iteration is therefore applied to determine the proper value of α. The value of x'_{w3} as obtained following the integration of Eq. (22) is compared in this routine with x_{w3}, the water level which is obtained following integration from the cathode end and applying the interfacial equilibrium condition at the cathode/membrane interface. These two values will be equal when the proper value of α is achieved by the iterative process. It is in the integration of Eq. (22) that the functional dependencies of $\xi(\lambda)$ and $D(\lambda)$ have to be well defined over a wide range of λ. Experimental derivation of these functions, described in detail in Section 5.3, has provided the parameter basis for the integration in this modeling effort.

Some key results of the iterative process to solve the profile of λ through the membrane are shown in Figs. 38 and 39. Figure 38 shows the steady-state profile of water in a Nafion$^{\text{TM}}$ 117 membrane as calculated with this model at four different current densities. The calculated profile of water is seen to become steeper as the current density increases, resulting in a significant depletion of water in the membrane near the anode. This is in spite of the hydrogen feed stream being saturated with water vapor. This situation is understandable. At higher current density, the drag of water becomes sufficiently large to prevent effective correction of the water level near the anode by the combined effects of back-diffusion and supply of water vapor with the hydrogen feed stream. The difficulty with back-diffusing enough water is strongly related to the thickness of the membrane. Figure 38 demonstrates the typical water profile in a relatively thick, Nafion$^{\text{TM}}$ 117 membrane, which served as the "workhorse" in most earlier experiments with PEFCs. Compared with the 175 μm-thick Nafion$^{\text{TM}}$ 117 membrane, Nafion$^{\text{TM}}$ 1100 membranes which are 100 μm thick or thinner, will suffer a much smaller problem of water depletion near the anode at high currents, although their intrinsic water transport characteristics are the same as in the Nafion$^{\text{TM}}$ 117 membrane. This is fully predicted by the model.

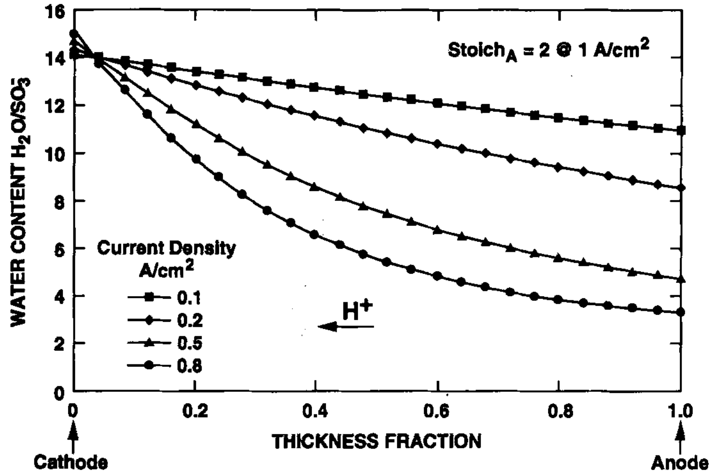

Fig. 38. Calculated water profiles in a Nafion™ 117 membrane within an operating PEFC as a function of current density. Cell and both hydrogen and air humidifiers are held at 80 °C [87]. (Reprinted by permission of the Electrochemical Society).

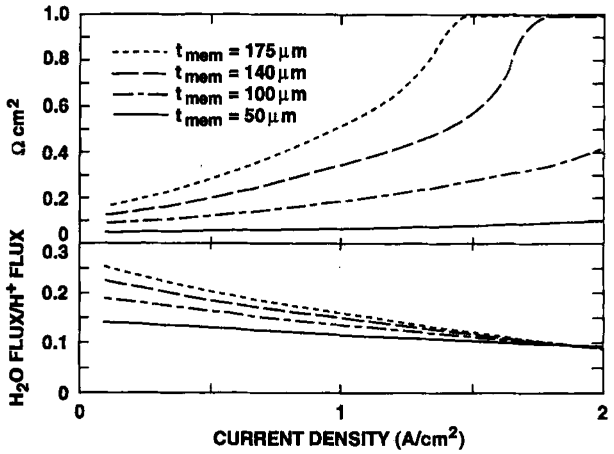

Fig. 39. Computed R_{cell} (upper panel) and H_2O/H^+ net flux ratio (lower part) for Nafion™ 1100 membranes of different thicknesses. Cell and saturator temperture, 80 °C. Unity fuel utilization [87]. (Reprinted by permission of the Electrochemical Society).

In Fig. 39 there are two families of four curves, showing the calculated high-frequency resistance of the cell (top) and the calculated net flux of water through the membrane (bottom) for membranes with identical transport properties differing in thickness only. To calculate the membrane (cell high-frequency) resistance, the dependence of the specific resistance of Nafion™ 1100 on λ was measured experimentally (see Fig. 32). The measurement of the high-frequency resistance of the cell is, in fact, the most effective experimental verification for the predictions of such a water profile model. This would be true as long as no method for direct observation of the water profile in the ionomeric membrane within the operating cell has been demonstrated. The top part of Fig. 39 shows that it is sufficient to lower the Nafion membrane thickness from 175 to 50 μm in order to eliminate completely any increase of membrane resistance with current density up to 2 A/cm^2. Results of measurements of high-frequency resistance in PEFCs with membranes of different thicknesses as a function of current density fully confirm the prediction of these model calculations. Obviously, improved water diffusivity in a membrane of given thickness would also facilitate the maintenance of a flatter water profile at higher current densities, as demonstrated in Fig. 38.

Measurements of the net water flux through the PEFC have been performed to limited extent. Results reported [87] have shown small net water fluxes associated with cell current, similar to the calculated ones shown in the bottom part of Fig. 39. Clearly, these net water fluxes per proton are significantly less than ξ^*. This is expected from the opposing effect of back-diffusion which, in the operating PEFC, tends to lower the net flux across the cell well below the level of the protonic drag of water (see Eq. (18)).

Some comments should be made on this detailed water profile modeling work by Springer and co-workers [87]. Firstly, the dependence of ξ^* on λ was assumed linear, corresponding to zero drag at zero water content and 2.5 H_2O/H^+ at $\lambda = 22$. More detailed measurements carried out since (see Section 5.3.2) have shown that the drag diminishes between $\lambda = 22$ and $\lambda = 14$ but then it seems to stay constant at 1.0 H_2O/H^+ between $\lambda = 14$ and $\lambda = 2$. These model calculations should be corrected accordingly. The difference in the resulting profile is not expected to be very substantial but could still be significant. The other two comments relate to processes which were not accounted for in this model. The first is evaporative losses of water: to account realistically for obseved overall water management in a PEFC under test, one has to consider such evaporative losses, which are particularly significant in hardware employing porous graphite plates. This explains why water has to be supplied to the cathode in most cases at a level higher than expected from model calculations which neglect evaporative losses and assume a perfectly isothermal system. This work [87] also disregarded the flow of liquid water through the electrodes, and the effects of such flow through electrodes and membrane, particularly under conditions of differential pressurization.

This last issue was treated in detail by Bernardi and Verbrugge as part of a detailed mathematical model for the PEFC [92, 105]. The results of their calculations, based on measured hydraulic permeabilities for both membrane and electrodes, are shown in Figs. 40 and 41. Figure 40 shows a pressure profile through a cell operated at 5 atm on the cathode side and 3 atm on the anode side. At 105 mA/cm^2, the flow of water through the cell will be from cathode to anode and so water has to be supplied with the cathode feed stream. In contrast, Bernardi and Verbrugge suggest that at 600 mA/cm^2 liquid water generation at the cathode could generate a buildup of hydrostatic pressure sustained by the hydrophobic nature of the cathode backing. Under such conditions, hydraulic flow of water will take place from the cathode catalyst in both the direction of the membrane and the direction of the outer face of the cathode. Under such conditions, there seems to be no need to supply water to the cathode (provided no water losses occur). Figure 41 shows calculations of liquid water velocity (hydraulic flow) through the fuel cell at three different current

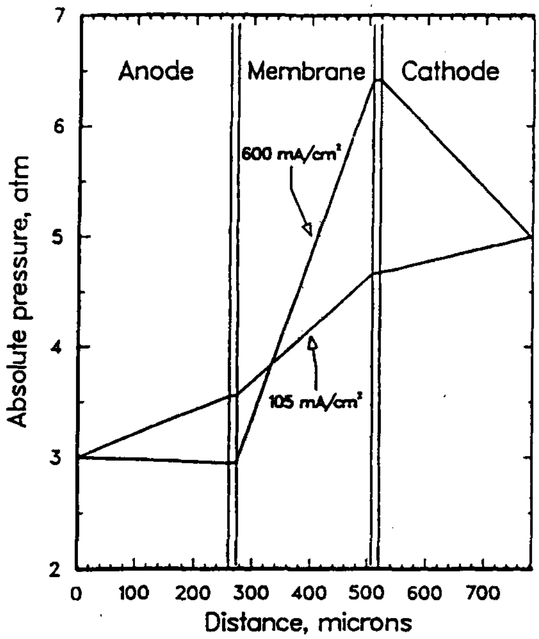

Fig. 40. Model calculations of hydraulic pressure throughout the PEFC for two current densities [105]. This calculation is for a Nafion 117 membrane, humidifier temperatures of 105 °C and cell temperature of 80 °C, air-side pressure of 5 atm and fuel-side pressure of 3 atm. (Reprinted by permission of the Electrochemical Society).

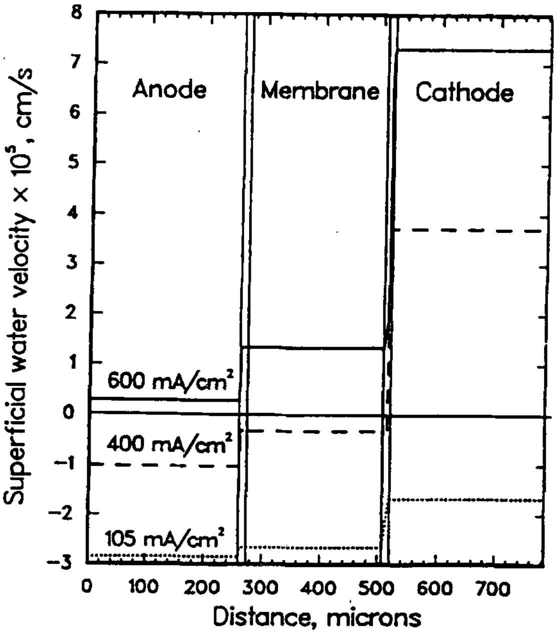

Fig. 41. Model calculations of water velocity throughout the PEFC for three current densities, under the cell operation conditions specified in the caption of Fig. 40 [105]. (Reprinted by permission of the Electrochemical Society).

densities. A unique situation could take place at a medium current density of 400 mA/cm^2. According to these calculations, at this current density the net flow of water is outwards in both the cathode and the anode compartments. This is so because some of the water generated at the cathode flows through the membrane and anode.

At 600 mA/cm^2, however, the electroosmotic drag already starts to have a stronger effect and this necessitates an external supply of water to the anode. Thus, the range of stable operation with no external water supply may be quite narrow. The results of the calculations shown in Figs. 40 and 41 clearly demonstrate that the hydraulic flow of liquid water in PEFCs could have a significant effect on the water profile and that such flow could be significant, not only in differentially pressurized cells but also because of the possibility of hydraulic pressure buildup at the cathode catalyst. It should be noticed, however, that, in spite of these intriguing calculations, in reality it is dufficult to operate single PEFCs at such current densities (0.4 A/cm^2) with no external water supply, at least to the anode. This is for two possible reasons: overestimation of the hydraulic permeabilities in the calculations and/or the evaporative loss of water from a PEFC which is not perfectly sealed.

6.2 Modeling of Electrode Losses

6.2.1 Modeling of Steady-State Polarization

Different approaches are possible in the complete modeling of the PEFC. One approach involves unified modeling of the losses in all the components of the cell, including electrode losses of all kinds and losses in the membrane. Such a unified approach can employ for diagnostics the polarization curve of the cell, which is affected by all cell losses. However, if a rigorous test of the model is to be performed, several polarization curves recorded under differnt operating conditions should be employed in testing of the model against cell performance. A unified approach to PEFC modeling has been described in the literature at two very different levels of sophistication. Srinivasan and co-workers [110] described the PEFC polarization curve in terms of only three parameters: ORR current density at 0.9 V, a (constant) Tafel slope, and an effective resistance that lumps together all the effects of membrane resistance plus all the different mass-transport losses in the air cathode. Although polarization curves could be fitted with this three-parameter approach by excluding the high-current-density domain, such an approach cannot yield detailed information on the nature and/or magnitude of cathode losses.

In contrast, the modeling work of Bernardi and Verbrugge [92] describes in great detail factors that could contribute to losses in the PEFC, using a unified model for the complete cell. This model extensively treats electrocatalysis and details of transport processes in both the gas and condensed phase within the cell cathode, together with ionic and electronic conductivity limitations in the membrane and in the electrodes. The model is tested against experiment by comparing against the cell polarization curve, but, again, excluding from the fit the high current density part of the polarization curve. This unified and detailed approach is elegant and has the advantage of simultaneous treatment of all possible sources of loss in the PEFC. A problem with such a unified model is with efficient cell diagnostics. Since the number of system parameters considered is, typically, around ten, it is easy to understand that evaluation of each of these parameters is practically impossible from a polarization curve of an operating cell. Tradeoffs between various parameters easily generate some given effect on cell polarization. A possible remedy for such problems is to resolve cell losses experimentally and to model separately experimentally resolved losses. For example, the high-frequency component of the cell impedance is measured (in addition to the polarization curve), and its dependence on cell current is fitted to a membrane model (see Fig. 39), whereas the iR-corrected polarization curve ($R =$ high-frequency resistance) is fitted to a model for cathode losses. This last approach is effective in resolving membrane losses from electrode losses before fitting to the cell model is attempted.

Springer and co-workers have recently implemented the latter approach, modelling in detail losses in the air cathode of the PEFC and fitting their PEFC cathode model to families of iR-corrected PEFC polarization curves recorded with a range of cathode feed streams [100]. These authors argued, on the basis of measurements of overall cell polarization and of cathode polarization (the latter obtained with an RHE reference in the cell), that the anode losses in a well-humidified PEFC with a pure H_2 feed are negligible. Therefore, under such experimental conditions, the iR-corrected polarization curve is equivalent to a cathode polarization curve. Another important element in their modeling/diagnostics approach was the use of a large experimental database which made it possible to maintain in the fit only such cell parameters that have in reality a significant effect on cell performance. Their model treats the cathode catalyst layer and gas-diffusion backing, as schematically presented in Fig. 42. The catalyst layer is considered in the model as a composite film, typically 4 to 7 μm thick, of Pt/C catalyst intermixed uniformly with recast ionomer [14,41,42]. The volume distribution of catalyst sites within this layer is uniform. The backing layer is a separate hydrophobized carbon cloth (about 300 μm thick) of about 40% porosity. However, the effective porosity of the backing layer in the operating cell may be significantly smaller because of possible "flooding" by liquid water. The cathode model considers losses caused by

- the rate of the oxygen reduction reaction (ORR) process at the Pt/ionomer interface,
- limited oxygen permeability and limited ionic conductivity within the catalyst layer,
- limited oxygen permeability through the hydrophobized backing layer, and
- the drop in oxygen concentration along the air/O_2 flow channel, caused by oxygen reactant consumption.

The key model parameters that describe these types of loss in the PEFC are as follows.

- Interfacial ORR losses:

i^*, the current density per cm^2 Pt at 0.9 V vs. a reversible hydrogen electrode (A/cm^2 atm) at an O_2 partial pressure $p_{ox} = 1$ atm;

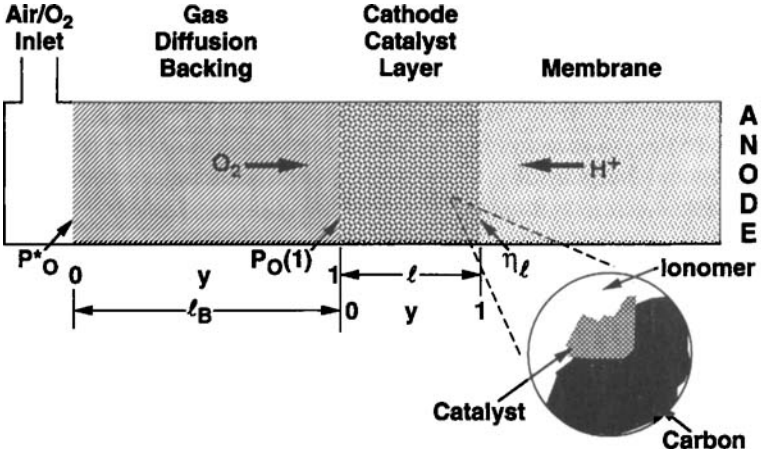

Fig. 42. Schematic of regions considered in PEFC air electrode modeling, including (from left to right): gas flow channel, gas-diffusion backing, and cathode catalyst layer. Oxygen is transported in the backing through the gas-phase component of a porous/tortuous medium and through the catalyst layer by diffusion through a condensed medium. The catalyst layer also transports protons and is assumed to have evenly distributed catalyst particles within its volume [100]. (Reprinted by permission of the Electrochemical Society).

A_r, the effective platinum surface area per unit geometric surface area (dimensionless); and
$\exp((0.9 - V)/b)$, or $\exp(f(V))$, the ORR rate dependence on potential relative to 0.9 V described by a constant Tafel slope of $2.3b$ (mV per decade), or by an experimentally determined $(f(V))$ measured at a model, smooth Pt/ionomer system [9].

- Catalyst layer transport losses:
  l_{cl}, the thickness of the catalyst layer (cm);
  DC^*, the product of the effective diffusion coefficient of oxygen (cm^2/s), and the equilibrium oxygen concentration (mol/cm^3 atm) in the catalyst layer at $P_{ox} = 1$ atm;
  σ, the effective protonic conductivity within the catalyst layer (S/cm).

- Backing layer transport losses:
  l_B, the thickness of the backing layer (cm); and
  $\varepsilon(J)$, the effective porosity of the backing (dimensionless).

The rest of the parameters which define the behavior of the cell for each set of operating conditions include the cathode inlet gas stream composition, flow rate, and total pressure; the degree of humidification of the inlet as stream; and the temperature of the cell. Some important assumptions made in choosing these parameters and in fitting them to the experimental data are the following:

- Interfacial ORR kinetic parameters (i^*, b) employed in the fit of the model to experimental PEFC polarization curves must be in reasonable agreement with the parameters measured in studies of the ORR at model Pt/ionomer interfaces [3–6, 9]

- The presence of liquid water in the cathode has an effect on oxygen transport through the effective porosity of the backing, which is an adjustable parameter in the model. In some of the fits, this effective porosity was also allowed to decrease with increase in cell current, to account for enhanced filling of pores in the backing layer with enhanced generation of water in the cathode. Gas transport through the backing layer is determined by the Stefan–Maxwell equations for multicomponent gas transport [111] and is confined to the part of the backing that is free of liquid water.

- Depletion of oxygen within the gas flow channel (Figs. 1, 42), caused by the consumption of the reactant gas as it flows along the active area, can be accurately described by defining an effective uniform concentration of oxygen in the flow channel equal to the average of cathode inlet and cathode outlet gas stream concentrations.

- Electronic conductivity losses within the catalyst layer, or within the backing, were both considered negligible, based on measured electronic vs. ionic resistivities in the composite catalyst layer.

The backing in this model is treated with the Stefan–Maxwell equation to yield the partial pressure of oxygen at the backing/catalyst layer interface from the total pressure P_{tot} in the gas flow channel, the backing characteristic current density, I_B, and the mole fractions of water vapor and of oxygen, x_{ws} and x_{on}, respectively:

$$P_{\text{ox}} = P_{\text{tot}}(1 - x_{\text{ws}})\{1 - (1 - x_{\text{on}})\exp[I/I_B]\} \tag{23}$$

The backing characteristic current density is given by:

$$I_B = nF\mathscr{D}_{\text{SON}}\varepsilon^{1.5}(T/T_S)^{0.823}/\mathscr{V}_m l_B \tag{24}$$

and is a function of the standard molar volume of an ideal gas, $\mathscr{V}_m$, the oxygen/nitrogen binary diffusion coefficient at standard conditions, $\mathscr{D}_{\text{SON}}$, the backing thickness, l_B and the backing porosity, ϵ. It is the effective porosity, ε, and the way it is affected by the accumulation of liquid water in the backing, which constitute important elements of this model and enable prediction of the lmiting current behavior. (Springer et al. [108] consider, in addition, the effect of water vapor in the backing. They also add, on the basis of impedence spectra analysis, effects of tortuosity in the backing layer, as described in Section 6.2.2.)

The key equations in this model describing limitations in the cathode catalyst layer are:

$$\frac{\partial \eta}{\partial y} = \frac{Il_{\text{cl}}}{\sigma} = IR_{\text{cl}} \tag{25}$$

$$\frac{\partial I}{\partial y} = p_{\text{ox}} i^* \frac{C}{C^*} A_{\text{r}} \exp\left[\mathscr{F}(\text{V}_0 - \eta)\right] \tag{26}$$

$$\frac{\partial C/C^*}{\partial y} = \frac{I - I_l}{p_{ox} I_D} \tag{27}$$

Equations (25) to (26) describe variations of parameters along the y coordinate of the catalyst layer ($y = z/l_{\text{cl}}$), where z is the catalyst layer thickness coordinate, $y = 0$ specifies catalyst layer/gas interface, and $y = 1$ specifies the catalyst layer/ionomeric membrane interface (see Fig. 42), in which $R_{\text{cl}} (= l_{\text{cl}}/\sigma)$ is the protonic resistance through a unit cross-sectional area of the catalyst layer, and $I_{\text{D}} (= nFDC^*/l_{\text{cl}})$ is defined as a characteristic diffusion current density. The thickness of the catalyst layer disappears from the equations by introducing R_{cl}, A_{r} and I_{D}. The variables considered include the overpotential η, the current density I, and the oxygen concentration C when $P_{\text{ox}} = 1$ atm at the catalyst layer/gas interface. The O_2 partial pressure, p_{ox}, at the catalyst layer/gas interface is a function of the cathode inlet gas stream and the backing transport characteristics and is derived from Eq. (23) above. Equation (25) is an ohmic relationship between local current density and the local variation of η, as determined by the protonic resistivity of the catalyst layer. Equation (26) describes the local rate of current generation within the catalyst layer in terms of the oxygen partial pressure at the catalyst layer/gas interface, the local concentration of oxygen relative to its concentration at the catalyst layer/gas interface, and the local overpotential. V_0 is an arbitrary reference cathode potential ($V_0 - \eta = V_{\text{cath}}$) chosen to be 0.9 V. Equation (27) describes the gradual transformation of the oxygen flux to a protonic current along y, such that the sum of the two fluxes is kept constant and equal to the oxygen flux at the catalyst layer/gas interface. The current density, concentration, and overpotential profiles through the catalyst layer are evaluated from these equations and boundary conditions.

To obtain better confidence in the fit of so many cathode parameters, Springer and co-workers fitted simultaneously families of iR-corrected polarization curves, recorded for the same cell with a wide range of cathode feed streams. Such a fit is shown in Fig. 43. It should be noticed that, unlike previous modeling efforts [110], this modeling covers the complete polarization curve and is capable of describing effectively the steep fall in cell voltage usually referred to as "limiting current." The caption shows the parameters which yielded the best fit to the model. Two important points to notice from the simultaneous fits to the four polarization curves in Fig. 43 are the qualitative characteristics which demonstrate transport limitations in the gas phase within the backing, and protonic conductivity limitations in the catalyst layer. Curves (c) and (d), obtained with diluted oxygen feed streams used for diagnostic, demonstrate that the limiting current depends not on oxygen partial pressure but, rather, on oxygen mole fraction. This is an immediate qualitative indication that

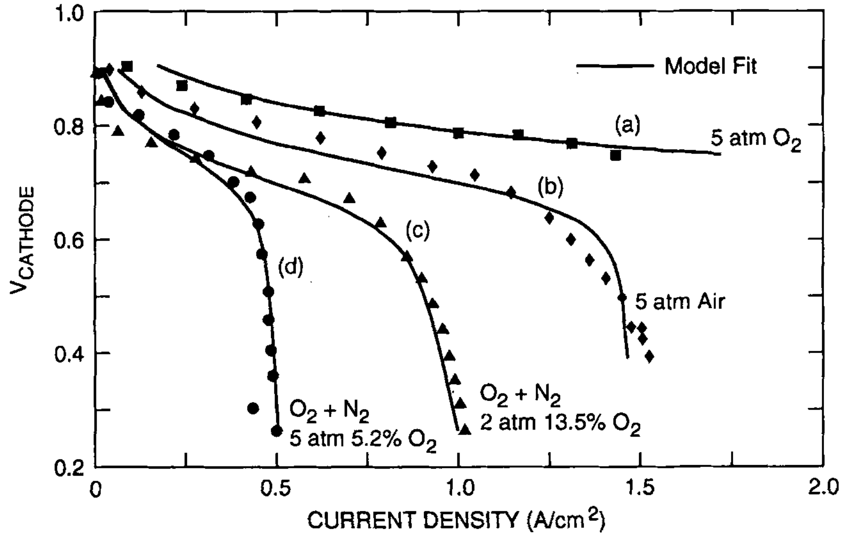

Fitted Parameters:

- Cathode catalytic activity @ 0.9 V: 90 mA/cm^2
- dV/dlogJ: 85 mV/decade
- $\sigma = 0.0013$ S/cm (protonic cond. in catalyst layer)
- DC* = 1.9×18^{-8} mol/cm-s-atm (gas perm. in catalyst layer)
- Backing porosity: 0.25 - 0.19 (assuming zero tortuosity)

Fig. 43. Simultaneous fit to four polarization curves for a PEFC with 300 μm thick backing layer and 7.5 μm-thick catalyst layer. Different cathode feed stream compositions are used and a simultaneous fit is demanded using the same physical and transport parameters for the backing layer and the catalyst layer [100]. (Reprinted by permission of the Electrochemical Society).

transport in the air cathode is limited at high current densities in the *gas-phase* component of the backing. On the other hand, comparison of curves (a) and (b) demonstrates the low enhancement in current observed at low overpotentials when switching from a 5 atm air to a 5 atm O_2 cathode. Instead of the five-fold increase in current under complete interfacial kinetics control, the observed increase is only about two-fold. This ratio could be modeled only by the effect of a limited protonic conductivity within the catalyst layer. The relative importance of such effects varies with cell operating conditions. Springer and co-workers noted the relative increase in significance of protinic conductivity limitations in the catalyst layer at low air pressures.

In this modeling work [100], Springer and co-workers have reduced the description of the complicated fuel cell system to the set of parameters that most strongly influences the behavior of the cells. These do not include anode parameters, but it should be realized that this would be true only for the conditions specified – well humidified cells with a pure H_2 feed stream. The accuracy of the model depends strongly on the representation of the ORR kinetics and the authors have stressed the use of realistic ORR parameters. For well-humidified H_2/air PEFCs, the model suggests the following general trends.

- Gas-phase transport limitations in the cathode backing determine the cell limiting current and also affect the slope of the polarization curve in the medium current density domain.
- Transport limitations originating from the catalyst layer are significant in the medium current density domain, particularly so at low air pressures.
- For neat oxygen, where backing effects are eliminated, losses from ionic resistance and premeability of the catalyst layer prevail.

Behavior indicative of "partial flooding" of the fuel cell could be modeled by assigning diminished porosity to the backing. It was felt that inclusion of this element is an important prerequisite for the complete modeling of the PEFC, particularly at high current densities.

Other elements of PEFC characeteristics which have been modeled recently are the variations of temperature and water content and the associated possible variations in protonic conductivity down the gas flow channel. These types of lateral thermal effects have been dealt with by Fuller and Newman [106] and by Nguyen and White [107].

6.2.2 Modeling and Diagnostics Based on Impedance Spectra Measurements

In a recent comprehensive measurement and analysis of ac impedence spectra of PEFCs, Springer et al. described the generic form of spectra measured for such fuel cells and their value for cell diagnostics [108]. The measurements were carried out using a combination of instruments enabling the determination of the impedance spectrum in the presence of large dc currents. The impedance spectrum of the air cathode was shown to contain two features: a higher-frequency loop determined by interfacial charge-transfer resistance and catalyst layer properties and a lower-frequency loop determined by gas-phase transport limitations in the backing. The lower-frequency loop is completely absent from the spectrum of cathodes operating on neat oxygen. A typical family of impedance spectra measured for PEM fuel cells with air cathodes is shown in Fig. 44. Measured impedance spectra were analyzed by adapting the polymer electrolyte fuel cell cathode model described in [100] for probing the effect of ac perturbation. Comparison of model predictions with observed data was made by simulataneous least-squares fitting of a set of spectra measured at several cathode potentials (see Figs. 44). The results revealed significant ionic-transport and oxygen-transport limitations in the cathode catalyst layer and significant gas-transport limitations in the hydrophobic cathode backing. Both findings had been reported previously from steady-state polarization data and modeling [100].

Two features of the fuel cell cathode were, however, highlighted uniquely by impedance spectra; the complex effect of cathode dehydration and the effect of backing tortuosity. Three different types of losses caused by insufficient cell hydration, related to cathode interfacial kinetics, proton conductivity in the catalyst

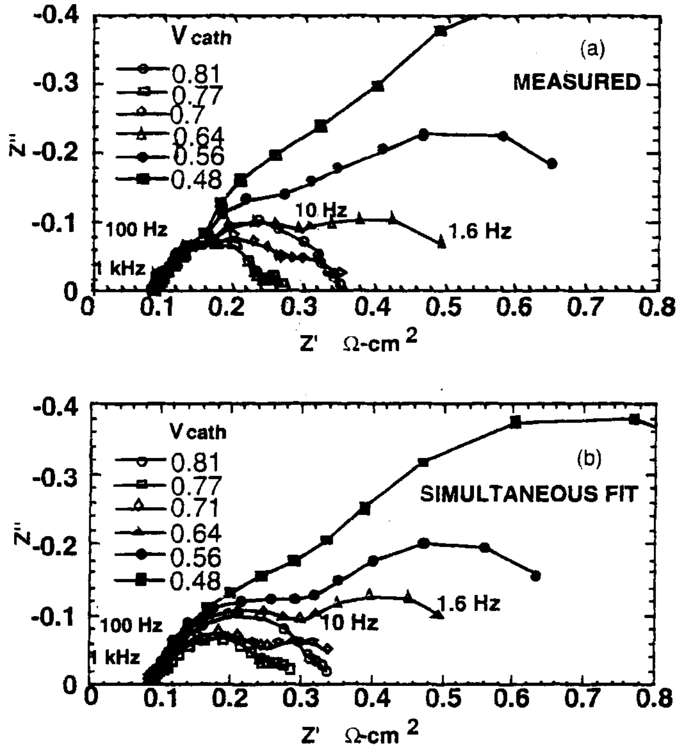

Fig. 44. (a) Measured impedance spectra for a PEFC air cathode potentials and (b) a simultaneous fit of these six spectra [108]. The two distinguishable features of the spectrum correspond to catalyst layer processes (high-frequency) and backing layer transport (low-frequency). (Reprinted by permission of the Electrochemical Society).

layer, and conductivity in the membrane, could be clearly resolved in the impedence spectra measured [108]. Significant tortuosity of the backing was revealed from backing transport dynamics, reflected from the well-resolved impedence feature at lower frequencies. In summary, analysis of impedance data for the PEFC has yielded parameters for electrocatalysis and for charge and mass transport in the air cathode which were in good agreement with those evaluated from steady-state polarization curves [108] and additional features, particularly the effect of tortuosity in the backing, could be identified and quantified from such impedance data.

7 PEFC Stack and Complete Power Systems

This section contains a brief description of some recent efforts in the building of PEFC stacks and of complete power systems based on such stacks. Most of this chapter is devoted to more fundamental, electrochemical aspects of PEFCs, and has focused on the electrode and single-cell levels of PEFC R & D. The brief discussion of systems aspects is added for the sake of completeness. Further detailed information on characteristics and specifications of stacks and systems should be obtained directly from developers/manufacturers.

7.1 Earlier History – Efforts at General Electric

General Electric's work in the field of polymer electrolyte fuel cells began in 1954, when W. T. Grubb began work on ion-exchange polymer electrolytes for H_2/O_2 cells. Further studies resulted in the development of electrode loading techniques. In 1959, Cairns and Douglas demonstrated the feasibility of larger cells.

Military and space applications were recognized at GE as promising fields for early introduction of the technology. A number of prototype fuel cells of substantial size were built between 1959 and 1964, increasing the cell area from 2 square inches (12.9 cm^2) to $1\frac{1}{2}$ square feet (0.14 m^2) to meet requirements of a power source developed for the US Navy. A typical performance in the early 1960s was 70 W/ft^2 (140 A/ft^2 at 0.5 V) for operation on neat hydrogen and oxygen. Air-breathing portable power sources based on polymer electrolyte fuel cells were delivered by GE to the US Army between 1961 and 1964 at a power level of 60–200 W.

The polymer electrolyte employed in these earlier projects was polystyrenesulfonate. The last GE fuel cell project employing this membrane was the Gemini fuel cell program (1962–1966). The power source included three 32-cell stacks in each of two 1 kW modules. The maximum current density was 45 mA/cm^2. This power source served in seven successful manned space flights and achieved 850 h of flight operation. Later GE technology was based on the Nafion PFSA membrane which was introduced by Dupont in 1966. The NASA Space Shuttle Fuel Cell Technology Project (1972–1974) was devoted to the demonstration of 5 kW modules (2 × $2\frac{1}{2}$ kW stacks), reaching 185 mA/cm^2 maximum current density on neat hydrogen and oxygen.

GE developed, in parallel, water electrolysis technology based on Nafion membranes, and developed oxygen and hydrogen generators based on this technology. Both the fuel cell and electrolysis technologies based on the Nafion electrolyte were further developed in the late 1970s and early 1980s. The NASA Advanced Fuel Cell Technology Program, which started in 1974, included bipolar design, elimination of gasket seals, thinner (5 mil; 0.13 mm) electrolyte sheets, 500 mA/cm^2 design current density, maximum current density of 1300 mA/cm^2 (on pressurized neat oxygen and hydrogen), and 1.1 ft^2 (0.1 m^2) cell area. The SPE® Hydrogen Generator System (water electrolyzer) unit developed at GE (now United Technology, Hamilton Standard) in parallel with these polymer electrolyte fuel cell developments, is a commercial unit with hydrogen generation rates ranging between 100 and 1000 scfh. Taking advantage of the effective barrier between hydrogen and oxygen as provided by the ionomeric membrane, hydrogen can be generated at variable pressures up to 100 psig and at a purity of 99.995%.

7.2 Further Developments During the 1980s and early 1990s

During the 1980s, new initiatives in the development of PEFC stacks and power systems emerged. The application of reformed carbonaceous fuels for the anode feed stream and the application of air at the cell cathode became important issues in the context of the possible conversion of the PEFC from a space to a terrestrial transportation and power generation technology. In a survey performed in 1991, six companies producing PEFC stacks were identified: Ballard (Canada), International Fuel Cells (USA), Hamilton Standard (USA), Ergenics (USA), Treadwell Corporation (USA), and Siemens (Germany). The largest stack size reported was 8.5 kW (Siemens), whereas the others have concentrated on sizes of 5 kW or less. All of these stacks were then at a developmental stage, with limited commercial availability. All of these PEFC stacks, other than Ballard's, required pure hydrogen fuel and pure oxygen as oxidant. The reason lay in the space and military applications for which they were developed.

Since the transfer of the GE PEFC technology to United Technology (UTC) in the 1980s, International Fuel Cells (IFC, a UTC subsidiary) has continued the development of PEFC stacks for military applications. IFC has developed a technology of water management in PEFC stacks based on transfer of water from the cathode flow channel to the cooling water channel through a porous graphite barrier. The Ballard stack development led in 1992 to a 35-cell stack including an integral gas humidification section.This stack is shown in Fig. 45: its dimensions are 10 in × 10 in × 18 in (25.4 cm × 25.4 cm × 45.7 cm), i.e., it has a volume of 29.5 liters, and the active electrode area is 232 cm^2 per cell. The bipolar plates are graphite with machined flow fields. The reported weight of the 1992 first-generation Ballard stack was 85 lb (38.3 kg). This yielded a power density of 170 W/liter and 130 W/kg (however, the newest-generation 20 kW Ballard PEFC stack was reported in 1995 with powder density increase factor of more than four, reaching 570 W/liter). Humidification is achieved in a section of plates at the end of the stack. The fuel gas is passed over membrane surfaces that are in contact with hot water (coolant water) on their other side. This mode of humidification may be efficient in eliminating the need for an external water source but is associated with a limit on the partial pressure of water in the gas stream. Typical performance data for the stack have been reported [112]. At an air pressure of 50 psig (4.4 atm) and a hydrogen pressure of 30 psig (3.0 atm) the stack is reported to produce 5 kW. If air is replaced by oxygen, the stack is reported to produce 10 kW of power.

Overall, PEFC stacks of 5–20 kW capacity were the state-of-the-art in 1995; the three stacks installed in the "Green Car," manufactured by Energy Partners (Florida) were 7 kW each, and a new stack reported by Ballard was 20 kW. The platinum loading in all of the above stacks is high. A first 10 kW stack that utilizes the low platinum loading technology was reported in 1996 by Mechanical Technology Inc. (MTI) of Albary, NY, USA. Based on the recent advances in the R&D work on low platinum loading membrane/electrode assemblies and, particularly, on the demonstration of longevity of such membrane/electrode assemblies (see Section 4.4), there is every reason to believe that PEFC stacks with such low platinum loading would

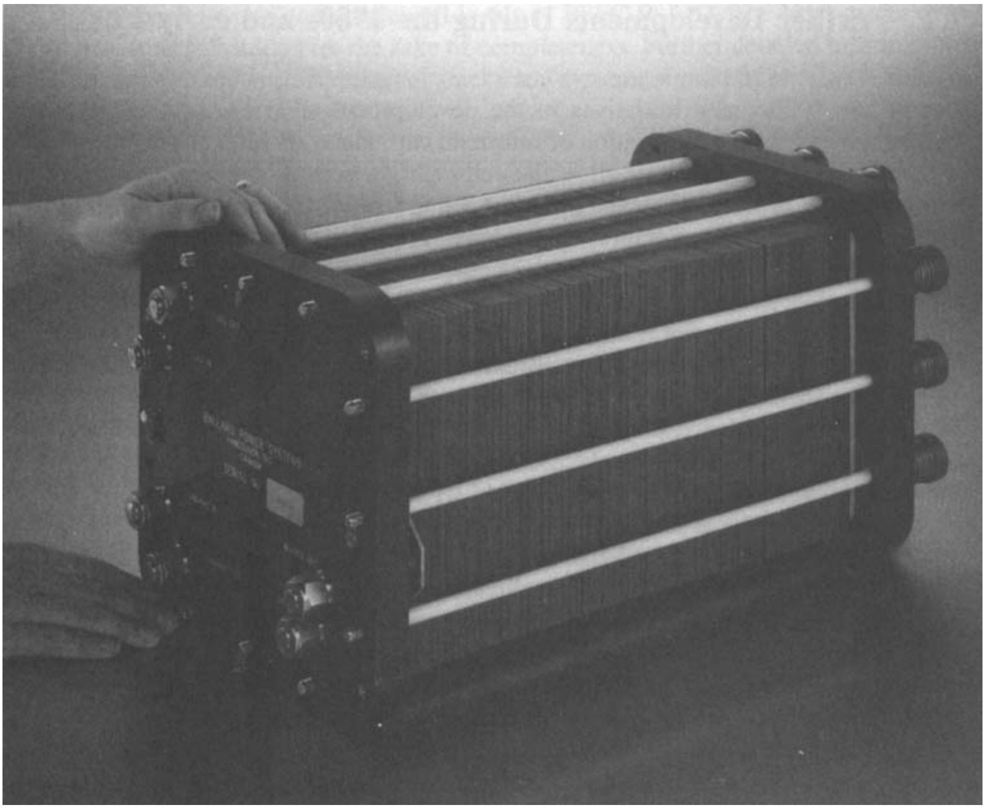

Fig. 45. The first-generation Ballard PEFC stack, nominally 5 kW for pressurized hydrogen/air operation. Reproduced by permission Ballard Power Systems.

provide similar performances to those demonstrated in platinum-rich stacks. MTI's report fully confirms these expectations. Similarly, a lower-cost formula will be required in the longer run for the bipolar plates, because machined graphite plates are too costly for large-scale transportation applications. Current densities recently reported for stacks have been similar to those reported for single-cell PEFC, ranging between 300 and 2000 mA/cm^2 at cell potentials of 0.6–0.8 V depending on the nature of the fuel and oxidant feed streams and their pressures. To achieve a high performance level, stacks need to be pressurized to at least two atmospheres on the fuel side and up to three to four atmospheres on the air side of H_2/air fuel cell stacks. Low-pressure operation could have obvious and significant engineering and cost advantages but would require further increase in cell performance at low air pressures to satisfy demands in transportation or even for stationary power generation. On the other hand, "air-breathing" PEFC stacks could conceivably serve as battery replacements with metal hydrides as hydrogen sources. This concept has been demonstrated recently by several teams.

Recent technology developments have brought the PEFC stack to the point of demonstration in complete power systems for electric vehicles and, most recently, in model electric vehicles. The latter include a bus demonstrated by Ballard, a passenger car demonstrated by Energy Partners, and a van demonstrated by Daimler Benz in Germany, all systems relying for the moment on hydrogen fuel on board the vehicle. A 10 kW power system was developed between 1991 and 1993 for the US Department of Energy by a team consisting of GM/Allison Turbines (primary contractor), Los Alamos National Laboratory, Ballard (supplier of PEFC stacks), and Dow Chemical. This power system is based on methanol fuel which is steam-reformed on board the vehicle. A conceptual scheme showing the components of such a power system is given in Fig. 46. It is suggested by this figure that the PEFC stacks are going to be only around 25% of the overall system weight or volume when steam-reformed

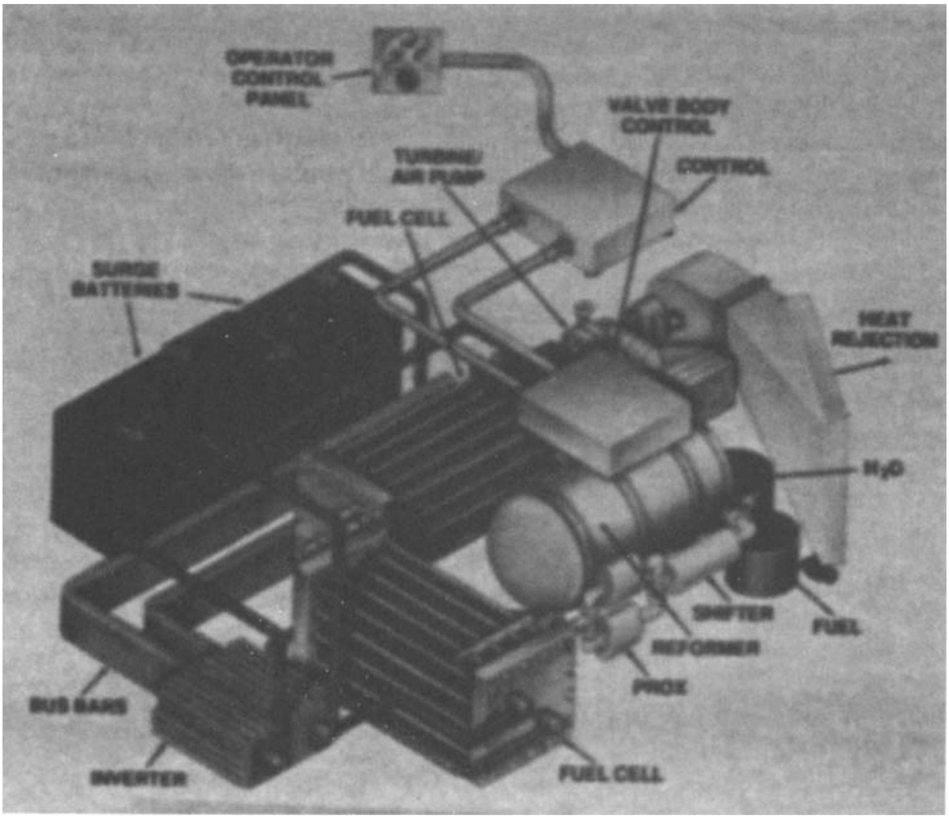
OPERATOR CONTROL PANEL
VALVE BODY CONTROL
TURBINE/ AIR PUMP
CONTROL
FUEL CELL
SURGE BATTERIES
HEAT REJECTION
H_2O
SHIFTER
FUEL
REFORMER
PROX
BUS BARS
INVERTER
FUEL CELL

Fig. 46. Conceptual design of a PEM fuel cell system (Reproduced by permission of US Department of Energy, Office of Transportation Technology).

methanol on board the vehicle is chosen as the hydrogen source. The scheme shows the need for polishing the reformate by a shift reactor and by preferential oxidation (see Section 3.3) to bring the level of CO in the fuel feed stream well below 100 ppm. Also, the system shown is a hybrid fuel cell/battery, where the battery is intended for cold start, for peak power and for energy storage by regenerative braking. The energy storage function cannot be fulfilled by a fuel cell stack but, on the other hand, the peak power requirements could be provided, in principle, by the PEFC stack. For a particular applications, cost and other systems considerations may dictate the choice of a hybrid fuel cell/battery over a pure PEFC power source or vice versa. The second phase of the General Motors project, devoted to a 30 kW system based on a methanol reformer and PEFC stacks began in 1995.

Early in 1993 the Ballard bus became the first electric vehicle demostrated which was powered purely by PEFC stacks. A scheme of this bus is shown in Fig. 47. The purpose of this Ballard bus program has been to achieve commercialization, by 1998, of Zero Emission Vehicle (ZEV) electric buses powered by the Ballard fuel cell. A commercially available 32-foot bus was selected for the first phase of the program, completed in March 1993, in which, the power plant used Ballard's 5 kW fuel cell stacks: 24 stacks were integrated into a 120 kW (160 hp) "electric engine" consisting of three eight-stack series strings connected electrically in parallel. Compressed hydrogen gas, selected by Ballard as the fuel for phase 1 of their bus demonstration project, was stored in DOT-approved fiberglass-wound aluminum cylinders, mounted under the floor of the bus. The range of the bus, at the time of writing, is 160 km but is expected to increase in the last phase of the project (1998) to 560 km. The phase-1 bus uses an 80 kW dc motor connected directly to an Allison four-speed transmission. The performance quoted by Ballard for their first-generation bus is 1–50 km/h in 20s,

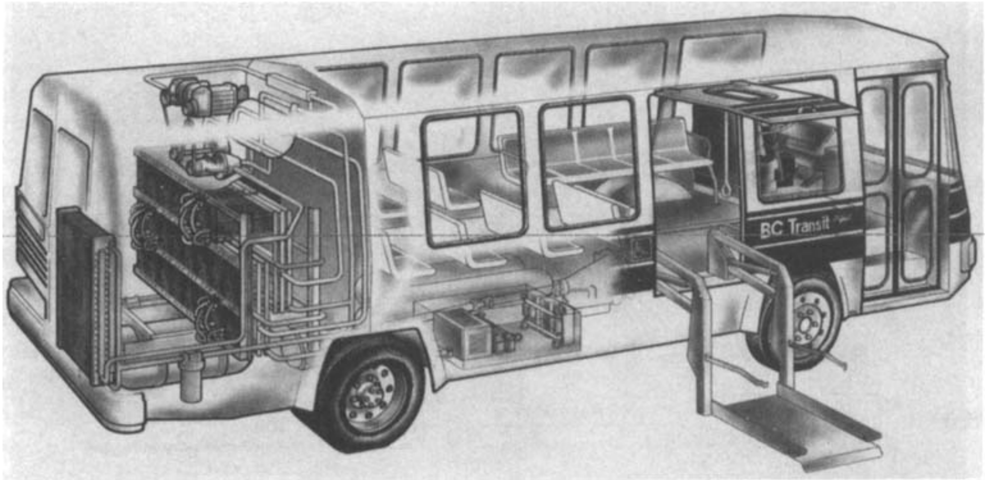

Fig. 47. Scheme of the first-generation Ballard bus. The 120 kW power system seen at the back was based on 24 PEFC stacks of 5 kW each Compressed-hydrogen cylinders were placed under the bus floor. See text for more details. Reproduced by permission of Ballard Power Sources.

a top speed of 70 km/h, a range of 160 km, and maintenance of 30 km/h on an 8% grade. Demonstration of the second-generation PEFC powered Ballard bus, using compressed hydrogen storage and an advanced 240 kW PEFC stack based power system, began in 1995.

8 The Polymer Electrolyte Direct Methanol Fuel Cell (DMFC)

In this section, recent advances in the field of polymer electrolyte direct methanol fuel cells, i.e., PEFCs based on direct anodic oxidation of methanol are discussed. A schematic of such a cell is shown in Fig. 48, together with the processes that take place in the cell. The DMFC has many facets, electrocatalysis materials and components which deserve a detailed treatment. The discussion here will be confined, however, to the very significant performance enhancement demostrated recently with polymer electrolyte DMFCs, and, as a result, to possible consideration of DMFCs as a nearer term technology.

Recent advancements in DMFC research and development have been quite dramatic, with the methanol/air fuel cell achieving a power density which is a very significant fraction of that achieved with methanol reformate/air fuel cells. The recent DMFC work has strongly focused on cells with polymeric (primarily PFSA) membrane electrolytes. More applied work, aimed primarily at the demonstration of

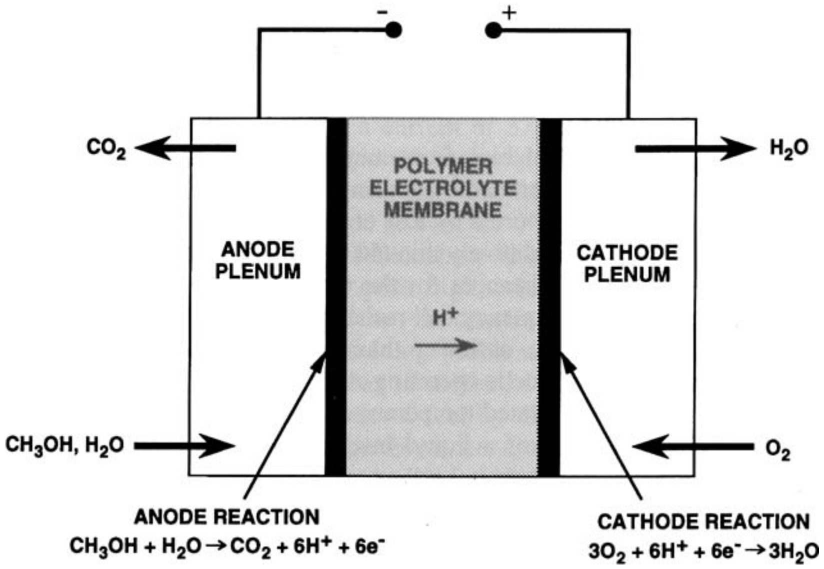
-
+
CO_2
H_2O
POLYMER ELECTROLYTE MEMBRANE
ANODE PLENUM
CATHODE PLENUM
H^+
CH_3OH, H_2O
O_2
ANODE REACTION
$CH_3OH + H_2O \rightarrow CO_2 + 6H^+ + 6e^-$
CATHODE REACTION
$3O_2 + 6H^+ + 6e^- \rightarrow 3H_2O$

Fig. 48. Schematic of a PEFC based on the direct oxidation of methanol.

enhanced, stable performance of DMFC single cells or stacks, has taken place in the USA in research institutes including the Jet Propulsion Laboratory [113, 114]. Case Western Reserve University [115], and Los Alamos National Laboratory [116, 117] in collaboration with industries such as International Fuel Cells (IFC) and Giner, Inc. Similar efforts in Europe resulted in a demonstration at Siemens [118] of a high-performance polymer electrolyte DMFC operating at temperatures above 120 °C.

The recent strong advances in DMFC performance have been achieved without any breakthroughs in electrocatalysis, i.e, by employing Pt–Ru anode catalysts [119] and platinum cathode catalysts. However, the use of these electrocatalysts in conjunction with polymer electrolyte membranes has resulted in very significant enhancements in DMFC performance when such cells are operated at temperatures as high as 120–140 °C, and particularly when catalyst layer composition and structure have been optimized. Operation at elevated temperatures is facilitated in such PEFCs by the anode being continously in contact with liquid methanol/water mixtures. In this section, recent results are described briefly, showing the high performances achievable from polymer electrolyte DMFCs. These results are then used to evaluate a polymer electrolyte DMFC stack comparatively vs. the system comprising a methanol reformer and a reformate/air polymer electrolyte fuel cell stack.

Thin-film catalysts bonded to the membrane by the decal method [14, 41, 42] provided best result in terms of catalyst utilization and cell performance in work reported recently by Ren et al. [116]. Nafion$^{\mathrm{TM}}$ 112, 115 and 117 membranes were cleaned and converted into the acid form, unsupported Pt–RuO$_x$ catalysts were used for the anode catalyst and platinum black was used for the cathode catalyst. The single-cell fuel cell hardware consisted of uncatalyzed carbon-cloth gas-diffusion backings and nuclear-grade graphite blocks with machined serpentine flow channels. The outlet flows could be controlled so as to impose a desired amount of back-pressure to ensure a two-phase liquid/vapor system on the anode side of the DMFC, securing a well-humidified membrane and thus good protonic conductivity at temperatures as high as 130 °C. The oxygen or air feeds to the cathodes were also humidified to provide water-vapor-saturated gas at temperatures 0–10 °C above the cell temperature.

Figure 49 shows polarization and high-frequency resistance curves of DMFCs operated at 130 °C with 5 atm oxygen cathodes using Nafion$^{\mathrm{TM}}$ 112, 115, and 117 membranes. The best performance reported by Ren et al. [116] (670 mA/cm^2 at 0.5 V cell voltage) was obtained using the relatively thin (50 μm) Nafion$^{\mathrm{TM}}$ 112 membranes. The high-frequency (8 kHz) cell resistances for the three cells are also depicted in Fig. 49 (open symbols). The high-frequency cell resistivities of the DMFCs operating at 130 °C are seen to be as low as, or lower than, those typically measured for conventional, well-humidified H$_2$/air cells operating at 80 °C. Clearly, the membranes were well hydrated even at these elevated temperatures, most probably as a result of the maintenance (by pressurization) of a liquid in the anode compartment. (Other workers [118] have operated direct methanol polymer electrolyte fuel cells at 130 °C on vaporized water/methanol feeds.) These results demonstrate that operation of polymer electrolyte fuel cells in the direct methanol mode is possible at temperatures well above 100 °C, a feature of significant importance considering the requirement of higher DMFC temperatures for enhancement of the anodic process. All of the cells

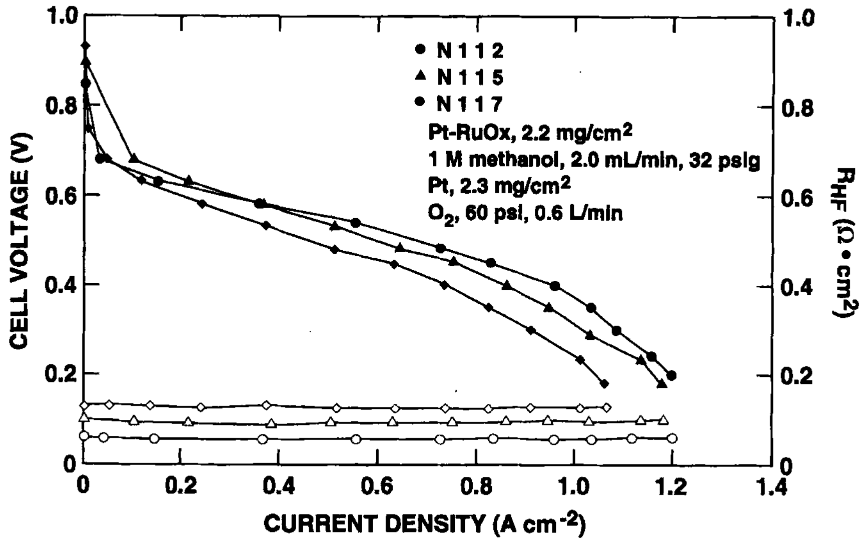

Fig. 49. performance of a methanol/oxygen PEFC operting at 130 °C with Nafion (N) membranes of three different thicknesses [116]. (Reprinted by permission of the Electrochemical Society).

described here demonstrated reasonable performance stability [116]. The performance of the Nafion™ 112-based cell dropped from 670 mA/cm^2 to 600 mA/cm^2 at constant (0.5 V) cell voltage after one week of running. The higher cell temperature could thus have a beneficial effect in enhancing and maintaining methanol anode activity. Figure 50 shows polymer electrolyte DMFC performances under conditions that may be more amenable to transportation applications. Air cathodes at only 3 atm were used instead of higher-pressure oxygen and the cell temperatures were also set somewhat lower, at 110 °C. Still, Fig. 50, shows that with the Nafion™ 112 membrane/electrode assembly, a current of 370 mA/cm^2 at 0.5 V cell voltage was obtained with a 1 M methanol feed. As shown in Fig. 51, the peak power output of this type of DMFC was almost 400 mW/cm^2 for the oxygen cathode at 130 °C and about 250 mW/cm^2 for the air cathode at 110 °C.

The results shown above demonstrate that the performance obtained from a polymer electrolyte DMFC is quite high, with the maximum area power density reaching about one-third of the maximum power densities demonstrated for reformate/air fuel cells. A remaining problem, however, with polymer electrolyte DMFCs is related to the high flux of methanol across polymeric PFSA membranes, which could cause a serious loss of fuel by direct fuel–oxygen recombination and could also hurt the air cathode performance. Quantification of this flux under various conditions has been reported recently for Nafion™ membranes under a range of experimental conditions [117]. The results have shown clearly that the membrane is the only significant barrier for methanol permeation in a polymer electrolyte DMFC and that the rates of penetration under open-circuit conditions are of the order of 100 mA/cm^2 in a Nafion™ 117 membrane and proportionately higher for thinner

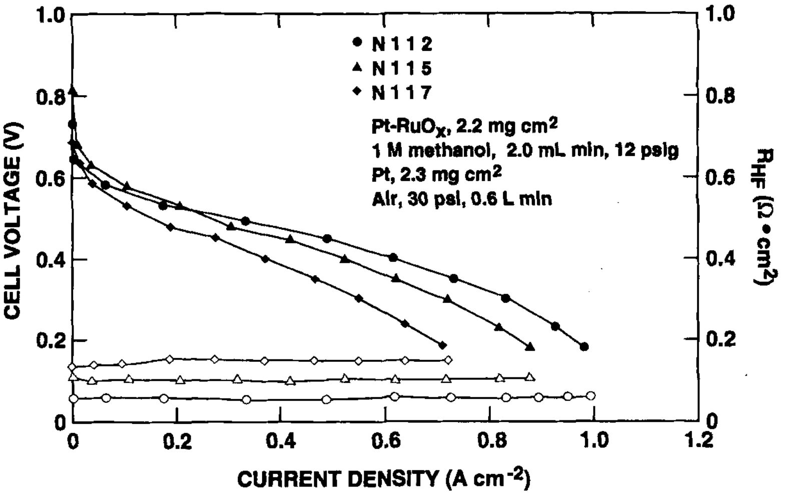

Fig. 50. Performance of a methanol/air PEFC opertaing at 110 °C with Nafion (N) membranes of three different thicknesses [116]. (Reprinted by permission of the Electrochemical Society).

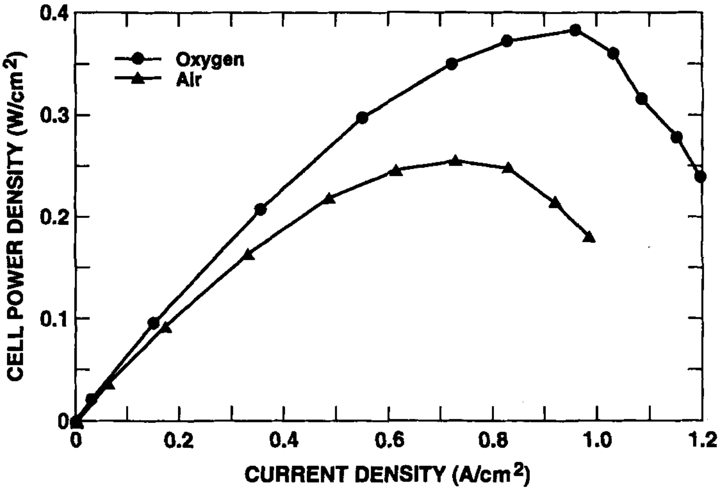

Fig. 51. Cell power densities for methanol/oxygen and methanol/air polymer electrolyte fuel cells with a Nafion 112 membrane [116]. (Reprinted by permission of the Electrochemical Society).

membranes of this type. The same authors have also reported that the degree of methanol crossover could be significantly cut down in a polymer electrolyte cell operating at sufficiently high temperatures, when the cell operates at high current densities. These findings are demonstrated in Fig. 52. This figure shows that, for lean feeds of methanol, the amount of methanol reaching the other side of the cell (the cathode compartment) decreases significantly with cell current density. This

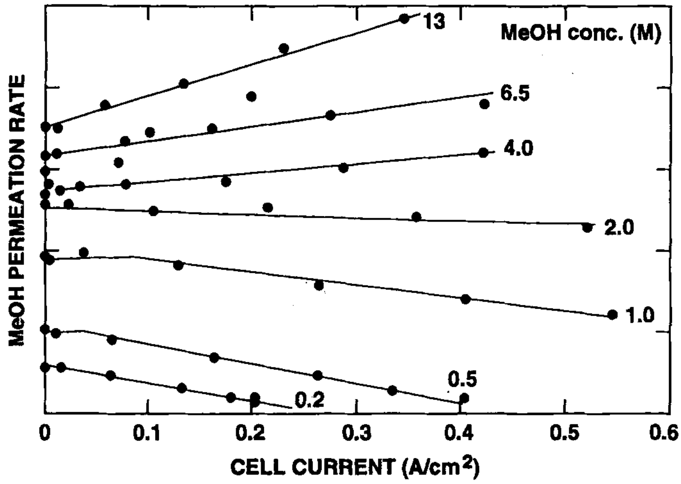

Fig. 52. Variation of methanol permeation rate in a polymer electrolyte fuel cell at elevated temperature with cell current density for different methanol feed concentrations. The results show that, for methanol concentrations under 1 m, methanol is effectively consumed at the anode, thus minimizing the permeation rate [117]. (Reprinted by permission of the Electrochemical Society).

demonstrates the important finding that, at least in principle, the degree of crossover can be minimized by operating at current corresponding to large drop of methanol concentration within the anode, thus lowering significantly methanol access to the membrane. Another approach to the minimization of crossover has quite recently been reported [115]: a polybenzimidazole (PBI) membrane doped with phosphoric acid has been used for the development of a polymer electrolyte DMFC operating unpressurized at temperatures close to 200 °C. This example of a polymer electrolyte DMFC presents advantages in that cell operation is under ambient conditions and methanol crossover is minimized thanks to low mobility of the methonol in the nonswollen PBI membrane. The main disadvantage is the rather low electrode activities, even at such high temperatures, apparently because of the nature of the water-lean PBI/phosphoric acid electrolyte.

The recent results demonstrated for polymer electrolyte DMFCs shed new light on the probability of this power source becoming a viable option in the near future for several applications. For example, concepts of PEFC-based power systems for transportation applications have been based in the past either on hydrogen carried on board the vehicle or on the steam-reforming of methanol to generate a mixture of hydrogen and CO_2 as the fuel feed stream for the fuel cell stack. The latter system has been considered an attractive option because of the high energy density of the fuel (methanol), its availability, and the relatively simple fuel distribution system required. However, the complexity and additional weight and volume associated with the reformer on board the vehicle have presented significant challenges in the implementation of this option. To date, the DMFC has not been considered a serious option for transportation applications due to its limited performance (low power density) in comparison with the reformate/air fuel cell. However, having obtained roughly one-third the maximum power densities of reformate/air fuel cells, the polymer electrolyte methanol/air cell shows promise in becoming a serious competitor to the on-board methanol-reforming system for methanol-fueled transportation applications. For these two different systems for conversion of methanol to dc power, it has been argued [116] that:

1. The mass or volume power densities are quite similar for:
   (i) a DMFC stacks operating at 0.25 W/cm^2, and
   (ii) a system comprising a methanol + reformer/air fuel cell (RAFC) stack generating 1.0W/cm^2.

2. The overall energy conversion efficiency for the complete process of mathanol chemical energy conversion dc electric energy will be similar (43%) for a system with an RAFC operating at 0.70 V and a DMFC operating at 0.55 V, provided the fuel efficiency in the DMFC is raised to 90% (the latter requirement could be possibly achieved by combination of anodic effects and membrane modification).

3. The cost per kilowatt predicted for the DMFC is significantly higher, as long as the areal power density remains lower by a factor of about three to four and the catalyst loading is not reduced significantly. However, the cost of the balance of plant is much higher in the case of the reformer-based system, lowering the cost differential between the two options significantly.

From the points made above, it seems that the DMFC could become a serious power source candidate for transportation applications, provided the following requirements are also met:

1. catalyst loading is further reduced (or alternative anode catalysts developed),
2. long-term stable performances (1000 h time scale) are demonstrated, and
3. fuel efficiencies are actually increased to the 90% level.

Acknowledgments

1. I was invited originally to write this chapter by Professors Tobias and Gerischer, two distinguished scholars who have since passed away. They provided important inspiration as world leaders in the field and as great teachers of electrochemistry.

2. My work on polymer electrolyte fuel cells has been part of a team effort at Los Alamos National Laboratory (The Electronic and Electrochemical Materials and Devices Group). The experience of working with all members of this team has been extremely rewarding. The team's achievements and their enthusiasm have provided the encouragement to invest the effort in writing this chapter.

3. I am indebted to Ross Lemons, Director of the Materials Science and Technology Division at Los Alamos, for his inspiring leadership, during the earlier days of

work on polymer electrolyte fuel cells at Los Alamos. His contributions to this field as technical leader and articulate technology promoter have been invaluable.

4. US Department of Energy Support for the Core Fuel Cell Research Program at Los Alamos dates from 1980. Most recently this support has come from the DOE Office of Transportation Technology. Dr. Albert Landgrebe served as DOE program manager for this program for many years. Two other recent sources of support for fuel cell R&D work at Los Alamos have been the Defense Advanced Research Project Agency (DARPA) and the US DOE Hydrogen Program.

5. Notes on the history of PEFC development at General Electric (Section 7.1) have been kindly provided by Dr. J. F. McElroy of Hamilton Standard.

6. Finally, My wife Marcia deserves special acknowledgment and thanks.

References

1. S. Gottesfeld, I. D. Raistrick, S. Srinivasan, J. Electrochem. Soc. 134, 1455 (1987).
2. W. K. Paik, T. E. Springer, S. Srinivasan, J. Electrochem. Soc. 136, 644 (1989).
3. A. Parthasarathy, C. R. Martin, S. Srinivasan, J. Electrochem. Soc. 138, 916 (1991).
4. A. Parthasarathy, B. Dave, S. Srinivasan, A. J. Appleby, C. R. Martin, J. Electrochem. Soc. 139, 1634 (1992).
5. A. Parthasarathy, S. Srinivasan, A. J. Appleby, C. R. Martin, J. Electrochem. Soc. 139, 2856 (1992).
6. A. Parthasarathy, S. Srinivasan, A. J. Appleby, C. R. Martin, J. Electrochem. Soc. 139, 2530 (1992).
7. F. Uribe, M. S. Wilson, T. E. Springer, S. Gottesfeld, Proc. Workshop on Structural Effects in Electrocatalysis and Oxygen Electrochemistry, Electrochemical Soc. Proc. Vol. 92–11, pp. 494–509 (1992).
8. Z. Ogumi, Z. Takehara, S. Yoshizawa, J. Electrochem. Soc. 131, 769 (1984); Z. Ogumi, T. Kuroe, S. Yoshizawa, J. Electrochem. Soc. 132, 2601 (1985).
9. F. A. Uribe, T. E. Springer, S. Gottesfeld, J. Electrochem. Soc. 139, 765 (1992).
10. K. L. Hsueh, H. H. Chang, D. T. Chin, S. Srinivasan, Electrochim Acta 30, 1137 (1985); M. A. Enayatullah, t. D. De Vilbiss, J. O'M Bockris, J. Electrochem. Soc. 136, 3369 (1989).
11. (a) A. K. Shukla, P. Stevens, A. Hamnett, J. B. Goodenough, J. Appl. Electrochem. 19, 383 (1989): (b) Data of PEFC testing at Los Alamos National Laboratory (1986–1987).
12. S. Mukerjee, S. Srinivasan, J. Electroanal. Chem. 357, 201 (1993); see also S. Mukerjee, S. Srinivasan, M. P. Soriaga, J. McBreen, J. Phys. Chem. 99. 4577 (1995).
13. M. T. Paffett, J. G. Beery, S. Gottesfeld, J. Electrochem. Soc. 135, 1431 (1988).
14. M. S. Wilson, S. Gottesfeld, J. Appl. Electrochem. 22 1 (1992).
15. I. D. Raistrick, Internal Report, Los Alamos National Loboratory, (1985).
16. N. E. Vanderborgh, J. Guante, R. E. Dean, R. D. Sutton, Abastracts of the Fuel Cell Seminar in Long-Beach, CA. Oct. 1988, Courtesy Associates, Inc., Washington, DC, p. 52.
17. S. Gottesfeld, J. Pafford, J. Electrochem. Soc. 135, 2651 (1988); S. Gottesfeld, US Patent 4 910 099 (March 20, 1990).

18. (a) W. Vogel, J. Lundquist, P. Ross, P. Stonehart, Electrochim. Acta 20, 79 (1975); (b) H. Igarashi, T. Fujino, M. Watanabe, J. Electroanal. Chem., 391, 119 (1995); (c) D. Thirumalai, T. A. Zawodzinski, T. E. Springer, S. Gottesfeld, Abstr. Electrochem. Soc. Meeting, Montreal (May 1997); (d) H. A. Gasteiger, N. M. Markovic, P. N. Ross, J. Phys. Chem. 99, 8290 (1995); (e) H. A. Gasteiger, N. M. Markovic, P. N. Ross, J. Phys. Chem. 99, 16757 (1995).
19. See, for example, P. J. Berlowitz, C. H. F. Peden, D. W. Goodman, J. Phys. Chem. 92, 5213 (1988).
20. M. T. Paffett, Los Alamos National Laboratory, Internal Report.
21. M. S. Wilson, T. E. Springer, T. A. Zawodzinski, S. Gottesfeld Proc. 28th Intersociety Energy Conversion Engineering Conf. 1993, Atlanta, Georgia, Vol. 1, pp. 1203–1208.
22. V. M. Schmidt, R. Ianniello, H. -F. Oetjen, H. Reger, U. Stimming, F. Trila p. 1.
23. M. Iwase, S. Kawatsu in: Proton Conducting Membrane Fuel Cells I, S. Gottesfeld, G. Halpert, A. Landgrebe (Eds), the Electrochemical Society, Pennington, NJ, Oct (1995), p. 12.
24. R. D. Sutton, Report at the Fuel Cell Seminar in Tucson, AZ (1992).
25. B. Z. Nikolic, H. Huang, D. Gervasio, A. Lin, C. Fierro, R. R. Adzic, E. B. Yeager J. Electroanal Chem. 295, 415 (1990).
26. A. LaConti, G. Smarz, F. Sribnik, New Membrane – Catalyst for Solid Polymer Electrolyte Systems, Final Report to Los Alamos National Laboratory from United Technologies, Hamilton, Standard, (1985).
27. C. M. Seymour et al. Abstracts of the Fuel Cell Seminar in Tucson, AZ, Courtesy Associates Inc., Washington, DC (1992), p. 446.
28. Abstracts of the PNGV Workshop on Fuel Processing for Proton Exchange Membrane (PEM) Fuel Cells, Dearborn, MI, October 1995, US DOE, Office of Transportation Technology.
29. Niedrach, US Patent 3, 297, 484 (1967).
30. R. J. Lawrence, US Patent 4 272 353 (June, 1981).
31. H. Takenaka, E. Torikai, Kokai Tokyo Koho (Japanese Patent) 55, 38943 (1980).
32. P. S. Fedkiw, W.-H Her, J. Electrochem. Soc. 136, 899 (1989).
33. P. Aldebert, F. Novel-Cattin, M. Pineri, R. Durand, Solid State Ionics 35, 3 (1989).
34. I. D. Raistrick, in: Diaphragms, Separators, and Ion Exchange Membranes, J. W. Van Zee, R. E. White, K. Kinoshita, H. S. Burney, (eds.). The Electrochemical Society Softbound Proc. Series, Pennington, NJ (1986), PV 86–13, p. 172.
35. S. Srinivasan, E. A. Ticianelli, C. R. Derouin, A. Redondo, J. Power Sources 22, 359 (1988).
36. E. A. Ticianelli, C. R. Derouin, A. Redondo, S. Srinivasan, J. Electrochem. Soc. 135, 2209 (1988).
37. E. A. Ticianelli, C. R. Derouin, S. Srinivasan, J. Electroanal. Chem. 251, 275 (1988).
38. S. Mukerjee, S. Srinivasan, A. J. Appleby, Electrochim. Acta, 38, 1661 (1993).
39. D. Rocco de Senna, E. A. Ticianelli E. R. Gonzalez, Abstracts of the Fuel Cell Seminar in Phoenix, AZ, Courtesy Associates Inc., Washington, DC (1990), p. 391.
40. E. J. Taylor, E. B. Anderson, N. R. K. Vilambi, J. Electrochem. Soc. 139, L45 (1992).
41. M. S. Wilson, S. Gottesfeld, J. Electrochem. Soc. 139, L28 (1992).
42. M. S. Wilson, J. A. Valerio, S. Gottesfeld, Electrochim. Acta 40, 355 (1995).
43. M. S. Wilson, US Patents. 5 211 984 and 5 234 777 (1993).
44. Abstracts of the US Department of Energy Hydrogen Program Review Meeting in Coral Gables, FL, April 1995.
45. J. F. McElroy, Abstracts of the Fuel Cell Seminar in Phoenix, AZ, Courtesy Associates, Inc., Washington, DC (1990), p. 282.

46. M. S. Wilson, F. Garzon, K. E. Sickafus, S. Gottesfeld, J. Electrochem. Soc. 140, 2872 (1993).
47. M. Reddy, J. a. Marinsky, J. Phys. Chem. 22, 3884 (1970).
48. J.-P. Randin, J. Electrochem. Soc. 129, 1215 (1982).
49. A. B. LaConti, A. R. Fragala, J. R. Boyack, in: Electrode Materials and Processes for Energy Conversion and Storage, J. D. E. McIntyre, S. Srinivasan, F. G. Will (eds.), The Electrochemical Society Softbound Proc., Pennington, NJ (1977) PV 77–6, p. 354.
50. G. G. Scherer, T. Mamose, K. Tomiie, J. Electrochem. Soc. 135, 3071 (1988).
51. T. Kyu in: Materials Science of Synthetic Membranes, D. R. Lloyd (ed.), ACS Symp. Ser. No. 269 (1985), p. 365.
52. R. S. Yeo, H. L. Yeager, Modern Aspects of Electrochem. 16, 437 (1985).
53. S. C. Yeo, A. Eisenberg, J. Appl. Polym. Sci. 21, 875 (1977).
54. K. A. Mauritz, C. E. Rogers, Macromolecules 18, 423 (1985).
55. H. L. Yeager, A. Steck, J. Electrochem. Soc. 128, 1880 (1981).
56. D. Wu, DuPont Central Research, private communication.
57. W. Grot, G. E. Munn, P. N. Walmsley, Abstracts of the ECS Meeting in Houston, TX, May, 1972.
58. T. A. Zawodzinski, Jr., C. Derouin, S. Radzinski, R. J. Sherman, T. Springer, S. Gottesfeld, J. Electrochem Soc. 140, 1041 (1993).
59. T. A. Zawodzinski, Jr., C. Lopez, R. Jestel, J. Valerio, S. Gottesfeld, J. Electrochem Soc. 140, 1981 (1993).
60. G. A. Eisman in: Diaphragms, Separators and Ion Exchange Membranes, J. W. Van Zee, R. E. White, K. Kinoshita, H. S. Burney (eds.), The Electrochemical Society Softbound Proc. Ser., Pennington, NJ (1986), PV 86–13, pp. 156–171.
61. M. Escoubes, M. Pineri in: Structure and Properties of Ionomers, M. Pineri, A. Eisenberg (eds.), Reidel, Dordrecht (1987), p. 341.
62. P. C. Rieke, N. E. Vanderborgh, J. Membr. Sci. 32 313 (1987).
63. K. K. Pushpa, D. Nandan, R. M. Iyer, J. Chem. Soc. Faraday Trans. 84, 2047 (1988).
64. T. A. Zawodzinski, M. Neeman, L. Sillerud, S. Gottesfeld, J. Phys. Chem. 95, 6040 (1991).
65. M. Heaney, Ph.D. Thesis, University of Colorado, Boulder (1993).
66. P. Schroeder, Z. Phys. Chem. 45, 75 (1903).
67. T. A. Zawodzinski, M. Shoichet, T. McCarthy, S. Gottesfeld, J. Appl. Electrochem. 23, 86 (1993).
68. T. A. Zawodzinski, Jr., S. Gottesfeld, Extended Abstr. of Electrochemical Society Meeting Canada, Fall 1992.
69. T. A. Zawodzinski, Jr., T. Springer, F. Uribe, S. Gottesfeld, Solid State Ionics 60, 199 (1993).
70. N. Sivashinsky, G. B. Tanny, J. Appl. Polym. Sci. 26. 2625 (1981).
71. N. G. Boyle, V. J. MacBrierty, D. C. Douglass, Macromolecules 16, 75 (1983).
72. R. C. T. Slade, A. Hardwick, P. G. Dickens, Solid State Ionics 9/10, 1093 (1983).
73. F. Valino, M. Pineri, A. J. Dainoux, J. Polym. Sci. 20, 481 (1982).
74. M. Falk, Can. J. Chem. 58. 1495 (1980).
75. R. S. Chen, J. P. Jayakody, S. G. Greenbaum, Y. S. Pak, G. Xu, M. G. McLin, J. J. Fontanella, Solid State Ionics (1993).
76. Y. S. Pak, G. Xu, J. Electrochem. Soc. 140, 1237 (1993).
77. M. Verbrugge, R. Hill, J. Electrochem. Soc. 137, 3770 (1990).
78. M. Verbrugge, E. W. Schneider, R. S. Conell, R. Hill, J. Electrochem. Soc. 139, 3421 (1992).
79. J. J. Fontanella, M. G. McLin, M. C. Wintersgill, J. P. Calame, S. G. Greenbaum, Solid State Ionics 66, 1 (1993).

80. J. J. Fontanella, M. G. McLin, M. C. Wintersgill, J. Polym. Sci. B: Polym. Phys. in press.
81. B. D. Cahan, J. S. Wainwright, J. Electrochem. Soc. 140, L185 (1993).
82. J. Crank, The Mathematics of Diffusion, 2nd edn, Clarendon, Oxford, (1975), Chapter 9.
83. M. Verbrugge, R. Hill, J. Phys. Chem. 92, 6778 (1988).
84. M. Verbrugge, J. Electrochem. Soc. 136, 417 (1989).
85. R. Hill, M. Verbrugge, J. Electrochem. Soc. 137, 886 and 893 (1990).
86. R. C. T. Slade, A. Hardwick, P. G. Dickens, Solid State Ionics (1990).
87. T. E. Springer, T. A. Zawodzinski, S. Gottesfeld, J. Electrochem. Soc. 138, 2334 (1991).
88. H. R. Zelsmann, M. Pineri, M. Thomas, M. Escoubes, J. Appl. Polym. Sci. 41, 1673 (1990).
89. K.-D. Kreuer, T. Dippel, W. Meyer, J. Maier, Mater. Res. Soc. Symp. Proc. 293, 273 (1993).
90. B. Breslau, I. Miller, Ind. Chem. Eng. Fundam. 10, 554 (1971).
91. F. Helferrich, Ion Exchange, McGraw-Hill, New York (1962).
92. D. Bernardi, M. Verbrugge, J. Electrochem. Soc. 139, 2477 (1992).
93. T. Okada, S. K. Ratjke, H. Nache-Olsen, J. Membr. Sci., 66, 179 (1992).
94. R. Mosdale, P. Stevens, F. Novel-Cattin, B. Loppinet, G. Gebel, P. Adelbert, M. Pineri, Proc. Eur. Space Power Conf., p. 479 (1991).
95. K. D. Kreuer, T. Dippel, J. Maier in: Proton Conducting Mambrane Fuel Cells I, S. Gottesfeld, G. Halpert, A. Landgrebe (eds.), The Electrochemical Society, Pennington, NJ (1995) 241.
96. T. Fuller, J. Newman, J. Electrochem. Soc. 139, 1332 (1992).
97. T. A. Zawodzinski, J. Davey, J. Valerio, S. Gottesfeld, Electrochim. Acta 40 297 (1995).
98. A. Sen, K. E. Leach, R. D. Varijan, Abstracts of the Spring 1995 Meeting of the MRS, San Francisco, CA (1995).
99. A. Steck, H. L. Yeager, Anal. Chem. 51, 869 (1979).
100. T. E. Springer, M. S. Wilson, S. Gottesfeld, J. Electrochem. Soc. 140, 3513 (1993).
101. R. F. Savinell, S. D. Fritts, J. Power Sources 22, 423 (1988).
102. D. Bernardi, J. Electrochem. Soc. 137, 3334 (1990).
103. D. M. Bernardi, M. W. Verbrugge, AIChe J. 37, 1151 (1991).
104. T. F. Fuller, J. Newman in: Proc. Symposium on Fuel Cells, R. E. White, A. J. Appleby (eds.), Electrochem. Soc. Proc. 89–14, 25 (1989).
105. D. Bernardi, M. Verbrugge, J. Electrochem. Soc. 139, 2477 (1992).
106. T. F. Fuller, J. Newman, J. Electrochem. Soc. 140, 1218 (1993).
107. T. V. Nguyen, R. E. White, J. Electrochem. Soc. 140, 2178 (1993).
108. T. E. Springer, T. A. Zawodzinski, M. S. Wilson, S. Gottesfeld in: Proton Conducting Membrane Fuel Cells I, S. Gottesfeld, G. Halpert, A. Landgrebe (eds.) The Electrochemical Society, Pennington, NJ (1995), p. 137; also, J. Electrochem. Soc., 143, 587 (1996).
109. J. L. Fales et al. in: Diaphragms, Separators, and Ion Exchange Membranes, J. W. Van Zee, R. E. White, K. Kinoshita, H. S. Burney (eds.) The Electrochemical Society Softbound Proc. Series, Pennington, NJ (1986), PV 86–13, p. 179.
110. E. A. Ticianelli, C. R. Derouin, A. Redondo, S. Srinivasan, J. Electrochem. Soc. 135, 2209 (1988); for more uses of the same approach see also E. A. Ticianelli, C. R. Derouin, S. Srinivasan, J. Electroanal. Chem. 251, 275 (1988), and S. Srinivasan, D. J. Manko, H. Koch, M. A. Enayatullah, A. J. Appleby, J. Power Sources 29, 367 (1990).
111. R. B. Bird, W. E. Stewart, E. N. Lightfoot, Transport Phenomena, Wiley, New York (1960), p. 570.
112. K. B. Prater, J. Power Sources 37, 181 (1992).
113. S. Surampudi, S. R. Narayanan, E. Vamos, H. Frank, G. Halpert, A. LaConti, J. Kosek, G. K. Surya Prakash, G. A. Olah, J. Power Sources 47, 377 (1994).

114. J. A. Kosek, C. C. Cropley, G. Wilson, A. B. LaConti, S. Narayan, E. Vamos S. Surampudi, H. Frank in: Proc. 28th Intersociety Energy Conversion Engineering Conference (IECEC), Atlanta, GA (1993), Vol. 1, p. 1209.
115. R. F. Savinell, E. Yeager, D. Tryk, U. Landau, J. S. Wainright, D. Weng, K. Lux, M. Litt, C. Rogers, J. Electrochem. Soc. 141. L46 (1994).
116. X. Ren, Mahlon S. Wilson, S. Gottesfeld in: Proton Conducting Membrane Fuel Cells I, S. Gottesfeld, G. Halpert, A. Landgrebe (eds.), The Electrochemical Society, Pennington, NJ 1995, p. 252.
117. X. Ren, T. A. Zawodzinski, F. Uribe, H. Dai, S. Gottesfeld in: Proton Conducting Membrane Fuel Cells I, S. Gottesfeld, G. Halpert, A. Landgrebe (eds.), The Electrochemical Society, Pennington, NJ (1995), p. 284.
118. H. Grüne, G. Luft, K. Mund, M. Waidhas, Program and Abstracts, Fuel Cell Seminar, San Diego, CA, Nov. 28 – Dec. 1, 1994, p. 474.
119. M. Watanabe, M. H. Uchida, S. Motoo, J. Electroanal. Chem. 229, 395 (1987).
120. M. Watanabe, M. H. Uchida, Y. Seki, m. Emori, P. Stonehart, J. Electrochem. Soc. 143, 3847 (1996).

Advances in Electrochemical Science and Engineering
Edited by Richard C. Alkire, Heinz Gerischer, Dieter M. Kolb and Charles W. Tobias
© WILEY-VCH Verlag GmbH, 1997

Graphite, Carbonaceous Materials and Organic Solids as Active Electrodes in Metal-Free Batteries

Fritz Beck

University of Duisburg, Fachgebiet Elektrochemie, D 47057 Duisburg,
Lotharstr. 1, Germany

Contents

1 Introduction . . . 306
  1.1 Charge Stoichiometry . . . 307
  1.2 Electron Transfer . . . 312
  1.3 Structures . . . 314
  1.4 Energetics . . . 319
  1.5 Kinetics . . . 322
2 Reversible Electroorganic Reactions . . . 329
3 Graphite Intercalation Compounds (GICs) . . . 335
  3.1 Acceptor (A)-Type GICs . . . 336
  3.2 Donor (D)-Type GICs . . . 342
4 Fullerenes . . . 347
5 Carbon Blacks . . . 349
6 Conducting Polymers . . . 351
  6.1 Polyacetylene, PPP, and other Polyaromatics . . . 355
  6.2 Polyheterocycles . . . 356
  6.3 PANI and other Polyarylamines . . . 358
  6.4 n-Doping . . . 359
7 Carbonaceous Materials . . . 360
8 Electrodes and Electrolytes . . . 369
9 Cells and Batteries . . . 373
  9.1 Lithium and Lithium-Ion Cells . . . 377
  9.2 Hybrid Cells . . . 382
  9.3 Cells Free of Metals and Inorganic Active Materials . . . 384
10 Conclusions . . . 388
11 References . . . 395

List of Symbols

A_s	specific surface area
b	charge mobility
c	concentration
C	double layer capacity; capacitance
d	thickness of active part of electrode; diameter
D	diffusion coefficient
E	energy

E_s	energy density
F	Faraday number
ΔG	reaction free enthalpy
ΔH	reaction enthalpy
j	current density
j_0	concentration-dependent exchange current density
j_{00}	standard exchange current density
k	Boltzmann constant; rate constant
k_het	heterogeneous rate constant
K	capacity of galvanic cell
$K_\mathrm{s,th}$	theoretical specific capacity
L	transport length; thickness
M	molar mass
m_A	mass of active materials per unit electrode area
n	stage number
p	degree of polymerization
P	porosity of active part of electrode
P_s	specific power
Q	electric charge
r	radius
R	gas constant; internal resistance of electrochemical system
ΔS	reaction entropy
t	time
T	temperature
U_cell	cell voltage
U_end	end voltage
U_R	potential versus a reference electrode
$U_\mathrm{R,0}$	electrode potential
$U_\mathrm{R,00}$	standard potential
U_0	equilibrium cell voltage
V	potential
V_OC	open circuit potential
W	Walden product
x	degree of polymerization; stoichiometry
y	degree of insertion
z	number of electrons
Z	frequency
α	degree of oxidation; charge-transfer coefficient; A h efficiency
γ	current efficiency
Γ	molar surface concentration
ϵ	permittivity constant
η	overvoltage; specific viscosity
κ	permeability of potential barrier at electrode
λ	reorganization energy
μ	active mass utilization
ν	stoichiometric number
ρ	density; resistivity
τ	time constant of electrochemical system
$\Delta\phi$	Galvani voltage

Abbreviations

AC	activated carbon
ACF	activated carbon fiber

A-GIC	acceptor-type GIC
AN	acenaphthene
Ant	anthrone
AQ	anthraquinone
$\mathrm{AQH_2}$	anthrahydroquinone
BET	Brunauer-Emmett-Teller
c.b.	carbon black
c.d.	current density
c.e.	current efficiency
CM	carbonaceous material
CPP	natural graphite-filled polypropylene
CuPc	copper phthalocyanine
CV	cyclic voltammetry, cyclic voltammogram
DEC	diethyl carbonate
DEE	diethoxyethane
D-GIC	donor-type GIC
DL	double layer
DMcT	dimercaptodithiazole
DMC	dimethyl carbonate
DME	dimethoxyethane
DMSO	dimethyl sulfoxide
EC	ethylene carbonate
ECDLC	electrochemical double layer capacitor
EIS	electrochemical impedance spectroscopy
$\mathrm{EMI^+}$	1-ethyl-3-methylimidazolium cation
GC	glassy carbon
GF	graphite fluoride
GIC	graphite intercalation compound
GO	graphite oxide
HOMO	highest occupied molecular orbital
HOPG	highly oriented pyrolytic graphite
IC	insertion of a counterion (process)
ICP	intrinsically conducting polymer
IR	ohmic voltage drop
LGH	linear graphite hybrid
LUMO	lowest unoccupied molecular orbital
Me	metal
MO	molecular orbital
NA	negative active materials
NG	natural graphite
NMP	*N*-methylpyrrolidone
OAR	overall reaction
PA	polyacetylene; positive active materials
PAN	polyacrylonitrile
PANI	polyaniline
PC	propylene carbonate
PEO	poly(ethylene oxide)
PFu	polyfuran
PH	phenol-formaldehyde resin
p-POD	*p*-phenylene oxadizole
P-3-FPT	poly[3-(4-fluorophenyl)thiophene]
PP	polypiopylene
PPAN	pyrolyzed polyacrylonitrile
PPO	poly(propylene oxide)
PPP	poly(*p*-phenylene)

PPS	poly(*p*-phenylene sulfide)
P-3-PT	poly(3-phenylthiophene)
PPy	polypyrrole
PT	polythiophene
PTFE	polytetrafluoroethylene
PVC	poly(vinyl chloride)
QMB/CV	quartz microbalance/cyclic voltammetry
r.b.	rechargeable battery
r.c.	rechargeable cell
RPP	carbon black/polypropylene composite
SES	solvent/electrolyte system
SHE	standard hydrogen electrode
SPE	solid polymer electrolyte
TCNQ	tetracyanoquinodimethane
XRD	X-ray diffraction

1 Introduction

The storage of electric energy plays a key role in modern energy technology. The direct storage in physical capacitors or coils suffers from relatively low energy densities and from shielding problems. Thus the electrochemical method must be favored, in spite of some losses in the course of two transitions: electrical to chemical energy and back in a charge/discharge cycle.

The principle of rechargeable batteries had been demonstrated by Ritter [1] at the very beginning of electrochemical history, making use of an all-copper pile. Planté [2] invented the lead acid accumulator as a solution of high practical relevance, just in time for the emerging age of electricity. The state at the end of the 19th century is nicely summarized by Wade [3]. Until recent times inorganic systems, mostly on the basis of metals for the negative and metal oxides for the positive electrode, were employed exclusively. The so-called "organic batteries", which were introduced in the 1950s, were characterized by organic (aprotic) solvents to balance the reactivity of alkali-metal negatives. Graphite powder or carbon black was employed only to improve the electronic conductivity of some oxides such as MnO_2 or NiOOH.

It was in the last decade that organic and graphite-type active materials were considered with increasing interest for rechargeable batteries. This development was pushed by the growing need for batteries totally free of the toxic "battery metals" such as lead, cadmium, mercury, and nickel, and their compounds. Environmental aspects began to play an important role. This holds for fabrication, application, and recycling of the batteries. In addition, availability of all these metals will be low in the future. Inorganic alternatives such as Zn/MnO_2, $Na/\beta\text{-}Al_2O_3/Na_2S_x$, or Li/MnO_2 do not suffer from such limitations, but many problems such as cycle life and operating temperature remain to be unsolved. Organic and graphite-type active materials would be another alternative; in principle, they could be manufactured on a large scale from renewable material sources. The organic chemical industry is well prepared for such an extension. Recycling or combustion of exhausted batteries would probably be less complicated than for inorganic systems after quantitative separation of the electrolyte. Thus the recent drive toward this development is readily understandable, as it leads unequivocally to metal-free batteries, with which all the problems associated with metals such as corrosion, toxicity, and lack of availability would not occur. In this chapter, only rechargeable batteries (r.b.s, accumulators, secondary cells) are considered due to their practical importance. Primary batteries are outside the scope of this presentation, which is the first comprehensive treatment in the field, after some preliminary summarizing publications in German [4–9] and in English [10].

The review is organized in an introductory section (Section 1), some material-oriented sections devoted to organic solids (Section 2), pure graphites and carbons (Sections 3–5) and other systems mainly with conjugated double bonds, involving heteroatoms such as O, N, S, etc. (Sections 6, 7). Polyacetylene and polybenzene at the beginning of Section 6 on conducting polymers will bridge these parts. Finally, electrochemical systems in terms of electrodes (Section 8) and cells and batteries (Section 9) will be covered. The final part (Section 10) includes, among others, a discussion on graphite oxide and graphite fluoride.

1.1 Charge Stoichiometry

Active materials are considered to be integrated as solids in the battery electrodes. Electrodes of the second kind and insertion electrodes are treated exclusively. Sometimes, it is believed [10] that this is the only way to arrive at practical battery designs. However, nowadays a continuous hybridization of the fuel cell type of design can be observed for conventional inorganic systems, e.g., dissolved active materials in flow cells, storage outside in a separate tank (especially for gaseous reactants) and so on. These versions will not be discussed in the present review, however, for they play no role for metal-free cells.

The capacity K of a galvanic cell is simply based on the electric charge, Q_{disch}, which can be restored in the course of the discharge process:

$$K = Q_{\mathrm{disch}} = f(m_{\mathrm{A}}, j, U_{\mathrm{end}}, \gamma, d, P, \ldots, T, \mathrm{SES}) \tag{1}$$

K depends in a rather complex way on many parameters such as the mass m_{A} of the active materials per unit electrode area, the current density j, the end voltages U_{end} upon charge and discharge, the current efficiency γ, which is a measure for the electrochemical side-reactions, the thickness d and the porosity P of the active part of the electrode, the temperature T, the solvent/electrolyte system (SES), etc. On the basis of Faraday's law, however, simple relationships for the so-called theoretical specific capacity $K_{\mathrm{s,th}}$ can be derived easily. $K_{\mathrm{s,th}}$ is identical to the reciprocal electrochemical equivalent m_{e}:

$$\frac{1}{K_{\mathrm{s,th}}} = m_{\mathrm{e}} = \frac{m_{\mathrm{A}}}{Q_{\mathrm{A}}} = \frac{M}{zF} \tag{2}$$

where M is the molar mass of the active material(s), z the electron number in the electrochemical conversion and F the Faraday constant. Below, three specific cases are discussed which are relevant to rechargeable batteries.

The first refers to *stoichiometric* redox processes (in the solid state) according to the overall reaction

$$\nu_1 M_1 + \nu_2 M_2 + \cdots = \nu_1' M_1' + \nu_2' M_2' + \cdots + ze^- \tag{3}$$

where the reduced moieties are on the left-hand side. Practical examples can be found in Section 2. Then $K_{s,th}$ is given by

$$K_{s,th} = \frac{zF}{\sum \nu_i M_i} \tag{4}$$

where z is the number of electrons in the overall reaction, M_i are the molar masses of the reactants and ν_i are stoichiometric factors. Clearly, $K_{s,th}$ is maximized by low equivalent weights $\nu_i M_i / z$.

The second category is due to *nonstoichiometric* insertion compounds. Their formation can be written for an acceptor-type reaction as

$$\mathrm{W} + y\mathrm{A}^- + \nu y \mathrm{S} \rightarrow [\mathrm{W}^{y+} \cdot y\mathrm{A}^- \cdot \nu y \mathrm{S}] + ye^- \tag{5}$$

Nonstoichiometry is considered by the degree of insertion y, the stoichiometric number ν of the co-inserted solvent molecules S and the molar mass M_W of the "characteristic host lattice unit" [12]. M_A is the molar mass of the anion, M_S that of the co-inserted solvent molecule S. Then $K_{s,th}$ is given by

$$K_{s,th} = \frac{yF}{M_W + yM_A + \nu y M_s} \tag{6}$$

Clearly, $K_{s,th}$ is maximized by a high y and low molar masses for all reactants. Figure 1 shows some typical examples [7]. Solvate molecules are neglected. Graphite, in comparison with inorganic systems, allows, high $K_{s,th}$ due to its light weight as a host lattice. Unfortunately, y is confined to 0.042 per C_1 unit in comparison with 0.5–1.0 for the lithium compounds. An early saturation is found for the heavy HSO_4^- anions. Conducting polymers have a somewhat higher y up to 0.1 (per C_1); cf. Table 1. A value of $y = 0.2$ is reported for poly-3-methoxythiophene) [13], but CH_2Cl_2 as a solvent of low nucleophilicity of necessary in this case, and the potential difference between the uncharged and charged states is as high as 3 V (cf. Section 6).

A third category which is primarily outside the scope of Faraday's law, must be considered. The charge is stored in this case in the electrochemical double layer capacitor (ECDLC). But it is bound again to atomic structures, which are also related to the corresponding masses. The capacitance increases with increasing specific surface A_s, which can be well above 1000 m^2/g in the case of carbon blacks. In addition to Eqs. (4) and (6), a third definition of specific charge is possible:

$$K_{s,th} = A_s \cdot C_{DL} \cdot U_{end} \tag{7}$$

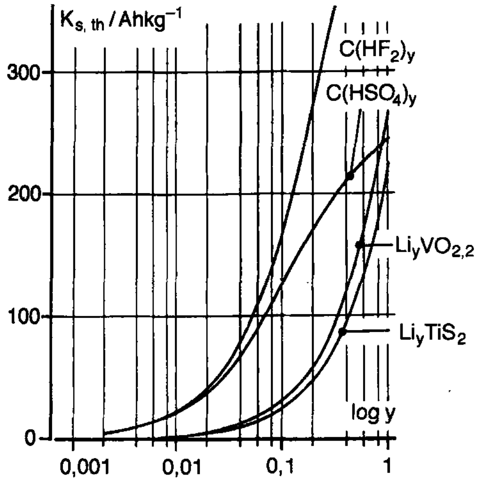

Fig. 1. Dependence of theoretical specific capacities $K_{s,th}$ for two graphite intercalation electrodes and two inorganic Li^+ insertion electrodes on the logarithm of the degree of insertion y.

where C_{DL} is the double layer capacitance (20 $\mu F/cm^2$ in concentrated electrolytes) and U_{end} is the end voltage. With $U_{end} = 1$ V, one obtains $K_{s,th} = 200$ C/g = 56 A h/kg for $A_s = 1000\ m^2/g$. The counterions are neglected in this calculation, but not in Table 1. A simple calculation, based on the formula for the specific surface of (a) spherical particles, radius r, and (b) fibres, radius $r(\rho = \text{density})$, leads to the following expressions for the specific surface area:

$$A_s = \frac{3}{r \cdot \rho} \tag{8a}$$

$$A_s = \frac{2}{r \cdot \rho} \tag{8b}$$

In the case of (b), the contributions of the end-capped circular areas are neglected. Numerical examples with $\rho = 1$ are: $r = 30\,nm$; $A_i = 100\,m^2/g$ and (b) $r = 2\,\mu m$; $A_i = 1\,m^2/g$. Clearly, a high proportion of inner surface area is responsible for the extremely high specific areas

"Supercaps" with a specific capacity higher by one order of magnitude are possible, if surface-bound redox systems are realizable, e.g., *o*-quinoid groups at the surface of carbon structures [14, 15]. This leads back to Faraday's law, which can be written in a two-dimensional form,

$$Q_A = z \cdot F \cdot \Gamma \tag{9}$$

where Γ is the molar surface concentration of these groups, and z is the number of electrons per redox reaction. A pseudocapacitance is derived therefrom:

$$C_{P,A} = \frac{dQ_A}{dU} = zF\frac{d\Gamma}{dU} \tag{10}$$

Table 1. Specific theoretical capacities $K_{s,th}$ for graphite, conducting polymers, and some quinones.[a]

No.	Active Material[b]	C_1 unit	y_{max} [per C_1]	$K_{s,th}$ [A h/kg]	Remarks
1	H_2 (combustion)	–	–	22.590	Hypothetical example
2	C, carbon (combustion)	($z = 4$)	–	8.930	Hypothetical example
3	CH_4 (combustion)	($z = 8$)	–	13.400	Hypothetical example
4[c]	C_x, graphite, A–GIC	C	0.021	39.1	2nd stage, aqueous electrolyte
5[c]	C_x, graphite, A–GIC	C	0.042	69.1	1st stage
6[c]	Polyacetylene	CH	0.1	116.5	
7[c]	Poly(p-phenylene)	$CH_{0.67}N_{0.25}$	0.08	104	
8[c]	Polypyrrole	$CH_{0.75}$	0.09	95	
9[c]	Polythiophene	$CH_{0.5}S_{0.25}$	0.13	111	
10[c]	Polyaniline	$CH_{0.67}N_{0.17}$	0.17 (0.33)	295 (285)	$1e^-(2e^-)$ step with H^+ (A^-), $A^- = HSO_4^-$
11	Benzohydroquinone	$CH_{1.0}O_{0.33}$	(0.33)	483	Not stable
12	Chloranil-hydroquinone	$CH_{0.33}Cl_{0.67}O_{0-33}$	(0.33)	213	
13	Anthrahydroquinone	$CH_{0.63}O_{0.14}$	(0.14)	252	
14	Coronene-hydroquinone	$CH_{0.5}O_{0.25}$	(0.25)	406	Hypothetical example
15	2,5-Dimercapto-1,3,4-thiadiazole	$CNS_{1.5}$	(1.0)	319[d]	
16[c]	C_x, graphite, D-GIC(LiC_6)	C	0.17	339	
17[c]	$C_x^+A^-$ (carbon black)	–	–	63.6	ECDLC, $A_s = 1500$ m²/g, $U_{end} = 1$ V
18[c]	$C_x^-H^+$ (carbon black)	–	–	83.1	ECDLC, $A_s = 1500$ m²/g, $U_{end} = 1$ V
19	Li TiS_2	–	1.0	225	
20	$Li_{0.5}VO_{2.17}$ ($Li_3V_6O_{13}$)	–	0.5	150	
21	PbO_2	–	–	224	
22	NiOOH	–	–	292	
23	Pb	–	–	259	
24	Zn	–	–	820	

[a] C_1 units and $M_A = 100$ are used for the calculations.
[b] Some inorganic active materials are shown for comparison.
[c] Co-insertion of solvents *not* considered.
[d] calculated as 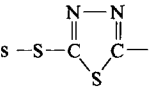 , 2 F/mol, cf. Section 2.

As in conventional batteries, charge is never stored as free charges, for this would lead to a space charge with an extremely high specific energy, which cannot be handled. Thus charges are compensated by counterions. Charged organic molecules (Section 2) in terms of radical ions are compensated by counterions, mostly the addition or release of protons or the formation of S–S bonds, leading to covalent

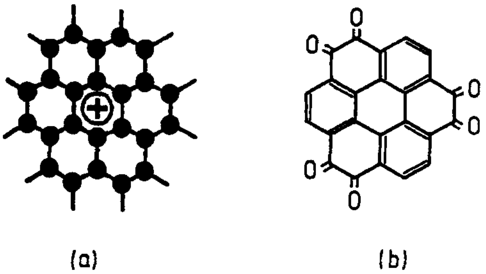

Fig. 2. Coronene model for GICs of the A-type (a) and of a hypothetical "coronene-quinone" (b), as an example of the *o*-quinoid surface groups on the graphite.

bonds, which can be easily cleaved in the course of the back-reaction. Charged structures are compensated through counterions. Actual examples are discussed in each of the Sections 3–7. A weak ionic bond is formed. Counterions must have weak electrophilicity and nucleophilicity to avoid the formation of strong covalent bounds. These two principles are summarized in Fig. 2 in terms of "coronene" structures. In graphite intercalation compounds of the acceptor type, one positive charge can be realized per 24 C atoms of the graphene layer. The $K_{s,th}$ value is rather low. Higher charging leads to the irreversible formation of graphite oxide. However, the hypothetical "coronene-quinone" due to oxidation at the rim of the molecule to form *o*-quinones would lead to a much higher specific capacity.

The highest capacities are due to hydrogen (cf. Table 1), but hydrogen is difficult to store, and a practical solution has only recently been found in metal hydride/nickel oxide accumulators, where $K_{s,th}$ for the metal hydride falls, unfortunately, to about 1% of the value for pure hydrogen. Carbon is a light element with a low equivalent weight of 3, but the total irreversibility of the reaction

$$CO_2 + 4\,H^+ + 4\,e^- = C + 2\,H_2O \tag{11}$$

at room temperature does not allow any practical application. A combination of both – the combustion of methane – is unfeasible even in fuel cells with catalyst electrodes. Consequently, larger molecules and host lattices must be employed, and Table 1 lists some characteristic examples. The values for graphite intercalation compounds of the acceptor type (A-GICs) Nos. 4 and 5 are low indeed, and they fall even further if solvents or solvent acid molecules are co-intercalated. This holds for D-GIC No. 16 too, which has a high value initially. These restrictions will be discussed further in Section 3. As already shown in Fig. 1, larger y values allow for elevated capacities in the case of inorganic systems (cf. Nos. 19 and 20). Conducting polymers (Nos. 6–9) are in between, around $K_{s,th} = 100$ A h/kg, but polyaniline (No. 10) is essentially above this value and similar to the quinones (Nos. 11–14) due to their chemical relationship. The polydisulfides (e.g., No. 15) are also in this order. Electrochemical double layer capacitors (ECDLCs) are based on highly dispersed carbon black particles. Their specific capacities are calculated with the aid of Eq. (7), and values for a positive and negative charge (Nos. 17 and 18, respectively) are shown. Nos. 21–24 are some conventional inorganic active materials, for comparison.

In conclusion, the charge density (charge/mass) follows immediately from $K_{s,th}$ on the basis of Faraday's law. Optimization of this important figure of merit is achieved by minimization of the equivalent masses, $\sum M_i/z$ (Eq. (4)) or the molar masses M_W, M_A and M_S (Eq. (6)). Lightweight systems such as H_2, Li, Al, F_2, etc., seem to be ideal for a maximum $K_{s,th}$. It is a consequence even of these simple stoichiometric considerations alone that (in sharp contrast to other devices for energy conversion and storage such as electrical machines, combustion motors, heat and pressure storage equipment, traditional capacitors, and coils) a molecular understanding of the electrochemical processes is absolutely necessary for the development of rechargeable batteries (r.b.s). The view in terms of a black box with two current leads is inadequate.

1.2 Electron Transfer

Redox reactions can be regarded as a kind of elementary reaction for metal-free batteries

$$\mathrm{Red} \rightleftarrows \mathrm{Ox} + ze^- \qquad (12)$$

Two cases are distinguishable according to Fig. 3. The conventional one (a) holds for all molecular systems, which will be treated in Section 2, e.g., quinones or disulfides. The redox partner reacts in the *dissolved* state; this means at low concentrations for electrodes of the second kind. The reactant is positioned in the outer Helmholtz plane, or even in the inner Helmholtz plane, as shown for adsorbed molecules. One example is the quinone/hydroquinone redox reaction according to Eq. (13):

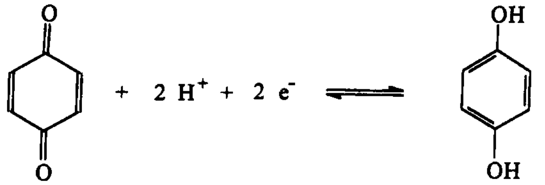

(13)

The quinoid reactant corresponds to Ox, *electrons* are tunnelling through the energy barrier ΔE (thickness d) at the phase boundary electrode (1)/electrolyte (2), and the counterions H^+ are provided from the electrolyte. The electrode is made of "inert" materials such as platinum, gold, or glassy carbon. This mechanism plays a major role in organic electrosynthesis, where the starting materials are provided mostly in the dissolved state. It holds also for fuel cells, but in organic batteries it is the exception rather than the rule.

A much more general mechanism for this kind of application is schematically represented in Fig. 3(b). A third phase (3) is inserted as an active material between the contact plane (1), made of metal or any inert metal-free material such as glassy carbon or carbon-black-filled polymers with a good electronic conductivity, and the

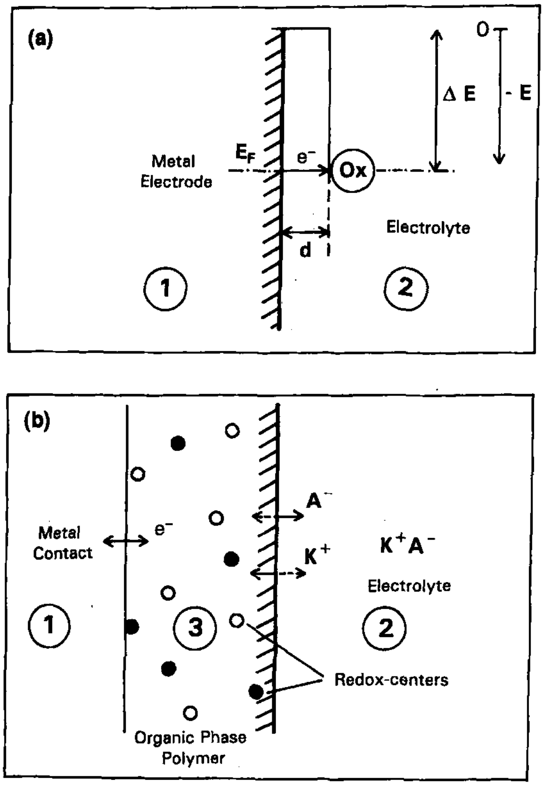

Fig. 3. Extrinsic (a) and intrinsic (b) electron-transfer reactions at a bare and a modified electrode. E_F = Fermi potential, ΔE = height and d = thickness of energy barrier. ①–③ are phase numbers. ○ and ● are oxidized and reduced redox centers in phase ③. A reduction is shown in both cases.

electrolyte (2). Electrons are provided from (1) in the case of reduction and are transported through (3) to the redox centers, which are distributed in this phase. The equivalent of anions A^- (cations K^+) cross the phase boundary (2)/(3). Again, transport processes in (2) and (3) proceed at the same time. The electrode has become now an *ion* electrode such as a metal electrode [16]. This kind of electrode is very common in organic batteries. Phase (3) provides a host lattice W for the insertion of ions. The whole process can be divided into two steps. Donor-electrodes ("n-type") are reduced via an *i*ntrinsic *r*edox (IR) process. It is followed by the *i*nsertion of a cation (Li^+, H^+) as a *c*ounterion (IC) to compensate the charge and to avoid space charges:

$$\mathrm{IR} : W_{OX} + e^- \rightleftarrows W^-_{red} \tag{14a}$$

$$\mathrm{IC} : W^-_{red} + Li^+ \rightleftarrows [W^- Li^+] \tag{14b}$$

$$\mathrm{OAR} : W + Li^+ + e^- \rightleftarrows [W^- Li^+] \tag{14}$$

Table 2. Graphite-type active materials.

Section[a]	System	H/C	Structure	κ[S/cm][b]
3	Graphite	< 0.01	Planar (sp^2) graphene layers	10^4 (10^5)
4	Fullerene	< 0.01	Globular molecular crystal	10^{-14} (≈ 1)
5	Carbon blacks	0.03	Limited graphene layers	Max. 20
6	Conducting polymers	0.5–1.0	Linear rigid chains	10^{-8}(10^{-3}–10^5)
7	Carbonaceous materials	0.1	Ladder- and band-type polymers	10^{-8} (10^{-3}–10)
10	Graphite oxide	0.1–1.0	Nonplanar (sp^3) C_2O layers	10^{-5}

(a) Section in which the material is discussed in this review.
(b) Specific electronic conductivity for undoped and, in parentheses, for doped materials.

The *o*ver*a*ll *r*eaction OAR becomes highly reversible, and is suitable for the reversible Li^+ storage of electric energy ("lithium ion batteries"). Accordingly, acceptor-electrodes ("p-type") are initially oxidized, and the charge is compensated by the insertion of anions. The overall reaction is written as:

$$W + A^- \rightleftarrows [W^+A^-] + e^- \qquad (15)$$

Graphite-type host lattices W are listed in Table 2. They are characterized by conjugated double bonds, $C=C$ in most cases, sometimes $C=N$, for instance as in polyaniline or phthalocyanines Nos. 3–5 in Table 2 are real graphite-type materials. Large polyaromatic molecules, forming a molecular lattice (cf. Fig. 6) also belong to this category. Aromatic compounds have formed a very extensive chapter in organic chemistry from the beginning. Planar π-systems, and in particular aromatic ones, are very important metal-free battery electrodes. In the last two decades nonplanar π-systems emerged as an interesting theme, but their relevance to battery electrodes is uncertain at the present stage. Entries 6 and 7 in Table 2 involve other systems, where heteroatoms appear in the overall structure, and where conjugated double bonds have lost their prevailing importance.

In conclusion, two types of metal-free battery electrodes have been defined in this section. Their combinations constitute metal-free rechargeable cells. Several types of such cells can be distinguished on the basis of the present considerations. They will be discussed in detail in Section 2 for quinone and similar cells, in Section 3 for all-carbon cells and in Section 6 for cells containing polypyrrole. In Section 9 a more general view of these aspects will be presented.

Of course, electron and ion transfer reactions imply many structural, energetic, and kinetic aspects. They will be treated in Sections 1.3–1.5.

1.3 Structures

An important macroscopic structural aspect concerns the arrangement and the contact design of the *current collector*, which has to supply the electrons from/to an external electrical circuit. These electrons are due to the driving redox reactions at or within the electrodes. Direct electron transfer between dissolved redox partners, e.g., in the

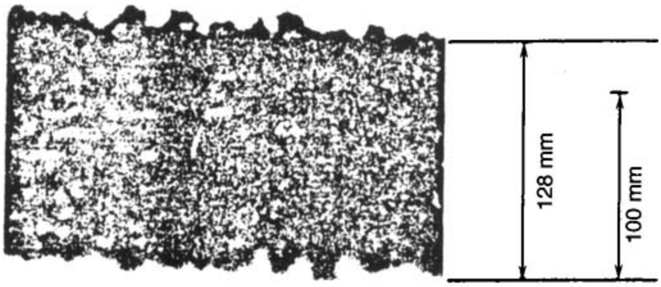

Fig. 4. Direct light micrograph (side view) of a platinum wire, diameter 1.00 mm, which is coated by a polypyrrole layer (standard conditions, d_n = 65μm). The layer is in the dry state (cf. [19]).

course of side-reactions, and corrosion reactions at the electrodes cannot provide any contribution to the external current. Effective systems with the highest disorder are inert current collectors, to be brought loosely into a (wet) contact with dissolved redox systems, dispersed particles, particle beds, or precompacted pellets made from particles. These designs are very simple, but they generally suffer from high ohmic and/or transport hindrances in most cases. The next step for an electrode design of higher-order current collector/active material is to introduce *porous electrodes*. The principles for inorganic [17] and carbonaceous systems [18] are well known. In the latter case, carbon aerogels (C-aerogels) are reported, which have an advantage over particulate systems: interparticulate resistivities are omitted.

Polypyrrole (PPy), as a standard example of a conducting polymer, is generally synthesized through film-forming anodic electropolymerization. The polymer layers are highly porous. Figure 4 shows such a PPy layer on a platinum wire with a diameter of 1.00 mm [19]. The uneven surface (in the side view) is due to the characteristic cauliflower structure. The real thickness d of the PPy layer can be easily derived therefrom. In comparison with the nominal thickness d_n for the compact material calculated with the aid of the experimental density and Faraday's law [20], appreciably higher d values were found, as shown by the correlation in Fig. 5 [19]. It must be concluded therefore that the material is highly porous. The degree of swelling (30 vol% change) is considered in this discussion. The high degree of porosity has interesting consequences with respect to the specific capacity [21, 22] and is one possible explanation for the high capacitive current in the cyclic voltammetry (CV) experiment for the doping/undoping process. Another explanation is that there is a superposition of redox processes along the potential axis [23], caused by the presence of appropriate redox centers in the solid. The findings of Bard et al. [24], according to which electrodes coated with PPy behave as the base material, provide a further argument for the highly porous material with pores which penetrate the entire substrate. In addition, the rest potential is for thin layers due to the basis electrode rather than due to the polymer itself for the same reason [25]. It should be mentioned that the density of PPy, which is reported in the literature (e.g., [26, 27]) to be 1.50 g/cm^3, is measured by the flotation method. Thus the pores are all filled by the mixed solvent, and closed pores are not present.

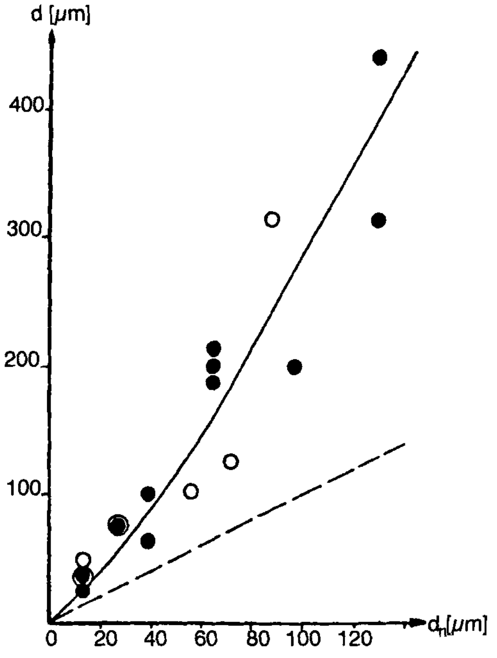

Fig. 5. A plot of the measured thicknesses *d* of the polypyrrole layers shown in Fig. 4, but in the wet state, vs. the nominal thickness d_n, which is calculated by applying Faraday's law. Current densities for electrodeposition: ○, 0.4 mA/cm^2; ●, 4 mA/cm^2. The 1:1 correlation is drawn as a broken line (cf. [19]).

The highest order in macroscopic electrode design is represented by *insertion electrodes*, according to Fig. 3(b). Redox reactions occur in the solid phase. The ions as redox partners form solid solutions. This does not exclude the possibility that in porous insertion electrodes both mechanisms are operative (cf. [28]).

The molecular structure of insertion electrodes can be divided into three categories:

1. layered (lamellar) lattices, e.g., graphite;
2. molecule lattices with leaf-type aromatic and heteroaromatic molecules, e.g., metal-free phthalocyanine;
3. molecule lattices with rigid chains, e.g., polypyrrole.

Category 2 continuously approaches graphite if the molecular weight of the molecules increases. This is also possible for category 3 by crosslinking (cf. Section 7). A schematic representation of these structural considerations is shown in Fig. 6. Graphite and polypyrrole (for categories 1 and 3) are represented as acceptor (A)-type insertion compounds and category 2 (metal-free phthalocyanine) as the corresponding donor (D)-type. The horizontal lines represent graphene layers or PPy chains. The sloping lines stand for a stack of leaf-type molecules. The volume expansion upon insertion of the counterions is demonstrated.

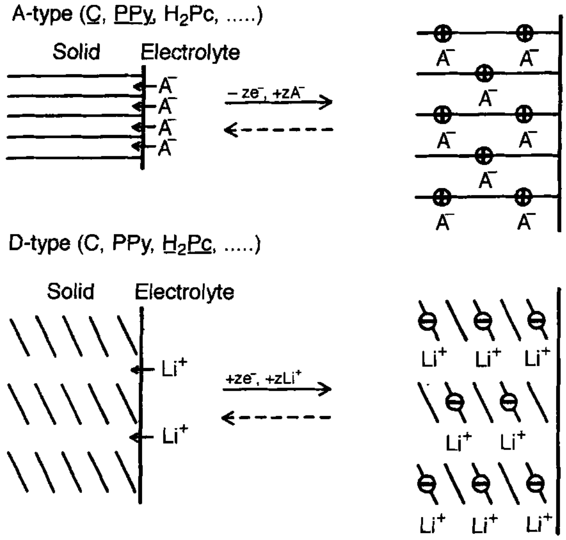

Fig. 6. Structural and stoichiometric aspects of graphitic and organic intercalation (insertion) compounds.

According to this mechanism, a "host lattice" can be established which accommodates ions as "guests", namely anions for oxidized host lattices and cations for reduced ones. In this case, the extrinsic electron transfer is changing to an intrinsic one according to Fig. 3(b). As was already pointed out in the previous section, ionic charges rather than electrons are now transferred at the electrode/electrolyte phase boundary. The counterions act merely to compensate the charge introduced in the organic layer and to avoid the formation of an energy-rich electric space charge. Nonstoichiometric insertion compounds from the acceptor type A or donor type D arise in this way. In the past, a great variety of inorganic systems, mostly of the donor type with Li^+ ions, have been described (cf. [29]). Their applications in secondary batteries have been reviewed by Desilvestro and Haas [30]. On the other hand, graphite and conducting organic polymers, mostly acceptor-type host lattices, have their own merits, as already discussed. The structural integrity in the course of electrochemical cycling and the high reversibility of the ion charge-transfer reactions at the electrode/electrolyte phase boundary seem to predestine these systems as ideal active materials for rechargeable batteries, as already foreseen by Whittingham [31].

A special structural aspect must be discussed in connection with the ECDLC. The importance of large specific surface areas A_s has already been stressed in Section 1.1, where the charge stoichiometry and the specific capacity of electroactive materials were presented cf. Eqs. (7) and (8). In principle, a "plate" of an atomic capacitor, carrying electronic charges, must be combined with another parallel plate, consisting of ionic charges. Their distance apart d is in the range of atomic dimensions. A first approach is the Helmholtz capacitor model of 1879, which correlates the charge density Q_A with the electric field strength $\Delta\varphi/d(\Delta\varphi =$ Galvani voltage) according to Gauss's law:

$$Q_A = \varepsilon \cdot \varepsilon_0 \cdot \Delta\varphi/d \tag{16}$$

If one assumes $\varepsilon = 6$ for the permittivity constant under these conditions, as usual, and $\Delta\varphi = 1$ V, Q_A is about 10% of the charge density which would be obtained if every surface atom carried just one elementary charge. Obviously this is due to a Coulombic repulsion. One way to overcome this limitation is to introduce surface-bound redox centers, where no free charges are established. This has already been developed in Section 1.1. All in all, a high specific surface area A_s is most important to utilize the potentialities of an ECDLC (cf. Eq. (7)). For graphitic carbon, the maximum value can be easily calculated, assuming spherical C atoms:

$$A_s = N_L^{1/3}\rho^{-2/3}M^{-1/3} \tag{17}$$

where $\rho = 2.26$, the density of graphite, $M = 12$ and $N_L =$ Loschmidt number. One obtains $A_s = 2170\,\mathrm{m^2/g}$. A geometric approach on the basis of graphene layers, $d_{C-C} = 0.139$ nm, leads to $1260\,\mathrm{m^2/g}$. Carbon black from industrial sources can reach $1500\,\mathrm{m^2/g}$. This demonstrates the possibility of approaching the upper theoretical limit. Dahn has shown recently [32] that fabrication is feasible on pyrolysis of organic precursors down to a critical $x = \mathrm{H/C}$ ratio of 0.2, corresponding to $y = 4$ shells (where benzene with zero shells has $x = 1$, coronene (Fig. 2) has one shell and $x = 1/2$; see fig. 7(a) etc). The remaining terminal C–H bonds stabilize the nanodisordered structure (Fig. 7(b)). The graphene layers carry $\mathrm{Li^+}$ from both sides. The specific capacity of the lamellar compound $\mathrm{LiC_6}$ (A) in ordered graphite is greatly enhanced in this way (B).

If precompacted carbon black pellets are charged and discharged galvanostatically in 10 M $\mathrm{H_2SO_4}$ [33], a capacity C_A is found from the slope of the charge/discharge curves

$$C_A = \frac{j}{\mathrm{d}U/\mathrm{d}t} \tag{18}$$

which corresponds to 80% of the theoretical value, calculated with the aid of Eq. (7), using the theoretical double layer capacitance for strong electrolytes, $C_{DL} = 20\,\mu\mathrm{F/cm^2}$. This result shows clearly that the real surface area of the nanoporous c.b. particles can be perfectly utilized [34]. A 1-mm layer of a c.b. with $A_s = 1500\,\mathrm{m^2/g}$, $\rho = 1\,\mathrm{g/cm^3}$, would lead to $C_A = 30\,\mathrm{F/cm^2}$. The same value is obtained for polypyrrole layers [19]; cf. Figs. 4–6. Electrolytic capacitors based on polyaniline have also been reported [35]. The in-plane order of such surfaces is much more complicated than for metal or graphite surfaces. Practical systems are mostly mixtures of carbon fibres, activated carbons, carbon blacks, polytetrafluoroethylene (PTFE); see for instance [36]. Further information about the double layer structure can be obtained by electrochemical impedance spectroscopy (EIS) [37] or solid-state NMR [38].

(a) **Fabrication**

Pyrolysis of monomer or polymer precursors under N_2 to 600 - 800 °C. Critical H/C-ratio = 0.2

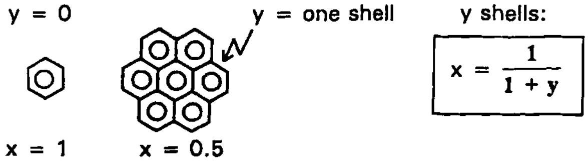
y = 0
y = one shell
y shells:
$x = \frac{1}{1+y}$
x = 1
x = 0.5

(b) **Electrochemical Equivalent m_e**

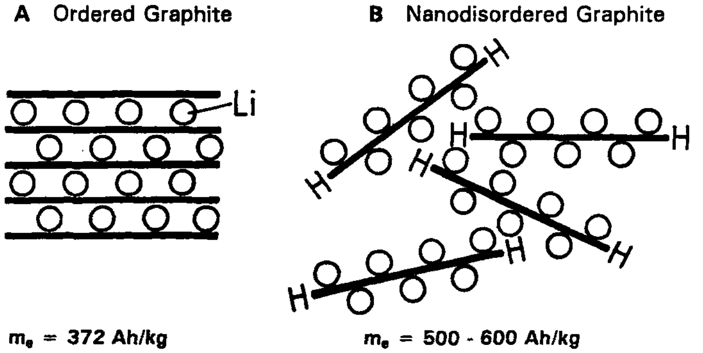
A Ordered Graphite
B Nanodisordered Graphite
Li
H
m_e = 372 Ah/kg
m_e = 500 - 600 Ah/kg

Fig. 7. (a) Definition of a critical H/C ratio x, e.g. $x = 0.5$ for coronene. After Dahn et al. [32]. (b) Nanodispersed graphites with inserted/adsorbed lithium.

1.4 Energetics

According to the Helmholtz model, the basic equation of electrochemical thermodynamics is as follows:

$$\Delta G = -zFU_0 = \Delta H - T\Delta S \tag{19}$$

where ΔG, ΔH, and ΔS are thermodynamic functions, namely reaction-free enthalpy, reaction enthalpy, and reaction entropy of the overall cell reaction, and U_0 is the equilibrium cell voltage. Maximum U_0 can be achieved with a large ΔG and $z = 1$.

According to the Nernst view, the potentials of the positive and the negative electrodes, respectively, must be strongly separated for this purpose:

$$U_0 = U_{R,0}^{+} - U_{R,0}^{-} \tag{20}$$

where U_R is the potential vs. a reference electrode. The Nernst equation yields the dependency on the activity a. In the case of a dissolved redox system (cf. Eq. (12)), the electrode potential is given by:

$$U_{R,0} = U_{R,00} + \frac{RT}{zF} \ln \frac{a_{ox}}{a_{red}} \tag{21}$$

where $U_{R,00}$ is the standard potential. This leads to a strong variation of the potential upon conversion of the system according to Eq. (12). If α is the degree of oxidation, the last quotient in Eq. (21) can be substituted by $\alpha/(1-\alpha)$. On the other hand, for electrodes of the second kind, both a_{ox} and a_{red} are nearly constant for an insoluble metal salt/metal system, in general for multiphase systems, and $U_{R,0}$ is nearly independent of the conversion of the active material. The discharge curve is "hard." This is a favorable situation for batteries.

For insertion electrodes according to Eq. (5), with y = degree of insertion (e.g., oxidation or reduction), another form of the Nernest equation is valid:

$$U_{R,0} = U_{R,00} + \frac{RT}{F} \ln\left(\frac{y}{1-y}\right) \tag{22}$$

At least for small y values, the potential is a logarithmic function of y. As a consequence, the electrode potential changes significantly on charging the electrode. The discharge curve becomes "soft," which is an unfavorable situation for batteries. This leads to straight lines in the semilogarithmic plots, shown for charge curves in Fig. 8. Examples (1)–(4) are due to acceptor-type compounds, but (5) and (6) hold for the donor type. The slope is greater than RT/F in any case, due to the choice of the stoichiometric reference. Deviations from the simple Eq. (22) are attributed to Coulombic interactions of the charged moieties [44–46].

Anodic charge of graphite leads to graphite intercalation compounds (GICs) of the A type. The formation of "stages" can be rationalized by the model of Rüdorff and Hofmann of 1938 [47], according to which the intercalation of anions in the solid proceeds in steps. The process begins with high stage numbers n, it goes further to lower ones, and it finishes at $n = 1$, when all interlamellar gaps are occupied. The number of unoccupied gaps between the graphene layers is $(n-1)$. The in plane order does not change (cf. Fig. 14). Along the charge curve, potential ramps are observed due to the alternating formation of one- and two-phase regions in the solid [48]. Further aspects of GICs, especially the peculiar dependency of $U_{R,0}$ on the acid concentration in the case of strong aqueous acids as electrolytes, will be discussed in Section 3.1 (cf. Fig. 18). The graphite behavior is an exception, however, for all the other insertion electrodes exhibit continuous charge and discharge curves.

The standard potentials $U_{R,00}$, which hold for $a_{ox} = a_{red}$ in Eq. (21) or $y = 1/2$ in Eq. (22), depend directly on the chemical nature of the compound. Consequently, they are linked to the corresponding electronic energy levels derived from the molecular orbital (MO) theory. A linear dependency between $U_{R,00}$ and the corresponding eigenvalue coefficients for the lowest unoccupied molecular orbital (LUMO) or highest occupied molecular orbital (HOMO) energy levels was found

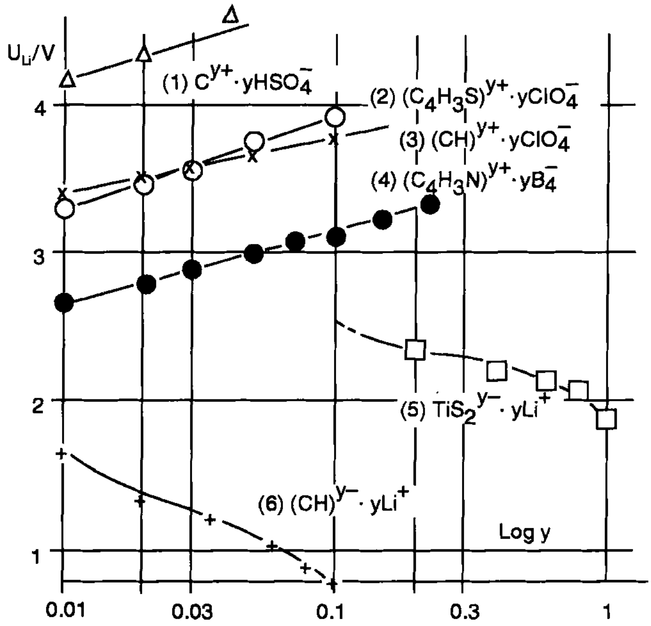

Fig. 8. Dependence of U_{Li} (equilibrium potential vs. Li) on the logarithm of the degree of insertion y of a variety of insertion electrodes. Sources of data: (1) [39]; (2) and (3) [40]; (4) [41]; (5) [31, 42]; (6) [43]. (1)–(4), Acceptor type; (5), (6), Donor type.

[49, 50]. The band structure of the solids can be derived from the MO model for polycondensed aromatic hydrocarbons. Parker [51] has pointed out that the HOMO and LUMO levels converge to a constant "middle potential" with increasing degree of condensation, and that they finally coincide with the Fermi level E_F of graphite (Fig. 9). The density of energy states in graphite is zero at E_F, and this is the reason for the relatively low electronic conductivity in comparison with metals. Intercalation of anions (cations) leads to a removal (injection) of electrons.

Recently, the chemical graph theory was systematically developed to characterize and evaluate polyene molecular structures [52], i.e., those compounds which play a central role in battery application. Especially for carbon electrodes, the role of inserted heteroatoms such as nitrogen was systematically investigated by Ukrainian workers [53, 54]. Such developments may adopt a high importance in future battery work.

Finally, a compilation of the relevant equilibrium potentials of active materials is shown in Table 3. The inorganic systems are arranged on the left-hand side, carbon, graphit, and organics on the right-hand side. It becomes evident that there are no fundamental differences concerning the possible range of potentials in the two cases. Perhaps it is easier to achieve negative potentials with the aid of metals that are not "noble." Some inorganic host lattices (Li/Mn spinel $Li_xMn_2O_4$, CoO_2, TiS_2, graphite have the same range of potentials (about 0.5 V) as intrinsically conducting polymers due to the insertion/release process (cf. Eq. (22)). In conclusion, such a table is of

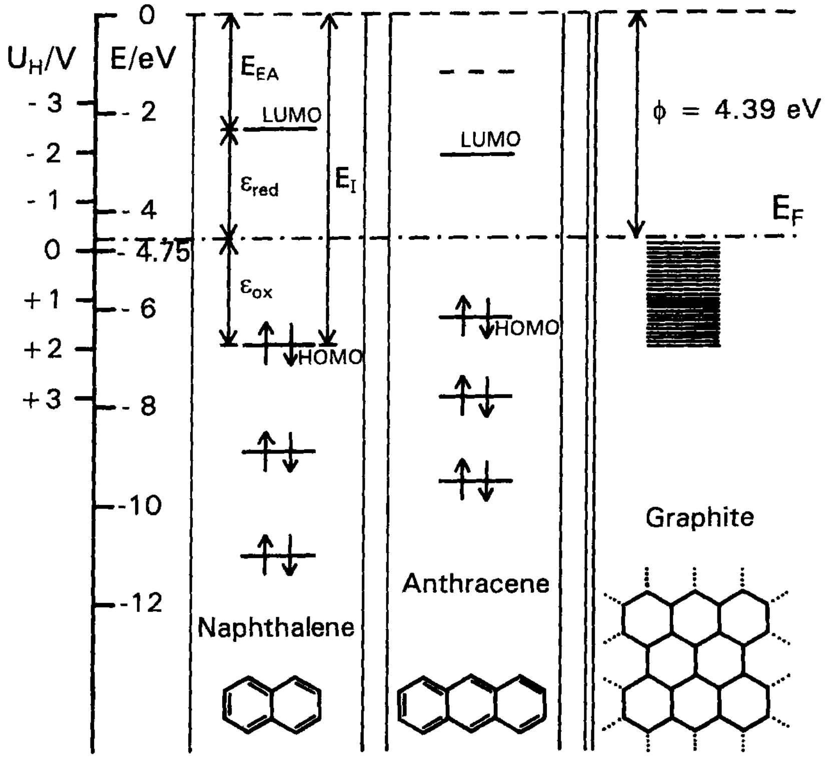

Fig. 9. Energy levels in aromatic radical cations and radical anions and in p- and n-doped graphite.

high practical value for an initial selection of active materials to be combined in a rechargeable battery with a considerable cell voltage.

1.5 Kinetics

Pure charge transfer for tunneling electrons (cf. Fig. 3(a)) in the case of dissolved aromatic molecules must be regarded as a very fast process. The Marcus theory provides the following equation for the heterogeneous rate constant (cm/s) with Z as the frequency of infra-red oscillations:

$$k_{\text{het}} = \kappa \exp\left(-\lambda/4kT\right) \cdot Z \cdot d_{\text{H}} \tag{23}$$

The first two factors are for a correction of the maximum value $Z \cdot d_{\text{H}}$ to be expected if an oscillating redox ion in the outer Helmhotz plane, $Z \sim 10^{13}\,\text{s}^{-1}$ (infrared) at a distance d_{H} (10^{-8} cm), the thickness of the Helmholtz layer, leads to an electron tunneling event for every oscillation. Thus K_{het} would become maximally 10^5 cm/s. The first correction factor is the permeability of the potential barrier at the electrode,

Table 3. Standard electrode potentials $U_0[V]$ (vs. SHE) of active materials in rechargeable batteries.[a]

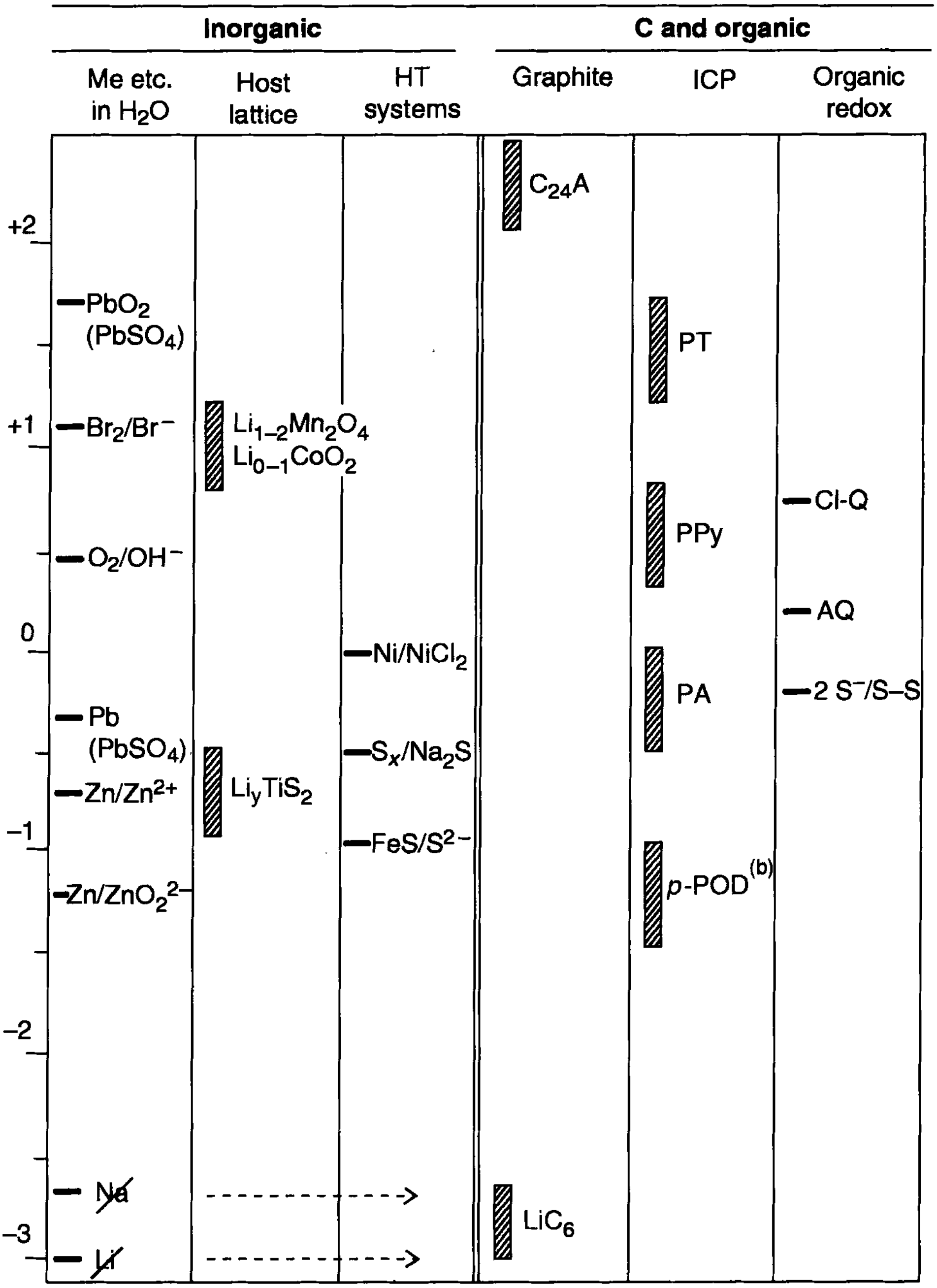

---

[a] The hatched rectangles indicate the potential range ≈ 0.5V for insertion compounds.

[b] p-POD = poly(phenyloxadiazol)

$\kappa \sim 10^{-2}$. The second correction factor is due to the reorganization energy λ of the solvate shells of the redox ions; λ is in the order of 0.5–1 eV. This factor then becomes 10^{-2} to 10^{-4}. Thus k_{het} drops in reality to 10–0.1. Most of the measured rate constants for aromatic systems (molecule/radical ion) are of this order of magnitude [55]. The molecular interpretation of such high rates is a stabilization of the radical ion in an (extended) aromatic system.

Deviations from this ideal case, which is not very characteristic for battery electrodes, are attributable to three reasons:

1. The reactive radical ions [56] undergo irreversible chemical follow-up reactions (ec mechanism). The whole electrode process becomes irreversible. In Section 2 it is shown that this is true at least for the formation of one or two covalent bonds containing at least one C atom, e.g., C–C or C–X, X = H, O, N, etc.
2. The electrode process is ion transfer rather than electron transfer. This is true for all insertion electrodes (cf. fig. 3(b)).
3. A further contribution to irreversibility arises if the inserted counterions are not inert, but have some nucleophilic (anionic) or electrophilic (cationic) behaviour. So at least partial covalence is possible. The polarons are not entirely free; the electronic conductivity decreases [57].

The charge-transfer kinetics of an electrochemical electrode can be formally treated on the basis of the Butler–Volmer equation. The overvoltage η_{CT} is then given by

$$\eta_{\text{CT}} = \frac{2.30RT}{(\alpha zF)} \log \frac{j_{\text{i}}}{j_0} \tag{24}$$

for an anodic polarization in the Tafel region, where α is the charge-transfer coefficient and j_0 stands for the concentration-dependent exchange current density. In practicle, the standard exchange current density j_{00} is found for battery electrodes in the range of 1 (low-melting metals) to 10^{-4} A/cm^2 (oxides), corresponding to $k = 10^{-2}$ to 10^{-6} cm/s. That is appreciably below the ideal data for aromatic radical ions, mentioned above.

The reversible main reaction in a rechargeable battery, characterized by the current density j_{m}, can be accompanied by side-reactions with the exchange current densities (c.d.) $j_{\text{s},1}$, $j_{\text{s},2}$. The current efficiency (c.e.) can be defined as

$$\gamma_i = \frac{j_i}{j} \tag{25}$$

where j is the overall current density and j_i the partial current density for the electrode reaction i. For the above mentioned main reaction, c.e. becomes

$$\gamma_{\text{m}} = \frac{j_{\text{m}}}{j} \tag{26}$$

and must be maximized. But for the side-reactions a minimization of γ_s,

$$\gamma_{s,i} = \frac{j_{s,i}}{j} \tag{27}$$

is absolutely necessary to achieve a long-term cyclability. Besides chemical analysis and the spectroscopic tools, a continuous method at the rotating ring/disk electrode was found recently [58, 59]. The disk is an insertion electrode in aprotic electrolytes. While the insertion process (anions or cations) does not involve any protons (cf. Eq. (5)), protons are injected in the case of irreversible anodic oxidation of organic (solvent) molecules "RH_2," according to

$$RH_2 \rightarrow R + 2H^+ + 2e^- \tag{28}$$

These protons can be reduced at the platinum ring [59]. The concept of individual current efficiencies for charge and discharge, λ and ε, for single electrodes will be treated in Section 9.

As the electrode process is a heterogeneous one, mass-transport steps must occur before both hand and thereafter. The rate constant k_T is simply defined according to Fick's first law as

$$k_T = \frac{D}{L} \tag{29}$$

where D is the diffusion coefficient and L is the transport length, e.g., the thickness of the Nernst diffusion layer δ_N. For stirred liquid electrolytes, D is about $10^{-5}\,\mathrm{cm^2/s^1}$, and L is about 10^{-2}–10^{-3} cm. Then k_T becomes 10^{-2}–$10^{-3}\,\mathrm{cm/s^1}$. For solids, however, D values entrace a wide range from 10^{-5} to $10^{-15}\,\mathrm{cm^2/s}$ [6, 60]. A diffusion overvoltage can easily be defined on this basis:

$$\eta_D = \frac{2.30\,RT}{zF}\log\left(1 - \frac{j}{j_{\mathrm{lim}}}\right) \tag{30}$$

Hence η_D becomes zero for $j = 0$, but $-\infty$ for $j \rightarrow j_{\mathrm{lim}}$. For stagnant electrolytes, L becomes time-dependent according to Fick's second law:

$$L = \sqrt{2Dt} \tag{31}$$

A diffusion layer grows into the bulk of the electrolyte phase. The practical solution of this transport problem is use of porous electrodes [17, 18]. A quantitative treatment of the problem of current density distribution is given on the basis of electrotechnique [17, 61] and of electrochemical kinetics [62, 63]. A simple but very useful model, assuming that the transport length L is about the pore diameter d_p, was given by Vetter [64]. This model is schematically represented in Fig. 10(a) for the case of an electrode of the second kind.

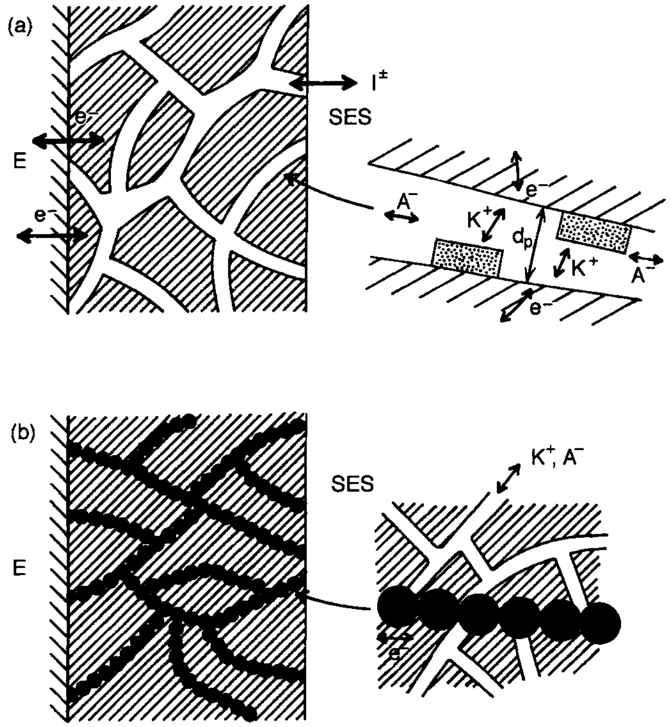

Fig. 10. Models for battery electrodes: (a) porous electrodes; (b) carbon-black-filled electrodes.

In the case of insertion electrodes, transport occurs exclusively in the solid phase, which is a solid solution of the guests in the host lattice. It is normally much slower [44–46]. However, in practice, insertion electrodes are porous as well, and the major proportion of transport proceeds in the electrolyte-filled pores [28]. A general consideration of porous electrode structures has already been provided in Section 1.3. Porous electrodes have a long tradition in battery science [3, 5, 6, 10, 17, 28, 30]. Conventional inorganic battery electrodes are porous electrodes, and an appreciable portion of the manufacturing costs is due to the processes for the attainment of porosity (milling, "formation", etc.) Examples for metal-free active materials are discussed in detail for polypropylene-bound natural graphite (CPP-Carbon/Polypropylene) in Section 3.1, for polypyrrole in Section 6.2 and for C-aerogels in Section 7. All such electrodes can be characterized by a practical figure of merit, called the active mass utilization μ [8–10, 17]:

$$\mu = \frac{K}{K_{s,th}} \tag{32}$$

The theoretical maximum values are given by Eqs. (4), (6) and (7), respectively. K depends on many parameters (cf. Eq. (1)). One of the most important is the nominal thickness d_n [20] of the active layer. If is possible to calculate the thickness dependency of μ (cf. [65]). The result is a $\mu = K \log d_n$ function, which was indeed found experimentally [28,158].

Charge transport is absolutely necessary as well. According to Ohm's law, the voltage drop ΔU in a layer of thickness L and of resistivity ρ is given by

$$\Delta U = \rho \cdot L \cdot j \tag{33}$$

This equation corresponds to Eqs. (24) and (30). No problems arise in the case of metals, PbO_2, or graphite with a high electronic conductivity. Figure 10(a) represents this situation well. However, it is highly problematic for poorly conducting materials such as $PbSO_4$, $Ni(OH)_2$, anthraquinone, or de-doped conducting polymers. If the reaction product is electronically conducting again, the process starts at the current collector, and it proceeds from there to the porous electrode/electrolyte phase boundary. However, a generally adopted solution of this problem is the admixture of about 5–30 wt% carbon black or special graphite powders (Lonza). According to Fig. 10(b), chains of carbon black or graphite particles, present at a concentration above the percolation threshold, do provide electronically conducting pathways. Electrolyte-filled pores, or solid electrolyte properties of the solid phase, are necessary again.

Of course an appropriate ionic conductivity in the active layer is important as well. Organic solid polymer electrolytes (SPEs) provide only $\kappa = 0.1\text{–}1$ mS/cm, and liquid organic electrolytes $\kappa = 1\text{–}10$ mS/cm. But aqueous electrolytes have much better values in the order of 10–100 mS/cm. One of the consequences of the low ionic conductivities of organic electrolytes is a minimization of transport length L (cf. Vetter's model [64]), or the capillary gap cell in organic electrosynthesis [4].

Heat transport in connection with the removal of reversible heat $T\Delta S$ and irreversible Joule heat, may become an additional problem. In contrast to metals, organics and polymers (or at least the conventional, insulating ones) suffer from relatively low specific heat conductivities. Again, graphite pathways and minimized L improve this unfavorable situation to some extent.

In conclusion, the cell voltage U_{cell} for a battery is given by

$$U_{\text{cell}} = U_0 - \sum_i \eta_i(j, d, P, \rho \cdots) \tag{34a}$$

The overvoltages η_i must be minimized, for all of them enter as subtrahends into this equation. A strong need for

- a minimization of j, current density, and
- a minimization of L, transport length

therefore exists. This is possible with the aid of porous electrode structures. Otherwise the practical cell voltage U_{cell} becomes exceedingly low, and the heat generation leads to an intolerable heating up of the cell.

A general kinetic aspect of high technical relevance, especially for electrotraction, is the rate capability of the rechargeable cell. Figure 11 shows a treatment in terms of

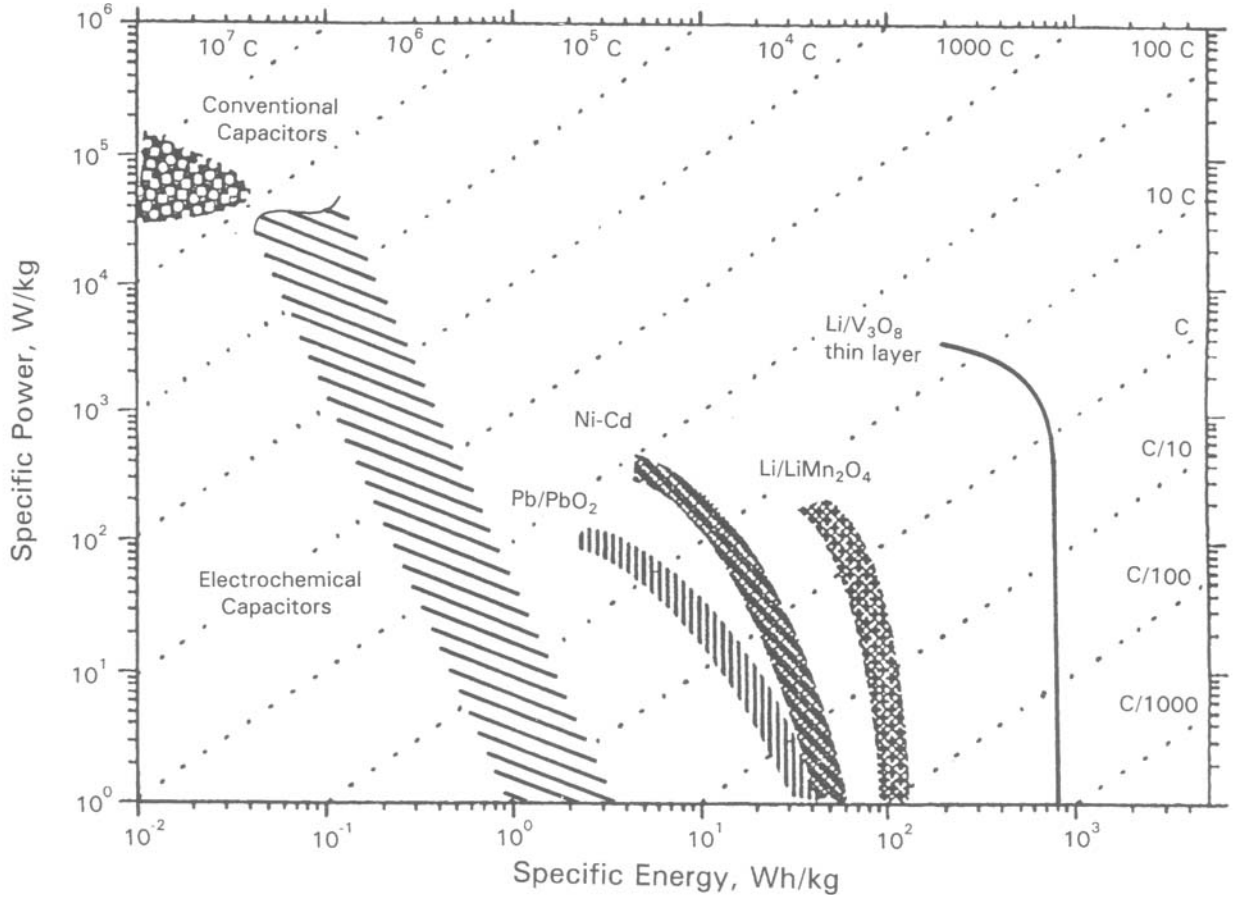

Fig. 11. Ragone functions for conventional batteries, lithium batteries, and capacitors. After Owens et al. [66].

a so-called Ragone plot [66]. Electrochemical capacitors have low specific energies, but allow for high power densities. Thin-layer Li/V_3O_8 cells lead to promising high energy densities and a high specific power at the same time [66]. The conventional accumulators are in between.

2 Reversible Electroorganic Reactions

Irreversible electrode reactions predominate in preparatively oriented organic electrochemistry [4, 67]. Examples are the cathodic hydrodimerization of acrylonitrile to yield adiponitrile:

$$2\,CH_2{=}CHCN + 2\,H_2O + 2\,e^- \rightarrow NCCH_2CH_2{-}CH_2CH_2CN + 2\,OH^- \qquad (34)$$

and the anodic epoxidation of propene with formation of propylene oxide:

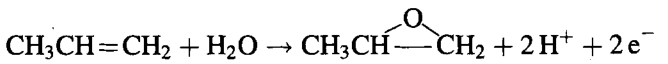

$$CH_3CH{=}CH_2 + H_2O \rightarrow CH_3CH\overset{O}{\text{—}}CH_2 + 2\,H^+ + 2\,e^- \qquad (35)$$

In general, the formation or cleavage of covalent bonds with at least one C atom as C–C (Eq. (34)), C–O (Eq. (35)), C–N, or C–H are strongly irreversible steps. However, reversible electrode reactions are needed in batteries, where two independent redox systems are operative at the two electrodes:

$$\text{Positive}: \mathrm{Red}_+ \underset{\text{disch}}{\overset{\text{ch}}{\rightleftarrows}} \mathrm{Ox}_+ + ze^- \qquad (36a)$$

$$\text{Negative}: \mathrm{Ox}_- + ze^- \underset{\text{disch}}{\overset{\text{ch}}{\rightleftarrows}} \mathrm{Red}_- \qquad (36b)$$

Such reversible organic redox systems are well known, but they are the exception rather than the rule. This section involves low-molecular-weight organic moieties forming a dissolved redox system or a molecular lattice in contrast to the host lattices composed of extended graphene layers (for graphite) or rigid polymer chains with conjugated double bonds (for polypyrrole or polyaniline). Some cases are in between, such as the leaf molecules of the phthalocyanines, as already pointed out in Section 1.3.

Prominent examples are the redox pairs *o*- or *p*-quinones/hydroquinones, the corresponding quinoneimines, the diimines and the azobenzenes and disulfides [68]. v. Stackelberg [69] has pointed out that the exclusive formation or cleavage of O–H, N–H, S–H, or S–S bonds is a necessary precondition for reversible organic redox partners. This can be clearly recognized in the case of the quinone/hydroquinone redox reaction (cf. Eq. (13)). Only O–H bonds are formed or cleaved. In contrast, in the case of the acetone/isopropanol redox system, O–H *and* C–H bonds participate,

Table 4. Standard potentials $U_{H,O}$ (vs. SHE) and theoretical specific capacities $K_{s,th}$ of molecular organic active materials.

Group	Organic molecule[a]	$U_{H,O}$[V]	$K_{s,th}$ [Ah/kg]	Electrolyte[b]	Remarks
Quinones	(2,3-Dicyano-5,6-dichloro-quinone)	1.27	236	A	unstable
	2,3,5,6-Tetrachloroquinone = chloranil (**A**)	0.67	218	A	
	Anthraquinone (**B**)	0.15	258	A	
	Anthraquinone (**B**)	−0.60	258	NA	
	Napthacene-quinone (5, 12) (**C**)	−0.32	208	A	unstable
N-Containing compounds	*m*-Dinitrobenzene	−0.20	1920	A	Irreversible
	N-Heptylviologen (**D**)	−0.33/−0.44	119	A	
	H_2Pc/Li^+(donor) (**E**)	−1.40	290	NA	Film
	CuPc/ClO_4^- (acceptor) (**E**)	1.18	18.2	NA	Film
	CuPc/ClO_{+}^{-} (acceptor) (**E**)	1.22	39.7	NA	Solution
	CuTPP/ClO_4^- (**F**)	1.30	23.5	NA	Film
	CuTPP/Clo_4^-(**F**)	1.15	34.5	NA	Solution
S-containing compounds	Cysteine/cystine	0.1	221	A	
	Thiourea/formamidine disulfide	0.42	353	A	
	Dithio compound (**G**)	−0.5	388	NA	
	Dithio compound DMcT (**H**)	±0	357	NA	
Radical ions	Perylene radical cation	−0.5	44	NA	

[a] Formulae (**A**)–(**H**) are shown below

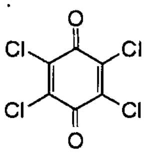

A

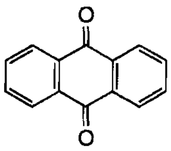

B

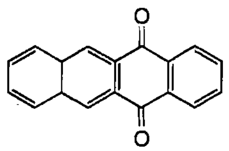

C

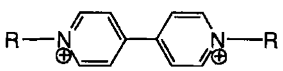

D

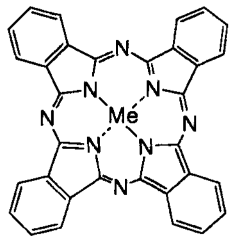

E

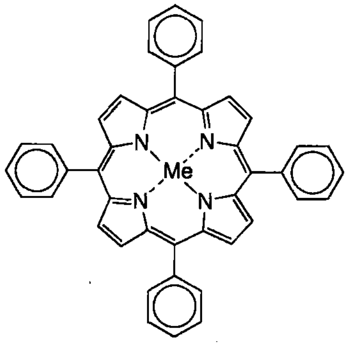

F

$(\text{—}SCH_2CH_2\text{—}O\text{—}CH_2CH_2S\text{—})_p$

G

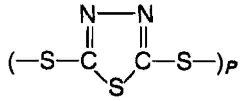

H

[b] A, aqueous; NA, nonaqueous.

turning the whole process back to be irreversible again:

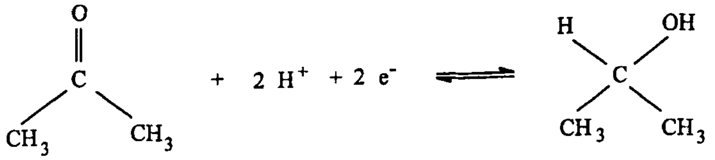

(37)

The redox potentials of quinones were measured [70] at an early stage. The stable systems fall in a voltage range of only about 0.5 V (Table 4). In the past, some attempts to build a quinone accumulator were undertaken by Sandstede et al. [71–74] and by two other groups [75, 76–78]. The stable combination chloranil/anthraquinone could be cycled in dilute sulfuric acid or in HCl:

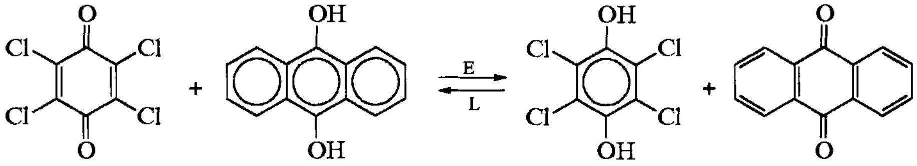

(38)

However, the voltage was only 0.52 V, and the theoretical energy density was relatively low, 61 W h/kg. Anthraquinone (AQ) was also combined with a PbO_2 positive [79] and a graphite (GIC)-positive [80]. The nonconducting active materials were intensively mixed with carbon black to achieve quantitative utilization of active mass [81]. In the case of the very poorly soluble anthraquinones, a Li^+ insertion in the solid state may be possible. Polarographic investigations in $LiClO_4$/DMF of dissolved AQ establish a reduction potential for

$$AQ + 2\,Li^+ + 2\,e^- \rightleftarrows AQLi_2 \tag{39}$$

of −0.6 V vs. SHE [82].

Unfortunately anthrahydroquinone is not very stable under acid conditions, which are needed for a reversible cyclization of the benzoquinone derivatives. There is an early preparative observation on the rapid formation of anthraquinone (AQ) **3** and anthrone (Ant) **4** from anthrahydroquinone (AQH_2) **1** in cold concentrated sulfuric acid [83] according the overall reaction

$$2\,AQH_2 \longrightarrow AQ + Ant + H_2O \tag{40}$$

A kinetic evaluation in 85% H_2SO_4 [84] led to a mechanism according to Fig. 12, which is characterized by a protonation step and a hydride transfer. Oxanthrol **2** is a tautomeric intermediate. The rate constants for this second-order reaction are, for 1, 5, and 15 M H_2SO_4, 0.9×10^{-3}, 1.9×10^{-3}, and 30×10^{-3} l/mol h, respectively [33, 80, 85]. The starting concentrations for these measurements with dissolved molecules were 6.0 mM. Due to its very low solubility in dilute sulfuric acid, the concentrations of the anthraquinone/anthrahydroquinone redox system would be

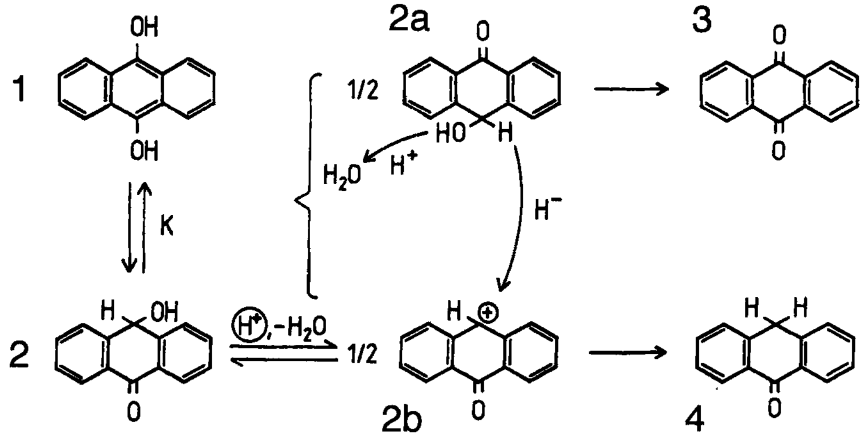

Fig. 12. Mechanism of the acid-catalyzed disproportionation of anthrahydroquinone **1** to anthraquinone **3** and anthrone **4**. Compound **2** is the tautomer, oxanthrol.

smaller by a factor of 10^{-2} for an electrode of the second kind. Therefore, the half-lifetime of about 30 h would increase to $> 10^5$ h. So anthraquinone is acceptable, and it already is an industrially important intermediate, in contrast to chloranil. While benzohydroquinone is decomposed in irreversible side-reactions in the alkaline region, this does not seem to be the case for anthrahydroquinone. The redox system is stable at high pH values [86]. The quinone electrode is an electrode of the second kind. The electrochemical conversion proceeds via dissolved organic molecules. Vetter's model [64] is applicable. Another viewpoint is reported in the literature, according to which the redox mechanism is some kind of solid-state reaction [87].

Nitrogen-containing organic compounds provide another interesting group. Aromatic nitro compounds such as *m*-dinitrobenzene are characterized by extremely high theoretical capacities, taking into account the reduction $RNO_2 \rightarrow RNH_2$ with 6 F/mol (cf. Table 4) [88]. Unfortunately, reoxidation to the nitroaromatic is not possible, but a polymer is formed. Nevertheless, these organic compounds were considered to be useful as positive electrodes for primary cells with magnesium. Addition of carbon black improved the rate capability up to 1 A/g [89]. A systematic investigation of aromatic and aliphatic nitro compounds as active materials in batteries was undertaken by Glicksman and Morehouse [90–93]. Aromatic compounds were also used for lithium primary batteries ($LiClO_4$/propylene carbonate) [94]. Methylene Blue showed the largest energy density, of 365 W h/kg.

The viologens are alkyl derivatives of the 4,4′-dipyridylium dication. The one- or two-electron reduction leads to a radical cation or a diamagnetic product, respectively [95]. This type of redox reaction has a good reversibility. In the phthalocyanines (PCs) and other N_4-chelates, the nitrogen is also a component of the ring system. Donor-type Li^+ insertion compounds of metal-free phthalocyanines were formed reversibly in $LiClO_4$/PC with up to six cations [96]. At the anode, copper phthalocyanine (CuPC) inserted reversibly $y = 0.42$ ClO_4^- anions/mol [97]. For copper tetraphenylporphyrin, $y = 0.65$ was found [98] (cf. Table 4). Composites of these

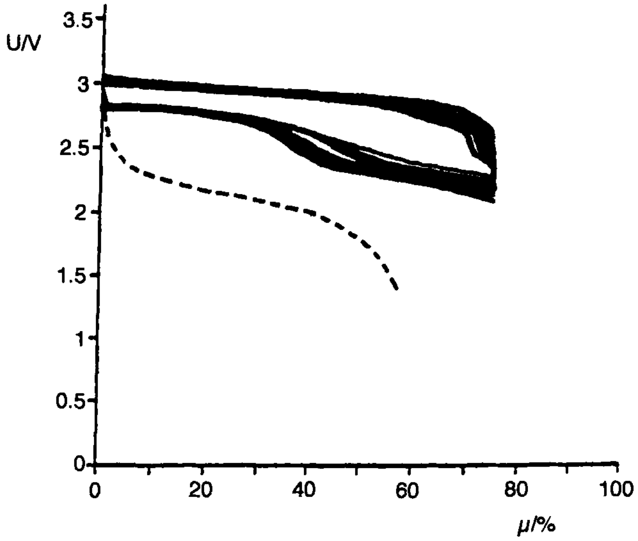

Fig. 13. Cyclic charge/discharge for the first 83 cycles of an Li/PEO + $LiN(SO_3CF_3)_2$/poly-(2,5-dimercaptodithiazole) cell at 80 °C. After de Jonghe et al. [102]. For comparison: – – – , Li/PEO/TiS_2, 80 °C.

insoluble, powdery materials with polymer binders exhibited a normal redox capacity beyond a concentration of 30 wt% [99], which is due to the percolation threshold.

Organic sulfur compounds are also able to form reversible redox systems. Mercaptans (monosulfides) are oxidized to disulfides according to

$$2R-SH \rightleftarrows R-S-S-R + 2H^+ + 2e^- \qquad (41)$$

Cysteine [100] and thiourea [101] are examples (cf. Table 4). The S–S bond can be easily cleaved at the cathode. Even more interesting are bifunctional sulfides, which can be anodically transformed to polymer disulfides [102–105]:

$$p\,^-S-X-S^- \rightleftarrows (-S-X-S-)_p + 2pe^- \qquad (42)$$

These systems work according to a novel, very interesting mechanism: the polymer chain is depolymerized cathodically through the quasireversible cleavage of the S–S bond. In the back-reaction the bifunctional α,ω-disulfides are anodically polymerized again (cf. Eq. (42), where X means a bifunctional organic block unit). The combination with a lithium negative electrode and the application of a polymer solid electrolyte (poly (ethylene oxide); PEO) has been developed. Figure 13 shows that the active mass utilization μ approaches 80% for an electrode which contains 25% carbon black, a value similar to that for quinones. This electrode is superior to a TiS_2 positive electrode with respect to μ as well as the potential level (the broken curve in Fig. 13). Due to the sluggish redox kinetics, an elevated temperature was employed. Typical examples are 2-mercaptoethyl ether and dimercaptodithiazole (DMcT). The corresponding polymer structures **7** and **8** are shown in Table 4. The redox potentials are −0.5 and 0 V vs. SHE, respectively. The theoretical specific capacities are 394 and 362 A h/kg (cf. Table 4). Cyclovoltammograms of the redox reaction according to Eq. (42) exhibit some irreversibility; the redox peaks have a separation of more than 1 V. A typical intermediate is the dimer. Some tendency to overoxidation of the polymer was found in addition [106]. However, improved rate capabilities were obtained by intensively mixing powders of DMcT and polyaniline (PANI), which acts as a redox mediator [107]. A further improvement was achieved by painting solutions of DMcT and PANI in NMP (*N*-methylpyrrolidone), a dark and viscous "ink", onto the base electrode. After drying, 80% of the theoretical capacities (as a sum of both individual $K_{s,th}$ values) were found [108]. A lithium cell based on this composite electrode had a practical average discharge voltage of 3.4 V, and an energy density of 900 Wh/kg could be calculated. It was also possible to reactivate spent PANI by cycling with DMcT [109]. The role of PANI could be also played by polypyrrole to some extent [110, 111].

Sodium sulfide/sodium polysulfide in aqueous systems can be cycled according to:

$$S_4^{2-} \rightleftarrows 2\,S_2^- \xrightleftharpoons{6e^-, 4H_2O} 4\,HS^- + 4\,OH^- \tag{43}$$

The standard potential is −0.52 V vs. SHE in this case [112].

Radical ion salts. are potential candidates for a battery application. The initial step in organic electrochemistry is usually pure electron transfer between dissolved or adsorbed molecules and the inert electrode. Radical ions are formed as typical intermediates, e.g., at the cathode a radical anion:

$$X + e^- \rightleftarrows X\cdot^- \xrightarrow{\varepsilon} \cdots \rightarrow P \tag{44}$$

These species remain in solution or they are adsorbed and undergo usually irreversible follow-up reactions with electrophiles ε to yield finally the product P. This conventional type of electron transfer is called "extrinsic" in Fig. 3(a). However, the reactivity of radical ions is weakened by using large aromatic molecules, and in the absence of any strong electrophilic or nucleophilic reaction partner the counterions merely associate, and the dissolved radical ion salt accumulates. One can even go a step further: using a relatively nonpolar solvent, the radical ion salt is electrodeposited as a salt layer. Examples of this so-called "electrocrystallization" are furnished by naphthalene [113] or perylene [114]. In both cases, a 2:1 molecular charge stoichiometry is established, e.g., $[(\text{perylene})_2]\cdot^+A^-$(cf. [115,116]). An application in batteries is conceivable, according to

$$2\,C_{20}H_{12} + ClO_4^- \rightarrow [(C_{20}H_{12})_2]^+ClO_4^- + e^- \tag{45}$$

(cf. Table 4). The salts form molecular stacks of ions; sec Fig. 6. Fluoranthene is another example for an arene [117], and numerous aromatic compounds are reported analogously to form radical-cation [118, 119] and radical-anion [120] salts. More recently, Marks and his group have extended this method of electrodeposition to the metal phthalocyanines [121, 122]. It should be mentioned, that charge-transfer complexes also involve radical ions as a limiting case. Phenazine/iodine [123] and poly(vinylpyridine)/iodine [124] are two systems which were discussed at an early stage for battery application. Tetracyanoquindimethane (TCNQ) salts involve radical anions, TCNQ$\cdot^-$, and have been used as polymer composites [125, 126]. It should be mentioned finally that application of the radical ion salts in batteries is severely hampered due to their solubility in polar solvents. However, they provide a better understanding of the systems with real intrinsic redox properties. The electronic conductivity of these "organic metals" can be rationalized [127]. If the molecule becomes larger, e.g., for polyacetylene or polycondensed aromatic hydrocarbons, insolubility will be the consequence, and a solid phase arises as shown in Fig. 3(b).

3 Graphite Intercalation Compounds (GICs)

It has already been pointed out in Section 1.4 that the MO model for polycondensed aromatic hydrocarbons leads directly to the concept of the so-called middle potential [51]. In graphite, graphene layers (Fig. 14) are stacked at a relatively large distance of 3.35 Å due to van der Waals forces. These layers in an insulated form would be oxidized or reduced at the same potential, the middle potential (identical with the Fermi potential, E_{F}, of the solid) of -0.2 V vs. SHE (cf. Fig. 9), to form the radical cation or anion. However, in the solid, the intercalation of the counterions leads to a strong positive (negative) shift of the potential, again of about 2 V. The two main reasons for this are [128, 129]:

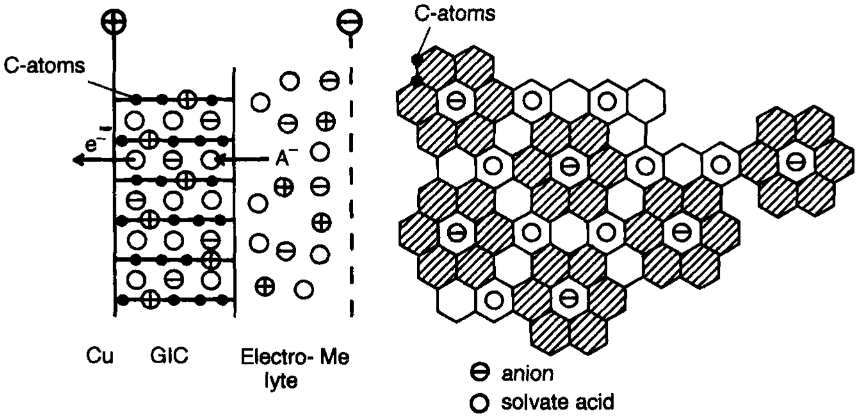

Fig. 14. Structural details for the distribution of charges ⊕, ⊖ and solvate acid molecules ○ in a graphite intercalation compound, first stage.

1. The density of states approaches zero at E_F, quite in contrast to metals.
2. Work must be provided against the van der Waals forces. The distance of the graphene layers is more than doubled to 7.98 Å in the case of HSO_4^- ions. Electrostatic interactions must be taken into consideration.

Among the (C-containing) host lattices which are listed in Table 2, graphite is of special importance. It has been known for a long time; it already served in the form of natural graphite as a black pigment in the Stone Age. It differs from all the others in the following ways.

- It contains no C–X heterobonds and no C–H bonds; thus stability against irreversible electrochemical oxidation or reduction is very high.
- The intrinsic redox processes according to Fig. 3 are strongly reversible, and battery application is straightforward.
- Chemical stability is excellent, e.g., against acids or bases, in contrast to metals and many oxides.
- It has a relatively high electronic conductivity.
- It is a readily available, cheap material.
- It forms both types of intercalation compounds, donor (D) and acceptor (A) type. This is quite in contrast to most of the other inorganic host lattice such as, for example, TiS_2 [31], V_3O_8, Cr_3O_8, MnO_2, CoO_2, and many others [29], where D-type compounds, mostly with Li^+, are absolutely preferred. The reason for this is that graphite is a metal, with a Fermi potential of about −0.2 V vs. SHE (see above), while the inorganic host lattices are oxide (sulfide etc. . . .) semiconductors, with a relatively large band gap, acceptor states in the conduction band (E_c) in an accessible potential region, but donor states in the valence band (E_v) at very positive potentials which are not compatible with the stability of the solvent/electrolyte systems.

As a consequence, this review of GIC compounds is organized in two parts: Section 3.1 to devoted to A-type systems, and Section 3.2 deals with the D-type systems.

3.1 Acceptor (A)-type GICs

Graphite intercalation compounds (GICs) of the A type are prepared by chemical or anodic oxidation of graphite. In strong acids and in the presence of appropriate anions such as $A^- = HSO_4^-, ClO_4^-, BF_4^-$, or HF_2^-, the so-called graphite salts are formed. The insertion of one anion is accompanied by the insertion of $\nu = 2$ solvate acids HA according to the overall reaction:

$$C_x + xy\ A^- + \nu xy\ HA \rightleftarrows [C^{y+} \cdot yA^- \cdot 2\nu y\ HA]_x + xy\, e^- \tag{46}$$

where x is the degree of polymerization, while y is the degree of insertion (stoichiometric number of anions for *one* C atom). A very general version of this equation was already shown as Eq. (5) in Section 1.1 Figure 14 displays the structure of these GICs in a side view and as an in-plane array. The latter demonstrates that each anion sits in the center of a coronene structure ($C_{24}^{+}\ A^{-}$), and these are interlinked without further C atoms and by six solvate acid molecules.

Unfortunately, a denser package seems not to be possible. Diluted structures have been observed, where not one graphene layer separates the guest layers, as shown in Fig. 14, but $n = 2, 3, 4, \ldots$. Thus the stoichiometries are $C_{48}A$, $C_{72}A$, in general C_{24n}, where n is the stage number, and they were originally determined via X-ray analysis by Rüdorff and Hofmann [47]. These authors were also the first to identify the electrochemical reaction (46) as a possible reversible process for battery electrodes (concentration cells). Reversibility decreases strongly with decreasing crystallinity of the graphite material in the order: natural graphite > HOPG (Highly Oriented Pyrolytic Graphite) > pyrolytic graphite > graphite foil, graphite fibers > Kish graphite > Acheson graphite [130]. Varieties of natural graphite such as thermally exfoliated (550 °C) natural graphite [131] or highly dispersed graphite powder [132] show also high reversibility. In the former case, the redox capacity due to –OH surface groups was only in the range of 0.1–10 A s/g C, much lower than expected; cf. GIC (graphite hydrogensulfate), 335 A s/g C. A useful composite material, "CPP", was developed [133], consisting of 80 wt% natural graphite and 20 wt% polypropylene. The nonporous material could be easily formed by a few galvanostatic cycles [134]. It was found that cycle life was increased by decreasing tensile strength and rigidity of the polymer binder [135].

Galvanostatic charging curves [48, 136, 137] clearly confirm this model. They show plateaus in the two-phase regions, but in the single-phase parts the potential rises linearly with time, as in the case of a capacitor [137]. The slope is given by:

$$\frac{dU}{dQ} = \frac{n}{C_1} \tag{47}$$

where C_1 is the capacity of the stage 1 moiety and n is the stage number (cf. Fig. 15). It is interesting to note that, according to Fig. 14, a GIC electrode can indeed be regarded as an atomic capacitor. One ensemble of plates is represented by the graphene planes, contacted by the metal lead, and the other "plates" are the ionic layers, "contacted" by the electrolyte. The energy density of a charged capacitor is given by

$$E_s = \frac{\varepsilon \cdot \varepsilon_0 \cdot U^2}{2d^2\rho} \tag{48}$$

With $U = 0.5$ V, $d = 0.36$ nm, $\rho = 1$ g/cm^3, and $\varepsilon = 10$ (electrostriction!), one obtains $E_s = 100$ W h/kg. This is of the right order of magnitude. But it does not mean that the mechanism is purely electrostatic, as was put forward by Schuldiner [138] for the analogous case of polyacetylene. The mechanism remains an electrochemical one: anions are transferred at the electrode/electrolyte phase boundary (2), as shown in Fig. 14. For a compact capacitor with $U = 100\,V$, $d = 1$ μm, and $\varepsilon = 100$, one obtains only $E_s = 0.5$ Wh/kg [6].

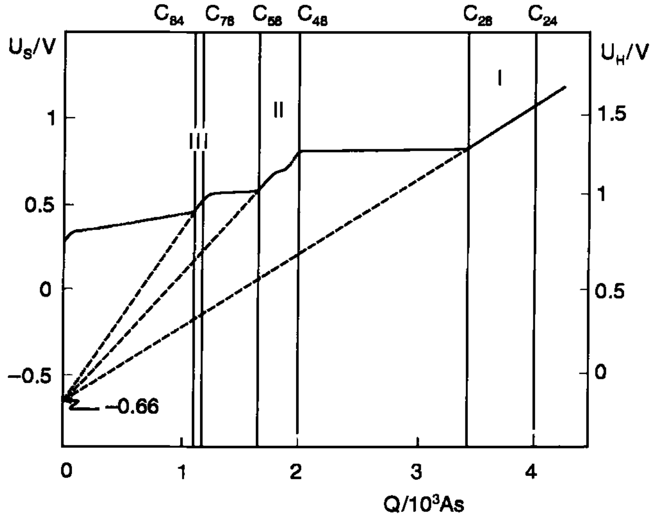

Fig. 15. Charging curve for an HOPG electrode in 97% sulfuric acid. $I = 30$ μA. After Métrot et al. [137]. Left voltage scale U_s vs. $Hg/Hg_2SO_4/18$ M H_2SO_4. Right-hand scale U_H vs. SHE. Abscissa: charge Q in coulombs per mole carbon. I, II and III are the stage numbers.

In analogy to the slow charging curves (Fig. 15), slow cyclic potentiodynamic curves such as those in Figs. 16 and 17 disclose the various stages as current peaks. If the potential difference from the first intercalation (high n) to the last peak is about 0.65 V, stage 1 is accomplished, but only in conc. (18 M) H_2SO_4 (cf. [139, 140]).

In the case of aqueous acids of medium concentration, only stage 2 can be obtained, and the potential difference between the first steep rise of current at the "intercalation potential" U_i (cf. the 10 M H_2SO_4 example in Fig. 16) and a final rise into the region of overoxidation is reduced to about 0.20 V. This is shown for six examples in Fig. 16. Recently, it was found that stage 1 is established again if H_2O as a solvent is substituted by a weaker nucleophile, e.g., in 12 M H_2SO_4 in CH_3COOH [8]. Interestingly, all these voltammetric curves reveal a strong linear dependency of U_i upon the analytical acid concentration c. Figure 18 shows that the slope of the U_i vs. c-curve is about 54 mV/m, with similar values for $HClO_4$ and HBF_4 and only 28 mV/M for H_2F_2 [130, 141, 142]. The explanation for this behavior is the influence of solvate acid HA on the Nernst potential according to Eq. (46) and the fact confirmed experimentally that c_{HA} rises exponentially with c:

$$c_{HA} = c_0 \exp(k \cdot c) \tag{49}$$

It was possible to match k from spectroscopic findings with this electrochemical model [141]. Recently, it was demonstrated that GICs which were fabricated via chemical oxidation (HNO_3) showed an analogous relationship to that in Fig. 18 in H_2SO_4, but the potentials were more positive by up to 0.5 V [143].

Similar linear curves were also found for some synthetic metals such as polyacetylene (PA) and poly (p-phenylene)(PPP) [144]. The slopes and two sets of

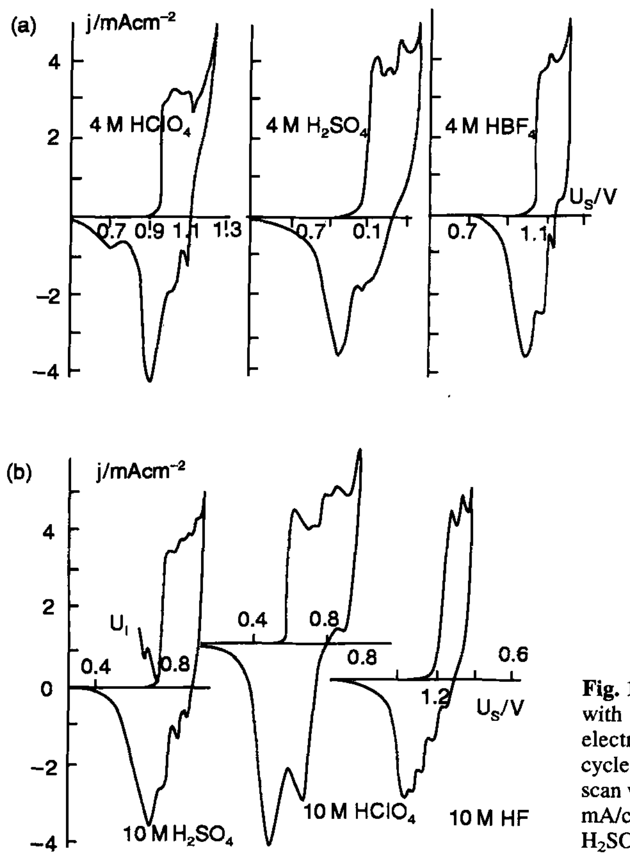

Fig. 16. Slow cyclic voltammetric curves with CPP, in 4 M (a) and 10 M (b) electrolyte acids as indicated, second cycle, $v_s = 1$ mV/s, 25 °C. The voltage scan was reversed at a current density of 5 mA/cm^2. Potential U_s vs. Hg/Hg_2SO_4/1 M H_2SO_4.

potential data for 10 and 15 M H_2SO_4 are summarized in Table 5. Interestingly, the aromatic systems are much more positive than PA by about 0.5 V. This is a consequence of the resonance energy in the former. The strong concentration effect represented by Fig. 18 was further developed toward an electrochemical sensor for the concentration of acids such as H_2SO_4 or H_2F_2 in the range from 0.1 M up to 100% [145, 146].

Besides the "classical" electrolyte acids mentioned above, several other acids such as trifluoroacetic acid, methanesulfonic acid, or hexafluorophosphoric acid were used for the anodic formation of GICs. Others like 4–7 M HNO_3, 4–48 M H_3PO_4, 0.75–0.15 M amido sulfonic acid, 1–2.8 M H_2SiF_6, etc., turned out to be unsuitable [16]. On changing the electrolyte to neutral aqueous solutions, it was shown that reversible cycling of GIC is feasible in such electrolytes as 8 M $NaClO_4$ or 5 M $NaBF_4$ [147]. Due to a lack of any solvate acid, the intercalation potential decreases logarithmically with increasing electrolyte concentration.

If electrolytes in aprotic solvents ($LiClO_4$ NEt_4PF_6) are employed, similar results are obtained according to Besenhard [148]. Relatively stable solvents such as dimethyl sulfoxide (DMSO) or propylene carbonate (PC) are used, but it is believed

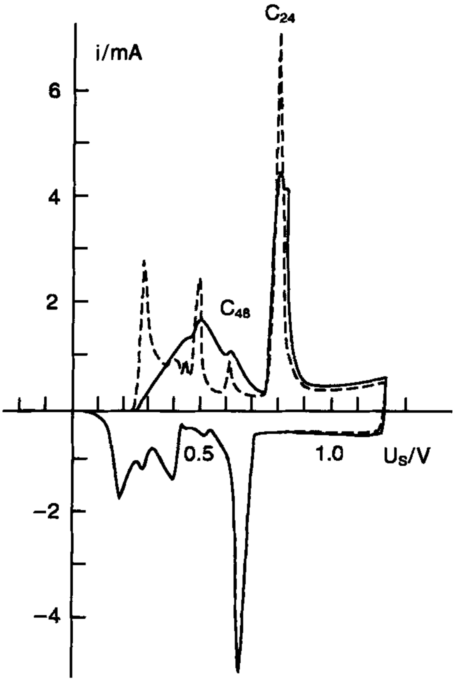

Fig. 17. Slow cyclic current-voltage curves for natural graphite CPP, $A = 0.5$ cm^2, in 18 M H_2SO_4; voltage scan rate $= 0.1$ mV/s, potential range $= -0.2 + \cdots + 1.2$ V; $m_{CPP} = 32.3$ mg;———, first cycle; – – –, second cycle. After Jiang et al. [139].

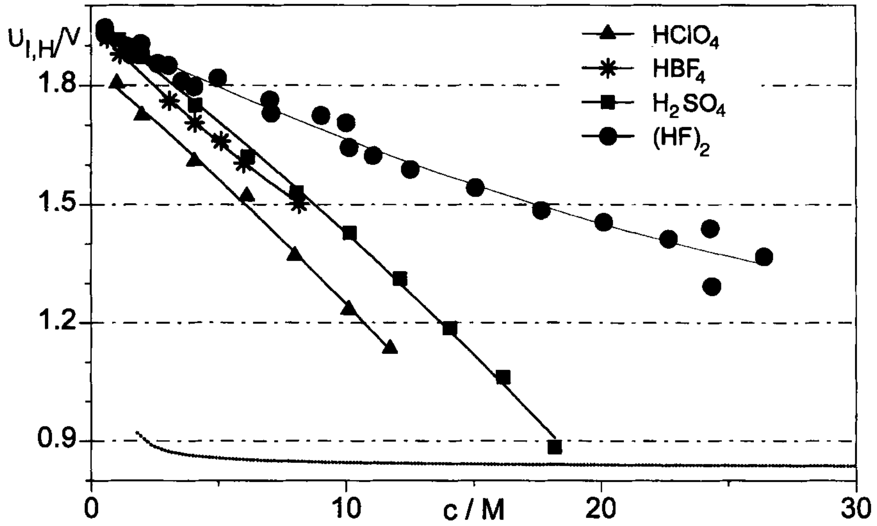

Fig. 18. Dependence of intercalation potential U_I (vs. SHE) on the molar acid concentration c, measured by slow cyclic voltammetry as in Figs. 16 and 17. The definition of U_I is indicated in Fig. 16, on the curve for 10 M H_2SO_4. The acids are shown in the key. The dotted line represents Nernst behavior.

Table 5. Relationship of intercalation potentials U_I (vs. SHE) to sulfuric acid molarity for three host lattices.

Host lattice	Slope [mV/M]	U_I[mV] vs. SHE in aqueous H_2SO_4	
		10 M	15 M
Graphite (C)	54	1380	1110
Poly(p-phenylene)(PPP)	64	1320	1000
Polyacetylene (PA)	42	770	450

that their slow oxidation at the very positive potentials (about 2 V vs. SHE) is the ultimate limit for their application. The relative stability of nitromethane in such systems was shown. Potentiodynamic measurements at thin layers of natural graphite in 0.2 M $LiClO_4$ in sulfolane demonstrate that stage 1 can indeed be obtained [149]. In the case of other aprotic solvents such as propylene carbonate or acetonitrile, anodic stability at the GIC is inferior, and this is reflected in the finding that only higher stages can be realized [149, 150].

Some kinetic aspects should be mentioned. Charge-transfer kinetics at the phase boundary electrode (GIC)/electrolyte is due to ions [16], and exchange current densities were measured of $i_0 = 0.6$ A/cm^2 in 18 M H_2SO_4 but 0.01–0.1 A/cm^2 in 1 M $LiClO_4$ in aprotic solvents [149, 151]. Concerning transport kinetics is in the solid, it was reported by Krohn [152] that the diffusion constant of intercalated anions in the order of 10^{-6}–10^{-7} cm^2/s. Normally, $D = 10^{-10}$–10^{-20} cm^2/s is found for diffusion in solids. The exceptionally high values in the case of graphite are attributed to the presence of "solvate acid" molecules in the solid, which provides a similar "medium" to the bulk of the electrolyte. More recently, it was demonstrated that the product of specific viscosity η and diffusion coefficient D, the so-called Walden product W ($\eta \cdot D = W$), is fairly constant for a couple of aprotic or strongly acid solvents [151]. This is discussed in terms of validity of Walden's rule even in the solid environment.

The application of A-type GIC materials in rechargeable batteries has frequently been investigated, namely in metal/graphite cells in concentrated sulfuric acid by Fujii (Me = Pd) [153, 154] and in acids of medium concentration by Beck and Krohn (Me = Pb or Zn) [155–157]. The latter electrolytes have an improved compatibility with the negative metal electrode. Metal-free accumulators with GIC as a positive electrode were built with anthraquinone in aqueous acids [80] and with polypyrrole in aprotic electrolytes [58, 158, 159]. General discussions of the potentialities of graphite-type active materials in rechargeable batteries have been published by Besenhard and Fritz [160] and Beck et al. [5–10]. At the end of this review (Section 9) the discussion relevant to batteries will be summarized.

The many ternary and higher-order GICs which are described in the preparation-oriented literature can be partially employed as host lattices for battery applications (cf. [161]). Equation (50) gives an example:

$$[C_x^+NiCl_3^-] + e^- \rightarrow C_x + NiCl_2 + Cl^- \qquad (50)$$

The stoichiometry $x = 7$ was found [162]. The Li/$C_7NiCl_{2.5}$ cell was tested in aprotic electrolytes ($U \sim 2.5$ V). $FeCl_3$ as an intercalant is another example. The chemical formation of the ternary GIC proceeds according to the overall reaction

$$C_x + m\,FeCl_3 \rightleftarrows [C_x^{y+}(FeCl_4^-)_y(FeCl_3)_{(m-y)}]_i + y\,FeCl_2 \tag{51}$$

Extended lists of such ternary compounds are reported [163]. $Mn(OH)_2$ [164] and $MnCl_2$ [165] lead to electrodes with some relationship to the well-known battery MnO_2 positive electrode. The last example, which is discussed further in the next section, is the reversible intercalation of Li^+ in the C_xVF_6 host lattice [166]:

$$[C_xVF_6 + yLi^+ + y\,e^- \rightleftarrows [C_x\,Li_y\,VF_6] \tag{52}$$

Specific capacities up to 400 A h/kg were determined at −0.5 V vs. SHE and 10 μA/cm^2. At present, no advantages can be recognized over the classical GICs, with respect to either specific electrochemical capacity or the potential level. Moreover, the stoichiometric presence of inorganic components spoils the principle of metal-free graphite-type active materials.

3.2 Donor (D)-Type GICs

Going from acceptor- to donor-type GICs, aqueous electrolytes cannot be used due to excessive hydrogen evolution. However, it was shown by Besenhard [148, 167, 168] (cf. [169]) that aprotic electrolytes, predominantly DMSO, with alkali, or quaternary ammonium, salts yield an intercalation of the cations and a co-intercalation of the solvent. More recently, Schoderböck and Boehm [170] were able to identify at least five stages, which are formed in succession in the 1 M $LiClO_4$ in DMSO electrolyte system (Fig. 19). The current efficiency was about 90%, indicating some cathodic decomposition, either electrochemical at negative potentials or chemical in the first stage. The overvoltage in the reverse direction seems to be somewhat higher (cf. Figs. 16 and 17).

The optimum stoichiometry corresponds to $[Li^+C_6^- \cdot \nu S]$, where ν is the stoichiometric number for co-intercalated solvent molecules S. The overall reaction is

$$C_x + Li^+ + e^- + \nu S \rightleftarrows [C_x^- \cdot Li^+ \cdot \nu S] \tag{53}$$

Figure 20 represents the hexal in-plane array of the intercalated Li^+ ions. Volume changes upon cycling are only 6%, while in the case of graphite hydrogensulfate they are about 140%, and for LiAl (as a typical example for negative electrode alloys) they are 97%. Layer spacing of Conoco XP coke decreases with increasing heat-treatment temperature T_t from 3.46 Å for $T_t = 1100$ °C to 3.36 Å for $T_t = 2600$–3000 °C, which is the limit for crystalline graphite [171]. The c-distance for petroleum coke rises nearly linearly with x; it is 3.46 Å for $x = 0$, and it reaches 3.65 Å for $x = 0.5$, corresponding to $\Delta V = 11\%$ for $x = 1$ [171, 172]. With respect to pure lithium with a specific capacity of 3860 Ah/kg, this value drops down to 340 Ah/kg, for $\nu = 0$.

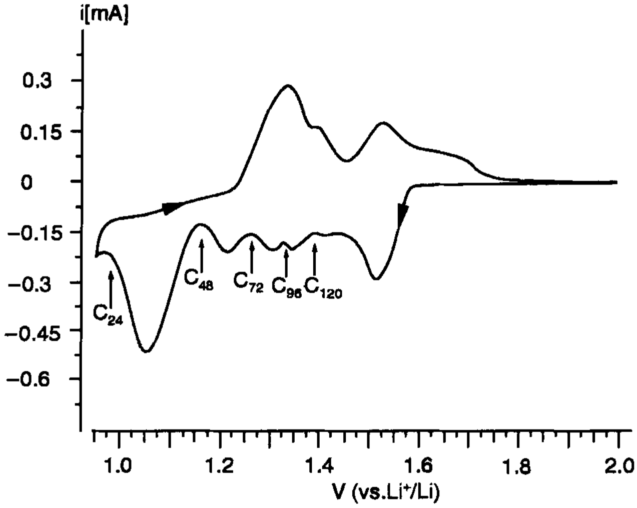

Fig. 19. Cyclovoltammogram of intercalation and de-intercalation of Li^+ into Madagascar flakes (electrolyte: 1 M $LiClO_4$/DMSO). 40 mg C, 0.01 Vs^{-1}, 22 °C.

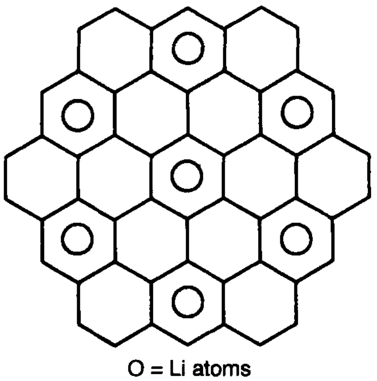

Fig. 20. In-plane array for donor-type Li^+GIC, C_6Li.

However, as lithium metal shows only poor cyclic behavior, LiC_6 has become a very interesting candidate for the negative electrode in rechargeable batteries. This point is stressed in two review articles, by Scrosati [173] and Fauteux and Koksbang [174].

With respect to the charge stoichiometry, the normal-value LiC_6 could be enhanced by nanodispersed graphites [32] to LiC_3, and even LiC_2 could be obtained at 30–60 kbar and 280 °C [175].

The solid-state character of the graphite material has a great influence on the electrochemical behavior of the LiC_x. Natural graphite (NG) has the highest crystallinity, and the specific capacity approaches the theoretical value $K_{s,th} = 339$ Ah/kg for LiC_6 [176]. Practical values around 350 Ah/kg are actually found. Staging, as determined by X-ray diffraction (XRD), is well developed. The potentials are close to the lithium potential, namely +85, +120, and +210, mV vs. Li for stages 1, 2, and 3–4, respectively [176]. Synthetic graphites, manufactured at 2700–3000 °C, such as mesophase pitch-based carbon microbeads [177, 178] or fibers with diameters of 1–10 μm [179–184], are nearly equivalent. The form factor is highly beneficial for any battery application, but the high manufacturing costs must be considered too. Powdery synthetic graphite materials such as Lonza KS 15 [185] are also useful. In contrast, carbons and carbonaceous materials with a small or even zero degree of crystallinity deviate from this ideal behavior in the following ways.

1. Suppression of staging in the LiC_x compound. In the exreme case, no staging at all is exhibited in the XRD diagram [171, 186].
2. The specific capacity is much lower, around 180–190 Ah/kg.
3. The pyrolysis temperature, starting from appropriate precursors, is normally below 1400 °C. Further examples will be discussed in Section 7.
4. The transport kinetics is much faster. Diffusion coefficients D_{Li^+} were reported to be 10^{-8} cm²/s for $x \rightarrow 0$ and 10^{-9} cm²/s for $x \approx 0.7$ for coke [172], but $10^{-11} - 10^{-12}$ cm²/s for graphite [187]. At 100 °C D for Li^+ and K^+ was 10^{-7} cm²/s but for Na^+ only 10^{-11} cm/s [188].

The coke materials discussed so far are made from coal. They are sometimes also called "active carbon", if they are employed for purification processes. Capacities as high as 300 Ah/kg are reported in the literature [189]. Some papers are of special interest, for a broad spectrum of graphites and carbons were evaluated in the same laboratory [190, 191]. Figure 21 shows that lithium–carbons are characterized by discharge curves with potentials which comprise a broader potential region of 0.1–1 V vs. Li. The lithium–graphite potential is "held" at 0.1–0.3 V vs. Li, as mentioned above.

Composites, in the usual sense, were proposed to improve the mechanical stability of the electrode. An example is 80 wt% coke powder in PVC [192]. Of greater interest are carbons with nanodispersed boron (via BCl_3, 900 °C). The compound $B_{0.17}C_{0.83}$ has a reversible specific capacity of 437 Ah/kg [193]. An even stronger enhancement of $K_{s,th}$ up to 500 Ah/kg could be achieved by silicon (via $SiCl_4$/via Me_2Cl_2Si, 950 °C) for the composition $Si_{0.11}C_{0.89}$ [194, 195]. Structural aspects are compiled in Fig. 22. The improved stoichiometry is attributed to the electron-acceptor capability of boron or silicon. Doping of petroleum-fuel green coke by phosphorus elevates K_s by 20% [191].

The important role of the solvent/electrolyte system is considered finally. In principle, none of the aprotic solvents which are commonly used is thermodynamically stable against lithium metal. The same is true for LiC_6, although some improved metastability is found. Binary mixtures of PC (propylene carbonate)/EC (ethylene carbonate) are widely used [196]. PC alone is not suitable, but it is convenient as a liquefier for the solid EC. Another binary system is EC/DEC (diethyl carbonate). 1 M $LiPF_6$ in 30–50 vol% EC has a specific conductivity of $\kappa = 7$ mS/cm at 20 °C. In DEC alone, κ is only 2 mS/cm. In this case, DEC is the stable thinner. Ternary systems comprising EC/PC . DEC (1 : 1 : 2–3 by volume) are also employed. In both cases, the co-insertion of solvent molecules is totally inhibited (see below). A test of

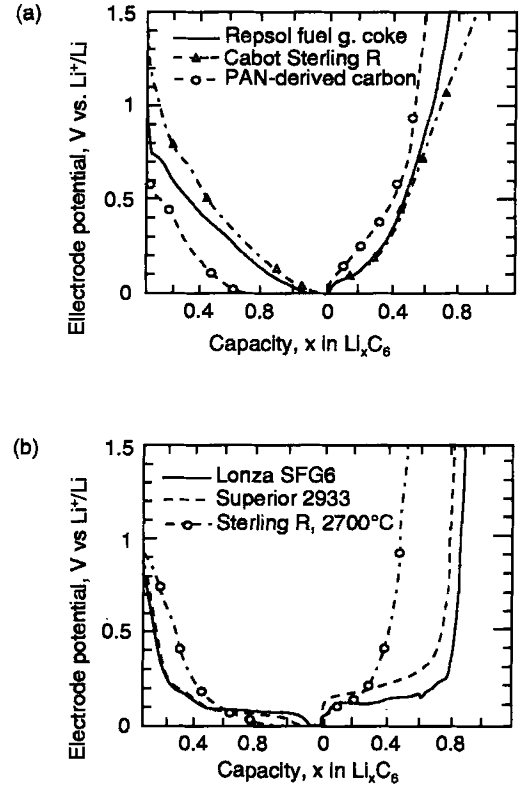

Fig. 21. Discharge/charge profiles of several anodes containing graphite and graphitized materials in 0.5 M $LiN(CF_3SO_2)_2$/(50:50) EC/DMC electrolytes. (a) Cokes and carbon materials; (b) graphite and graphitized materials. C/24 rate, after [191].

the shelf life of a Li/needle coke electrode led to the following results [210].

- Self discharge at 20 °C is moderate (5% per month).
- At 60 °C for 13 days, stability decreased in the following order of liquid electrolytes: $LiAsF_6$, PC > $LiClO_4$, PC $\gg$ $LiAsF_6$, 2Me-THF.

Impedance spectroscopy (EIS) reveals the presence of a protecting layer at the surface of a fully charged C_6Li electrode, as is the case for lithium metal itself (cf. [201–203, 210, 211]). Thus Peled's former model for lithium metal [204, 205] can be extended to LiC_x, which has a similar strong reactivity with respect to the aprotic solvent/electrolyte system. The protecting films are predominantly built up by an irreversible cathodic process at the end of the first charge. This is revealed by a large excess of this charge (160–130%) over the steady-state capacity (cf. [206]). A thorough study of the nature of these films was performed by Aurbach et al. by FTIR and EIS [206–209]. A DEC/EC electrolyte led to a layer of composition $(CH_2OCOOLi)_2$ [209]. Modification of the layer under the influence of additives, mainly small molecules such as CO_2, N_2O, etc., was also tried [209–211]. Li_2CO_3 was found as a component of the film in the case of CO_2 bubbling. Finally, a "chemical" proof for the in-situ formation of a protecting layer on C_6Li should be

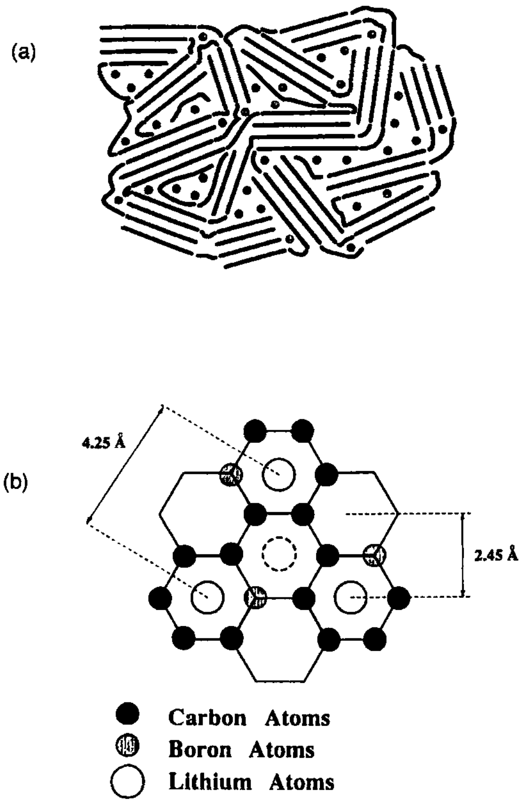

Fig. 22. (a) Franklin's model for pregraphitic carbon; stacked graphene layers are represented by straight lines. Bent or curved lines represent tetrahedrally bonded carbon chains or buckled graphene layers. The nanodispersed silicon atoms are represented as shaded dots. After Wilson and Dahn [194]. (b) Schematic drawing of the lithium sites on a single layer of boron-substituted carbon. The broken circle represents the site for additional lithium beyond $x = 1$ in $Li_x(B_zC_{1-z})_6$. After Dahn et al. [195].

mentioned: no change in the golden color of C_6Li (prepared from Li + HOPG at 200 °C) was observed after three months of immersion in an electrolyte composed of 1 M $LiBF_4$ in PC/EC/DME (1:1:2 by volume) [212].

The co-intercalation of solvent molecules S as shown in Eq. (53) in the charge direction was observed mainly for crystalline graphite. The presence of 4–6 molecules of S in the strongly expanded interlamellar compound was found analytically [213]. Such a co-intercalation (cf. [214] and [216]) leads to further, dramatic breakdown of the theoretical capacity (see Table 6), so it must be avoided as much as possible. There are three strategies available.

1. The composition of the solvent/electrolyte system may be adjusted. For EC-containing electrolytes, a cathodic pre-step is discussed for liquid electrolytes,

$$(Li(S)y)^+ + e^- \longrightarrow Li_{ad} + yS \qquad (54)$$

Only the adsorbed naked Li atoms are intercalated in the C-lattice.
2. From solid polymer electrolytes [198, 199] no co-intercalation is observed either [216], for only "naked" ions are present in the SPE phase.
3. If carbonaceous materials are employed as a host lattice, no co-intercalation of solvents occurs. This is attributed to the protecting layer in this case [216].

Table 6. Theoretical specific capacities $K_{s,th}$ for D-type GICs: the problem of co-intercalation of solvent molecules.

D-type GIC	$K_{s,th}$ [A h/kg]	Ref.
(Li metal)	3862	
$[Li^+C_2^-]$	1157	[175, 425]
$[Li^+C_3^-]$	623	[32]
$[Li^+C_6^-]$	339	
$[(Li(PC)_6)^+C_6^-]$	44.5(a)	[214]

(a) PC, propylene carbonate, $M = 86$.

Thus, strong issues are available through a proper choice of the host lattice and the electrolyte to arrive at a LiC_6 composition.

4 Fullerenes

A few years ago, a novel molecular structure of carbon was detected. Globular C_{60} molecules (or C_{70} and other sizes) form a molecular lattice. The C_{60} "buckyballs" have a diameter of 1 nm. Within the C_{60} moieties, the polyaromatic structure sp^2 is fully retained in annealed five- and six-membered rings. The fullerene molecule resembles a football in design. The close analogy to graphite, with sp^2-structures of 100% C, justifies a treatment immediately following Section 3 on graphite.

It was in 1990 that Krätschmer et al. [217, 218] reported the first macroscopic preparation of C_{60} in gram quantities by contact-arc vaporization of a graphite rod in a 100 Torr atmosphere of helium, followed by extraction of the resultant "soot" with toluene. Fullerene ions could also be detected by mass spectrometry in low-pressure hydrocarbon flames [219]. The door was opened by, Krätschmer and co-workers preparative success to extensive studies of the electrochemical behavior of the new materials. Cyclic voltammetry of molecular solutions of C_{60} in aprotic electrolytes, e.g., methylene chloride/quaternary ammonium salts, revealed the reversible cathodic formation of anionic species, the radical anion, the dianion, etc. (cf. [220, 221]). Finally, an uptake of six electrons in the potential range of 1–3.3 V vs. SHE in MeCN/toluene at $-10\,^\circ C$ to form the hexavalent anion was reported by Xie et al. [222]. This was in full accordance with MO calculations. A parametric study of the electroreduction of C_{60} in aprotic solvents was performed [223]. No reversible oxidation of C_{60} was possible, not even to the radical cation. However, the stability of di- and trications with special counterions, in the $Li/PEO/C_{60}^{3+} \cdot 3\ MoF_7^-$ cell, was claimed later [224].

Even more important for a possible application in rechargeable batteries was the finding that solid C_{60} films (from solution) on platinum electrodes could be reversibly cycled in $MeCN/NBu_4AsF_6$ [225, 226]. The main difference from the C_{60} solutions

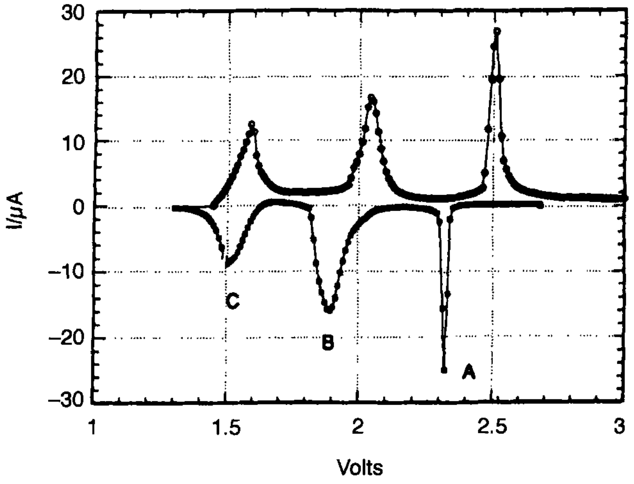

Fig. 23. Cyclic voltammogram for the first cycle of the solid-state secondary cell described in the text. The potential steps were confined to the range 1.3–3.0 V. V_{oc} open circuit potential relaxed to only 1.4 V after reducing to 1.3 V.

was a much bigger peak separation (0.3–0.6V) of the reduction and the corresponding reoxidation peaks. This was attributed to solid-state reorganization processes. The fast decay of peak intensity upon cycling was indicative of an electrochemical destruction mechanism of the solid film. Again, no reversible oxidation peaks could be detected. The charge stoichiometry for each of the two redox pairs was found to be 0.5 electrons per C_{60} [227]. Chabre et al. [228] were able to measure a voltammogram according to Fig. 23 in an all-solid-state electrochemical cell (−) $Li/P(EO)_8$, $LiClO_4/C_{60}$ (+). The positive electrode was a composite made from 60% "active material" and 40% solid electrolyte. Obviously, the peak separation is much smaller, only 0.1–0.2 V. This is attributed to the absence of any solvent molecules. Co-insertion of these molecules, which is partially responsible for the reorganization processes mentioned above, is therefore impossible under these conditions. Stable layers of C_{60}, entrapped in an *N*-substituted polypyrrole, are reported by Deronzier and Moutet [229].

It should be mentioned that the possible application of C_{60} (solid) as an active material in a rechargeable battery is at present far from any practical reality due to the following reasons:

1. Even if we assume a stoichiometry $C_{60}Li_{60}$ – it is reported that only the monoanion ($C_{60}Li$) can be reversibly cycled – the specific capacity $K_{S,th} = 211$ Ah/kg is inferior to that of the D-GIC, LiC_6, which is 339 Ah/kg. A comparative study of both host lattices, graphite and fullerene, is published elsewhere [230].

2. Excessive costs.

3. The discharge potential difference exceeds 3 V.

Recently, fluorinated fullerenes, e. g. $C_{60}F_{40}$, were proposed as an active material in primary lithium cells. In a mixture with graphite, discharge capacities (Li^+ – intercalation and LiF formation) of 560 Ah/kg were reported [231].

However, a much more promising physical application of fullerenes is emerging in the field of superconductivity. Superconducting transitions up to $T_c = 33$ K for Rb_3C_{60} are now known [232, 233], after the initial report of $T_c = 18$ K for K_3C_{60} in 1991 [234]. This is well above the corresponding T_c values for D-type GICs, e.g., 5 K for C_2Na or 0.13 K for K_8C [235]. It should be mentioned that fullerene is an insulator, $\kappa_{25} \approx 10^{-14}$ S/cm [236], but upon n-doping, the conductivity jumps to $\kappa_{25} \approx 1$ S/cm.

5 Carbon Blacks

These highly dispersed materials are composed of practically pure carbon (cf. Table 2); in this respect they are related to graphite and fullerene, which have been discussed extensively in Sections 3 and 4. However, the order of organization is greatly inferior to these. The structure of the individual particles is characterized by graphitized zones, as discussed in Section 1.3, and by amorphous interregions. Very important are a variety of oxygen-containing surface groups (cf. [237–239]), which are all located at the plane edges. *o*-Quinone/hydroquinone surface groups undergo reversible redox transitions in aqueous electrolytes at about 0.7 V vs. SHE at pH 0. Other surface groups are only irreversibly oxidized (–OH, phenolic) or reduced (–COOH, –CO–O, lactonic). The redox capacity is negligible in comparison with that provided by intercalation and double layer (DL) charging [131]. Interestingly, precompacted carbon black pellets showed hardly any redox capacity at 0.7 V in 10 M H_2SO_4 [33], while anodically activated glassy carbon exhibited a strong redox response in 3 M H_2SO_4 at that potential [240]. Acheson graphite, on the other hand, exhibited several peak signals in the slow CV [241]. A recent review focuses on the chemical and physicochemical methods for the assessment and identification of these surface functional groups [242].

Carbon blacks (c.b.s) have been known since ancient times, for preparing Indian ink. From the 1920s, c.b. has been fabricated industrially on a large scale by the thermal decomposition of hydrocarbons (natural gas) or aromatic hydrocarbons. Of the total production, 90% goes into the rubber industry, and most of this is employed for the reinforcement of tires. Production capacity is at present 7.2 million tonnes/y and the annual production is 6.1 million tonnes/y [244]; 95% of this global fabrication is by the furnace c.b. process [245]. The specific surface area A_s (m^2/g) in this case covers a range from a few tens up to more than 1500. It should be mentioned that c.b. is used as a filler for conducting polymers [246].

It is, however, only recently that c.b.s became interesting as materials in rechargeable batteries and capacitors. C.b. as a positive electrode is reported for rechargeable lithium cells [247, 248]. With Ketjen Black (950 m^2/g), a discharge

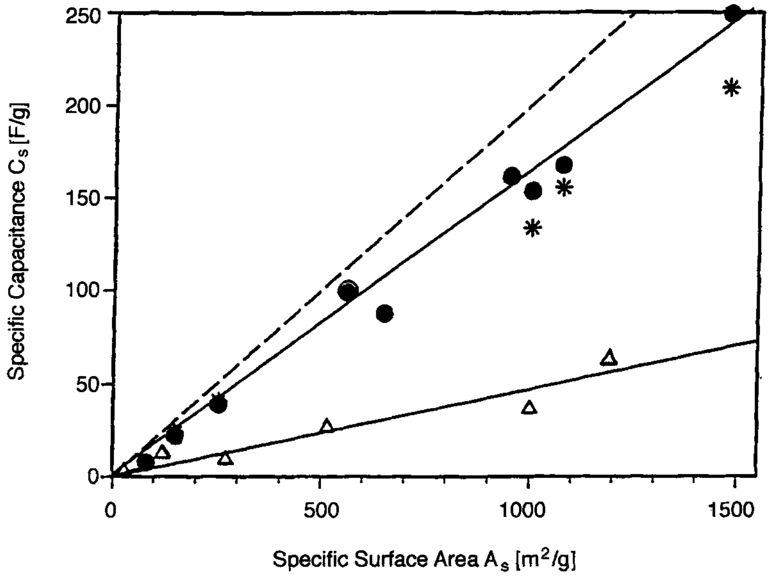

Fig. 24. Specific capacitance C_s vs. specific area A_S of carbon black single electrodes: ●,*, precompacted c.b. electrodes; p_{PP} = 440 MPa; Pt mesh contact in 10 M H_2SO_4 (●) and 3 M H_2SO_4 (*) [33]; △, c.b. in aprotic electrolyte, 1 M $LiCF_3SO_3$ in PC [249]; – – – –, theoretical line, $C_{A,DL}$ = 20 μF/cm²

capacity of up to 400 Ah/kg was achieved in $LiClO_4$/PC. The c.b. electrode contained a binder, polyethyleneglycol. The mechanism of the c.b. electrode is considered to be due to a charge/discharge of the electrochemical double layer capacitors (ECDLCs). The theoretical physical specific capacitance (in F/g) is given by

$$C_{s,th} = A_s \cdot C_{A,DL} \tag{55}$$

where A_s is the specific surface area of the c.b. and $C_{A,DL}$ is the area specific double layer capacitance: a value of 20 μF/cm² is considered normal in concentrated electrolytes (cf. Eq. (7)). The measured C_s data, e.g., from the slopes of the galvanostatic cycling curves (cf. Eq. (18)), reach 80% of the theory. The proportionality between C_s and A_s was confirmed (Fig. 24) with precompacted c.b. pellets [33] is aqueous H_2SO_4 and carbon black in general [249] in aprotic electrolytes.

The latter data are only about 30% of the former although both were acquired with measurements at single electrodes. From this it must be concluded that electrodes in aprotic electrolytes have double layer capacity $C_{A,DL} < 20 \mu F/cm^2$. The virtual advantage of higher voltages U (2–3 V versus 1–1.5 V), which enter as U^2 in the energy density, is at least partially jeopardized in this way. Heydecke and Beck investigated carbon blacks in detail as a slurry electrode by cyclovoltammetric measurements in dilute acids [250, 251]. Anodic oxidation and, with a large overvoltage, cathodic re-reduction were observed. The redox capacity was found to be proportional to the BET surface. An interesting observation was the linear rise at the beginning of the positive scan, instead of a limiting current according to the potentiodynamic charge of the double layer capacity which was expected in advance:

$$j = C_A \cdot v_s \qquad (56)$$

The supercapacitor makes use of an additional pseudocapacitance

$$C_P = Q_{\mathrm{Redox,A}} U^{-1} = zF\Gamma U^{-1} \qquad (57)$$

in analogy to Eq. (9), where $Q_{\mathrm{Redox,A}}$ is the electrochemical redox capacity of redox active surface groups, mentioned above, which have a molar surface concentration Γ. It is possible therefore to increase the double layer capacity by a factor of 10 to 20. The pure double layer capacitance, maximum 20 $\mu F/cm^2$, is confined by the lateral repulsion of surface charges. Only 10% of the surface atoms can be charged. But neutral redox systems of the type $Q + 2\,H^+ + 2\,e^- \rightleftharpoons H_2Q$ do not suffer from such a limitation [14]. It should be noted that the rate of anodic oxidation of carbon black surfaces increases with increasing surface concentration of the already-present surface groups mentioned above [252].

In conclusion, carbon blacks are very interesting materials for ECDLCs. Carbon blacks have moderate prices, DM 6–28/kg, at the time of writing, depending on A_s [33]. Exotic variants such as fullerene black – a side-product representing a tenfold increase in yield, which is obtained in the course of the fullerene synthesis [253] – should also be mentioned. A further extension to conducting polymers and to carbonaceous materials will be described in the next two sections. The corrosion in acids is negligible, in strong contrast to the early developments with Raney materials [254]. The intrinsic instability of a double layer "wet" capacitor is of course a drawback to a physical "dry" capacitor. But, as shown in Sections 1.1 and 1.3, it is not possible to achieve such high specific charge densities with the latter.

6 Conducting Polymers

Polymers with intrinsic electronic conductivities (ICPs) have been known for twenty years. The intensive research in this field has been reviewed by Wegner [255], Skotheim [256], Heinze [40] and Evans [257]. Table 7 gives a summary of the most important systems, which are all characterized by conjugated double bonds, mostly C=C, sometimes also C=N. Polyacetylene (PA) is chemically synthesized by polymerization of acetylene in the presence of Ziegler – Natta or Luttinger catalysts, while the others can be obtained by chemical or anodic oxidation of aromatic or heterocyclic compounds. Chemical/preparative aspects are reported by Naarmann [258], physical aspects by Roth and Filzmoser [259]. A regular structure is expected, but not proven in the great majority of cases. As an example, the film-forming anodic polymerization of pyrrole to polypyrrole is due to the overall reaction represented by

Table 7. The basic ICP systems, their specific electrical conducturties κ_{25} and theoretical electrochemical capacities $K_{s,th}$.

Structural Formula	"C_1"	κ_{25} [S/cm] $y = 0^{(a)}$	$y = 0.01^{(a)}$	y_{max} [C_1!]	$U_{Redox}{}^{(a)}$ vs. SHE [V]	$K_{s,th}$ [Ah/kg]	Ref.
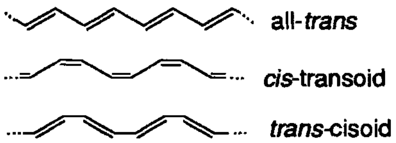 Polyacetylene, PA	CH	10^{-5}	10^3–10^5	0.13	0.8	116.5	McDiarmid et al., 1979
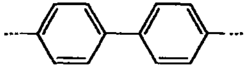 Poly (*p*-phenylene), PPP	$CH_{0.67}$	10^{-10}	500	0.08	1.4	103.6	Shacklette et al., 1980
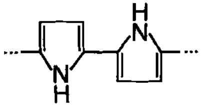 Polypyrrole, PPy	$CH_{0.75}N_{0.25}$	10^{-8}	100	0.09	0.1	95.3	Diaz, 1979
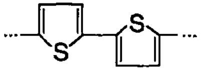 Polythiophene, PT	$CH_{0.50}S_{0.25}$	10^{-8}	50	0.13	1.15	110.6	Diaz, 1979 Garnier, 1982
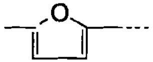 Polyfuran, PFu	$CH_{0.50}O_{0.25}$	10^{-10}	50		1.8		Garnier, 1982
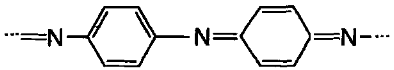 Polyaniline, PANI	$CH_{0.67}N_{0.17}$	10^{-10}	0.01	0.17	0.35	294	Diaz, 1980
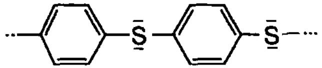 Poly (*p*-phenylene sulfide), PPS	$CH_{0.67}S_{0.17}$	10^{-10}	1	0.06	1.5	67	Shacklette et al., 1980

(a) p-Doping. y = degree of insertion.

Eq. (58), which is composed of an oxidative coupling of the monomer in the α, α' position and a simultaneous doping of the polymer:

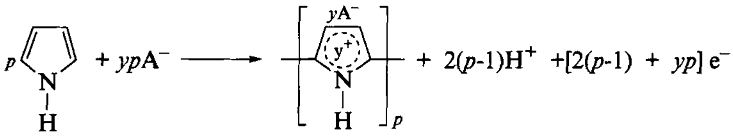

(58)

where p is the degree of polymerization, and y the degree of insertion. Clearly, a deficit of protons is generated, which turns the anodic diffusion layer acid but, rather unexpectedly, the bulk pH never exceeds 5 [260]. Acid-catalyzed chemical polymerizations of pyrrole to oligomers may arise, where the conjugation is lost [260, 261].

Numerous applications of these materials were proposed from the beginning, but only a few were realized. The application of ICPs in rechargeable batteries turned out to be much more complicated and critical than most of the other possibilities. This is due to the strong electrochemical strain in this case. The reversible intrinsic redox reaction can be written for the case of p-doped (A-type) polypyrrole as

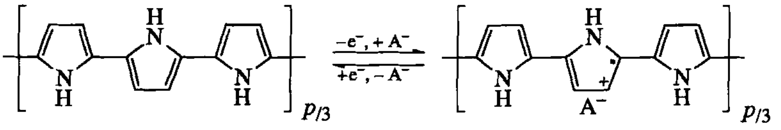

(59)

where p has the same meaning as before. In most cases y is in the range 0.1–0.35, with respect to one ring unit. According to Eq. (6), improved theoretical redox capacities could be realized at higher y values. They are possible in principle for extremely weak nucleophiles such as methylene chloride for the solvent, where $y = 1$ was found for thin films of poly (3-methoxythiophene) at 0 °C. However, the redox processes were spread over nearly 3 V, extending from -0.3 to 2.7 V vs. SHE [13]. It was suggested by Métrot [262] that the intrinsic redox reactions for graphite, mostly referred to as intercalation of ions and discussed extensively in Section 3 of this review, could serve as a model for the reaction of Eq. (59). This reversible redox process may be accompanied by irreversible electrochemical side-reactions, even more for ICPs (due to the presence of C–H and C–X bonds) than for graphite. Polypyrrole (PPy) again as a typical example, may be overoxidized according to

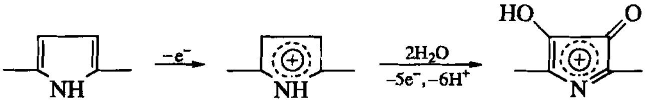

(60)

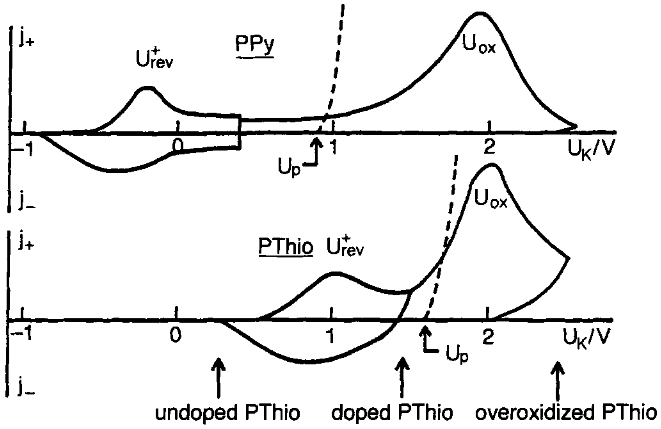

Fig. 25. Potential domains for reversible cycling (left) and for irreversible overoxidation (right) in the case of polypyrrole (PPy) and of polythiophene (PThio).

4-hydroxypyrrolin-3-ones are formed at every third ring starting from the radical cation (1 F) through a further 5 F reaction. A chemical attack by nucleophiles or electrophiles in solution may occur in addition, and irreversible chemical reactions with "environmental" species such as oxygen or water may proceed, even on standing. Such side-reactions of the host lattice must be carefully minimized for any application in rechargeable batteries, otherwise only a limited number of cycles can be achieved. Figure 25 shows that anodic overoxidation proceeds at positive potentials relative to the reversible intrinsic redox process. Both electrode reactions are well separated in the case of PPy, but not for polythiophene (PT), because of the positive redox potential for the latter. On the other hand, PT becomes stable even in the undoped state in this way, as already mentioned above, but Fig. 25 makes it clear that redox switching and overoxidation are close to each other [263]. Systematic research into the huge number of reaction possibilities began only recently. In case of polyacetylene [144], poly (*p*-phenylene) [264] and polypyrrole [265–269], modification of the backbone by carbonyls, etc., is observed, while polyaniline undergoes a dissolution of monomer units from the chain terminals, leading to the formation of quinones [270–273]. A similar cleavage of the polymer chain is discussed for the overoxidation of polypyrrole in dilute sulfuric acid. Maleimide and succinimide have been identified in the electrolyte [269]. An interesting aspect is the chemical modification of the material in this way. Recently, electrochemical stability and degradation of conducting polymers were treated in a review article [274]. Section 6.1 will be devoted to polymer hydrocarbons with conjugated C=C double bonds, which are closely related to the materials mentioned in Section 3–5. For the first time, however synthesis has been achieved starting from well-defined monomers. In Sections 6.2 and 6.3 heteroatoms are introduced (cf. Table 7). All these systems are p-doped (A-type); but in Section 6.4 the relatively rare cases of n-doping are reviewed.

Coming back to Table 7, it should be emphasized that the simple cases shown there are the most important. None of the numerous derivatives obtained hitherto via monomer modification, copolymerization or codeposition of dispersed solids to form composites [258] showed improved properties relevant to batteries. Therefore the basic systems shown in Table 7 represent the optimum in terms of redox capacity, potential and long-term stability.

6.1 Polyacetylene, PPP and other Polyaromatics

As already, mentioned, these polymer hydrocarbons with conjugated double bonds link this section on the synthetic polymers, starting from appropriate monomers, to the preceding sections on graphite, fullerene, and carbon black. Development in the field of ICPs started in 1977/1978 with the efforts of McDiarmid and Heeger to employ polyacetylene as an active battery material. Preparative aspects were predominant [275]. Polyacetylene (PA) had the simplest composition of all the conducting polymers. Reversible cycling (Eq. (61); without possible co-insertion of solvent molecules) is completely analogous to that of graphite, as already mentioned:

$$(\mathrm{CH})_x + xy\,\mathrm{ClO}_4^- \rightleftharpoons [(\mathrm{CH})^{y+}\cdot y\,\mathrm{ClO}_4^-]_x + xy\mathrm{e}^- \tag{61}$$

Battery-relevant galvanostatic cycling of these materials in contact with platinum was demonstrated [276, 277]. Figure 26 displays a typical example. The reversible potential is about 3 V vs. Li or 0 V vs. SHE. However, it should be noted that the cycles were rather flat, varying from $y = 4.1$ to 5.0%. It was expected, at that time, that a "novel lightweight accumulator" should be realizable on the basis of this finding (cf. McDiarmid et al. [278]). A dramatic drawback of PA is, however, its instability under environmental conditions, in the doped state as well as in the undoped state. This instability is confined to the undoped state in the case of PPy, while PT is stable in the doped and in the undoped states. A special form of the polymer, the so-called Shirakawa foil [279, 280], was favored in the early strages, but soon it became clear that the powdery precipitated polymers could be fabricated under cheaper conditions. The density of PA is only 0.4 g/cm^3 and fibrils of only 20 nm diameter were identified. Besides the combination Li/p-PA (Fig. 26), a metal-free system n-PA/p-PA was checked in aprotic electrolytes [277, 281–283]. It was found that cyclic behavior was rather poor. This was attributed to the high reactivity of the undoped PA toward traces of oxygen and to overoxidation at the anode [284]. This holds also for aqueous acids [144]. The rate of autoxidation is much higher than for

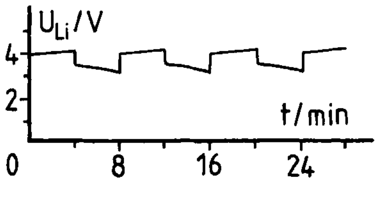

Fig. 26. Partial cyclic curves for the p-PA/Li cell in 0.3 M LiClO$_4$ in PC, c.d. 0.55 mA/cm^2, $y_{\max} = 50\%$, $y_{\min} = 4.1\%$, 100 cycles. After [277].

PPP [5] (cf. below). The highly conducting PA found by Naarmann in 1987 [285, 286] could not make up for this disadvantage. Such a high conductivity is not at all necessary for battery applications. The rate of electrochemical doping/undoping (anions) is rather low due to the extremely small diffusion coefficient in the fabrils [287]. Today, the earlier interest in this material for batteries has totally disappeared.

Poly(p-phenylene) (PPP) can be synthesized from benzene following Kovacic's method [288] through chemical oxidative coupling. The oxidant is $CuCl_2$ or $FeCl_3$ in the presence of $AlCl_3$. Anodic polymerization is also possible in conc. $H_2SO_4 + HF$ (two phases) [289–291] and in liquid SO_2 containing CF_3SO_3H [292]. p-Doping of pellets from PPP powders was performed in aprotic electrolytes [293] and in aqueous acids (16 M H_2SO_4) [294]. The potential was about 1 V and 0.7 V vs. SHE, respectively. However, no advantage over polyheterocycles (see Section 6.2) or graphite could be detected. n-Doping is also possible, similarly to the case of polyacetylene. The following interesting application of this property was reported [295, 296]: a mixture of NaPb alloy powder, PPP powder, and polypropylene binder (a negative electrode) showed highly improved cyclability. PPP acted as a redox catalyst. Extended preparative work by Müllen and his group led to defined aromatic oligomers of the poly(*p*-phenylene) type [297, 298], poly(1,4-naphthylene) type [299, 300], the poly(9,10-anthrylene) type [301] and the poly(phenylene-vinylene)s [300, 302]. Further condensation to ribbon- and ladder-type strutures is reported. Redox switching is possible. An application in rechargeable batteries is not seen due to limitations of cost and mass.

6.2 Polyheterocycles

Polypyrrole can be synthesized by galvanostatic film-forming polymerization of pyrrole in aqueous acids [303, 304] or in aprotic electrolytes [305, 306], e.g., $LiClO_4$ or NR_4BF_4 in acetonitrile or propylene carbonate. The latter films, with a typical "cauliflower structure," seem, however, more appropriate to battery applications. The aprotic electrolytes were optimized [307, 308] and should contain water as an additive (10–100 mM). This empirical finding was rationalized in terms of a modification of the permittivity number in the electrochemical double layer to decrease the electrostatic repulsion of the two $Pt^{\cdot+}$ (radical cation of pyrrole), which dimerize radical cations in the rate-determining step [309]. The rate of this step is low, and this is reflected in maximum current densities of 1 mA/cm^2 for electrosynthesis. Higher current densities lead to partially overoxidized products. Electrocatalysis is possible, e.g., on the basis of bromide ions in small concentrations, typically 1 mM [310, 311], or quinones [312] as redox catalysts. The structure of polypyrrole (PPy) is linear, but cyclic structures are claimed too [313]. Cyclic behavior according to Eq. (59) is excellent for the "Diaz-type" PPy [314]. This holds also for its stability in aqueous electrolytes with pH < 8 and in aprotic solvents. This was proven for aqueous electrolytes in 1 M $NaBF_4$ [19] fand for aprotic solvents by 0.1 M $LiClO_4$ or NBu_4BF_4 in acetonitrile [308, 314]. It is for this reason that PPy as an electrochemically generated layer on appropriate base electrodes was combined as a positive electrode with lithium negative electrodes to form a rechargeable battery

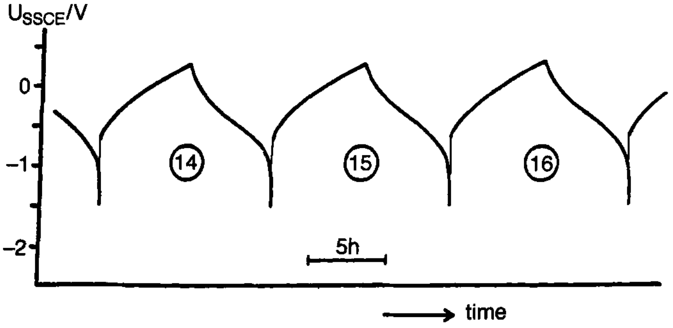

Fig. 27. Cyclic curves for polypyrrole/c.b. composites, $d_n = 300$ µm, $\mu = 71\%$, $j = 0.5$ mA/cm^2. Electrolyte: 0.2 M $LiClO_4$ in PC. The base electrode is c.b.-filled PP.

[315–320]. The necessary porosity for thicker layers was introduced by appropriate current densities [321–323], by co-deposition of composites with carbon black [28, 324] (cf. Fig. 27), by electrodeposition into carbon felt [28], and by fabrication of pellets from chemically synthesized PPy powders with added carbon black [325]. Practical capacities of 90–100 Ah/kg could be achieved in this way even for thicker layers. Self-discharge of PPy was low, as mentioned. However, in lithium cells with solid polymer electrolytes (PEO), high values were reported also [326]. This was attributed to reduction products at the negative electrode to yield a shuttle transport to the positive electrode. The kinetics of the doping/undoping process based on Eq. (59) is normally fast, but complications due to the combined insertion/release of both ions [327–330] or the presence of a large and a small anion [331] may arise. Techniques such as QMB/CV(Quartz Micro Balance/Cyclic Voltammetry) [331] or resistometry [332] have been employed to elucidate the various mechanisms.

It should be mentioned that PPy has been used as a binder for co-deposited MnO_2 powder. Both materials contributed to the electrochemical capacity of the composite electrode [333].

The electrosynthesis of polythiophene (PT) from thiophene must be performed under extremely anhydrous conditions, quite in contrast to polypyrrole [334]. Polymerization of 3-methylthiophene and bithiophene is much less sensitive to water. The advantage of PT is a higher theoretical capacity and a very positive potential (cf. Table 7). It is for these reasons that its application as a positive electrode in rechargeable lithium batteries [335–338] and in a metal-free PPy/PT cell [339] has been considered. Derivatives such as dithienothiophene [340] or *trans*-1,2-di(2-thienyl)ethylene [341] have also been polymerized, but the polymer materials suffer from low theoretical capacities [337].

Recently, the application of poly(3-arylthiophene)s [342, 343] and of the above-mentioned condensed products [344, 345] as super capacitors were reported by Gottesfeld et al. and by Mastragostino et al. The materials are p-doped at the positive electrode and n-doped at the negative electrode. The advantage is a high voltage of 2–3 V and good reversibilities at both electrodes.

PPy/PANI bilayer systems show additive properties compared with the individual polymers [346].

6.3 PANI and other Polyarylamines

According to the late Eugene Genies, the advantages of polyaniline as an active material are attributable to the following properties [347]:

- a higher theoretical capacity (290 Ah/kg) than any other conducting polymer because of the proton exchanges which decresase the Coulombic interactions;
- a higher stability compared with the other conducting polymers;
- a high specific conductivity, which can be more than 100 S/cm;
- large facilities for the processing, because it is possible to prepare films or composites, either from solution or by injection molding.
- fibrillar morphology;
- compatibility with some other materials already used as positive electrodes having a potential in the range 2.5–4 V vs. lithium;
- low specific weight of the polymer and a low cost for the preparation.

Synthesis is performed in 0.1–1 M H_2SO_4 at the anode, mostly potentiodynamically (cf. [348]) or chemically with persulfates. The material has known as aniline black for more than a century, and it is an intermediate for the synthesis of quinone. Benzidine, a carcinogen, may be a side-product, but it was possible to minimize this

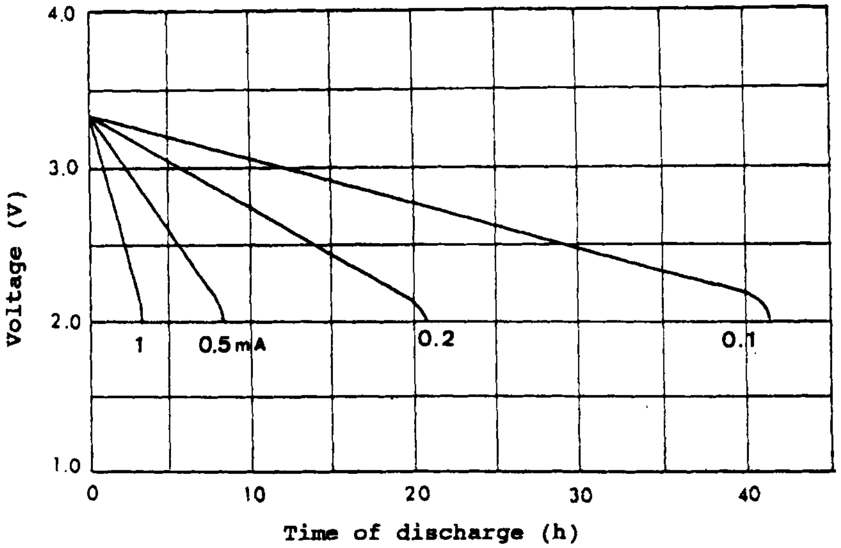

Fig. 28. Discharge curves of an Li/PANI button cell (Bridgestone), after [354]. Charge: 10 h, 0.5 mA. Discharge: 0.1–1 mA, down to 2.0 V.

to < 100 ppm [349]. Unfortunately this low-benzidine material did not have a sufficient charge storage capability.

In the past, numerous efforts to utilize PANI as a positive electrode in rechargeable batteries were undertaken, mainly with lithium, LiAl, or LiC_6 negative electrodes [350–354]. Li^+ was inserted in carbonaceous materials in the last example [354]. Bridgestone/Seiko's development [355] was commercialized as a button cell, but there was no great advantage over the Li/c.b. and Li/PPy versions, which have been discussed in Sections 5 and 6.2. Figure 28 displays typical discharge curves with a linear character, similar to those for a capacitor. According to Oyama et al. [106–109, 356], who claim the usefulness of sulfur additives, especially disulfides, in PANI batteries, the reversibility of the sulfur compound is improved. PANI itself has fast charge/discharge kinetics [357]. Numerous examples in the patent literature refer to multiple-component systems. As an example, a mixture of 10 PANI, 2 PT, 1 c.b., and 1 PTFE is claimed as a positive electrode with $PC/LiBF_4$ as an electrolyte and LiAl as negative electrode [358]. Further discussion of PANI batteries, and also of aqueous electrolytes, is postponed to Section 9. *o*-Phenylenediamine was polymerized to form a ladder polymer (alternating annealed phenylene and pyrazine rings [359]). Benzoquinone could be incorporated [360].

6.4 n-Doping

All the materials described hitherto in Section 6 are p-doped. The relatively rare cases of n-doping are compiled in this section. Polyacetylene $[Li_{0.2}(C_2H_2)]_p$ [43, 361] and poly(*p*-phenylene)(PPP)$[Na_{0.4}(C_6H_4)]_p$ [362] are examples for polyhydrocarbons. Polypyrrole was claimed by Wu and Xi [363] to act as a donor-type host lattice, but it

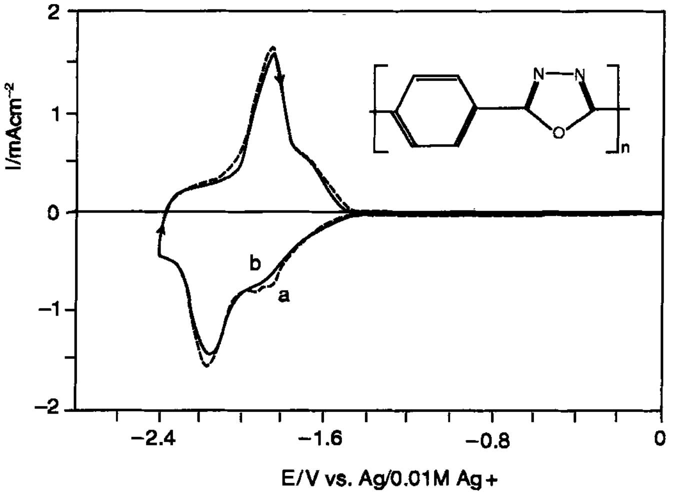

Fig. 29. Cyclic voltammograms of a p-POD (*p*-phenylene oxadiazole) film on a glassy carbon electrode. Voltammograms were measured in 0.1 M Bu_4NClO_4 in acetonitrile with a scan rate of 10 mV/sec. Curve **a** is the first cycle and curve **b** is the sixth cycle.

seems to be doubtful whether such a system is stable in the presence of traces of water, for the activated C=C double bond can be easily hydrogenated. However, an elegant indirect route is very well known: electrosynthesis is performed in the presence of a Nafion™ membrane [364, 365], dodecyl sulfate [366], and poly(styrene sulfonate) [367–369]. The large anions that are incorporated cannot be released again, and further cycling is due to Li^+ ions. The same strategy with a polystyrene dopant was successful in the case of polyaniline [370]. The last three examples are due to chemical polymerization. All three exhibit very negative redox potentials. For some poly(pyrimidine-2,5-diyl)s they were −1.6 to −2.2 V vs. SHE [371]. For the related poly(methylpyridine-2,5-diyl)s about −2.1 V vs. SHE was observed [372]. Another category is represented by the poly(phenylene-1,3,4-oxadiazole) shown as an insert in Fig. 29 [373]. This material is of interest also for light-emitting diodes (LEDs). It shows a redox potential of −2.0 V vs. SHE. Interestingly, the redox cycling with NBu_4^+ is reversible, but not for Li^+.

7 Carbonaceous Materials

Carbonaceous materials (CMs) are sometimes also named "polymeric carbons." They are mostly prepared by thermal decomposition of organic precursors. One strategy is pyrolysis of gaseous or vaporized hydrocarbons at the surface of heated substrates, a second is heating (pyrolysis) of natural or synthetic polymers, both in an inert atmosphere. The latter is of special interest, and according to Miyabayashi et al. [374], precursors such as condensed polycyclic hydrocarbons, polymeric heterocyclic compounds, phenol–formaldehyde resins, polyacrylonitrile or polyphenylene are heated to 300–3000 °C for 0.15–20 h. Sometimes, a temperature/time profile is run. The temperature range must be divided into two domains, namely

1. $\theta_P = 300\text{–}1350$ °C, sometimes up to 2000 °C, at which functional groups and heteroatoms are retained, and
2. $\theta_P = 2000\text{–}3000$ °C, at which more and more graphitic structures are obtained.

These materials were first discussed in Section 3.2 as host lattices for D-type GICs, mainly Li^+ compounds LiC_x, $x = 2, \ldots 10$. It has already been stated there that CMs are much more interesting than crystalline graphite. The very diversified activities worldwide in this field justify devotion of a separate section to these materials. There are a few recent reviews specializing in battery applications [374–376]. However, earlier monographs on industrial carbons do not mention this possibility, which has gained such an importance in our time [243–245, 377]. As already shown, the pyrolysis temperature determines the properties of the material. This is demonstrated in Table 8 [375] for three temperatures and two feedstock compounds, of which one acenaphthene (in coal pitch), is graphitizable, but the other, a phenol–formaldehyde resin, is not. Accordingly, only in the former case was a dense graphitic material

Table 8. Characteristics of model carbons graphitized at 2870 °C and carbonized at 1000 and 800 °C, and discharge capacities K_s (from [375]).

Feedstock[a]	$T_p(N_2,1\ h)$ [°C]	XRD data			ρ[b] [g/cm^3]	p[c] [Vol.%]	K_s[d] [Ah/kg]
		d_{002} [Å]	c [Å]	a [Å]			
AN	2870	3.37	23.3	1.0	2.22	2.6	316.5
	1000	3.43	21.8	20.1	1.91	41.0	264.3
	800	3.39	21.7	19.7	1.65	49.7	497.4
PH	2870	3.44	25.8	40.0	1.42	49.8	134.4
	1000	3.52	20.0	20.0	1.43	55.5	282.1
	800	3.55	11.1	19.6	1.54	57.0	385.7

[a] The carbonaceous products were obtained by pyrolysis at temperature of AN T_p (acenaphthene) and PH (phenol–formaldehyde resin); those from PH were nongraphitizable.
[b] Specific gravity.
[c] Cavity index.
[c] Discharge capacity.

obtained. The great difference in the discharge capacity between $T_P = 1000$ and 800 °C is remarkable. The same effect is observed for pyrolyzed polyacrylonitrile, PPAN (Fig. 30) [378]. Further discussion of this material follows below.

From investigations of this kind, model structures for CM could be derived. Figure 31 shows an example for the glassy carbon type, manufactured by pyrolysis of polyfurfuryl alcohol [379]. The components of the materials have a ribbon-like structure. Layered elements can be identified too. Li^+ is the counterion in negative CM, and two possibilities arise, either intercalation into the graphitized portions of CM or "adsorption" at "inner surfaces", especially in the case of a large specific surface. The corresponding electrode reactions were studied in detail in $LiClO_4$/PC + DME electrolytes [380, 381] (DME = dimethoxyethane). The initial cycle showed a redox capacity of 600 Ah/kg, but a steady-state value of only 140 Ah/kg was measured in the fifth cycle (cf. [382]). Kamo and co-workers found a relatively broad variation of the potential, as in Fig. 30 for 1000 °C, with an average of about −2 V vs. SHE, which is about 3 V more negative with respect to the example in Fig. 30. It is believed that carbonaceous materials make possible the formation of C_6Li free of co-inserted solvent molecules.

The CMs are discussed below in nine sections: (1–6) starting from an appropriate ensemble of precursors, or (7–9) grouped according to the mode of fabrication.

1. Activated carbon (AC) is fabricated from natural polymer sources based on cellulose, e.g., wood or coconut shells, which also provide an interesting cellular or fibrous texture. The dried starting materials are pyrolyzed (carbonized) at $T_P = 600$–830 °C. The yield of AC is 50–80%. Specific surfaces of 10–1000 m^2/g are obtained. The great advantage of this route is of course the possibility of obtaining a low-cost material, which is applied industrially in large quantities for adsorption and purification of streams of material [383, 384]. However, the employment for ECDLCs was patented at an early stage [385], and it is realized in commercialized products, in the so-called "Gold Cap" [386, 387]. Pretreatment of carbons, either oxidative (O_2,

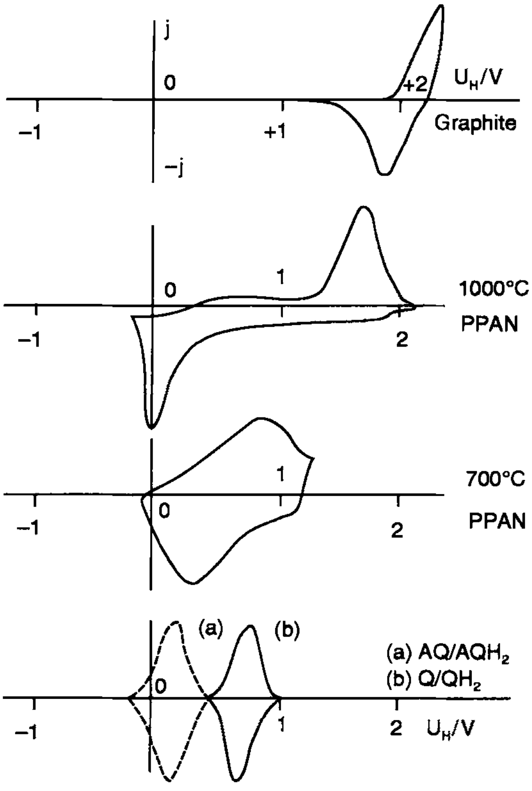

Fig. 30. Slow cyclic voltammetry (1 mV/s) in 1 M H_2SO_4 for various solid redox active substances, schematically. U_H is the potential vs. SHE.

air, HNO_3) or thermal, is of great importance (cf. [388]). Activation is also achieved by treatment with water and/or CO_2 at 800–1000 °C. Another natural source is pitch coke and pitch, based on coal tar; cf. Nos. 1 and 2 in Table 9 [389, 390].

2. Synthetic polymers are also suitable as an interesting starting material for the fabrication of activated carbons and carbonaceous materials. The pyrolysis is performed in an inert atmosphere. The higher order of these synthetic polymers should assist in the production of a more defined CM. Inexpensive candidates are the phenol–formaldehyde resins via the resol stage. Crosslinked polymers are obtained throughout. Examples of this were found in the following investigations (in parentheses: temperature of pyrolysis T_P): namely, Yata et al. [391] (450–800 °C), Zhang et al. [392] (1100 °C), Zheng et al. [393] (700–1100 °C), and Chu et al. [394] (500–750 °C). Pyrolysis yields were over 50%. Mixing of a powdery phenol resin with active carbon powder prior to the carbonization is sometimes recommended [395]. Furthermore, two examples via *o*-cresol–formaldehyde (Novolac) are listed in Table 9 as Nos. 3 and 4, taken from the Japanese patent literature [396, 397]. The pyrolysis temperature is as high as 1700 °C in both cases. A very interesting material,

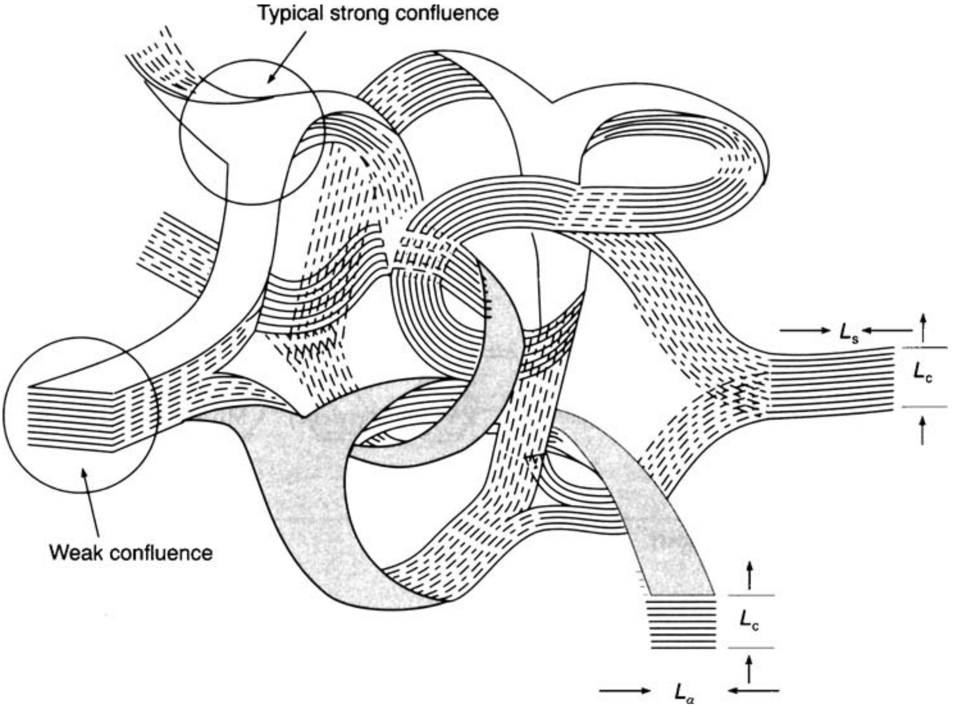

Fig. 31. Structure of carbonaceous materials. After [379].

which is called a carbon aerogel, also originates from a phenol–formaldehyde (mole ratio, 1:2) resin; the phenol is mostly resorcinol. However, the mode of fabrication seems to be rather complicated [18, 398, 399]. The following steps are essential:

- Curing. An aqueous solution of resorcinol/HCHO (1:2) + Na_2CO_3 (catalyst) is held for five days at temperatures of 20–90 °C.
- The transparent gels are subject to a supercritical drying after the substitution of water by acetone, which is then removed by CO_2.
- Pyrolysis at 1050 °C.

The material has a *priori* a continuous C-phase with a low resistivity. The specific surface is 100–700 m^2/g.

3. Another group of synthetic polymers have a linear structure. Poly(furfuryl alcohol), already mentioned in connection with Fig. 31 [377], belongs to this group, as of course do the vinyl polymers, e.g., PVC. Schuster has described the admixture of active carbon powder to overcome the agglutination of the thermoplastic polymers upon heating [400, 401]. The pyrolysis temperatures were rather low: 40 (?) to

Table 9. Carbonaceous materials for the negative electrode in rechargeable lithium batteries, with proposals for the positive electrode (selected from Japanese patent literature, 1988–1991).

No.	Precursor	T_p [°C]	Positive electrode (suggestion)	Reference
1	Pitch (→ coke)	1500	$LiMn_2O_4$	Nagaura, 1991 [389]
2	Pitch, based on coal tar (→ fibers)	1000	–	Ozaki, 1991 [390]
3	Novolac from *o*-cresol + formaldehyde	1700	V_2O_5	Inada, 1988 [396]
4	*o*-Cresol/CH_2O resin	1700	Carbon black	Morimoto, 1990 [397]
5	Poly(vinylidene fluoride)	800	–	Yamamoto, 1988 [402]
6	Benzene	1000	PANI (polyaniline)	Tajima, 1988 [441]
7	Benzene	1700	CrO_3	Tanaka, 1990 [442]
8	Polyacetylene	1500	TiS_2	Miyabayashi, 1988 [418]
9	Novolac for the negative electrode	800/1500	PA (polyacetylene)	Miyabayashi, 1988 [419]
10	Poly(p-phenylene)→ LGH (linear graphite hybrid)	700	V_2O_5	Inada, 1988 [424, 425]

* Metal-free rechargeable battery

300 °C. A pressure typically of 200 bar was used. The black, dense products exhibited, in an aqueous electrolyte (LiCl), a reversible redox capacity of up to 50 Ah/kg, which is a relatively low value. Table 9 contains an example (No. 5), starting from poly(vinylidene fluoride) [402].

Another method to improve the structural order of CMs is the conversion of the precursors to fibers prior to the pyrolysis step [377]. The precursor polymer may be stretched in addition. Carbon fibers are manufactured in large quantities as reinforcements in composite materials, after Bowen [403] and Fitzer [404]. Surface and bulk activation can be accomplished by anodic oxidation in dilute aqueous electrolytes (cf. Besenhard et al. [405, 406]). But carbon fibers with various degrees of graphitization have also been employed recently in rechargeable batteries [407–411] and in electrochemical double layer capacitors [18, 412–416]. This takes advantage of two fiber specific effects, namely

- The specific area of this kind of structurized material increases strongly with decreasing fiber diameter, cf. Eq. (8b).
- The resistivity is essentially reduced, for the material is a continuum along one individual fiber [417].

A relatively nonexpensive version starts from coal tar pitch. Activated carbon fibers (ACFs) are reviewed in [410]. Skundin has reported a felt texture to be an optimum for CM.

4. If polymers with conjugated C = C double bonds are employed, an even higher order should be achieved in the CM.

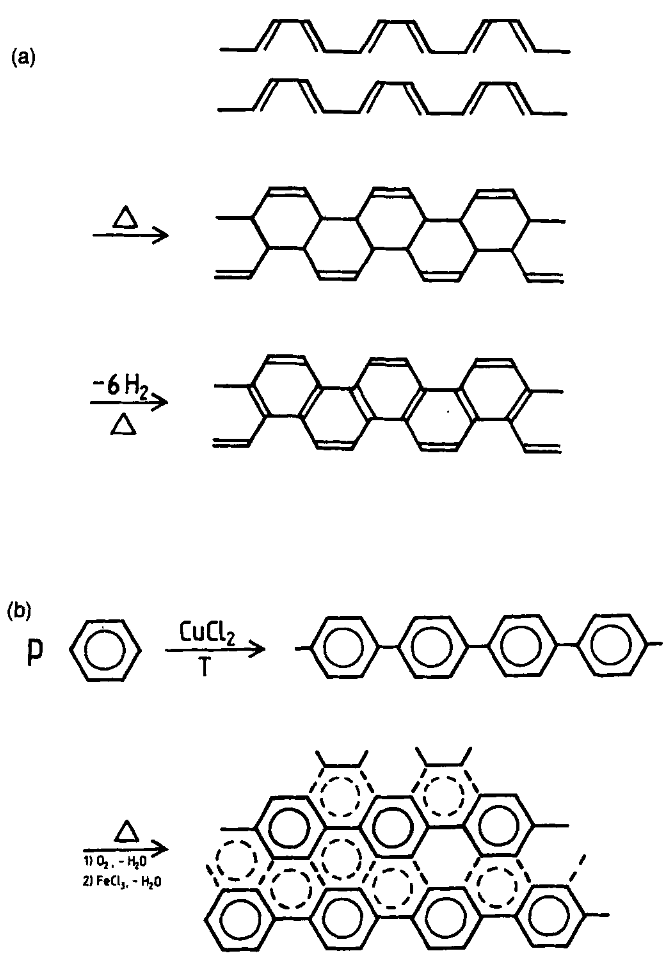

Fig. 32. Pyrolysis products of (a) polyacetylene and of (b) poly(*p*-phenylene).

Polyacetylene (98% *cis*) was carbonized by heating for 1 h at 800–1500 °C under N_2 (cf. Fig. 32 (a) [418, 419]). The 1500 °C product served as a negative electrode in an Li(CM)–TiS_2 battery, while the 800 °C product was a positive electrode (intercalation of ClO_4^-) in a metal-free battery with Li(CM) as the negative. In the latter case, CM was formed by pyrolysis of Novolac; cf. Table 9. The mechanistic aspects of carbonization of polyacetylene are summarized in Fig. 32 (a).

Poly(*p*-phenylene) (PPP), prepared from benzene according to Kovacic method [288, 420], was shown by Naarmann to turn from yellow to brown and finally to black with increasing reaction temperatures in an autoclave [421]. The conductivity increased accordingly [422]. This was attributed to a further condensation of the PPP chains to yield band graphite structures (cf. Fig. 32(b)). This kind of thermal structurization of PPP was also reported by Fitzer et al. [377, 423]. The temperature was 600–700 °C, and a yield of 90% was obtained. The ribbon tape graphite is also called "linear graphite hybrid (LGH)" [424]. With respect to LiC_x compounds made therefrom at 700 °C, ^7Li NMR reveals the existence of Li_2 molecules in the material [425]. The charge density is much higher and approaches the stoichiometry LiC_2 (cf. Table 6). This is attributed to a structure in which each Li in the LiC_6 structure, which is shown in Fig. 20, is surrounded by three Li–Li molecules. Every C_6 ring is then coordinated with one lithium.

A third way to synthesize band-type aromatic structures is starting from appropriate aromatic monomers. Müllen et al., especially, have demonstrated this possibility [297–301, 426].

5. Polyacrylonitrile is another precursor of CM that has been frequently investigated for the fabrication of carbon fibers [377]. Depending on the temperature, relatively defined intermediates can be prepared. Ladder-type polymers for a pyrolysis at 500–700 °C (naphthyridine ring structures) are obtained, as claimed by Becher and Mark [427] and by Topchiev [428]. This early work was further elaborated for battery applications by Schwarzenberg et al. [429] and by Jobst et al. [430, 431]. More extended condensation is achieved at higher temperatures and/or longer pyrolysis times. Structural details of this conventional concept are given in Fig. 33. The resistivity of the black product, which is obtained at 700 °C, is rather low, at about 5Ω cm [429]. EIS measurements are evaluated in terms of an influence of the porous structure [429, 432]. An application in electrochemical double layer capacitors is described [430]. The CV profiles in $LiClO_4$/PC extend from −2 V to 1.5 V vs. SHE with large hystereses.

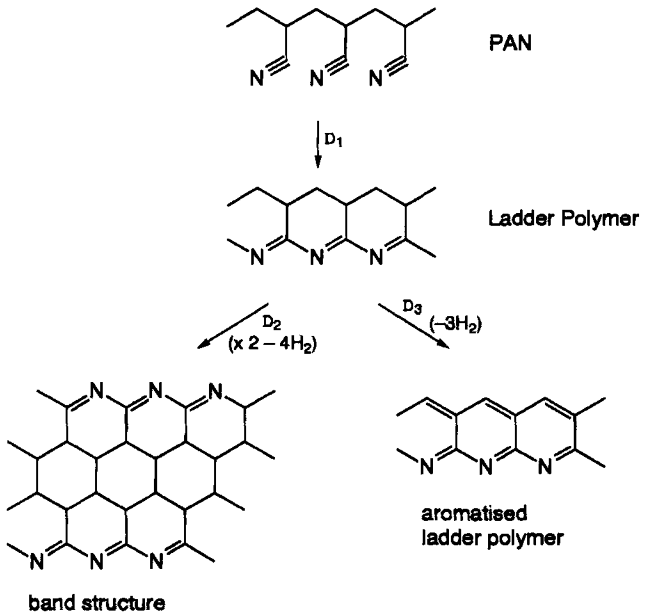

Fig. 33. Conventional structure of pyrolyzed polyacrylonitrile (700 °C).

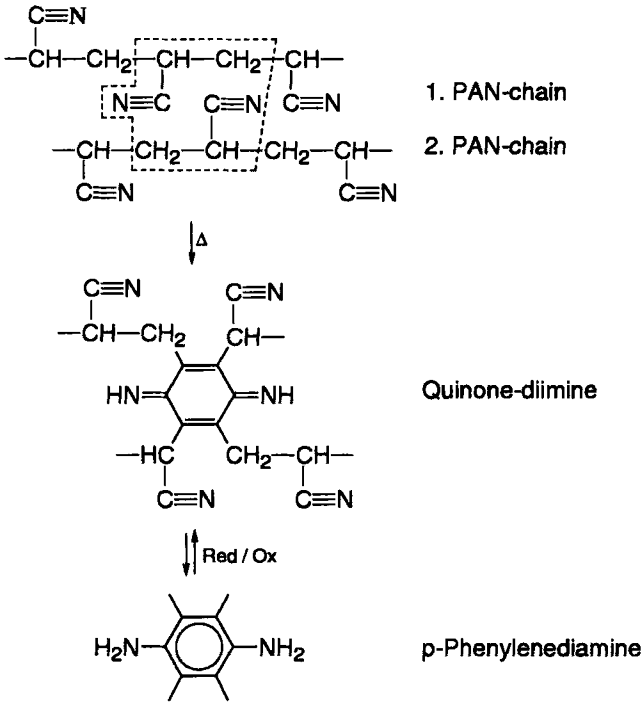

Fig. 34. Novel proposal for the structure of pyrolyzed polyacrylonitrile.

However, it is also possible to cycle CM made from pyrolyzed polyacrylonitrile in aqueous electrolytes, according to Beck and Zahedi [378]. Figure 30 shows relatively flat redox peaks around the quinone/hydroquinone center ($U_s \simeq 0$ V, about 0.7 V vs. SHE). Protons are the counterions in this case. A polyquinonimine structure is concluded from (electro)chemical and FTIR data (cf. Fig. 34). These acceptor-type compounds have relatively high specific capacities of about 300 Ah/kg in the steady state. The initial capacities are even higher. It should be mentioned that graphite nanotubules were synthesized in the nanopores of a porous Al_2O_3 matrix at 250/600 °C [433].

6. Interesting porous structures are achieved by anodic activation of glassy carbon (GC) in 3 M H_2SO_4 at +1.98 V vs. SCE. The porous layers are well contacted by the pristine GC basis behind this layer [240, 434]. Application in electrochemical double layer capacitors seems to be straightforward. However, maximum capacitances are only about 1 F/cm^2. This is due to the limitation of the layer thickness. In comparison to the maximum in Fig. 24 in the same electrolyte, namely 200 F/cm^3, this means a layer thickness of only 50 μm. Thicker layers become instable due to scaling.

It should be mentioned that the wide field of anodic overoxidation of conducting polymers [144, 263–274] may also serve to modify a polymer layer the ICP type to achieve a highly porous material on the previous base electrode, containing a high concentration of functional groups.

7. An interesting electrochemical alternative is the cathodic reduction of halogenated polymers, e.g., PTFE. The formation of black layers through wet (electrolytic) contacts of screen cathodes was reported [435, 436]. Pyrolysis of poly(2-chloro-1-phenylacetylene) [437] or, as already mentioned, of PVC [400, 401] are non-electrochemical routes, starting from halogen-containing polymers.

In summary, all the reaction routes (1–7) discussed hitherto start from polymeric structures. A subdivision seems feasible into

- controlled thermal/pyrolytic polymer degradation (1–3) with a mass yield of 90–20%, and
- intrinsic conversion of PA, PPP, PAN (polyacrylonitrile), and other precursors (4–7) with much higher mass yields.

The resulting thermostructured CM is characterized by graphite structures with a limited extension (10–20 nm) and a typical distance of layers in the *c*-direction of $d_{002} > 337$ pm, a specific surface of one-tenth several hundreds of square meters per gram, and an H/C ratio of < 0.15. This is due to nongraphitic regions between the pseudo-graphitic unit cells, which provide additional electrochemical activity. The in-plane order of the graphene layers is nearly perfect, but the staging structure deviates from crystalline graphite by shifts and by twists. The argon laser Raman spectrum exhibits two peaks at 1580 and 1360 cm^{-1} with an intensity ratio of from 0.4 up to 1. Strong paramagnetism is found in CM due to the high concentration of unpaired electrons, according to Murata et al. [438]. An Li/CM electrode has a golden color in the charged state, and it turns black after discharge. This has been proposed as a charge indicator. The electrochemical capacity of these materials was reported in some cases to be beyond C_6Li, either by an extreme dispersion of the CM [32, 439] or through a more densely packed in-plane order [425].

In the final part of this section, the starting materials are small molecules or monomers, and CMs are synthesized through polymerization. For route 7, this is achieved with hexachlorobuta-1,3-diene, which is cathodically polymerized in $LiBF_4$/CH_3CN to form a cation-doped black polymer [440].

In addition, there are two more methods.

8. Pyrolysis of gaseous hydrocarbons at 1000–1700 °C is a common route (cf. Nos. 6 and 7 in Table 9, where two examples involving benzene are considered [441, 442]). The substrate was nickel, and dense black layers were obtained to serve as a host lattice for the lithium negative electrode. The pyrolytic carbon from benzene at 1000 °C gave a lithium GIC (C_6Li) and could be cycled at 99% current efficiency [407]. Pyrolysis of epoxy Novolac resin and epoxy-functionalized silane gave a material containing silicon with a capacity of 770 mAh/g for the lithiated form [443].

9. The condensation of aromatic acid anhydrides, e.g., phthalic anhydride, with aromatic hydrocarbons, e.g., napthalene, in the presence of $ZnCl_2$ led to black polymer semiconductors of the polyacene quinone radical type [444, 445]. Resistivities in the order of 10^5–$10^{10}\Omega$ cm were measured. High spin densities are characteristic [446]. An evaluation as active materials has not yet been performed.

8 Electrodes and Electrolytes

All the **active materials** which have been discussed in this review have two features in common: they contain carbon, either alone (see Table 2) or in conjunction with oxygen, nitrogen, sulfur, etc.; and they are in the solid state. The latter is extremely beneficial for a practical accumulator. However, the density of the solids is in the range of only 1–2 g/cm^3, far below that of inorganic systems, and this leads unequivocally to relatively low-volume specific redox capacities [338].

Electric conductivity is an essential precondition. There is no problem with graphite or doped conducting polymers (see Table 1). In the case of insulating materials such as undoped π-systems or quinones, for example, two strategies have been known for a long time to provide charge transport:

- Electrolyte pathways in the porous electrodes, which shunt the insulating material down to the electronically conducting zone of the electrode.
- Admixing of 3–25% carbon black, thus generating a percolating network of electronically conducting inert material (cf. [477]).

General aspects of charge transport in active materials have already been discussed in Section 1.5 (cf. Fig. 10). According to this, porous structures are extremely important in this field, as shown in Section 1.3 (cf. Figs. 4 and 5). In the following, four groups of active materials are briefly discussed in connection with their transfer to practical electrode designs:

1. Graphite is an interesting host lattice for GICs. Natural-graphite-filled polyolefins ("CPP"; C/polyolefin 80:20, m/m) were developed [133, 134] as battery electrodes. It was found that long-term cyclic behavior was strongly influenced by the tensile strength of the polymer material [448]. In contrast to natural graphite blocks or pressed pellets, the periodic volume changes did not lead to any early mechanical disintegration, and thousands of cycles were indeed possible. Porosiy was introduced by in-situ formation (five to ten galvanostatic cycles [134]) or by the common method via pore builders [28, 339], e.g., powdery Na_2SO_4. The cyclic behavior was dramatically improved (Fig. 35). Recently a very interesting method for the fabrication of quasi-natural graphite electrodes was developed by Kaneko et al. [449]. Graphite powder and CM precursors like furan resins (from polyfurfuryl alcohol; cf. Fig. 31) were mixed 1:1 and carbonized at 1000 °C under N_2. The binder is then like glassy carbon, and test CVs, e.g., for ferro/ferricyanide, were identical with those at HOPG.

2. This leads to a group of electrodes in which porous carbonaceous material itself provides the active materials. The carbon aerogels [18, 398, 399] are representative of this phenomenon. Storck have developed a mathematical model for the potential distribution in an activated-carbon packed-bed electrode [450]. An intraparticle porosity as well as an interparticle macroporosity are treated. It is a general problem

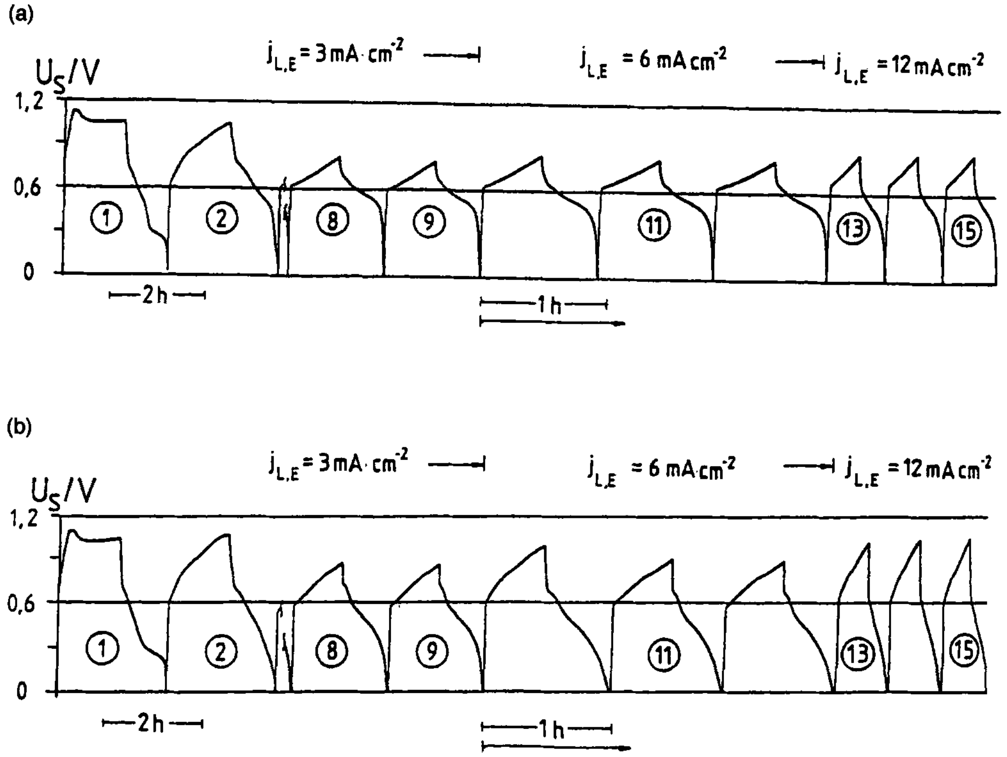

Fig. 35. Cycling of CPP electrodes (80 C/20 PP) in 12 M H_2SO_4: (a) porous, 9% Na_2SO_4, leached; (b) nonporous.

for "handling" of highly dispersed materials as electrodes. A direct application of the dispersion electrode, after Gerischer [451, 452], was tried for carbon black dispersions in 1 M H_3PO_4 [453]. However, the curves exhibited large overvoltages due to the adherence of c.b. particles at the feeder. A typical battery solution was found for precompacted c.b. electrodes (with 10% PTFE), which are employed in electrochemical double layer capacitors [33]. Their resistivity is as low as 0.03 Ω cm, which is comparable with glassy carbon [454].

3. A third category comprises conducting polymers. The film-forming anodic polymerization of monomers, e.g., pyrrole, leads in the majority of cases to porous or even biporous [28] polymer layers, adhering to the substrate. The porosity can be improved at higher current densities, but the overoxidation limit must be considered. Another improvement is possible in terms of the application of graphite felt as a substrate [28, 58, 455]. Last but not least, the co-deposition of dispersed c.b.s in the electrolyte leads to composites with up to 65 wt% c.b. in the polymer layer for

$d = 0.1$ mm [58, 324, 339]. It is possible with these strategies to reach acceptable active mass utilizations μ even for relatively thick layers, e.g., $d = 0.1$ mm. It was found that μ decreases linearly with log d. An interesting composite of polypyrrole/MnO_2 powder (up to 1:1), the components of which are both redox-active at similar potentials, was systematically evaluated by Yoneyama and co-workers [333]. A superposition of both K_s-values was observed, albeit with a relatively low efficiency in the case of MnO_2. A composite PANI/polydisulfide was investigated by Oyama et al., as was discussed extensively in Section 6.3. Redox catalysis via the more reversible PANI component was found. Another mechanism of this kind was suggested for a NaPb/PPP composite with PP binder (cf. Section 6.1) [295, 296].

4. Low-molecular-weight organics need a priori carbon black as an additive. An example is anthraquinone, which is used together with a carbon black. For many inorganic electrodes such as MnO_2, NiOOH, TiS_2, or CF_x the same strategy is followed up. Matveev et al. have provided a systematic study [81] of this system. An interesting feature is the possible presence of *o*-quinones at the surface of carbon particles, which transfers a double layer capacitor to much more interesting version with large pseudocapacitances [14]. Unfortunately, only relatively unspecific chemical activation is available at the present for this purpose.

Current collectors are a second component that is of great technical importance in a battery cell. The following properties are essential:

1. high electronic conductivity;
2. chemical/electrochemical inertness;
3. nonporosity for application as wall in bipolar designs;
4. good adherence to the active materials;
5. including no metals or inorganic conductors.

It is not easy to verify such a material. The common practical solution of the problem is on the basis of carbon-black-filled polymers [Mayr [455a]]. However, condition 2 excludes graphitic fillers. The binder may be polypropylene as an optimum. Unfortunately, the electronic conductivity is a factor 10^7 below that of a metal and 10^5 below graphite or PbO_2. This is prohibitive for side current leads, but bipolar designs are straightforward [456–458]. The problem might be solved by inserting a metal sheet, preferably made of aluminum; however, the principle of a metal-free battery would be jeopardized in this case. The c.b. concentration is 15–30 wt% to achieve a satisfying percolation behavior (cf. Fig. 36). Systematic studies are due to Skyllas-Kazakos and co-workers [456, 457] and to Beck et al. [458]. Closed pores may serve as a buffer for volume changes. These composites are more flexible than the conventional electrode carbons or variants such as glassy carbon [459] or reticulated vitreous carbon [460]. Hydrophobically modified silica gels are employed in a sol–gel process to form an extremely inert binder for carbon composite electrodes [461]. Polypyrrole/PVC blends are reported in the literature [462], but the filler is certainly not inert. A general review of polymer blends is given in [463].

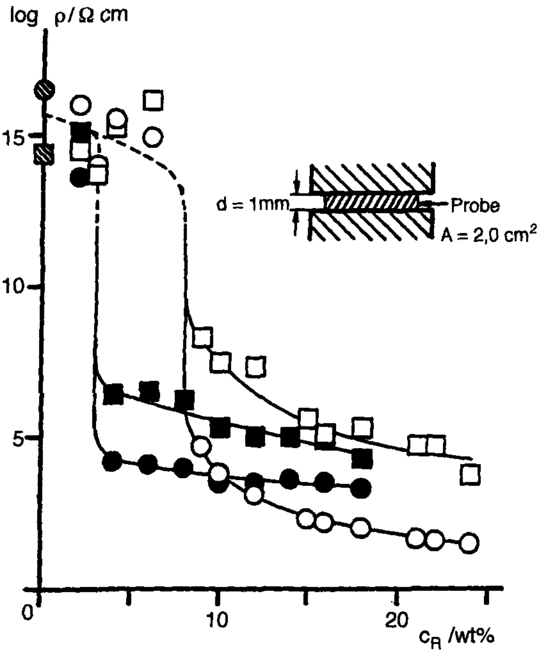

Fig. 36. Percolation curves for carbon-black-filled polypropylene Novolen 1120 HX, showing dependence of the logarithm of the resistivity ρ on the c.b. concentration: ○, Corax L, untreated; □, Corax L, emerified; ●, Ketjen Black, Untreated; ■, Ketjen Black, emerified. The configuration of the electrodes is shown schematically in the insert.

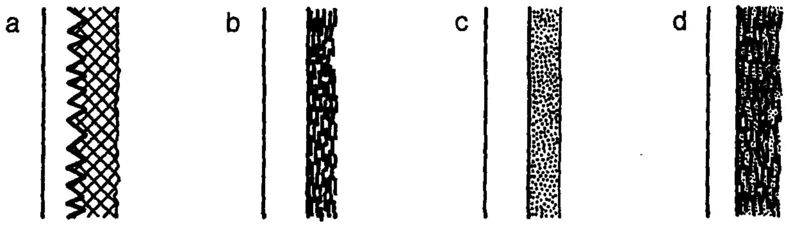

Fig. 37. Composite base electrode (left) and active materials (right) for batteries (a)–(d); for details, see the text.

The active materials can be deposited in different ways onto the base material (current collector). Figure 37 shows four examples: (a) painting of a slurry of active material plus carbon black plus binder onto a base electrode with "wafer" structure; (b) pressing of graphite flakes at higher temperature, where the van der Waals forces between the *ab* planes of the graphite flakes support their compaction; (c) anodic deposition of a (porous) layer of a conducting polymer; (d) a polyolefin-bound natural graphite layer with a backing made of carbon-black-filled polyolefin, designed to avoid migration of the anions.

The third part of a battery cell is devoted to the **electrolyte**. Liquid electrolytes, which include aqueous electrolytes such as 1 M H_2SO_4 or aprotic electrolytes such as

0.1 M $LiClO_4$ or $LiBF_4$ in PC (propylene carbonate) and others, have the highest specific conductivities, especially the aqueous systems. They range up to some 100 mS/cm and to about 10 mS/cm, respectively. The Li^+ ion has a relatively high mobility, and the transference number is also high, $t_+ = 0.7$. Quaternary ammonium ions exhibit ion association, which decreases with increasing ion size [464]. Admixing of pyrogenic silica such as Aerosil^{RTM} with liquid organic Li^+ electrolytes immobilizes these systems and enhances the conductivity somewhat [465].

Going on to solid polymer electrolytes, a broad variety of PEO-based systems is available since their introduction by Armand. Bisamino PEO/PPO polymers are reported [466]. Strong coordinatioin of the Li^+ ions to the ether functions leads to an unexpectedly low mobility of the cation, $t_+ < t_-$ (cf. [467]). The solid polymer electrolytes (SPEs) are being extensively developed at present; a special issue of *Electrochimica Acta* [468], more than 400 pages, has been exclusively devoted to this topic. The specific conductivities, however, are rather low, in the order of 10^{-5}–10^{-6} S/cm.

Recently, a solution of this problem was envisaged with the so-called "gel electrolytes" [469–471]. An organic solvents such as PC is employed as a plasticizer for the basic polymer, e.g., polyacrylonitrile. The specific conductivity is appreciably enhanced and may exceed 1 mS/cm. A similar strategy was used for inorganic systems, namely sol–gel vanadium oxide blended with SPE [472]. Interestingly, inorganic fillers such as Al_2O_3 or mica-type silicates [473] may also improve the ionic conductivity of PEO. A remarkable development in the field of solid polymer electrolytes was achieved by dissolving a polymer-like poly(propylene oxide) in a salt mixture. The rubbery solid electrolyte improves the contact with the solid electrodes [474].

Finally it should be noted that ambient-temperature molten salts such as 1-ethyl-3-methylimidazolium chloride have been studied in connection with the solution of organics such as anthracene [475] or dimethylaniline [476]. Naturally, the classical high-temperature salt melts are prohibitive for organic batteries, which must work near room temperature.

9 Cells and Batteries

Rechargeable batteries (r.b.s) contain an appropriate combination of reversible negative and positive electrodes. The energy density is given by Eq. (62):

$$E_s = UX \frac{\mu_+ K^+ \cdot \mu_- K^-}{\mu_+ K^+ + \mu_- K^-} \tag{62}$$

where U is the cell voltage, K^+ and K^- are the theoretical capacities, which are to be defined according to Eqs. (1)–(7), μ_+ and μ_- are the active mass utilizations for the positive and negative electrodes, respectively [477], and X is a factor depending on the cell design and the dilution of the electrolyte. X may be in the range 1.5–10; conventional accumulators have $X = 5$–6. For the calculation of the theoretical energy density $E_{\mathrm{s,th}}, X = 1, U = U_0$ (the thermodynamic equilibrium voltage) and $\mu = 1$ must be used. Clearly, the energy density of the r.b. is governed by that electrode with the highest K. This is especially clear in lithium-metal batteries (see Table 10(a), below), where normally $K^- \gg K^+$, and Eq. (62) reduces to $E_s \simeq UXK^+\mu_+$, if μ_+ and μ_- are of the same order. The second point is the extremely negative potential of the metal. These are the only two reasons why lithium batteries are favored by many groups.

A general classification of most of the metal-free batteries is based on the electrode categories defined in Section 1.2 along with Eqs. (14) and (15). The terminology "donor", "acceptor" (D, A) is used again, in spite of its shortcomings [10]. The other nomenclature, e.g. p-type instead of A-type and n-type instead of D-type, is omitted, however, for it suggests a propinquity to semiconductor physics which does not exist.

The two types of electrodes according to Eqs. (14) and (15) can be combined in the following three types of rechargeable batteries:

– *(A) D/D Batteries*

$$[\mathrm{W_p^- Li^+}] + \mathrm{W_n} \underset{\text{discharge}}{\overset{\text{charge (1)}}{\rightleftarrows}} \mathrm{W_p} + [\mathrm{W_n^- Li^+}] \tag{63}$$

In particular, the host lattice of the negative electrode and the lithium-insertion compound of the positive electrode is used, when the battery is mounted. This corresponds to the discharged state. It is at a lower energy level and therefore more stable than the charged state. The upper arrow corresponds to the first charge. $\mathrm{Li^+}$ migrates upon cycling in both directions ($\mathrm{Li^+}$ swing, $\mathrm{Li^+}$ shuttle, $\mathrm{Li^+}$ rocking-chair mechanism).

– *(B) A/A Batteries*

$$[\mathrm{W_n^- A^-}] + \mathrm{W_p} \underset{\text{discharge}}{\overset{\text{charge (1)}}{\rightleftarrows}} \mathrm{W_n} + [\mathrm{W_p^+ A^-}] \tag{64}$$

On mounting the electrodes to form the battery, the host lattice of the positive electrodes and the acceptor-type insertion compound of the negative electrode are employed. This corresponds to the discharged state, which is stable. The upper arrow corresponds to the first charge. On cycling, the anion migrates this time between the two electrodes (anion shuttle mechanism).

In each of these two systems (A) and (B) the electrolyte remains invariant if the stoichiometric factor for the co-inserted solvent molecules (not shown here) is identical. This great advantage, which, particularly in lithium systems, is also an advantage for the mass of the system, is lost in system (C):

– *(C) D/A Batteries*

$$W_n + W_p + Li^+ + A^- \underset{\text{discharge}}{\overset{\text{charge(1)}}{\rightleftarrows}} [W_n^- \, Li^+] + [W_p^+ \, A^-] \qquad (65)$$

The electrolyte salt will be consumed stoichiometrically upon charge. Normally A forms the positive and D the negative electrode. For mounting the electrodes in the battery cell, the undoped host lattices are used in conjuction with the concentrated electrolyte. As an alternative, the doped materials are employed, together with the diluted electrolyte. In this case, cycling starts in the discharge direction.

It should be mentioned that Gottesfeld et al. (cf. Section 9.3) have proposed a related scheme, which is confined to the development of ECDLCs based on conducting polymers. Indeed, their "group III" is essentially identical to the present category (C).

It is highly appropriate to define individual current efficiencies for the processes at the battery electrodes in the charge direction (λ) and the discharge direction (ϵ) [17, 58, 158]. The number of moles (n) of active materials generated, e.g., at the positive electrode on charging is then given according to Faraday's law by:

$$n_+ = \lambda_+ \cdot Q_{\text{ch}}/zF \qquad (66)$$

Discharge starts from the same amount of active material to yield an electric charge:

$$Q_{\text{disch}} = \epsilon_+ \cdot n_+ \cdot zF \qquad (67)$$

The Ah efficiency α can be derived:

$$\alpha_+ = Q_{\text{disch}}/Q_{\text{ch}} = \epsilon_+ \cdot \lambda_+ \qquad (68)$$

Thus α becomes inefficient if one or both electrode current efficiencies are below unity, and the cyclability of the cell is only possible if

$$\alpha_+ = \alpha_- \qquad (69)$$

Otherwise, nonreacted active materials will accumulate at one side.

Figure 38 identifies to some extent the possible cell designs in r.b.s. Conventional accumulators are composed of porous electrodes of the second kind [3, 11, 17] (1), but in the case of metal-free cells this is more or less the exception, and solid-state electrodes (A), (B) or (C) are combined, porous or not (2). The theory was developed by Atlung et al. [44–46]. (1) and (2) are based on electrochemical reactions. But electrodes with a high specific surface area, based on active carbon, carbon blacks, or other materials, allow for the special design of an ECDLC (3), where primarily electrochemical reactions are not involved. As indicated in Figure 38, the amount of electrolyte will be medium; (i.e. between case (1) and (2)).

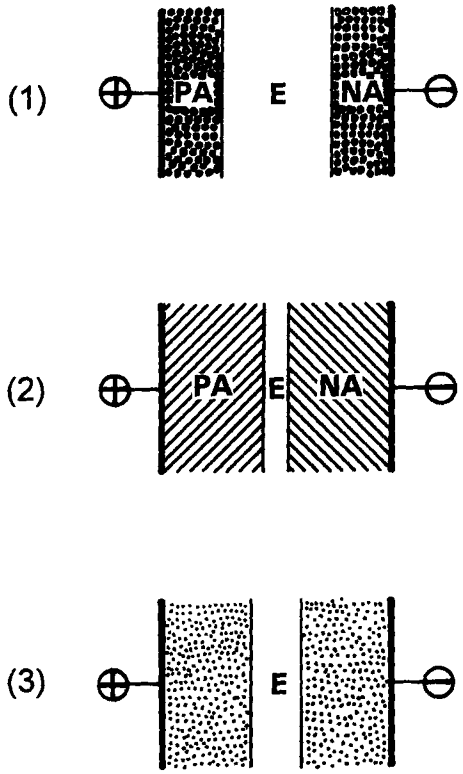

Fig. 38. Symmetrical combinations of positive and negative active materials, PA and NA, in (1) conventional accumulators, (2) swing accumulators and (3) electrochemical double layer capacitors. The relative electrolyte (E) volume is shown schematically. The thick, vertical lines represent the current collector (schematically).

Of special interest is the bipolar electrode design, anticipated already by Alessandro Volta in his voltaic pile. There are several pronounced advantages [478]:

- no bus bars or intercell connectors;
- no resistance losses along or across electrode plates, and minimal voltage losses from one cell to the next;
- uniform distributions of current and potential;
- improved rate capability of the battery, especially in D/D and A/A types.

In spite of this, the practical verification of the idea has been severely hampered to the present-day, mainly due to material problems for the so-called "bipolar wall." Even for the lead–acid accumulator, the development is only at the initial stages [479]. Metal-free batteries suffer somewhat from poor electronic conductivities of the current collectors, as already pointed out in the previous section, and this feature alone would highly justify the introduction of bipolar cell designs.

Sections 9.1 and 9.2 will deal with hybrid systems, in which one electrode is a metal or an inorganic compound such as PbO_2 or TiS_2. "Lithium systems" are treated separately (Section 9.1) from the others (Section 9.2) because of their great diversification (cf. Tables 10 and 11). Though this is not the place to cover all the many inorganic systems known today [480], some examples for exclusively inorganic lithium batteries are presented in order to have a suitable basis for comparative evaluations. It is only Section 9.3 which provides a survey of entirely metal-free rechargeable batteries (cf. Table 12).

9.1 Lithium and Lithium-Ion Cells

These rechargeable batteries have gained considerable interest in recent years due to their potential high energy densities. A possible application would be in electrotraction. The "clean air acts" for the State of California and others (originally 1997 but probably 2000 or 2003) provide a strong driving force for this development. However, numerous technical problems inhibit industrial realization and scaling-up to a battery of the order of a some 10 kWh which is needed to meet their commercial introduction for electric cars. As shown in Tables 10–12, commercialized batteries are presently in the 1–10 Wh range, to be useful for portable electronics rather than for electrotraction. At present and in the near future no lithium or lithium-ion batteries will be available for electric vehicles [480a].

The highest energy density could be achieved with lithium-metal electrodes. The first section (a) of Table 10 is devoted to such systems. It should be mentioned that the examples given there are partly a matter of historical development, e.g., earlier r.b.s with a lithium negative electrode would be built today with the more stable negative electrodes of the LiAl or LiC_6 type; cf. sections (b) and (c) of Table 10.

The problem of finding a really stable lithium electrode in *organic* solvent/electrolyte systems remains unsolved: Peled [203–205] and Aurbach and co-workers [206–209], for example, have identified protecting layers on the lithium metal surface as a consequence of the extreme reactivity of the alkali metal. Recently, on the other hand, Pletcher et al. have demonstrated, at least at microelectrodes, that the Li/Li^+ couple in $PC/LiAsF_6$ has fast kinetics, and surface film effects are practically excluded [481]. The only really stable lithium system at room temperature seems to be the totally inorganic system No. 1 in Table 10 (with a CoO_2 positive electrode) [482, 483]. Unfortunately, the much more interesting MnO_2 as a positive electrode is prohibited due to chemical reduction by the SO_2 component. The following five examples (Nos. 2–6) also have inorganic positive electrodes, but the electrolyte is organic. It is instable at both electrodes. As an example, CoO_2 has a positive potential of about 4 V vs. Li, and achievement of at least a relative stability is attempted by using an exotic electrolyte as listed in Table 10. All positive electrodes function as host lattices for Li^+ ions, and in the cell, on charge, Li^+ ions move to the negative electrode for plating, and on discharge, they come back to the positive electrode to be inserted. The charge stoichiometry for MnO_2 is only 0.5 F/MeO_x, but for the others it is about 1 F/MeO_x or TiS_2.

In spite of the numerous difficulties that exist for lithium-metal systems, three examples, Nos. 7–9, were temporarily commercialized. A large *primary* reserve battery, Li/MnO_2 with an organic electrolyte system, was developed by the Hoppecke Co. (data: 16 kWh, 100 V, 1.5–6 kW, 55 kg); 34 cells with 200 Ah and 270 Wh/kg

Table 10. Data for lithium and lithium-ion cells.

No.	Type	Negative electrode[a]	Positive electrode	Electrolyte	U_0 [V]	$E_{s,th}$ [Wh/kg]	Ref.	Remarks
(a) *With lithium-metal electrodes*								
1	ai	Li metal	CoO_2	$LiAlCl_4/SO_2$	4.0	1096	[482, 483]	99% c.e. for Li cycling at 40 mA/cm^2
2	ai	Li metal	CoO_2	$LiAsF_6$+$LiBF_4$ in methyl formate	4.0	1096	[484]	E_s is 250% of that of AgO/Zn
3	ai	Li metal	V_2O_5	1 M $LiAsF_6$, PC/EC/DME (1:1:2)	3.8	1041	[485]	Spirally wound cylindrical cells
4	ai	Li metal	MnO_2	1 M $LiClO_4$, PC/CME (1:1)	3.0	445	[486]	Design as primary cell
5	ai	Li metal	TiS_2	$LiAsF_6$, 2-MeTHF/EC (9:1)	2.2	496	[487]	Cell design as in No. 4
6	ai	Li metal	Cr_3O_8	1 M Li ClO_4, PC/DME (1:1)	2.7	712	[488]	Cr_3O_8 from CrO_3, thermal decomposition
7	ai	Li metal	MoS_2	?	1.8	289	–	Commercialized, Moli Energy, Canada
8	ai	Li metal	MnO_2	?	3.0	445	–	Commercialized, Tadiran, Rehovot, Israel
9	ai	Li metal	VO_x	?	3.8	1041	–	Commercialized, Hydroquebec, Canada
10	ai	Li metal	Ternary GIC	–	2–3	–	[161]	A-type
11	meO	Li metal	C_nA^-	$LiClO_4$, PC	5.2	353	[489–494]	$E_{s,th}$ holds for $Li/C_{24}ClO_4$
12	meO	Li metal	Polyacetylene$^+ClO_4^-$	$LiClO_4$, PC	3.0	340	[276–278]	$y = 0.2$ (one ClO_4^- per five $-C_2H_2-$)
13	meO	Li metal	$PPy^+ClO_4^-$	$LiClO_4$, PC	3.0	267	[314–320, 496–501]	$y = 0.33$ (one ClO_4^- per three $-C_4H_3N-$)
14	meO	Li metal	PPy^+, large anion ($C_{12}SO_3^-$), Li^+	$LiClO_4$, PC	3.0	178	[502, 503]	$y = 0.33$ (one dodecylbenzene sulfonate per three $-C_4H_3N-$)
15	meO	Li metal	$PThio^+$ ClO_4^-	$LiClO_4/PEO$	3.5	266	[504, 505]	
16	meO	Li metal	$PANI^+ClO_4^-$	$LiClO_4$, PC	3.0	(a) 820 (b) 816	[508, 513]	Calculated for (a) $z = 1.0$ and (b) $z = 2.0$ ($y = 0$ and 1 ClO_4^-) per C_6 ring; cf. Eq. (66)
17	meO	Li metal	Polydisulfide	$LiN(SO_2CF_3)_2/PEO$	2.5	–	[102–105]	
17a	meO	Li metal	Polydisulfide + PANI	$LiClO_4$,PC	3.4	900	[106–108]	Composite electrode
(b) *With lithium-alloy electrodes*								
18	meC	Li/Wood's metal	Carbon black	$LiClO_4$/?	3.0	113	[247, 248]	Commercialized, Matsushita, K^+ up to 50 Ah/kg; K^-: $Li_l(Bi, PB, Sn, Cd)_l$
19	meO	LiAl	$PANI^+ClO_4^-$	$LiBF_4$/PC + DME	3.2	(a) 692 (b) 664	[514–517]	Commercialized by Seiko/Bridgestone (a) 1 F/unit; (b) 2 F/unit; cf. Eq. (70)
20	ai	LiAl	MnO_2	?	3.0	374	[519]	$E_{s,th}$ calculated by $LiAl/LiMn_2O_4$; commercialized by Sanyo Corp.
(c) *Lithium-ion cells*								
21	Ci	LiC_6	$LiMn_2O_4$	Salts in PC/DEE or EC/DEE	3.6	372	[525–531]	
22	Ci	LiC_6	CoO_2	?	3.6	568	[533, 534]	Commercialized by Sony Energy Tec
23	Ci	LiC_6	NiO_2	?	3.6	569	[535]	
24	Ci	LiC_6	TiS_2	–	1.8	253	[536]	
25	CO	LiC_6	PPy	$LiClO_4$/PC	2.6	187	[541]	$y = 0.33$ for PPy, $A^- = ClO_4^-$

[a] Abbreviations: ai, all inorganic; meO, metal/organic; meC, metal/carbon; Ci, carbon/inorganic; CO, carbon/organic.

were switched in series. It was designed for the HERMES space shuttle (EC program).

Flandrois [161] has reviewed lithium cells with ternary GICs, mostly with inorganic components, as the last example (No. 10) for all-inorganic systems. A combination of lithium with "graphite salts," A-type GICs $C_n^+A^-$, should lead to extremely high voltages, $U_0 > 5\,\text{V}$. About 100 examples are collected in [489]. Bennion and co-workers [490–492] and Japanese workers [493] have studied these combinations in detail. The carbon positive electrode can also be fabricated from graphite fibers [495]. The main problems are again the stability of the solvent/electrolyte system at the negative and now, in addition, at the positive electrode.

Intrinsically conducting polymers (ICPs) have also frequently been combined with lithium negative electrodes. Entry 12 in Table 10 gives an example for polyacetylene (PA) [276–278]; cf. Section 6.1. In spite of the moderate PA potential, the positive electrode decomposes on cycling, due to overoxidation [284]. The cyclic curve shown in Fig. 26 refers only to a partial conversion of $\simeq 20\%$ ($y = 0.05-0.041$) of the PA positive. Many proposals were made in connection with a Li/polypyrrole rechargeable battery, for PPy is some kind of a standard ICP, and it is relatively stable. BASF together with VARTA temporarily commercialized such a battery [319–321], and other efforts have been reported [315–318, 495–501]. However, the lithium metal negative was not really reversible, and the energy density was rather low. An excess of lithium foil was provided to buffer the metal losses for each cycle. The usual liquid electrolyte, $PC/LiClO_4$, was employed, but in some cases also conventional solid-state electrolytes based on poly(ethylene oxide) [495, 496], where the transference number t_+ was only 0.19, but $t_- = 0.81$. The current collector for the polypyrrole had a large surface in terms of porous carbon [497] or carbon cloth [498, 499]. Foils of PPy, made by the continuous anodic process, were used to provide a spirally wound design of the positive electrode [500]. The lithium was in the form of a coaxial cylinder in the center. A similar cell was built with PPy, deposited on a glass fiber separator by vapor-phase polymerization of pyrrole using $FeCl_3$ as an oxidant [501]. A mathematical model of the Li/PPy cell was reported [502].

While all these proposals refer to a D/A battery, with a stoichiometric conversion of the electrolyte, some authors construct a D/D battery (cf. No. 14 in Table 10), were large anions, such as poly(styrene sulfonate) [503] or dodecylbenzene sulfonate are irreversibly inserted in the course of the electropolymerization [504], and the Li^+ ion is reversibly cycled.

Polythiophene (from bithiophene) was also proposed as the positive electrode in a rechargeable lithium battery [505, 506]. All solid-state batteries were assembled with $PEO/LiClO_4$. Poly(3-methylthiophene) was used in Li/SO_2 rechargeable cells [507].

Organic polydisulfides were combined with lithium metal in solid-polymer electrolytes [102–105]; cf. No. 17 in Table 10 and Section 2. The cells were cycled at 80 °C.

Polyaniline is frequently used in r.b.s with lithium negative electrodes. However, in the course of the development of a commercialized system (Seiko/Bridgestone), there have only been a few examples with true lithium-metal negative electrodes, but many for the more practical LiAl alloy electrodes. The redox processes of PANI are basically the same in aqueous electrolytes and in Li^+-containing organic solutions.

However, only the latter can be employed in conjunction with lithium, LiAl or LiC_6 negative electrodes A two-step redox process is discussed according to Section 6.3 and Eq. (70). The first two-electron step leads to the (green) emeraldine form, where the *N*-protons have disappeared and an alternating chain of benzoid and quinoid C_6 rings have formed. The second two-electron process leads to an anion-doped

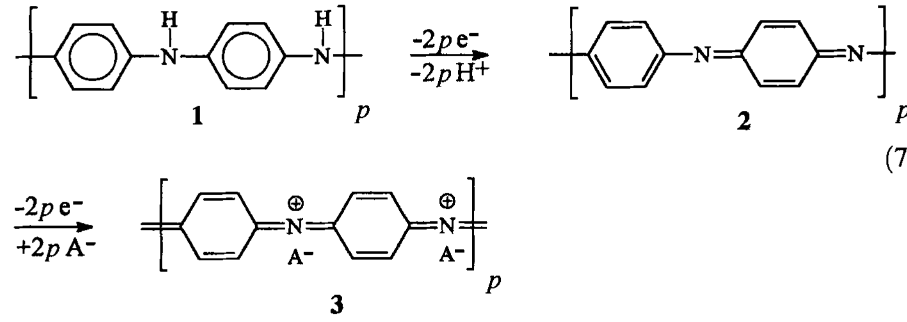

(70)

polymer, where all rings are in the quinoid state, as shown in Eq. (70). It should be mentioned that this presentation is only formal; the all-quinoid state is not realistic, but it reflects the theoretical charge stoichiometry in accordance with the monomer model hydroquinone (for $HO(C_6H_4)NH_2$, the hydrolysis product of PANI) → semiquinone → quinone. The theoretical capacity is then as high as 295 A h/kg for the transition **1** → **2** (1 F per monomer unit) and 285 A h/kg for **1** → **3**, $A^- = HSO_4^-$ (2 F per monomer unit); cf. Table 1. However, other calculations [351, 545] are based on the transition of leucoemeraldine (**1**) to emeraldine base,

$$\left[(C_6H_4)\text{-NH-}(C_6H_4)\text{-NH-}(C_6H_4)\text{-N} = (C_6H_4) = \text{N}\right]_p$$

which is described in depth in the classical preparative organic literature. In this case, only 0.5 F per monomer unit is transferred, and the theoretical capacity drops to 147 Ah/kg. Practical capacities of about 100 Ah/kg are reported [351, 545], but this may be a matter of incomplete active mass utilization.

Thus, in analogy with the monomer quinone/hydroquinone redox couple, two electrons per monomer unit are assumed to be transferred finally. Examples for lithium metal negative electrodes in combination with PANI are reported in [508–510]. Details of the preparation of PANI positive electrodes are given in the patent literature (e.g., [358, 511–513]).

Switching to lithium-alloy negative electrodes, some voltage loss must be noted. LiAl has $U_{Li} = +385\,mV$, $Li_{4.5}Pb$ has $U_{Li} = 388\,mV$. Entries 18–20 in Table 10(b) represent three examples of rechargeable cells, which have been, at least temporarily, commercialized. The first (No. 18) is due to a lithium alloy/carbon black battery commercialized by the Matsushita Co. [248]. The lithium alloy components are Pb + Cd + Bi + Sn (Wood's alloy). Button cells in the range 0.3 to 2.5 mAh were offered. The electrolyte was $LiClO_4$ in an unknown solvent. The practical energy densities, $\simeq 2$ Wh/kg, were rather low. The c.b. positive electrode acts as a double layer capacitor. For a sample with $1000\,m^2/g$, $\simeq 50$ Ah/kg is claimed [247]. This is nearly the same value as for *aqueous* systems shown in Fig. 24. However, as nonaqueous electrolytes lead to lower values, a contribution of pseudocapacitances must be assumed. The second system was a LiAl/PANI cell from Seiko/Bridgestone [514, 515]. A factor of 3 was claimed with regard to the specific energy of the Li/c.b. cell. Electrochemical [516] and chemical [517] syntheses of PANI were thoroughly elaborated. A capacity of 120 Ah/kg was reported for the former; this is only 43% of the second step in Eq. (70). A ternary alloy, Li(Al/Mg), was also employed in a PANI battery [518]. A third example is the LiAl/Mn_2O_4 cell of Sanyo. Cells with 20 and 70 mAh are on the market [519]. The practical energy density is only 33–49 Wh/kg. Interestingly, the LiAl negative is doped with manganese to improve the cyclability. A systematic discussion of lithium alloys for r.b.s with oxide positive electrodes, mainly LiAl/Mn_2O_4, NiO_2, or CoO_2, is given in [520] (cf. [174]).

The polybenzene cell reported by Shacklette et al. [293] also has a LiAl negative electrode.

LiC_6 as a donor-type GIC is an alternative negative material, which has been a favorite for years due to its excellent cyclic behavior [173, 174]. Combinations with graphite or ICPs afford an entirely metal-free battery and as such should be treated in Section 9.3 but, on the other hand, they are essentially types of "Li^+-ion batteries", and are therefore discussed here. The material for the host lattice may be crystalline graphite (cf. Section 3.2), but particularly carbon black (Section 5) or carbonaceous materials (CMs, Section 7). Many examples have been dealt with there, and only two further should be mentioned now. A rechargeable lithium battery with a positive bed of powdery carbonaceous materials is claimed in [521] in combination with a MnO_2 positive. Another patent [522] describes a battery with a mixture of CM and Li_4Pb powder as the negative and V_2O_5 as the positive material. The electrolyte was 1.5 M $LiPF_6$ in 2-methyltetrahydrofuran. The first attempt to employ LiC_6 negative electrodes originates from 1983 [523]. A review on rechargeable lithium batteries [524] stresses the usefulness of Li–Mn spinels $LiMn_2O_4$ as positive materials, and this special combination seems to be scheduled for the development of large cells, as is demonstrated by the many publications in the field [520, 525–531] (cf. No. 21 in Table 10 (c)). Propylene carbonate (PC) or 1:1 mixture of PC/DEE (diethoxyethane) or EC/DEE (EC = ethylene carbonate) were employed as aprotic solvents. Another candidate for the positive material is the layered oxide, CoO_2; this battery was the first to be commercialized [532] by Sony Energytec [533]. The capacities of these LiC_6/CoO_2 accumulators for electronic equipment range from 0.4 to 1.08 Ah, much higher than for LiAl/MnO_2. The nominal cell voltage was 3.6 V. The practical energy densities were between 78 and 99 Wh/kg. Besides the solvents mentioned above, PC/DME was used [534]. A similar LiC_6/NiO_2 cell is also reported [535]. The potentials of the oxide positive materials are rather high in all three cases, about 1.0 V vs. SHE. The danger arises of oxidative degradation of the organic solvent. If one substitutes LiC_6 by $LiTiS_2$ in the same battery, the cell voltage drops to 1.8 V [536]. The current density is as low as $0.02\,mA/cm^2$.

Finally some engineering aspects should be considered. Transport problems in Li/MeO_x [537] and LiC_6/MeO_x [538, 539] cells have been discussed thoroughly. The beneficial bipolar lithium-ion batteries are considered in this connection [540].

Only a few examples with organic positive electrodes are known. A representative one is the LiC_6/PPy r.b. [541]. An ambient-temperature, all-solid-state r.b. with a PPy positive electrode, a gelatinous PAN-based solid electrolyte, and lithium is described in [542]. The current densities are relatively high, at 0.1 mA/cm^2.

9.2 Hybrid Cells

A hybrid cell can be defined as a system in which only one electrode of the secondary cell is graphitic, carbonaceous, or organic, but the other is inorganic. The most important cells have metals as negative electrodes. Lithium cells of this kind have already been discussed in detail in Section 9.1 (cf. Table 10(a)). In this section, systems with other metals as the negative are considered; see Table 11(a). They are organized in the same order as in this review.

Starting with a quinone electrode (No. 1), the copper salt/diaphragm/hydroquinone r.b. is claimed in a patent [543]. The cyclability is excellent, but the voltage is less than 0.5 V. One advantage is the impossibility of generation of H_2, a gas which cannot easily be recycled in an r.b. An alternative to the quinone accumulator (cf. Sections 2 and 9.3) is the Zn/chloranil cell [71–74].

Metal/graphite cells (cf. Section 3.1) in concentrated sulfuric acid have been discussed by Fujii [153, 154], and in medium-concentration H_2SO_4 by Beck and Krohn [155–157]. The metals were copper, iron, lead, and zinc [155, 156]. But really good cyclability was found in the system Pb/60% H_2F_2/A-GIC [156]. More than 3000 cycles, in one case nearly 6000 (1.4 years), 1/1 h, (1 hour charge/1 hour discharge) could be achieved. The current density was 3 mA/cm^2. The medium discharge voltage was 1.7 V initially. The "CPP" positive electrode (natural graphite/polypropylene, 80:20 m/m) survived all these cycles [133, 134, 448]; cf. Section 8. Cyclic curves are shown in Fig. 39. The practical energy density was about 25 Wh/kg. The combinations of D–GIC (LiC_6) with MnO_2, TiS_2, or PPy have already been discussed in Table 10(c).

Proceeding to the conducting polymers, it is predominantly polyaniline that has been combined with zinc in aqueous electrolytes [544–548]. The aqueous electrolyte was 1 M $ZnCl_2$ or saturated $ZnCl_2$ [547]. A weak acid electrolyte was important for optimum cyclability of PANI. The final goal of this development was to find a substitute for the conventional (primary) Zn/MnO_2 cell. However, the current density was rather low (1 mA/cm^2), as was the voltage ($\simeq$ 1 V), but a relatively high practical energy density could be achieved, about 70 Wh/kg, which must be compared with the theoretical one quoted in Table 11(a). An Al/PANI battery was reported, too [549, 550]. The electrolyte was an ambient-temperature salt melt in this case (cf. Section 8). The rechargeability of the aluminium electrode in this electrolyte seems to be satisfactory. However, the cell voltage remains at a low level, $U_0 = 1$ V.

Besides metal negative electrodes, *inorganic positive* electrodes have also been combined with organic materials (Table 11(b)). Lead dioxide was used in combination with anthraquinone [79, 551] in H_2SO_4. Construction of sealed cells was possible due to the fact that anthrahydroquinone reacts rapidly with O_2 coming from the positive PbO_2 on overcharging. A similar PbO_2/PANI cell has been reported

Table 11. Data for hybrid cells: combinations with metal negative electrodes other than lithium (Table 10) or PbO_2 and TiS_2 positive electrodes.

No.	Type[a]	Negative electrode	Positive electrode	Electrolyte	U_0 [V]	$E_{s,the}$ [Wh/kg]	Ref.	Remarks
(a) *With metal negative electrodes*								
1	meO	$Cu(SO_4)$	*p*-Benzoquinone	$CuSO_4/H_2SO_4$	0.5	99	[543]	
2	meO	$Zn(SO_4)$	Chloranil	$ZnSO_4/H_2SO_4$	1.5	197	[71–74]	
3	meC	$Pb(F_2)$	Graphite	60% HF	1.7	63	[156]	Graphite; 2nd stage[b]
4	meC	$Zn(SO_4)$	Graphite	12 M H_2SO_4	2.2	84	[155, 156]	Graphite; 2nd stage[b]
5	(H)C	Pd(H)	Graphite	Conc. H_2SO_4	0.8	44	[153, 154]	PdH, graphite; 1st stage[b]
6	meO	$Zn(Cl_2)$	PANI	$ZnCl_2$ (1 M to satd.)	1.0	(a) 168 (b) 236	[544–549]	(a) 1 F per C_6H_4NH unit (b) 2 F per C_6H_4NCl unit
7	meO	Al	PANI	RT salt melt (Cl^- anion)	1.0	(a) 198 298	[550–551]	see No. 6
(b) *With inorganic positive electrodes*								
8	Oi	Anthraquinone	PbO_2	4 M H_2SO_4	1.5	179	[79, 552]	
9	Oi	PANI	PbO_2	4 M H_2SO_4	1.5	194	[547]	PANI: 1 F per C_6H_4NH unit
10	Oi	Polyacetylene	TiS_2	THF/$NaPF_6$	0.7	78	[43]	PA: $y = 0.1$ per C, $NaTiS_2$

[a] For abbreviations, see Table 10. Oi, Organic/inorganic.

[b] No HA co-intercalation assumed.

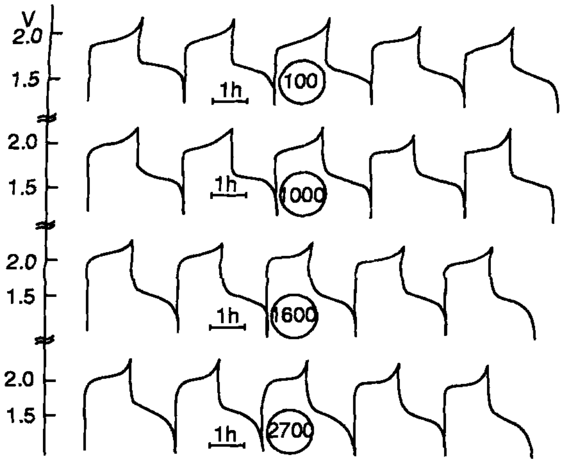

Fig. 39. Long-term cyclization of the cell Pb/60% H_2F_2/CPP. The current densities on charge (1 h) and discharge (down to 1 V) were each 3 mA/cm^2. Cycle numbers are indicated by ring numerals. After [157].

[544]. Polyacetylene/TiS_2 was successfully cycled in THF + $NaPF_6$ [43]; the cell voltage, however, was only 0.7 V. A CoO_2 positive electrode was combined with a Na_xPb-alloy negative electrode [295, 296]; PPP as an additive improved rechargeability (cf. Section 6.1). Such cells were developed to some extent at Allied Signal Co. (USA). Practical energy densities up to 70 Wh/kg were realized.

Lead plates coated with a thin PANI interlayer were recommended for the lead–acid accumulator [552].

9.3 Cells Free of Metals and Inorganic Active Materials

The ultimate goal of this review and present results in terms of r.b.s will be discussed in this section. The material is organized in two main parts, Symmetric cells (Table 12(a)) and Mixed systems (Table 12(b)). "Symmetric cells" should be understood in a wide sense. Thus the "all-carbon accumulators" group comprises all cells in which both electrodes are made of pure carbon and graphite materials. Totally symmetric cells such as graphite/graphite or carbon black/carbon black are arranged at the beginning. Thereafter, the "asymmetric" examples such as CM/graphite or carbon black/CM follow. The second column shows the type of cell according to the "A, D" classification, which was outlined at the beginning of Section 9. Within each of the groups resulting from combination of (a) or (b) with D/D, A/A or D/A, the material is listed in order corresponding to this review.

The "quinone accumulator" is commonly defined in the special composition shown as No. 1 in Table 12 [71–78]. The cyclic behavior is good; thick quinone/c.b. layers, up to 7 mm, were cycled at 10 mA/cm^2 for up to 300 cycles [76,77]. However, The specific energy is rather low due to the low voltage. Moreover, stability of AQ/AQH_2 in the acid is problematic (cf. Section 2). *p*-Benzoquinone cannot be used because of its anodic instability, and employment of the heavier chloranil is raises

Table 12. Data for entirely graphitic, carbonaceous, and organic cells.

Type	No.	Negative electrode	Positive electrode	Electrolyte	U_0 [V]	$E_{s,th}$ [Wh/kg]	Ref.	Remarks
(a) *Symmetric cells*								
D/D	1	Anthraquinone	Chloranil	1.5 M H_2SO_4	0.52	61	[71–78]	Mixed with c.b.
D/A	2	Graphite	Graphite	Aprotic solvent, $LiClO_4$	4.5	259	–	$Li^+C_6^-$ / C_{24}^+ ClO_4^-
D/A	3	Graphite	Graphite	Room-temp. salt melt	3.5	147	[553]	EMI^+C_6 / $C_{24}^+ClO_4^-$
D/A	4	C felt	C felt	NBu_4ClO_4/PC	4.0	75	[554]	ECDLC, $K = 50$ Ah/kg
D/A	5	Polyacetylene	Polyacetylene	$Li(NBu_4)ClO_4$/PC	2.0	146	[277,281–283]	$(Li_{0.1}\,CH)_x/[(CHClO_4)_{0.1})_x]$
D/A	6	PPy	PPy	$LiClO_4$/MeCN	1.5	80	[557–559]	$(C_4NH_3^{y-}Li_{0.33}^+?)[C_4NH_3^{y+}(ClO_4^-)]_{0.33}$
A/A	7	PPy (undoped)	PPy (doped)	$LiClO_4$/MeCN	1.1–0	29	[559,562,563]	$y = 33\%$
A/A	8	PPy (undoped)	PT (doped)	$LiClO_4$/MeCN	2.0–0	45	[562,563]	$y = 33\%$
D/A	9	PT	PT	$LiClO_4$/MeCN	2.5	(113)	[564]	Cf. Fig. 40; the negative electrode is problematic
D/A	10	P-3-FPT[a]	P-3-FPT[a]	1 M TMATFMS[a]/MeCN	2.5	82	[562,563]	Cf. Fig. 40
(b) *Mixed systems*								
D/A	11	Anthraquinone	Graphite	50% H_2F_2	1.9	63	[80,153]	$C_{24}^+HF_2^-$ 2 H_2F_2, aqueous electrolyte
D/A	12	Graphite	PANI	1 M $LiClO_4$/PC	3.8	(a) 603 (b) 587	[566]	LiC_6, K_+ = (a) 1 F, (b) 2 F/unit
D/A	13	Polyacetylene	PANI	1.5 M $LiAsF_6$/PC	1.6	(a) 105	[567–569]	Cf. No. 12 for PANI, No. 5 for PA
A/A	14	PPy	Graphite	0.2 M $LiClO_4$/PC	1.7	80	[58,158, 159]	$y = 0.33$

[a] $NMe_4CF_3SO_3$

environmental problems. It should be mentioned that a proton-shuttle mechanism is operative in the cell.

As already pointed out in Section 3, graphite is an ideal host lattice for D- and A-type intercalation compounds, because of its stability. Unfortunately, the charge stoichiometries are rather unfavorable, and only relatively modest theoretical energy densities can be achieved, even for the ideal case (No. 2 in Table 12). The potentials are -2.5 V and $+2.0$ V [149, 150] vs. SHE, respectively. It is difficult to realize such systems in aprotic organic electrolytes due to the instability of the solvents relative to both charged electrodes. It should be mentioned that a relatively large proportion of $E_{s,th}$ can be retained as the practical value. An example [553] involves room-temperature salt melts in terms of 1-ethyl-3-methylimidazolium (EMI^+) tetrachloroaluminate (No. 3). Many other systems with (partially) nongraphitized Carbon materials are known, which work as ECDLCs. An early example [554] is given as No. 4 in the Table. It is assumed, as in earlier sections, that carbon felt has a high specific area, and a capacity of $K = 50$ A h/kg "electrodes" seems to be reasonable. The mass equivalent of the ions must be added. A similar system with activated carbon fibers (ACFs) is reported in [555].

The same kinds of highly symmetric carbon systems for ECDLCs are also known for activated carbons [15, 249, 385], carbon blacks [33, 249], carbonaceous materials ("aerogels") from phenol–formaldehyde resins via pyrolysis [18], and pyrolyzed PAN [430]. Another system, but with a rather low $E_{s,th}$, was built with two activated glassy carbon plates [240, 434] (cf. Section 7, group 6).

Many other ECDLC-type cells have different carbon materials at both electrodes, but function accordingly. Examples are (negative/positive): Li/CM (Novolak)/carbon black [397] and the aqueous system carbon black/graphite (CPP) with a voltage of about 1.5 V. The electrolyte is medium concentration H_2SO_4 [556].

The next group of materials comprises conducting polymers (ICP). Systems with identical polymers have often been reported for polyacetylene. It is known that this ICP forms insertion compounds of the A and D types (see Section 6.4, and No. 5 in Table 12). Cells of this kind were successfully cycled [277, 281–283]. However, the current efficiency was only 35%; heavy losses were observed due to an overoxidation of the PA [284]. In other cases as for polypyrrole (PPy), the formation of D-PPy was anticipated but did not occur [557, 558]. Entry (6) in Table 12 represents some kind of ideal model. A PPy/PPy cell with alkyl or aryl sulfates or sulfonates rather than perchlorates is claimed in [559]. Similar results were obtained with symmetric polyaniline (PANI) cells [560, 561]. Symmetric PPy and PANI cells yield about 60% current efficiency, much more than with PA. An undoped PPy/A-doped PPy combination yields an anion-concentration cell [562, 563], in analogy to graphite [47], (cf. No. 7). The same principle can be applied with the PPy/PT combination [562, 563] (cf. No. 8). Kaneto et al. [564] have reported in an early paper the combination of two polythiophene (PT) thin layers (< 1 μm), but the chargeability was relatively poor (Fig. 40, and No. 9 in Table 12). A pronounced improvement was due to Gottesfeld et al. [342, 343, 562, 563], who employed poly[3-(4-fluorophenyl)thiophene], P-3-FPT, in combination with a stable salt electrolyte (but in acetonitrile; cf. Fig. 40 and No. 10 in Table 12). In all practical cases, however, $E_{s,th}$ was below 100 Wh/kg.

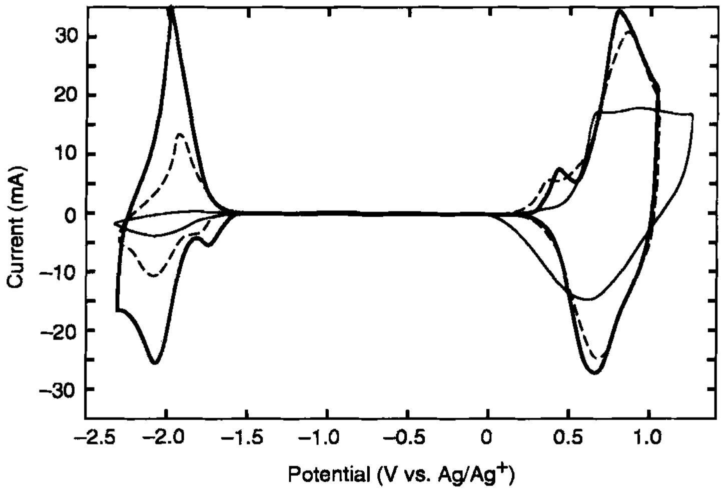

Fig. 40. Cyclic voltammograms at 25 mV/s. Films of (—) polythiophene(PT), (– – – –) poly(3-phenylthiophene)(P-3-PT) and (—) poly[3-(4-fluorophenyl)thiophene](P-3-FPT) in 1.0 M TMATFMS ($Me_4NCF_3SO_3$) in acetonitrile. The carbon paper electrode is 75 μm thick and has a cross-sectional area of 1.0 cm^2. After [563].

Finally, some mixed systems must be discussed. A combination of an anthraquinone (AQ)-negative with an A-GIC-positive material in aqueous acids leads to an r.b. of voltage 1.9 V. This is essentially a combination of the organic electrodes of the hybrid cells Pb/GIC [156] and AQ/PbO_2 [79, 502], respectively. As the negative electrode needs a low acidity (cf. Section 2), but the GIC needs a high one (cf. Section 3.1), the optimization of the electrolyte is not easy to perform [80, 159]. Attempts with buffered 50% HF are reported [565]. The highest energy density is due to unbuffered 50% HF [80] (No. 11). Many systems consist of layers of conducting polymer on the one hand and graphite intercalation compounds (GIC) on the other. The negative electrode may be a D-GIC, mostly LiC_6. The cell with a PPy positive electrode [541] was already discussed as No. 25 in Table 10. The theoretical energy density was relatively high: $E_{s,th} = 187$ Wh/kg. In analogy to this, a Li-in-CM/PPy was described [440]. Other examples are Li-in-CM/pyrolyzed PA [419], Li-in-CM/PANI [441] and pyrolyzed benzene (800 °C)/PANI [566]. The latter example is included in Table 12 as No. 12. The current efficiency was 96%. The energy density is much higher than in the case of LiC_6/PPy, which was mentioned above. Some Japanese patents claim a polyacetylene/PANI cell, where D-GIC is substituted by PA, which can be analogously D-doped [567–569]; cf. No. 13 in Table 12. An example of an A^- shuttle is given in the PPy/A-GIC cell. The mechanism is presented in Fig. 41. Clearly, the electrolyte is (nearly) invariant. A slight variation may occur due to different stoichiometries of co-inserted solvate molecules. Data are given in Table 12, No. 14. In the discharged state, the anions are located in the negative, electrode, and in the positive electrode for the charged state. The organic electrolyte is unstable at the very positive potential of the A-GIC, and the capacity of the cell decreases slowly due to the accumulation of residual anions in the PPy

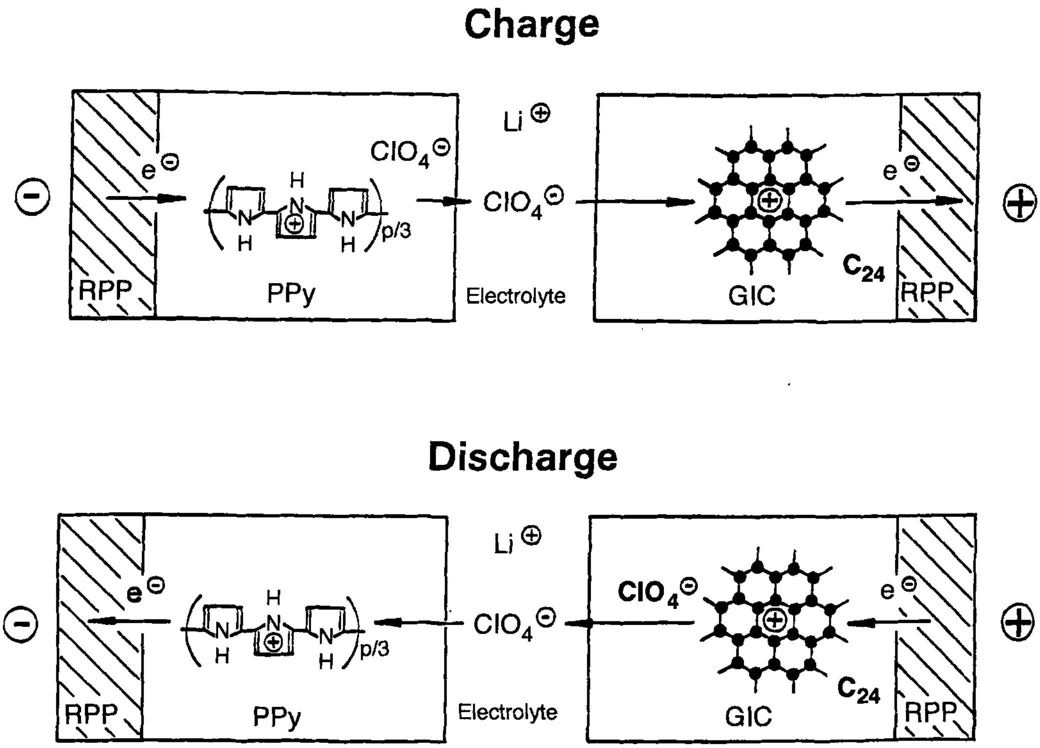
Charge
⊖
e⊖
H
N
H
H
p/3
$ClO_4^{\ominus}$
RPP
PPy
Li⊕
$ClO_4^{\ominus}$
Electrolyte
GIC
C_{24}
e⊖
RPP
⊕
Discharge
⊖
e⊖
H
N
H
H
p/3
RPP
PPy
Li⊕
$ClO_4^{\ominus}$
Electrolyte
$ClO_4^{\ominus}$
GIC
C_{24}
e⊖
RPP
⊕

Fig. 41. Schematic representation of the anion shuttle in the PPy/GIC battery on charge and discharge.

negative electrode. If one evaluates the system PPy/PT, $U \simeq 1$ V, the electrolyte is stable at the lower potential of the positive electrode, and cyclability is greatly improved [570]. A combination of two donor-type electrodes would lead to a cation-shuttle mechanism. This case is very common with inorganic systems (cf. Table 10), e.g., $LiC_6/LiMn_2O_4$. But for carbon aqueous or organic systems, it is very rare, as pointed out in Section 1.

10 Conclusions

The most important figure of merit in r.b.s is the theoretical energy density $E_{s,th}$. As shown in Tables 10–12, where inorganic examples are included for comparison, the metal-free systems seems to have some limitations. However, the top inorganic

Table 13. Volume specific capacities K_v (charge densities per volume), after [6].

Active Material	M [g/mol]	ρ[g/cm^3]	$\bar{\rho}$ [g/cm^3]	z	K_v [Ah/dm^3]
Zn	65	7.1	4	2	3300
Li	7	0.53	0.5	1	1900
Pb	207	11.3	7	2	1800
MnO_2	87	5.0	3	2	1800
PbO_2	239	9.35	5.5	2	1200
$LiTiS_2$	119	–	3	1	680
$Li_3V_6O_{13}$	535	–	3	3	450
D-GIC LiC_6	79	1.2	1	1	339
PANI $C_6H_4N(H)(H_2O)$	91	–	1	1	295
Anthrahydroquinone	210	1.4	1	2	260
PPy $(C_4H_3N)_3ClO_4$	294	1.5	1	1	90
A-GIC $C_{24}ClO_4$	675	1.5	1	1	40

examples such as Li, H_2, O_2, or F_2 are absolutely impractical, and a confinement to LiC_6, H_xLaNi_5, MnO_2 or PbO_2 has been performed for many years. Insofar, both topics approach each other again. As $E_{s,th}$ is composed of two factors, the equilibrium cell voltage U_0 and the theoretical capacity $K_{s,th}$, the question arises, which of the two determines more strongly $E_{s,th}$. It is the latter. Table 1 shows clearly, that many good, highly reversible, active materials actually have a $K_{s,th}$ of only 50–100 Ah/kg, while the $K_{s,th}$ of inorganic materials is well above that range. The reasons for this have already been stressed in the introductory section. The U_o values are normal (Table 3) and cover the same range (−3 to +2 V vs. SHE) as the inorganic examples. The negative region is, however, not so densely occupied.

It should be remembered that the practical energy density E_s in metal-free batteries is often closer to the theoretical value than in the case of conventional systems. This can be rationalized in terms of higher active mass utilizations through thin-layer technology (via thermoplastic binders, for instance), lighter current collectors (at least in bipolar systems), and so on. The lead–acid accumulator has a ratio $\alpha = E_{s(5h)}/E_{s,th} \approx 15\%$; thus $E_s = 25$ Wh/kg. But a metal-free system with $E_{s,th} = 80$ Wh/kg may allow $E_s = 40$ Wh/kg, if α is 50% in this way.

A somewhat problematic point is the volume-specific energy density E_v. Some typical examples are compiled in Table 13. They are calculated with the aid of Eq. (71):

$$K_v = K_{s,th} \cdot \bar{\rho} \tag{71}$$

making use of an empirical true density $\bar{\rho}$ which is 60% of the density of the compact material (lithium is excepted). Clearly, the K_v data of nonmetallic materials are lower by a factor of 5–83 with respect to metals etc. due to the fact that the densities are 1–2, and 5–11, respectively. This may possibly lead to constructional problems in electric vehicles or electronic equipment.

Table 14. Mass increments [g/F] for metal-free rechargeable batteries.

Type	Composition for 1 F in the discharged state, negative ⊖/positive ⊕	U_0 [V]	Specific mass (g/F)			$E_{s,th}$ [Wh/kg]
			⊖	⊕	Electrolyte	
D/D	$[LiC_6/Li_2Mn_2O_4]$	3	72	188	–	309
	$C_6/[(C_4H_3N)_3^0 \ldots C_8H_7SO_3^-Li^+]_{p/3}$	2.5	72	386	–	146
	$C_6/((C_6H_5)_5^-Li^+)_{p/5}$	1.5	72	342	–	97
A/A	$[(C_4H_3N)_3^+ClO_4^-]_{p/3}/C_{24}$	1.7	295	288	–	78
D/A	$LiC_6/C_{24}(ClO_4)$	4.5	72	288	500[(a)]	33.5
	AQ/C_{48}[(d)]	1.5	104	576	360[(b)]	39
	AQ/C_{48}[(e)]	1.5	104	576	2115[(c)]	14
	AQ/C_{24}[(f)]	1.5	104	288	112[(b)]	80
	AQ/C_{24}(g)	1.5	104	288	705[(c)]	37

[(a)] 2.2–0.2 M $LiClO_4$, $\rho = 1$.

[(b)] 65–35% HF (40–20 M HF).

[(c)] 8 M (50%) HBF_4–6M HBF_4.

[(d)] Charged: $C_{48}^+ \cdot HF_2^- \cdot 2H_2 \cdot H_2F_2$.

[(e)] Charged: $C_{48}^+ \cdot BF_4^- \cdot 2\ HBF_4$.

[(f)] Charged: $C_{24}^+ \cdot HF_2^-$.

[(g)] Charged: $C_{24}^+ \cdot BF_4^-$.

Table 14 presents some typical theoretical energy densities in a special form. The mass increments are listed separately for the two electrodes and the electrolyte, if any. The electrolyte, of course, is virtually absent for the D/D and A/A systems, i.e., for systems with an ion-shuttle mechanism. As a consequence, relatively high E_s values are obtained. The $LiC_6/LiMn_2O_4$ cell is also shown, for comparison. The other systems with a D/A mechanism, where the electrolyte enters, at least partially, into the overall process, exhibit much lower figures for E_s. In some cases, a large volume of the electrolyte is necessary. The relative optimum is aqueous HF, where high molar concentrations are possible. The upper practical limit (~ 60 wt%) is given by the vapor pressure of HF. Another strategy for escaping from this limitation is to employ a (salt) slurry. The need for cyclic recrystallization of small particles may be problematic.

The specific power P_s(W/kg) is an important figure of merit, in addition. It governs the short-term availability of the stored energy, and is given by

$$P_s = \frac{E_s}{\tau} = \frac{E_s}{RC} \tag{72}$$

where τ is the time constant of the electrochemical system, which is the product of its capacitance C and the internal resistance R. In the case of capacitors, $E = \frac{1}{2}\ CU^2$, and C cancels out, but the resistance R is retained. The minimization of R is difficult in metal-free systems and with organic or polymeric materials and organic liquid or solid electrolytes. Charge mobility b and diffusion coefficient D are interconnected by the Nernst–Einstein equation,

$$D = bRT/F \tag{73}$$

Armand has shown [571] that D can vary widely, from 10^{-7} to 10^{-17} cm^2/s in the solid state. A great influence of co-intercalated solvents in the GIC phases [151] and of plasticizers in polymers can be observed. Other strategies are available to minimize the internal resistance of a battery, namely bipolar switching of the electrodes, thin-layer electrolytes and current collectors, and again systems with a shuttle mechanism. Due to its importance, it should be tried in every individual design for such systems. Table 15 presents four characteristic examples. In Nos. 1 and 2, protons are involved in No. 3 Li^+ ions (albeit PPy is originally A-type), and in No. 4 anions. The gain in energy density is much stronger for D/D than for A/A, for in the former case the heavier anions are eliminated.

Costs of the active materials and, in the case of D/A-systems, of the solvent/electrolyte system, are for any practical case extremely important, for they are proportional to the charge to be stored. Cost aspects in batteries are comprehensively treated in [477]. The specific cost per Ah is reduced at high cycle numbers. Thus good cyclability is important, too. Graphite, H_2SO_4, or, with some restrictions, carbon blacks and carbonaceous materials are inexpensive materials. PANI is an inexpensive ICP, but this does not generally apply for all other ICPs as erroneously stated in the literature [562, 563]. The pure material costs for a lead–acid battery are below 4 DM/kWh. But it is nearly impossible to meet this cost level in the case of a polyacetylene battery, for the polymer should then be as cheap as < 0.3 DM/kg.

Table 15. Selected examples of metal-free batteries with shuttle mechanisms, after [4]. $\rightleftarrows$ charge direction

No.	Electrode reactions	
	$\ominus$ $AQ + 2H^+ + 2e^-$	$\overset{L}{\rightleftarrows}$ AQH_2
	$\oplus$ QH_2	$\overset{L}{\rightleftarrows}$ $Q + 2H^+ + 2e^-$
1	$AQ + QH_2$	$\overset{L}{\rightleftarrows}$ $AQH_2 + Q$
	$-$ $\sim\sim S\text{–}S \sim\sim + 2H^+ + 2e^-$	$\overset{L}{\rightleftarrows}$ $2 \sim\sim SH$
	$\oplus$ QH_2 $^-$	$\overset{L}{\rightleftarrows}$ $Q + 2H^+ + 2e^-$
2	$QH_2 \sim\sim S\text{–}S \sim\sim + 2e^-$	$\overset{L}{\rightleftarrows}$ $Q + 2 \sim\sim Sh$
	$\ominus$ $C_x + Li^+ e^-$	$\overset{L}{\rightleftarrows}$ $[C_x^- Li^+]$
	$\oplus$ $[py_3p^-\ SO_3^-\ Li^+]$	$\overset{L}{\rightleftarrows}$ $[py_3^+ p^-\ SO_3] + Li^+ + e^-$
3	$C_x + [py_3p^- SO_3^-\ Li^+]$	$\overset{L}{\rightleftarrows}$ $[C_x^- Li^+] + [py_3^+ p^- SO_3^-]$
	$\ominus$ $[py_3^+ A \cdot \nu S] + e^-$	$\overset{L}{\rightleftarrows}$ $[py_3] + A^- + \nu S$
	$\oplus$ $C_{24} + A^- \cdot \nu' S$	$\overset{L}{\rightleftarrows}$ $[C_{24}^+ A^- \cdot \nu' S] + e^-$
4	$[py_3^+ A^- \cdot \nu S] + C_{24}$	$\overset{L}{\rightleftarrows}$ $[py_3] + [C_{24}^+ A^- \nu' S] + (\nu - \nu')\, S$

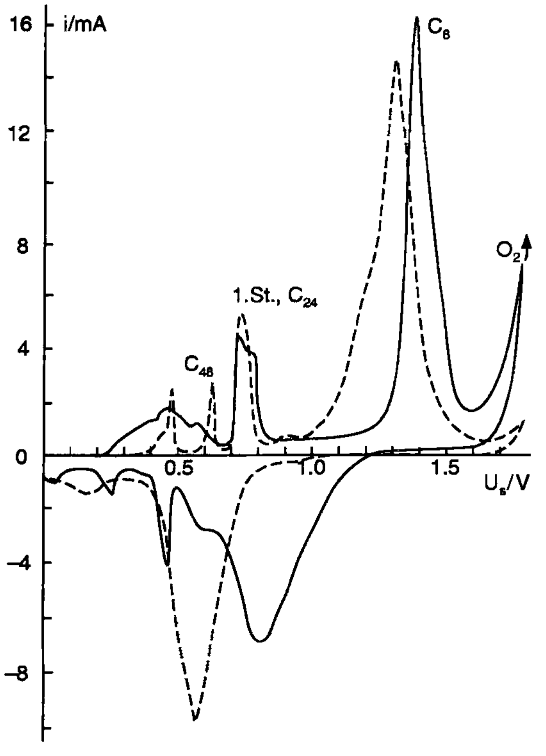

Fig. 42. Slow cyclic current vs. voltage curves for natural graphite (CPP), $A = 0.5$ cm^2, in 18 M H_2SO_4; voltage scan rate = 0.1 mV/s, potential range = 0.0 to +1.8 V, $m_{CPP} = 33.6$ mg: —— first cycle; - - - second cycle.

This chapter provides a strong foundation for the selection of materials. Cost considerations play a prominent role, but the scientific and industrial background must be acknowledged at all times. Two examples of this are given as illustrations. The application of negative lithium-insertion compounds does not necessarily lead to aprotic electrolytes, with their high resistivity. Dahn and co-workers [572] have shown nicely that an appropriate choice of the host lattice allows for the design of "rechargeable lithium batteries with aqueous electrolytes." The system was $LiVO_2$/$Li_{(1-x)}Mn_2O_4$ in aqueous $LiNO_3$. The cell voltage was about 1.5 V. The negative electrode had a potential of −0.5 V vs. SHE.

The second example relates to graphite oxide (GO). The original idea was to extend the capacity $K_{s,th}$ of the A-GIC, e.g., $C_{24}^+HSO_4^-$ (cf. Section 3.1). Measurements in concentrated sulfuric acid [139] identified a phase $C_8^+HSO_4^-$, just ahead of the anodic gas evolution. The slow CV is depicted in Fig. 42. It corresponds to Fig. 17, which is continued to more positive potentials. Unfortunately, the overvoltage for the re-reduction was high (0.5–1 V), and the redox capacity decreased from cycle to cycle. Higher oxidation states toward $C_{2.5}HSO_4$ were realized in a graphite-bed electrode [573] by galvanostatic charge, but the irreversibility was very pronounced from the beginning (cf. [160]). GO and graphite fluoride are direct derivatives of the parent graphite lattice, not with ionic bonding of the reaction partners as in the GICs (graphite salts or LiC_6), but with covalent bonding of O or F. Thus the mobile π-electrons are totally consumed, and the solid is a nonconducting material. The planar sp^2 configuration of the carbon atoms in graphite adopts a nonplanar sp^3 structure. The main stoichiometries are C_8O_3 and C_2O (COH) for graphite oxide and CF, C_2F and C_4F for graphite fluoride (GF). Graphite oxide may eventually contain 4–40 wt% swelling water, with a layer distance of 630–900 pm, respectively [574]. It can be prepared chemically, e.g., with $HNO_3 + H_2SO_4$ at a low water concentration. The various chemical methods, which are alternatives to the anodic process, have been critically reviewed by Boehm and Scholz [575].

GO does not seem to be suitable as a reversible battery electrode. The reason is the irreversible formation of covalent C–O(H) bonds in the course of anodic formation. According to Boehm and to Ubbelohde, graphite intercalation compounds do play the role of a precursor:

$$\begin{aligned} &C_{24} + A^- \longrightarrow C_{24}^+A^- + e^- \xrightarrow[-HA]{H_2O} \cdot C_{24}^+OH^-(sp^2) \\ &\longrightarrow C_{24} - OH(sp^3) \xrightarrow{OX} C_8O_{1.5} \xrightarrow{OX} C_8O_3 \end{aligned} \tag{73}$$

After cathodic cleavage of the covalent bonds, a very distorted graphite lattice is left behind. However, according to Jiang et al. [139], it does not seem to be totally impossible, that a set of conditions will be found in the future that allow for the reversible cycling of the electrode with a stoichiometry somewhere between $C_{24}A$ and CA. In this way, one would solve the problem of the relatively poor electrochemical capacity of the A-GICs. The potential oscillations, which are frequently observed upon galvanostatic oxidation of graphite in the potential region of GO formation, were recently discussed in terms of fluctuating anion- and water-transport overvoltages [576].

If GO is used as a host lattice for Li^+ in aprotic electrolytes, reversibility is improved [577]. The potential level is distinctly more positive than with donor GIC, at about -1 V vs. SHE. An all-solid-state Li/GO battery with PEO/$LiClO_4$ as solid electrolyte was reported by Mermoux and Touzain [578], but rechargeability is poor. Recently, the structure of graphite oxide was studied by its fluorination at 50–200 °C [579]. C–OH bonds were transformed into C–F bonds. The examples, in conjunction with Section 2, show that the formation or cleavage of covalent C–O (C–F) bonds makes the whole electrochemical process irreversible. Application was attempted in lithium primary batteries, which have a voltage of 2–2.5 V. Really reversible electrodes are only possible, however, with graphite intercalation compounds, which are characterized by weak polar bonds.

Finally, some technical features should be discussed; each of them is important, and a thorough optimization must be performed on the way to achieving a successful r.b. Side-reactions must be minimized due to their irreversible nature. The irreversible chemical disproportionation of anthrahydroquinone was discussed in detail in Section 2. Graphite electrodes, which form the negative pole in Li^+ion batteries, decompose

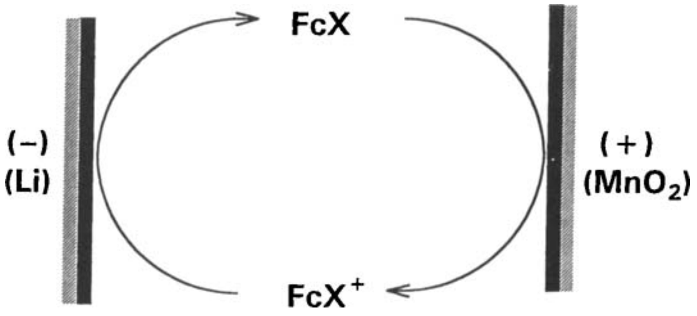

Fig. 43. Mechanism of overcharge protection (redox additive). After [586].

the aprotic, organic solvent/electrolyte system as much [580] as A-GICs at the positive electrode, as discussed in Sections 3.1 and 3.2. The discrimination between a chemical and an electrochemical mechanism is not straightforward in either case. The expectation that the very positive potentials are jeopardized by the poor catalytic properties of graphite in comparison with transition-metal oxides seems to be unrealistic.

Self-discharge is a matter of corrosion of the active materials, mostly in the charged state. The mechanisms for A-GICs [581] and for conducting polymers [582–584] have been clarified. Self-discharge is a superposition of a cathodic process (deintercalation, undoping) and an anodic one (overoxidation of the host lattice and/or decomposition of the solvent/electrolyte system). D-GICs may corrode according to an analogous mechanism: anodic undoping vs. overreduction of the host lattice and/or $H_2O \rightarrow H_2$. Shelf life of the active materials therefore depends on the electrochemical conditions, but also to some extent on the presence of impurities.

A secondary battery is sensitive to overcharging in the standard case. The active material and/or the electrolyte will be decomposed. Various strategies for overcharge protection have been followed. A simple one is the introduction of an overpressure valve, which interrupts the charge current if an in-cell pressure is built up. In another case, a LiAl/PANI cell was protected by an element switched in parallel, which is conductive at $U > 2.7$ V, but insulating at $U < 2.7$ V [585]. A third proposal is to include a redox additive in the electrolyte [586] in the form of a ferrocene derivative, FcX. For a Li/Li_xMnO_2 cell, dimethylaminomethylferrocene with a standard potential $U_{Li} = 3.44$ V was optimum. Figure 43 depicts schematically the mechanism as an "electrochemical short circuit."

One of the strong driving forces for the development of metal-free batteries has been the problematic history of battery metals such as lead and cadmium. Zinc is an interesting metal, which does not suffer from such shortcomings, although its environmental problems are not completely negligible. Developments such as the rechargeable Zn/MnO_2 accumulator [587, 588] or a Zn/air battery (with mechanically exchanged zinc plates) [589, 590] are of great interest. These are aqueous systems with high energy and power densities. But the present metal-free systems will find their market.

Acknowledgments. The present review article is written in memory to Professor Dr. Heinz Gerischer, my academic teacher, who died on September 14, 1994. I look back to the happy days in Stuttgart, 1956–1960. They were followed by a shaping period of 18 years in industrial R&D (Ludwigshafen) and subsequently 18 years back in the academic world. His strong encouragement since 1991 was the solid foundation of this work.

The strong technical support from Dr. Krohn and Dr. Wermeckes as well as from some of my Ph.D. students has been appreciated over the years. Financial support of our relevant research work in Duisburg by DFG, MWF (Düsseldorf) and AIF (Bonn) is gratefully acknowledged.

References

1. J. W. Ritter, Voigts Magazin für den neuesten Zustand der Naturkunde 6, 97 and 181 (1803).
2. G. Planté, Compt. Rend. 50, 640 (1860).
3. E. J. Wade, Secondary Batteries, Their Theory, Construction and Use, The Electrician Printing and Publishing Co., London (1902).
4. F. Beck, Elektroorganische Chemie, Verlag Chemie, Weinheim (1974), pp. 314–323.
5. F. Beck in: Notsromversorgung mit Batterien, Viertes Technisches Symposium 28./29.3.1985, München, K. Eberts (ed.), VDE-Verlag, Berlin (1986), p. 263.
6. F. Beck, Ber. Bunsenges. Phys. Chem. 92, 1283 (1988).
7. F. Beck, H. Krohn, M. Oberst in: Elektrisch leitende Kunststoffe, H. J. Mair, S. Roth (eds.). Hanser, München (1989), p. 403.
8. F. Beck, T. Boinowitz, U. Tormim, DECHEMA Monogr. 128, 287 (1993).
9. F. Beck in: Anwendungstechnik Batterien unter besonderer Berücksichtigung der Notstromversorgung, Internationales Technisches Symposium March 11–12, 1993, München, W. Jacobi (ed.), privately published, Soest (1994), p. 357.
10. F. Beck in: Proc. NATO Advanced Research Workshop, Kiev, May 14–17, 1995, on New Promising Electrochemical Systems for Rechargeable Batteries, V. Z. Barsukov, F. Beck (eds.), Kluwer, Dordrecht (1996), pp. 393–417.
11. G. Kortüm, Lehrbuch der Elektrochemie, 1st edn. Verlag Chemie, Weinheim (1952), p. 376.
12. F. Beck, H. Krohn, A. Pruß, DECHEMA Monogr. 102, 585 (1986).
13. J. Heinze, M. Dietrich, K. Hinkelmann, K. Meerholz, F. Rashwan, DECHEMA Monogr. 112, 61 (1989).
14. B. E. Conway, J. Electrochem. Soc. 138, 1539 (1991).
15. M. F. R. Rose, C. Johnson, T. Owens, B. Stephens, J. Power Sources 47, 303 (1994).
16. F. Beck, H. Krohn in: The Electrochemistry of Carbon, Workshop, August 1983, Cleveland, Ohio, S. Sarangapani et al. (eds.), The Electrochemical Society, Pennington, NJ (1984)
17. F. Beck, K. J. Euler, Electrochemische Energiespeicher, VCH, Weinheim (1984), pp. 138–153.
18. S. T. Mayer, R. W. Pekala, J. L. Kaschmitter, J. Electrochem. Soc. 140, 446 (1993).

19. F. Beck, M. Oberst, P. Braun, DECHEMA Monogr. 109, 457 (1987).
20. F. Beck, M. Oberst, Makromol. Chem., Macromol. Symp. 8, 97 (1987).
21. B. J. Feldman, P. Burgmayer, R. W. Murray, J. Am. Chem. Soc. 107, 872 (1985).
22. S. Feldberg, J. Am. Chem. Soc. 106, 4671 (1984).
23. J. Heinze, K. Hinkelmann, M. Dietrich, J. Mortensen, DECHEMA Monogr. 102, 209 (1986).
24. R. A. Bull, R. F. Fan, A. J. Bard, J. Electrochem. Soc. 129, 1009 (1982).
25. F. Beck, J. Jiang, M. Kolberg, H. Krohn, F. Schloten, Z. Phys. Chem. NF 160, 83 (1988).
26. K. K. Kanazawa, A. F. Diaz, R. H. Geiss, W. D. Gill, J. F. Kwak, J. A. Logan, J. F. Rabolt, G. B. Street, J. Chem. S., Chem. Commun. 854 (1979).
27. M. Salmon, A. F. Diaz, A. J. Logan, M. Krounbi, J. Bargon, Mol. Cryst. Liq. Cryst. 83, 265 (1982).
28. F. Beck, T. Boinowitz, G. tom Suden, E. Abdelmula, GDCh Monogr. 2, 223 (1995).
29. R. Schöllhorn, Angew. Chem. 92, 1015 (1990); Angew. Chem., Int. Ed. Engl. 19, 983 (1990).
30. J. Desilvestro, O. Haas, J. Electrochem. Soc. 137, 5C (1990).
31. M. S. Whittingham, Science, 192, 1126; J. Electrochem. Soc. 123, 315 (1976).
32. J. R. Dahn, Extended Abstract No. 85, Electrochemical Society Meeting, Miami Beach, October 1994.
33. F. Krüger, F. Beck in: Proc. NATO Advanced Research Workshop, Kiev, May 14–17, 1995, on New Promising Electrochemical Systems for Rechargeable Batteries, V. Z. Barsukov, F. Beck (eds.), Kluwer, Dordrecht (1996), pp. 373–389.
34. S. Trasatti, O. A. Petrii, J. Electroanal. Chem. 327, 353 (1992).
35. J. Li, J.-Z. Zhang Y.-H, Geng, L.-X. Wang, X.-B. Jing, F. S. Wang, Synth. Metals 69, 245 (1995).
36. K. Hiratsuka, T. Morimoto, Y. Sanada, K. Kurihara, Extended Abstract 21-13-09 (p. 1178), 39th Annual Meeting Int. Soc. Electrochemistry (ISE), Kyoto, September, 1989.
37. T. Pajkossy, J. Electroanal. Chem. 364, 111 (1994).
38. K. Franaszczuk, A. Wickowski, Extend. Abstr. VII-38, 45th Annual Meeting of the Int. Soc. Electrochemistry (ISE), Porto, September, 1995.
39. F. Beck, H. Krohn, Synth. Metals 7, 193 (1983).
40. J. Heinze, Topics Curr. Chem. 152, 1 (1990).
41. F. Beck, M. Oberst, P. Braun, DECHEMA Monogr. 109, 457 (1987).
42. K. M. Abraham, J. S. Foos, J. L. Saldman, J. Electrochem. Soc. 131, 2197 (1984).
43. J. Caja, R. B. Kaner, A. G. McDiarmid, J. Electrochem. Soc. 131, 2744 (1984).
44. S. Atlung, K. West, T. Jacobsen, J. Electrochem. Soc. 126, 1311 (1979).
45. K. West, T. Jacobsen, S. Atlung, J. Electrochem. Soc. 129, 1480 (1982).
46. S. Atlung, T. Jacobsen, K. West, B. Zachau-Christiansen, DECHEMA Monogr. 109, 333 (1987).
47. W. Rüdorff, U. Hofmann, Z. Anorg. Allg. Chem. 238, 1 (1938).
48. A. R. Ubbelohde, M. J. Homley, G. S. Parry, D. A. Young, J. Chem. Soc. 5674 (1963).
49. E. S. Pysh, N. C. Yang, J. Am. Chem. Soc. 85, 2124 (1963).
50. B. Case, N. S. Hush, R. Parsons, M. E. Peover, J. Electroanal. Chem. 10, 360 (1965).
51. V. D. Parker, J. Am. Chem. Soc. 98, 98 (1976).
52. J. R. Dias, Molecular Orbital Calculations Using Chemical Graph Theory, Springer Heidelberg (1993).
53. V. V. Strelko, E. D. Lavrinenko-Ometsinskaya, J. Mol. Struct. (Theochem.) 188, 193 (1989).
54. K. Kazdobin, V. Volkov, V. Belyakov in: Proc. NATO Advanced Research Workshop, Kiev, May 14–17, 1995, on New Promising Electrochemical Systems for Rechargeable Batteries, V. Z. Barsukov, F. Beck (eds.), Kluwer, Dordrecht (1996), pp. 349–362.

55. M. E. Peover in Electroanalytical Chemistry, 2, A. J. Bard (ed.), Marcel Dekker, New York (1967).
56. L. Kevan in Radical Ions, E. T. Kaiser, L. Kevan (eds.), Interscience, New York (1968).
57. S. Kuwubata, J. Nakamura, H. Yoneyama, J. Chem. Soc., Chem. Commun. 779 (1988).
58. T. Boinowitz, Ph.D. Thesis, University of Duisburg (1996).
59. F. Beck, M. Oberst, J. Electroanal. Chem. 285, 177 (1990).
60. M. B. Armand, J. Power Sources 14, 11 (1985).
61. K. J. Euler, W. Nonnenmacher, Electrochim. Acta 2, 268 (1960).
62. J. Newman, C. W. Tobias, J. Electrochem. Soc. 109, 1183 (1960).
63. J. Newman, Electrochemical Systems, Prentice Hall, New York (1973).
64. K. J. Vetter, Z. Elektrochem. 52, 797 (1952).
65. K. Mund. F. v. Sturm, Electrochim. Acta 20, 463 (1975).
66. B. W. Owens, S. Passerini, W. H. Smyrl, A. L. Xidis in Rechargeable Lithium Ion Batteries, S. Megahead et al. (eds.), Proc. 94–28, The Electrochemical Society, Pennington, NJ (1995), p. 277.
67. M. M. Baizer, H. Lund, (eds.), Organic Electrochemistry, 3rd edn., Marcel Dekker, New York (1990).
68. W. M. Clark, Oxidation–Reduction Potentials of Organic Systems, William & Wilkins, Baltimore (1960).
69. M. v. Stackelberg in Houben-Weyl, Methoden der Organischen Chemie, III 2 (1955), p. 225.
70. J. B. Conant, L. F. Fieser, J. Am. Chem. Soc. 45, 2194 (1923); 46, 1858 (1924).
71. H. Alt, H. Binder, A. Köhling, G. Sandstede, J. Electrochem. Soc. 12, 1950 (1971).
72. H. Alt, H. Binder, A. Köhling, G. Sandstede, Electrochim. Acta 17, 873 (1972).
73. H. Alt, H. Binder, G. Klempert, A. Köhling, G. Sandstede, J. Applied Electrochem. 2, 193 (1972).
74. Battelle, Frankfurt, German Patent 2 240 614 (August, 1972).
75. G. Matricicali, M. M. Dieng, J. F. Dufeu, M. Guillou, Electrochim. Acta 21, 943 (1976).
76. O. S. Ksenzhek, V. M. Gurskii, S. A. Petrova, Vopr. Khim. Khim. Tekhnol. 92, 3 (1990); Chem. Abstr. 115, 259839p (1991).
77. O. S. Ksenzhek, V. M. Gurskii, S. A. Petrove, V. S. Gevod, Vopr. Khim. Khim. Tekhnol. 92, 9 (1990); Chem. Abstr. 115, 259840g.
78. Dnjepropetrovsk, USSR Patent 624 322 (December, 1976).
79. V. Z. Barsukow, S. A. Dunovsky, N. Sayoyan, A. I. Trepalin, I. A. Aguf, V. A. Smolkowa, USA Patent 4 227 546 (July, 1981).
80. H. Krohn, E. Ther, U. Tormin, B. Wermeckes, F. Beck in Proc. NATO Advanced Research Workshop, Kiev, May 14–17, 1995, on New Promising Electrochemical Systems for Rechargeable Batteries, V. Z. Barsukov, F. Beck (eds.), Kluwer Dordrecht (1996), pp. 433–450.
81. V. V. Matveev, N. V. Korneev, V. Z. Barsukov, N. B. Ilyuk, J. Power Sources, to be published.
82. M. E. Peover, J. D. Davies, J. Electroanal. Chem 6, 46 (1963).
83. M. A. Matthews, J. Chem. Soc. (Lond.) 1926, 237.
84. F. Beck, G. Heydecke, Ber. Bunsenges. Phys. Chem. 91, 37 (1987).
85. B. Wermeckes, F. Beck, Denki Kagaku 62, 1202 (1994).
86. S. I. Bailey, Chem. Aust. 50, 202 (1983).
87. V. Z. Barsukov, Extended Abstracts, 31st ISE Meeting (Int. Soc. Electrochemistry), Venice, 1980, Vol. 2, p. 675.
88. E. Voss, Chem.-Ing.-Tech. 42, 199 (1970).
89. M. A. Gutjahr, K. D. Beccu, Chem.-Ing.-Tech. 42, 202 (1970).
90. R. Glicksman, C. K. Morehouse, J. Electrochem. Soc. 105, 299 (1958).
91. R. Glicksman, C. K. Morehouse, J. Electrochem. Soc. 106, 288 (1959).

92. R. Glicksman, C. K. Morehouse, J. Electrochem. Soc. 107, 717 (1960).
93. R. Glicksman, J. Electrochem. Soc. 108, 1 (1961).
94. S.-I. Tobishima, J.-I. Yamaki, A. Yamaji, J. Appl. Electrochem. 14, 721 (1984).
95. R. J. Jasinski, J. Electrochem. Soc. 124, 637 (1977).
96. H. Djellab, F. Dalard, J. Electrochem. 221, 105 (1987).
97. R. Jansen, F. Beck, Synth. Metals 41–43, 2903 (1991).
98. R. Jansen, F. Beck, Electrochim. Acta 38, 907 (1993).
99. F. Beck, R. Jansen, Adv. Mater. 3, 385 (1991).
100. M. v. Stackelberg, Angew. Chem. 54, 76 (1941).
101. R. Glicksman, J. Electrochem. Soc. 110, 353 (1963).
102. M. Liu, S. J. Visco, L. C. De Jonghe, J. Electrochem. Soc. 138, 1891 (1991).
103. M. Liu, S. J. Visco, L. C. De Jonghe, J. Electrochem. Soc. 138, 1896 (1991).
104. M. M. Doeff, S. J. Visco, L. C. De Jonghe, J. Appl. Electrochem. 22, 307 (1992).
105. M. M. Doeff, M. M. Lerner, S. J. Visco, L. C. De Jonghe, J. Electrochem. Soc. 139, 2077 (1992).
106. K. Naoi, Y. Oura, Y. Iwamizu, N. Oyama, J. Electrochem. Soc. 142, 354 (1995).
107. K. Naoi, Y. Oura, N. Oyama in: Rechargeable Lithium Ion Batteries, S. Megahead et al. (eds.), Proc. 94–28, The Electrochemical Society, Pennington, NJ (1995), p. 312.
108. N. Oyama, T. Tatsuma, T. Sato, T. Sotomura, Nature (London) 373, 598 (1995).
109. A. Kaminaga, T. Tatsuma, T. Sotomura, N. Oyama, J. Electrochem. Soc. 142, L47 (1995).
110. S. Ye, D. Bélanger, J. Electrochem. Soc. 141, L49 (1994).
111. T. Tatsuma, T. Sotomura, T. Sato, D. A. Buttry, N. Oyama, J. Electrochem. Soc. 142, L182 (1995).
112. P. M. Lessner, F. R. McLarnon, J. Winnick, E. J. Cairns, J. Electrochem. Soc. 140, 1847 (1993).
113. H. P. Fritz, H. Gebauer, P. Friedrich, P. Ecker, R. Artes, U. Schubert, Z. Naturforsch., Teil B 33, 498 (1978).
114. H. D. Keller, D. Nöthe, K. Wehe, M. Werner, P. Koch, D. Schweitzer, Mol. Cryst. Liq. Cryst. 62, 81 (1980).
115. E. W. Grabner, E. Brauer, Ber. Bunsenges. Phys. Chem. 76, 106, 111 (1972).
116. S. Kotowski, E. W. Grabner, H.-D. Brauer, Ber. Bunsenges. Phys. Chem. 84, 1140 (1980).
117. V. Enkelmann, B. S. Morra, Ch. Kröhnke, G. Wegner, J. Heinze, Chem. Phys. 66, 303 (1982).
118. H. Awano, H. Murakami, T. Yamashita, H. Ohigashi, Synth. Metals 39, 327 (1991).
119. G. Heywang, S. Roth, Angew. Chem. 103, 201 (1991).
120. P. Erk, H. Meixner, T. Metzenthin, S. Hünig, U. Langohr, J. U. von Schütz, H.-P. Werner, H. C. Wolf, R. Burkert, H. W. Helberg, G. Schaumburg, Adv. Mater. 3, 311 (1991).
121. T. Inable, S. Nakamura, W. B. Liang, T. J. Marks, R. L. Burton, C. R. Kannewurf, K. I. Imaeda, J. Am. Chem. Soc. 107, 7224 (1985).
122. M. Almeida, M. G. Kanatzidis, L. M. Tonge, T. J. Marks, H. O. Marcy, W. J. McCarthy, C. R. Kannewurf, Solid State Commun. 63, 457 (1987).
123. M. Pampallona, A. Ricci, B. Scrosati, C. A. Vincent. J. Appl. Electrochem. 6, 269 (1976).
124. A. A. Schneider, W. Greatbach, R. Mead, J. Power Sources 651 (1974).
125. O.-K. Kim, R. B. Fox, J. Polym. Sci., Polym. Chem. Ed. 20, 2765 (1982).
126. O.-K. Kim, J. Polym. Sci., Polym. Lett. 21, 575 (1983).
127. J. H. Perlstein, Angew. Chem. 89, 534 (1977).
128. A. R. Ubbelohde, F. A. Lewis, Graphite and its Crystal Compounds, Clarendon Press, Oxford (1960).
129. M. S. Dresselhaus, G. Dresselhaus, Adv. Phys. 30, 139 (1981).

130. F. Beck, H. Junge, H. Krohn, Electrochim. Acta 26, 799 (1981).
131. E. Frackowiak, W. Kaiser, H. Krohn, F. Beck, Mol. Cryst. Liq. Cryst. 244, 221 (1994).
132. G. Furdin, J. F. Marêché, A. Mabchour, A. Hérold, Mol. Cryst. Liq. Cryst. 245, 219 (1994).
133. F. Beck, K. Wurmb, K. Boehlke, German Patent 2 532 512 (BASF AG) (1975).
134. F. Beck, H. Krohn, W. Kaiser, J. Appl. Electrochem. 12, 505 (1982).
135. H. Krohn, F. Beck, A. Zahn, Angew. Makromol. Chem. 164, 143 (1988).
136. W. Biberacher, A. Lerf, J. O. Besenhard, H. Möhwald, T. Butz, Mater. Res. Bull. 17, 1385 (1982).
137. A. Métrot, A. Inioui, A. Storck, Electrochim. Acta 27, 1247 (1982).
138. S. Schuldiner, J. Electrochem. Soc. 129, 1270 (1982).
139. J. Jiang, F. Beck, H. Krohn, J. Indian Chem. Soc. 66, 603 (1989).
140. J. Jiang, F. Beck, Carbon 30, 223 (1992).
141. F. Beck, H. Krohn, Synth. Metals 14, 137 (1986).
142. F. Beck, W. Kaiser, H. Krohn, Angew. Chem. Suppl. 57, 1982; cf. Angew. Chem. 94, 83 (1982).
143. M. Inagaki, N. Iwashita, Mol. Cryst. Liq. Cryst. 244, 89 (1994).
144. K. H. Dietz, F. Beck, J. Appl. Electrochem. 15, 159 (1985).
145. F. Beck, H. Krohn, R. Wanger, D. Nann (Hagen Batterie AG), German Patent 3 809 247 (February 1988).
146. H. Krohn, F. Beck, Synth. Metals 34, 707 (1989).
147. H. Krohn, F. Beck, H. Junge, Ber. Bunsenges. Phys. Chem. 86, 704 (1982).
148. J. O. Besenhard, Habilitationsschrift, T. U. München (1978).
149. U. Tormin, Ph.D. Thesis, University of Duisburg (1997).
150. Z. Zhang, M. M. Lerner, J. Electrochem. Soc. 140, 1955 (1995).
151. U. Tormin, F. Beck, Electrochim. Acta 40, 1955 (1995).
152. H. Krohn, Carbon 23, 449 (1985).
153. R. Fujii, Report Government. Industr. Res. Inst. Osaka 353, 1 (1978).
154. R. Fujii, Denki Kagaku 40, 380, 705 (1972).
155. F. Beck, H. Krohn, DECHEMA Monogr. 92, 57 (1982).
156. F. Beck, Elektrotechniek (Netherlands) 61, 178 (1983).
157. F. Beck, H. Krohn, J. Power Sources 12, 9 (1984).
158. T. Boinowitz, G. tom Suden, U. Tormin, H. Krohn, F. Beck, J. Power Sources 56, 179 (1995).
159. F. Beck, T. Boinowitz, H. Krohn, U. Tormin, E. Ther, Mol. Cryst. Liq. Cryst. 245, 177 (1994).
160. J. O. Besenhard, H. P. Fritz, Angew. Chem. 95, 954; Angew. Chem., Int. Ed. Engl. 22, 950 (1983).
161. S. Flandrois, Synth. Metals 4, 255 (1982).
162. R. Yazami, P. Touzain, Solid State Ionics 9–10, 489 (1983).
163. M. Armand, P. Touzain, Mater. Sci. Engng. 31, 319 (1977).
164. N. Iwashita, M. Inagaki, Electrochim. Acta 36, 591 (1991).
165. F. Baron, European Patent 94 291 (1982).
166. R. Yazami, T. Nakajima, Extended Abstract, 40th ISE Meeting, Kyoto (1989), p. 516.
167. J. O. Besenhard, Carbon 14, 111 (1976).
168. J. O. Besenhard, M. Möhwald, J. J. Nickl, Carbon 18, 399 (1980).
169. N. Okuyama, T. Takahashi, S. Kanayama, H. Yasunaga, Physica B + C 105, 298 (1981).
170. K. Schoderböck, H. P. Boehm, Synth. Metals 44, 239 (1991).
171. J. R. Dahn, R. Fong, M. J. Spoon, Phys. Review B, 42, 6424 (1990).
172. D. Guyomard, J. M. Tarascon, J. Electrochem. Soc. 139, 937 (1992).
173. B. Scrosati, J. Electrochem. Soc. 139, 2276 (1992).
174. D. Fauteux, R. Koksbang, J. Appl. Electrochem. 23, 1 (1993).

175. P. Scharff, Chem.-Ing.-Tech. 67, 930 (1995).
176. T. Ohzuku, Y. Iwakoshi, K. Sawai, J. Electrochem. Soc. 140, 2490 (1993).
177. J. Yamaura, Y. Ozaki, A. Morita, A. Ohta, J. Power Sources 43–44, 233 (1993).
178. K. Tatsumi, N. Iwashita, H. Sakaebe, H. Shioyama, S. Higuchi, A. Mabuchi, H. Fujimoto, J. Electrochem. Soc. 142, 716 (1995).
179. R. Kanno, Y. Kawamoto, Y. Takeda, S. Ohashi, N. Imanishi, O. Yamamoto, J. Electrochem. Soc. 139, 3397 (1992).
180. M. Morita, N. Nishimura, Y. Matsuda, Electrochim. Acta 38, 1721 (1993).
181. M. Endo, J.-I. Nakamura, A. Emori, Y. Sasabe, K. Takeuchi, M. Inagaki, Mol. Cryst. Liq. Cryst. 245, 171 (1994).
182. N. Takami, A. Satoh, M. Hara, T. Ohsaki, J. Electrochem. Soc. 142, 2564 (1995).
183. T. Takamura in Rechargeable Lithium and Lithium-Ion Batteries, S. Megahead et al. (eds.), Proceedings Vol. 94–28, The Electrochemical Society, Pennington, NJ (1995), p. 213.
184. K. Tatsumi in Rechargeable Lithium and Lithium-Ion Batteries, S. Megahead et al. (eds.), Proceedings Vol. 94–28, The Electrochemical Society, Pennington, NJ (1995), p. 97.
185. H. Mao, P. Juric, U. von Sacken, Extended Abstracts, Fall Meeting in New Orleans, The Electrochemical Society, October 10–15, 1993.
186. J. R. Dahn, Phys. Rev. B 44, 9170 (1991).
187. M. Endo, Y. Okada, H. Nakamura, Synth. Metals 34, 739 (1989).
188. R. Yazami, P. Touzain, Solid State Ionics 9–10, 489 (1983).
189. Y. Takasu, M. Shiinoki, Y. Matsuda, J. Electrochem. Soc. 131, 959 (1984).
190. J. R. Dahn, A. K. Sleigh, H. Shi, J. N. Reimers, Q. Zhong, B. M. Way, Electrochim. Acta 38, 1179 (1993).
191. T. D. Tran, J. H. Feikert, S. T. Mayer, X. Song, K. Kinoshita in Rechargeable Lithium and Lithium-Ion Batteries, S. Megahead et al. (eds.), Proceedings Vol. 94–28, The Electrochemical Society, Pennington, NJ (1995), p. 110.
192. S. Passerini, J. M. Rosolen, B. Scrosati, J. Power Sources 45, 333 (1993).
193. B. M. Way, J. R. Dahn, J. Electrochem. Soc. 141, 907 (1994).
194. A. M. Wilson, J. R. Dahn, J. Electrochem. Soc. 142, 326 (1995).
195. A. M. Wilson, J. R. Dahn in Rechargeable Lithium and Lithium-Ion Batteries, S. Megahead et al. (eds.), Proceedings Vol. 94–28, The Electrochemical Society, Pennington, NJ (1995), p. 158.
196. Z.-I. Takehara, K. Kanamura, Electrochim. Acta 38, 1169 (1993).
197. M. Jean, C. Desnoyer, A. Tranchant, R. Messina, J. Electrochem. Soc. 142, 2122 (1995).
198. R. Yazami, P. Touzain, J. Power Sources 9, 365 (1983).
199. Z. Jiang, M. Alamgir, K. M. Abraham, J. Electrochem. Soc. 142, 333 (1995).
200. R. Bittihin, R. Herr, D. Hoge, J. Power Sources 43–44, 409 (1993).
201. R. Fong, U. von Sacken, J. R. Dahn, J. Electrochem. Soc. 137, 2009 (1990).
202. J. R. Dahn, U. von Sacken, M. W. Juzkow, H. A. Janaby, J. Electrochem. Soc. 138, 2207 (1991).
203. E. Peled in Rechargeable Lithium and Lithium-Ion Batteries, S. Megahead et al. (eds.), Proceedings Vol. 94–28, The Electrochemical Society, Pennington, NJ (1995), p. 1.
204. E. Peled, J. Electrochem. Soc. 126, 2047 (1979).
205. E. Peled, J. Power Sources 9, 253 (1983).
206. D. Aurbach, Y. Ein-Eli, O. Chusid (Youngman), Y. Garmeli, M. Babai, H. Yamin, J. Electrochem. Soc. 141, 603 (1994).
207. D. Aurbach, I. Weissman, A. Zaban, O. Chusid (Youngman), Electrochim. Acta 39, 51 (1994).
208. Y. Ein-Eli, B. Markovsky, D. Aurbach, Y. Carmeli, H. Yamin, S. Luski, Electrochim. Acta 39, 2559 (1994).

209. D. Aurbach, Y. Ein-Eli, B. Markovsky, A. Zaban A. Schechter in Rechargeable Lithium and Lithium-Ion Batteries, S. Megahead et al. (eds.), Proceedings Vol. 94–28, The Electrochemical Society, Pennington, NJ (1995), p. 26.
210. J. O. Bessenhard, M. W. Wagner, M. Winter, J. Power Sources 43–44, 413 (1993).
211. B. Simon, J. P. Boeuve, J. Power Sources 43–44, 65 (1993).
212. R. Yazami, D. Guerard, Extended Abstract No. 24, Battery Division, ECS Meeting, Toronto, October, 1992, p. 32.
213. J. O. Besenhard, H. Möhwald, J. J. Nickl, Synth. Metals 3, 187 (1981).
214. J. O. Besenhard, M. Winter, J. Yang, W. Biberacher, J. Power Sources 54, 228 (1995).
215. D. Billaud, F. Henry, P. Willmann, Mol. Cryst. Liq. Cryst. 245, 159 (1994).
216. R. Yazami, D. Guérard, J. Power Sources 43–44, 39 (1993).
217. W. Krätschmer, K. Fostiropoulous, D. R. Huffman, Chem. Phys. Lett. 170, 167 (1990).
218. W. Krätschmer, D. L. Lamb, K. Fostiropoulous, D. R. Huffman, Nature (London) 347, 354 (1990).
219. T. Baum, S. Löffler, P. Löffler, P. Weilmünster, K.-H. Homann, Ber. Bunsenges. Phys. Chem. 96, 841 (1992).
220. R. E. Haufler, J. Conceicao, L. P. F. Chibante, Y. Chai, N. E. Byrne, S. Flanagan, M. M. Haley, S. C. O'Brien, C. Pan, Z. Xiao, W. E. Billups, M. A. Ciufolini, R. H. Hauge, J. L. Margrave, L. J. Wilson, R. F. Curl, R. E. Smalley, J. Phys. Chem. 94, 8634 (1990).
221. R. D. Johnson, G. Meijer, D. S. Bethune, J. Am. Chem. Soc. 121, 8983 (1990).
222. Q. Xie, M. Perez-Cordero, L. Echegoyen, J. Am. Chem. Soc. 114, 3978 (1992).
223. D. Dubois, G. Moninot, W. Kutner, M. T. Jones, K. M. Kadish, J. Phys. Chem. 96, 7137 (1992).
224. A. Hamwi, G. Dondainas, J. Dupuis, Mol. Cryst. Liq. Cryst. 245, 301 (1994).
225. Ch. Jehoulet, A. J. Bard, F. Wudl, J. Am. Chem. Soc. 113, 5456 (1991).
226. Ch. Jehoulet, Y. S. Obeng, Y.-T. Kim, F. Zhou, A. J. Bard, J. Am. Chem. Soc. 114, 4237 (1991).
227. R. G. Compton, A. Spackman, R. G. Wellington, J. Turner, J. Electroanal. Chem. 327, 337 (1992).
228. Y. Chabre, D. Djurado, M. Armand, W. R. Romanow, N. Coustel, J. P. McCauley, J. E. Fischer, A. B. Smith, J. Am. Chem. Soc. 114, 764 (1992).
229. A. Deronzier, J.-C. Moutet, J. Am. Chem. Soc. 116, 5019 (1994).
230. S. Lemont, J. Ghanbaja, D. Billaud, Mol. Cryst. Liq. Cryst. 244, 203 (1994).
231. Y. Matsuo, T. Nakajima, Electrochim. Acta 41, 15 (1996).
232. M. S. Dresselhaus, G. Dresselhaus, Mol. Cryst. Liq. Cryst. 244, 1 (1994).
233. K. Lüders, Phys. Bl. 50, 166 (1994).
234. A. F. Hebard, M. J. Rossenski, R. C. Haddon, Nature (London) 350, 600 (1991).
235. I. T. Belash, A. D. Bronnikov, O. V. Zharikov, A. V. Palnichenko, Extended Abstracts, 5th Int. Symp. on Graphite Intercalation Compounds, Berlin, May, 1989, p. 70.
236. J. Mort, R. Ziolo, M. Machon Kin, D. R. Huffman, M. I. Ferguson, Chem. Phys. Lett. 186, 284 (1991).
237. V. A. Garten, D. E. Weiss, Aust. J. Chem. 8, 68 (1955).
238. V. A. Garten, D. E. Weiss, Aust. J. Chem. 10, 309 (1957).
239. J. V. Hallum, H. V. Drushel, J. Phys. Chem. 62, 110, 1502 (1958).
240. M. Sullivan, R. Kötz, O. Haas, Extended Abstract No. 60, ECS Meeting, Chicago, October, 1995.
241. K. F. Blurton, Electrochim. Acta 18, 869 (1973).
242. H. P. Boehm, Carbon 32, 759 (1994).
243. C. L. Mantell, Industrial Carbon, van Nostrand, New York (1947).
244. G. Kühner, M. Voll, Manufacture of carbon black, in: Carbon Black, J.-B. Donnet, R. C. Bansal, M.-J. Wang (eds.), 2nd edn., Marcel Dekker, New York (1993), pp. 1–66.

245. G. Collin, M. Zander, Chem.-Ing.-Tech. 63, 539 (1991).
246. H. J. Mair, S. Roth (eds.), Elektrisch leitende Kunststoffe, 2nd edn., Carl Hanser, München (1989).
247. A. Watanabe, K. Mori, H. Ishikawa, Y. Nakamura, J. Electrochem. Soc. 134, 1318 (1987).
248. Anon. Li/Carbon Black-Battery, Data Sheet Matsushita Co. (1988).
249. X. Andrieu, L. Josset, Extended Abstract No. 57, ECS Meeting, Chicago, October, 1995.
250. F. Beck, G. Heydecke, Ber. Bunsenges. Phys. Chem. 92, 1418 (1988).
251. G. Heydecke, F. Beck, Carbon 28, 301 (1990).
252. N. Giordano, P. L. Antonucci, E. Passalacqua, L. Pino, A. S. Arico, K. Kinoshita, Electrochim. Acta 36, 1931 (1991).
253. M. Kanowski, G. Buntkowsky, H. Werner, M. Wohlers, R. Schlögl, H. M. Vieth, K. Lüders, Mol. Cryst. Liq. Cryst. 245, 271 (1994).
254. K. Mund, G. Richter, DECHEMA Monogr. 90, 173 (1981).
255. G. Wegner, Angew. Chem. 93, 352 (1981).
256. T. A. Skotheim (ed.), Handbook of Conducting Polymers, Marcel Dekker, New York (1986), Vols. 1 and 2.
257. G. P. Evans, The electrochemistry of conducting polymers, in: Advances in Electrochemical Science and Engineering, H. Gerischer, C. W. Tobias (eds.), VCH, Weinheim (1990).
258. H. Naarmann, Makromol. Chem., Macromol Symp., 8, 1 (1987).
259. S. Roth, M. Filzmoser, Adv. Mater. 2, 356 (1990).
260. F. Beck, B. Wermeckes, M. Schirmeisen in: Electroorganic Synthesis, R. D. Little, N. L. Weinberg (eds.) (M. Baizer Memorial Book), Marcel Dekker, New York (1990), p. 397.
261. H. A. Potts, G. F. Smith, J. Chem. Soc. 4018 (1957).
262. A. Métrot, Makromol. Chem., Macromol. Symp. 8, 39 (1987).
263. U. Barsch, F. Beck, Electrochim. Acta 41, 1761 (1996).
264. F. Beck, A. Pruß, J. Electroanal. Chem. 216, 157 (1987).
265. F. Beck, P. Braun, M. Oberst, Ber. Bunsenges. Phys. Chem. 91, 967 (1987).
266. V. V. Krasko, A. A. Yakovleva, Ya. M. Kolotyrkin, Elektrokhimija 22, 1432 (1986).
267. J. B. Schlenoff, Y. Fong, H. Xu, Polym. Mater. Sci. Engng. 63, 411 (1990).
268. J. B. Schlenoff, H. Xu, J. Electrochem. Soc. 139, 2397 (1992).
269. D.-S. Park, Y.-B. Shim, S.-M. Park, J. Electrochem. Soc. 140, 609 (1993).
270. T. Kobayashi, H. Yoneyama, H. Tamura, J. Electroanal. Chem. 177, 293 (1984).
271. D. E. Stilwell, S.-M. Park, J. Electrochem. Soc. 135, 2497 (1988).
272. D. E. Stilwell, S.-M. Park, J. Electrochem. Soc. 136, 688 (1989).
273. Y.-B. Shim, M.-S. Won, S.-M. Park, J. Electrochem. Soc. 137, 538 (1990).
274. A. A. Pud, Synth. Metals 66, 1 (1994).
275. H. Naarmann, Angew. Makromol. Chem. 109/110, 295 (1982).
276. P. J. Nigrey, A. G. McDiarmid, A. J. Heeger, J. Chem. Soc., Chem. Commun. 594 (1979).
277. P. J. Nigrey, D. McInnes, D. P. Nairns, A. G. McDiarmid, A. J. Heeger, J. Electrochem. Soc. 128, 1651 (1981).
278. A. G. McDiarmid, A. J. Heeger, P. J. Nigrey (University Patents Inc., Norwalk, Connecticut), European Patent 36 118 (February, 1981).
279. H. Shirakawa, S. Ikeda, Polym. J. 2, 231 (1971).
280. T. Ito, H. Shirakawa, S. Ikeda, J. Polym. Sci., Polym. Chem. Ed. 12, 11 (1974).
281. D. McInnes, M. A. Druy, D. P. Nairns, A. G. McDiarmid, A. J. Heeger, J. Chem. Soc., Chem. Commun. 317 (1981).
282. B. Broich, J. Hocker, Ber. Bunsenges. Phys. Chem. 88, 497 (1984).

283. T. Nagatomo, K. Negishi, H. Kakehata, O. Omoto, Proc. Symp. Advances in Battery Materials and Proc., J. McBreen et al. (eds.), The Electrochemical Society, Pennington, NJ (1984), p. 34.
284. R. Bittihn, D. Naegele, G. Köhler, R. Denig, Mol. Cryst. Liq. Cryst. 121, 221 (1985).
285. Anon. Chem. Engng. News 20 (1987).
286. H. Naarmann, Adv. Mater. 2, 345 (1990).
287. F. G. Will, J. Electrochem. Soc. 132, 2093 (1985).
288. P. Kovacic, A. Kyriakis, J. Am. Chem. Soc. 85, 454 (1963).
289. I. Rubinstein, J. Electrochem. Soc. 130, 1509 (1983).
290. I. Rubinstein, J. Polym. Sci., Polym. Chem. Ed. 21, 3035 (1983).
291. M. D. Levi, E. Yu. Pisarevskaya, E. B. Molodkina, A. I. Danilov, J. Chem. Soc., Chem. Commun. 149 (1992).
292. S. Hara, S. Aeiyach, P. C. Lacaze, J. Electroanal. Chem. 364, 223 (1994).
293. L. W. Shacklette, R. L. Elsenbaumer, R. R. Chance, J. M. Sowa, D. M. Ivory, G. G. Miller, R. H. Baughmann, J. Chem. Soc., Chem. Commun. 361 (1982).
294. F. Beck, A. Pruß, Electrochim. Acta 28, 1847 (1983).
295. T. R. Jow, L. W. Shacklette, M. Maxfield, D. Vernick, J. Electrochem. Soc. 134, 1730 (1987).
296. M. Maxfield, T. R. Jow, M. G. Sewchok, L. W. Shacklette, J. Power Sources 26, 93 (1989).
297. A. Bohnen, H. J. Räder, K. Müllen, Synth. Metals 47, 37 (1992).
298. H. Gregorius, W. Heitz, K. Müllen, Adv. Mater. 5, 279 (1993).
299. K.-H. Koch, K. Müllen, Chem. Ber. 124, 2091 (1991).
300. U. Scherf, K. Müllen, Synthesis 1992, 23.
301. M. Baumgarten, U. Müller, A. Bohnen, K. Müllen, Angew. Chem. 104, 482 (1992).
302. A. V. Vannikov, A. Yu. Kryukov, H.-H. Hörhold, Synth. Metals 41–43, 331 (1991).
303. A. Dall'Olio, Y. Dascota, V. Varacca, V. Bocchi, C.R. Acad. Sci., Ser. C. 267, 433 (1968).
304. L. F. Warren, D. P. Anderson, J. Electrochem. Soc. 134, 101 (1987).
305. A. F. Diaz, K. K. Kanazawa, G. P. Gardini, J. Chem. Soc., Chem. Commun. 635 (1979).
306. A. F. Diaz, Chem. Scr. 17, 145 (1981).
307. E. M. Genies, G. Bidan, A. F. Diaz, J. Electroanal. Chem. 149, 101 (1983).
308. F. Beck, M. Oberst, Macromol. Chem. Macromol. Symp. 8, 97 (1987).
309. F. Beck, M. Oberst, R. Jansen, Electrochim. Acta 35, 1841 (1990).
310. M. Oberst, F. Beck, Angew. Chem., Int. Ed. Engl. 26, 1031 (1987).
311. F. Beck, M. Oberst, J. Appl. Electrochem. 22, 332 (1992).
312. B. Zinger, Synth. Metals 28, C37 (1989).
313. G. Paasch, D. Schmeißer, A. Bartl, H. Naarmann, L. Dunsch, W. Göpel, Synth. Metals 66, 135 (1994).
314. A. F. Diaz, J. I. Castillo, J. A. Logan, W.-Y. Lee, J. Electroanal. Chem. 129, 115 (1981).
315. G. Mengoli, M. M. Musiani, M. Fleischmann, D. Pletcher, J. Appl. Electrochem. 14, 285 (1984).
316. S. Hiroshi, K. Naoi, T. Hirabayashi, T. Osaka, Denki Kagaku 54, 75 (1986).
317. F. Trinidad, J. Alonso-Lopez, M. Nebot, J. Appl. Electrochem. 17, 215 (1987).
318. S. Panero, P. Prosperi, F. Bonino, B. Scrosati, Electrochim. Acta 32, 1007 (1987).
319. H. Münstedt, G. Koehler, H. Moehwald, D. Naegele, R. Bittihn, G. Ely, E. Meissner, Synth. Metals 18, 259 (1987).
320. R. Bittihn, G. Ely, F. Woeffler, H. Münstedt, H. Naarmann, D. Naegele, Makromol. Chem., Macromol. Symp. 8, 51 (1987).
321. R. Bittihn, Kunststoffe 79, 6 (1989).
322. Petr Novák, W. Vielstich, J. Electrochem. Soc. 137, 1681 (1990).

323. K. West, T. Jacobsen, B. Zachau-Christiansen, M. A. Careem, S. Skaarup, Synth. Metals 55–57, 1412 (1993).
324. W. A. Wampler, C. Wei, K. Rajeshwar, J. Electrochem. Soc. 141, L13 (1994).
325. N. Mermilliod, J. Tanguy, J. Electrochem. Soc. 133, 1073 (1986).
326. P. Novák, O. Inganäs, J. Electrochem. Soc. 135, 2485 (1988).
327. J. Heinze, R. Bilger, Ber. Bunsenges. Phys. Chem. 97, 502 (1993).
328. R. Bilger, J. Heinze, Synth. Metals 55–57, 1424 (1993).
329. F. Beck, M. Dahlhaus, J. Electroanal. Chem. 357, 289 (1993).
330. M. Hepel, Electrochim. Acta 41, 63 (1996).
331. M. A. Vorotyntsev, E. Vieil, J. Heinze, in: Proceedings of the NATO Advanced Research Workshop, Kiev, May 14–17, 1995, on New Promising Electrochemical Systems for Rechargeable Batteries, V. Z. Barsukov, F. Beck (eds.), Kluwer Dordrecht (1996), pp. 333–346.
332. R. John, G. G. Wallace, J. Electroanal. Chem. 354, 145 (1993).
333. S. Kuwabata, A. Kishimoto, T. Tanaka, H. Yoneyama, J. Electrochem. Soc. 141, 10 (1994).
334. F. Beck, U. Barsch, Makromol. Chem. 194, 2725 (1993).
335. J. Roncali, Chem. Rev. 92, 711 (1992).
336. S. Panero, P. Prosperi, B. Klaptse, B. Scrosati, Electrochim. Acta 31, 1597 (1986).
337. A. Corradini, M. Mastragostino, A. S. Panero, P. Prosperi, B. Scrosati, Synth. Metals 18, 625 (1987).
338. P. Passiniemi, J.-E. Österholm, Synth. Metals 18, 637 (1987).
339. F. Beck, M. Dahlhaus, E. Abdelmula, GDCh Monogr. 3, 581 (1996).
340. F. Buttol, M. Mastragostino, A. S. Panero, B. Scrosati, Electrochim. Acta 31, 783 (1986).
341. T. Kawai, T. Iwasa, M. Onada, T. Sakamoto, K. Yoshino, J. Electrochem. Soc. 139, 3404 (1992).
342. X. Ren, J. Davey, S. Gottesfeld, J. Ferraris, Extended Abstract No. 53, ECS Meeting, Chicago, October, 1995, p. 84.
343. X. Ren, J. Davey, S. Gottesfeld, J. Ferraris, Extended Abstract No. 54, ECS Meeting, Chicago, October, 1995 p. 85.
344. C. Arbizzani, M. Catellani, M. Mastragostino, C. Mingazzini, Electrochim. Acta 40, 1871 (1995).
345. C. Arbizzani, M. Mastragostino, L. Meneghello, Electrochim. Acta 41, 21 (1996).
346. Z. Gao, J. Bobacka, A. Ivaska, J. Electroanal. Chem. 364, 127 (1994).
347. E. Genies in: Proc. NATO Advanced Research Workshop, Kiev, May 14–17, 1995, on New Promising Electrochemical Systems for Rechargeable Batteries, V. Z. Barsukov, F. Beck (eds.). Kluwer, Dordrecht (1996), pp. 306–307.
348. E. Genies, M. Lapkowski, C. Santier, E. Vieil, Synth. Metals 18, 631 (1987).
349. S. Roth, W. Graupner, Synth. Metals 55–57, 3623 (1993).
350. M. Jozefowicz, J. Perichon, L. T. Yu, R. Buvet, French Parent 1 216 569 (1970); R. de Surville, M. Josefowicz, L. T. Yu, J. Perichon, R. Buvet, Electrochim. Acta 13, 1451 (1958).
351. A. G. McDiarmid, S. L. Mu, N. L. D. Somasiri, W. Wu, Mol. Cryst. Liq. Cryst. 121, 187 (1985).
352. E. Genies, C. Tsintavis, J. Electroanal. Chem. 195, 109 (1985).
353. E. M. Genies, P. Hany, G. Santier, J. Appl. Electrochem. 18, 751 (1988).
354. Y. Echigo, K. Asami, H. Takahashi, K. Inoue, T. Kabata, O. Kimura, T. Ohsawa, Synth. Metals, 55–77, 3611 (1993).
355. T. Enomoto, D. P. Aller, Bridgestone, Corp., Bridgestone News Release (Sept. 9, 1987), 10-1-Kobayashi, 1-Chome, Chuo-Ku-Tokyo 104.
356. E. M. Genies, P. Hany, C. Santier, J. Appl. Electrochem. 18, 751 (1988).

357. O. Genz, M. M. Lohrengel, J. W. Schultze in: Proc. NATO Advanced Research Workshop, Kiev, May 14–17, 1995, on New Promising Electrochemical Systems for Rechargeable Batteries, V. Z. Barsukov, F. Beck (eds.), Kluwer, Dordrecht 1996, pp. 321–331.
358. R. Shishikura, H. Konuma, T. Sakai, H. Nakamura, M. Takeuchi, M. Kobayashi, (Showa Denko K.K.; Hitachi, Ltd.) Japanese Patent 62/10 862 (January, 1987).
359. J. Yano, K. Ogura, A. Kitani, K. Sasaki, Synth. Metals 51b, 51e.
360. K. L. N. Phani, S. Pitchumany, S. Muralidharan, S. Ravichandran, S. V. K. Iyer, J. Electroanal. Chem. 353, 315 (1995).
361. R. Huq, G. C. Farrington, J. Electrochem. Soc. 132, 1432 (1985).
362. R. L. Elsenbaumer, L. W. Shacklette in Handbook of Conducting Polymers, T. A. Skotheim (ed.), Marcel Dekker, New York (1986), Vol. 1, p. 231.
363. H. Wu, X. Qu, Huaxue Xuebao (Acta Chim. Sin.) 45, 631 (1987).
364. P. Aldebert, P. Audebert, M. Armand, G. Bidan, M. Pineri, J. Chem. Soc., Chem. Commun. 1636 (1986).
365. T. Hirai, S. Kuwabata, H. Yoneyama, J. Electrochem. Soc. 135, 1132 (1998).
366. S. Panero, P. Prosperi, B. Scrosati, Electrochim. Acta 37, 419 (1992).
367. X. Ren, G. Pickup, J. Phys. Chem. 97, 5356 (1993).
368. K. Takeshita, W. Wernet, N. Oyama, J. Electrochem. Soc. 141, 2004 (1994).
369. T. Shimidzu, A. Ohtani, K. Honda, J. Electroanal. Chem., 251, 323 (1988).
370. M. Morita, S. Miyazaki, H. Tanoue, M. Ishikawa, Y. Matsuda, J. Electrochem. Soc. 141, 1409 (1994).
371. T. Kanbara, T. Kushida, N. Saito, I. Kuwajima, K. Kubota, T. Yamamoto, Chem. Lett. 583 (1992).
372. T. Muruyama, Z.-h. Zhou, K. Kubota, T. Yamamoto, Chem. Lett. 643 (1992).
373. S. Janietz, B. Schulz, M. Törrönen, G. Sundholm, Eur. Polym. J. 29, 545 (1993).
374. M. Miyabayashi, A. Itsubo, Y. Nakano, M. Masami, M. Ueda (Mitsubishi Petrochemical Co. Ltd.), European, Patent 165 047 (December 1985). Cf. Japanese Patent 84-230 293 (November, 1984); Chem. Abstr. 104, 71831y (1986).
375. K. Tokumitsu, A. Mabuchi, H. Fujimoto, T. Kasuh in: Rechargeable Lithium and Lithium-Ion Batteries, S. Megahead et al. (eds.), Proceedings/Vol. 94–28, The Electrochem. Soc., Pennington, NJ (1995), p. 136.
376. T. D. Tran, J. H. Feikert, S. T. Mayer, X. Song, K. Kinoshita in: Rechargeable Lithium and Lithium-Ion Batteries, S. Megahead et al. (eds.), Proceedings Vol. 94–28, The Electrochemical Society, Pennington, NJ (1995), p. 110.
377. E. Fitzer, Angew. Chem. 92, 375 (1980).
378. F. Beck, N. Zahedi, Polymer 37 (1996), in press.
379. G. M. Jenkins, K. Kawamura, Polymeric Carbons, Cambridge University Press Cambridge (1976).
380. O. Yamamoto, Y. Takeda, R. Kanno, K. Nakanishi, T. Ichikawa in: Proc. Symp. on Primary and Secondary Ambient Temperature Lithium Batteries, 1987, Proceedings, Vol. 88–6, The Electrochemical Society Pennington, NJ (1988), p. 754.
381. O. Yamamoto, Extended Abstract, 40th ISE Meeting, Kyoto, 1989, p. 510.
382. R. Kanno, Y. Takeda, T. Ischikawa, K. Kakanishi, O. Yamamoto, J. Power Sources 26, 535 (1989).
383. J. S. Mattson, H. B. Mark Jr., Activated Carbon, Marcel Dekker, New York (1971).
384. H. Kienle, E. Bader Aktivkohle und ihre industrielle Anwendung, F. Enke Verlag, Stuttgart (1980).
385. D. L. Boos, US Patent 3 536 953 (1970).
386. S. Sekido, T. Muranaka, Y. Yoshino, H. Mori, Nat. Techn. Report 26, 220 (1980).
387. Anon. Gold Cap from Matsushita Company (Panasonic), in: Electronic Aktuell (February, 1993), pp. 23–27.

388. K. Kinoshita, X. Chu, Extended Abstract No. 56, ECS Meeting, Chicago, October, 1995.
389. T. Nagaura, M. Anzai (Sony Corp.), Japanese Patent 89-220216, (1989/1991); Chem. Abstr. 115, 53476j (1991).
390. Y. Ozaki, N. Eda (Matsushita Electric Industrial Co., Ltd.), Japanese Patent 89-272 837 (1989); Chem. Abstr. 115, 139653b (1991).
391. S. Yata et al., Synth. Metals 38, 169, 177, 185 (1990).
392. S. S. Zhang, Q. G. Liu, L. L. Yang, J. Electrochem. Soc. 140, L107 (1993).
393. T. Zheng, Q. Zhong, J. R. Dahn, J. Electrochem. Soc. 142, L211 (1995).
394. X. Chu, L. D. Schmidt, W. H. Smyrl in: Rechargeable Lithium and Lithium-Ion Batteries, S. Megahead et al. (eds.), Proceedings Vol. 94–28, The Electrochem. Soc., Pennington, NJ (1995), p. 196.
395. I. Tanahashi, A. Yoshida, A. Nishino, Bull. Chem. Soc. Jpn. 63, 2755 (1990).
396. K. Inada et al. (Toshiba Battery Co.), Japanese Patent 87-138 181 (1988); Chem. Abstr. 110, 234643d (1989).
397. T. Morimoto, N. Yoshida (Asahi Glass Co.), Japanese Patent 89-84 648 (1989); Chem. Abstr. 114, 232041q (1991).
398. R. W. Pekala, J. Mater. Sci. 24, 3221 (1989).
399. S. T. Mayer, J. L. Kaschmitter, R. W. Pekala, Extended Abstract No. 500, ECS Meeting Miami Beach, October, 1994.
400. D. Schuster, German Patent 3809 758 (1988).
401. D. Schuster, D 6741 Frankweiler, Information Sheet (1991); German Patent 4 102 958 (1991).
402. O. Yamamoto, Y. Takeda, R. Kanno, K. Nakanishi, T. Ichikawa, Proc. Electrochem. Soc. 88–6, 754 (1987).
403. D. D. Bowen in: Concise Encyclopedia of Composite Materials, A. Kelly, R. W. Cahn, M. B. Bever (eds.), Pergamon Press, Oxford (1989), pp. 175–185.
404. E. Fitzer, M. Heine in: Fibre Reinforcements for Composite Materials, Composite Materials Series, Vol. 2, A. R. Burnell (ed.) Elsevier, Amsterdam (1988), p. 73.
405. J. O. Besenhard, J. Jakob, U. Krebber, P. Möller, R. F. Sauter, N. Kanani, H. Meyer, J. K. H. Hörber, A. D. Jannakoudakis, Z. Naturforsch. Teil B44, 729 (1989).
406. O. Besenhard, P. D. Jannakoudakis, A. D. Jannakoudakis, E. Theodoridou, J. Appl. Electrochem. 19, 341 (1989).
407. N. Mohri, N. Yanagisawa, Y. Tajima, H. Tanaka, T. Mitate, S. Nakajima, M. Yoshida, Y. Yoshimoto, T. Suzuki, H. Wada, J. Power Sources 26, 545 (1989).
408. R. Kanno, Y. Kawamoto, Y. Takedo, S. Ohashi, N. Imanishi, O. Yamamoto, J. Electrochem. Soc. 139, 3397 (1992).
409. M. Morita, N. Nashimura, Y. Matsuda, Electrochim. Acta 38, 1721 (1993).
410. M. Suzuki, Carbon 32, 577 (1994).
411. A. M. Skundin, Proc. of the NATO Advanced Research Workshop, Kiev, May 14–17, 1995, on New Promising Electrochemical Systems for Rechargeable Batteries, V. Z. Barsukov, F. Beck (eds.), Kluwer, Dordrecht (1996), p. 373.
412. K. Hiratsuka, T. Morimoto, Y. Sanada, K. Kurihara, Extended Abstract 40th ISE Meeting, Kyoto, 1989, p. 1178.
413. X. Shui, D. D. L. Chung, C. A. Frysz, J. Power Sources 47, 313 (1994).
414. S. M. Lipka, R. Karan, R. Kashauer, Extended Abstract No. 499, ECS Meeting, Miami Beach, October, 1994.
415. S. M. Lipka, D. I. Zawacki, Extended, Abstract No. 59, ECS Meeting, Chicago, October, 1995.
416. Y. A. Maletin, N. G. Strizhakova, V. Y. Izotov, S. G. Kozachkov, A. A. Mironova, V. V. Danilin, Proc. of the Advanced Research Workshop, NATO Kiev, May 14–17, 1995, on

New Promising Electrochemical Systems for Rechargeable Batteries, V. Z. Barsukov, F. Beck (eds.), Kluwer, Dordrecht (1996), p. 363.
417. C. J. Marrion, D. R. Cahela, S. Ahn, B. J. Tatarchuk, J. Power Sources 47, 297 (1994).
418. M. Miyabayashi, A. Itsubo, H. Yui, J. Sato, K. Inada, K. Ikeda (Petrochemical Co. and Toshiba Batt. Co.), Japanese Patent 86-169 864 (1988); Chem. Abstr. 108, 189925t (1988).
419. M. Miyabayashi, A. Itsubo, H. Yui, J. Sato, K. Inada, K. Ikeda (Mitsubishi Petrochemical Co. and Toshiba Batt. Co.), Japanese Patent 86-142 643 (1988); Chem. Atstr. 108, 153662r (1988).
420. M. B. Jones, P. Kovacic, D. Lanska, J. Polym. Sci., Polym. Chem. Ed. 19, 89 (1981).
421. H. Naarmann, Ber. Bunsenges, Phys. Chem. 68, 558 (1979).
422. F. Beck, Ber Bunsenges. 68, 558 (1964).
423. E. Fitzer, J. Kalka, High Temp. - High Press. 3, 53 (1971).
424. K. Inada, K. Ikeda, S. Inomata. T. Nishii, M. Miyabayashi, H. Yui in: Practical Lithium Batteries, Y. Matsuda, C. R. Schlaikjer (eds.), JEC Press, Cleveland, OH (1988), pp. 96–99.
425. K. Sato, M. Noguchi, A. Demachi, N. Oki, M. Endo, Science 264, 556 (1994).
426. U. Anton, A. Bohnen, K.-H. Koch, H. Naarmann, H. J. Räder, K. Müllen, Adv. Mater. 4, 91 (1992).
427. M. Becher, H. F. Mark, Angew. Chem. 73, 641 (1961).
428. A. V. Topchiev, J. Polym. Sci., Part A 1, 591 (1963).
429. M. Schwarzenberg, K. Jobst, L. Sawtschenko, Electrochim. Acta 35, 403 (1990).
430. K. Jobst, L. Sawtschenko, M. Schwarzenberg, G. Paasch, Synth. Metals 47, 297 (1992).
431. K. Jobst, L. Sawtschenko, M. Schwarzenberg, G. Paasch, L. Wuckel, Synth. Metals 51, 425 (1992).
432. G. Paasch, K. Micka, M. Schwarzenberg, K. Jobst, L. Sawtschenko, Electrochim. Acta 37, 2453 (1992).
433. R. V. Parthasarathy, K. L. N. Phani, C. R. Martin, Adv. Mater. 7, 896 (1995).
434. C. Barbero, R. Kötz, J. Electrochem. Soc. 140, 1 (1993).
435. A. A. Pud, G. S. Shapoval, Elektrokhimiya 28, 654 (1992); (Engl. Translat.) p. 529.
436. A. A. Pud, G. S. Shapoval, V. P. Kukhar, O. E. Mikulina, L. L. Gervits, Electrochim. Acta 40, 1157 (1995).
437. R. Kanno, Y. Takeda, T. Ichidawa, K. Nakanishi, O. Yamamoto, J. Power Sources 26, 535 (1989).
438. K. Murata, H. Ueda, K. Kawaguchi, Synth. Metals 44, 357 (1991).
439. T. Zheng, Y. Liu, E. W. Fuller, S. Tseng, U. von Sacken, J. R. Dahn, J. Electrochem. Soc. 142, 2581 (1995).
440. H. Nishihara, K. Ohashi, S. Kaneko, F. Tanaka, K. Aramaki, Synth. Metals 41–43, 1495 (1991).
441. Y. Tajima, M. Mori, H. Tanaka (Sharp. Corp.), Japanese Patent 86-269 425 (1988); Chem. Abstr. 109, 113473u (1988).
442. H. Tanaka, T. Mitate, N. Yanagisawa (Sharp. Corp.), European Patent 90-404 578 (1990); Chem. Abstr. 114, 85403d (1991).
443. J. S. Xue, K. Myrtle, J. R. Dahn, J. Electrochem. Soc. 142, 2927 (1995).
444. H. A. Pohl, E. H. Engelhardt, J. Phys. Chem. 66, 2085 (1962).
445. H. A. Pohl, D. A. Opp, J. Phys. Chem. 66, 2121 (1962).
446. G. Kossmehl, G. Manecke, Chem.-Ing.-Tech. 39, 1041, 1079 (1967).
447. Rohm & Haas Co., European, Patent 50 441 (1980).
448. H. Krohn, F. Beck, A. Zahn, Angew. Makromol. Chem. 164, 143 (1988).
449. H. Kaneko, A. Negishi, Y. Suda, T. Kawakubo, Denki Kagaku 61, 920 (1993).
450. J. C. Card, G. Valentin, A. Strock, J. Electrochem. Soc. 137, 2736 (1990).

451. H. Gerischer, Ber. Bunsenges. Phys. Chem. 67, 164 (1963).
452. J. Held, H. Gerischer, Ber. Bunsenges. Phys. Chem. 67, 921 (1963).
453. G. Heydecke, F. Beck, Ber. Bunsenges. Phys. Chem. 92, 1418 (1988).
454. F. Beck, F. Krüger, GDCh Monogr. 3, 465 (1996).
455. B. Coffey, P. V. Madsen, T. O. Poehler, P. C. Searson, J. Electrochem. Soc. 142, 321 (1995).
455a. H. J. Main, S. Roth Elektrisch leitende Kunshaffe Carl Hanser Verlag Munich, 1989.
456. S. Zhong, M. Kazacos, R. P. Burford, M. Skyllas-Kazacos, J. Power Sources 36, 29 (1991).
457. V. Haddadi-Asl, M. Kazacos, M. Skyllas-Kazacos, J. Appl. Electrochem. 25, 29 (1995).
458. F. Beck, G. tom Suden, U. Tormin, T. Boinowitz, Electrochim. Acta 41 933 (1996).
459. M. Mitzlaff, J. Cramer, R. Pistorius, Chem.-Ing.-Tech. 54, 601 (1982).
460. J. Wang, Electrochim. Acta 26, 1721 (1981).
461. G. Gun, M. Tsionsky, O. Lev, Anal. Chim. Acta 294, 261 (1994).
462. C. S. C. Bose, S. Basak, K. Rajesiwar, J. Electrochem. Soc. 139, L75 (1992).
463. B. Wessling, Synth. Metals 45, 119 (1991).
464. M. Ue, Electrochim. Acta 39, 2083 (1994).
465. H. P. Fritz, K. Stein, R. Herr, J. Power Sources 37, 315 (1992).
466. C. Arbizzani, M. Mastragostino, L. Meneghello, X. Andrieu, T. Vićedo, J. Power Sources 45, 161 (1993).
467. H. Akashi, S. L. Hsu, W. J. MacKnight, M. Watanabe, N. Ogata, J. Electrochem. Soc. 142, L205 (1995).
468. Electrochim. Acta 40, 2031–2454 (1995).
469. S. Passerini, F. Croce, B. Scrosati, Extended Abstract No. 23, ECS Meeting, New Orleans, October 10–15, 1993.
470. F. Croce, F. Gerace, G. Dautzemberg, S. Passerini, G. B. Appetecchi, B. Scrosati, Electrochim. Acta 39, 2187 (1994).
471. M. Ishikawa, M. Ihara, M. Morita, Y. Matsuda, Electrochim. Acta 40, 2217 (1995).
472. M. G. Minett, J. R. Owen, J. Power Sources 28, 397 (1989).
473. R. A. Vaia, S. Vasudevan, W. Krawiec, L. G. Scanlon, E. P. Giannelis, Adv. Mater. 7, 154 (1995).
474. C. A. Angell, C. Liu, E. Sanchez, Nature (London) 362, 137 (1993).
475. R. T. Carlin, P. C. Truelove, R. A. Osteryoung, Electrochim. Acta 37, 2615 (1992).
476. S.-G. Park, P. C. Truelove, R. T. Carlin, R. A. Osteryoung, J. Am. Chem. Soc. 113, 3334 (1991).
477. F. Beck in: Notstromversorgung mit Batterien, Fünftes Technisches Symposium K. Eberts (ed.), VDE-Verlag, München (1987).
478. S. Hossain, Extended Abstract No. 31, ECS Meeting, New Orleans, October, 1993.
479. H. Döring, H. Clasen, M. Zweynert, J. Garche, L. Jörissen in: Proc. of the NATO Advanced Research Workshop, Kiev, May 14–17, 1995, on New Promising Electrochemical Systems for Rechargeable Batteries, V. Z. Barsukov, F. Beck (eds.), Kluwer, Dordrecht (1996), pp. 3–14.
480a. J. P. Gabano (ed.), Lithium Batteries, Academic Press, London (1983).
480. a F. R. Kalhammer, A. Kozawa, C. B. Moyer, B. B. Owens, Performance and Availability of Batteries for Electric Vehicles: A Report of the Technical Advisory Panel (Dec. 11, 1995).
481. D. Pletcher, J. F. Rohan, A. G. Ritchie, Electrochim. Acta 39, 2015 (1994).
482. G. Hambitzer, J. Dreher, J. Dünger, U. Schriever, Extended Abstracts P:III.1.14, ISE Meeting, Berlin, September, 1993.
483. G. Hambitzer, J. Dreher, J. Dünger, B. Hefer in: Proc. of the NATO Advanced Research Workshop, Kiev, May 14–17, 1995, on New Promising Electrochemical Systems for

Rechargeable Batteries, V. Z. Barsukov, F. Beck (eds.), Kluwer, Dordrecht (1996). pp. 117–128.

484. P. Smith, D. Chua, W. Ebner, S. James in Power Sources 13, T. Keily, B. W. Baxter (eds.), 17th International Power Sources Symposium, sponsored by the Joint Services Electrical Power Sources Committee, Bournemouth, 1991, p. 437.
485. M. Broussely, J. Labat, J. M. Bodet, J. M. Cocciantelli, ibid., p. 429.
486. Y. M. Kim, H. Y. Kang, ibid, p. 383.
487. G. Halpert, S. Surampudi, A. Attia, ibid, p. 419.
488. J. O. Besenhard, M. Buser, M. Schwake, DECHEMA Monogr. 124, 725 (1991).
489. M. Armand, P. Touzain, Mater. Sci. Engng. 31, 319 (1977).
490. J. S. Dunning, W. H. Tiedemann, L. Hsueh, D. N. Bennion, J. Electrochem. Soc. 118, 1886 (1971).
491. D. N. Bennion, R. K. Hebbar, S. L. Deshpande, US Patent 4 009 323 (1977).
492. S. L. Deshpande, D. N. Bennion, J. Electrochem. Soc. 125, 689 (1978).
493. T. Ohzuku, Z. Takehara, S. Yoshizawa, Denki Kagaku 46, 438 (1978).
494. Y. Matsuda, M. Morita, H. Katsuma, J. Electrochem. Soc. 131, 104 (1984).
495. R. Shishikura (Showa Denko K.K. and Hitachi Ltd.), Japanese Patent 86-297 917 (1986); Chem. Abstr. 109, 213593b.
496. C. Arbizzani, A. M. Marinangeli, M. Mastragostino, L. Meneghello, T. Hamaide, A. Guyot, J. Power Sources 43–44, 453 (1993).
497. S. Furukawa, K. Nishio, M. Fujimoto, T. Suzuki, K. Hasegawa (Mitsubishi), Japanese Patent 86-15 324, (1986); Chem. Abstr. 107, 158390q.
498. A. Sekino, Y. Ozeki (Nippon Steel) Japanese Patent 84-2039, (1984); Chem. Abstr. 103 218330z (1985).
499. A. Demachi, T. Oishi (Honda), Japanese Patent 88-271 467 (1988); Chem. Abstr. 113, 100955k (1990).
500. H. Naarmann, G. Koehler (BASF), German Patent 85-3528462, (1985).
501. H.-M. Wu, H.-J. Shy, H.-W. Ko, J. Power Sources 27, 59 (1989).
502. T. Yeu, R. E. White, J. Electrochem. Soc. 137, 1327 (1990).
503. A. Shimizu, K. Yamataka, M. Kohno, Bull. Chem. Soc. Jpn. 61, 4401 (1988).
504. R. C. D. Peres, M.-A. De Paoli, S. Panero, B. Scrosati, J. Power Sources 40, 299 (1992).
505. C. Arbizzani, M. Mastragostino, Electrochim. Acta 35, 251 (1990).
506. C. Arbizzani, M. Mastragostino, T. Hamaide, A. Guyot, Electrochim. Acta 35, 1781 (1990).
507. C. W. Walker Jr., J. Electrochem. Soc. 138, 1559 (1991).
508. T. Boschi, M. L. Di Vona, P. Tagliatesta, J. Power Sources 24, 185 (1988).
509. C. Li, B. Zhang, B. Wang, J. Power Sources 39, 255 and 259 (1992).
510. C. Li, B. Zhang, B. Wang, J. Power Sources 43–44, 669 (1993).
511. K. Taniguchi, O. Kimura, T. Kahata (Ricoh Co. Ltd.), Japanese Patent 89-114 160 (1989); Chem. Abstr. 115, 12381f (1991).
512. T. Osawa, S. Yoneyama, M. Sachiko, M. Yoshino, F. Masubuchi, T. Kahata (Ricoh Co. Ltd.), Japanese Patent 89-180 401 (1989); Chem. Abstr. 114, 250743z (1991).
513. K. Taniguchi, S. Yoneyama, F. Masabuchi (Ricoh Co. Ltd.), Japanese Patent 89-301 927 (1989); Chem. Abstr. 115, 211884x (1991).
514. T. Nakajima, T. Kawagoe, Extended Abstract, ICS, Meeting, Santa Fe, 1988.
515. T. Nakajima, T. Kawagoe, Synth. Metals 28, C629 (1989).
516. T. Osaka, S. Ogano, K. Naoi, N. Oyama, J. Electrochem. Soc. 136, 306 (1989).
517. K. Nishio, M. Fujimoto, N. Yoshinaga, N. Furukawa, O. Ando, H. Ono, T. Suzuki, Extended Abstract, 40th ISE Meeting, Kyoto, September, 1989, p. 553.
518. M. Mizumoto, M. Namba, S. Nishimura, H. Miyadera, M. Koseki, Y. Kobayashi, Synth. Metals 28, C639 (1989).

519. Anon., JEC Newsletter, JEC Press, Brunswick, OH (1989), No. 3, p. 17.
520. D. Rahner, S. Machill, K. Siury, M. Kloß, W. Plieth in: Proc. of the NATO Advanced Research Workshop, Kiev, May 14–17, 1995, on New Promising Electrochemical Systems for Rechargeable Batteries, V. Z. Barsukov, F. Beck (eds.), Kluwer, Dordrecht (1996), pp. 35–61.
521. M. Miyabayashi, H. Yui, K. Inada, K. Ikeda, H. Nose (Mitsubishi, Petrochemical Co. Ltd. and Toshiba Battery Co. Ltd.), Japanese Patent 89-50 056 (1989); Chem. Abstr. 114, 167870 t (1991).
522. M. Takeuchi, R. Shishikura, H. Konuma, M. Kameyama (Showa Denko K.K. and Hitachi, Ltd.), Japanese Patent 88-74 768 (1988); Chem. Abstr. 112, 81016r (1990).
523. S. Basu (AT & T Bell), US Patent 4 423 125, (1983).
524. K. M. Abraham, Electrochim. Acta 38, 1233 (1993).
525. D. Guyomard, J. M. Tarascon, J. Electrochem. Soc. 139, 937 (1992).
526. M. M. Thackeray, A. de Kock, M. H. Rossouw, D. Liles, R. Bitthin, D. Hoge, J. Electrochem. Soc. 139, 363 (1992).
527. J. M. Tarascon, D. Guyomard, G. L. Baker, J. Power Sources 43–44, 689 (1993).
528. Q. Xu, G. Wan, J. Power Sources 41, 315 (1993).
529. J. M. Tarascon, D. Guyomard, Electrochim. Acta 38, 1221 (1993).
530. J. M. Tarascon, W. R. McKinnon, F. Coowar, T. N. Bowmwer, G. Amatucci, D. Guyomard, J. Electrochem. Soc. 141, 1421 (1994).
531. D. Guyomard, J. M. Tarascon, Adv. Mater. 6, 408 (1994).
532. Y. Nishi, H. Azuma, A. Omaru (Sony) US Patent 4 959 281 (1990).
533. Anon., JEC Battery Newsletter No. 3, p. 37/137 (1994).
534. H. Yang, X. Ai, M. Lei, S. Li, J. Power Sources 43–44, 399 (1993).
535. J. R. Dahn, U. von Sacken, M. W. Juzkow, H. Al-Janaby, J. Electrochem. Soc. 138, 2207 (1991).
536. F. Croce, S. Passerini, B. Scrosati, J. Electrochem. Soc. 141, 1405 (1994).
537. M. Doyle, T. F. Fuller, J. Newman, Electrochim. Acta 39, 2073 (1994).
538. T. F. Fuller, M. Doyle, J. Newman, J. Electrochem. Soc. 141, 1 (1994).
539. T. F. Fuller, M. Doyle, J. Newman, J. Electrochem. Soc. 141, 982 (1994).
540. S. Hossain, Extended Abstract No. 31, ECS Meeting, New Orleans, October, 1993, p. 51.
541. H. Münstedt, H. Gebhard (BASF), German Patent 3 545 902 (December, 1985).
542. S. Kakuda, T. Momma, T. Osaka, G. B. Appetecchi, B. Scrosati, J. Electrochem. Soc. 142, L1 (1995).
543. W. Kristen, German Patent 3 017 725 (May, 1980).
544. A. Kitani, M. Kaya, K. Sasahi, J. Electrochem. Soc. 133, 1069 (1986).
545. N. L. D. Somasiri, A. G. MacDiarmid, J. Appl. Electrochem. 18, 92 (1988); F. Trinidad, M. C. Montemayor, E. Fatas, J. Electrochem. Soc. 138, 3186 (1991).
546. B. Wang, G. Li, C. Li, F. Wang, J. Power Sources 24, 115 (1988).
547. R. Wang, C. Li, G. Li, F. Wang, Extended, Abstract, 40th ISE Meeting, Kyoto, September, 1989, p. 1238.
548. S. Mu, J. Ye, Y. Wang, J. Power Sources 45, 153 (1993).
549. N. Koura, H. Ejiri, Extended Abstract 40th ISE Meeting, Kyoto, September, 1989, p. 1240.
550. N. Koura, H. Ejiri, Extended Abstract No. 901, ECS Meeting, Montreal, May, 90.
551. V. Z. Barsukov, S. A. Dunovsky, L. N. Sagoyan, V. N. Korneew, Extended, Abstract No. 7.1, 38th ISE Meeting, Maastricht, September, 1987.
552. S. Sarkar, I. N. Basumallick, J. Power Sources 31, 89 (1990).
553. R. T. Carlin, H. C. De Long, J. Fuller, P. C. Truelove, J. Electrochem. Soc. 141, L73 (1994).
554. R. Bosch GmbH, German Patent 3 215 126A (1982).
555. M. Nawa, T. Nogami, H. Mikawa, J. Electrochem. Soc. 131, 1457 (1984).

556. F. Beck, F. Krüger, unpublished work (1996).
557. A. Mohammadi, O. Inganäs, I. Lundström, J. Electrochem. Soc. 133, 947 (1986).
558. J. Y. Lee, L. H. Ong, G. K. Chuah, J. Appl. Electrochem. 22, 738 (1992).
559. E. Hannecart, E. Destryker, J. Fauvarque, A. De Guibert, X. Andrieu (Solvay) European Patent Application 413 382 (1991).
560. R. de Surville, M. Josefowicz, L. T. Yu, J. Perichon, R. Buvet, Electrochim. Acta 13, 1451 (1968).
561. N. Li, J. Y. Lee, L. H. Ong, J. Appl. Electrochem. 22, 512 (1992).
562. A. Rudge, I. Raistrick, S. Gottesfeld, J. P. Ferraris, Electrochim. Acta 39, 273 (1994).
563. A. Rudge, J. Davey, I. Raistrick, S. Gottesfeld, J. P. Ferraris, J. Power Sources 47, 89 (1994).
564. K. Kaneto, K. Yoshino, Y. Inuishi, Jap. J. Appl. Phys. 2 22, L567 (1983).
565. F. Beck, E. Ther, GDCh Monogr. 3 462 (1996).
566. Tajima, Japanese Patent 85-214 312 (1985).
567. Showa Denko K.K. and Hitachi Ltd., Japanese Patent 88-80 441 (1988).
568. Showa Denko K.K. and Hitachi, Ltd., Japanese Patent 86-106 847 (1986).
569. Showa Denko K.K. and Hitachi Ltd., Japanese Patent 86-20 264 (1986).
570. F. Beck, H. Krohn, E. Abdelmula, GDCh Monograph 3 581 (1996).
571. M. B. Armand, J. Power Sources 14, 11 (1985).
572. W. Li, J. R. Dahn, D. S. Wainwright, Science 264, 1115 (1994).
573. H. Krohn, F. Beck, R. Herrmann, Chem.-Ing.-Tech. 54, 530 (1982).
574. W. Scholz, H. P. Boehm, Z. Anorg. Allg. Chem. 369, 327 (1969).
575. H. P. Boehm, W. Scholz, Justus Liebigs, Ann. Chem. 691, 1 (1966).
576. F. Beck, J. Jiang, H. Krohn, J. Electroanal. Chem. 389, 161 (1995).
577. J. O. Besenhard, E. Theodoridou, H. Möhwald, J. J. Nickl, Synth, Metals, 4, 211 (1982).
578. M. Mermoux, P. Touzain, J. Power sources 26, 529 (1989).
579. T. Nakajima, Y. Matsuo, Carbon 32, 469 (1994).
580. Y. Matsmura, S. Wang, J. Mondori, J. Electrochem. Soc. 142, 2914 (1995).
581. F. Beck, H. Krohn, E. Zimmer, Electrochim. Acta 31, 371 (1986).
582. F. Beck, R. Michaelis, Werkstoffe Korros. 42, 341 (1991).
583. F. Beck, U. Barsch, Synth. Metals 55–57, 1299 (1993).
584. F. Beck, U. Barsch, R. Michaelis, J. Electroanal. Chem. 351, 169 (1993).
585. T. Nagai, H. Hatsutori, A. Kawakami, (Hitachi Maxell Ltd.), Japanese Patent 89-18 671 (1989); Chem. Abstr. 114, 146984t (1991).
586. M. N. Golovin, D. P. Wilkinson, J. T. Dudley, D. Holonko, S. Woo, J. Electrochem. Soc. 139, 5 (1992).
587. Y. F. Yao, N. Gupta, H. S. Wroblowa, J. Electroanal. Chem. 223, 107 (1987).
588. C. G. Castledine, B. E. Conway, J. Appl. Electrochem. 25, 707 (1995).
589. B. Koretz, Y. Harats, J. R. Goldstein, M. Korall in: Proc. NATO Advanced Research Workshop, Kiev, May 14–17, 1995, on New Promising Electrochemical Systems for Rechargeable Batteries, V. Z. Barsukov, F. Beck (Eds.), Kluwer, Dordrecht (1996).
590. J. R. Goldstein, I. Gektin, B. Koretz, GDCh Monogr. 3 (1996), in press.

Advances in Electrochemical Science and Engineering
Edited by Richard C. Alkire, Heinz Gerischer, Dieter M. Kolb and Charles W. Tobias
© WILEY-VCH Verlag GmbH, 1997

Index

Active mass utilization 326, 371, 373
Active material 369, 376
Advanced Mixed Potential Model (AMPM) 152
Air cathode diagnostics 278
Alloys 76, 137
Alloy-600 140, 146, 169
Alternate hydrocarbon approximation 29, 43
Angular velocity 133
Anode poisoning 219, 243
Anthraquinone 329
Aprotic solvent 339
Aromatic compound 314
Aromatic hydrocarbon 24
Aspect ratio 171

Bipolar
- electrode 376
- plate 201
- wall 376

Boiling-Water Reactor (BWR) 146, 152
Breakdown potential 147

Capacity 307, 373
Carbonaceous material 360
Carbon
- aerogel 363, 369
- black 310, 314, 318, 349, 371
- fiber 364, 366
- steel (A 508 Cl. 2) 158, 184

Catalyst
- loading 236
- ripening 242

Charge stoichiometry 307
Charge-transfer
- absorption 12
- complex 335
- emission 12, 24
- kinetics 323, 341

Chemiluminescence 3
Coke material 344
Corrosion fatigue 127, 157
CO tolerance 225, 228
CO_2 effect 225
CO_2 tolerance 227
Coulomb
- energy 21, 35, 51
- repulsion 46, 52, 53, 318

Coupled Environment Fracture Model (CEFM) 187
Critical
- *potential* 142, 156
- nucleus 157, 171

Cryoelectrochemistry 69, 72
Current anomaly 71
Current collector 314, 371
- plate 201

Damage 130
- *function analysis* 127

Debye equation 17, 31
Degradation 99
Dendrites 102
Diffusion
- water in membrane 265

Diffusivity 134
Direct Methanol Fuel Cell (DMFC) 291
Dispersion electrode 370

Electroanalysis 104, 105
Electrocatalysis 202
- hydrogen anode 202, 217
- oxygen cathode 203

Electrochemical Corrosion Potential (ECP) 142, 151, 152, 173, 176, 188
Electrochemiluminescence 4, 18
Electrocrystallization 89, 90
Electronic conductivity 327
Electronic coupling element 17, 39, 40, 41, 44
Electronic matrix element 6
Electron transfer 312
Electroorganic reaction 329
Electroosmosis 268
Electrooxidation 79
Electropolymerization 102

Electrosynthesis 75, 79, 312
Energetics 319
Energy
- density 373, 389
- operator 6
Extrinsic electron transfer 317

Feldberg plot 23, 24, 35
Franck-Condon principle 5, 6, 10
Franck-Condon factor 10, 53, 54
FRASTA 160
Freeze-thaw test 244
Friction factor 135
Fullerene 107, 347

Gas diffusion electrode 231
Gibbs energy 7, 8, 9, 20, 21, 26, 35
Glassy carbon 367
Graphene layer 318, 336
Graphite 369
- intercalation compound 320, 335, 393
- nanodispersed 319, 343
- oxide 311, 314, 392

High temperature aqueous system 139
Humidification 213
- oxygen cathode
Hybrid cell 382
Hydrocarbon 368
Hydrodynamics 131
Hydrogen evolution reaction 69

Impedance 209, 217
- spectroscopy 284
Initiation 157
Insertion compounds 308, 323
Insertion electrode 316, 320, 326
Intercalation potential 338, 341
Intergranular attack 147
Intramolecular charge-transfer state 33, 35, 37, 55
Intramolecular donor-acceptor systems 33
Ionic conductivity 327
Ionomeric membrane 245

Kinematic viscosity 130, 134, 139

Light-emitting diode 360
Light-water reactor 127
Lithium 88
- cell 377
- ion cell 377
- ion swing 374
- graphite 343
Localized corrosion 127
Longitudinal relaxation time 14, 38
Long crack 186
Low pressure steam turbine 172

Marcus region
- normal 3, 8, 15, 16, 17, 29, 36
- inverted 3, 8, 10, 11, 15, 16, 17, 18, 25, 29, 33 36, 38, 47, 49, 55
Marcus theory 322
Mass transfer 131
- coefficient 133
- correlation 133, 135, 140
Metallization 101
M&E Assembly (MEA) 199, 229, 241
MEA preparation 230
Membran surface composition 257
Membran water
- content 249, 272
- uptake 250
Methanol permeation 295
Microelectrode 210
Mixed Potential Model (MPM) 151, 155
Model
- air cathode 278
- cell polarization 278
Modeling 221, 271
- CO effects 221
Molybdenum(II) halide cluster ion 49

NMR relaxation measurement 258
Navier-Stokes equation 132, 179
Overoxidation 353, 367, 379
Overpotential 166
Overvoltage 327
Oxygen
- bleeding 22, 228
- deficiency 65

Passivation 103
Passivity 130
- breakdown 130, 157, 163, 168

Paste electrode 66
Perfluorosulfonic acid (PFSA) 200, 245
Perovskite 63, 67, 68, 81, 83
Phthalocyanine 332
Pitting 128, 180
Point defect model 163
Poisson's equation 132
Polyacetylene 310, 352, 354, 365
Polyacrylonitrile 361, 366
Polyaniline 379
Polymer Electrolyte Fuel Cell (PEFC) 197
- life testing 241
- polarization curve 238
- stack 285
Polymeric
- carbon 360
- membrane 200
Polythiophene 379
Poly(p-phenylene) 310, 352, 356, 365
Polypropylene 371
Porosity 326
Porous backing layer 201
Porous electrode 315
Potential oscillation 393
Precursor complex 16, 21
Pressure-vessel steels 146
Pressurized Water Reaktor (PWR) 146, 149
Proton conductivity 69, 241, 245, 260
Proximity effect 75
Pseudocapacitance 309
Pt/recast ionomer interface 215

Quantum effects 11
Quinone 329, 367

Radiative electron transfer 11
Ragone plot 329
Rechargeable batteries 306, 307
Reorganization energy
- inner 7
- outer 7
Reynolds number 134
Rotating cylinder electrode 155
Ruthenium(II) chelates 44

Self-discharge 394
Sherwood number 134
Short crack 175, 183
Shuttle mechanism 391
Slurry electrode 350
Solvent molecular dynamics 14
Spin-orbit coupling 20
Stainless steel 127, 128, 140, 142, 154, 160, 175, 185 188
Standard electrode potential 323
Stanton number 134
Streamline flow pattern 177
Stress corrosion cracking 127, 157
Stress intensity ratio 171
Sulfides 333
Supercaps 309
Surface-bound redox system 309

Theoretical specific capacity 307
Triple-potential-step technique 23
Triplet-triplet annihilation 4, 20, 25, 26, 30, 33
Tungsten halide cluster ions 54
Two-level tunneling 73

Vetter's model 325, 332
Viologens 332

Wagner-Traud hypothesis 151